ORGANIC MATTER CYCLING AND NUTRIENT DYNAMICS

IN MARINE SEDIMENTS

A DISSERTATION SUBMITTED TO THE GRADUATE DIVISION OF THE UNIVERSITY OF HAWAI'I IN PARTIAL FULFILLMENT OF THE REQUIREMENTS FOR THE DEGREE OF

DOCTOR OF PHILOSOPHY

IN

OCEANOGRAPHY

MAY 2008

By
Angelos K. Hannides

Dissertation Committee:

Francis J. Sansone, Chairperson
Kathleen C. Ruttenberg
Craig R. Smith
Eric J. Gaidos
Gregory E. Ravizza

5033

We certify that we have read this dissertation and that, in our opinion, it is satisfactory in scope and quality as a dissertation for the Degree of Doctor of Philosophy in Oceanography.

DISSERTATION COMMITTEE

_____
Chairperson

_____

_____

_____

_____

Dedication

To Cecelia.

Acknowledgements

I would like to thank whole-heartedly the members of my Dissertation Committee, Preliminary Qualifying Exam Committee and Advisory Committee for their mentorship, guidance and advice throughout my sojourn at the Department of Oceanography of the University of Hawaii at Manoa: F. Sansone, C. Smith, E. Gaidos, K. Ruttenberg, G. Ravizza, M. McManus, G. Stewart, F. Mackenzie, R. Grigg, and R. Lukas. Also, I would like to thank A. Rusch, S. Brown, A. Hebert, K. Selph, B. Popp, T. Rust, and N. Wallsgrove, who provided invaluable support in the field, in the laboratory, and in discussions, and their role was indispensable in the research presented in this dissertation. The following individuals supported me during various stages of my graduate experience in Hawaii, and I am indebted to them: M. Grabowski, R. Briggs, D. Sulak, C. Colgrove, M. O' Brien, I. Herzfeld, S. Lecas, E. Pawlak, M. Swanson, K. Millikan, T. Hilmer, J. Sevadjian, P. Bienfang, S. de Felice, J. Drazen, E. de Carlo, R. Solomon, R. Tom, R. Chock, M. Hatfield, J. Falter, K. Sørensen, B. Glazer, S. Ogata, W.F.X.E. Misa, C. Fletcher, M. Dyer, C. Conger, M. Engels, Bochiccio, E. Grabowski, S. Curless, T. Clemente, D. Sadler, D. Karl, K. Bjørkman, A. Baco-Taylor, S. Mincks, I. Altamira, A. Demopoulos, A. Bernardino, F. de Leo, A. Glover, T. Treude, A. Boetius, B. Bidigare, S. Christensen, R. Wallsgrove, L. Levin, and the crews of the R/V Gordon Sproul, R/V Western Flyer, ROV Tiburon, RRS Charles Darwin, R/V Kilo Moana, R/V Melville, and F/S Meteor. I am particularly grateful for the generous moral and material support I enjoyed from the Department of Oceanography Chairs between the years of 2001 to 2007: C. Measures, E. Laws, L. Magaard, and F. Sansone. I spent half of my

doctoral student years (2001-2, 2003-4, 2005-6) as a Teaching Assistant for the course Science of the Sea, OCN 201, and in turn half of that as Teaching Assistant Coordinator. The course coordinators, lecturers, and teaching assistants provided guidance, inspiration, and a pleasant respite from research during this invaluable teaching experience. The administrative personnel – N. Koike, K. Kozuma, A. Sullivan, and J. Turk – was reliable and prompt in calm and turbulent times. Special thanks go to my Cypriot colleagues for their understanding during the last stages of my dissertation completion: G. Georgiou, M. Hadjichristoforou, and M. Argyrou from the Department of Fisheries and Marine Research of the Ministry of Agriculture, Natural Resources and the Environment, as well as G. Zodiatis, and D. Hayes, of the Oceanography Centre of the University of Cyprus. Funding for research, conferences, and personal stipends, was provided by NOAA, NSF, Sea Grant, SOEST, the University of Hawaii, NERC, RPF, and DFG.

Abstract

This dissertation explores two recently recognized pathways of organic matter supply to marine sediments and their impact on sedimentary biogeochemistry: The entrapment and decomposition of particulate organic matter in permeable sediments and the resulting nutrient dynamics were investigated with a specially designed experimental laboratory microcosm that allows permeable sediment incubation under controlled physical forcing. Microcosm generated enhanced solute transport rates were roughly proportional to sediment column permeability. Comparison with field observations revealed that the enhanced transport rates induced by the experimental conditions were lower than those observed in the field, and this was also reflected in the enhanced build-up of pore water nutrients relative to concentrations in field sediments. Particulate organic matter and nutrient enrichment experiments, conducted with the microcosm, demonstrated the rapid uptake of both particles and solutes by the permeable sediment column under physical forcing, the rapid decomposition of the removed particles, and the lack of regenerated nutrient build-up. Nutrient enrichment experiments with sediment plug chambers demonstrated the rapid uptake and retention of nutrients by surface permeable sediments, as well as the loss of nitrogen though benthic denitrification in sediment grain microzones. The processing of large organic matter packages on the deep-sea floor by deep-sea communities was investigated using natural and experimental whale, kelp and wood falls in the California Borderland Basins region, focusing on their quality and its impact on sedimentary organic enrichment and redox shifts. Labile organic material generated by the processing of whale falls and kelp falls generated substantial

pore water sulfide levels in impacted sediment, despite a small organic enrichment signal. In contrast, wood derived material input did not result in sulfidic conditions, despite generating very high organic enrichment in impacted sediments, due to its refractory nature. A constructed model incorporating metazoan processing and dispersal of fragmented material revealed that whale fall processing is characterized by higher rates of tissue removal, organic carbon release, and carbon sedimentation rates than wood fall processing. However, organic carbon release rates, when normalized to fall weight, are similar between the two types of falls, due to differences in their carbon content and in absorption rates during metazoan ingestion.

Table of Contents

List of Tables

List of Figures

Chapter 1 – Introduction

1.1 Preface

The oceanic regime is characterized by many diverse depositional environments and processes (e.g., Aller 2004). However, most research efforts have concentrated on a few major, well-defined pathways by which particulate organic matter (POM) is delivered to the sea floor. Attention is usually focused on the gravitational settling of sub-centimeter size POM, quantified by sediment traps (e.g., U.S. GOFS 1989; Gardner et al. 1997) or by radioisotope techniques (e.g., Lao et al. 1993). The main paradigm that describes organic matter cycling in sedimentary settings focuses on the gravitational supply of POM to the sea floor, its decomposition during settling and after sedimentation (primarily by microbes), the regeneration of nutrients, and their release back to the water column, where they will be used anew in primary production (e.g., Rowe et al. 1975).

Research during the last two decades, however, has changed our view of decomposition-mediated carbon exchange and cycling between sediments and the water column. For example, while comparing two edited books, both titled "Benthic Boundary Layer" but published 25 years apart (McCave 1976; Boudreau and Jørgensen 2001), one finds many cases of such view changes and advances in technology in the more recent but not in the older publication. Extensive discussions on the role of sedimentary permeability on solute and particle exchange between sediments and overlying water (Huettel and Webster 2001), the role of microbenthic primary productivity on regional and global carbon cycling (Jahnke 2001), and the varied use of micro-sensors for environmental observation (Kühl and Revsbech 2001) are a few notable examples.

Recent changes in perspective are most dramatic in the shallower waters of the continental margins, which are the most productive and most frequently ignored regions in global flux calculations (e.g., Jahnke 1996). Previously unappreciated pathways of matter deposition could have biogeochemical and ecological implications very different from those that the main paradigm would suggest. This dissertation explores two recently recognized pathways of organic matter supply to marine sediments and their impact on sedimentary biogeochemistry: the entrapment and decomposition of POM in permeable sediments, and the gravitational deposition of massive packages of organic matter on the deep-sea floor and their processing by deep-sea communities.

1.2 Organic matter deposition and processing in permeable sediments

The first recently recognized pathway is POM entrapment and decomposition in permeable sediments. Permeable sediments are characterized by grain sizes > 62 μm (i.e., sandy or coarser) and by permeabilities > 10^{-12} m^2 (Huettel et al. 1998). Moreover, permeable sediments of the continental shelf are also characterized by simultaneous low organic matter content and high oxygen consumption rates (e.g., Rusch et al. 2006). These have lead to the comparison of these sediments with "familiar trickling filters in sewage plants" (Boudreau et al. 2001). It is now evident that the cause of the paradoxically simultaneous low organic matter content and high oxygen consumption rate is the high turnover rate of organic matter, which was originally proposed four decades ago by Webb and Theodor (Webb and Theodor 1968). The occurrence of high organic matter turnover is supported by fragmentary evidence for enhanced solute

transport and trapping of POM in permeable sediments (e.g., Bacon et al. 1994; Reimers et al. 2004; Hebert et al. 2007), and the correlation between consumption of oxygen and the concentration of available dissolved organics (Rusch et al. 2006). It follows that POM degradation is likely to lead to nutrient regeneration as in fine-grained sediments (Berner 1980). Despite the above, the hypothesis that physical forcing over permeable sediments drives both enhanced POM trapping and mineralization in these "reactors" and the subsequent release of nutrients to the water column remains untested and undocumented.

Part I (Chapters 2-4) of my dissertation focuses on the testing of the permeable sediment nutrient regeneration hypothesis. Chapter 2 provides a general overview of permeable sediments, their geology, physics, and biogeochemistry. Chapter 3 describes the design, operation and assessment of a new experimental laboratory microcosm for the investigation of permeable sedimentary biogeochemical processes under controlled physical forcing. Chapter 4 discusses how the microcosm, in conjunction with sediment plug incubations, was used to test the combined effect of physical forcing and sediment permeability on nutrient regeneration by organic matter decomposition.

1.3 Massive organic matter processing and the generation of reducing biogenic habitats in deep-sea sediments

The second recently recognized pathway of POM supply to the seafloor is the deposition and subsequent exploitation of organic matter contained in large falls, which generate reducing conditions in surrounding sediments (e.g., Smith et al. 1989). Large falls consist of massive packages of organic matter that reach the seafloor and cannot be ingested wholly by any fauna present. Instead, these falls require substantial

fragmentation processing that may differ in rate or intensity, depending upon fall quality (physical and biochemical characteristics). In turn, the geochemical response of the sediments will be affected by the fall processing rate.

Part II (Chapters 5-7) of this dissertation investigates the role of fall quality in the interaction between falls and sea floor communities, and the subsequent generation of reducing biogenic habitats. Chapter 5 provides an introduction to large organic falls, their character, processing, and impact on sedimentary biogeochemistry. The extent to which different fall types (e.g., kelp, wood, and whale carcasses) cause the same geochemical response in the surrounding sediments was tested using two data sets, and is described in Chapter 6. Chapter 7 further explores the rise, intensity and duration of biogenic reducing habitats through the use of a mathematical model.

1.4 Mathematical notations used in this dissertation

Numerous derived quantities have to be used throughout this dissertation in different applications and contexts, and consequently they have to be expressed in different units. When these quantities are first introduced in the text, they are defined by the basic quantities in parentheses, as shown in Table 1.1. A list of all the derived quantities used in this dissertation and their expression by basic quantities is given in Appendix A. The International System of Units (SI) is followed to the greatest extent possible, along with all the conventions for printing and expressing them, as described by Taylor (1995). A notable violation of the SI conventions that appears in this dissertation is the use of the unit "ppm" to express gas concentrations in air (Taylor 1995, p. 20-21; see Intergovernmental Panel on Climate Change 2001).

Table 1.1 Base quantities of the International System of Units used in this dissertation, their symbols (used in definitions of derived quantities), and their official units (Taylor 1995, p. 4). See Appendix I for derived quantities and additional SI-compliant units used throughout the dissertation.

		SI base unit	
Base quantity	**Symbol**	**Name**	**Symbol**
Length	Le	meter	m
Mass	M	kilogram	kg
Time	T	second	s
Temperature	T_K	kelvin	K
Amount of substance	N	mole	mol

1.5 References

Aller, R. C. (2004) Conceptual models of early diagenetic processes: The muddy seafloor as an unsteady, batch reactor. Journal of Marine Research, 62: 815-835.

Bacon, M. P., R. A. Belastock and M. H. Bothner (1994) ^{210}Pb balance and implications for particle transport on the continental shelf, U.S. Middle Atlantic Bight. Deep-Sea Research II, 41: 511-535.

Berner, R. A. (1980) Early diagenesis. Princeton University Press, Princeton, New Jersey, U.S.A., pp. 241.

Boudreau, B. P., M. Huettel, S. Forster, R. A. Jahnke, A. McLachlan, J. J. Middelburg, P. Nielsen, F. J. Sansone, G. L. Taghon, W. Van Raaphorst, I. T. Webster, J. M. Weslawski, P. Wiberg and B. Sundby (2001) Permeable marine sediments: overturning an old paradigm. Eos, Transactions of the American Geophysical Union, 82: 133, 135-136.

Boudreau, B. P. and B. B. Jørgensen [eds.] (2001) The benthic boundary layer, Oxford University Press, New York, New York, U.S.A., pp. 404.

Gardner, W. D., P. E. Biscaye and M. J. Richardson (1997) A sediment trap experiment in the Vema Channel to evaluate the effect of horizontal particle fluxes on measured vertical fluxes. Journal of Marine Research, 55: 995-1028.

Hebert, A. B., F. J. Sansone and G. R. Pawlak (2007) Tracer dispersal in sandy sediment porewater under enhanced physical forcing. Continental Shelf Research, 27: 2278-2287.

Huettel, M., W. Ziebis, S. Forster and G. W. Luther III (1998) Advective transport affecting metal and nutrient distributions and interfacial fluxes in permeable sediments. Geochimica et Cosmochimica Acta, 62: 613-631.

Huettel, M. and I. T. Webster (2001) Porewater flow in permeable sediments, p. 144-179. *In* Boudreau, B. P. and B. B. Jørgensen [eds.], The Benthic Boundary Layer. Oxford University Press, New York, New York, U.S.A.

Intergovernmental Panel on Climate Change (2001) Climate change: the science of climate change. Cambridge University Press, New York, New York, U.S.A.

Jahnke, R. A. (1996) The global ocean flux of particulate organic carbon: Areal distribution and magnitude. Global Biogeochemical Cycles, 10: 71-88.

Jahnke, R. A. (2001) Constraining organic matter cycling with benthic fluxes, p. 302-319. *In* Boudreau, B. P. and B. B. Jørgensen [eds.], The Benthic Boundary Layer. Oxford University Press, New York, New York, U.S.A.

Kühl, M. and N. P. Revsbech (2001) Biogeochemical microsensors for boundary layer studies, p. 183-210. *In* Boudreau, B. P. and B. B. Jørgensen [eds.], The Benthic Boundary Layer. Oxford University Press, New York, New York, U.S.A.

Lao, Y. F., R. F. Anderson, W. S. Broecker, H. J. Hofmann and W. Wolfli (1993) Particulate fluxes of ^{230}Th, ^{231}Pa, and ^{10}Be in the northeastern Pacific Ocean. Geochimica et Cosmochimica Acta, 57: 205-217.

McCave, I. N. [ed.] (1976) The benthic boundary layer, Plenum Press, New York, New York, U.S.A., pp. 323.

Reimers, C. E., H. A. Stecher III, G. L. Taghon, C. M. Fuller, M. Huettel, A. Rusch, N. Ryckelynck and C. Wild (2004) In situ measurements of advective solute transport in permeable shelf sands. Continental Shelf Research, 24: 183-201.

Rowe, G. T., C. H. Clifford, K. L. J. Smith and P. L. Hamilton (1975) Benthic nutrient regeneration and its coupling to primary productivity in coastal waters. Nature, 255: 215-217.

Rusch, A., M. Huettel, C. Wild and C. E. Reimers (2006) Benthic oxygen consumption and organic matter turnover in organic-poor, permeable shelf sands. Aquatic Geochemistry, 12: 1-19.

Smith, C. R., H. Kukert, R. A. Wheatcroft, P. A. Jumars and J. W. Deming (1989) Vent fauna on whale remains. Nature, 341: 27-28.

Taylor, B. N. (1995) Guide for the use of the International System of Units (SI). NIST Special Publication 811, 1995 Edition. U.S. Government Printing Office, Washington, D.C., U.S.A., pp. 74.

U.S. GOFS (1989) Sediment Trap Technology and Sampling, Report of the U.S. GOFS Working Group on Sediment Trap Technology and Sampling, George Knauer and Vernon Asper (Co-Chairmen). Planning Report Number 10, Woods Hole Oceanographic Institution, Woods Hole, Massachusetts, U.S.A., pp. 94.

Webb, J. E. and J. Theodor (1968) Irrigation of marine submerged sands through wave action. Nature, 220: 682-683.

Chapter 2 – An overview of permeable sediments: their geology, physics, and biogeochemistry

2.1 Introduction

Permeable sediments cover approximately 70 % of the area of continental shelves (Emery 1968; Riedl et al. 1972), and underlie some of the most productive regions of the oceans (Ryther 1969). Despite their spatial preponderance, they have been relatively understudied (Boudreau et al. 2001; Reimers et al. 2004a). This bias against their study can be attributed to two major reasons. The first is the poor applicability of observing and sampling methodologies used in fine-grained sediments: cores cannot be retrieved without loss of pore water, while benthic flux chambers cannot enclose an area of the seafloor without affecting the physical conditions which influence exchange across the sediment-water-interface (e.g., Saager et al. 1990; Malan and McLachlan 1991). The second reason concerns the misinterpretation of early observations of permeable sediment geochemistry and microbiology. The fact that the organic matter content and microbial biomass of coarse-grained sediments are lower than those of fine-grained sediments has been repeatedly established (e.g., ZoBell 1938; Newell 1965; Meyer-Reil 1986). A common interpretation of this has been that the productivity of these sediments is fairly low (e.g., Newell 1965), while another explanation, namely that turnover rates are very high in these sediments (Webb and Theodor 1968), has been largely ignored. This chapter provides an overview of permeable sediments and argues for the interpretation of low stocks of organic matter and biomass as evidence for high activity rates of permeable sediments.

2.2 Characterization of permeable sediments

2.2.1 Geological and hydrological characteristics

Permeable sediments are coarse-grained sediments, i.e., sediments with grain sizes > 62 μm (Table 2.1). Since sands (grain diameters between 63 and 2000 μm), are the most common type of permeable sediments, the term "sandy sediments" is commonly used interchangeably with "permeable sediments" (see Boudreau et al. 2001 for an example). However, this is not always accurate. Many unconsolidated permeable sediments, such as those associated with coral reefs, don't strictly qualify as sandy. They are mostly coarser than the sand fraction but also contain a detectable amount of silt and clay. Figure 2.1 illustrates grain size property differences between two types of permeable sediments from the Hawaiian Islands. The diameter at which half the grains in the sample are coarser and half are finer is defined as the median grain diameter, ϕ_{50}. The median can be most easily determined on a cumulative grain size distribution plot (Figure 2.1b) from the 50 % line. In the samples compared in Figure 2.1b, ϕ_{50} may be an inadequate descriptor, because the spread of the particle distribution in each case is different. This spread is referred to as the sorting, σ_ϕ which is defined as (McManus 1988):

$$\sigma_\phi = \frac{\phi_{84} - \phi_{16}}{2} \qquad 2.1$$

where ϕ_{84} and ϕ_{16} can be determined from the points of intersection with the 84 % and 16 % lines on the cumulative grain size distribution plot (Figure 2.1b). The poorer the sorting of the sediment sampling, the greater the value of σ_ϕ is. The values of σ_ϕ for

Table 2.1 Sediment grain size classification as summarized by McManus (1988). The dimensionless grain size scale of ϕ was originally introduced by Krumbein (1934) and simplifies the statistical analysis of grain size distributions that span many orders of magnitude (McManus 1963; Krumbein 1964). The definition of ϕ is (McManus 1988):

$$\phi = -\log_2\left(\frac{d}{d_o}\right)$$

where d is the grain diameter in mm, and d_o is the diameter of a 1 mm grain.

	Range of grain diameters	
Grain size fraction	**μm**	**ϕ**
Boulders	$> 256\times10^3$	-8
Cobbles	64×10^3 to 256×10^3	-6 to -8
Pebbles	2×10^3 to 64×10^3	-1 to -6
Sand	63 to 2000	4 to -1
Silt	2 to 62	9 to 4
Clay	< 2	> 9

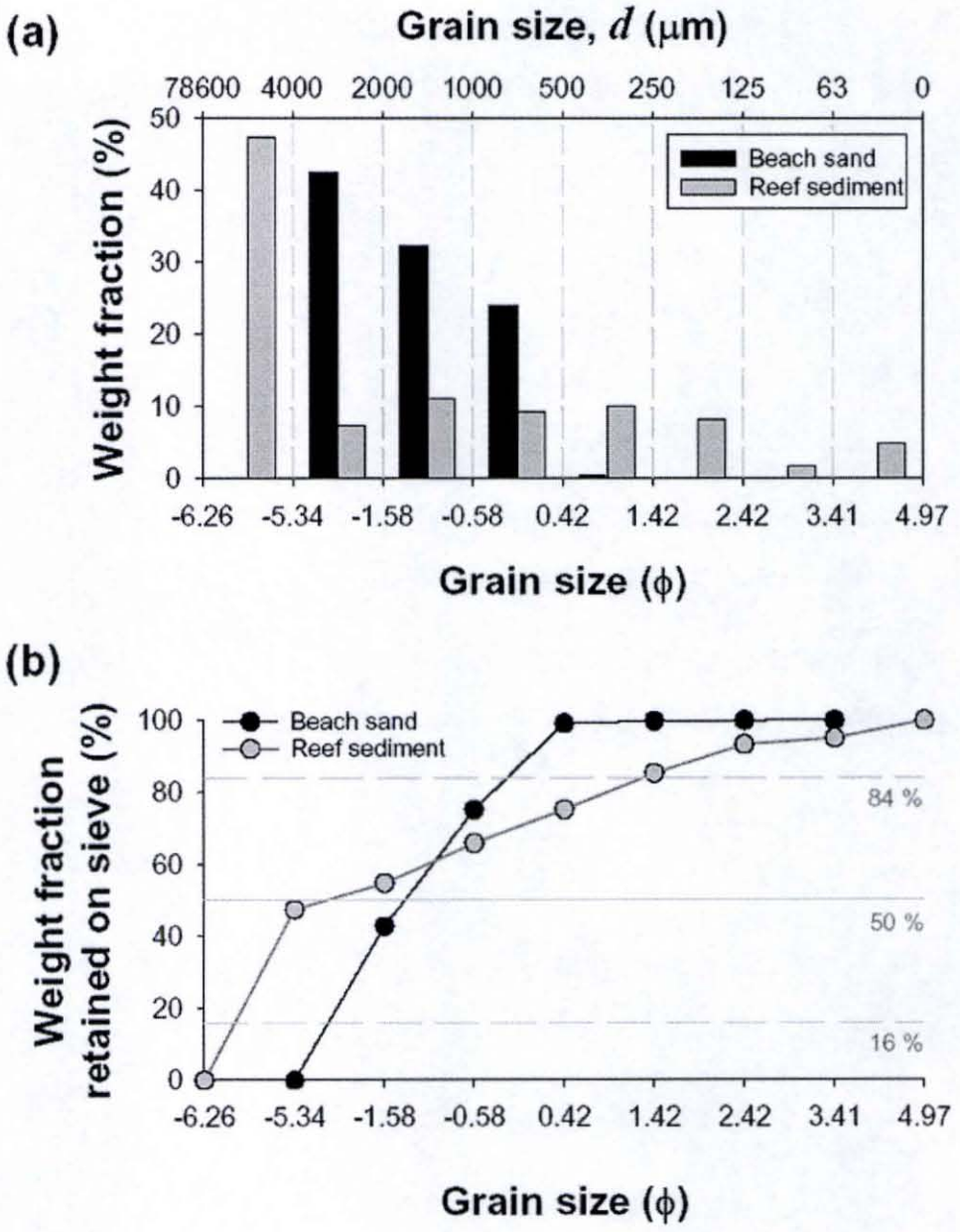

Figure 2.1 A comparison of grain size distributions of beach sand (O'ahu) and reef sediment (Moloka'i fringing reef): (a) Weight fraction (%) distribution among various size classes; (b) Cumulative grain size distribution plot of the data in (a). See Table 2.1 for grain size classification.

beach sand and reef sediment are 1.00 and 3.35 respectively, and indicate that although reef sediment is coarser than beach sand, it also includes non-negligible fractions of very large and very fine particles. Therefore, reef sediment does not qualify as sandy. Instead, what renders it similar to beach sand, in terms of physical and biogeochemical function, is permeability.

Permeability, k (Le^2), is the property which determines the ability of a fluid to pass through a porous medium (McManus 1988). Although materials with no permeability do theoretically exist, natural geological materials are all permeable to a certain degree (Table 2.2). Permeable sediments are those unconsolidated sediments that are characterized by a high degree of permeability, "high degree" having been operationally defined as a value greater than 10^{-12} m^2 (since Huettel et al. 1998).

Table 2.2 Permeabilities, k, of commonly-occurring consolidated and unconsolidated sediments (data from Blatt et al. 1972).

Medium	k **(m^2)**
Cemented limestone	10^{-21}
Limestone	10^{-16} to 1.5×10^{-13}
Sandstone	10^{-14} to 3×10^{-13}
Mud	10^{-17} to 3×10^{-14}
Sand	$> 10^{-12}$

Permeability, k, is calculated from the hydraulic conductivity, K ($Le \cdot T^{-1}$), which in turn is commonly determined using constant- or falling-head permeameters and the Darcy equation (Hubbert 1940):

$$v = \frac{q}{A} = -K\left(\frac{H}{l}\right) \qquad 2.2$$

where v is the velocity ($Le \cdot T^{-1}$) of the fluid, q ($Le^3 \cdot T^{-1}$) is the volume flow rate, A (Le^2) is the cross sectional area of the column, H (Le) is the head difference between reservoirs, and l (Le) is the length of the column whose conductivity is being measured (Boudreau 1997, p. 132). K is, in turn, related to k, as follows:

$$K = \frac{k\rho g}{\mu} \qquad 2.3$$

where ρ is the density of the fluid used ($M \cdot Le^{-3}$), μ its dynamic viscosity ($M \cdot Le^{-1} \cdot T^{-1}$), and g is the acceleration due to gravity ($Le \cdot T^{-2}$) (Boudreau 1997, p. 132). The significance of Eq. 2.3 lies in the normalization of a measurement of hydraulic conductivity, which was performed with a liquid of a specific temperature and salinity, in terms of properties affected by temperature and salinity, such as viscosity and density. This normalization produces a fluid-independent measure of "the ability of a fluid to pass through a porous medium" (McManus 1988), permeability.

Permeability is primarily controlled by grain size and sorting, while porosity, grain shape, and packing arrangement play a lesser role (Krumbein and Monk 1943; Beard and Weyl 1973; McManus 1988). Relationships between permeability and some commonly determined sedimentary parameters are illustrated in Figure 2.2. Notice the low values of the correlation coefficients in all these relationships. These low values

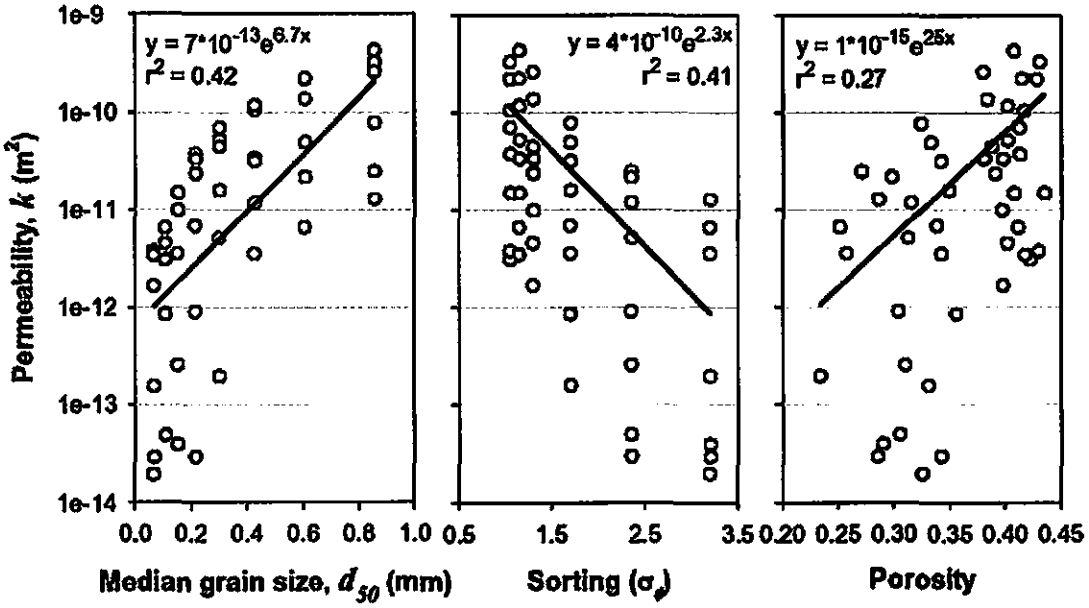

Figure 2.2 Relationships between commonly determined sedimentary parameters and measured permeability. Relationships were generated using the data from Beard and Weyl (1973), after converting permeability values to SI units from darcies. An early unit of permeability, 1 darcy = 9.875×10^{-13} m^2, may still occasionally appear in the literature (e.g., Blevins 1984, p. 495).

suggest that a single grain size composition property cannot be used to reliably predict the permeability of a sedimentary sample. The median or mean grain size is almost meaningless, unless used alongside the dimensionless sorting parameter, as in the famous Krumbein and Monk (1943) relationship (modified to give k in m^2):

$$k = 7.505 \times 10^{-10} d_{mean}{}^{2} e^{-1.31\sigma_\phi} \qquad 2.4$$

where d_{mean} is the mean grain diameter (mm).

Even when using both grain size and sorting, the calculated estimates of permeability may deviate significantly from actual measurements (Rusch et al. 2001). A characteristic case is sediment with a very small but detectable fraction of fine grains. The fact that they are present in small amount may mean that they don't affect the estimates of d_{mean} and σ_ϕ. However, they affect permeability disproportionately to their contribution to overall sediment weight because they fill pore water channels between larger grains (Burmister 1955). Despite problems with using relationships such as Eq. 2.4, permeability itself is not commonly measured, and researchers have often used empirical relationships such as Eq. 2.4 to estimate permeability and apply these estimates to varying degrees of spatial scale (e.g., Riedl et al. 1972). It has been suggested that observed deviations of estimates from actual measurements (Rusch et al. 2001) are acceptable depending on the objectives of a study (see the discussion by Burdige 2006, p. 56-58).

2.2.2 Physical exchange

A multitude of evidence suggests that the transport of solutes in permeable sediments is higher than predicted by molecular diffusion. This was first demonstrated by

simple yet elegant dye injection experiments in the sandy sea floor of the Mediterranean coast of France (Webb and Theodor 1968). Under common sea state conditions, they observed the dye, which was injected several centimeters below the sediment-water interface (SWI), emerge into the water column several seconds to minutes after injection. They attributed the "irrigation of these sands ... (to) the action of surface waves." At present, waves are generally accepted to be one of three physical phenomena that induce enhanced transport of matter in permeable sediments, the other two being bottom currents and density-driven convection (Huettel and Webster 2001). The following is a brief description of the effect of wave- and current-induced enhanced transport in permeable sediments.

2.2.2.1 Wave-induced transport

Two major mechanisms have been proposed to account for wave-induced transport. They are believed to occur simultaneously and to complement one another in generating enhanced transport of matter across the SWI (Webster 2003). The first mechanism is rotational dispersion. The idea was first proposed and treated mathematically by Putnam (1949). However, it was only developed and tested on permeable sediments with a wave tank experiment several decades later by Webster and Taylor (1992), who also coined the term "rotational dispersion." The operation of rotational dispersion is shown in Figure 2.3. It is occasionally assumed to be the principal mechanism of enhanced transport in permeable sediments (e.g., Boudreau 1997, p. 39-41). This is perhaps a hasty assumption in that the major proof of rotational dispersion, namely a record of the rotating direction of the pressure gradient in a sediment column

(Webster and Taylor 1992), has not been attainable due to the lack of suitable observational instrumentation.

The second mechanism believed to contribute to wave-induced transport is shear dispersion (Figure 2.4). Enhanced transport by shear dispersion was mathematically explored by Watson (1983) and demonstrated by Joshi et al. (1983) in a cylinder. Webster (2003) constructed a model which envisioned pore spaces as interconnected cylinders, and was used to determine transport by shear dispersion for a given sediment grain size, porosity and permeability, and wave amplitude and period. Shear dispersion was also tested on permeable sediments with a wave tank experiment during a study by Sutherland and colleagues that unfortunately remains unpublished (see Sutherland et al. 1999).

2.2.2.2 Current-induced transport

A current flowing over a flat sediment surface can penetrate into the sediment through shear, and can cause slip flow, forming what is termed the Brinkman layer (Huettel and Webster 2001). However, exchange is much stronger in the presence of surface roughness elements, e.g., sand ripples (Figure 2.5). These elements induce variations in the pressure field that cause net advection of water into and out of the sediment (Huettel and Webster 2001). The interplay between currents and surface topography reinforces the importance of considering three-dimensionality when sediment surface processes are studied in the presence of currents.

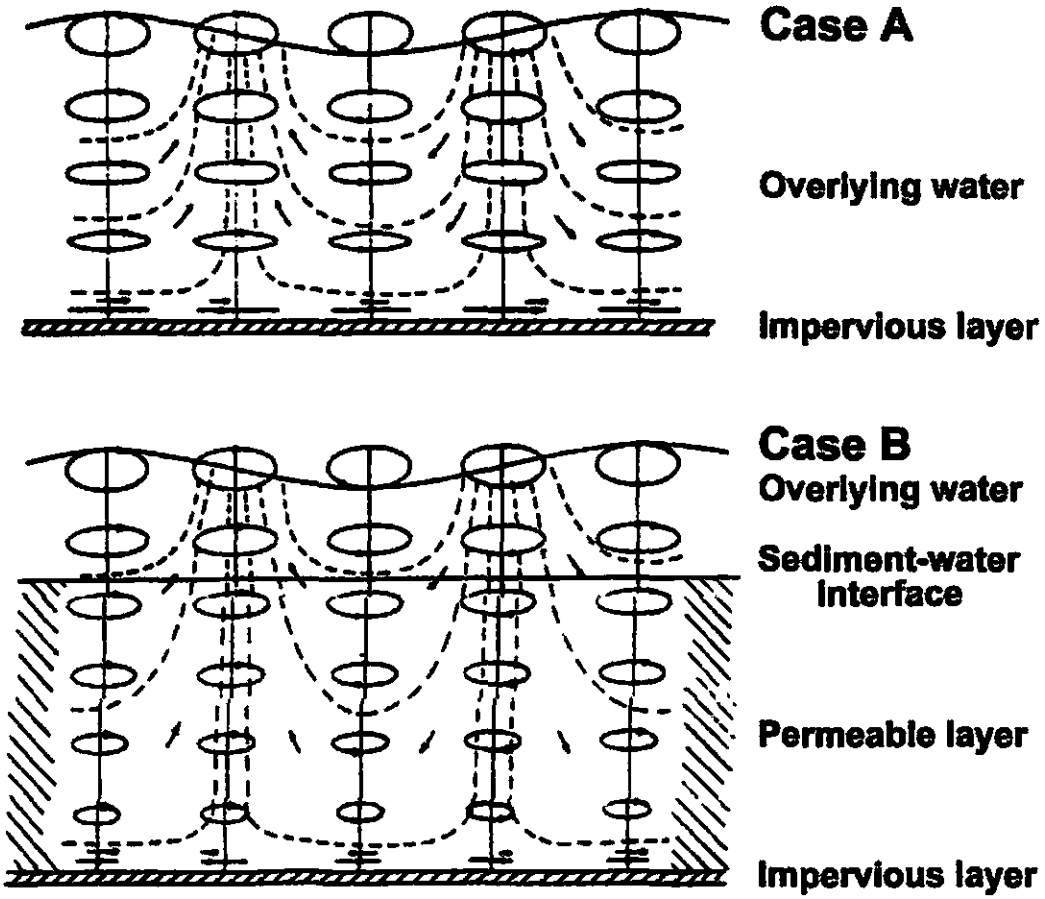

Figure 2.3 How rotational dispersion is believed to operate in permeable sediments (modified from Haberstroh 1994). Case A (top): the wave-induced elliptical motion of water slowly flattens as it reaches an impervious surface, such as muddy sediment or bedrock; Case B (bottom): if a permeable layer is present, the elliptical motions do not flatten out at the SWI, but extend into the sediment. There, as in the water column, the water does not return to exactly the same position from which it started, but is slightly displaced, and in the process disperses pore water and solutes (Webster and Taylor 1992; Boudreau 1997, p. 39-41).

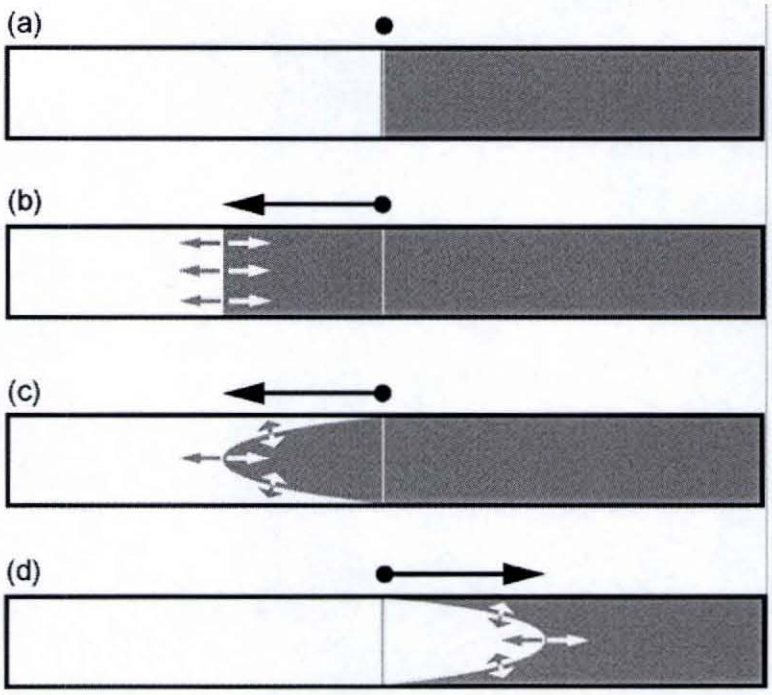

Figure 2.4 How shear dispersion is believed to operate across a cylinder (based on a description by Webster 2003): (a) A cylinder contains two solutions of different concentrations separated by a sharp front at a mean point (indicated by the black circle); (b) This front is forced to oscillate about this mean point by an invisible piston. The black arrow indicates the extent of oscillation. In the hypothetical absence of shear, the front moves uniformly across the cross section of the cylinder. Solute exchange, indicated by the white and grey arrows, takes place at the front by molecular diffusion; (c) & (d) Frictional shear, due to the walls of the cylinder, forces the fluid along the perimeter to move more slowly than the fluid in the center. Shear deforms the front and sets up a radial gradient in flow velocity and concentration. Dispersion and molecular diffusion operate against this gradient to mix the two solutions at rates much higher than those achieved in the hypothetical "no shear" case illustrated in (b).

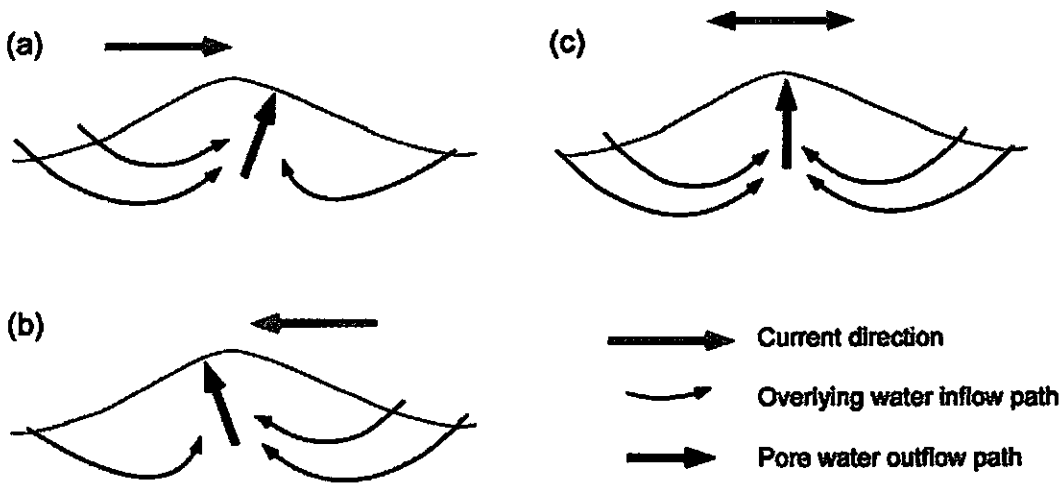

Figure 2.5 How current-induced transport operates across sediment ripples (modified from Precht and Huettel 2004) (a) & (b) Unidirectional bottom currents cause a pressure increase up-current from the ripple crest and a pressure drop down-current from the crest. As a consequence, overlying water is forced in at the high pressure point and pore water is forced out of the sediment at the low pressure point; (c) In the presence of oscillatory boundary flows, such as those induced by waves, the pattern becomes symmetric about the crest.

2.2.2.3 Degree of transport enhancement

In the case of sediments of low permeability (< 10^{-12} m^2), transport of solutes across the permeable sediment-water-interface is dictated by molecular diffusion, and by bioirrigation and bioturbation in the presence of animals (e.g., Berner 1980). Transport of particles to the sediment in this setting is generally dictated by gravity, which causes particles to settle on the sediment-water interface (see Eq. 2.5). Burial below the SWI is accomplished either by continuing accumulation of sediment or by bioturbation. In the case of permeable sediments, transport of both solutes and particles is greatly enhanced relative to that typical of low permeability sediments (Rusch and Huettel 2000; Huettel and Webster 2001). Although this has been known for almost four decades now (Webb and Theodor 1968), there is a dearth of field measurements that would allow constraints to be placed on estimates of this enhancement. From the data that are available, a general impression can be obtained. In the case of solutes, physical activity enhances transport of solutes by 2 to 3 orders of magnitude over the rates achieved by molecular diffusion alone, and matches rates achieved by bio-irrigating infauna (Table 2.3).

Enhanced particle transport is more difficult to evaluate. Rusch and Huettel (2000) measured diatom transport rates of 2.02 $g \cdot m^{-2} \cdot d^{-1}$ in clean sand implanted in an intertidal/subtidal sand flat in the North Sea. I conducted a thought experiment to obtain an approximate value of the flux of these diatoms by gravitational settling. I calculated the gravitational settling flux of these diatoms by conceptually re-suspending 2.02 g of diatoms evenly into the water column (1 m depth at this location) above 1 m^2 of the sea floor, and multiplying this amount by the distance settled during 1 d. The distance settled

was calculated by the sinking velocity, u ($m \cdot s^{-1}$), estimated using Stokes' Law (McCave 1975):

$$u = \frac{gd^2(\rho - \rho_0)}{18\mu} \qquad 2.5$$

where g is the acceleration due to gravity (9.81 $m \cdot s^{-2}$), d is the diameter of the sinking particles (17.5×10^{-6} m), ρ is the density of the particle material (1.1×10^{6} $g \cdot m^{-3}$), ρ_0 is the density of seawater (1.028×10^{6} $g \cdot m^{-3}$), and μ is the dynamic fluid viscosity (1.3012 $g \cdot m^{-1} \cdot s^{-1}$) (see Rusch and Huettel 2000 for site-specific parameters). I estimated that gravitational settling under ideal conditions (i.e., no resuspension) could result in a diatom flux of 1.02 $g \cdot m^{-2} \cdot d^{-1}$. Considering that resuspension is probably inevitable at this

Table 2.3 Wind- and current-induced transport velocities of dissolved conservative tracers at three permeable sediment settings. Typical transport velocities induced by bio-irrigating benthos and by molecular diffusion are also given for comparison.

Setting	Velocity ($cm \cdot h^{-1}$)	References
Coastal sub-tidal (water depth 3 m)	130	Webb and Theodor (1968)
Inter-tidal sand flat	26	Precht and Huettel (2004)
Continental shelf (water depth 15 m)	12.6	Reimers et al. (2004b)
Bio-irrigation (*Arenicola marina*)	16	Riisgård et al. (1996)
Diffusion	0.14	Precht and Huettel (2004)

physically dynamic site, it is evident that enhanced transport could at least double the flux of particles in the sediment at this location. Rusch et al. (2000) have also estimated that physically-enhanced transport rates in North Sea sand flats match those of bioturbation-driven transport.

The comparable magnitude of physically- and biologically- enhanced transport of solutes and particles indicates that the relative importance of physical versus biological transport processes deserves more study, especially in coastal locations where fauna are typically abundant. Finally, it is worth noting that the cotemporaneous transport of solutes and particles has not been explored. Interestingly, the data in Rusch and Huettel (2000) suggest that enhanced particle transport is as extensive as enhanced solute transport in permeable sediments, even though observations and measurements were not carried out on the same sediment core (Table 2.4).

Table 2.4 Penetration depth of dye and particles in Sylt Island sand during in situ experiments (Rusch and Huettel 2000). The depths shown are indicative of enhanced transport. Observations and measurements took place 2 d after the release of rhodamine dye, and 13 h after the release of particles (see Table 3 in Rusch and Huettel 2000).

Material	Penetration depth (cm)
Rhodamine dye	1.0-1.5
30 μm beads	2.35 ± 1.38
3 μm beads	2.62 ± 1.03
1 μm beads	3.10 ± 1.44
Diatoms	2.19 ± 0.29

I'd like to close the section on transport enhancement with a flow chart which describes the procedure of assessing the permeability, k, of the sea floor at a specific setting and a specific time, while relating k to physical forcing, enhanced transport, and the presence of suspended fine particles in the overlying water (Figure 2.6). Enhanced transport is represented by the coefficient, ε, which, when multiplied by the molecular diffusion coefficient, D ($Le^2 \cdot T^{-1}$), yields a quantitative measure of enhanced transport (ε is used extensively in Chapter 3). The flow chart helps highlight the following points:

a) Increased permeability ($k > 10^{-12}$ m^2) of sediment, as it is calculated from grain size composition or measured by hydraulic conductivity, is not sufficient by its self to generate enhanced transport, but physical forcing from waves, currents, etc. is also needed.

b) The degree of enhanced transport will be affected not just by physical forcing but also by the presence of particles suspended in the overlying water. These particles may be entrained and trapped in the sedimentary column and affect the permeability, k, beyond the effect of grain size characteristics.

c) Permeability and its impact on exchange across the SWI at a specific site should probably be discussed in the context of the range of physical and biogeochemical conditions at that site.

It is quite possible that the grain size composition of the sea floor at a specific site is linked with the prevalent physical conditions, i.e., wave-impacted shores and tidal channels are likely to have coarse-grained bottoms while sheltered embayments may be characterized by finer-grained bottoms. However, daily to seasonal changes in parameters

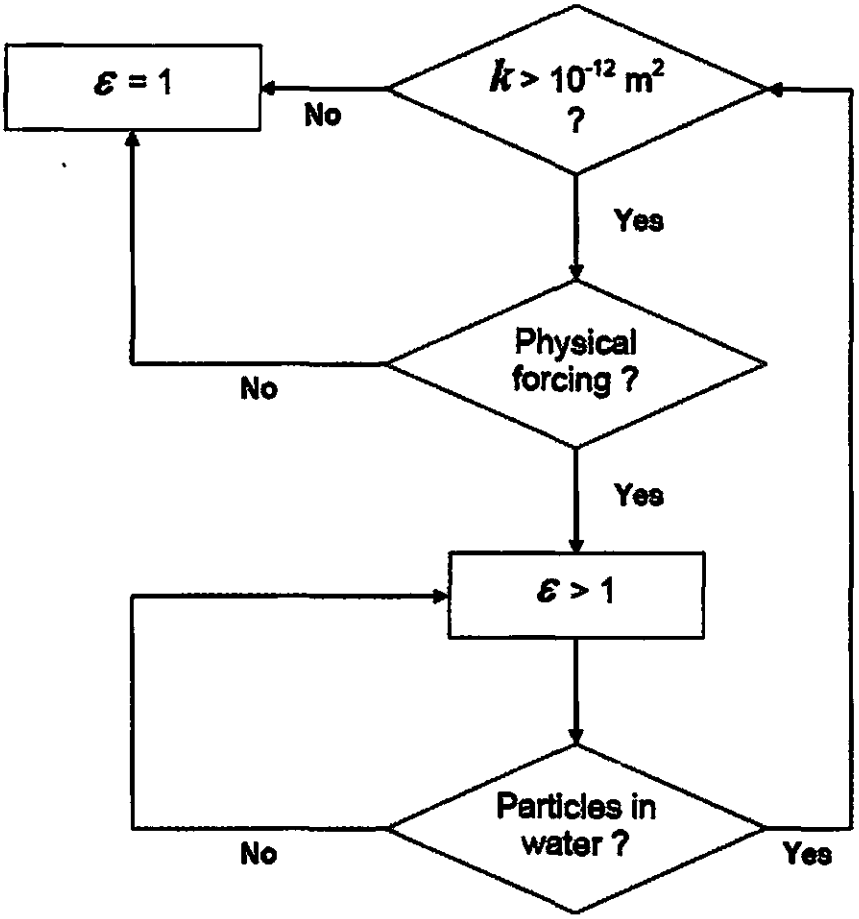

Figure 2.6 A flow chart that aids the visualization of the relationship between the permeability, k, physical forcing, enhanced transport, ε, and the presence of suspended fine particles in the overlying water (see text for discussion).

such as physical forcing (due to weather and climatic cycles) and suspended particle concentrations in the overlying water (e.g., due to algal blooms, terrestrial input, etc.) are probably the norm in most locations. Therefore, regardless of the prevalent conditions at a site, the range of conditions is likely be broad and to cause fluctuations in permeability and material exchange across the SWI over annual time periods, thus creating a more complex physical framework than molecular diffusion and gravitational settling, over which one must superimpose biogeochemical processes.

2.2.3 Biogeochemistry

Permeable sediments are commonly characterized by low organic matter content and low biomass (Figure 2.7), as compared to finer-grained sediments (e.g., ZoBell 1938; Newell 1965; Meyer-Reil 1986). The widely accepted interpretation of this observation has been that permeable sediments are generally characterized by low activity and productivity (e.g., Newell 1965). Oxygen profiles from permeable sediments could be viewed as supporting evidence for this explanation (Figure 2.8). More specifically, in fine-grained sediments, oxygen penetrates slowly into the sediment by molecular diffusion, while being consumed by the abundant microbial populations inhabiting the grain surfaces. As a consequence, the resulting oxycline is only a few millimeters thick (Figure 2.8a). In permeable sediments, however, oxygen can penetrate several centimeters into the sediment by enhanced transport, while it is consumed at low rates due to low organic matter content and low microbial abundances. The outcome is an oxic-suboxic layer several centimeters thick (Figure 2.8b and c). Profiles of other solutes,

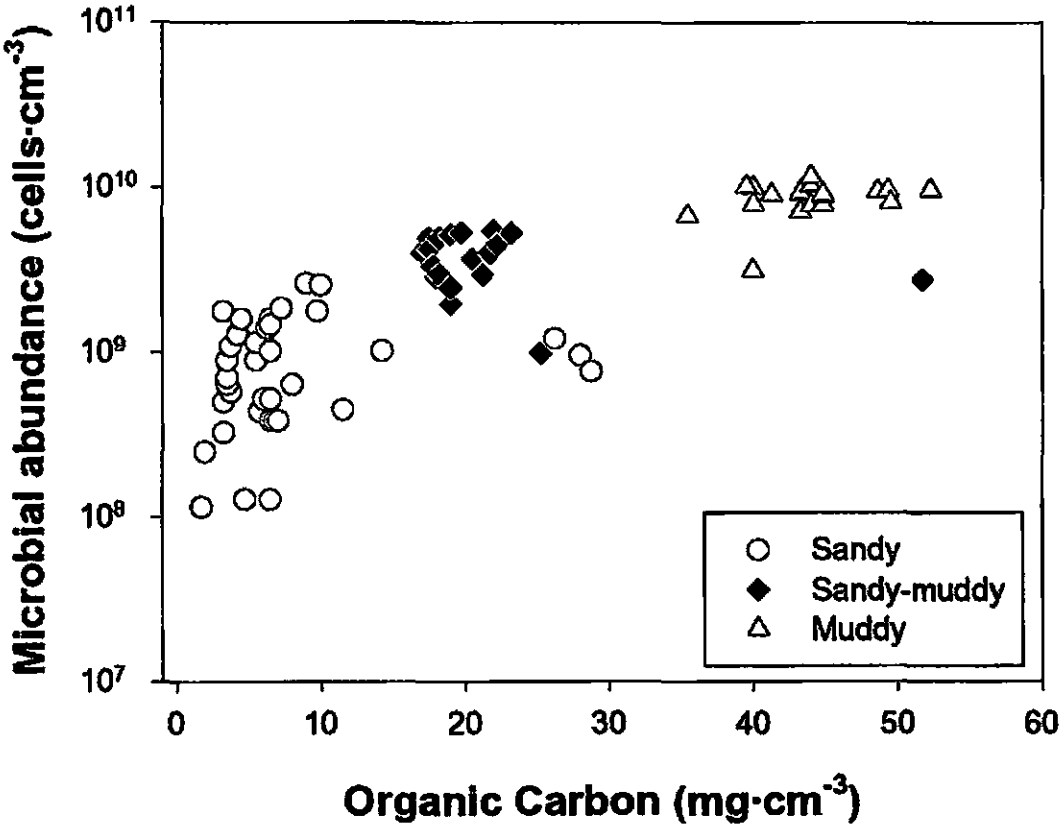

Figure 2.7 Sedimentary organic carbon content versus microbial cell abundance in three sediment types in Kiel Bight (modified from Meyer-Reil 1986).

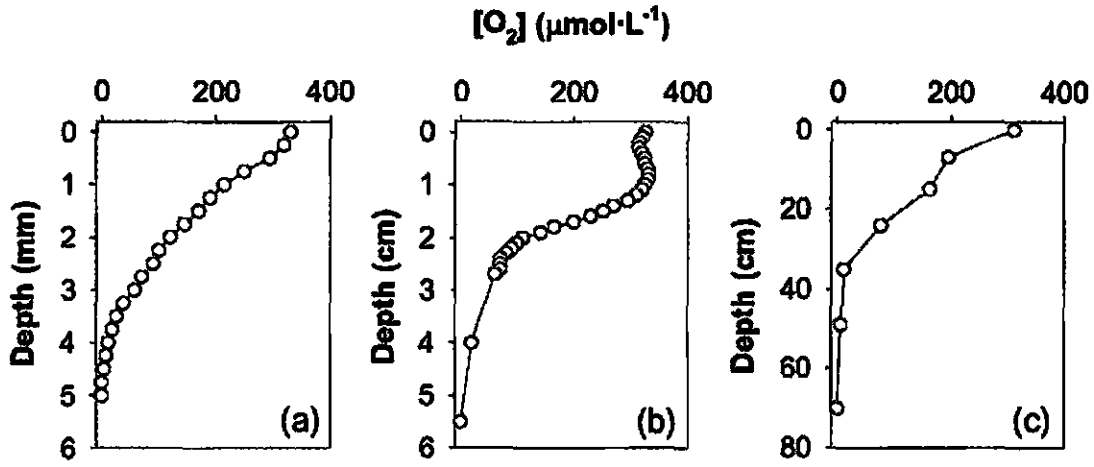

Figure 2.8 Typical profiles of pore water oxygen concentration with depth in three different types of sediment: (a) A profile from a silty site (Station 13; water depth 19 m) in the North Sea (Lohse et al. 1996); (b) A profile from a sandy site (Station 4; water depth 58 m) in the North Sea (Lohse et al. 1996); (c) A profile from a sand-and-rubble carbonate reef sediment site (Array SB; water depth 1 m) on Checker Reef in Kane'ohe Bay, O'ahu, Hawai'i (Falter and Sansone 2000). Note the differences in the depth scales.

such as ammonium, nitrite and nitrate, whose concentrations are sensitive to redox conditions, corroborate this pattern (e.g., Falter and Sansone 2000).

The predominant interpretation of these observations has overshadowed an alternative explanation, proposed early on by Webb and Theodor (1968) but effectively ignored. They suggested that the reason for low standing stocks of organic matter is high organic matter turnover and rapid conversion into nutrients. Direct evidence for this explanation was lacking until oxygen consumption rates were measured in permeable sediments (Table 2.5). These measurements indicate that oxygen consumption in permeable sediments is among the highest recorded across sedimentary settings in the world's oceans, and this evidence supports the view of permeable sediments as massive bio-catalytic converters of organic matter into nutrients (Reimers et al. 2004b; Rusch et al. 2006).

Table 2.5 Typical oxygen fluxes into the sediment in major oceanic sedimentary regimes.

Sea floor setting	O_2 flux ($mmol \cdot m^{-2} \cdot d^{-1}$)	References
Abyssal plain	0.1 – 2	Smith (1987)
Rise and slope	0.3 – 3	Reimers et al. (1992)
Deltas	5 – 50	Aller et al. (1996; 2004b)
Mobile mud belts	7 – 20	Aller et al. (2004a)
Estuaries	10 – 40	Aller (1994)
Continental shelf (permeable sediments)	10 – 120	Reimers et al. (2004b); Rusch et al. (2006)

The controlling dynamics of the bio-catalytic ability of permeable sediments are still unclear. Physical forcing has been observed to affect permeable sediment oxygen consumption non-linearly: as physical forcing increases, oxygen consumption plateaus (Rusch et al. 2006). The asymptotic nature of the relationship suggests that permeable sediments could become saturated with oxygen, which then builds up, even though organic material may still be present for degradation. The hypothesis that oxygen could build up through physical forcing, in the presence of organic material is supported by the study of Falter and Sansone (2000), which demonstrated the build up of pore water oxygen with increasing physical forcing (e.g., Figure 2.8c). In the case particulate organic matter is present in the water column, it could be trapped into the sediment under the effect of increased physical forcing, leading to the hypothesis that increasing forcing will result in increasing flux of organic material into the sediment. Combining the findings of Rusch et al. (2006) and Falter and Sansone (2000) leads to the hypothesis that increased physical forcing could lead to the simultaneous increase in oxygen flux and organic matter flux across the SWI, accompanied by the build-up of oxygen and organic matter in the sediment column. This topic is explored further in Chapters 3 and 4.

2.2.4 Global distribution and importance

Emery (1968) estimated that relict sediments cover 70 % of the area of the world's shelves. Recent data syntheses of sediment type distributions of the North American continental shelf show that more than 50 % of the area is covered by "mostly sandy" sediment, the latter defined as sediment with a sand weight fraction greater than 60 % (Jenkins et al. 2003; Reimers et al. 2004a, p. 3). This spatial extent, in conjunction

with the fact that the shelves underlie some of the most productive regions of the Earth's oceans (Ryther 1969), suggest that shelf permeable sediments must be the recipients of significant fluxes of organic carbon. However, the low organic carbon content and high oxygen consumption rates of these sediments suggest that shelves do not store carbon, but bio-catalytically oxidize it instead. Therefore, it is possible that the role of continental shelves as carbon sinks has been overestimated (de Haas et al. 2002), and that most of the carbon sequestration in continent-ocean margins is restricted to deltaic regions (Aller 2004).

The discrepancy in accumulation regimes is amply illustrated by a comparison between two major sections of the Atlantic shelf. The Middle Atlantic Bight (MAB) and the Amazon shelf both receive ample amounts of organic carbon, 7.5×10^7 t·y^{-1} and 2×10^8 t·y^{-1} respectively, from terrestrial inputs as well as from marine primary productivity (Showers and Angle 1986; de Haas et al. 2002). Whereas organic carbon accumulation on the MAB shelf is virtually non-existent, a substantial amount of organic carbon settle on the Amazon shelf sediments, with ultimately 4.5×10^6 t·y^{-1} of organic carbon (or 2.25 % of the original Amazon shelf input) accumulating on the shelf (Showers and Angle 1986; de Haas et al. 2002). Special hydrological reasons play their role in this discrepancy, e.g., shelf currents channel fine-grained, organic-carbon rich particles off the shelf and onto the slope in the case of the MAB, while retaining them on the shelf in the case of the Amazon shelf (de Haas et al. 2002). However, it is also likely that a substantial fraction of the 7.5×10^7 t of carbon received annually by the MAB is trapped and remineralized rapidly by the coarse sediments of this region. Considering that these sediments have recently been shown to act as efficient denitrifiers as well (Rao 2006; Rao

et al. 2007), it is likely that rapid trapping and remineralization of organic matter on permeable sediment shelves may account for significant amounts of remineralized carbon and nitrogen, and that this process should be taken into account in future marine production-respiration balance calculations.

2.3 References

Aller, R. C. (1994) The sedimentary Mn cycle in Long Island Sound: Its role as intermediate oxidant and the influence of bioturbation, O_2, and C_{org} flux on diagenetic reaction balances. Journal of Marine Research, 52: 259-295.

Aller, R. C., N. E. Blair, Q. Xia and P. D. Rude (1996) Remineralization rates, recycling, and storage of carbon in Amazon shelf sediments. Continental Shelf Research, 16: 753-786.

Aller, R. C., C. E. Heilbrun, C. Panzeca, Z. Zhu and F. Baltzer (2004a) Coupling between sedimentary dynamics, early diagenetic processes, and biogeochemical cycling in the Amazon–Guianas mobile mud belt: coastal French Guiana. Marine Geology, 208: 331-360.

Aller, R. C. (2004) Conceptual models of early diagenetic processes: The muddy seafloor as an unsteady, batch reactor. Journal of Marine Research, 62: 815-835.

Aller, R. C., A. K. Hannides, C. E. Heilbrun and C. Panzeca (2004b) Coupling of early diagenetic processes and sedimentary dynamics in tropical shelf environments: the Gulf of Papua deltaic complex. Continental Shelf Research, 24: 2455-2486.

Beard, D. C. and P. K. Weyl (1973) Influence of texture on porosity and permeability of unconsolidated sand. American Association of Petroleum Geologists Bulletin, 52: 349-369.

Berner, R. A. (1980) Early diagenesis. Princeton University Press, Princeton, New Jersey, U.S.A., pp. 241.

Blatt, H., G. Middleton and R. Murray (1972) Origin of sedimentary rocks. Prentice-Hall, Englewood Cliffs, New Jersey, U.S.A., pp. 634.

Blevins, R. D. (1984) Applied Fluid Mechanics Handbook. Van Nostrand Reinhold Company, New York, New York, U.S.A., pp. 558.

Boudreau, B. P. (1997) Diagenetic models and their implementation. Springer, Berlin, Germany, pp. 414.

Boudreau, B. P., M. Huettel, S. Forster, R. A. Jahnke, A. McLachlan, J. J. Middelburg, P. Nielsen, F. J. Sansone, G. L. Taghon, W. Van Raaphorst, I. T. Webster, J. M. Weslawski, P. Wiberg and B. Sundby (2001) Permeable marine sediments: overturning an old paradigm. Eos, Transactions of the American Geophysical Union, 82: 133, 135-136.

Burdige, D. J. (2006) Geochemistry of marine sediments. Princeton University Press, Princeton, New Jersey, U.S.A., pp. 609.

Burmister, D. M. (1955) Principles of permeability testing of soils, p. 3-20. *In* Barber, E. S. [ed.], Symposium on permeability of soils. ASTM Special Technical Publication No. 163. American Society for Testing Materials, Philadelphia, Pennsylvania, U.S.A.

de Haas, H., T. C. E. van Weering and H. de Stigter (2002) Organic carbon in shelf seas: sinks or sources, processes and products. Continental Shelf Research, 22: 691-717.

Emery, K. O. (1968) Relict sediments on continental shelves of the world. American Association of Petroleum Geologists Bulletin, 52: 445-464.

Falter, J. L. and F. J. Sansone (2000) Hydraulic control of pore water geochemistry within the oxic-suboxic zone of a permeable sediment. Limnology and Oceanography, 45: 550-557.

Haberstroh, P. R. (1994) Wave-forced porewater mixing and nutrient flux in a coral reef framework. Ph.D. Dissertation, University of Hawai'i, pp. 248.

Hubbert, M. K. (1940) The theory of ground water motion. Journal of Geology, 48: 785-944.

Huettel, M., W. Ziebis, S. Forster and G. W. Luther III (1998) Advective transport affecting metal and nutrient distributions and interfacial fluxes in permeable sediments. Geochimica et Cosmochimica Acta, 62: 613-631.

Huettel, M. and I. T. Webster (2001) Porewater flow in permeable sediments, p. 144-179. *In* Boudreau, B. P. and B. B. Jørgensen [eds.], The Benthic Boundary Layer. Oxford University Press, New York, New York, U.S.A.

Jenkins, C. J., A. J. Kettner, C. Moore and G. Sharman (2003) goSEABED World Seabed Data Browser. University of Colorado Institute of Arctic and Alpine Research, Boulder, Colorado, U.S.A.

Joshi, C. H., R. D. Kamm, J. M. Drazen and A. S. Slutsky (1983) An experimental study of gas exchange in laminar oscillatory flow. Journal of Fluid Mechanics, 133: 245-254.

Krumbein, W. C. (1934) Size frequency distributions of sediment. Journal of Sedimentary Petrology, 4: 65-77.

Krumbein, W. C. and G. D. Monk (1943) Permeability as a function of the size parameters of unconsolidated sand. Transactions of the American Institute of Mining and Metallurgical Engineers, 151: 153-163.

Krumbein, W. C. (1964) Some remarks on the phi notation. Journal of Sedimentary Petrology, 34: 195-197.

Lohse, L., E. H. G. Epping, W. Helder and W. Van Raaphorst (1996) Oxygen pore water profiles in continental shelf sediments of the North Sea: turbulent versus molecular diffusion. Marine Ecology Progress Series, 145: 63-75.

Malan, D. E. and A. McLachlan (1991) In situ benthic oxygen fluxes in a nearshore coastal marine system: a new approach to quantify the effect of wave action. Marine Ecology Progress Series, 73: 69-81.

McCave, I. N. (1975) Vertical flux of particles in the ocean. Deep-Sea Research, 22: 491-502.

McManus, D. A. (1963) A criticism of certain usage of the phi notation. Journal of Sedimentary Petrology, 33: 670-674.

McManus, J. (1988) Grain size determination and interpretation, p. 63-85. *In* Tucker, M. [ed.], Techniques in sedimentology. Blackwell Scientific Publications, Oxford, U.K.

Meyer-Reil, L.-A. (1986) Spatial and temporal distribution of bacterial populations in marine shallow water surface sediments, p. 141-160. *In* Lasserre, P. and J.-M.

Martin [eds.], Biogeochemical processes at the land-sea boundary. Elsevier Press, Amsterdam, Netherlands.

Newell, R. (1965) The role of detritus in the nutrition of two marine deposit feeders, the prosobranch *Hydrobia ulvae* and the bivalve *Macoma balthica*. Proceedings of the Zoological Society of London, 144: 25-45.

Precht, E. and M. Huettel (2004) Rapid wave-driven advective pore water exchange in a permeable coastal sediment. Journal of Sea Research, 51: 93-107.

Putnam, J. A. (1949) Loss of wave energy due to percolation in a permeable sea bottom. Eos, Transactions of the American Geophysical Union, 30: 349-356.

Rao, A. M. F. (2006) Carbon and nitrogen cycling in permeable continental shelf sediments and porewater solute exchange across the sediment-water interface. Ph.D. Dissertation, Georgia Institute of Technology, pp. 228.

Rao, A. M. F., M. J. McCarthy, W. S. Gardner and R. A. Jahnke (2007) Respiration and denitrification in permeable continental shelf deposits on the South Atlantic Bight: Rates of carbon and nitrogen cycling from sediment column experiments. Continental Shelf Research, 27: 1801-1819.

Reimers, C., C. Friedrichs, B. Bebout, P. Howd, M. Huettel, R. Jahnke, P. MacCready, K. Ruttenberg, L. Sanford and J. Trowbridge (2004a) Coastal Benthic Exchange Dynamics. Report TR-04-01, Skidaway Institute of Oceanography, pp. 92.

Reimers, C. E., R. A. Jahnke and D. C. McCorkle (1992) Carbon fluxes and burial rates over the continental slope and rise off Central California with implications for the global carbon cycle. Global Biogeochemical Cycles, 6: 199-224.

Reimers, C. E., H. A. Stecher III, G. L. Taghon, C. M. Fuller, M. Huettel, A. Rusch, N. Ryckelynck and C. Wild (2004b) In situ measurements of advective solute transport in permeable shelf sands. Continental Shelf Research, 24: 183-201.

Riedl, R. J., N. Huang and R. Machan (1972) The subtidal pump: a mechanism of interstitial water exchange by wave action. Marine Biology, 13: 210-221.

Riisgård, H. U., I. Berntsen and B. Tarp (1996) The lugworm (*Arenicola marina*) pump: characteristics, modeling and energy cost. Marine Ecology Progress Series, 138: 149-156.

Rusch, A., M. Huettel and S. Forster (2000) Particulate organic matter in permeable marine sands - dynamics in time and depth. Estuarine, Coastal and Shelf Science, 51: 399-414.

Rusch, A. and M. Huettel (2000) Advective particle transport into permeable sediments - evidence from experiments in an intertidal sandflat. Limnology and Oceanography, 45: 525-533.

Rusch, A., S. Forster and M. Huettel (2001) Bacteria, diatoms and detritus in an intertidal sandflat subject to advective transport across the water-sediment interface. Biogeochemistry, 55: 1-27.

Rusch, A., M. Huettel, C. Wild and C. E. Reimers (2006) Benthic oxygen consumption and organic matter turnover in organic-poor, permeable shelf sands. Aquatic Geochemistry, 12: 1-19.

Ryther, J. H. (1969) Photosynthesis and fish production in the sea. Science, 166: 72-76.

Saager, P. M., J. P. Sweerts and H. J. Ellermeijer (1990) A simple pore-water sampler for coarse, sandy sediments of low porosity. Limnology and Oceanography, 35: 747-751.

Showers, W. S. and D. G. Angle (1986) Stable isotopic characterization of organic carbon accumulation on the Amazon continental shelf. Continental Shelf Research, 6: 227-244.

Smith, K. L. (1987) Food energy supply and demand: a discrepancy between particulate organic carbon flux and sediment community oxygen consumption in the deep ocean. Limnology and Oceanography, 32: 201-220.

Sutherland, D. A., M. A. Merrifield and F. J. Sansone (1999) Wave-induced porewater transport in permeable sediments. Eos, Transactions of the American Geophysical Union, December 8th-12th, 2003, 80(49), Fall Meeting Supplement, Abstract OS12F-09.

Watson, E. J. (1983) Diffusion in oscillatory pipe flow. Journal of Fluid Mechanics, 133: 233-244.

Webb, J. E. and J. Theodor (1968) Irrigation of marine submerged sands through wave action. Nature, 220: 682-683.

Webster, I. T. and J. H. Taylor (1992) Rotational dispersion in porous media due to fluctuating flows. Water Resources Research, 28: 109-119.

Webster, I. T. (2003) Wave enhancement of diffusivities within surficial sediments. Environmental Fluid Mechanics, 3: 269-288.

ZoBell, C. E. (1938) Studies on the bacterial flora of marine bottom sediments. Journal of Sedimentary Petrology, 8: 10-18.

Chapter 3 – A microcosm method for the study of permeable sediments under controlled physical forcing

3.1 Introduction

Many continental shelf and carbonate reef sediments are often highly permeable relative to fine-grained sediments (Jenkins et al. 2003; Reimers et al. 2004a, p. 3). Permeable sediments are defined as sediments with grain diameter > 62 μm (sandy or coarser) with permeability greater than 10^{-12} m^2 (Huettel et al. 1998). Greater permeability leads to enhanced exchange between overlying water and pore water due to dynamic water column conditions. These exchange rates far exceed those by molecular diffusion, which dominate transport in fine-grained sediments (Webb and Theodor 1968; 1972; Webster and Taylor 1992; Precht and Huettel 2004; Reimers et al. 2004b). It is now evident that the relatively low organic matter content of permeable sediments is not due to low productivity, but due to rapid turnover rates of organic material (Webb and Theodor 1968). Therefore, it is probable that the role of permeable sediments in biogeochemical cycling has been underestimated, especially in view of the funding preference traditionally shown to investigations of fine-grained sediment.

One reason for the bias against permeable sediment investigations is technical: traditional field methods employed in the retrieval and study of fine-grained sediments cannot be applied directly to permeable sedimentary settings. For example, rigid-cased benthic chambers used for the measurement of fluxes across the sediment-water interface (SWI) interfere with the dynamic relationship between water-column physical conditions and interstitial flows in sedimentary pore water (Burdige et al. 1992). Proposed solutions

to this problem have included flexible-top benthic chambers (Malan and McLachlan 1991) and stirred chambers that induce a radial exchange pattern across the SWI that is estimated to simulate the non-diffusive mixing of the setting under study (Wild et al. 2004). The sampling of pore water has also been problematic because of the rapid loss of pore water when a conventional sediment core is retrieved. However, numerous samplers have been designed to sample permeable sediment pore water from various settings (Saager et al. 1990; Marinelli et al. 1998; Haberstroh and Sansone 1999; Falter and Sansone 2000a; Berg and McGlathery 2001; Martin et al. 2003).

3.1.1 Existing laboratory methods

The technical impediments described above have slowed down the study of permeable sediments in situ. As a result, investigators have resorted to laboratory studies that have elegantly demonstrated the physical and biogeochemical functioning of permeable sediments (see Huettel and Webster 2001 for a review). A description and comparison of the most widely used laboratory methods in permeable sediment research can be seen in Table 3.1. With the exception of flow-through chambers, they allow the bidirectional exchange of both dissolved and particulate material between overlying water and sediments. Most frequently, they have been employed in the investigation of material exchange across sediment topography, such as ripples, which takes place through net advection in the direction dictated by the small-scale pressure fields over the sea floor (Huettel et al. 1998; Huettel and Rusch 2000; Reimers et al. 2004b; Rusch et al. 2006).

Table 3.1 Laboratory methods used in the study of permeable sediments.

Method description	Studied process	Sediment source	Depth (cm)		Notes	Selected references
			Sediment	Overlying water		
Recirculating flume	Current over sediment topography	Intertidal sand; beach sand; coastal subtidal sand	15-20	10-12	Allows exchange of solutes and particles; large amounts of material needed	Huettel and Gust (1992b), Huettel et al. (1996; 1998)
Wave flume	Waves over flat sediment	Quartz sand	10-15	15-25	Same as for recirculating flume	Sutherland et al. (1999), Hebert et al. (2007)
Stirred chamber	Advective transport	Inter/sub-tidal sands (sieved and unsieved)	14-18	8-10	Stirring rate based on assumptions of flow path length across ripples	Huettel and Gust (1992b), Huettel and Rusch (2000), Wild et al. (2004)
Flow-through chamber	Advective transport	Continental shelf sands	6-32	0	Flow rate based on assumptions of flow path length across ripples; no bidirectional exchange possible	Reimers et al. (2004b), Rao (2006), Rusch et al. (2006)

Despite their successful application so far, they all appear to have significant limitations that prohibit their application in the study of carbonate reef sediments exposed to widely variable physical conditions, from open ocean swell to flat water (Grigg 1998; Falter and Sansone 2000b). Carbonate reef sediments exhibit redox gradients that extend over decimeters to a meter (Haberstroh and Sansone 1999; Falter and Sansone 2000b), in contrast to the millimeter-to-centimeter-scale gradients in other permeable sediments and fine-grained sediments (e.g., Figure 2.7; Lohse et al. 1996). The exact physical mechanisms contributing to the establishment of these deep redox gradients are not known. According to Webster (2003), it is unlikely to be the shallow topography-induced advection proposed for rippled tidal flat and shelf sediments (e.g., Huettel et al. 1998). Instead, he proposed that the mechanism most likely to dominate solute transport several decimeters below the SWI is shear dispersion. Indeed, maximum depths at which net advection due to sediment topography have been documented to impact pore water chemistry are on the order of several centimeters (Precht and Huettel 2004; Reimers et al. 2004b). Therefore, the study of carbonate reef sediments requires a system that permits the incubation of deep columns of carbonate reef sediments under physical forcing that can be controlled and can induce enhanced exchange to a depth of decimeters.

3.1.2 Characteristics and purpose of the new microcosm

The microcosm method presented in this chapter allows the incubation of meter-deep sediment columns, while simultaneously controlling the magnitude of physical forcing in the form of oscillatory pressure gradients above the SWI. It also permits the non-destructive monitoring and sampling of pore water and overlying water during

experiments. Since three-dimensional sedimentary features are most likely ineffectual in deep transport processes (Precht and Huettel 2004; Reimers et al. 2004b), this method focuses on processes along the vertical space dimension, such as solute and particle exchange across the SWI, and the underlying decimeters-deep redox gradients.

The study of material exchange across the SWI in permeable sediments has been identified as a research priority by the scientific community (Reimers et al. 2004b). The relative simplicity of the microcosm described here renders such research affordable and feasible. Like flumes, stirred chambers and flow-through chambers, it allows permeable sediment incubation under controlled physical conditions of enhanced solute exchange. Unlike current flumes, stirred chambers and flow-through chambers, which create advective flow, the microcosm creates oscillatory flow across the SWI over a meter-deep sediment column much more simply than by placing such a column in a wave-generating flume (an untenable feat for most researchers). Chapter 3 describes the design, development and testing of this microcosm method. Detailed information on all steps of its construction and operation, as well as pertinent findings from all assessment studies and experiments, are included for the benefit of future users.

3.2 An early microcosm design

3.2.1 Motivation

The motivation for the design, construction, and testing of this microcosm emerged from the idea of testing the response of carbonate sediments to the rise of pCO_2 in the atmosphere (E. Gaidos, personal communication). While previous work on this

phenomenon has been restricted to the direct effects of carbonate stability on calcifying reef organisms (e.g., Kleypas et al. 1999; Leclercq et al. 2002; Langdon and Atkinson 2005), the impact of rising pCO_2 may extend to carbonate sediment permeability, hydraulics and biogeochemistry. Such impacts may result in changes in the efficiency of nutrient recycling in reef ecosystems and the subsequent ability of reefs to sustain high productivity and biodiversity. Past studies of carbonate reef sediment biogeochemistry (Haberstroh and Sansone 1999; Falter and Sansone 2000a) provided the observations that dictated the features such an incubator should have (see Sections *3.1.1 – 3.1.2*), and guided the effort to design, develop and test such a microcosm for weeks-to-months-long incubations of sediments.

3.2.2 Methods for construction and operation – technical information

3.2.2.1 Principles of operation

In its early design, the microcosm (Figure 3.1) consists of two connected columns, each approximately 2 m high: a "live" column, here-on referred to as Column A, and an "auxiliary" column, here-on referred to as Column B. The full column height is typically constrained by the ceiling height of conventional laboratories. Column A, which is studded with sampling ports, contains the material under study, whether it is "live" sediment collected from the field or model sediment from a merchant. The actual sediment column height is limited to a maximum of 1 m to allow space for sufficient overlying water. Column B contains previously combusted silica sand grains and prevents direct hydraulic and chemical communication between the bottom of the sediment in Column A and the overlying water. The two columns can thus be thought of

as representing two locations along the sea floor separated by half a wavelength of a surface wave.

Water is added to a height of 50 cm above the SWI in Column A. This overlying water is pumped between the two columns by peristaltic Pump A (Connection II, Figure 3.1) to create an oscillatory head with a height of a few to tens of centimeters, similar to that over low-energy natural patch reefs (e.g., Falter and Sansone 2000b). The difference in head between the two columns induces an oscillatory flow of pore water through the sediment about a mean point. The system is sealed from direct contact with the atmosphere, and equal pressure in the two columns is maintained by a headspace connection (Connection III, Figure 3.1). A second peristaltic pump, Pump B, circulates seawater through the entire system by supplying Column A with seawater from a reservoir while removing water from Column B at the same rate (Connection IV, Figure 3.1). The reservoir can be used to manipulate the composition of incoming overlying water, e.g., by altered particle content, dissolved gas concentration, etc.

3.2.2.2 Materials

Columns and reservoir – Each column is made of two segments of transparent Schedule 40 polyvinyl chloride (PVC) pipe with an internal diameter of 7.68 cm (3 in) and a wall thickness of 6.4 mm (0.25 in) (Harvel Plastics, Easton, Pennsylvania, U.S.A.). The two segments are connected by LASCOtite compression pressure couplings (LASCO Fittings, Brownsville, Tennessee, U.S.A.). Two column segments are used for ease of machining; a single segment may otherwise be preferred. The lower and upper ends of each column are threaded to accept commercially available pipe fittings, and the tops

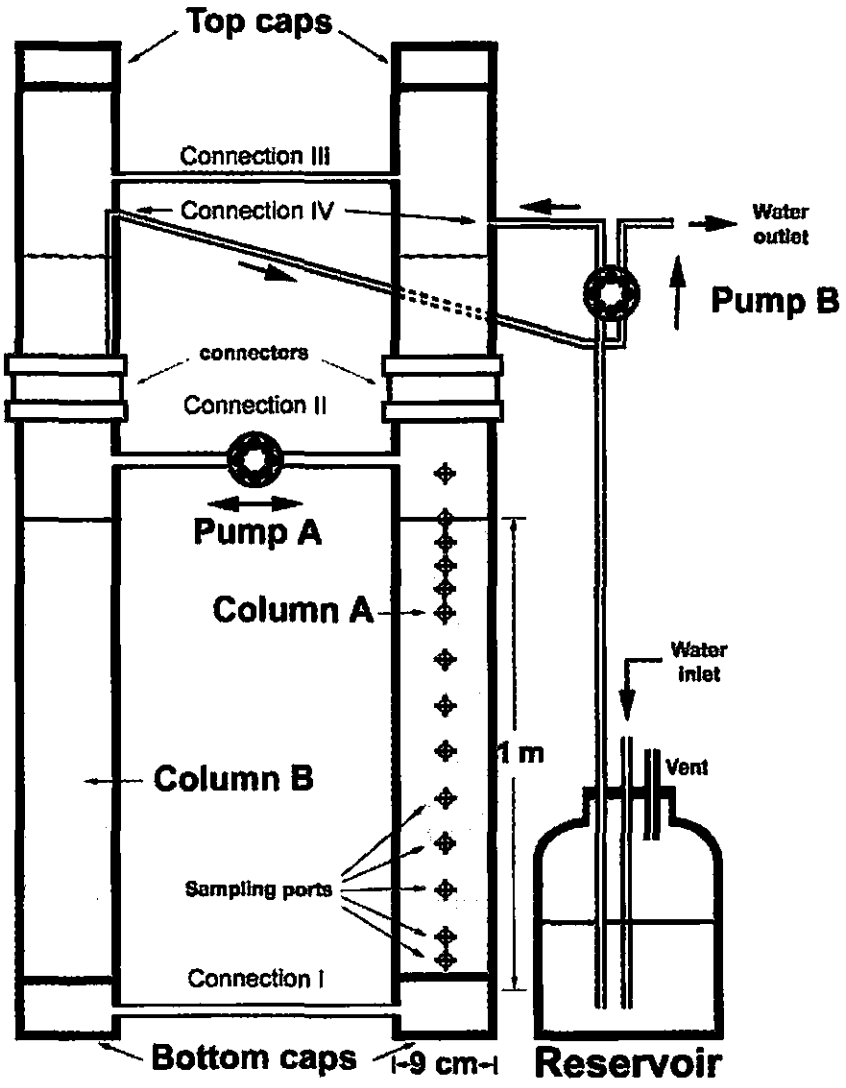

Figure 3.1 Schematic diagram of the prototype microcosm. See text for description of components and materials.

capped with threaded opaque PVC threaded end-caps (U.S. Plastics Corp., Lima, Ohio, U.S.A.). To form each bottom end cap, a female acrylonitrile butadiene styrene (ABS) reducer coupling (the part to be screwed onto the pipe) is glued into an unthreaded ABS end cap using ABS cement (the actual material is not critical). This design allows enough space on the bottom caps to connect the components that form Connection I (Figure 3.1).

Before the bottom caps are screwed into place, mesh stoppers are added to the bottom of the pipe to hold the sediment in place while allowing water to flow through. The mesh stoppers are made by cutting the center out of 7.68-cm (3-in) pipe stoppers and gluing 0.25-mm mesh screen over the opening. Finally, numerous apertures are drilled and threaded on both columns for connections and sampling ports, as described in a later paragraph (see *Sampling ports*). The columns are secured upright on a level surface with Castaloy three-prong extension clamps (Fisher Scientific, Pittsburgh, Pennsylvania, U.S.A.), attached to a custom-made aluminum frame. During operation, the columns are covered with aluminum foil or aluminum tape to exclude ambient light, thereby preventing the growth of photoautotrophs.

The reservoir is a vacuum-tight, autoclavable polypropylene, 20-L Nalgene carboy, capped by a Top Works Fluid Transfer System consisting of a closure with a silicone stopper with two drop tubes and a vent tube (Nalge Nunc International, Rochester, New York, U.S.A.). This carboy's thick wall ensures relatively high gas impermeability, while the use of this particular closure simplifies the exchange of liquids between the reservoir and other components.

Connectors, tubing and pumps – Tubing connections at 0.1 m below the column top ends, 1.12 m above the column bottom ends, and at the bottom caps (Connections I-

III in Figure 3.1) are 1.28-cm (0.5-in NPT) high-density polyethylene male pipe adapters with 0.96-cm (0.375-in) barbed fittings (Cole-Parmer Instrument Co., Vernon Hills, Illinois, U.S.A.). The adapters at Connections I and III are connected using butyl rubber tubing, selected for its low gas permeability, while the adapters at Connection II are connected through Pump A with Norprene pump tubing L/S 36 (internal diameter 9.5 mm) (Masterflex, Cole-Parmer Instrument Co., Vernon Hills, Illinois, U.S.A.). The columns are connected to the reservoir with 0.32-cm (0.125-in NPT) polypropylene male pipe adapters with 0.32-cm (0.125-in) barbed fittings (Cole-Parmer Instrument Co.), along with L/S 14 Norprene tubing (internal diameter 1.6 mm) (Masterflex, Cole-Parmer Instrument Co.) (Connection IV in Figure 3.1). Norprene tubing is used for its low gas permeability and resistance to abrasion by the pump head during continuous pumping. The tubing section leading from Column B to Pump B at Connection IV originates well below the water level in that column, ensuring that only water is drawn and that the outflow rate into the microcosm equals the inflow. Pumps A and B are L/S computer-compatible/programmable brushless drives (Model no. 07550-30, Masterflex, Cole-Parmer Instrument Co.) with Standard Masterflex pump heads (Masterflex, Cole-Parmer Instrument Co.). Complex pumping routines are executed using Linkable Instrument Network (Win LIN), a Microsoft Windows-based software program supplied by the pump manufacturer.

Sampling ports – Eleven sampling port holes were drilled at 10-cm intervals from the bottom of Column A, with an additional three ports at 5, 85 and 95 cm from the bottom. Each sampling port consists of a 1-way male Luer-lock stopcock (Cole Parmer Instrument Co.) mated to a 1/4-28 UTF female Luer fitting (Cole-Parmer Instrument

Co.). There is a possibility that sampling of the fluid adjacent to the inner wall of the column may be subject to wall and edge effects (e.g., Huettel and Gust 1992a), although for permeable sediments this effect has been demonstrated to be negligible (Rocha et al. 2005). To avoid the former, in case it is true, Fisherbrand Turnover septa (Fisher Scientific), fitted to the female Luer fittings and secured in place using cable ties, permit sampling from the center of the core with syringe needles. Alternatively, 1/4-28 UTF Mininert threaded valves with septa (VICI Precision Sampling, Baton Rouge, Louisiana, U.S.A.) can be used.

Sediments – During experiments, Column A holds the sediments under study in a column as high as 1 m. Column B is always packed with commercial silica sand combusted overnight at 500 °C to remove organic material. Oxidized iron in combusted sand imparts a reddish-yellow color. After several days' exposure to anoxic, sulfidic conditions, the column assumes a grey color, presumably due to the oxidized iron becoming reduced to FeS and FeS_2. This color change can act as an indirect indicator of anoxic conditions at the bottom of Column B and the functioning of the connection between Columns A and B. The use of silica sand may be problematic, if iron dynamics are of interest. Since iron and phosphorus cycling is tightly coupled (Ruttenberg 2001), it is likely that the presence of iron in this column may interfere with nutrient dynamics and particularly phosphorus mobility and availability for uptake by single cells. A good alternative to iron-containing sand is quartz beads, which are widely available in a variety of grain size ranges.

3.2.2.3 Operating procedures

Column assembly and monitoring – The microcosm is assembled from the bottom up. First, the mesh stoppers are attached to the lower segments of the two columns, and the bottom caps are screwed on. After connecting the bottom caps together (Connection I, Figure 3.1), the two columns are filled with water up to 1 m, either by pouring it from a container or by using a peristaltic pump. Any bubbles trapped under the mesh stoppers can be released by gentle tapping. The sediment under study and silica sand are added to Columns A and B respectively, taking care to accommodate any water overflowing from the ports of Connection II (Figure 3.1). After loading the sediment, the top and bottom column segments are connected using the LASCOtite couplings, and the two columns are connected to each other through Connection III and to Pump B through Connection IV (Figure 3.1). More seawater is then added to the columns to the desired height of overlying water (typically 50 cm above the SWI in Column A) either by pouring it in from the top or by using Pump B. After the top caps are in place, both pumps are programmed according to the experiment's requirements and are activated, while ensuring that the reservoir is full. This time point marks the beginning of an experiment.

The microcosm is monitored for leaks, particularly at the bottom of the columns where the pressure is greatest. Leaks can be prevented by tightening the connections and by using Teflon tape on all threaded parts. Silicon grease can also be used, but only on surfaces not in contact with the microcosm contents, since it may react with and bind various monitored components such as dyes, or be used as substrate by microbial assemblages (M. Huettel, personal communication). The sections of tubing in the

peristaltic pumps are inspected for excessive wear or softness every 1-4 days and replaced as necessary. This issue is discussed further in Section *3.2.4.5*.

Sediment loading –The lower segment of Column A can be used as a core liner for field sediment sampling after blocking the threaded sampling ports with suitable plugs. However, a major problem encountered by researchers who work with permeable sediments is post-sampling loss of pore water from cores (e.g., Saager et al. 1990; Berg and McGlathery 2001; Martin et al. 2003). This water must be replaced in the core, either by pumping from below or by dispensing from above. Additionally, simple coring is impossible in the case of carbonate reef sediments, which may be partly lithified (Moore 2001, p. 106-110) or may contain sizeable rubble (personal observations). Instead, drilling has been used to retrieve sediments from such locations (Engels et al. 2004), with interstitial water being lost in the process. In this situation, sediments can be loaded via the top of the core, followed by filling with water from below. The biggest issue with this step is the potential inclusion of air pockets in the sediment column, which will interfere with the column's hydrodynamics and will alter the pore water dissolved gas composition. One solution to this problem is the addition of sediments to a column already filled with water, which is the approach that was followed in this study. Sorting by grain size during settling can be minimized by adding the sediment in small aliquots (50-100 mL). During loading, the application of gentle vibrations by tapping the column's side helps to compact the sediment (Huettel and Rusch 2000). This eliminates depth-dependent variability in compaction-related parameters such as porosity and permeability, and generates a homogeneous sediment column.

Table 3.2 Experiments conducted using the first microcosm design: the material used (see Figure 3.2, and Table 3.3), sediment column heights (l_A: Column A; l_B: Column B), experiment duration (t), and objectives. Column B always contained silica sand, unless otherwise noted.

Exp No.	Column A material	l_A (cm)	l_B (cm)	t (d)	Experiment objectives
1	Beach sand (O'ahu)	100	75	2	Enhanced solute exchange – proof of concept
2	Carbonate reef sediment (Moloka'i)	100	75	3	Biogeochemistry of incubated sediments; redox gradient extent
3	Carbonate reef sediment (Moloka'i)	97	75	6	Biogeochemistry of incubated sediments; redox gradient extent
4	Carbonate reef sediment (Moloka'i)	97	75	55	Long-term redox gradient extent and development; microbiology
5	Silica sand	72	-	6	Solute molecular diffusion control
6	Silica sand	99	75	1	Solute enhanced transport
7	Beach (O'ahu) and reef (Moloka'i) sand mix	93	75	7	CO_2 detection and monitoring in overhead gas – proof of concept
8	Carbonate reef sediment (O'ahu)	95	45	100	Maximum incubation limit with CO_2 detection and monitoring
9	No sediment	-	-	22	O_2 intrusion

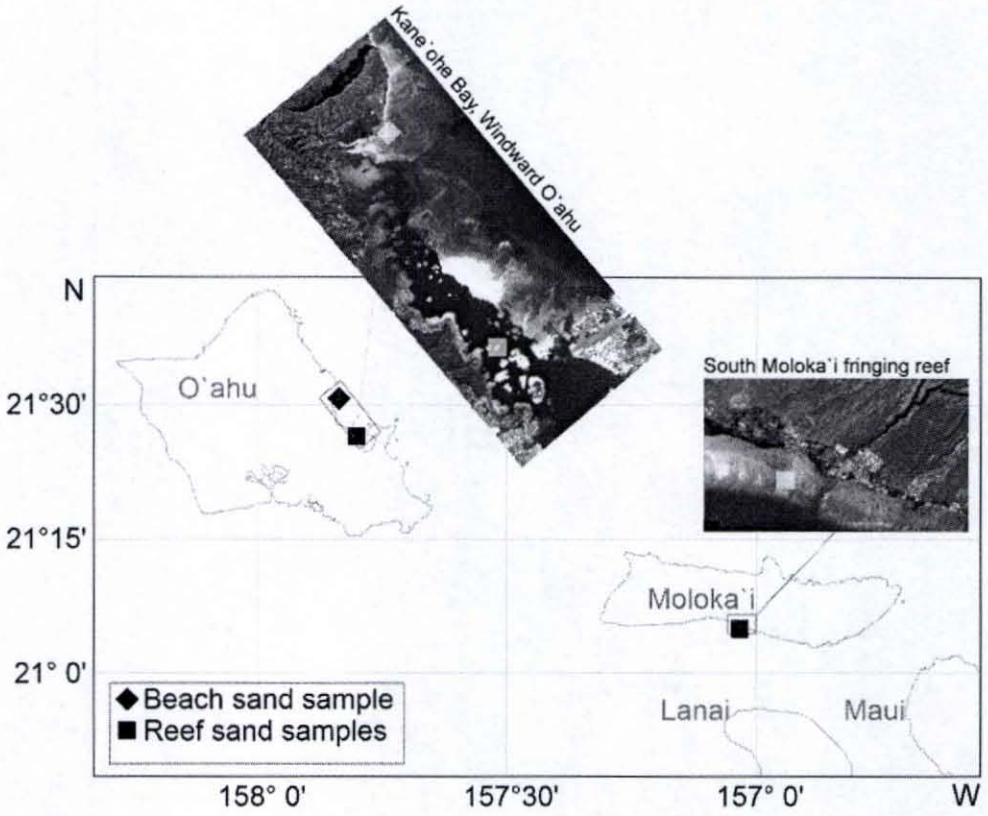

Figure 3.2 Sites of sources of the sedimentary materials used in experiments with the first microcosm design (see Table 3.3 for details). Semi-transparent symbols on satellite photographs indicate the site locations, described in more detail in Table 3.3 (satellite photographs courtesy of P. Mouginis-Mark). The average water depth at both coral reef sites was 0.5 m.

Table 3.3 Physical characteristics of the sediments used in the assessment experiments of the first microcosm design.

Sediment type (Exp. No.)	Source location	Grain size[a] (mm)		σ_1 [b]	φ [c]	k [d] (m^2)
		Median	Mean			
Silica sand (5-6)	Merchant	0.60	0.56	0.59	0.46	2.5×10^{-10}
Beach sand, Kealoa, O'ahu (1, 7)	21° 30.67' N 157° 50.15' W	1.90	2.11	0.91	0.52	6.6×10^{-10}
Fringing reef sediment, Moloka'i (2-4, 7)	21° 04.95' N 157° 01.95' W	9.26 [e] 3.13 [f]	7.93 [e] 2.89 [f]	2.29 [e] 3.16 [f]	0.54 [e]	1.3×10^{-9} [e] 2.7×10^{-11} [f]
Patch reef sediment, O'ahu (8)	21° 26.74' N 157° 48.06' W	7.44 [e] 4.17 [f]	6.01 [e] 3.40 [f]	2.65 [e] 2.95 [f]	0.52 [e]	1.1×10^{-9} [e]

[a] Grain size was determined by wet sieving. Median = d_{50}, and mean = d_{mean}, where d_x is defined as the size of the grain that is coarser than weight fraction x (%) of all the grains (McManus 1988).

[b] Sorting is defined as $\sigma_1 = \frac{\phi_{84} - \phi_{16}}{4} + \frac{\phi_{95} - \phi_5}{6.6}$, where $\phi = -\log_2\left(\frac{d}{d_o}\right)$, an alternative grain size scale suitable for sediments with broad ranges in grain size (McManus 1988).

[c] Porosity, φ, is defined as the portion of total volume that is occupied by water, and is determined gravimetrically (Breitzke 2000).

[d] Permeability, k, was calculated for sieved sediments from hydraulic conductivity, measured on sediment columns with pressure gradient relaxation tests (see Section *3.2.3.1*).

[e] Sediments sieved through a 500 μm sieve (see Sections *3.2.3.2* and *3.2.3.3*).

[f] Unsieved sediments.

3.2.3 Methods for assessment experiments

The utility of this microcosm system hinges on its ability to reproduce two observed properties of permeable marine sediments: the enhanced exchange between overlying and pore water, and establishment of a redox gradient spanning tens of centimeters, rather than the millimeters commonly observed in fine-grained sediments. Nine experiments were conducted to test the design of the microcosm system, the construction materials and sampling procedures for their general ease-of-use and suitability, as well as for the generation of the desired features of enhanced exchange and decimeters wide redox gradients (Table 3.2). The sediments used during these experiments were collected from marine settings on two Hawaiian islands, O'ahu and Moloka'i, as well as sand purchased from a commercial supplier (Figure 3.2, Table 3.3).

The experiments were divided into three categories, based on their goals and objectives. The first category (Exp. 1, 5 and 6) involved the observation and quantification of enhanced exchange between overlying water and sediments. The second category (Exp. 2-4) involved the incubation of reef sediments over periods of days to weeks, the determination of geochemical and microbial patterns during this period, and the evaluation of the microcosm's suitability for biogeochemical investigations. Additionally, a three-week-long experiment (Exp. 9) was conducted to investigate the intrusion of O_2 from the atmosphere into the microcosm, a process which may affect O_2 flux estimates across the SWI. The third category (Exp. 7 and 8) tested the feasibility of the detection and monitoring of pCO_2 in the overhead gas of Column A during long-term incubation of live sediments, The long-term sediment incubation during Exp. 8 presented

an additional opportunity to carry out biogeochemical and microbial observations and analyses.

3.2.3.1 Characterization of sediment column hydraulics

Every experiment should begin with the hydraulic characterization of the assembled microcosm. This must include the determination of the hydraulic conductivity (and, consequently, the permeability) of the sediment and silica sand columns, and the flow velocity field imparted by water level oscillations. Pressure sensors and flow meters in-line with the microcosm would greatly facilitate this characterization. In their absence, cost-effective but equally efficient methods must be devised. Such a method, which relies on pressure gradient relaxation and which does not require any additional devices, was developed and tested during the assessment experiments, and is described further in the following paragraphs.

It is best to conduct pressure gradient relaxation tests after Column A is assembled and while Column B is filled with silica sand, preferably at more than two silica sand column heights (see below for further explanation). Each test consists of blocking Connection I (Figure 3.1), setting a water level difference between the two columns using Pump A, marking the starting water level, removing the block, and recording the changing water level at known time points. The rate of water flow, $q(t)$ ($mL \cdot s^{-1}$), from the one column to the other (through Connection I) decreases with time as the water levels in the two columns equilibrate. The flow rate function, and the consequent relaxation time needed for equilibration, are related to the permeability of the

porous material (e.g., Dinariev et al. 1989), in this case the sediment and silica sand columns, by Darcy's law (Hubbert 1940):

$$K = \frac{q(t)}{A}\frac{l}{H(t)} = v(t)\frac{l}{H(t)} \qquad 3.1$$

where K is the hydraulic conductivity ($cm \cdot s^{-1}$), A is the cross-sectional area of the column (46.3 cm^2 in this prototype), $H(t)$ is the head difference between the two columns (cm), l is the length of the column of porous material (cm), and $v(t)$ is the flow velocity ($cm \cdot s^{-1}$).

In the case of communicating vessels such as these, the change in water level of one column is a consequence of an equal amount of change in the other column, but in the opposite direction. Therefore, Eq. 3.1 could not be solved using relationships used in permeametry for hydraulic conductivity determination (where the water level of at least one column is held constant). Instead, a numerical solution in four steps was developed, by which water-level data were used to determine the optimal value of K for the whole system (both columns) and, eventually, k values for each of the two columns.

Step One: Data evaluation – The first step in solving Eq. 3.1 is to evaluate the water-level data collected during a pressure gradient relaxation run. The reason for this is that, as in permeametry, the precise determination of the head difference between the two columns, $H(t)$, is very important. Determining $H(t)$ as precisely as possible in this microcosm application could be achieved with the use of pressure sensors in-line with the two columns. In the absence of these, where water levels are recorded manually on tape attached on the column wall, curve fitting can be employed. The two data sets of water heights dropping (h_A) and rising (h_B) with time (t) are fit with exponential decay and exponential growth equations, respectively:

$$h_A = y_{0A} + a_A e^{-b_A t} \quad 3.2$$

$$h_B = y_{0B} + a_B\left(1 - e^{-b_B t}\right) \quad 3.3$$

The asymptotes of these relationships (y_{0A} for Eq. 3.2 and $y_{0B} + a_B$ for Eq. 3.3) must be equal if the water level measurements are perfectly adjusted to each other. The difference between the asymptotes is calculated and an adjustment is performed using half the difference, h_{adj}, adding it or subtracting it to the data of the heights rising and dropping with time respectively:

$$h_{adj} = \frac{y_{0A} - (y_{0B} + a_B)}{2} \quad 3.4$$

The magnitude of h_{adj} is an indication of the precision of manually recorded water levels. Based on numerous observations throughout the course of this study, height determination errors on the part of the operator could explain as much as $h_{adj} = 2.5$ cm. This is an outcome of the water-level equilibrium height being off-set between the two columns. Above $h_{adj} = 2.5$ cm the system should be considered to be under the influence of additional pressure effects than the ones outlined in this section (see Section *3.3.3.1* for such a case).

Step Two: Optimal conductivity determination – The next step is to run a simple two-box model of the heights of the two columns, h_{Amodel} and h_{Bmodel}, at a user-determined range of K values, with the initial conditions:

$$h_{Amodel}(0) = h_A(0)$$

$$h_{Bmodel}(0) = h_B(0)$$

$$l = l_T = l_A + l_B$$

$$v(0) = \frac{K(h_{A\,model}(0) - h_{B\,model}(0))}{l_T}$$

where $h_A(0)$ and $h_B(0)$ are taken from the data, l_A and l_B are sediment column lengths in Columns A and B lengths respectively, and $v(0)$ is a re-arrangement of Eq. 3.1.

At one-second time intervals, the following calculations are made:

$$h_{Amodel}(t) = h_{Amodel}(t\text{-}1) - v(t\text{-}1) \qquad 3.5$$

$$h_{Bmodel}(t) = h_{Bmodel}(t\text{-}1) + v(t\text{-}1) \qquad 3.6$$

$$v(t) = \frac{K(h_{A\,model}(t) - h_{B\,model}(t))}{l_T} \qquad 3.7$$

At t=f, and before proceeding to the next K value in the range, the modeled heights, h_{Amodel} and h_{Bmodel}, are compared with the data values, h_A and h_B, by calculating the average Summed Square of Residuals (SSR) for the two sets:

$$SSR = \frac{\sum_{t=0}^{t=f}(h_A(t) - h_{A\,model}(t))^2 + \sum_{t=0}^{t=f}(h_B(t) - h_{B\,model}(t))^2}{2} \qquad 3.8$$

Upon completion of the model run at all the K values determined by the user, the K value at which the SSR is at a minimum is selected as the best fit, and it describes the composite hydraulic conductivity (K_T) of the whole system, i.e., both the sediment and silica sand columns.

Step Three: Calculation of flow velocity at optimal K – Values of K can be used to estimate permeability, k, using the following relationship (Boudreau 1997):

$$K = \frac{k\rho g}{\mu} \qquad 3.9$$

where ρ is the density of the fluid used ($g \cdot cm^{-3}$), μ its dynamic viscosity ($g \cdot cm^{-1} \cdot s^{-1}$), and g is the acceleration due to gravity (981 $cm \cdot s^{-2}$). Values used in these assessment experiments are shown in Table 3.4. The permeability, k, is independent of the fluid characteristics, and is more appropriate when comparing the results of the assessment experiments, some of which were conducted with fresh water and others with sea water.

Step Four: Determination of individual k values – Finally, when measurements are done at more than one silica sand column length, best values for the individual permeabilities of these two components (k_A and k_B for Columns A and B respectively) can be estimated. The contribution of individual conductivities to k_T is related to their lengths (Rocha et al. 2005):

$$k_T = \frac{l_T}{\frac{l_A}{k_A} + \frac{l_B}{k_B}} \qquad 3.10$$

Table 3.4 Viscosity and density values used in assessment experiments of the first microcosm design.

Exp. No.	Salinity	Temperature (°C)	μ [a] ($g \cdot cm^{-1} \cdot s^{-1}$)	ρ [b] ($g \cdot cm^{-3}$)
1	0	21	0.00978	1.000
2, 3, 4	33	21	0.01043	1.023
8	35	25	0.00957	1.022

[a] Viscosity values were obtained from the relationships in Riley and Skirrow (1975, p. 576);

[b] Densities were obtained from the tables in Fleming (1939).

The two unknowns, k_A and k_B, are determined by fitting the data of l_T versus k_T with Equation 3.5 using a non-linear least-squares fitting approach.

The hydraulic characterization method outlined above was used in Exp. 1-4 and 8. The mathematical computations were compiled using MATLAB (Mathworks Inc., Natick, Massachusetts, U.S.A.) into two routines: routine 1 (see Appendix B) uses the data from a single relaxation test to adjust the water level data if necessary, generating an estimate of the total hydraulic conductivity, and a flow velocity-water height difference relationship (Eq. 3.2-3.8); routine 2 (see Appendix C) uses all the hydraulic conductivity estimates from a single experiment to calculate the individual hydraulic conductivities and permeabilities of the two columns (Eq. 3.9-3.10).

The reliability of the pressure gradient relaxation method in determining the hydraulic conductivity of the whole microcosm and the individual columns was assessed in two ways. First, the different estimates of permeability of silica sand, k_B, from Exp. 1-4 were compared to obtain a sense of the replicability of this method. Second, in Exp. 8, the value of K_T measured with this method was compared to K_T determined by constant head permeametry to ensure that comparable values are obtained. This was achieved by connecting Pump A to a water reservoir and programming it to direct water into Column A at Connection II. The rate of pumping was adjusted such that the head difference, H (cm), between the two columns remained constant with time. Water was collected from Column B at the port of Connection II so that the volume, V (mL), flowing through the system during a known time period, T (s), was measured using a graduated cylinder. The hydraulic conductivity is given by the following equation (a alternative formulation of Eq. 3.1) (Klute and Dirksen 1986):

$$K_T = \frac{Vl_T}{ATH} \tag{3.11}$$

Several replicate measurements were made on each of two dates 30 days apart, and also served to test whether hydraulic changes do occur during a single experiment. Finally, the efficacy of the manual water level recording method was assessed by inspecting the h_{adj} values.

3.2.3.2 Enhanced exchange experiments

The exchange between the overlying water column and the sediment pore water was studied by adding a pulse of fluorescein dye (C.I. 45350) to the overlying water and monitoring its concentration with time in pore water. After an initial exploratory experiment (Exp. 1), a control experiment was conducted (Exp. 5) to compare observations under conditions of no pumping with predictions based on the theory of molecular diffusion. A subsequent experiment (Exp. 6) observed the penetration patterns under oscillatory conditions (generated by active pumping of overlying water between the two columns), which were compared with those of the control (Exp. 5).

Initial experiment – Exp. 1 used tap water, a 1-m column of poorly sorted beach sand in Column A, and a 75-cm column of silica sand in Column B (Table 3.2). Male Luer-lock stopcocks were used at the sampling ports, and water exchange between microcosm and reservoir did not take place during the experiment. A very dilute solution of fluorescein was added to the overlying water of both columns and was mixed by slowly pumping between the two columns for 2 min with Pump A, the end of which marked t = 0. At this point, Pump A was stopped, and was restarted after 8 h, in an oscillatory mode with a period of 30 s and a pumping rate that produced an 11-cm height

oscillation. Pore water (1-2 mL) was sampled from all depths at 4-h intervals, and fluorescence intensity was immediately measured with a Hitachi L-7480 fluorescence detector (Hitachi Instruments, San Jose, California, U.S.A.) by exciting the sample at 494 nm and detecting the emission intensity at 520 nm. Fluorescein concentrations were calculated using the intensities measured and a calibration curve created with appropriate standards. All samples exceeding the range of the calibration curve were diluted. The experiment was terminated at 36 h when dye was detected at the lowest sampling port in Column A.

Control experiment – In Exp. 5, Connections I and II between Columns A and B were blocked. The sampling port at 70 cm from the bottom was fitted with a septum-sealed Luer adaptor to allow sampling with a syringe needle at a point 1 cm within the sediment column. The remaining sampling ports were sealed with plugs. Coastal seawater was filtered with a 0.2-μm polycarbonate filter and used in column A, along with a 72-cm column of silica sand, such that the sampling port was at 2 cm below the sediment-water interface. At $t = 0$, a dilute solution of fluorescein was injected into the overlying seawater. The initial overlying water fluorescein concentration was estimated using the injected solution's concentration and the pre-existing overlying water volume. One-milliliter samples of pore water were retrieved from 2 cm sediment depth at 24-h intervals and were analyzed immediately for fluorescein as described previously. The experiment was terminated when the detected fluorescein concentration reached a maximum and started declining.

Active pumping experiment – In Exp. 6, both Columns A and B were loaded with silica sand to heights of 99 cm and 75 cm, respectively. Enough filtered seawater was

added to bring the total overlying water column height to 50 cm above the sediment surface in Column A. Pump A was programmed to create an oscillatory head with a height of 11 cm and a period of 30 s. After 15 h of pumping, a concentrated fluorescein solution was added to the overlying water of Column B, and the pumping action distributed the dye throughout the overlying water volume within 15 min. The end of this mixing period was considered to be the starting point of the experiment (t = 0). Pore water samples (1 mL) were collected from 29-, 49- and 69-cm depths approximately every 30 min and analyzed for fluorescein as described previously. The experiment was terminated after the dye front passed the 69-cm depth mark.

Data analysis – Tracer transport during Exp. 5 (in which only molecular diffusion was expected to take place) was modeled using Fick's Second Law of diffusion (Berner 1981, p. 32):

$$\frac{\partial C}{\partial t} = D_s \frac{\partial^2 C}{\partial z^2} \qquad 3.12$$

where C = concentration ($N \cdot Le^{-3}$), t = time (T), z = depth (Le), and D_s is the sedimentary diffusion coefficient ($Le^2 \cdot T^{-1}$). $D_s = D_0 \cdot \theta^{-2}$, where D_0 is the free solution diffusion coefficient ($Le^2 \cdot T^{-1}$), and θ is the dimensionless sediment tortuosity (Berner 1981, p. 36). The solution of Eq. 3.12 with the initial condition:

$$C = 0, \; z > 0, t = 0,$$

and the boundary condition:

$$C = C_0, z > 0, \; t = 0,$$

is (Crank 1957, p. 18-19):

$$C = C_0 erfc \frac{z}{2\sqrt{(D_s t)}} \qquad 3.13$$

where C_0 is the initial overlying water concentration ($N \cdot Le^{-3}$) and erfc is the complementary error function.

No change in C_0 was analytically detected during Exp. 5 due to the very high value of C_0, and the very shallow sediment depth at which C was measured (2 cm). This and the large overlying water volume allowed the assumption that C_0 remained constant throughout the experiment, and permitted the use of Eq. 3.13. A value of D_s was calculated by a least-squares fit of Eq. 3.13 to the concentration-time curve and comparing this with values of the free solution diffusion coefficient, D_0, and an estimate of θ^2. Published values of D_0 for fluorescein range between 1.52×10^{-2} and 1.93×10^{-2} $cm^2 \cdot h^{-1}$ (average of 1.73×10^{-2} $cm^2 \cdot h^{-1}$) at 22 °C (the temperature in which these experiments took place) (Kaiser and Maurice 1964; Soeller et al. 2003). The value of θ^2, was estimated to be 2.195 using $\theta^2 = 1/\varphi$, which is applicable when porosity, φ, is ≤ 0.7 (Ullman and Aller 1982). The silica sand porosity used in this calculation was determined to be 0.46 (Table 3.3). The overlying water fluorescein concentration was estimated to be 2 $\mu mol \cdot L^{-1}$, while the depth of observation, z, was 2 cm.

One should not assume that enhanced exchange, predicted to occur when actively pumping, can be modeled using Eq. 3.12. However, more elaborate models allowing for the concomitant change in overlying water concentration (e.g., Rao and Jahnke 2004) could not be used because of the unknown flux into Column B sand. Instead, the Column A concentration-time data were analyzed by calculating a tracer migration rate, v_m ($Le \cdot T^{-1}$) (Reimers et al. 2004b):

$$v_m = \frac{z}{t_M} \tag{3.14}$$

where t_M (T; the time at which the leading edge of the tracer peak arrives at depth z) is estimated visually from the data. A displacement coefficient, D_χ ($Le^2 \cdot T^{-2}$), analogous to a diffusion coefficient, was also calculated, based on the Einstein-Smoluchowski relation (Boudreau 1997, p. 101-102):

$$D_\chi = \frac{z^2}{2t_D} \tag{3.15}$$

where z is linear displacement of the concentration impulse (Le), and t_D is the elapsed time or breakthrough time (T), defined to be the time-axis intercept (at $C = 0$) of a fit of the linear portion of the concentration-time curve (Meier et al. 1988; Meier et al. 1991; Fritsche et al. 2001; Reimers et al. 2004b). The data points of each curve falling on this linear portion were fitted with a linear regression, and t_D was determined from the model equation and is used to calculate D_χ. Although Reimers et al. (2004b) refer to this coefficient as "the dispersion coefficient," I hesitate to follow suit because it suggests that dispersion is the dominant process responsible for enhanced transport in the case of sediments, an assertion about which there is no consensus (e.g., Webster and Taylor 1992; Webster 2003).

3.2.3.3 Sediment biogeochemistry and microbiology

The biogeochemistry and microbiology assessment experiments (Exp. 2-4) focused on redox geochemistry and microbial abundance dynamics. These experiments took place indoors in a temperature-controlled laboratory (21 °C ± 1 °C).

The carbonate reef sediments used in Column A were collected using a coring drill (Engels et al. 2004) from the fringing reef of southern Moloka'i (Table 3.2; Figure 3.2). Reef material from numerous cores up to 75 cm-deep was collected. Disruption and compression of sediment columns during drilling and retrieval meant that sediments retrieved from different depths were mixed. Grain size composition analysis indicated that this sediment was poorly sorted and fairly coarse (Table 3.3). The retrieved sediment included a fine-grained sediment fraction of paste-like consistency, which presumably was generated by the abrasive action of the drill. Its inclusion in Column A during a preliminary experiment (Exp. 2) rendered the reconstructed core functionally impermeable. Therefore, experimental sediment was wet-sieved to remove grains finer than 500 μm before use. Sediment was temporarily stored as necessary in aerated seawater at 4 °C.

The seawater used in these experiments was obtained from the Waikiki Aquarium (Honolulu, Hawai'i). This water is drawn from a 14 m-deep coastal well and treated for aquarium use by aeration to remove sulfide and excess carbon dioxide (the water is essentially free of particulates; Atkinson et al. 1995; J.C. Delbeek, personal communication). Seawater was added to the microcosm without deoxygenating it, since the studied permeable sediments are frequently exposed to oxygen-rich water during high energy events (Falter and Sansone 2000b), and the associated microbiota have been shown to consume it rapidly (Sansone et al. 1990). In case this is a concern, de-aeration or de-oxygenation of the water supplied to deeper portions of the sediment columns may be advisable.

One-way male Luer stopcocks were used as the main sampling ports. Septum-sealed Luer fittings and Mininert valves were used on parallel sampling ports to assess their functionality (see Section *3.2.2.2*). The sediment was mixed in a container to evenly distribute grains of different sizes and was loaded into Column A to form a 100 cm-high sediment column. Column B was filled with previously combusted silica sand to a height of 75 cm. Pump A was programmed to maintain an oscillatory head of height, $h = 11$ cm and frequency, $f = 2$ min^{-1}, and Pump B transferred water from the columns at a rate of 7 mL·min^{-1}, such that the turnover time of the overlying water was approximately 14 h.

Sampling and analyses – Sampling was conducted daily during the early stages of each experiment and at least twice weekly during the late stages. Dissolved oxygen was determined by Winkler titration (Winkler 1888; Hansen 1999), modified to accommodate the small sample sizes. Overlying and pore water samples for oxygen analysis were withdrawn using 10-mL Luer-lock syringes. Immediately after retrieval, each sample was dispensed from the syringe into a 20-mL vial (containing a magnetic stirrer) via a syringe needle, which ensured minimum exchange with the atmosphere. Before stirring, 0.25 mL of 3 mol·L^{-1} $MnCl_2$ and 0.25 mL of 4 mol·L^{-1} alkaline iodide were added to the sample. The sample was stirred for 1-2 s and 0.75 mL of 50 % sulfuric acid was then added to dissolve the precipitate. Using a starch indicator, the solution was titrated with 2.5 mmol·L^{-1} thiosulfate using a digital micropipette. The concentration of thiosulfate, originally 2.5 mmol·L^{-1}, was accurately determined on every analysis date using a potassium iodate standard since it may change with time.

Oxygenation of the sample during sampling and analysis was corrected for by analyzing 2-4 samples from a container of seawater that was deoxygenated by bubbling

with nitrogen gas for 30-45 min. The container was outfitted with a sampling port similar to the one used in these experiments, and otherwise used sampling and analytical procedures identical to those used with the microcosm samples. The average volume of titrant used was taken to represent the amount of oxygen that dissolved into the sample during the sampling and analysis process, and was subtracted from all the samples.

Overlying and pore water samples were analyzed for sulfide (ΣH_2S) using the methylene blue method of Cline (1969). One-milliliter samples were retrieved using a 3-mL syringe already containing 0.5 mL of 0.05 $mol \cdot L^{-1}$ zinc acetate to instantly fix any sulfide present, and stored in plastic scintillation vials at 4 °C for a few days to weeks before analysis. Fifty microliters of a diamine reagent (4 g of anhydrous ferric chloride and 1.6 g of N,N-dimethyl-p-phenylene diamine sulfate in 100 mL of 6 $mol \cdot L^{-1}$ HCl) were added to each sample. After 20 min, 2 mL of deionized water (DIW) were added, and the sample allowed to sit for 15 min before measuring its absorbance at 670 nm on a spectrophotometer. Calibration curves were constructed by analyzing standards with the above procedure. Standards were made by dissolving 0.12 g of $Na_2S.9H_2O$ in 100 mL of deoxygenated DIW to make a 5 $mmol \cdot L^{-1}$ sulfide solution. This solution was diluted to 500 $\mu mol \cdot L^{-1}$ by adding 5 mL to 45 mL of deoxygenated DW, and then aliquots appropriate for the required range of sulfide concentrations were dispensed to scintillation vials containing 0.5 ml of 0.05 $mol \cdot L^{-1}$ zinc acetate, and brought up to a total volume of 1.5 mL with DIW. Standards were stored with the samples and analyzed on the same date.

Microbial cell counts were conducted on 1-mL duplicate pore water samples collected from several depths with sterile 3-mL syringes. Samples were fixed with

glutaraldehyde (final volume concentration = 1 %) and stored at 4 °C until analysis. One set of samples was analyzed using flow cytometry (Monger and Landry 1993), and another set by epifluorescent microscopy (Hobbie et al. 1977; Porter and Feig 1980). In preparation for flow cytometry, 0.8 mL of sample was stained with the DNA stain Hoechst 33342 (Molecular Probes, Eugene, Oregon, U.S.A.) to a final stain concentration of 1 $\mu g \cdot mL^{-1}$, and incubated for 1 h at room temperature in the dark. Samples were analyzed with a Beckman-Coulter Epics-Altra dual-laser flow cytometer (Beckman Coulter Inc., Fullerton, California, U.S.A.) equipped with two argon ion lasers, one tuned to deliver 1 W of 488 nm light and the other, 200 mW of UV excitation. The flow rate of the sample (50 $\mu l \cdot min^{-1}$) was controlled with a Harvard Apparatus syringe pump (Harvard Apparatus, Holliston, Massachusetts, U.S.A.). Fluorescent signals were normalized with 0.5- and 1-μm polystyrene beads (Polysciences Inc., Warrington, Pennsylvania, U.S.A.). For epifluorescent microscopy, 25 μl of 0.2 $mg \cdot mL^{-1}$ 4'-6-diamidino-2-phenylindole (DAPI) (Pierce Chemical Company, Rockford, Illinois, U.S.A.) were added to each 1-mL sample, mixed well and incubated at room temperature for 10 min. A portion (0.9-0.95 ml) of the stained sample was diluted with 5-6 mL of 0.2 μm-filtered seawater, the mixture filtered through a black Isopore 0.2 μm filter (Millipore, Bedford, Massachusetts, U.S.A.), and the filter mounted on a glass slide using immersion oil. Direct cell counts were performed using an Olympus BX51 epifluorescence microscope (Olympus America Inc., Melville, New York, U.S.A.).

Microbial cell counts were also conducted in pore water from Exp. 8, collected as the microcosm was dismantled, as well as on sediments collected at assembly and at dismantling. Sediment samples were treated as follows for cell extraction. The sediments

were washed in Phosphate Buffered Saline (PBS; VWR International, San Diego, California, U.S.A.) to remove the formalin preservative. After adding 5 mL of twice-filtered (0.2 μm) seawater, samples were centrifuged at 10,000 rpm for 1 minute, the supernatant was collected with a Pasteur pipette and discarded, and the process was repeated. After adding 5 mL of twice-filtered (0.2 μm) seawater to each sample, along with a few drops of the dispersant Tween (VWR International), each sample was sonicated 4 times, for 5 seconds each time, in an ice bath, and vortex-mixed between each sonication. Samples were quick-spun by ramping up spinning to 10,000 rpm, at which point the centrifuge was allowed to decelerate to 0 rpm. Lower spinning velocities (1,000, 2,500, and 5,000 rpm) were rejected because the suspensions were deemed too cloudy. The supernatant was removed and treated as for the pore water samples for cell enumeration. The remaining sediment sample was weighed wet and dry using a drying oven at 60 °C to allow normalization of cell counts to the amount of sediment.

3.2.3.4 Carbon dioxide detection and monitoring in overhead gas

The constant need of the microcosm for seawater encouraged the move of the microcosm to Kewalo Marine Laboratory, a facility on the south shore of O'ahu with a continuous seawater supply from a pipe intake at 100 m offshore. The microcosm was set up outdoors in a westward-facing, mostly shaded location (Figure 3.3). However, it was subject to periodic direct exposure to sunlight (approximately between 14:00-17:00) and to temperature variations between day and night, as well as momentary variations due to cloud cover (see results in section *0* for further information). The overall temperature variability was 25 °C ± 3 °C for the duration of the experiments.

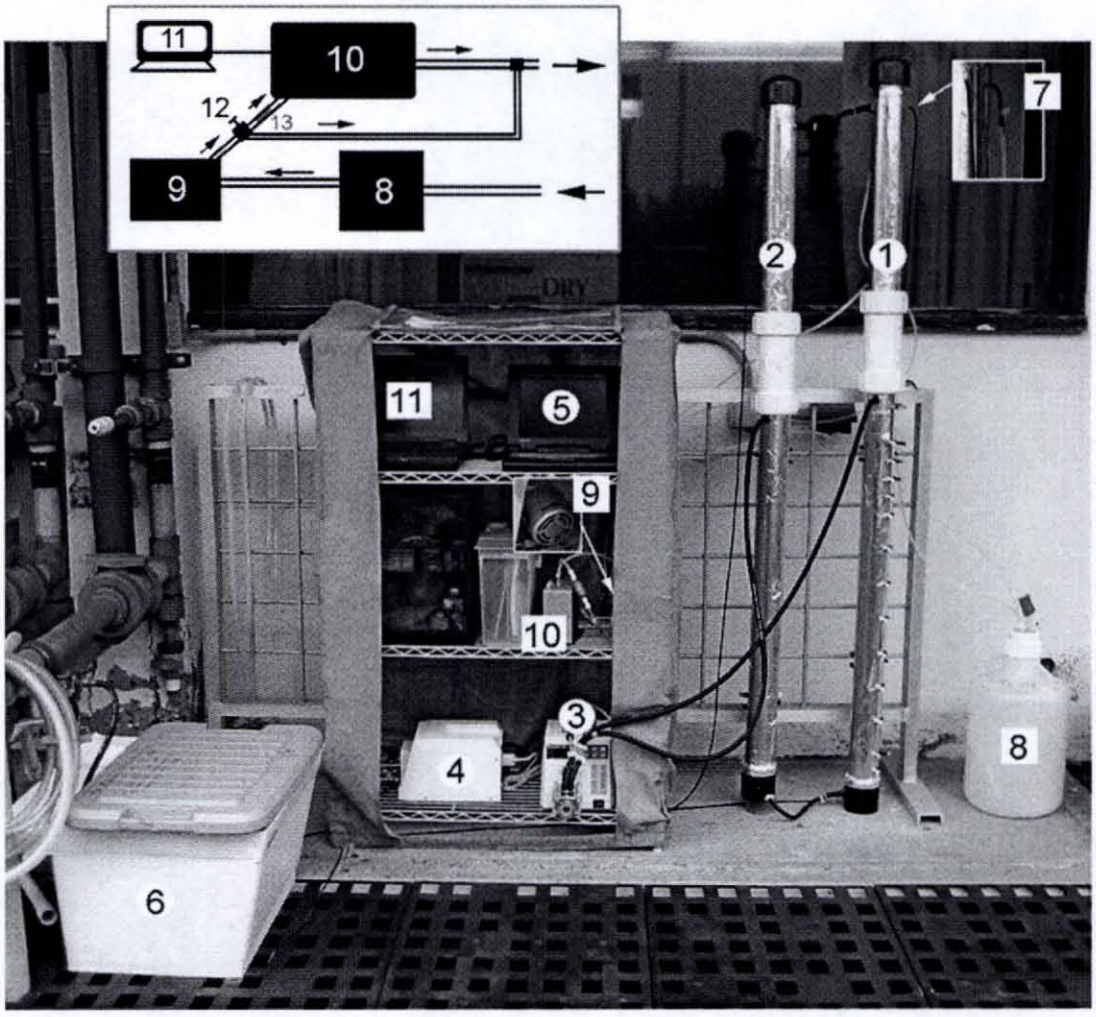

Figure 3.3 The microcosm at Kewalo Marine Laboratory, including the pCO_2 monitoring loop (inset). Legend: 1-Column A, 2-Column B, 3-Pump A, 4-Pump B, 5-Pump-controlling computer, 6-Reservoir, 7-Overhead gas outtake and intake, 8-Gas trap, 9-Gas pump, 10-LI-820 CO_2 detector, 11-LI-820-controlling computer, 12-flow valve, 13-Dryerite column. Not shown: Balston disposable air filter between the Dryerite column and the LI-820. Compare this photograph to Figure 3.1.

The sediment used during Exp. 7 consisted of swash zone beach sand from Kualoa Park, north Kane'ohe Bay, O'ahu, supplemented with fringing reef sediment from south Moloka'i (Figure 3.2). Sediment used in Exp. 8 was obtained by drilling from a patch reef in Kane'ohe Bay, O'ahu, as described in Section *3.2.2.3* (Figure 3.2). Sediment was wet-sieved on site using a 500 μm sieve. Both experiments were conducted under an oscillatory head of $h = 11$ cm and $f = 2$ min^{-1}, and an overlying water transfer rate of 7 mL·min^{-1}, such that the residence time of the overlying water was 14 h. The facility's seawater was treated only by pumping through a settling tank, and directly afterwards was supplied to the microcosm's reservoir without further treatment.

Carbon dioxide was monitored using a LI-820 CO_2 detector (LICOR, Lincoln, Nebraska, U.S.A.). The LI-820 is a non-dispersive, infrared gas analyzer, capable of detecting up to 1000 ppm of CO_2 using a 14 cm optical path. Its operation, standardization and data recording routines are controlled through a Microsoft Windows-based software interface. Prior to use, the detector was calibrated using 0 and 1000 ppm CO_2 gas standards, and was tested frequently with measurements of the CO_2 content of ambient air, which does not deviate significantly from 380 ppm (Fagan and Mackenzie 2007). A CO_2 detection loop was set up to circulate overhead gas from Column A through the LI-820 using a pneumatic pump (see inset in Figure 3.3). The incoming air was treated by passing it through a Dryerite column and a Balston air filter (supplied by LICOR), in that order, which were replaced or restored as necessary. Temperature and pCO_2 were recorded once a minute during the two experiments.

3.2.3.5 Design and materials assessment

Column hydraulics – After weeks of incubation, the occurrence of various processes, such as mineral precipitation and dissolution, biofilm development, and particle trapping and flushing, may cause a shift in the hydraulic conductivity of the columns. Such a shift may affect overlying and pore water exchange and, consequently, material transport rates. The conductivity of the whole system (i.e., both columns in series) was monitored for such a shift during Exp. 8, a three-month long incubation. Specifically, the hydraulic conductivities measured by the pressure gradient relaxation test at the beginning of the experiment, and by the constant head method at two time points 35 days apart during the latter part of the experiment, were compared (see section *3.2.3.1* for methods).

Microcosm gas permeability – The sedimentary oxygen consumption rates reported in the previous section assumed that exchange between atmosphere and microcosm was negligible. That assumption was tested with an oxygen intrusion experiment (Exp. 9). The microcosm components were chemically sterilized with ethanol and assembled as usual. The two columns were filled with filtered tap water to a height of 1.2 m (total volume = 11.1 L). This water was de-aerated by bubbling nitrogen gas at the bottom of the column and exchanging water between the two columns at 200 $mL \cdot min^{-1}$. De-aeration ceased when the water did not produce a yellow solution when fixed for Winkler titration and acidified (after approximately 2 h). The microcosm was then immediately sealed and the pumps programmed to run as in the biogeochemistry and microbiology experiments described in the previous sections. Water was sampled from

the microcosm at regular time intervals and measured for dissolved oxygen by Winkler titration, as described above.

Pumps, tubing, and sampling ports – The durability of the Masterflex pumps, pump heads, and various types of tubing was tested under the experimental conditions, specifically weeks of constant pumping with frequent (one or more per minute) reversals in pumping direction. The performance of various types of the male Luer-lock stopcocks, septum-sealed Luer fittings, and Mininert valves during weeks-long experiments was also assessed. Attention was focused on water leaks and on the coloration of sediment in the immediate vicinity of the ports; different sediment color could indicate different redox conditions due to oxygen intrusion.

3.2.4 Results

3.2.4.1 Microcosm hydraulic characterization

Five of the nine conducted experiments (Exp. 1-4, 8) provided insights in the hydraulic operation of the microcosm, through a combination of pressure gradient relaxation tests and permeametry tests. The results of the hydraulic tests were analyzed with specially prepared mathematical tools, in the form of two modeling routines. Examples of the output of MATLAB routines 1 and 2 are shown in Figure 3.4 and Figure 3.5 and respectively; the results are summarized in Table 3.5. With one exception, the values of h_{adj} (0.01 cm ± 0.36 cm) are well below the maximum acceptable limit (h_{adj} = 2.5 cm), suggesting that the manual recording of water levels is a satisfactory replacement of more precise instruments such as pressure sensors. The exception was Exp. 2, which involved unsieved Moloka'i fringing reef sand. The permeability of this

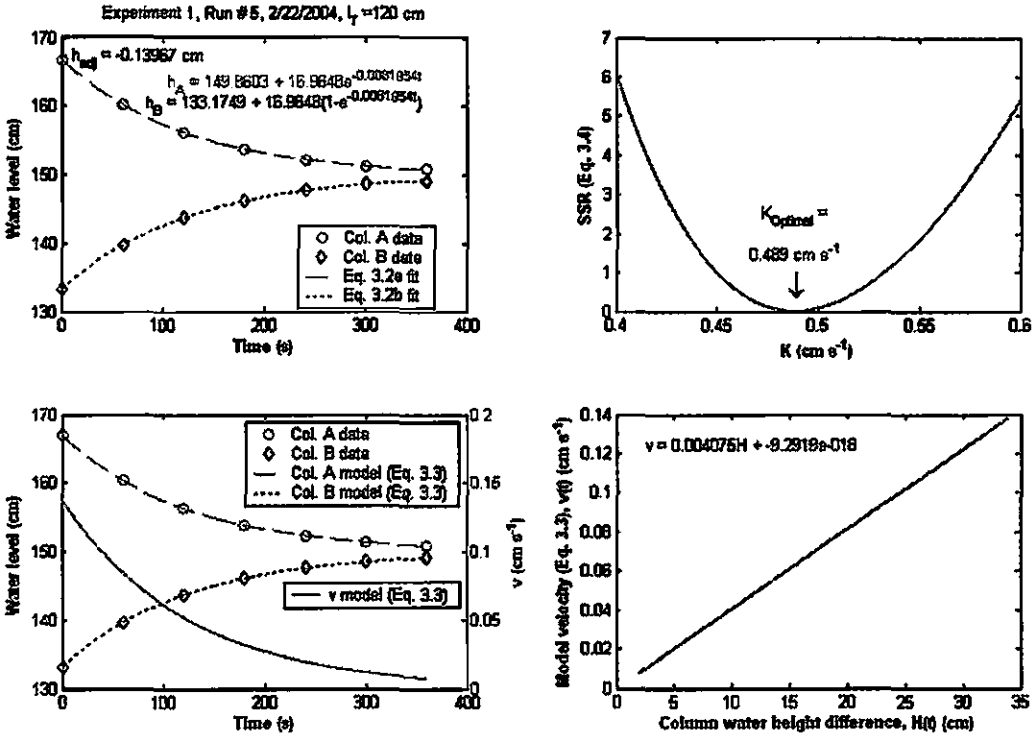

Figure 3.4 Example of the output of MATLAB routine 1, which processes the data from a single relaxation run, in this case run 5 of Exp. 1, to yield the optimal value of total hydraulic conductivity (K_T) and the relationship between flow velocity, $v(t)$, and the height difference, $H(t)$ (see Section *3.2.3.1*). Top left: data fits with Eq. 3.2 and 3.3, and calculation of h_{adj} (Eq. 3.4); Top right: variation of *SSR* within the range of K with which the box model (Eq. 3.5-3.7) was run, and selection of the best K value; Bottom left: output of the box model using the best K value, and variation of v with time; Bottom right: relationship of $v(t)$ with $H(t)$. Note that the significant figures of the values generated by the model output do not necessarily reflect the precision of the various parameters (compare with the values reported in Table 3.5).

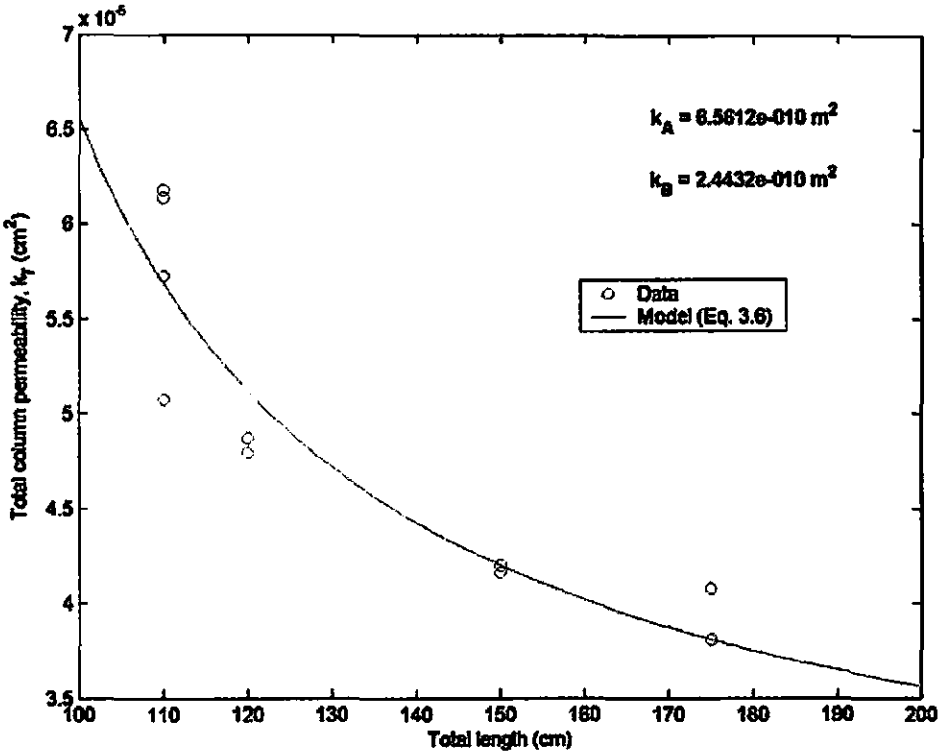

Figure 3.5 Example of the output of MATLAB routine 2, which receives total system permeability values, k_T, as they are generated from routine 1, paired with values of l_T. Routine 2 fits these data to Eq. 3.10 and generates the best estimates for the permeabilities of Column A and B materials (k_A and k_B respectively; see Table 3.5 for summary). This example is for Exp. 1, in which Column A contained beach sand and Column B contained silica sand (Table 3.2). Note that the significant figures of the values generated by the model output do not necessarily reflect the precision of the various parameters (compare with the values reported in Table 3.5).

Table 3.5 Summary of the results of pressure gradient relaxation tests and the assessment of this method for hydraulic characterization of the microcosm system. See Table 3.2 and Table 3.3 for more information about the experiments and microcosm contents.

Exp.		Mean h_{adj}	At maximum l_T:					
No.	n	(cm)	n	l_T (cm)	K_T (cm·s^{-1}) [a]	v/H (s^{-1}) [a]	k_A (m^2)	k_B (m^2)
1	10	-0.05 ± 0.36	2	175	0.40 ± 0.02	0.0023 ± 0.0001	6.6×10^{-10}	2.4×10^{-10}
2 [b]	1	5.55	1	110	0.03	0.0003	1.2×10^{-11}	- [c]
3	6	0.18 ± 0.50	2	172	0.42 ± 0.04	0.0025 ± 0.0002	1.3×10^{-9}	2.6×10^{-10}
4	8	0.00 ± 0.26	2	172	0.68 ± 0.02	0.0040 ± 0.0001	1.4×10^{-9}	4.2×10^{-10}
8	2	-0.15 ± 0.17	2	145	0.61 ± 0.13	0.0042 ± 0.0008	1.1×10^{-9}	- [c]

[a] Values for these parameters are reported as the mean ± SD of n measurements at maximum l_T.

[b] Exp. 2 was terminated soon after assembly because of the very low permeability of the sediment in Column A. Flow of water through the whole microcosm was extremely slow, as is indicated by the very low K_T and v/H values, while fits during routine 1 failed to converge. Although the sediment was still permeable by definition (i.e., $k > 10^{-12}$ m^2), it was deemed to be operationally non-functional for this particular microcosm application. This is primarily due to the length of the sediment column.

[c] Due to the lack of runs at different l_T values, Eq. 3.10 could not be used. Instead, the average k_B from Exp. 1, 3, and 4 (3.1×10^{-10} m^2) was used to calculate k_A by re-arranging Eq. 3.10 as follows:

$$k_A = \frac{l_A}{\frac{l_T}{k_T} - \frac{l_B}{k_B}}.$$

sediment column was deemed too low for this particular microcosm application, and the experiment was terminated after a brief geochemical assessment. Replicate estimates of the silica sand permeability using data from Exp. 1, 3, and 4 were quite similar (Table 3.5) and yielded an average of 3.0×10^{-10} m^2 $\pm$ 9.5×10^{-11} m^2.

Estimates of the microcosm K_T during Exp. 8 by both methods are shown in Table 3.6. Although a trend of very slight increase of mean conductivity with time seems evident, this trend is not statistically significant, due to daily measurement variability. Unfortunately, variability in the values obtained using pressure gradient relaxation tests during this experiment was unusually large (compare with other variabilities in K_T on Table 3.5). However, comparing the K_T standard deviations of Exp. 1, 3 and 4 (Table 3.5) with those obtained by constant head permeametry in Exp. 8 (Table 3.6), one sees that the two methods yield equally replicable and variable estimates of hydraulic conductivity and permeability. Therefore, pressure gradient relaxation tests can be used to estimate the hydraulic conductivity, K, (and consequently the permeability, k) of the sediment columns in the microcosm, if proper permeability tests cannot be performed. One such occasion would arise if a measurement of permeability is required during a microcosm experiment. A constant head permeability test would essentially flush out a significant portion of the pore water and its replacement with oxygenated overlying water, thus disrupting the biogeochemical conditions in the sediment column. Relaxation tests, on the other hand, can yield a reliable enough estimate, without a significant exchange of water between the overlying water and pore water reservoir.

Table 3.6 Estimates of K_T (mean ± standard deviation) during Exp. 8 in 2005 using two methods. A linear regression of the mean K_T vs. time indicated a slight change (K_T = $0.00043t + 0.62$, $r^2 = 1.00$, n =3). However, single-factor ANOVA comparison of the three sets of K_T values showed that they are not statistically different (p = 0.74, $F_{1,5}$ = 0.32).

Date	t (d)	Method	n	K_T (cm·s^{-1})	k_T (×10^{-10} m^2)
March 24	0	Pressure gradient relaxation tests	2	0.61 ± 0.13 [a]	5.8 ± 1.2
May 25	62	Constant head permeametry	4	0.64 ± 0.03	6.1 ± 0.3
June 30	98	Constant head permeametry	3	0.65 ± 0.01	6.2 ± 0.1

[a] From Table 3.4.

3.2.4.2 Enhanced transport

The results of the initial experiment (Exp. 1) are shown in Figure 3.6. Fluorescein was undetectable at 5 cm during the 8 h-long pre-pumping period. After pumping was initiated, the penetration of fluorescein to successive depths was monitored until it reached the bottom of the column after 28 h. The tracer data unequivocally demonstrate the enhanced exchange of overlying water with sediment pore water during pumping. Tracer penetration speeds (Eq. 3.14) and displacement coefficient values (Eq. 3.15) calculated from the concentration-time curves in Figure 3.6 were 2 to 3 orders of magnitude higher than the values generated for the molecular diffusion model at z = 2 cm (Table 3.7).

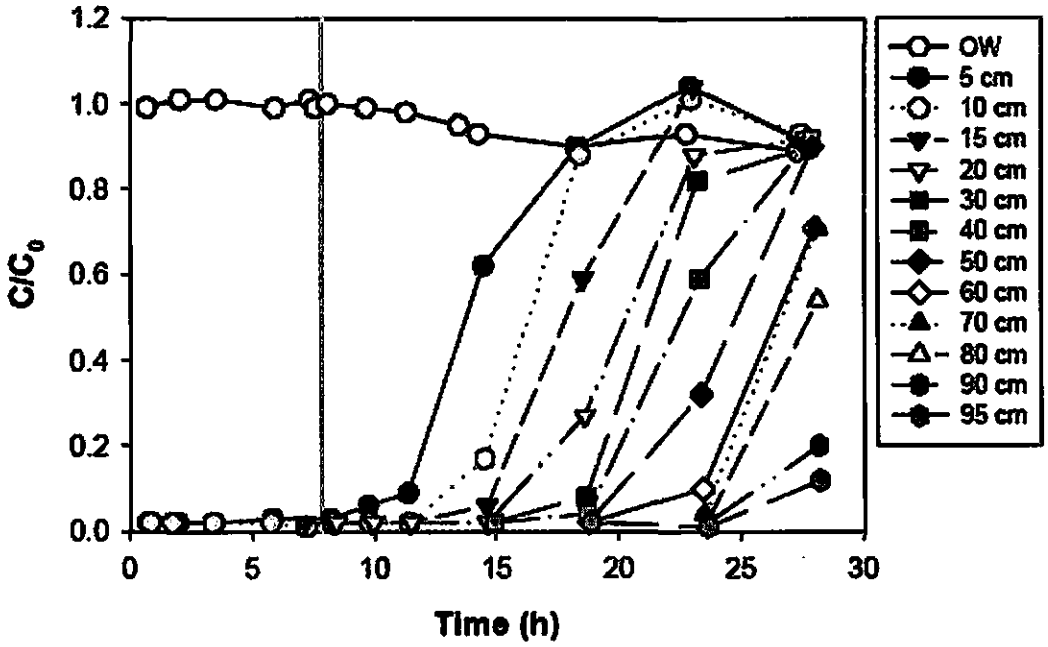

Figure 3.6 Fluorescein concentration vs. time at successive depths during the initial, proof-of-concept experiment (Exp. 1). Fluorescein concentrations (C) have been normalized to the initial concentration of the dye in overlying water (C_0). The time of the initiation of pumping is marked by the thick grey line.

The results of the control and active pumping experiments (Exp. 5 and 6 respectively) are shown in Figure 3.7 and Table 3.7. The best fit of Eq. 3.13 to the control data (Exp. 5) has a D_0 value of 9.7×10^{-2} $cm^2 \cdot h^{-1}$, which is approximately 5 times greater than the reported values of the molecular diffusion coefficient of fluorescein (Kaiser and Maurice 1964; Soeller et al. 2003). Also, the calculated displacement coefficient, D_p, for Exp. 5 is approximately 2.7 times greater than that calculated using the average theoretical value for the D_0 of fluorescein ("Model," Table 3.7).

However, the discrepancies between theoretical and calculated displacement coefficients in Exp. 5 are dwarfed by the difference in dye migration between the cases of active pumping (Exp. 6) and passive diffusion (Exp. 5). Due to the unanticipated high penetration speed, the arrival of the dye at depths 29 and 49 cm was not recorded satisfactorily. Based on the data from a depth of 69 cm, values for v_m and D_χ under active pumping conditions were 2 to 4 orders of magnitude greater than those under molecular diffusion-controlled conditions (Table 3.7). The calculated v_m value, 19 $cm \cdot h^{-1}$, at $z = 69$ cm, falls within the range of 6-53 $cm \cdot h^{-1}$ measured by Reimers et al. (2004b) in surface sediments of the Middle Atlantic Bight.

A substantial proportion of the discrepancy between anticipated (through theory) and measured displacement of dye in Exp. 1, 5 and 6 is due to pore water sample removal, which could induce dye penetration in excess of that caused by the physical forcing. Sample removal rates during Exp. 1 were 2.7 and 3.7 $mL \cdot h^{-1}$ during the static and pumping phases respectively. These rates translated to sampling-induced dye penetration speeds of 0.11 and 0.15 $cm \cdot h^{-1}$ for the static and pumping phases respectively, based on a porosity of 0.52 (Table 3.3) and a sedimentary surface area of 46.32 cm^2. These

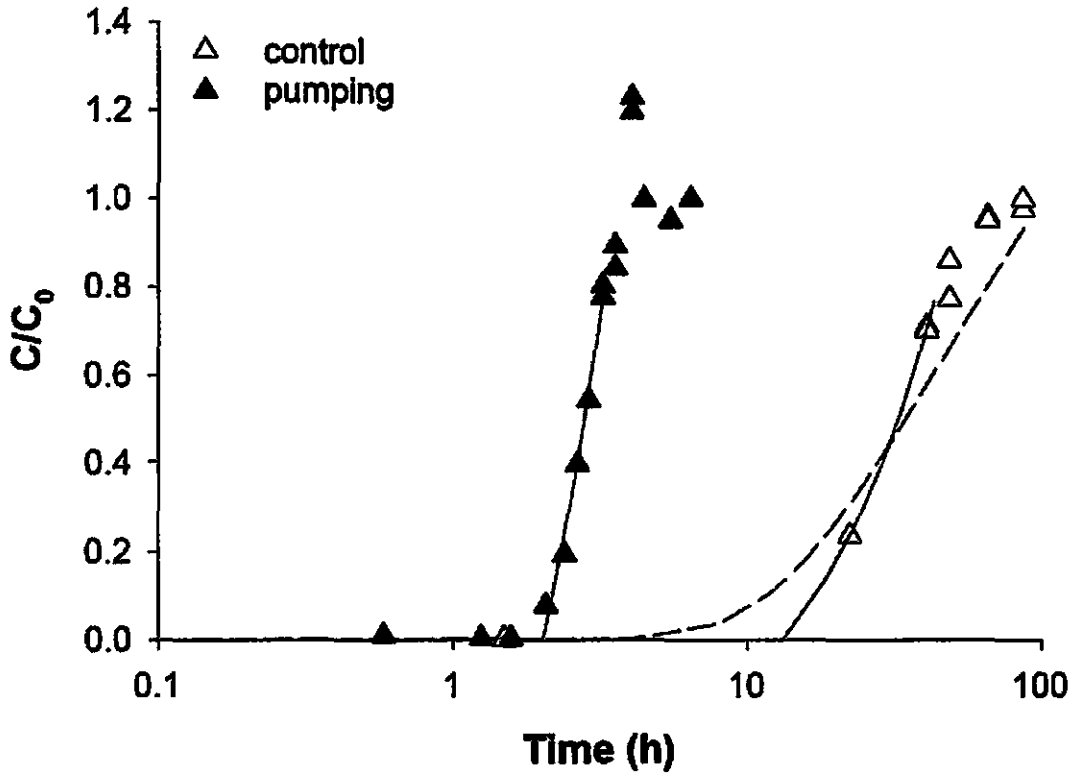

Figure 3.7 Fluorescein concentration vs. time for control (z = 2 cm) and active pumping (z = 69 cm) experiments (Exp. 5 and 6 respectively). Fluorescein concentrations (C) have been normalized to the initial concentration of the dye in overlying water (C_0). Solid lines indicate best fits of the data in the linear portions of the curves. These fits are used to estimate the time lag before breakthrough (t_D) and, ultimately, D_χ. The dashed line indicates the best least-squares fit to the control concentration-time data using Eq. 3.13, which results in an estimated D_0 value of 9.7×10^{-2} $cm^2 \cdot h^{-1}$.

Table 3.7 Results of data analyses for Exp. 1, 5 and 6, and molecular diffusion model calculations. The parameters shown are the depth of observation, z, the tracer peak arrival time, t_M (Eq. 3.14), the tracer breakthrough time, t_D (Eq. 3.15), the tracer migration rate, v_m (Eq. 3.14), and the displacement coefficient, D_χ (Eq. 3.15). The Pumping/Control ratio was calculated by dividing the values for v_m and D_χ of the active pumping experiment by those of the control experiment. Transport by molecular diffusion was modeled using Eq. 3.13, the average reported value for D_0 of fluorescein (1.73×10^{-2} $cm^2 \cdot h^{-1}$) and $\theta^2 = 2.195$.

Exp. No. (description)	**z (cm)**	**t_M (h)**	**t_D (h)**	**v_m ($cm \cdot h^{-1}$)**	**D_χ ($cm^2 \cdot h^{-1}$)**
1 (Initial)	-	-	-	0.48-3.5	5.8-240
5 (Control)	2	87.3	13.3	0.023	0.15
6 (Active pumping)	69	4.08	2.0	17	1200
Pumping/Control ratio	-	-	-	*740*	*8000*
Modeled diffusion	2	-	36.4	-	0.055

sampling-induced penetration speeds could account for a significant fraction (4-31 %) of the total tracer vertical migration rates, v_m, calculated from the data (Table 3.7). After the experience of the initial experiment (Exp. 1), sampling-induced penetration speed during the control experiment (Exp. 5) was greatly minimized by drawing very few samples (14) of smaller volume (1 mL) over the course of the experiment (141.5 h). Based on a porosity of 0.45 (Table 3.3), sampling-induced penetration speed was calculated at 0.005 $cm \cdot h^{-1}$, which would could account for only 10 % of the observed v_m (Table 3.7). Other possible explanations for higher-than-theoretical values include localized suction of pore water during sample removal and a lower actual value of tortuosity. During the active pumping experiment (Exp. 6), the sampling-induced tracer penetration speed (0.06 $cm \cdot h^{-1}$, based on 29 1-mL samples drawn over 23.8 h, assuming $\varphi = 0.45$) was only 0.3 % of the observed v_m (Table 3.7), and demonstrated the diminishing effect of the sampling methodology with increasing pumping activity. Regardless, the methodology of these conservative tracer experiments, including sample volume and sampling frequency, should be modified to limit the impact of sampling on the measured process as much as possible (see Section *3.3.2.3* for a solution).

3.2.4.3 Biogeochemistry and microbiology

Dissolved oxygen penetration depths in the incubated sediments were 10-50 cm (Figure 3.8a). These values compare favorably with depths of 15-50 cm observed by Falter and Sansone (2000b) in patch reef sediments. It is noteworthy that such profiles were attained very soon (hours-days) after experimental set-up with aerated (i.e., oxygen-rich) water. In view of the previously reported high oxygen demand in such sediments

(Sansone et al. 1990), this is hardly surprising. It should also be mentioned that the overlying water oxygen concentration in Figure 3.8a (97 $\mu mol \cdot L^{-1}$) was lower than that in the reservoir supplying the microcosm (155 $\mu mol \cdot L^{-1}$). I interpret this deficit as indicating that microbial populations in the sediment column and the silica sand column were consuming oxygen at a rate not compensated by the overlying water turnover rate during the experiments. The rate of O_2 consumption was estimated at (155-97) $\mu mol \cdot L^{-1} \times 7$ $mL \cdot min^{-1}$ (the overlying water turnover rate) $\times$ 60 min = 24 $\mu mol \cdot h^{-1}$, or 62 $mmol \cdot d^{-1} \cdot m^{-2}$, which lies in the upper end of the range of previously reported values for permeable sediments (Precht et al. 2004; Reimers et al. 2004b; Polerecky et al. 2005; Rusch et al. 2006). This observation highlights the need to maintain a minimum turnover rate of overlying water to maintain oxygen saturation in the overlying water. In turn, increasing the turnover rate suggests an increased demand for seawater by the microcosm and sets an upper limit on the time needed to manipulate reservoir water, if this is needed. The calculation above also demonstrates the ability to easily determine oxygen consumption, if the consumption of oxygen by the silica sand column is known. Also, such flux measurements require that exchange of gases between the microcosm and the surrounding atmosphere is negligible or known (this issue is addressed in Section *3.2.4.5*).

Free pore water sulfide was detected at levels between 1 and 6 $\mu mol \cdot L^{-1}$ (Figure 3.8a). These levels agree with those observed in a variety of coral reef-associated lithified frameworks (1-10 $\mu mol \cdot L^{-1}$) (Sansone et al. 1990) and fore-reef settings (3-16 $\mu mol \cdot L^{-1}$) (Tribble et al. 1990)

Cell abundances were measured in pore water from two experiments, Exp. 4 and 8 (Figure 3.8b-c). However, it is not clear what these abundances represent. Grain-surface biofilms and matrices, many of which can be released by microbes themselves, ensure that most of the population remains attached on the sediment grains (e.g., Findlay et al. 1992). These abundances ranged between 10^5-10^6 cells·mL^{-1} in sieved Moloka'i fringing reef sediment (Figure 3.8b), and between 1×10^4-3×10^4 cells·mL^{-1} in sieved O'ahu patch reef sediment (Figure 3.8c). The difference between the two sediments can perhaps be explained by differences in the grain size distribution of the unsieved sediments (Table 3.3). Moloka'i fringing reef sediment was finer and more poorly sorted than O'ahu patch reef sediment, and these properties have been connected to organic matter content and cell abundances (e.g., Hargrave 1972; Dale 1974). Even though these sediments were sieved prior to use in the microcosm, the relative properties of bulk sediment perhaps carry over to the coarser sediment grains and are reflected in such analyses. At this point, this is pure speculation since nothing is known about grain interactions in such poorly sorted sediments.

Both pore water (Figure 3.8c-d) and sediment-extracted cell profiles (Figure 3.8d) generally displayed a decreasing trend with increasing depth at the end of the experiments. Since these sediments were incubated with non-filtered sea water for the duration of the experiments, they may have been supplied with organic matter that presumably was mostly concentrated at or right below the SWI. Therefore, surface sediment populations are supplied with enough excess organic material to grow detectably above the original variability in cell abundances, e.g., 2.2×10^{-5}-6.5×10^{-5} cells·mL^{-1} at the start of Exp. 8 (Figure 3.8d). This trend of decreasing abundance with

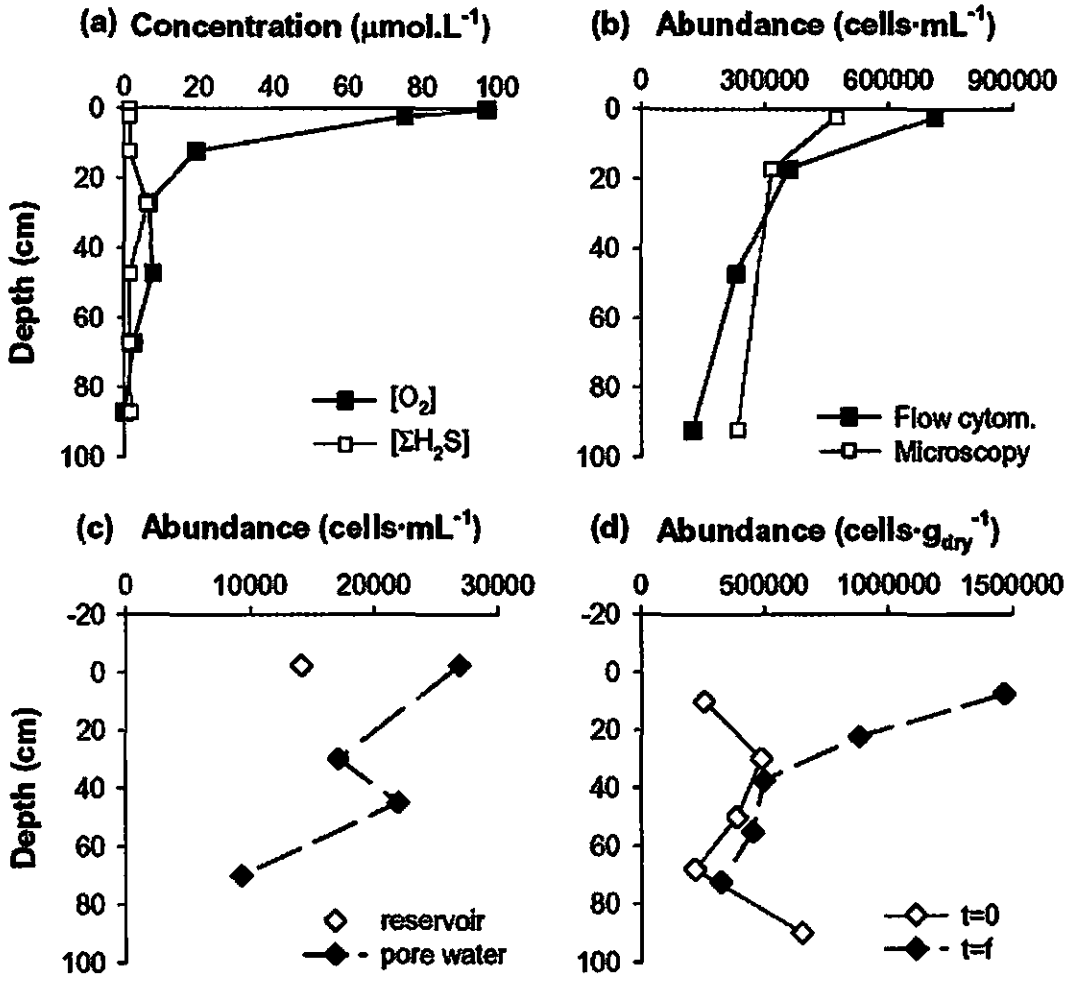

Figure 3.8 Typical profiles of measured parameters during carbonate reef sediment microcosm experiments: (a) typical profiles of dissolved oxygen and sulfide (Exp. 4); (b) typical pore water microbial abundance profiles (Exp. 4) measured by flow cytometry and epifluorescence microscopy; (c) typical pore water microbial abundance profiles (Exp. 8) measured by epifluorescence microscopy; and (d) sediment grain microbial abundance profiles (Exp. 8) at the start (t=0) and the end (t=f) of the experiment, measured by epifluorescence microscopy.

increasing depth has been recently reported for Kane'ohe Bay reef sediments (Sørensen et al. 2007), as well as in other sandy sediments (e.g., Meyer-Reil 1986; Rusch et al. 2003). However, recent measurements in Kane'ohe Bay sediments revealed highly variable trends in cell abundance with depth, including mid-depth minima, mid-depth maxima, increases with depth and decreases with depth (A. Rusch, personal communication).

It should be noted that the abundances recorded in the microcosm are approximately two orders of magnitude lower than those reported by Sørensen et al. (2007) in carbonate reef sediments. Since the microcosm cell counts were performed, research has shown that carbonate sediments have a much rougher surface than silicate sediments, providing refuges for microbes (Wild et al. 2006). Thus, additional extraction treatment (Wild et al. 2006; A. Rusch, personal communication) that was not used at this stage was incorporated in all future measurements.

3.2.4.4 Carbon dioxide detection and monitoring

Data collected during Exp. 7 (Figure 3.9) indicated that the pCO_2 in the overhead gas of the microcosm is at least 20 ppm higher than atmospheric levels, measured at 380 ppm with the LI-820 detector before the experiment. Moreover, a daily periodic cycle was observed, with elevated readings in the afternoon hours (15:00-18:00) which later dropped to the lowest levels measured. The afternoon hours which registered the highest readings coincided with periods of direct sunlight in the area of the microcosm (see section *3.2.3.4*). This cycle underlay a pattern of seemingly irregular and unpredictable fluctuations of pCO2, ranging from a few ppm to 50 ppm (Figure 3.9).

To explore this pattern further, longer pCO_2 records were obtained during Exp. 8. One such record is shown in Figure 3.10a. The following features were observed:

a) The daily pattern of peaks during the afternoon hours, observed during Exp. 7, was also present during Exp. 8. A detailed look at one such daily cycle (Figure 3.10b) shows that pCO_2 peak periods underlay smaller scale variations.

b) This pattern occasionally coincides with variations in instrument temperature over minute-to-hour-scales (see section *3.2.3.4*).

c) The baseline pCO_2 reading varies according to the integrity of the sampling loop. Upon assembly on March 24, pCO_2 climbed rapidly to a baseline reading of 500-550 ppm (much higher than atmospheric values of 375-380 ppm, Fagan and Mackenzie 2007). On March 29, a partial dissembling of the sampling loop (to replace the Dryerite column) was accompanied by an immediate baseline shift: from 490-530 ppm to 390-420 ppm (closer to ambient).

These observations are an initial indication that this microcosm, as constructed at the time, was partly capable of containing gases with partial pressures higher or lower than atmospheric, and that these partial pressures were susceptible to various perturbations that are easily detectable by an instrument as sensitive as the LI-820. One such regular perturbation, the pCO_2 increases during the afternoon hours, may have occurred due to actual pCO_2 fluctuations in the overhead gas due to heating of the various microcosm components in the afternoon hours. To investigate this further, I recorded the temperature of various microcosm components during the afternoon period, while recording pCO_2 using the LI-820 detector. To record the temperature of the gas trap-overhead gas, overlying water, and pore water at 90 cm depth, I used a Digi-sense

thermocouple thermometer (Cole-Parmer, Vernon Hills, Illinois, U.S.A.). I also recorded the ambient temperature and the water reservoir temperature using a regular mercury thermometer.

The results of this experiment are shown in Figure 3.11. With the exception of the water reservoir, all components underwent changes of several degrees during the monitored time period. This is especially true of air circulating between the gas trap and the overhead space of the microcosm, which appears to co-vary with its pCO_2 content (Figure 3.10), and is also very sensitive to illumination shifts due to passing clouds, as indicated by the error bars. The co-variation of temperature and pCO_2 in the overhead gas over the period of observation confirms that there could be a pressurization effect on gas concentrations due to heating during the afternoon hours.

A more disconcerting observation is the drop in the microcosm pore water temperature at 90 cm depth early in the run (Figure 3.11). My sole explanation for this cooling is the rearrangement of water masses in the microcosm as an afternoon progresses and as differential heating of the different parts of the microcosm system takes place. This would affect the physical transport controlled by the pumps and the exchange rates of material between overlying and pore water, rendering experimentation with this set-up unreliable and unfeasible.

Additional evidence for the problematic status of this design's ability to detect and monitor overhead gases was provided by measurements of pCO_2 during induced changes in the volume of overlying water, and consequently overhead gas. Variation in volume was achieved by constricting the outflow tubing (Figure 3.1) and increasing the rate of water supply to the microcosm through the inflow. The change in water level was

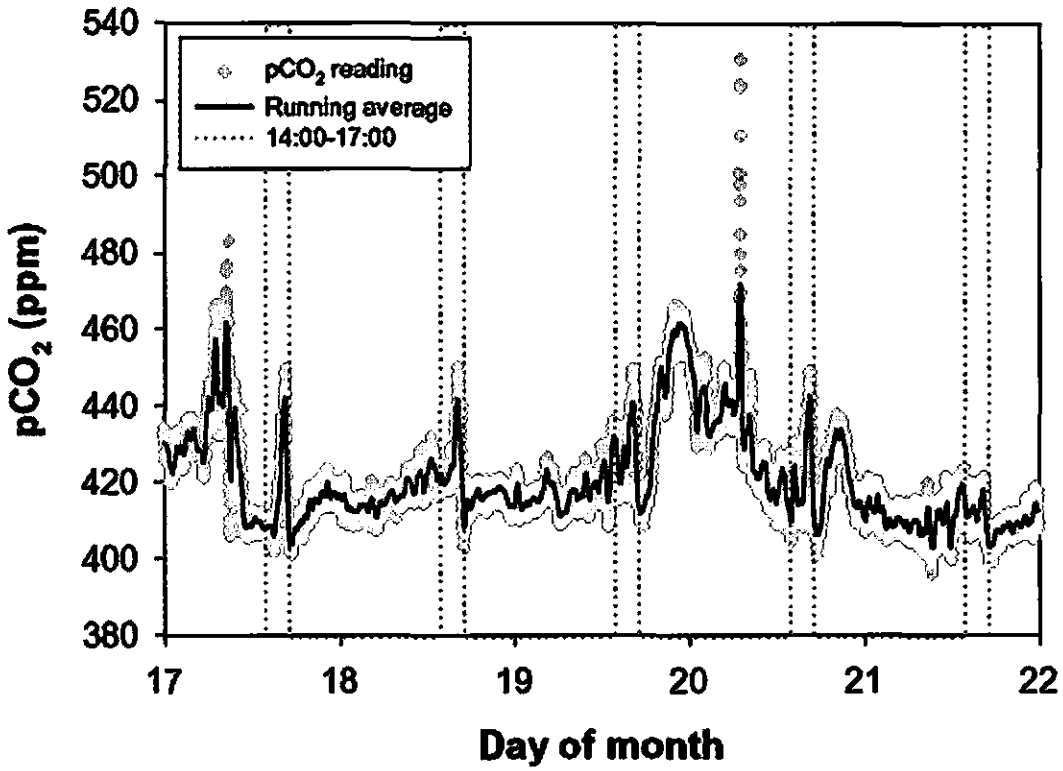

Figure 3.9 The pCO_2 record in the overhead gas of the microcosm during Exp. 7. Readings were taken at 1-min intervals. The data are overlain with a 30-minute running average. The daily time interval of 14:00-17:00 h is enveloped by the dotted lines. It corresponds to the period of direct sunlight (see section *3.2.3.4*) in the area of the microcosm and coincides with abrupt shifts in pCO_2 readings, overlying a more widely fluctuating record. Atmospheric pCO_2 was measured by the detector before this experiment at 379-381 ppm.

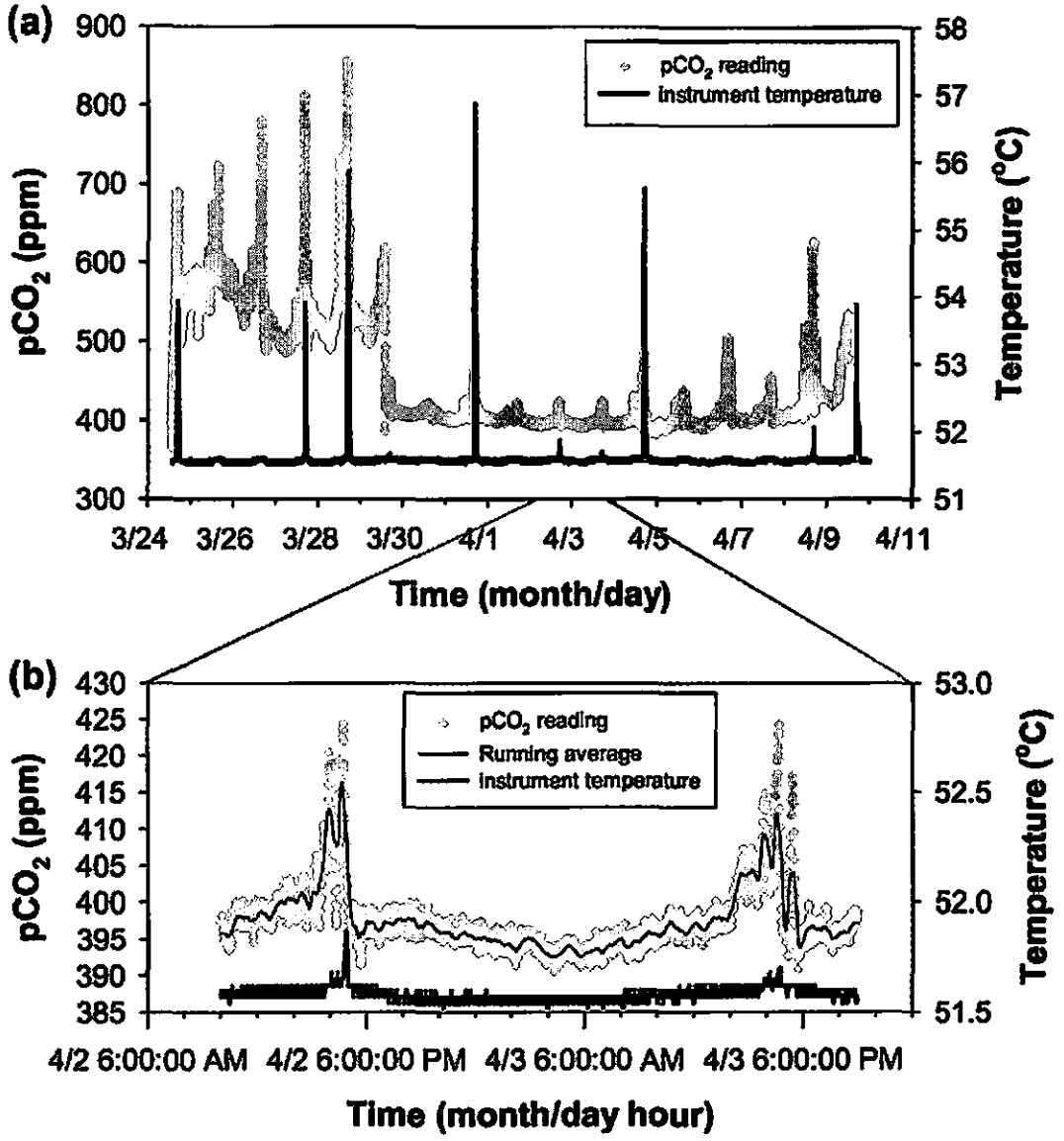

Figure 3.10 (a) The CO_2 record in the overhead gas of the microcosm and the instrument temperature during Exp. 8. Readings were taken at 1-min intervals. Note the coincident pCO_2 and temperature spikes and the irregularity with which the latter occur, (b) A detail of the record in (a). A running average of the pCO_2 data over 30-min intervals is also shown. Note the complexity of the pCO_2 spikes.

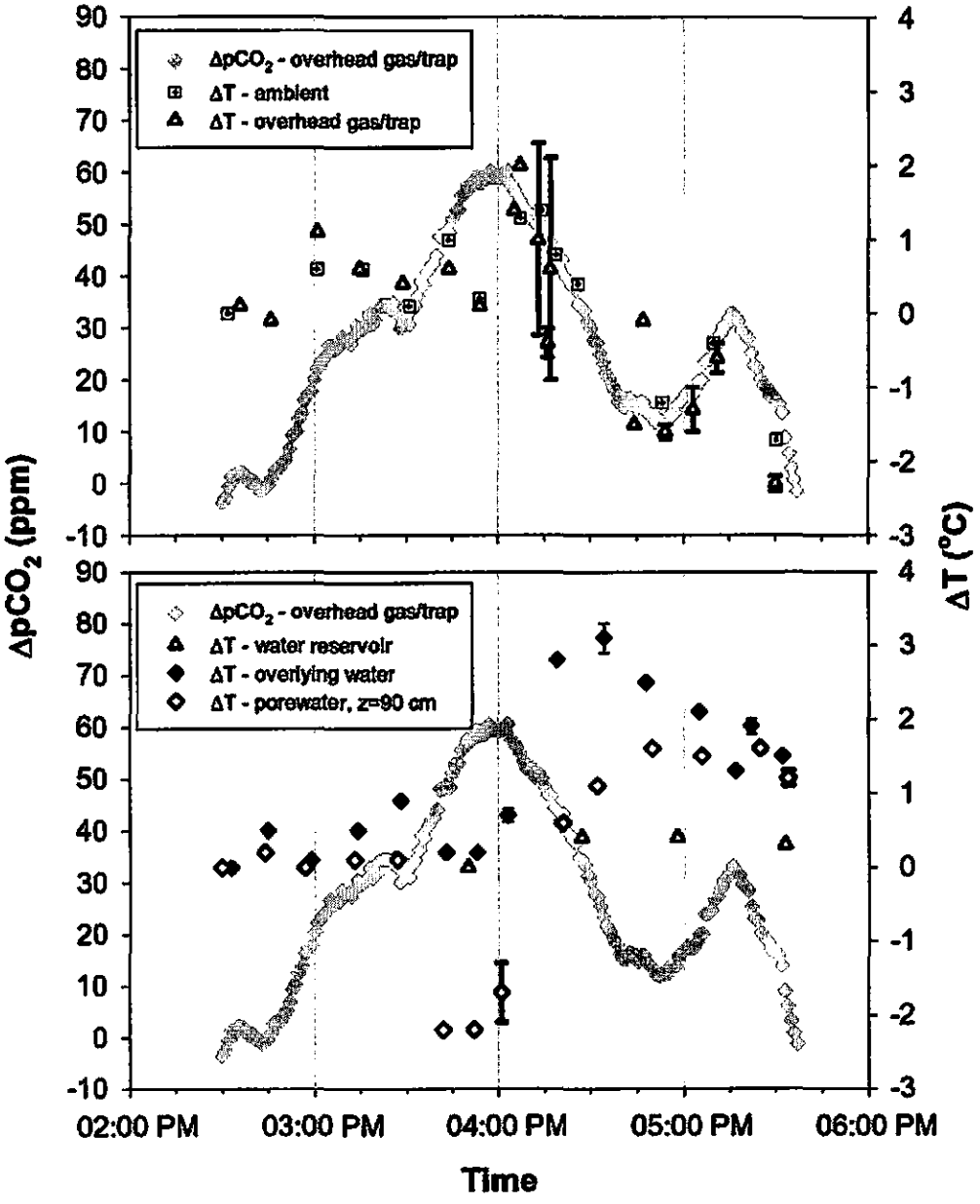

Figure 3.11 Temperature changes in various microcosm components during the afternoon of April 7th, 2005, superimposed on changes in overhead gas pCO_2. Data are shown on two plots for greater clarity. Error bars indicate the range of values recorded during a single minute. These second-to-second fluctuations correlated well with illumination changes due to passing clouds.

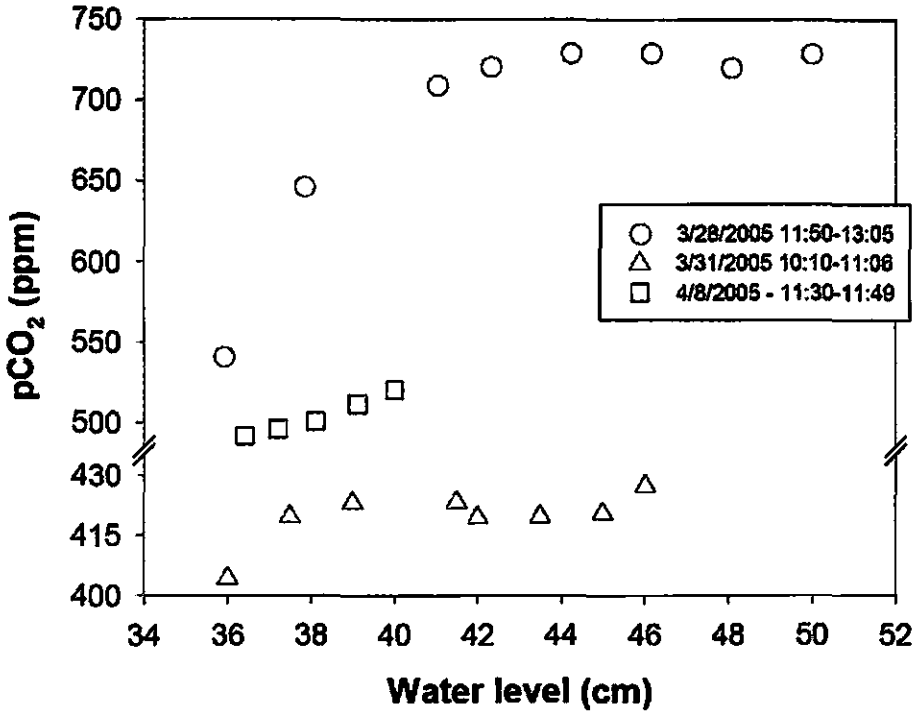

Figure 3.12 Changes in pCO_2 vs. overlying water level on three separate dates during Exp. 8. A rise of 1 cm in water level equals a reduction of 92.6 cm^3 in overhead gas volume (based on a microcosm column cross-sectional area of 46.3 cm^2).

similar to fluctuations during oscillatory pumping (10-15 cm). This test was carried out on three separate dates, and the results are shown in Figure 3.12.

Assuming that the recorded pCO_2 changes during these short time intervals are – for the most part – the combined result of compression of overhead gas and partial release of this pressure through the existing vent, they are not easily predictable. While in all three cases, the overall effect of decreasing volume is an increase in pCO_2, this happens at varying rates and patterns. These rates and patterns appear to be related to the

average water level, to the starting pCO_2, and to variations in temperature during the measurements (although the latter were relatively stable during these readings).

Resolving the influences of each of these individual parameters on overhead gas pCO_2 posed a technological/logistical problem of the microcosm design that could not be solved with the instrumentation and resources available at the time. It is important to note the significance of these effects in case, for example, variation in temperature during experimentation is desirable, since such variations are the norm in nature. The construction of the microcosm in a temperature-controlled room and the variation of temperature during an experiment should be preceded by the careful examination of the effects of this temperature variation on different parts of the microcosm and the determination of the impact on the microcosm operation.

3.2.4.5 Design and materials assessment

Column hydraulics – The hydraulic conductivity of the whole system was measured at three time points, several weeks apart from each other, during Exp. 8. As previously discussed (see Section *3.2.4.1*; Table 3.6), although a slight increase in mean hydraulic conductivity was observed (6.6 % over 98 days), the difference between the measurements on those three days was statistically insignificant. Nevertheless, these results demonstrate that column hydraulic conductivity could be affected by long-term incubations, and should be monitored when lengthy experiments are conducted.

Microcosm gas permeability – During the oxygen intrusion experiment (Exp.9), dissolved oxygen concentrations in the sealed microcosm increased at a rate of 1.6 $\mu mol \cdot L^{-1} \cdot d^{-1}$ after degassing, corresponding to 19.5 $\mu mol \cdot d^{-1}$ in the 12.0 L of water in the

microcosm. At experimental temperatures (25 °C ± 3), it would take 4-5 months for this water to reach saturation with respect to oxygen. The measured rate of oxygen intrusion is not significant when compared to the measured overlying water-to-sediment O_2 fluxes of 576 μmol·d^{-1} reported for Exp. 4 (3 % in this case). Therefore, for practical purposes, gas impermeability of the microcosm can be safely assumed, but the assumption must be tested every time considerable design or material modifications are made that could compromise the permeability of the microcosm significantly.

Pumps and tubing – The pumps were capable of running continuously for at least 30 d without problems. During this period, Pump A was reversing direction four times per minute and pumping a total volume of 2 L·min^{-1}. The Masterflex Standard pump heads were preferable to the Easy-Load II pump heads because they caused less wear of the tubing, resulting in longer tubing life. The original tubing selection, Masterflex silicon, was rejected due to high gas permeability, translucence and, most importantly, only a tenth of the tolerance of Norprene to abrasion, which resulted in rupturing every 2-3 d. The lifetime of Norprene tubing under the pumping conditions described for Pump A was at least 25 d. The tolerance of the tubing used in Pump B was not as critical since its pumping rate (7-15 mL·min^{-1}) was very close to the lower end of its specifications. One problem with Norprene was the release of shavings from its inner wall during the first several hours of operation. This problem was successfully minimized by using a new section of tubing for 48 h to pump water through a carboy. The release of shavings stopped after this period of time and the treated sections could be safely used in incubations.

Sampling ports – The mechanical performance of the male Luer-lock stopcocks was satisfactory. However, this method of sampling may pull water along the inner wall of the column, thus bypassing the interior of the sediment column (a wall or edge effect) (e.g., Huettel and Gust 1992a) . The "dead" volume of the Luer-lock stopcocks (0.5 mL) may also be an issue with sample volumes smaller than 1 mL. When sampling, I avoided collecting old water contained in the stopcocks by allowing 2-4 drops of pore water to pass through and flush the sampling ports. I found that the use of either septum-sealed Luer fittings or septum-containing valves (e.g. Mininert, VICI Precision Sampling, Baton Rouge, Louisiana, U.S.A.) alleviated both of these concerns, although the septa must be replaced after several weeks of intermittent sampling.

3.2.5 Discussion and conclusion

The evaluation experiments demonstrated that:

a) the method of physical forcing employed is capable of inducing enhanced exchange between the overlying water and the pore water in incubated sediments.

b) the microcosm can be sampled non-destructively during experiments for pore water; however, sample removal rates during fluorescein tracer experiments could account for a non-negligible fraction of the measured enhanced transport rates, thus interfering with the determination of enhanced transport relative to molecular diffusion.

c) the composition of the overhead gas is very sensitive to pressure and temperature changes that must be taken into account if changes in composition are to be interpreted geochemically.

This microcosm makes the study of biogeochemical cycling in permeable sediments possible, by allowing mass balance calculations of dissolved species during experiments (an example for dissolved oxygen uptake was given in Section *3.2.4.3*). A major impediment in attributing changes in overlying water chemistry to the live sediment incubated in Column A is the changing biogeochemistry of silica sand in Column B during experiments. Iron contained in this sand was routinely observed to change in color from orange-red to grey-black during experiments, in what is presumably a reduction due to the presence of dissolved sulfide in pore water. The issue of redox changes in Column B may actually be more complex, since iron cycling frequently affects phosphorus (a major nutrient) cycling directly (Ruttenberg 2001). The shift in silica sand activity during experiments may be further aggravated by the very likely colonization and build-up of microbial populations from the "live" sediment column (e.g., Findlay et al. 1992), despite being originally sterilized by combustion. This change in activity was not monitored by this design and posed a significant problem for the use of the microcosm for biogeochemical investigations. The removal of the silica sand column would greatly improve this method, by isolating the "live" sediment column as the cause of observed biogeochemical changes in the microcosm.

3.3 An improved microcosm design

3.3.1 Introduction

The unknown effects of the changing biogeochemical character of the silica sand in Column B during experiments forced a re-assessment of the microcosm design. The

removal of silica sand required its replacement with a hydraulically active but chemically impervious barrier. The chosen replacement was a five-layer-coextruded plastic membrane, DuraShield 45, developed and mass-produced by the Scholle Corporation for the food industry (Scholle Packaging Inc., Northlake, Illinois, U.S.A.). This membrane is an evolution of a three-layer-coextruded membrane previously used in this research field. In a study by Malan and McLachlan (1991), the latter replaced the rigid tops of benthic chambers to allow the overlying water volume to change when a sample was removed. The membrane is both gas-impermeable and flexible, matching exactly the requirements for its application to the microcosm.

It was preferable to place the membrane fairly low in Column B in order to minimize the volume of microcosm "bottom water" (the water contained beneath the meshed stoppers in the bottom caps, Figure 3.1). The pool of "bottom water" may create pore water concentration gradients of solutes, thus distorting solute profiles. The smaller its volume the smaller the concentration gradients and, consequently, the smaller the distortion of solute profiles will be. While diminishing the volume of the bottom water reservoir of the microcosm by placing the membrane low in Column B, the volume of water above the membrane is greatly enlarged. This poses a problem because of the way the oscillatory head is created in the first microcosm design (Figure 3.1): it requires that this body of water (in Column B) be directly mixed with the water overlying the sediment in Column A (Connection II, Figure 3.1). Consequently, the volume of overlying water in the modified design would actually increase by approximately 100 % over the first design. If a solute is fluxing across the SWI into the overlying water it would be diluted twice as much in the modified design, and increased analytical sensitivity would be

required to detect near-detection limit concentrations. Therefore, a way was sought by which to induce the pressure oscillations over the sediment column while not pumping the water between Columns A and B. This problem was solved by introducing a third column, Column C, into the microcosm as an auxiliary overlying water reservoir (Figure 3.13).

Finally, the continuous replacement of overlying water with water from a reservoir was stopped for two major reasons. First, the very small size of the tubing used in that microcosm component made it susceptible to frequent clogging due to biofilm formation. Second, the latter problem, along with the maintenance of an additional pump and reservoir loop (see Figure 3.1), rendered this a rather inefficient way of manipulating overlying water chemical composition, and was inadequate for oxygenating the overlying water (see Section 3.2.2.1). Moreover, the continuous replacement of overlying water could make the detection of material fluxing into the overlying water from the sediment difficult by preventing its accumulation to significant levels. Therefore, the modified microcosm features the direct oxygenation of overlying water in Column C with an air pump, while a sampling port allows both the retrieval as well as the addition of water from this column, if this is desired.

3.3.2 Methods for construction and assessment of the new microcosm design

3.3.2.1 Technical information

Flexible membrane – A circle approximately 25 cm in diameter was cut from a sheet of DuraShield 45 membrane, obtained from the manufacturer. The center of the circle was pushed in to form a cup shape and the membrane invaginations along the edge

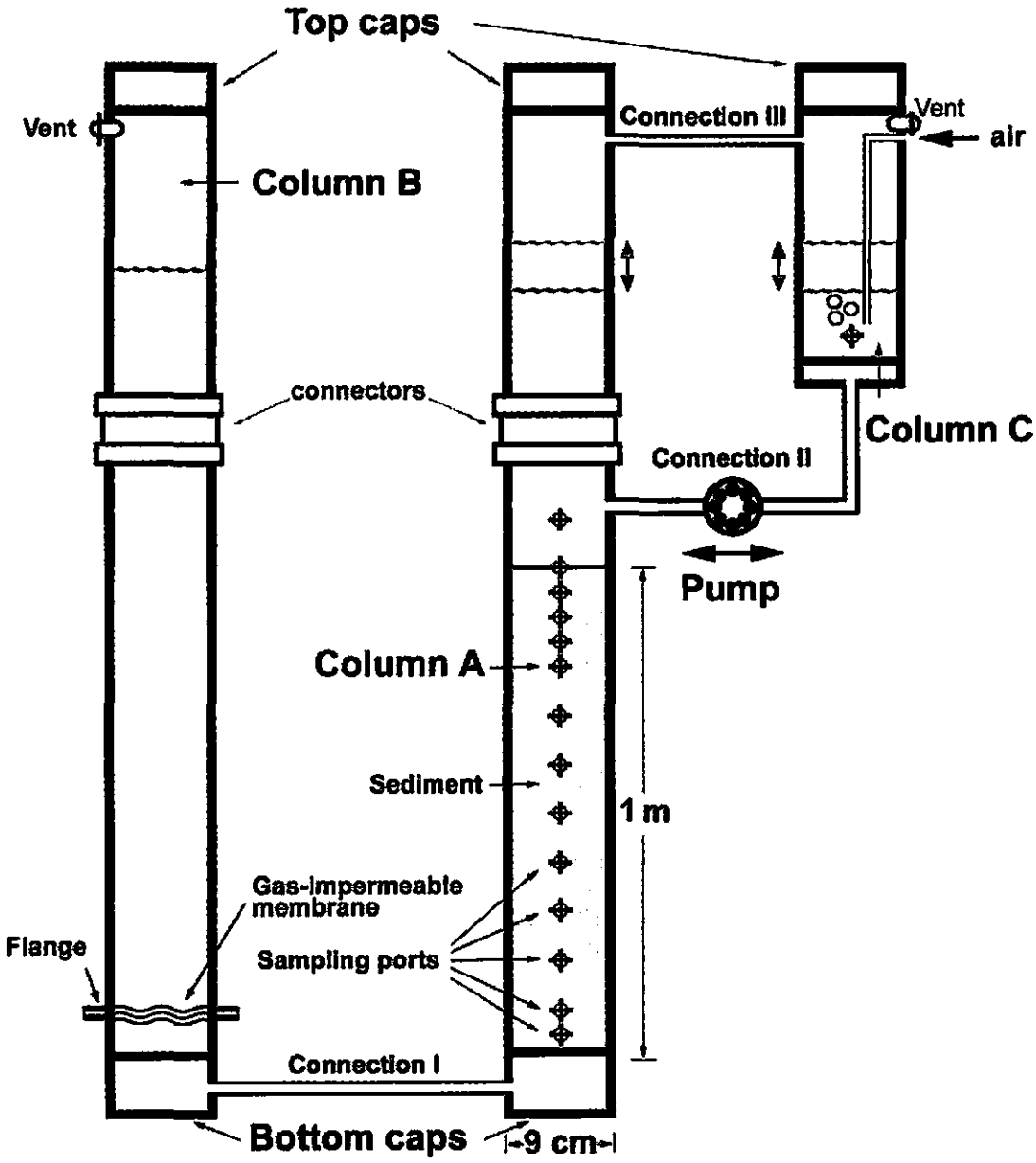

Figure 3.13 The modified microcosm design (compare to Figure 3.1). The silica sand in Column B has been replaced with a gas-impermeable membrane. Oscillatory pressure at the SWI is produced by pumping water between Column A and the newly-introduced Column C.

were pressed between hand made rubber gaskets. The gaskets were pressed together by two PVC pipe flanges (Harvel Plastics, Easton, Pennsylvania, U.S.A.), which were held in place by four sets of nuts and bolts. Column B was cut approximately 10 cm above the ABS bottom cap, and the two newly-cut edges of the column were fitted into the pipe flanges. When the invaginated membrane is fully inflated, it can hold a volume ≥ 600 mL, thus accommodating the flow of 1.2 L of water or more past it, if necessary, though that was in excess of what was needed for this study.

Column C – Column C was made from the same material as the other two columns of the microcosm (see Section *3.2.2.2*). A 60-cm section of transparent Schedule 40 PVC pipe with an internal diameter of 7.68 cm (3 in) and a wall thickness of 6.4 mm (0.25 in) was cut and threaded on one end. The threaded end received a bottom end cap, made by gluing a female acrylonitrile butadiene styrene (ABS) reducer coupling into an unthreaded ABS end cap using ABS cement. The flat surface of the bottom cap was threaded in the center to accept a 1.28-cm (0.5-in NPT) high-density polyethylene male pipe adapter with 0.96-cm (0.375-in) barbed fittings (Cole-Parmer Instrument Co.). A similar adapter was placed near the top of the column to form Connection III between the overhead gases of Columns A and C. A threaded 0.32-cm (0.125-in NPT) polypropylene male pipe adapter with 0.32-cm (0.125-in) barbed fittings (Cole-Parmer Instrument Co.) was placed at the same height as Connection III and was connected to an air pump. A 30 cm-long section of L/S 16 Norprene tubing (Masterflex, Cole-Parmer Instrument Co.) was fitted on the inside, terminating in an aquarium aeration stone. A sampling port, consisting of a 1-way male Luer-lock stopcock (Cole Parmer Instrument Co.) mated to a 1/4-28 UTF female Luer fitting (Cole-Parmer Instrument Co.), was placed approximately

5 cm above the top of the bottom cap. Finally, the top was sealed with an opaque 7.68-cm (3-in) PVC pipe stopper.

3.3.2.2 Assembly and operating procedures

The modification of the microcosm prompted an optimization of the assembly steps (see Section *3.2.2.3*). To facilitate the assembly of the modified microcosm, the tubing forming Connection I was split into three segments (Figure 3.14), which were incorporated at different stages in the assembly.

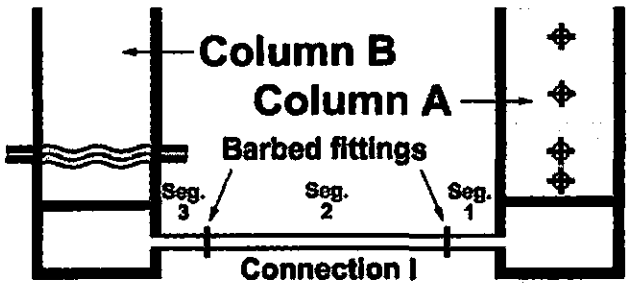

Figure 3.14 The segmentation of butyl tubing that forms Connection I. See the description of the assembly process in the text.

Step One: Sediment loading – The first step in the assembly of the microcosm is the loading of sediment in Column A. This is done while Connection I is blocked by constricting Segment 1 (Figure 3.14). After sediment loading, the bottom and top segments of this column are joined by the LASCOtite coupling. Norprene tubing is used to connect the end of Segment 1 to the bottom of Column C to set up an arrangement which allows the measurement of permeability (Figure 3.15). While blocking the

Norprene tubing, filtered seawater is added to both columns, so that the level in Column C is flush with the sampling port and that the level in Column A is 20-30 cm higher than the level in Column C.

Step Two: Permeability determination – Permeability may be measured with a falling head or a constant head, the latter (Eq. 3.11) being the appropriate method in the case of permeable sediments (Klute and Dirksen 1986). However, the height of the sediment column in Column A is typically 1 m, and this does make it possible to measure hydraulic conductivity using the former method: according to Burmister (1955), any ratio of head difference (H) to sediment column height (l_A) less than 0.4 will result in Darcian flow that allows the use of a falling head experiment. From a practical standpoint, this is done by releasing the constriction in the tubing connecting the two columns, and recording the height difference at known time points after the release. The data can be used to calculate the hydraulic conductivity, K, using the following equation (Klute and Dirksen 1986; Rocha et al. 2005):

$$K = \frac{\ln\left(\frac{H_0}{H}\right) l_A}{t} \qquad 3.16$$

where H_0 is the head difference (cm) at time $t = 0$. Examples of computations are given in the results section (Figure 3.21). If constant head measurements are desired, filtered seawater can be pumped continuously from a reservoir into Column A so that H remains fixed. The volume of water flowing out from the sampling port over a certain time period must be measured and used to calculate K with Eq. 3.11.

Before proceeding to the next phase of microcosm assembly, Segment 1 is clamped and the tubing connecting it to Column C removed. A shorter segment of

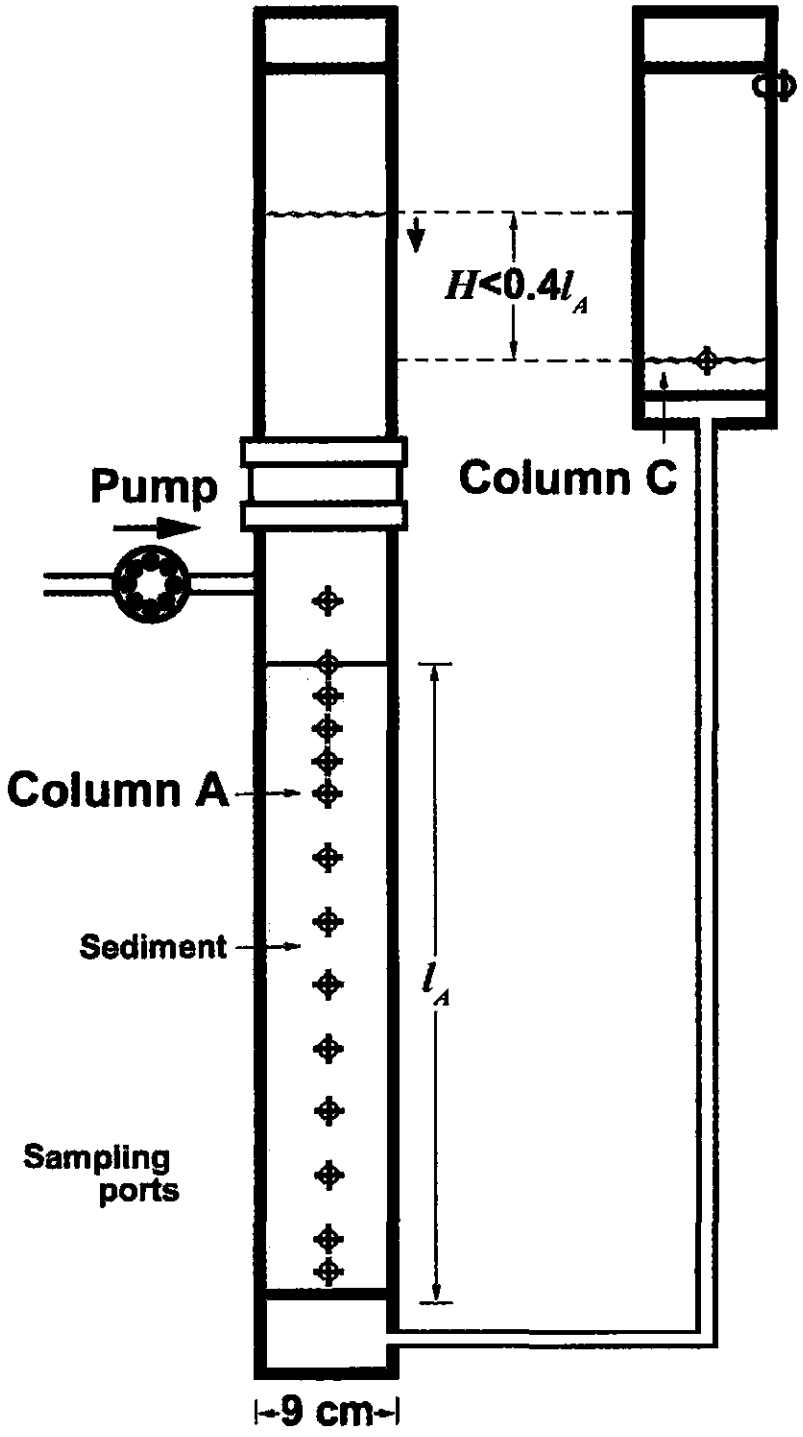

Figure 3.15 Configuration of the microcosm for the measurement of permeability.

Norprene tubing is used to connect the bottom cap of Column C to the pump head, which is already connected to Column A, thus forming Connection II.

Step Three: Connecting Columns A and B – The most important task of this step is the filling of the bottom chamber of Column B. The easiest way to achieve this with no gas bubbles is to lay this column on its side with the opening of Connection I on top, fully inflating the membrane by adding air under pressure through the opening, and slowly adding filtered seawater to the chamber. When it is almost full, the fitting (with Segment 3 attached; Figure 3.14) is screwed onto the opening to a level that is flush with the interior of the bottom cap. The bottom cap is continuously moved up and down with the opening always on top, in such a way so as to direct any remaining gas into Segment 3. Adding more filtered seawater to the chamber while doing this will slowly displace any remaining gas from the reservoir. When no more gas is evident and Segment 3 is full, Segment 2 (Figure 3.14) is added and filled with filtered seawater to the edge, and clamped shut. After Column B is secured in the upright position, Segments 1 and 2 can be topped with filtered seawater and connected.

Step Four: Completion of microcosm assembly – The top segment of Column B can now be connected to the bottom segment via a LASCOtite connector. This column can be filled with filtered seawater or an isopycnic solution made using tap water and salt (NaCl) to allow the levels in Columns A and B to be the same and thus directly comparable. This is desirable because it greatly simplifies the execution of pressure gradient relaxation tests, and the determination of velocity vs. head difference relationships, as described in Section *3.2.3.1*.

Before experimentation may begin, the three columns must be filled to the same level. To do so, the tubing forming Connection II is released from the pump head to allow water to flow freely between Columns A and C. The final step is the adjustment of the amount of water in Columns A and B such that the membrane is not extended in either direction and that the level in Column A is approximately 50 cm above the SWI (unless otherwise desired).

3.3.2.3 Simultaneous assessment of enhanced transport and biogeochemistry

During the assessment of the first microcosm design, enhanced transport and biogeochemistry were not investigated simultaneously but during separate experiments (Table 3.2). The investigator using this microcosm would benefit by conducting conservative tracer experiments at the same time as manipulating the column biogeochemically, because the simultaneous measurements of chemicals and their physical exchange rates across the SWI could allow the calculation of fluxes. However, fluorescein, rhodamine, and other dyes commonly used as tracers in groundwater research are toxic to living organisms (Flury and Wai 2003) and their presence may also interfere with colorimetric analyses of other chemical tracers. Therefore, they are unsuitable for cases in which biogeochemical analyses are taking place in the same samples. Moreover, the relatively large volumes required for their detection interfered with the calculation of enhanced transport rates during experimentation with the original microcosm design (see Section *3.2.4.2* for data and discussion). Consequently, the alternative to dye tracers should not only be inert with respect to biogeochemical processes, but should also be reliably detectable using very small volumes.

Bromide is a commonly used conservative tracer for transport studies in marine sediments (Martin and Banta 1992; Aller et al. 2004; Rao and Jahnke 2004). Bromide has a number of advantages when used to trace solute transport in marine sediments:

a) It is a conservative ion: there are no known significant sinks or sources in marine sediments (Martin and Banta 1992).

b) It is not surface-reactive, so absorption and adsorption can effectively be ignored.

c) Its concentration in seawater is approximately 0.85 $mmol \cdot L^{-1}$ in seawater, and therefore even a tripling of its concentration does not change salinity or density levels significantly.

d) Its detection by spectrophotometry is straight-forward (Balatre 1936; Presley 1971).

The modified microcosm design allows the use of a model developed by Rao and Jahnke (2004) to calculate enhanced transport in benthic chamber studies. This one-dimensional, grid-centered, finite difference model calculates the loss into the sediment of a pulse of bromide released in the overlying water of a chamber. It corrects for bromide removal by sampling, and allows the incorporation of non-local exchange effects caused by macrofaunal activity. The model generates the overlying water bromide concentration with time, as well as a pore water bromide profile at the final time-point. Model optimization is done using a χ^2 statistical scheme. For the needs of this study, the simplest module of the model was used, which includes the effects of physically enhanced transport, and excludes macrofaunal effects (Rao and Jahnke 2004):

$$\varphi \frac{\partial C}{\partial t} = \varepsilon D_0 \frac{\partial}{\partial z}\left(\frac{\varphi}{\theta^2}\frac{\partial C}{\partial z}\right) \qquad 3.17$$

where ε is a dimensionless diffusion enhancement factor (compare to Eq. 3.12). The value of ε is the unknown coefficient that yields an estimate of transport in excess of molecular diffusion, and should be positively correlated to permeability and physical forcing (see Chapter 2). Boudreau (1997) refers to ε (his symbol, $D^* = \varepsilon D_0$) as the effective dispersion coefficient and demonstrates why it can be used as a diffusion-like coefficient, as is the case in Eq. 3.17.

3.3.2.4 Assessment experiments

Design usability and hydraulic characterization – The new design and its performance during experimentation were assessed during six microcosm experiments (Table 3.8), mostly using permeable sediments from the Kilo Nalu observatory site on the south shore of O'ahu (Figure 3.16, Table 3.9). Exp. 10 aimed at evaluating the sequence of assembly steps described in section *3.3.2.2*. It also tested the assertion that the estimated permeability of 1 m-long sediment columns is not affected by the type of permeability test used (based on Burmister's ratio of $H/l_A < 0.4$; see Section *3.3.2.2, Step One: Sediment loading*). The assertion was tested by performing falling and constant head permeability tests on two silica sand columns of lengths l_A=50 cm and l_A=101 cm, and by comparing the two sets of permeability values using box plots (Moore and McCabe 1999, p. 44-51). The remaining experiments (11-15) were designed to simultaneously determine the physical exchange rates between overlying water and pore water and the biogeochemistry of incubated sediments. Bromide tracer experiments were conducted at multiple time-points during these experiments, and pore water samples were collected for biogeochemical analyses.

Table 3.8 Assessment experiments performed with the modified microcosm design. The material included in Column A, the sedimentary column height (l_A), experimental duration (t), pump settings (h = oscillation height, cm; f = oscillation frequency, min^{-1}), and experiment objectives are summarized. All carbonate reef sediment used was collected from Kilo Nalu (see Figure 3.16).

Exp			t	Pump		
No.	Column A material	l_A (cm)	(d)	h	f	Experiment objectives
10	Silica sand	50, 101	-	-	-	Hydraulic conductivity testing
11	Sand field carbonate reef sediment	99.5	78	8.5	2	Solute enhanced transport; sediment biogeochemistry
12	Sand pocket carbonate reef sediment	99	15	8.5	2	Solute enhanced transport; sediment biogeochemistry
13	Sieved sand pocket carbonate reef sediment	100	8	8.5	2	Solute enhanced transport; sediment biogeochemistry
14[a]	Sieved sand pocket carbonate reef sediment	99.5	15	10.5	3	Solute enhanced transport
15[a]	Sieved sand pocket carbonate reef sediment	99	16	10.5	1	Solute enhanced transport

[a] Exp. 14 and 15 were conducted by A. Rusch. This study reports only the conservative tracer experiments performed by A. K. Hannides during those incubations.

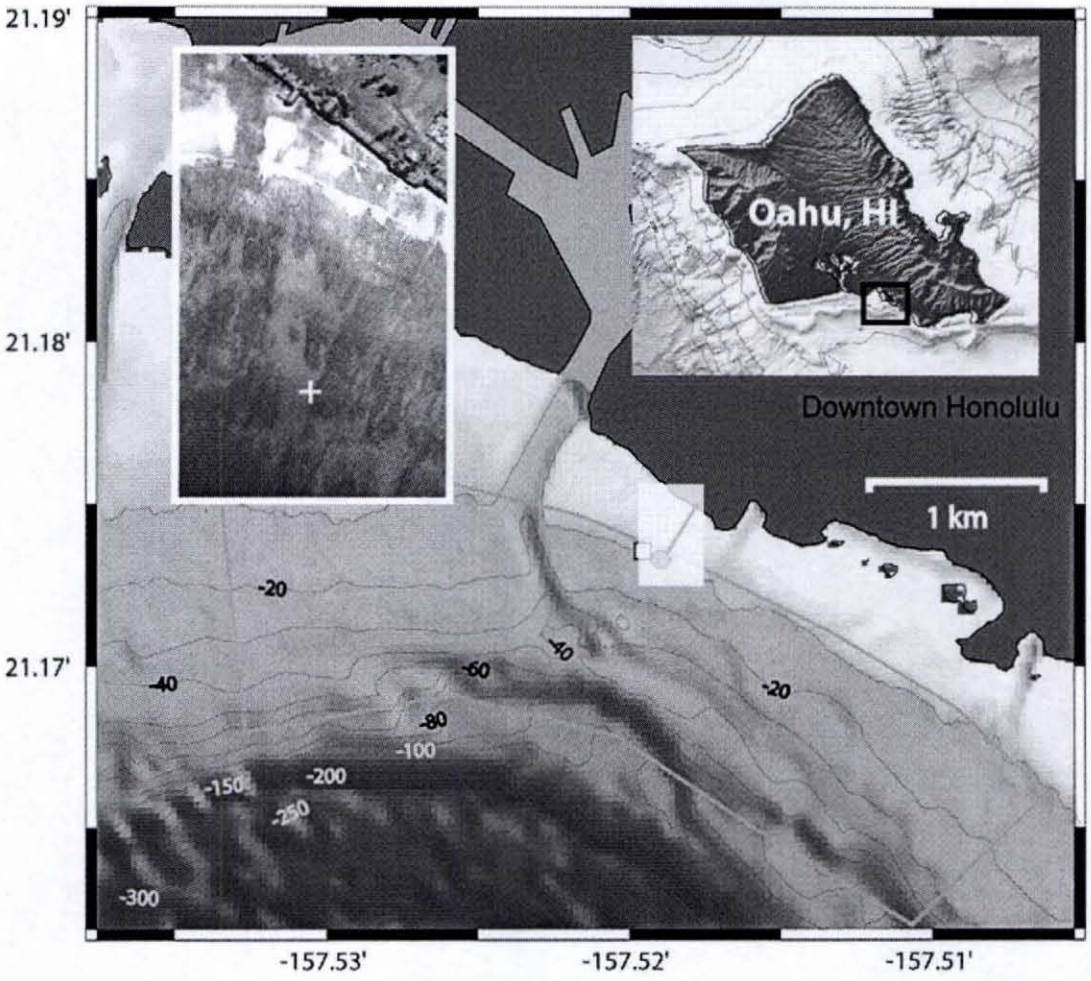

Figure 3.16 The Kilo Nalu observatory site on the south shore of O'ahu (maps and satellite photograph courtesy of G. Pawlak and A. Hebert). The inset shows a satellite photograph of the region indicated by the semi-transparent rectangle. Notice the light-colored sand field surrounded by dark-colored coral reefs. The cross indicates the location of sediment sampling, which is adjacent to the 10-m node of the observatory.

Table 3.9 Physical characteristics of the sediments used in the assessment experiments of the modified microcosm design. See Table 3.3, for definitions of physical characteristics. The sand field and sand pocket sediments were collected 6 m from each other along a transect across the boundary between the sand field and the adjacent coral reef (see Chapter 4). Sand pocket sediments are unconsolidated sediments that accumulate between individual or aggregated coral heads in the coral reef.

Sediment type (Exp. No.)	Source location	Grain size (mm)		σ_I	φ	k[a] (m^2)
		Median	Mean			
Silica sand (10)	Merchant	0.61	0.57	0.58	0.43	2.0×10^{-10}
Sand field sediment[b], Kilo Nalu (11)	21° 10.4' N 157° 31.1' W	0.23	0.24	0.78	0.51	4.3×10^{-11}
Sand pocket sediment[b], Kilo Nalu (12)	21° 10.4' N 157° 31.1' W	0.81	0.82	1.12	0.49	6.0×10^{-11}
Sieved sand pocket sediment[c], Kilo Nalu (13-15)	21° 10.4' N 157° 31.1' W	0.83	0.85	1.08	0.47	1.7×10^{-10}

[a] Permeability, k, was calculated from hydraulic conductivity measured on sediment columns before experiments by falling and constant head experiments (see Section *3.3.3.1*).

[b] Rubble larger than 1.5 cm in the smallest dimension was removed from the sediment.

[c] The sediment fraction smaller than 250 μm was removed by wet sieving in twice-filtered 0.2 μm seawater and discarded, as well as rubble larger than 1.5 cm in the smallest dimension.

Enhanced exchange – Bromide tracer experiments were conducted during microcosm Exp. 11-15 by injecting a very small amount of bromide in the overlying water (through the port positioned 10 cm above the SWI) and tracing its transport into the pore water. A common problem with tracer experiments is the initial sinking of the injected plug of tracer to the sediment surface because of its greater density. This problem was solved by taking a number of remedial steps. Typical overlying water concentrations upon addition of a tracer pulse in other studies have varied between 2 and 6 mmol·L^{-1} (Rao and Jahnke 2004). During Exp. 11-15, these concentrations were kept at 0.8-1.2 mmol·L^{-1}, thus minimizing the amount of tracer added. Moreover, this small amount of tracer was added to the microcosm after being diluted in 30-35 mL of microcosm overlying water, which was retrieved immediately preceding the tracer addition. Finally, the tracer experiments were conducted when active pumping was taking place, during which water was vigorously exchanged between the two columns at rates of 26 mL·s^{-1} (in the case of h = 8.5 cm and f = 2 min^{-1}). Slow (1 min) delivery of the pulse ensured that this transfer rate rapidly mixed the tracer with the overlying water of the microcosm (e.g., an overlying water volume of 3.5 L would pass through Connection II in 2.25 min at an exchange of 26 mL·s^{-1} yielding a mixing time on the order of minutes).

Two types of data were collected during these experiments. The first type consisted of bromide concentration time-series at a certain depth in the sediment column, typically the first pore water sampling port below the SWI (z = 4 to z = 5 cm, depending on l_A). The second type consisted of pore water bromide profiles at successive time points. The Rao and Jahnke (2004) model (Eq. 3.17, Appendix D) was used to obtain best estimates of enhanced diffusion coefficients that would explain the tracer experiment

data, using a free solution diffusion coefficient of bromide, $D_0 = 6.934\ mm^2 \cdot h^{-1}$ (Boudreau 1997, p. 116) and porosities, φ, from measurements on sediment columns Table 3.9. Model output was compared to the data using a χ^2 statistical scheme. In more than one case, estimates using both types of data were available and compared. Finally, the enhanced diffusion/transport coefficients were compared to estimates of *k* and pumping parameters (*h* and *f*) to decipher relationships between these parameters.

Biogeochemical response – Pore water samples were collected from the microcosm throughout the experiments, before and after tracer experiments. In the case of Exp. 11, in which Kilo Nalu sand-field sediment was incubated, the pore water profiles of selected solutes were compared to in situ profiles. Six sampling wells were installed in the vicinity of the 10-m node of the observatory in early Spring 2006 (for methods, see Haberstroh and Sansone 1999; Falter and Sansone 2000a). The wells were installed approximately 5 m from the boundary with the adjacent coral reef (see Figure 3.16). The wells allowed pore water sampling from sediment depths of 7.5, 15, 20, 30, 40, and 50 cm. These wells were sampled during three field trips to the observatory between April and August 2006. Oxygen and nutrient profiles from the field and the microcosm were compared for similarities or differences in concentration levels and curvature. More details about the laboratory and field analytical methods are given in section *3.3.2.5*.

3.3.2.5 Analytical methods

The limited availability of sample volume dictated the analytical approach towards solute quantification. Conventional analytical methods were modified to accommodate analysis on small-volume samples. During a typical sampling session, the

microcosm was sampled using pre-cleaned 5 mL syringes fitted with 25-gauge needles (0.24 mm outer diameter). After the oxygen concentration measurement (see below), the sample was filtered using 0.2-μm, small-volume, in-line filters, and split into aliquots for nutrient analyses and bromide, when needed. A similar sequence of analyses was followed during field sampling, in which oxygen was measured using part of the sample, while the rest was filtered and stored on ice for nutrient analyses. All solutes, except oxygen, were analyzed by manual spectrophotometry. All standards used during colorimetric analyses were made in artificial seawater (ASW) to eliminate matrix effects during spectrophotometric measurements (e.g., see Section *3.3.2.5 Ammonium*). Artificial seawater was made using the composition table in Parsons et al. (1984, p. 159). A summary of the analytical methods used and quality control parameters is given in Table 3.10, while more details for each analysis follow.

Dissolved oxygen – Oxygen was measured using an Orion 820 dissolved oxygen meter with a probe containing a Clark-type polarographic electrode (Clark Jr. et al. 1953; Thermo Electron Corp., Beverly, Massachusetts, U.S.A.). This catalytic gold-surface electrode detects oxygen by electrolytically reducing it after it passes from the sample to the KCl electrolyte through a permeable membrane (see Figure 3.17). The electrode was air-calibrated before each use while inserting the probe in a wetted sleeve provided by the manufacturer (according to the manufacturer's instructions). The meter was set to provide readings in units of $mg \cdot L^{-1}$ at an appropriate salinity (32-35), while a built-in temperature sensor automatically corrected the reading for temperature. While not in use, the probe was kept in the calibration sleeve and its reading monitored for drift. If the meter drifted by more than 0.2 $mg \cdot L^{-1}$, it was immediately recalibrated.

Table 3.10 Summary of analytical methods, sample volumes (V) and quality control parameters for solutes routinely analyzed during microcosm experiments. See the text for more information on specific methods.

Solute	V (mL)	Analytical method	LD [a] $\mu mol \cdot L^{-1}$ (n)	Precision [b] ± % (n)
Bromide	0.1	Spectrophotometry (Phenol-red)	90 (28) [c]	3 (39) [d]
Oxygen	1.0	Polarography (Clarke-type electrode)	5 (21)	3 (288)
Nitrate	1.2	Spectrophotometry (Cd reduction)	0.14 (8)	2 (10)
Nitrite	1.0	Spectrophotometry (azo dye)	0.03 (8)	3 (25)
Ammonium	1.0	Spectrophotometry (indophenol)	0.14 (8)	3 (32)
Phosphate	1.0	Spectrophotometry (molybdenum blue)	0.08 (9)	4 (38)

[a] The limit of detection (LD) is defined as the lowest measurable concentration that is different from a blank (Brügmann and Kremling 1999), and is calculated as the mean value of the blank (measured over several analytical sessions) plus 3 standard deviations.

[b] Precision is defined as the standard deviation of replicates of a sample, averaged for numerous samples over several analytical sessions, divided by each sample's average value, and multiplied by 100 (Brügmann and Kremling 1999).

[c] All samples analyzed for bromide during this study contained normal seawater levels (~ 850 $\mu mol \cdot L^{-1}$) or greater (as in the case of tracer experiments).

[d] The precision for bromide was calculated using 39 values for a stock of twice-filtered (0.2-µm) Waikiki Aquarium seawater, analyzed during 21 analytical sessions over 4 months, and found to be 866 ± 26 $\mu mol \cdot L^{-1}$ (mean ± SD).

The meter was used in two different ways. The first use of the meter involved measuring oxygen in very small samples (<5 mL) retrieved during microcosm sampling. Before each measurement, the probe was rinsed thoroughly with DIW and placed upright, membrane-down in a clean and empty 10-mL syringe barrel (Figure 3.17a). This particular type of syringe barrel was selected because its internal diameter was only slightly larger (15.87 mm) than the external diameter of the probe (15.36 mm), and this minimized the volume needed for a reliable oxygen reading (~ 1 mL). The tip of the barrel was fitted with a short section of tubing, which was used to connect the barrel with the 5-mL sampling syringe after the needle was removed. The sample was transferred immediately after sampling to the barrel and injected at a rate of 0.1-0.2 $mL \cdot s^{-1}$. Injection continued well after the sample covered the meter's temperature sensor (up to 6.5 cm), at which point a reading was taken. In a few cases, withdrawing and re-injecting the sample was possible and yielded a second reading on the same sample. The measurement was generally completed at most 30 s after sampling.

The second use involved measuring oxygen during field trips to the Kilo Nalu field site. Samples were drawn from the six sand field wells, as well as from the overlying water, into 140-mL syringes by divers. The syringes were delivered to the surface within minutes of sampling, and stored in the dark while each one was analyzed for dissolved oxygen. During analysis, each sample was dispensed into a 60-mL Biological Oxygen Demand (BOD) bottle using a short (< 10 cm) piece of tubing, and allowed to overflow by half the volume of the BOD bottle, thus using a total of 90 mL. Measurement of O_2 using the meter took place in identical fashion as that of Falter and Sansone (2000a). The probe, fitted with a plastic sleeve, was inserted into the BOD bottle

so that it sealed the bottle opening snugly, while ensuring that no air bubbles were trapped (Figure 3.17b). The sample was stirred using a portable battery-operated field stirrer and a small magnetic stirring bar, and a reading was taken within 15 s.

As in the previous use of this electrode in the field and lab (Falter and Sansone 2000a), the readings were calibrated by comparing them to oxygen concentrations obtained by Winkler titrations. A 4-liter glass reservoir with an opening at the bottom (Figure 3.18a) was outfitted for this calibration as follows. The top was blocked with a stopper with three openings. One opening held tubing feeding helium gas into the reservoir through an air stone. The second opening was outfitted with a section of butyl rubber tubing on the lower end, and with a three-way valve on the upper end. One tip of the valve was fitted on the reservoir, the second was fitted with a waste syringe (50 mL) to hold water discarded during sampling, and the third was reserved for the sampling syringe (60 mL). The third opening on the stopper was left open for venting. The bottom opening of the reservoir was fitted with a Y-connection. One of the two outlets was sealed by a septum, similar to the ones on the sampling ports of the microcosm. The second outlet was fitted with Tygon tubing and a clamp, and was reserved for sampling reservoir water in BOD bottles for Winkler titrations.

The reservoir was filled with twice-filtered (0.2 μm) seawater and placed on a stirring plate. The water in the reservoir was stirred gently at approximately 100 rpm by a large Teflon-coated stirring bar. The sampling syringe was used to draw 10-15 mL from the reservoir, which was discarded into the waste syringe (the dead volume of the tubing was measured to be 8 mL). Another 60 mL was drawn and dispensed into a 60-mL BOD bottle using the same length of silicon tubing used on field trips. This BOD bottle already

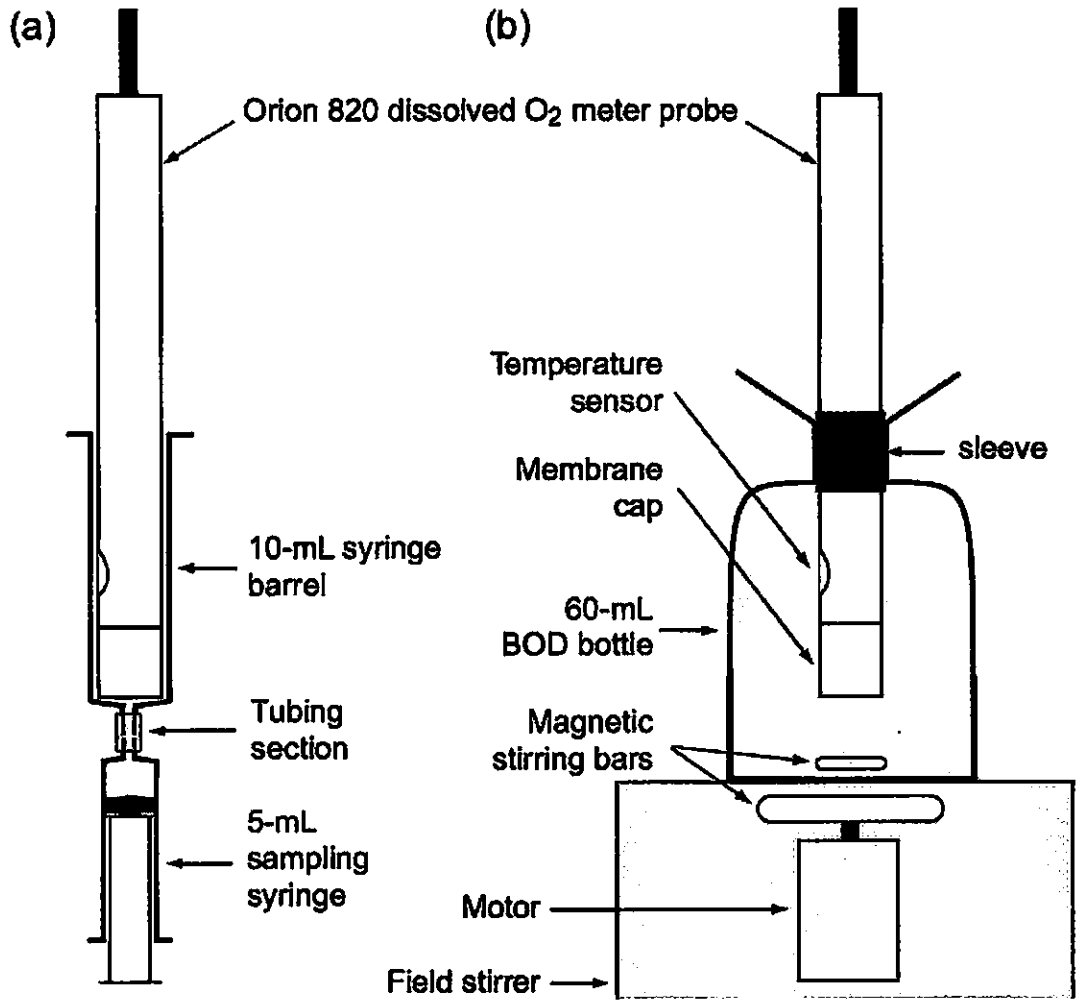

Figure 3.17 Uses of the Orion 820 dissolved oxygen meter during this study: (a) Small samples (< 5 mL) were analyzed by injecting them into a syringe barrel that held the meter, membrane facing down; (b) Larger sample volumes (> 60 mL) were analyzed by filling a 60-mL BOD bottle, with the electrode sealing the bottle opening with the help of a plastic sleeve.

contained a stirring bar and was resting on the portable stirrer. The probe was fitted with a removable plastic sleeve and fitted onto the BOD bottle, with the sleeve providing a tight seal. Stirring was started and a measurement was made as soon as the reading stabilized (within 15 s).

At that point, the probe was removed and placed in the syringe barrel. A 5 mL sample was retrieved from the septum-sealed bottom opening using a 5 mL syringe and a 25-Gauge needle. The needle was removed, and the sample injected into the piston at 0.1-0.2 $mL \cdot s^{-1}$, in a manner identical to that during the microcosm experiments. A reading was taken after the sample level covered the temperature sensor of the probe.

Simultaneously with the extraction of the 60-mL syringe sample, a helper (R. Solomon) filled a BOD bottle directly from the reservoir through the bottom opening. The seawater was allowed to overflow by 1.5 BOD bottle volumes, and the BOD bottle contents were then fixed with Winkler titration reagents (see Section *3.2.3.3*). After a first sample was taken from the reservoir, a slow and steady stream of helium was allowed to bubble through the reservoir. The reservoir water was sampled every 5-6 min, an adequate time interval for the oxygen concentration to change detectably. The experiment was terminated after the meter indicated the lowest value it could record when exposed to a de-aerated sample.

All of the BOD bottles were sealed and clamped shut, some additional water was added around the tops of the bottles, and the bottles were stored in the dark. The contents were analyzed 20 h later by titration with thiosulfate after acidification. The thiosulfate solution was standardized using an iodate standard. A reagent blank was taken at the end of the experiment when the sample's dissolved oxygen concentration (6.6 $\mu mol \cdot L^{-1}$)

could not be driven lower. According to R. Solomon (personal communication), this is well within the oxygen content of Winkler titration reagents. The BOD bottle volumes were determined gravimetrically with DIW. The results of the calibration are shown in Figure 3.18b and c, and are very similar to those obtained previously with this meter (Falter and Sansone 2000a). The relationships between meter readings and Winkler titration-determined concentrations are linear, with slopes of 0.030-0.031 (a "1:1" slope would equal 0.032). The results of this calibration experiment verified the reliability of this meter for oxygen measurements by the methods employed in this study. It is useful to note here that the meter reading (whose resolution is 0.1 $mg \cdot L^{-1}$) could fluctuate between as much as $\pm$ 0.2 $mg \cdot L^{-1}$ during a measurement of well-oxygenated samples. This brings the error of measurement to approximately 3 %. It should also be noted that, during this calibration experiment, the minimum value of detection of the meter was 0.4 $mg \cdot L^{-1}$. The minimum detection limit of this electrode has never been observed to reach 0.0 $mg \cdot L^{-1}$ (personal observations; F. Sansone and A. Rusch, personal communication), and varies within the relatively narrow range of 0.2-0.8 $mg \cdot L^{-1}$ (personal observations; Falter and Sansone 2000a). It is fortuitous that, during this study, almost all sampling events included at least one sample which was almost certainly anoxic (as evidenced by the scent of sulfide), so that the detection limit of the meter on that particular day could be observed and recorded. On those occasions, the limit of detection was taken as the meter-reading-vs.-concentration relationship intercept, and the rest of the concentrations calculated using the slopes determined during the calibration.

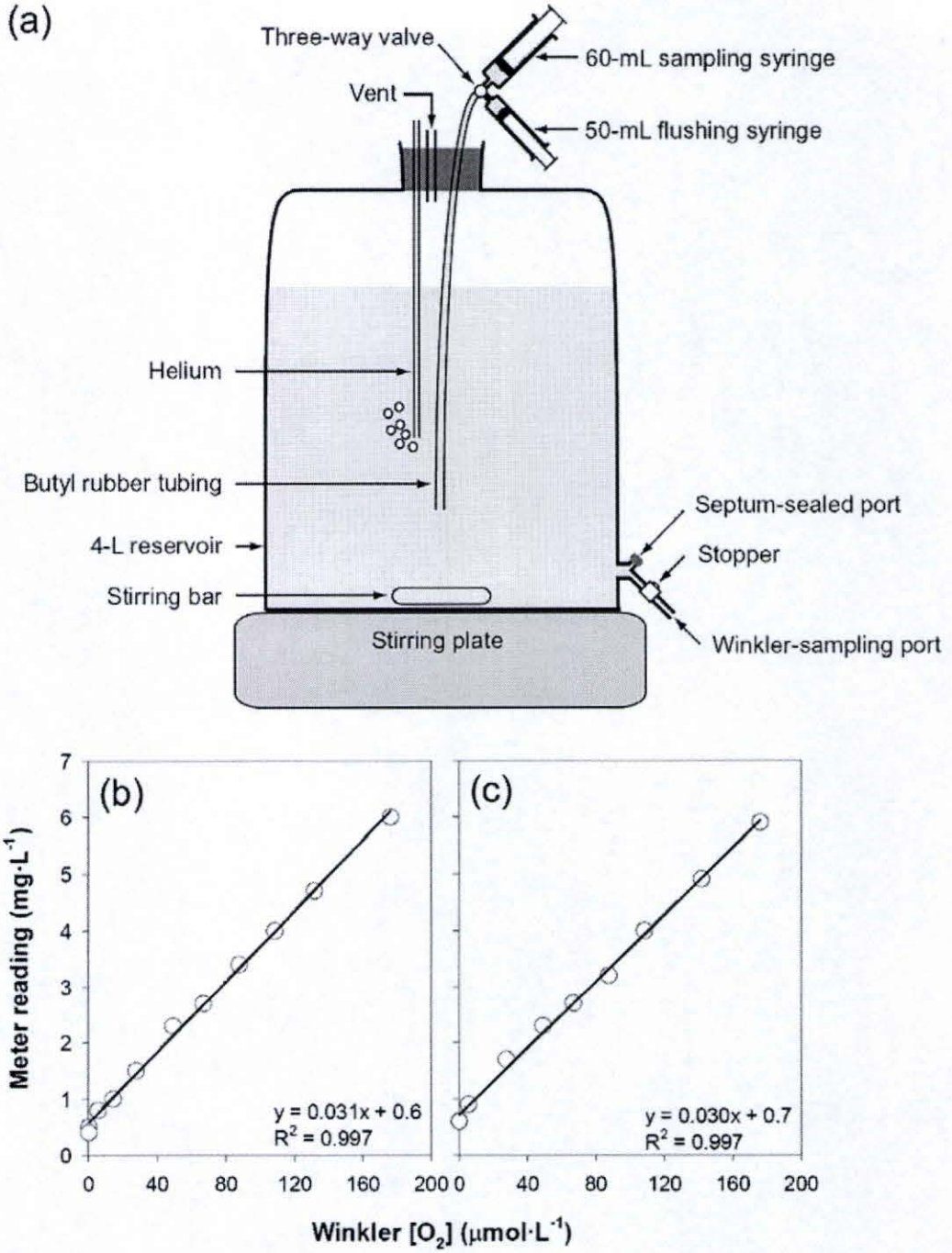

Figure 3.18 (a) Laboratory set-up used for the calibration of the Orion meter readings; Concentrations obtained by Winkler titration were compared to meter readings obtained by (b) sample injection, and (c) sample stirring (Figure 3.17a and b respectively).

The syringes used for well sampling in the field were also tested for oxygen penetration as follows. Filtered seawater was de-aerated and sampled with three field syringes as above. The contents of one field syringe were tested for oxygen immediately with the field stirrer method. The other two field syringes were placed in a container full of aerated water to simulate exposure to oxygenated overlying water at the field site. After 50 min, the average estimated period between sampling at the dive site and measurement on the field boat, their contents were analyzed for oxygen, and were found to be have been oxygenated by 18 ± 9 $\mu mol \cdot L^{-1}$ over the 50 min period. This value indicated that these syringes do take up oxygen from their surroundings, and that the uptake may vary from syringe to syringe. The oxygen values measured during field trips were corrected for this oxygenation by subtracting 18 $\mu mol \cdot L^{-1}$ from each measurement and taking into account the error of $\pm$ 9 $\mu mol \cdot L^{-1}$ when interpreting the results.

Bromide – Bromide was measured by the phenol red colorimetric analysis of Balatre (1936; Presley 1971). All of the reagent concentrations were maintained as in past protocols but their volumes were downsized accordingly. The volume available for bromide analysis during tracer experiments was 100 µl or smaller, and the reason for this was to limit as much as possible the interference of pore water removal at depth with the physically driven penetration of tracer (see the assessment of this issue in section *3.2.4.2*). The quality of the analysis, as well as the stability of the reagents, was evaluated throughout the duration of the study by always analyzing a stock of twice-filtered Waikiki Aquarium seawater alongside the analytical standards. Based on 39 measurements over 21 analytical sessions, this standard's concentration was determined to be 866 $\mu mol \cdot L^{-1} \pm 26$ $\mu mol \cdot L^{-1}$ (mean ± standard deviation). This analytical

uncertainty is slightly better than that of ± 47 $\mu mol \cdot L^{-1}$ reported by Rao and Jahnke (2004) in their review of bromide use during in situ tracer studies, and corresponds to a precision of 3 %.

Nitrate and nitrite – These nutrients are commonly reported jointly since there is no direct colorimetric analysis for nitrate. Instead, nitrate is reduced to nitrite and the reduced product (plus pre-existing nitrite) is reacted with sulfanilamide and N-(1-naphthyl)-ethylenediamine dihydrochloride (NEDA) to form an azo dye, which is quantified spectrophotometrically (Bendschneider and Robinson 1952). This yields the sum of nitrate and nitrite concentrations in the sample. If an unreduced sample is also analyzed, the actual nitrate concentration can be obtained by subtracting the unreduced (i.e., only nitrite) from the reduced sample's concentration. The challenge with measuring nitrate in small volumes lies in the reduction process. At present, the universally acceptable method of reduction is the contact of the sample with copper-coated Cd granules, which are loaded in a column several centimeters long (Parsons et al. 1984; Hansen and Koroleff 1999). These textbook protocols require sample volumes ranging from 25 mL (for concentrations greater than 15 μM) to 100 mL. Such large sample sizes during sedimentary investigations are almost never available. Jones (1984) developed an alternative way to bring smaller sample volumes (10-25 mL) in contact with the reducing agent. Each sample and standard is shaken with activated Cd granules in a vial for 90 minutes. A trial of this method during this study proved it to be very labor-intensive when applied to samples of 1-1.5 mL. Additional uncertainties emerged from relatively minor differences in the weight of Cd added. The resolution of this issue would make this

process even more inefficient time-wise. Instead, the downsizing of the Cd column reduction method (Parsons et al. 1984) was pursued, as follows.

Approximately 3 g of Cd granules (Sigma-Aldrich, St. Louis, Missouri, U.S.A.) were rinsed with 1 M HCl, and then with an 80 $mmol \cdot L^{-1}$ solution of $CuSO_4$. After immersing in a 117 $mmol \cdot L^{-1}$ solution of NH_4Cl (the buffer solution), the pellets were loaded in an inverted 1-mL glass syringe to form a Cd column with a total volume of 0.7 mL. A 2-cm section of tubing was connected to the tip of the syringe and fitted with a threaded stopper, so that the opening and closing of the tubing could be easily controlled. The column was rinsed thoroughly before use by passing several milliliters of the buffer through it. Before reduction, 60 µL of 4.67 $mol \cdot L^{-1}$ NH_4Cl solution were added to 1.2 mL of sample or standard to provide the alkaline conditions necessary for the strict reduction of nitrate to nitrite (Hansen and Koroleff 1999). The level of the buffer was brought flush with the top of the Cd column. After pipetting 0.5 mL of sample or standard on top of the column, the water level was brought back to the top of the Cd column and the effluent discarded. The rest of the sample (0.76 mL) was added to the column and the effluent collected in a 1.5 mL vial, again bringing the level to the top of the Cd column. Finally, 0.3 mL of the buffer was delivered to the column and the effluent added to the 1.5 mL vial, while the level was returned to the top of the Cd column. This yielded a total of 1.06 mL of sample, ready for nitrite analysis. The flow rate of sample or standard in the column was slower than the 2 $mL \cdot min^{-1}$ suggested by Hansen and Koroleff (1999), and routinely resulted in conversion efficiencies over 90 % (94 ± 10 % based on 63 standards), which were more than satisfactory for the purposes of this study.

Ammonium – The prevalence of ammonium in modern buildings makes ammonium detection particularly susceptible to contamination effects from the surroundings (Hansen and Koroleff 1999). This frequently results in relatively high uncertainties and detection limits, as well as low precisions. Consequently, simple precautions were taken to minimize contamination during analysis. The 1.5-mL vials in which the reaction and color development took place were kept capped at all times, and only opened to add reagents. All reagents and standard stock were stored in screw-cap vials. Finally, all used equipment was thoroughly washed with DIW immediately before use.

Ammonium was analyzed by indophenol blue formation using phenol and hypochlorite (Berthelot 1859). I tested two versions of the protocol that uses nitroprusside as a catalyst (Solórzano 1969). These versions differ in the sequence in which the reagents are added. The first, compiled by Parsons et al. (1984), advises the separate addition of the phenol and the nitroprusside solutions to the sample, prior to adding the mixed hypochlorite-citrate solution. The second, as outlined by Koroleff (1976b), urges the addition of an alkaline citrate solution, a mixed phenol-nitrorpusside solution, and finally the hypochlorite solution in that particular order. The Parsons et al. (1984) procedure routinely yielded precisions of the order of 15-20 %, while the Koroleff (1976b) procedure was much more consistent, giving a much better precision of 3 %. One cannot be certain whether it is the composition of the reagent solutions or the sequence of their addition that can explain this difference in reproducibility and stability. Actually, the reaction mechanism still cannot be fully explained (Hansen and Koroleff 1999). What is certain is that even after allowing for 5 h of reaction, the Parsons et al. (1984) procedure

still yielded widely varying standard absorptions, leading me to adopt the Koroleff (1976b) procedure. Finally, the effect of the matrix was also tested during this experimentation (since salt in seawater will interfere with the reaction) by comparing standards made in DIW with those in ASW. Absorbances of standards made in DIW were higher than those made in ASW by a factor of 1.1 (Figure 3.19), which agrees well with published salt-effect factors for salinity differences of 32-35 ‰ (1.08-1.09; Koroleff 1976b).

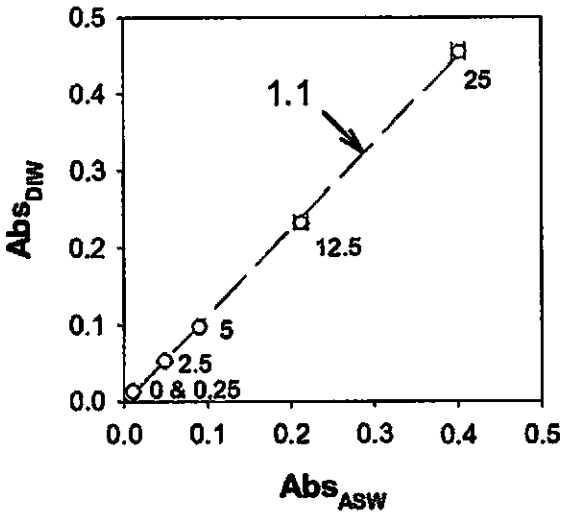

Figure 3.19 Comparison of absorbances at 630 nm of ammonium standards made in distilled water (Abs_{DIW}) and artificial seawater (Abs_{ASW}) with the indophenol blue method. Values next to symbols indicate the standard concentration ($\mu mol \cdot L^{-1}$). Linear regression of the data is shown by the dashed line, which has a slope of 1.1.

Phosphate – Phosphate was analyzed by the molybdenum blue complexation method with ascorbic acid as the reductant (Murphy and Riley 1962; Koroleff 1976a). The reaction involved adding two solutions to unacidified samples. The first solution was a mixed reagent of sulfuric acid, ammonium molybdate and antimonyl tartrate. The second was an ascorbic acid solution. During this study, no interferences or complications were observed with this method. Although the limit of detection was relatively high (0.08 $\mu mol \cdot L^{-1}$; Table 3.10), as compared to values of 0.01 $\mu mol \cdot L^{-1}$ mentioned in the literature (Hansen and Koroleff 1999), it was sufficiently low for the needs of this study.

3.3.3 Assessment of the new microcosm design – Results and discussion

3.3.3.1 Design operability and column hydraulics assessment

The new design works satisfactorily in principle and major shortcomings were not evident from this set of assessment experiments. The assembly steps accommodated the permeametry tests performed on the sediment column during experimental setup. The results of the permeametry tests (Exp. 10) are shown in Figure 3.20. The main observation is that the permeability estimates for the 101-cm column are similar for the constant- and falling-head tests. In the 50-cm column, however, the constant head test yielded a statistically different estimate than the falling head test.

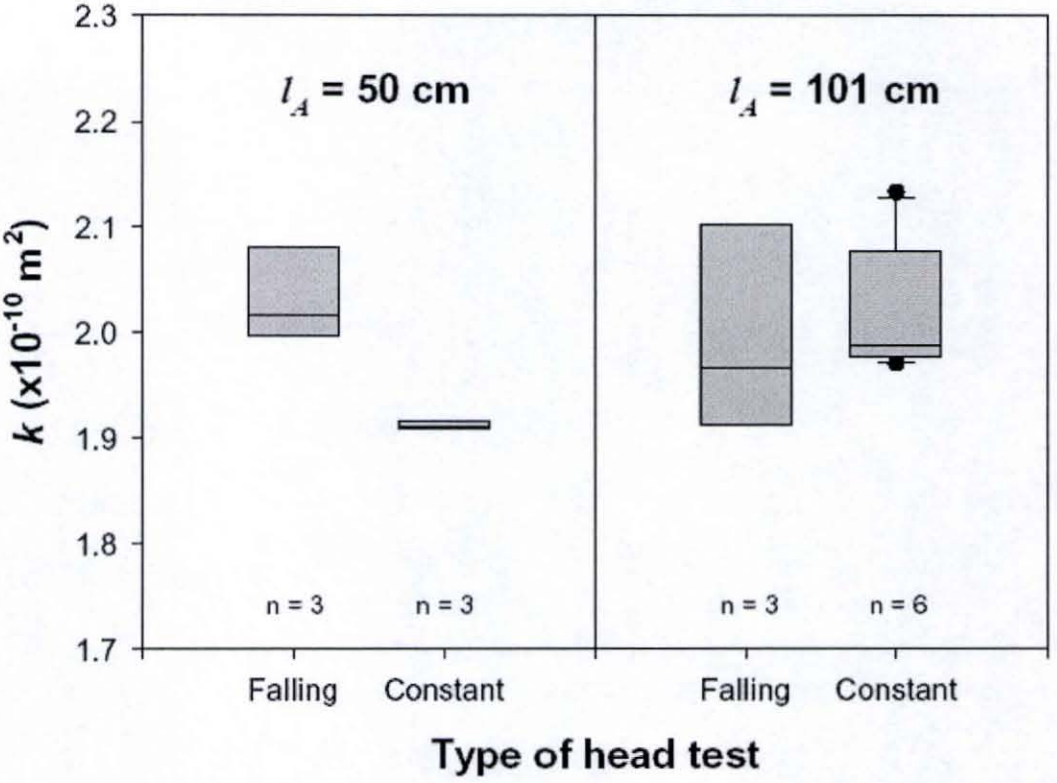

Figure 3.20 Results of permeametry tests conducted during Exp. 10 on a silica sand column. Two types of tests, falling head and constant head, were conducted with the column during two stages of its construction: with l_A=50 cm and l_A=101 cm. The ratio of H/l_A during all tests was always less than 0.4. Hydraulic conductivities were calculated from the data using Eq. 3.1 and 3.16 for constant head and falling head, respectively. Permeabilities were calculated from hydraulic conductivities using Eq. 3.9, with viscosity, $\mu = 0.01043$ g·cm^{-1}·s^{-1}, and density, $\rho = 1.023$ g·cm^{-3} (the same values as those used in Exp. 2-4, Table 3.4).

Interestingly, all measurements, binned together regardless of test type and column length, yielded an average permeability estimate of 2.0×10^{-10} with a standard deviation of 8.1×10^{-12} m^2 (a precision of 4 %, which compares favorably with 20 % for the pressure gradient relaxation method discussed in section *3.2.4.1*). The important finding of this experiment is that the permeability of 1 m-long columns can be measured with either constant or falling head permeametry after sediment column assembly, and allows for the use of the falling head method, which is logistically more straightforward.

The falling head method was employed as outlined in section *3.3.2.2* to measure the permeabilities of columns used in subsequent Exp. 11-13. The change of head difference, H, between columns A and C with time was used to obtain hydraulic conductivities for the sediment columns in Exp. 11-13 (Eq. 3.16, Figure 3.21). In turn, these conductivities were used to calculate permeabilities (Eq. 3.9), using viscosity and density values as for Exp. 2-4 (Table 3.4). The final permeability values are shown in Table 3.9.

The oxygen-impermeable membrane was visually observed to respond quickly to large head differences between Columns A and B. However, during pressure gradient relaxation tests (see section *3.2.3.1* for method), large variations in relaxation times (and, consequently, velocities) were noticed. The results of nine tests run during four experiments are shown in Table 3.11. A third of these tests yielded h_{adj} values in excess of 2.5 cm, the maximum that can be explained by height determination errors on the part of the operator. The remainder of the tests yielded $h_{adj} = 0.50 \pm 1.30$ cm (n = 6), which is approximately four times more variable compared to values obtained with relaxation tests on the first microcosm design (Table 3.5).

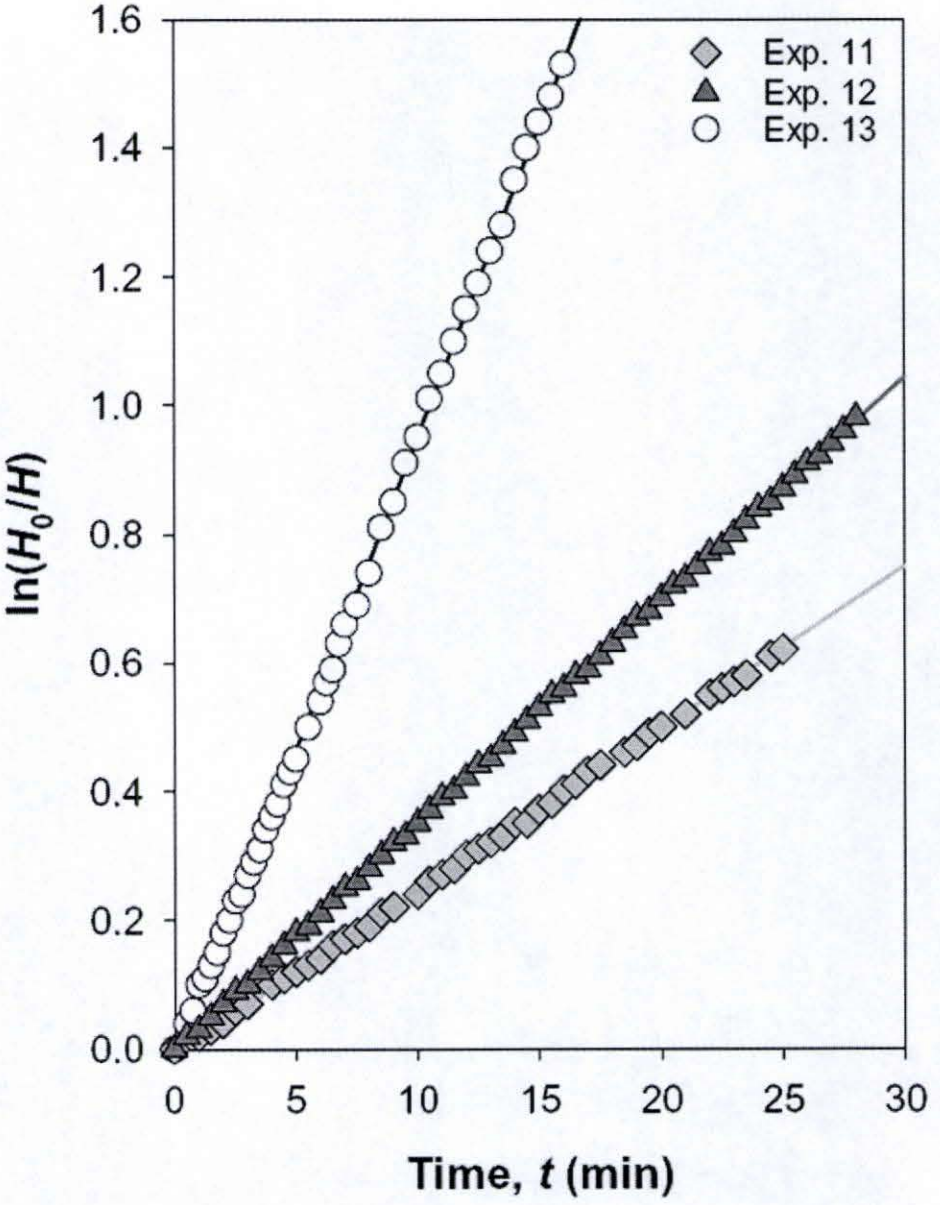

Figure 3.21 Results of falling head hydraulic conductivity measurements on the sediment columns used in Exp. 11-13. The straight lines correspond to linear regressions fitted through the data. The slopes of the three lines (0.0252, 0.0347, and 0.0968 min^{-1} for Exp. 11, 12 and 13, respectively), when multiplied by the column lengths (Table 3.8), yield the hydraulic conductivity for each column (Eq. 3.16).

Table 3.11 Results of relaxation tests performed on sediment columns of four experiments during the assessment of the modified microcosm design. Data were processed as described in section *3.2.3.1*. The permeability values of each column (k) as they were measured using the falling head method (Figure 3.21, Table 3.9) are given for comparison. Tests yielding height adjustments (h_{adj}) greater than 2.5 cm were not processed.

			Relaxation test results			
Exp. No.	l_A **(cm)**	k **(m²)**	h_{adj} **(cm)**	K_T **(cm·s⁻¹)**	v/H **(s⁻¹)**	k_T **(m²)**
11	99.5	4.3×10^{-11}	0.59	0.04	0.0004	4.2×10^{-11}
			3.68	-	-	-
12	99	6.0×10^{-11}	2.38	0.06	0.0006	6.2×10^{-11}
			-1.41	0.04	0.0004	4.2×10^{-11}
13	100	1.7×10^{-10}	1.41	0.19	0.0019	1.9×10^{-10}
			4.61	-	-	-
			-0.06	0.18	0.0018	1.9×10^{-10}
15 [a]	99	- [b]	6.07	-	-	-
			0.08	0.15	0.0015	1.6×10^{-10}

[a] Experiment and relaxation test performed by A. Rusch.

[b] Sediment was obtained from the reef sediment pocket, as in Exp. 13, and handled identically (see Table 3.9). Compare k_T values with the k for Exp. 13.

I suggest that the unusually high h_{adj} values obtained during these tests were mostly due to the conformation of the gas-impermeable membrane when forced towards the mid-point position. In this situation, this flexible membrane provides additional resistance because of a large number of invaginations of its internal surface area. These invaginations enclose water semi-permanently and substantially retard the relaxation of the pressure gradient. The solution to this problem would be to minimize the invaginations by decreasing the gross surface area of the membrane, currently 380 cm^2. A side-effect of this action would be to decrease the maximum inflation volume of the membrane (currently 1.2 L). This would not impact the microcosm operation at all, since the volume that needs to be accommodated during operation of the microcosm is much smaller (see section *3.3.2.1 Membrane incorporation*).

A minor fraction of the magnitude and variability in h_{adj} could be due to differences in the density between the seawater used in Column A and the NaCl solution used in Column B. If, for example, the two columns exert the same pressure but the density of one differs from the other by 0.001 $g \cdot cm^{-3}$, this would result in a difference in height of 0.1 cm. In that case, changes in water level in one column are not directly comparable to changes in the other. This could be resolved by using the same seawater in Column B as used in Column A.

The problem highlighted in this section does not affect significantly the operation of the microcosm and its use in experiments with permeable sediments. Two lines of evidence are provided to support this statement. Firstly, the volume of water passing the SWI during an oscillation cycle (as a result of pressure gradients between the two columns) is proportional to the ratio of v/H, derived from the data for each of the

relaxation tests (Table 3.5; Table 3.11). In turn, v/H is proportional to the total column permeability, k_T (Figure 3.22). This roughly linear proportionality indicates that, all else being the same, water exchange differences between experiments with columns of different permeabilities are an outcome of differences in k_T. Secondly, conservative tracer experiments conducted during the assessment of the modified microcosm indicate that enhanced exchange of solutes is also proportional to permeability (see section *3.3.3.2*). In conclusion, this problem is more of a nuisance than an interference. It can easily be solved as recommended in previous paragraphs, and therefore does not negate the utility of this method.

3.3.3.2 Enhanced exchange performance

During initial runs of the Rao and Jahnke (2004) tracer transport model, the model output became unstable, especially in the case of high ε values ($> 10^{2.3}$). This problem was solved by adjusting the time step of the model, dt, every time the value of ε was changed, based on the following modulus (A.M.F. Rao, personal communication; Boudreau 1997, p. 341):

$$dt \leq \frac{dz^2}{2\varepsilon \frac{D_0}{\theta^2}} \qquad 3.18$$

These initial runs also indicated that the profile data were better explained by assuming that the sediment column is experiencing enhanced transport heterogeneously. Specifically, instead of one ε value for the whole column, an upper layer with high ε was assumed to overlie a lower layer with a lower ε value. An initial value for the depth separating the two layers, z_{layer}, was selected by visually inspecting the data. This initial

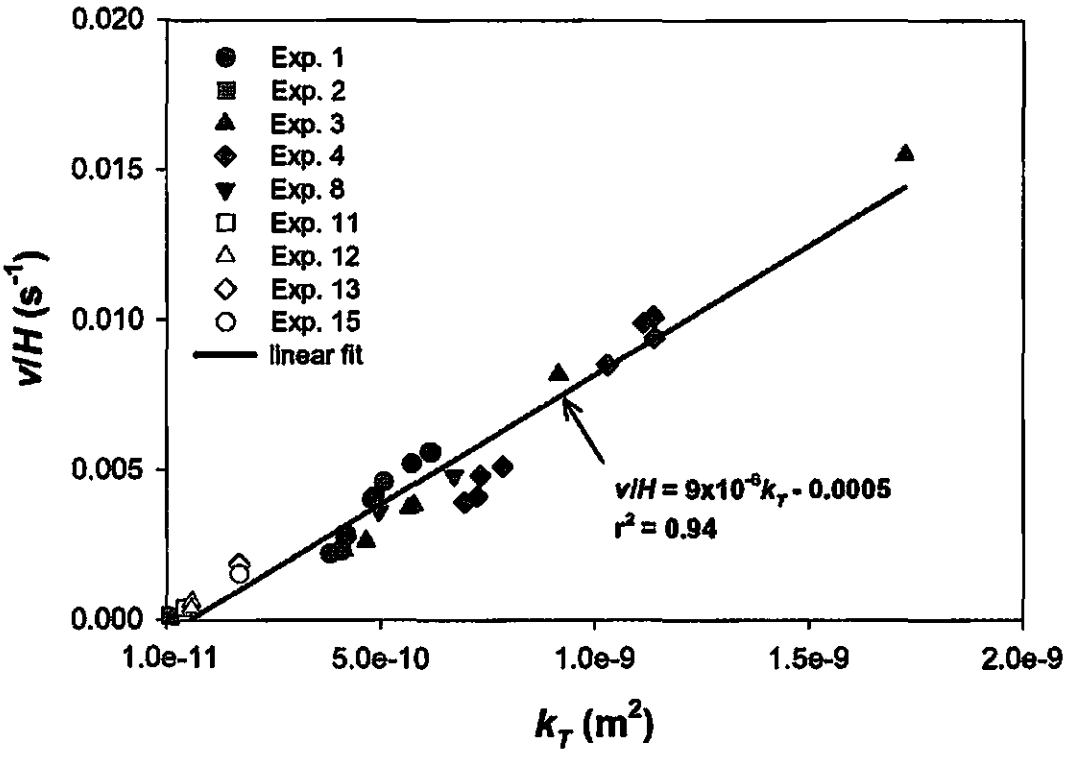

Figure 3.22 The ratio of *v/H* plotted against total permeability for each relaxation test of this study. See Section *3.2.3.1* for methods. Data from experiments using the original microcosm are plotted with filled symbols, and those from experiments using the modified microcosm with open symbols. Values of the two parameters are linearly related over a permeability range of two orders of magnitude (2×10^{-11} m^2 to 2×10^{-9} m^2).

value was optimized by running the model within an optimization routine which tested for the best-fit values of z_{layer}, and ε_{upper} and ε_{lower} (the diffusion enhancement factors for the upper and lower layer respectively) using a χ^2 statistic. An example of profile data fitted with one- and two-layer models is shown in Figure 3.23. Single-depth time-series data were processed with a one-layer model only, because of the lack of depth resolution that would justify the determination of z_{layer}, ε_{upper}, and ε_{lower}.

Detailed model run results are shown in Table 3.12, and they are summarized in Table 3.13 along with sedimentary column permeabilities. It is notable that the difference in χ^2 for 1-layer and 2-layer models becomes more distinct at greater k_A. The greater success of 2-layer models in simulating the data suggests that the mechanism that causes the presence of more than one "hydraulic layer" is a permanent feature of this microcosm. This mechanism is most likely turbulence caused by the pumping of water into Column A at Connection II (Figure 3.13) at rates of tens of milliliters per second. The effect becomes more evident as k_A increases, and this increase is manifested in higher values for z_{layer} and ε_{upper} necessary to simulate the data (Table 3.12). It should be pointed out that the success of the two-layer fit is not necessarily an indication that only two layers with distinct hydraulic characteristics exist in the column, but rather that this assumption statistically reproduces the observed changes due to transport.

Changes in pumping parameters also affect the values of z_{layer} and ε_{upper}. Specifically, dropping f from 3 min^{-1} to 1 min^{-1} (from Tracer Exp. 14-1 to 15-1 respectively) increases the ε_{upper} value markedly (Table 3.12). On the other hand, the combined increases of h and f between Exp. 13-14 did not yield a substantial change in

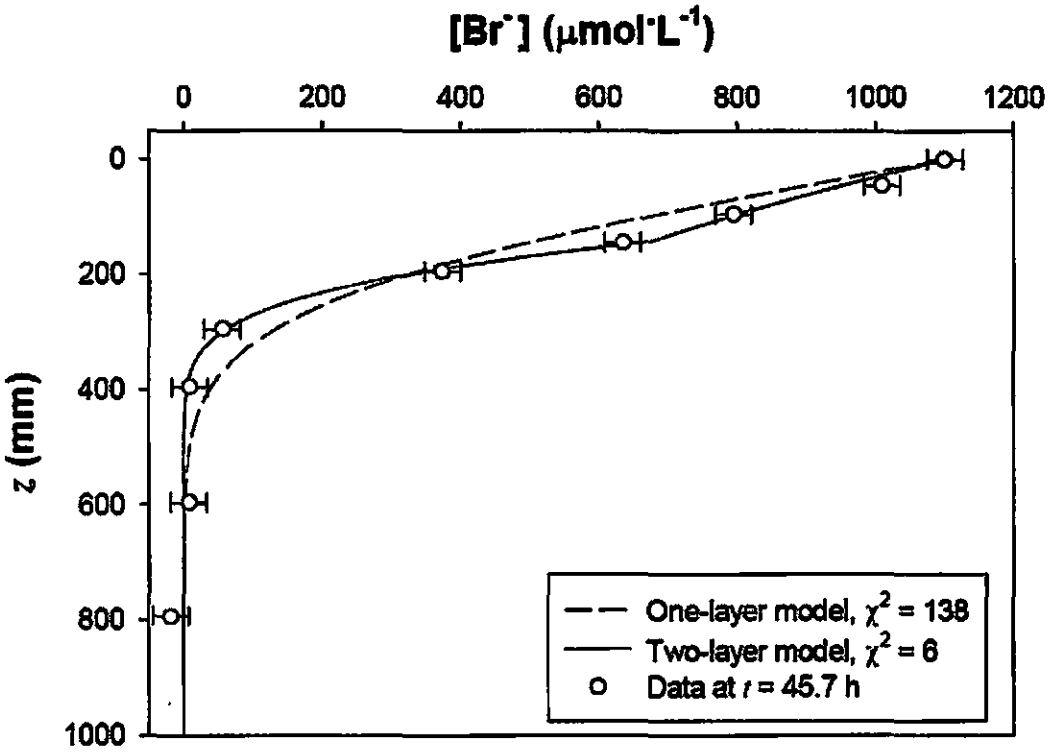

Figure 3.23 Model results for tracer experiment 14-1 (Table 3.12), superimposed on the data of bromide concentration, $[Br^-]$, with depth, z, at $t = 45.7$ h. The horizontal error bars on the data points indicate the analytical error ($\pm$ 26 $\mu mol \cdot L^{-1}$).

Table 3.12 Enhancement factors for Exp. 11-15. Both 1- and 2-layer fits are given for profile data (compare χ^2 values).

Exp. #	Tracer Exp. #	h (cm)	f (min^{-1})	Data type	z^a (cm)	1-layer fit		2-layer fit			
						ε	χ^2	z_{layer} (mm)	ε_{upper}	ε_{lower}	χ^2
11	11-1	0.6	2	time-series	4.5	13	49	-	-	-	-
11	11-3	8.5	2	profiles	-	90	58	75	90	16	49
12	12-1	8.5	2	profiles	-	14	26	10	55	13	20
12	12-1	8.5	2	time-series	4.0	28	35	-	-	-	-
13	13-1	8.5	2	profiles	-	213	38	55	426	176	7
13	13-1	8.5	2	time-series	5.0	139	27	-	-	-	-
13	13-2[b]	8.5	2	time-series	5.0	66	27	-	-	-	-
14	14-1	10.5	3	profiles	-	248	138	145	287	100	6
15	15-2	10.5	1	profiles	-	566	270	145	795	100	31

[a] Depth, z, at which time-series data were recorded;

[b] Tracer experiment 13-2 was conducted after the addition of a *Dunaliella* culture to the overlying water of the microcosm (see text for details).

Table 3.13 Comparison of sediment column permeabilities (k_A), with tracer transport experiment parameters (oscillation height, h, and frequency, f) and model-generated enhancement factors, ε.

Tracer Exp. #	k_A (m^2)	h (cm)	f (min^{-1})	ε (log)
11-1	4.3×10^{-11}	0.6	2	1.1
11-3	4.3×10^{-11}	8.5	2	1.2-2.0
12-1	6.0×10^{-11}	8.5	2	1.1-1.7
13-1	1.7×10^{-10}	8.5	2	2.1-2.6
14-1	1.7×10^{-10}	10.5	3	2.0-2.5
15-1	1.7×10^{-10}	10.5	1	2.0-2.9

the range of ε (Table 3.13). This suggests that rapid changes in pressure gradient induced by higher f do not enhance transport as much as longer periods (lower f) would under the same pressure gradient. Above and beyond the presence of two hydraulically active layers, the values of ε generally increase with k_A for both the upper and lower layers of hydraulic activity (Table 3.13), indicating that the enhanced transport of solutes is experienced throughout the sediment column.

The results for Tracer Exp. 12-1 yield lower ε values than those of Tracer Exp. 11-3, a pattern inverse of that predicted by k_A. However, Exp. 12 was interrupted by a power failure due to an earthquake (October 15, 2006). Pumping ceased for 20 h, and – more importantly – the temperature rose by 4-5 °C over the same period of time. This

may have had an adverse effect on the permeability of the column, perhaps by encouraging faster growth of biofilms within the column and impeding solute exchange after this point. Additional support for the adverse effects of this 20 h-long increase in temperature is available from particle transport data, collected during enrichment experiments described in Chapter 4.

Data from those enrichment experiments may also explain the decrease in ε recorded between two tracer experiments, 13-1 and 13-2 (Table 3.12). At a time point between 13-1 and 13-2, a culture of the chlorophyte *Dunaliella* was added in the overlying water, to yield abundances of 50000 cells·mL^{-1}. Based on cell counts on samples from the microcosm experiment and from control experiments (data not shown), these cells disappeared from the overlying water within 2 d, and a significant portion entered the sediments where they degraded. It is possible that the presence of these algae, and the resulting biofilm development by sedimentary microbiota during their degradation, may have caused a decrease in hydraulic conductivity of the sediment column at the SWI, resulting in a lower ε value.

The values of ε at fixed pumping settings could vary during an incubation experiment as a consequence of changes in the sedimentary column's permeability. Processes which may account for changes in permeability, and consequently ε, during an incubation experiment include biofilm disruption and formation, carbonate dissolution, and compaction. It is possible that, during field sediment sampling and column assembly, sediment grain aggregations held together by biofilms may be disaggregated thus causing an increase in permeability. These biofilms may form relatively quickly after assembly, especially if the microbial biomass is still present (e.g., Yingst and Rhoads 1980; Findlay

et al. 1992), thus causing a drop in ε values by restricting the localized exchange of water that drives enhanced exchange. Carbonate dissolution by metabolic CO_2 (generated during organic matter degradation) may slowly bring down the average grain size, and thus decrease permeability (Figure 2.2). At the same time, grain roughness which is fairly high in coralligenous carbonate grains, may be reduced resulting in an increase in permeability (Beard and Weyl 1973). If dissolution, which would result in the overall decrease in the amount of material, is not accompanied by a change in volume, it may result in an increase in permeability due to an increase in porosity (Figure 2.2). Alternatively, if dissolution leads to compaction of the sediment column, along with a decrease in average grain size, it may lead to a decrease in permeability. The above processes are not mutually exclusive and could all work simultaneously to affect a change in permeability. The data which are available from experimentation with the microcosm (Exp. 8, Table 3.6) suggest that a slight, statistically non-significant increase in the permeability of a carbonate reef sediment column takes place over a period of 100 d. Therefore, ε is not likely to change significantly by simple incubation of the originally used sedimentary material. External manipulation may be required, such as the addition of organics which act as stimulants of microbial activity including biofilm formation, or the input of very fine particulates which may be trapped in the sediment column and form a low permeability layer.

Field measurements of enhanced transport at Kilo Nalu have recently been completed (Hebert et al. 2007). A fluorescent dye injection and monitoring system was used to conduct enhanced transport experiments at the location where sediments for Exp. 11 were collected (Kilo Nalu sand field, Table 3.9) and at a sediment depth of 15 cm. At

the time field experiments were conducted, waves were characterized by heights of 0.4-1.3 m, and periods of 15 s. I converted the reported enhanced transport rates to ε values using a free solution diffusion coefficient of fluorescein of 1.73 $cm^2 \cdot h^{-1}$, and contrasted them with ε values obtained from conservative tracer experiments during Exp. 11 (Table 3.12), relating each ε value to the corresponding wave or oscillation height, h (Figure 3.24).

It is important to point out that the values of h used in the relationship of Figure 3.24 correspond to the oscillation at the water column surface and not at the sediment depth at which the experiments took place. Specifically, the water column at Kilo Nalu is 10 m deep and experimental measurements took place at z = 15 cm. In contrast, during Exp. 11, the overlying water height was 50 cm, and the measurements took place both at a fixed depth (z = 4.5 cm), i.e., in a manner analogous to that used by Hebert et al. (2007), as well as by using depth-integrated changes in tracer concentration (the profile technique, Table 3.12). If the wavelength, λ, corresponding to each h in the field were known, it would be possible to correct for h attenuation with depth using the relationship:

$$h(w) = h_0 e^{-k^* w} \qquad 3.19$$

where h_0 and $h(w)$ are wave heights at depths 0 and w respectively, and the wave number, $k^* = 2\pi \div \lambda$. It is likely that h(10 m) would be greatly reduced, relative to the values used in Figure 3.24. Even after correcting for attenuation with w, the problem of comparing transport conditions at different sediment depths, z, would persist. Application of the Rao and Jahnke (2004) model to microcosm conservative tracer experiments has shown that multi-ε solutions yield results that are more representative of the observations than a

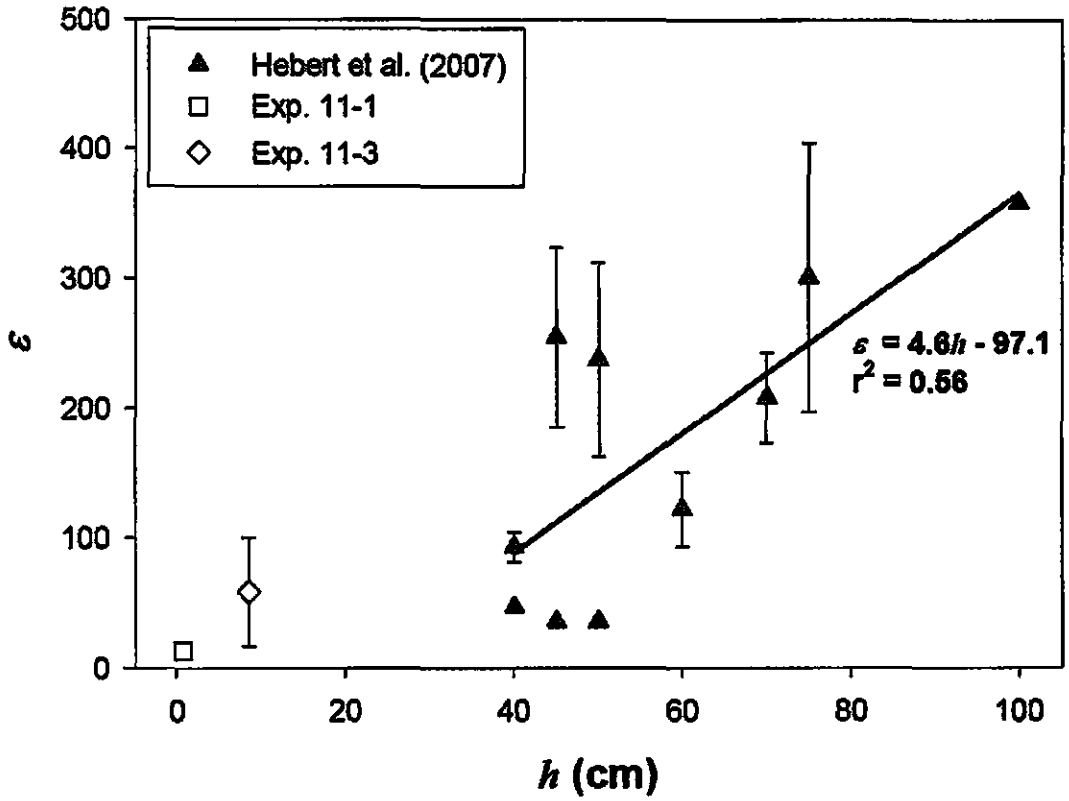

Figure 3.24 Relationship between wave or oscillation height, h (cm), and enhancement factor, ε, in data from solute tracer experiments using Kilo Nalu sand field sediment. Experiments were conducted in the field (closed symbols, Hebert et al. 2007) and the laboratory (open symbols, Exp. 11, Table 3.12). The values of h for the field data correspond to the average significant wave height for the duration of each tracer experiment.

single-ε solution (Figure 3.23). The topic of physical pore water solute transport remains one of the major questions in permeable sediment studies (Huettel and Webster 2001)

Therefore, based on the discussion in the previous paragraph, it is with caution that the comparison illustrated in Figure 3.24 is made and the following statements are put forth. It is evident that the degree of enhanced transport achieved by the microcosm with the pumping settings of Exp. 11 (Table 3.12) is on the lower end of those observed in the field. The presence of advective forcing in the form of currents (Hebert et al. 2007), as well as the interaction of these currents with sand ripples, may account for the greater enhancement factors observed in the field. Overall, all the enhanced transport conservative tracer experiments conducted with the microcosm demonstrate that the microcosm design can cause enhanced transport 1-3 orders of magnitude greater than that caused by molecular diffusion, and that the degree of enhancement is roughly proportional to the permeability of the sediment column in Column A (Table 3.13). The tracer transport model successfully reproduces the observed enhanced transport pattern by using two sedimentary layers with distinct degrees of enhanced transport (Eq. 3.17). The success of the model described by Eq. 3.17 proves that the solute transport process in the microcosm is a diffusion-like process and can be modeled as such (Boudreau 1997, p. 39-41). To simulate enhanced transport observed under open ocean waves and swell, the pumping parameters must be changed from those used in these experiments, by decreasing the oscillation frequency and increasing the oscillation height.

3.3.3.3 Biogeochemical response of sediments to microcosm incubation

A comparison of field data from the Kilo Nalu Observatory and microcosm Exp. 11 data is shown in Figure 3.25. The sediment incubated during Exp. 11 came from the vicinity of the wells, which were sampled to generate the Kilo Nalu pore water data. The field and microcosm data are similar in dissolved oxygen concentrations but differ in ammonium and phosphate concentrations. Whereas oxygen was depleted by a depth of 4.5 cm in the microcosm, oxygen was occasionally detectable at 7.5 cm depth in the field. Despite the apparently high sedimentary oxygen consumption rate, oxygen levels were maintained at a near-saturation level in the overlying water throughout Exp. 11 (data not shown). On the other hand, ammonium in the microcosm pore water builds up to concentrations three to four times those of Kilo Nalu pore water, and the same pattern is observed for phosphate.

One obvious explanation for these observations is that the physical forcing and the subsequent flushing of solutes out of the sediments is greater in the field than in the microcosm (since permeability is the same in both). This actually can be predicted from the results of the conservative tracer experiments described in the previous section. Those experiments showed that the induced exchange in the microcosm was one order of magnitude less intense than that measured in the field (Hebert et al. 2007). The difference observed in pore water solute concentrations is further enhanced by the timing of the field sampling. Summer on the south shores of the Hawaiian Islands is a period of maximum exposure to open-ocean, long-period swell generated from Southern Ocean storms (Grigg 1998). It is likely that oxygen penetration is highest during this time period, which is when the in situ samples were collected.

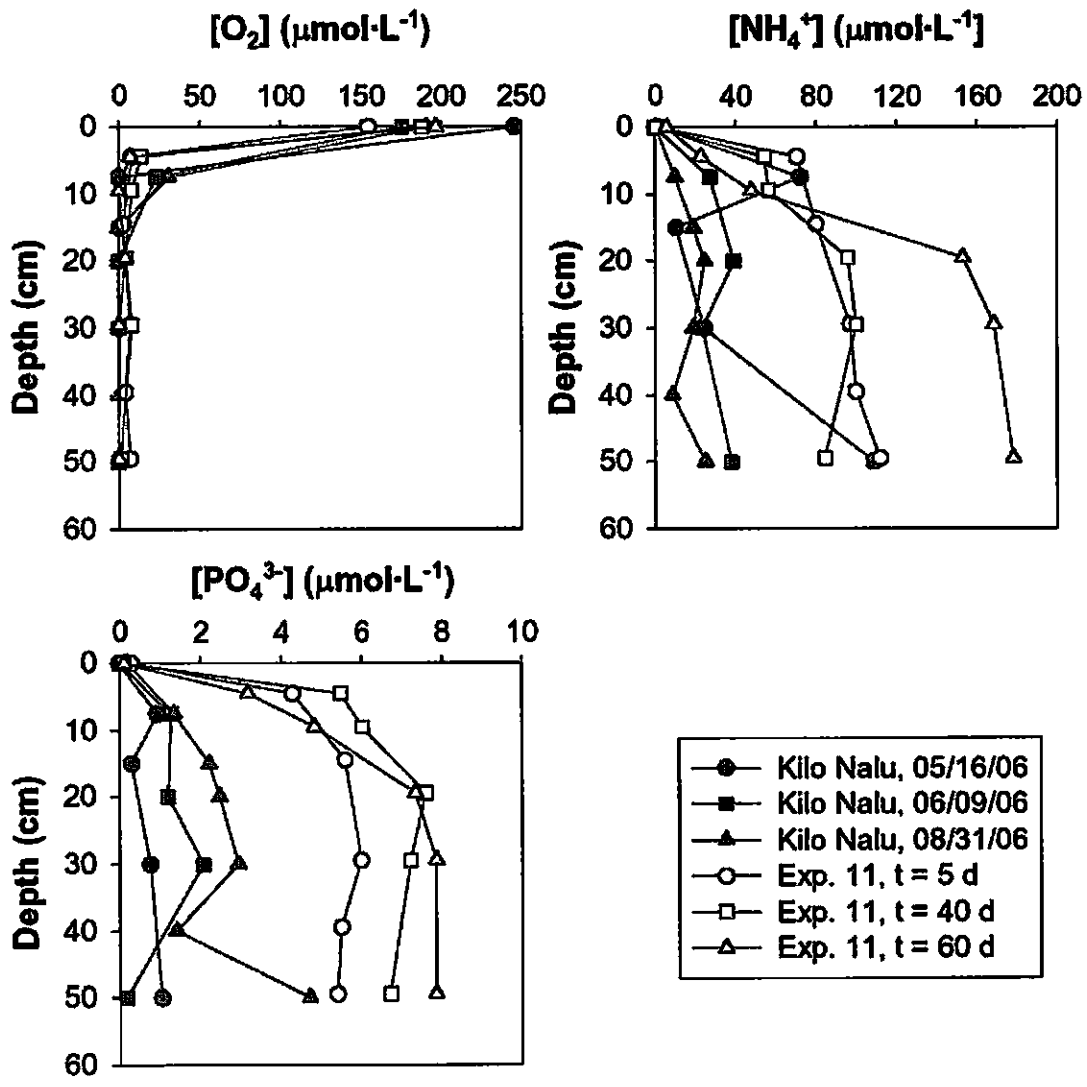

Figure 3.25 A comparison of the concentrations of oxygen, ammonium, and phosphate in Kilo Nalu pore water and microcosm pore water. The sediment used in the microcosm during Exp. 11 was collected from the vicinity of the wells sampled for pore water at Kilo Nalu. Kilo Nalu samples were collected during three field trips to the Observatory's 10-m node (May 16th, June 9th, and August 31st, 2006). Microcosm samples were collected at three well-spaced time-points during Exp. 11 (5, 40, and 60 days after t=0).

The build-up of phosphate and ammonium in the anoxic section of the microcosm column (most likely an outcome of organic matter decomposition) is suggestive of the relatively high reaction potential of these sediments (e.g., Marinelli et al. 1998). Interestingly enough, nitrate and nitrite concentrations were very low or undetectable (<1 $\mu mol \cdot L^{-1}$ and <0.07 $\mu mol \cdot L^{-1}$ respectively) in both field and microcosm profiles, which is consistent with the lack of dissolved oxygen in these sediments (e.g., Sansone et al. 1990; Tribble et al. 1990). In addition, all nutrients were undetectable in the overlying water in both cases. The shape of the solute profiles in Figure 3.25 is suggestive of nutrient fluxes away from the center of the sediment column towards the sub-oxic surface layer and the overlying water (e.g., Berner 1980). In the absence of appreciable nitrate and nitrate, it must be surmised that these nutrients are removed from the dissolved inorganic solute pool. One potential destination is the particulate pool, whether it is biotic uptake by subaerobic or aerobic biota or abiotic precipitation in the case of phosphate (e.g., Ogrinc and Faganeli 2006). Another possible sink for ammonium is denitrification through nitrification (Rao 2006).

With respect to the assessment of the microcosm design, it is important to realize that the absence of the exchange of overlying water renders the modified microcosm a "closed system," with respect to the elements that are not affected by gas exchange. The pools of elements, such as phosphorus, iron and manganese, will remain constant in the microcosm throughout incubation. However, the individual atoms will be redistributed, based primarily on redox conditions that dictate their mobilization or immobilization. For example reduced iron and manganese are soluble, albeit highly adsorptive (Burdige 2006, p. 108), and could diffuse away from the anoxic layers of the column. Phosphorus, whose

cycling is closely tied to that of iron (Slomp et al. 1996; Ruttenberg 2003), is strongly bound by iron oxides. In the case of regeneration during anaerobic organic matter degradation, phosphate will drift upwards towards the oxic surface layer of the sediment column, where it will be bound by oxidized iron (this is very likely one of the explanations for the phosphate profiles observed during Exp. 11, Figure 3.25). The absence of any significant signal of phosphate in the overlying water illustrates how the microcosm can be used to demonstrate frequently surmised processes, such as the phosphate removal process by iron oxides which greatly attenuates phosphate flux across the SWI (Burdige 2006, p. 468). In the case of elements such as iron, manganese and phosphorus, incubation of an originally homogeneous sediment column in the microcosm will result in their redistribution along the sediment column, based on their individual properties primarily in relation to redox conditions. The elemental redistribution process should be kept in mind when designing long-term experiments that could be affected by the localized accumulation of these elements with incubation time and how it could affect the conducted experiments and their results. In the case of the examples mentioned in this paragraph, this redistribution is perfectly natural over the time scales of the typical experiments (days-weeks).

On the contrary, examples of elements affected by gas exchange are carbon and nitrogen. The processes of organic matter degradation and denitrification could lead to the depletion of the carbon and nitrogen pools in the microcosm, through their loss as the gases CO_2 and N_2 respectively. The aeration of the overlying water of the microcosm renders it an open system with regards to such elements that would otherwise accumulate

in the gaseous phase. In other words, analysis of the composition of the overhead gas during incubation is unlikely to yield meaningful or defensible results.

3.3.4 Conclusions on the modified microcosm method

The modified design is overall an improvement, compared to the original design, in that it removed unknown biogeochemical sinks or sources from the silica sand column in Column B, while it retained useful characteristics from the original design (e.g., the generation of enhanced solute transport across the SWI, and the capability to sample pore water non-destructively during the course of an experiment). Moreover, streamlined procedures for the assembly and operation of the microcosm were developed, including the determination of important hydraulic parameters using specially compiled mathematical tools, and the testing of suitable protocols for the analysis of solutes of interest.

The complete elimination of the reservoir and the continuous exchange of Column A overlying water with replacement water (Figure 3.1) permitted the demonstration of the lack of accumulation of nutrients from the sediment pore water in the overlying water, which, in conjunction with nutrient profiles, points at their removal at the surface layers of the sediment column by biotic and abiotic processes. Accumulation of nutrients in the overlying water would not be detectable with the prototype microcosm due to their continuous removal and dilution through Connection IV (Figure 3.1). The microcosm acts as a closed system for elements such as iron, manganese, and phosphorus, which are not affected by gas exchange. Elements in the latter group include carbon and nitrogen which can be lost during microbial exploitation

in the gas phase as ΣCO_2 and N_2 respectively. The microcosm, as it is configured in its modified form, does not allow the reliable monitoring of compositional changes in the overhead gas.

The oxygen-impermeable membrane functioned well as a hydraulically active but chemically impervious barrier, but its inflation volume may need to be minimized in order to prevent interference with the hydraulic function of the column under certain configurations. One such configuration may be pumping frequencies, f, lower than those tested in this study. Measurements of enhanced transport and pore water biogeochemistry during incubation of Kilo Nalu sediments in the microcosm were compared with field measurements and indicated that the pumping parameters used in the incubations did not generate adequate solute exchange across the SWI to match in situ values. Values of $f < 1$ min^{-1} may be necessary in order to generate field-level enhanced exchange with this modified microcosm design. The effect of $f < 1$ min^{-1} on the hydraulic function of the microcosm should be investigated with the hydraulic characterization methods described in this chapter, to assess whether the proposed decrease of the inflation volume of the membrane allows the non-disrupted function of the microcosm.

3.3.5 Future methodological developments

Future efforts in understanding the biogeochemical function of permeable sediments would benefit by the use of the microcosm described in this chapter. The major innovation is the oscillating flow across the SWI (as opposed to the unidirectional flow of flow-through chambers and stirred chambers) while using a relatively small amount of sediment (as opposed to flumes). Achieving the oscillating flow at the present stage of

development requires constant supervision (see discussion in section *3.3.3.1*). The automation of water level control with the use of a pressure sensor that interfaces with the pump operation software would greatly improve the reliability of the method without constant inspection.

The microcosm method could be modified to generate oscillatory flows of greater magnitude by the replacement of the peristaltic pump with a more reliable dispenser such as a syringe pump (M. Huettel, personal communication). Such a pump (e.g., NE-515 OEM, New Era Pump Systems) could replace Column B completely and connect Column A with a small, flexible, oxygen-impermeable reservoir (e.g., a Durashield 45 bag from Scholle Corporation) at Connection III. The computer-controlled pump could force an oscillatory pore water motion through the sediment column, in the same way pistons have been used to generate shear dispersion through pipes in past experiments (Joshi et al. 1983). I suspect that very low pumping rates (impossible by the Masterflex drives used in this study) by such a syringe pump will induce enhanced transport rates several orders of magnitude greater than molecular diffusion. The proposed modification could produce an oscillating-flow platform that enables studies of nutrient dynamics and organic enrichment directly comparable with those performed using flow-through chambers (e.g., Rao 2006; Rusch et al. 2006). Such a comparison would highlight the differences between oscillatory, wave-induced flow (simulated by the oscillating-flow platform) and advective flow through sediment (simulated by flow-through chambers) and their effects on sedimentary biogeochemistry. Microbes occupying a certain position in the sediment column would experience a relatively constant redox environment under unidirectional flow in a flow-through chamber, whereas in an oscillating-flow chamber they would

experience oscillatory redox conditions, which have been shown to affect sedimentary respiration significantly (Aller 1994).

Although the adaptation of conventional analytical techniques helped satisfy the need for assessment of the concentrations of various solutes, the same goal could be achieved at a much greater spatial and temporal resolution with the use of microelectrodes. With the need to remove water samples for analysis gone, more ports can be drilled in Column A through which the pore water at many more depths can be interrogated at will for a variety of parameters. If numerous microelectrodes are available, concentrations can be recorded at various depths simultaneously. Microelectrode arrays could allow the careful observation of the physical and biogeochemical response of the column to changes in the oscillation parameters in a manner not possible with the present configuration (due to the large amount of pore water sample that would be required).

Finally, fluorescent bead particles of various sizes (e.g., Rusch and Huettel 2000)could be used in conjunction with fluorescence microelectrodes to detect particle penetration patterns in the sediment column in response to specific oscillation settings. Experimentation with such beads would allow the development of refined specifications regarding the experimentation with particles of various sizes and their penetration depths at different oscillation settings.

3.4 Conclusions

The microcosm described in this study allows experimentation with permeable sediments in a simple and affordable manner. Sediment columns of permeability $k > 10^{-11}$

m^2 can be assembled and incubated for several days to weeks under controlled physical forcing. Conservative tracer experiments demonstrated the generation of enhanced transport of solutes across the SWI and the quantification of this enhancement using specially developed mathematical tools. Relatively deep gradients in pore water solute concentrations have been recorded using non-destructive pore water sampling simultaneously with conservative tracer experiments. Comparison of microcosm incubation data with data collected in the field indicates that the physical forcing used during the assessment incubations may not be sufficient to reproduce the magnitude of enhanced transport and pore water gradients observed at the relatively high-energy site of the Kilo Nalu Observatory 10-m node, but should adequately match exchange rates at lower energy sites.

The physical forcing control of the microcosm could be enhanced using the modified design and operation procedures (i.e., by changing the pumping parameters). However, the microcosm method would benefit greatly by advances in the determination of the physical mechanisms responsible for enhanced transport in coral reef-associated sediments and the generation of deep and broad redox gradients such as those observed by Falter and Sansone (2000b). Modification of the pumping mechanism by replacement of the peristaltic pump with a syringe pump could perhaps allow the induction of enhanced transport rates several orders of magnitude greater than molecular diffusion. The resulting oscillating-flow platform would allow a comparison with the operation of flow-through chambers and could highlight the differences between oscillatory, wave-induced flow and advective flow through sediment and their effects on sedimentary biogeochemistry.

The microcosm method described in this chapter would also benefit greatly by the use of the increasingly versatile array of microelectrodes. Microelectrodes, inserted into Column A through multiple air-tight ports for the duration of an experiment, could continuously monitor the concentrations of a variety of dissolved species at multiple depths in the microcosm. The use of microelectrodes could solve the problem of sample volume limitation (imposed by the water budget of the microcosm) that restricts the number of analyses that could be performed on any one sample. Microelectrode-generated solute records would also enable experimentation that aims to connect changes in enhanced transport with shifts in redox conditions by providing the necessary high-frequency data in as non-invasive a manner as possible.

The current design of the microcosm allows the satisfactory design and execution of incubation experiments with permeable sediments. While it is an open system with respect to dissolved gases, it allows the measurement of elemental budgets for biogeochemically significant solutes such as nutrients, and the elucidation of consumption or production processes of these nutrients during early diagenesis. Chapter 4 includes the description of a set of enrichment experiments performed using the microcosm, and further demonstrates its utility.

3.5 References

Aller, R. C. (1994) Bioturbation and remineralization of sedimentary organic matter: effects of redox oscillation. Chemical Geology, 114: 331-345.

Aller, R. C., A. K. Hannides, C. E. Heilbrun and C. Panzeca (2004) Coupling of early diagenetic processes and sedimentary dynamics in tropical shelf environments: the Gulf of Papua deltaic complex. Continental Shelf Research, 24: 2455-2486.

Atkinson, M. J., B. Carlson and G. L. Crow (1995) Coral growth in high-nutrient, low-pH seawater: A case study of corals cultured at the Waikiki Aquarium, Honolulu, Hawai'i. Coral Reefs, 14: 215-223.

Balatre, M. P. (1936) Sur le dosage colorimétrique de petites quantités de Brome en présence d'un grand excès de Chlore. Journal de Pharmacie et de Chimie, 23: 409-413.

Beard, D. C. and P. K. Weyl (1973) Influence of texture on porosity and permeability of unconsolidated sand. American Association of Petroleum Geologists Bulletin, 52: 349-369.

Bendschneider, K. and R. J. Robinson (1952) A new spectrophotometric method for the determination of nitrite in seawater. Journal of Marine Research, 11: 87-96.

Berg, P. and K. J. McGlathery (2001) A high-resolution pore water sampler for sandy sediments. Limnology and Oceanography, 46: 203-210.

Berner, R. A. (1980) Early diagenesis. Princeton University Press, Princeton, New Jersey, U.S.A., pp. 241.

Berner, R. A. (1981) Early diagenesis. Princeton University Press, pp. 241.

Berthelot, M. P. E. (1859) Violet d'aniline. Répertoire de Chimie Appliquée, 1: 284-284.

Boudreau, B. P. (1997) Diagenetic models and their implementation. Springer, Berlin, Germany, pp. 414.

Breitzke, M. (2000) Physical properties of marine sediments, p. 29-72. *In* Schulz, H. D. and M. Zabel [eds.], Marine Geochemistry. Springer-Verlag, Berlin, Germany.

Brügmann, L. and K. Kremling (1999) Sampling, p. 1-25. *In* Grasshoff, K., K. Kremling and M. Ehrhardt [eds.], Methods of seawater analysis. Wiley-VCH, Weinheim, Germany.

Burdige, D. J., M. J. Alperin, J. Homstead and C. S. Martens (1992) The role of benthic fluxes of dissolved organic carbon in oceanic and sedimentary carbon cycling. Geophysical Research Letters, 19: 1851-1854.

Burdige, D. J. (2006) Geochemistry of marine sediments. Princeton University Press, Princeton, New Jersey, U.S.A., pp. 609.

Burmister, D. M. (1955) Principles of permeability testing of soils, p. 3-20. *In* Barber, E. S. [ed.], Symposium on permeability of soils. ASTM Special Technical Publication No. 163. American Society for Testing Materials, Philadelphia, Pennsylvania, U.S.A.

Clark Jr., L. C., R. Wolf, D. Granger and Z. Taylor (1953) Continuous recording of blood oxygen tensions by polarography. Journal of Applied Physiology, 6: 189-193.

Cline, J. D. (1969) Spectrophotometric determination of hydrogen sulfide in natural waters. Limnology and Oceanography, 14: 454-458.

Crank, J. (1957) The mathematics of diffusion. Oxford University Press, London, U.K., pp. 347.

Dale, N. G. (1974) Bacteria in intertidal sediments: factors related to their distributions. Limnology and Oceanography, 19: 509-518.

Dinariev, O. Y., A. B. Mosolov and O. V. Nikolaev (1989) Filtration through a porous barrier between two communicating vessels. Journal of Applied Mechanics and Technical Physics, 30: 143-147.

Engels, M. S., C. H. Fletcher, M. E. Field, C. D. Storlazzi, E. E. Grossman, J. J. B. Rooney, C. L. Conger and C. Glenn (2004) Holocene reef accretion: Southwest Molokai, Hawaii, U.S.A. Journal of Sedimentary Research, 74: 255-269.

Fagan, K. E. and F. T. Mackenzie (2007) Air-sea CO_2 exchange in a subtropical estuarine-coral reef system, Kaneohe Bay, Oahu, Hawaii. Marine Chemistry, 106: 174-191.

Falter, J. L. and F. J. Sansone (2000a) Shallow pore water sampling in reef sediments. Coral Reefs, 19: 93-97.

Falter, J. L. and F. J. Sansone (2000b) Hydraulic control of pore water geochemistry within the oxic-suboxic zone of a permeable sediment. Limnology and Oceanography, 45: 550-557.

Findlay, R. H., S. L. Kim and C. A. Butman (1992) Colonization of freshly deposited barite and silica sediments by marine microorganisms in a laboratory flume flow. Marine Ecology Progress Series, 90: 73-88.

Fleming, R. T. (1939) Tables for sigma-t. Journal of Marine Research, 2: 9-11.

Flury, M. and N. N. Wai (2003) Dyes as tracers for vadose zone hydrology. Reviews of Geophysics, 41: 1002, doi:10.1029/2001RG000109.

Fritsche, U., A. Koschinsky and A. Winkler (2001) The different diffusive transport behaviors of some metals in layers of Peru Basin surface sediment. Deep-Sea Research II, 48: 3653-3681.

Grigg, R. W. (1998) Holocene coral reef accretion in Hawaii: a function of wave exposure and sea level history. Coral Reefs, 17: 263-272.

Haberstroh, P. R. and F. J. Sansone (1999) Reef framework diagenesis across wave-flushed oxic-suboxic-anoxic transition zones. Coral Reefs, 18: 229-240.

Hansen, H. P. (1999) Determination of oxygen, p. 75-89. *In* Grasshoff, K., K. Kremling and M. Ehrhardt [eds.], Methods of seawater analysis. Wiley-VCH, Weinheim, Germany.

Hansen, H. P. and F. Koroleff (1999) Determination of nutrients, p. 159-228. *In* Grasshoff, K., K. Kremling and M. Ehrhardt [eds.], Methods of seawater analysis. Wiley-VCH, Weinheim, Germany.

Hargrave, B. T. (1972) Aerobic decomposition of sediment and detritus as a function of particle surface area and organic content. Limnology and Oceanography, 17: 583-596.

Hebert, A. B., F. J. Sansone and G. R. Pawlak (2007) Tracer dispersal in sandy sediment porewater under enhanced physical forcing. Continental Shelf Research, 27: 2278-2287.

Hobbie, J. E., R. Daley and S. Jasper (1977) Use of Nuclepore filters for counting bacteria by fluorescence microscopy. Applied and Environmental Microbiology, 33: 1225-1228.

Hubbert, M. K. (1940) The theory of ground water motion. Journal of Geology, 48: 785-944.

Huettel, M. and G. Gust (1992a) Solute release mechanisms from confined sediment cores in stirred benthic chambers and flume flows. Marine Ecology Progress Series, 82: 187-197.

Huettel, M. and G. Gust (1992b) Impact of bioroughness on interfacial solute exchange in permeable sediments. Marine Ecology Progress Series, 89: 253-267.

Huettel, M., W. Ziebis and S. Forster (1996) Flow-induced uptake of particulate matter in permeable sediments. Limnology and Oceanography, 41: 309-321.

Huettel, M., W. Ziebis, S. Forster and G. W. Luther III (1998) Advective transport affecting metal and nutrient distributions and interfacial fluxes in permeable sediments. Geochimica et Cosmochimica Acta, 62: 613-631.

Huettel, M. and A. Rusch (2000) Transport and degradation of phytoplankton in permeable sediment. Limnology and Oceanography, 45: 534-549.

Huettel, M. and I. T. Webster (2001) Porewater flow in permeable sediments, p. 144-179. *In* Boudreau, B. P. and B. B. Jørgensen [eds.], The Benthic Boundary Layer. Oxford University Press, New York, New York, U.S.A.

Jenkins, C. J., A. J. Kettner, C. Moore and G. Sharman (2003) goSEABED World Seabed Data Browser. University of Colorado Institute of Arctic and Alpine Research, Boulder, Colorado, U.S.A.

Jones, M. N. (1984) Nitrate reduction by shaking with cadmium: Alternative to cadmium columns. Water Research, 18: 643-646.

Joshi, C. H., R. D. Kamm, J. M. Drazen and A. S. Slutsky (1983) An experimental study of gas exchange in laminar oscillatory flow. Journal of Fluid Mechanics, 133: 245-254.

Kaiser, R. J. and D. M. Maurice (1964) The diffusion of fluorescein in the lens. Experimental Eye Research, 3: 156-165.

Kleypas, J. A., R. W. Buddemeier, D. Archer, J. P. Gattuso, C. Langdon and B. N. Opdyke (1999) Geochemical consequences of increased atmospheric carbon dioxide on coral reefs. Science, 284: 118-120.

Klute, A. and C. Dirksen (1986) Hydraulic conductivity and diffusivity: laboratory methods, p. 687-734. *In* Klute, A. [ed.], Methods of soil analysis, Part 1: Physical and mineralogical methods. American Society of Agronomy - Soil Science Society of America, Madison, Wisconsin, U.S.A.

Koroleff, F. (1976a) Determination of phosphate, p. 117-122. *In* Grasshoff, K. [ed.], Methods of seawater analysis. Verlag-Chemie, Weinheim, Germany.

Koroleff, F. (1976b) Determination of ammonia, p. 126-133. *In* Grasshoff, K. [ed.], Methods of seawater analysis. Verlag-Chemie, Weinheim, Germany.

Langdon, C. and M. J. Atkinson (2005) Effect of elevated pCO_2 on photosynthesis and calcification of corals and interactions with seasonal change in temperature/irradiance and nutrient enrichment. Journal of Geophysical Research - Oceans, 110: C09004, doi:10.1029/2004JC002640.

Leclercq, N., J. P. Gattuso and J. Jaubert (2002) Primary production, respiration, and calcification of a coral reef mesocosm under increased CO_2 partial pressure. Limnology and Oceanography, 47: 558-564.

Lohse, L., E. H. G. Epping, W. Helder and W. Van Raaphorst (1996) Oxygen pore water profiles in continental shelf sediments of the North Sea: turbulent versus molecular diffusion. Marine Ecology Progress Series, 145: 63-75.

Malan, D. E. and A. McLachlan (1991) In situ benthic oxygen fluxes in a nearshore coastal marine system: a new approach to quantify the effect of wave action. Marine Ecology Progress Series, 73: 69-81.

Marinelli, R. L., R. A. Jahnke, D. B. Craven, J. R. Nelson and J. E. Eckman (1998) Sediment nutrient dynamics on the South Atlantic Bight continental shelf. Limnology and Oceanography, 43: 1305-1320.

Martin, J. B., K. M. Hartl, D. R. Corbett, P. W. Swarzenski and J. E. Cable (2003) A multi-level pore-water sampler for permeable sediments. Journal of Sedimentary Research, 73: 128-132.

Martin, W. R. and G. T. Banta (1992) The measurement of sediment irrigation rates: a comparison of the BR^- tracer and $^{222}RN/^{226}RA$ disequilibrium techniques. Journal of Marine Research, 50: 125-154.

McManus, J. (1988) Grain size determination and interpretation, p. 63-85. *In* Tucker, M. [ed.], Techniques in sedimentology. Blackwell Scientific Publications, Oxford, U.K.

Meier, H., E. Zimmerhackl, W. Hecker, G. Zeitler and P. Menge (1988) Measurement of diffusion of radionuclides in sediment rocks. Radiochimica Acta, 44/45: 239-244.

Meier, H., E. Zimmerhackl, G. Zeitler and P. Menge (1991) Diffusion measurements of radionuclides in site-specific sediment/groundwater-systems. Material Research Society Symposium Proceedings, 212: 617-622.

Meyer-Reil, L.-A. (1986) Spatial and temporal distribution of bacterial populations in marine shallow water surface sediments, p. 141-160. *In* Lasserre, P. and J.-M.

Martin [eds.], Biogeochemical processes at the land-sea boundary. Elsevier Press, Amsterdam, Netherlands.

Monger, B. C. and M. R. Landry (1993) Flow cytometric analysis of marine bacteria with Hoechst 33342. Applied and Environmental Microbiology, 59: 905-911.

Moore, C. H. (2001) Carbonate reservoirs: porosity, evolution and diagenesis in a sequence stratigraphic framework. Elsevier Press, Amsterdam, Netherlands, pp. 444.

Moore, D. S. and G. P. McCabe (1999) Introduction to the practice of statistics (3rd edition). W. H. Freeman and Company, New York, New York, U.S.A., pp. 825.

Murphy, J. and J. P. Riley (1962) A modified single solution method for the determination of phosphate in natural waters. Analytica Chimica Acta, 27: 31-36.

Ogrinc, N. and J. Faganeli (2006) Phosphorus regeneration and burial in near-shore marine sediments (the Gulf of Trieste, northern Adriatic Sea). Estuarine, Coastal and Shelf Science, 67: 579-588.

Parsons, T. R., Y. Maita and C. M. Lalli (1984) A manual of chemical and biological methods for seawater analysis. Pergamon Press, Oxford, U.K., pp. 173.

Polerecky, L., U. Franke, U. Werner, B. Grunwald and D. de Beer (2005) High spatial resolution measurement of oxygen consumption rates in permeable sediments. Limnology and Oceanography Methods, 3: 75-85.

Porter, K. G. and Y. S. Feig (1980) The use of DAPI for identifying and counting aquatic microflora. Limnology and Oceanography, 25: 943-948.

Precht, E. and M. Huettel (2004) Rapid wave-driven advective pore water exchange in a permeable coastal sediment. Journal of Sea Research, 51: 93-107.

Precht, E., U. Franke, L. Polerecky and M. Huettel (2004) Oxygen dynamics in permeable sediments with wave-driven pore water exchange. Limnology and Oceanography, 49: 693–705.

Presley, B. J. (1971) Appendix: Techniques for Analyzing Interstitial Water Samples. Part I: Determination of Selected Minor and Major Inorganic Constituents, p. 1749-1755. *In* Winterer, E. L. and e. al. [eds.], Initial Reports of the Deep Sea Drilling Project, Volume VII. U.S. Government Printing Office, Washington, D.C., U.S.A.

Rao, A. M. F. and R. A. Jahnke (2004) Quantifying porewater exchange across the sediment-water interface in the deep sea with in situ tracer studies. Limnology and Oceanography Methods, 2: 75-90.

Rao, A. M. F. (2006) Carbon and nitrogen cycling in permeable continental shelf sediments and porewater solute exchange across the sediment-water interface. Ph.D. Dissertation, Georgia Institute of Technology, pp. 228.

Reimers, C., C. Friedrichs, B. Bebout, P. Howd, M. Huettel, R. Jahnke, P. MacCready, K. Ruttenberg, L. Sanford and J. Trowbridge (2004a) Coastal Benthic Exchange Dynamics. Report TR-04-01, Skidaway Institute of Oceanography, pp. 92.

Reimers, C. E., H. A. Stecher III, G. L. Taghon, C. M. Fuller, M. Huettel, A. Rusch, N. Ryckelynck and C. Wild (2004b) In situ measurements of advective solute transport in permeable shelf sands. Continental Shelf Research, 24: 183-201.

Riley, J. P. and G. Skirrow (1975) Chemical Oceanography, Volume 1. Academic Press, New York, New York, U.S.A., pp. 647.

Rocha, C., S. Forster, E. Koning and E. Epping (2005) High-resolution permeability determination and two-dimensional porewater flow in sandy sediments. Limnology and Oceanography Methods, 3: 10-23.

Rusch, A. and M. Huettel (2000) Advective particle transport into permeable sediments - evidence from experiments in an intertidal sandflat. Limnology and Oceanography, 45: 525-533.

Rusch, A., M. Huettel, C. E. Reimers, G. L. Taghon and C. M. Fuller (2003) Activity and distribution of bacterial populations in Middle Atlantic Bight shelf sands. FEMS Microbiology Ecology, 44: 89-100.

Rusch, A., M. Huettel, C. Wild and C. E. Reimers (2006) Benthic oxygen consumption and organic matter turnover in organic-poor, permeable shelf sands. Aquatic Geochemistry, 12: 1-19.

Ruttenberg, K. C. (2001) Phosphorus cycle, p. 2149-2162. *In* Steele, J. H., K. K. Turekian and S. A. Thorpe [eds.], Encyclopedia of Ocean Sciences, Vol. 4. Academic Press, London, U.K.

Ruttenberg, K. C. (2003) The global phosphorus cycle, p. 585-643. *In* Schlesinger, W. C. [ed.], Treatise on Geochemistry, Vol. 8. Elsevier, Amsterdam, Netherlands.

Saager, P. M., J. P. Sweerts and H. J. Ellermeijer (1990) A simple pore-water sampler for coarse, sandy sediments of low porosity. Limnology and Oceanography, 35: 747-751.

Sansone, F. J., G. W. Tribble, C. C. Andrews and J. P. Chanton (1990) Anaerobic diagenesis within Recent, Pleistocene, and Eocene marine carbonate frameworks. Sedimentology, 37: 997-1009.

Slomp, C. P., E. H. G. Epping, W. Helder and W. Van Raaphorst (1996) A key role for iron-bound phosphorus in authigenic apatite formation in North Atlantic continental platform sediments. Journal of Marine Research, 54: 1179-1205.

Soeller, C., M. D. Jacobs, P. J. Donaldson, M. B. Cannell, K. T. Jones and G. C. R. Ellis-Davies (2003) Application of two-photon flash photolysis to reveal intercellular communication and intracellular Ca^{2+} movements. Journal of Biomedical Optics, 8: 418-427.

Solórzano, L. (1969) Determination of ammonia in natural waters by the phenolhypochlorite method. Limnology and Oceanography, 14: 799-801.

Sørensen, K. B., B. Glazer, A. Hannides and E. Gaidos (2007) Spatial structure of the microbial community in sandy carbonate sediment. Marine Ecology Progress Series: in press.

Sutherland, D. A., M. A. Merrifield and F. J. Sansone (1999) Wave-induced porewater transport in permeable sediments. Eos, Transactions of the American Geophysical Union, December 8th-12th, 2003, 80(49), Fall Meeting Supplement, Abstract OS12F-09.

Tribble, G. W., F. J. Sansone and S. W. Smith (1990) Stoichiometric modeling of carbon diagenesis within a coral reef framework. Geochimica et Cosmochimica Acta, 54: 2439-2449.

Ullman, W. J. and R. C. Aller (1982) Diffusion coefficients in nearshore marine sediments. Limnology and Oceanography, 27: 552-556.

Webb, J. E. and J. Theodor (1968) Irrigation of marine submerged sands through wave action. Nature, 220: 682-683.

Webb, J. E. and J. L. Theodor (1972) Wave-induced circulation in submerged sands. Journal of the Marine Biological Association of the United Kingdom, 52: 903-914.

Webster, I. T. and J. H. Taylor (1992) Rotational dispersion in porous media due to fluctuating flows. Water Resources Research, 28: 109-119.

Webster, I. T. (2003) Wave enhancement of diffusivities within surficial sediments. Environmental Fluid Mechanics, 3: 269-288.

Wild, C., M. Rasheed, W. U., U. Franke, R. Johnstone and M. Huettel (2004) Degradation and mineralization of coral mucus in reef environments. Marine Ecology Progress Series, 267: 159-171.

Wild, C., C. Laforsch and M. Huettel (2006) Detection and enumeration of microbial cells within highly porous calcareous reef sands. Marine and Freshwater Research, 57: 415-420.

Winkler, L. W. (1888) Die Bestimmung des in Wasser gelösten Sauerstoffes. Berichte der Deutschen Chemischen Gesellschaft, 21: 2843-2855.

Yingst, J. Y. and D. C. Rhoads (1980) The role of bioturbation in the enhancement of bacterial growth rates in marine sediments, p. 407-421. *In* Tenore, K. R. and B. C. Coull [eds.], Marine benthic dynamics. University of South Carolina Press, Columbia, South Carolina, U.S.A.

Chapter 4 – Nutrient dynamics in permeable sediments: remineralization of suspended particulate organic matter and nutrient processing

4.1 Introduction

Permeable sediments are coarse-grained sediments (grain diameter > 62 μm) with permeabilities higher than 10^{-12} m^2 (Huettel et al. 1998). Their global distribution is wide, but they are most in shallow waters on continental shelves and carbonate reefs, where they constitute the majority of the sediment (Emery 1968; Riedl et al. 1972; Boudreau et al. 2001; Jenkins et al. 2003). The fact that these waters are classified among the most productive regions of the world's oceans (e.g., Ryther 1969; Lalli and Parsons 1997, p. 68, 218) implies that the underlying seafloor may affect and be affected by this productivity. Despite these indications, scientific investigations of the role of permeable sediments in global biogeochemical cycling have been disproportionately few relative to these sediments' spatial extent, for methodological reasons (Section *3.1*). This realization has led to recent efforts to initiate, coordinate and accelerate research in this field (Boudreau et al. 2001). In 2004, the Coastal Ocean Processes Program organized a research planning workshop, titled "Coastal Benthic Exchange Dynamics" (Reimers et al. 2004a). Among other findings, this workshop highlighted the need to learn more about permeable sediments, including the exchange of various solutes such as oxidants, nutrients, and organic material, across the sediment-water interface (SWI), and organic matter decomposition within permeable sediment columns (Reimers et al. 2004a, p. 2).

The recent establishment of a coastal observatory, Kilo Nalu, on the south shore of O'ahu, Hawai'i (Figure 3.16) is part of the effort to supply much-needed knowledge of permeable sediments and their biogeochemical functioning. Work at this observatory focuses on benthic boundary layer processes, including the exchange of matter across the SWI. The observatory is situated at a region characterized by extensive living reef areas interspersed with sand fields tens of meters wide. The reef areas consist of living coral heads surrounding sediment pockets tens of centimeters to a meter wide. The 10 m-deep site at Kilo Nalu spreads across the boundary between a reef region and a sand field approximately 90 m wide. The sand field sediments are currently the location of in-situ measurements of pore water transport dynamics and biogeochemical observations (e.g., Hebert et al. 2007).

This chapter describes how sediments from the observatory site were used to investigate the uptake and utilization of particulate organic matter (POM) and nutrients by reef-associated carbonate permeable sediments. Experiments conducted using a specially constructed microcosm studied the role of permeability in POM processing and nutrient regeneration, while sediment plug incubations assessed sedimentary nutrient regeneration and demand. Together, they provide insights into the biogeochemical functioning of permeable sediments, as well as the means to interpret field observations and to direct future studies at the Kilo Nalu Observatory.

4.1.1 Organic matter cycling in permeable sediments

The most significant distinction between permeable and fine-grained sediments is that the former are characterized by enhanced exchange between the moving overlying

water and the sediment pore water, whereas the latter are characterized by transport via molecular diffusion, bioturbation and bioirrigation, etc. (Webb and Theodor 1968; Webb and Theodor 1972; Shum 1992; Webster and Taylor 1992; Huettel and Webster 2001; Precht and Huettel 2003; Precht et al. 2004). In fine-grained sediments, particulate organic matter (POM) supply is driven by gravitational settling of particles to the sediment surface and incorporation to greater depths into the sediment by further sedimentation or by bioturbation (Berner 1980). In permeable sediments, however, overlying water motion can force POM and suspended organic matter (SOM) through the sedimentary matrix, where it often accumulates below the SWI (Bacon et al. 1994; Huettel and Rusch 2000; Rusch and Huettel 2000; Rusch et al. 2000; Rusch et al. 2001). The supply rate of this "physical injection" of particles into sediment at depth could be analogous to that effected by bioturbation in settings such as intertidal sand flats (e.g., Rusch et al. 2000). Therefore, this physical process must be a dominant driver of biogeochemical processes in permeable sediments.

Increased exchange of solutes and particles across the SWI of permeable sediments is commonly accompanied by low sedimentary POM content and high sedimentary oxygen consumption (SOC) rates, the latter being 1-2 orders of magnitude greater than SOC rates in a variety of other marine sedimentary settings (Reimers et al. 2004b; Rusch et al. 2006; Table 2.5). These facts suggest that one of the major ecosystem functions of permeable sediments in the global ocean must be nutrient regeneration by both aerobic and anaerobic organic matter remineralization, a role not accepted until recently (Marinelli et al. 1998; Boudreau et al. 2001). The commonly invoked steps of sedimentary organic matter cycling include:

a) The deposition of organic matter onto the sediment;

b) Sedimentary organic matter decomposition;

c) Nutrient regeneration during decomposition; and

d) The release of those nutrients to the pore water and, subsequently, the water column.

The enhanced exchange of solutes and particles at permeable sedimentary settings should accelerate the rates of all of these steps, relative to fine-grained sedimentary settings. Specifically, POM would not simply be deposited onto the SWI but would actually be driven into the permeable sediment and filtered by the sedimentary column (Boudreau et al. 2001). The resulting supply rate of POM per unit area of seafloor could exceed that of gravitational deposition (e.g., Rusch and Huettel 2000). Enhanced solute exchange would also accelerate the decomposition of POM and resultant nutrient regeneration, by supplying oxygen and removing metabolic inhibitors (e.g., ammonium, sulfide; Jørgensen 1983) at rates exceeding those that molecular diffusion alone could achieve. The same enhanced solute exchange rates could, in turn, accelerate the transport of nutrients from pore water to overlying water.

4.1.2 Nutrient regeneration in permeable sediments

The nutrient regeneration paradigm has been repeatedly examined in fine-grained sediments, and evidence in its favor has been frequently produced (e.g., Rowe et al. 1975; 1977; Nixon et al. 1980; Hopkinson 1987). Recent attempts to investigate nutrient cycling in permeable sediments have been fragmentary but suggestive of the occurrence of some of the steps of organic matter cycling listed above. Specifically, during stirred

chamber POM enrichment experiments, Huettel and Rusch (2000) demonstrated that sedimentary permeability is proportional to POM flux into the sediment and to POM decomposition rate. In addition, the characteristic pore water nutrient pools indicative of organic matter degradation (observed during fine-grained sediment nutrient regeneration studies; e.g., Rowe et al. 1975) have been documented in a variety of permeable sediment settings (e.g., Marinelli et al. 1998; Falter and Sansone 2000).

However, nutrient fluxes in permeable sedimentary settings have not been as readily observed and demonstrated as the above. Perhaps the clearest demonstration of nutrient fluxes out of permeable sediments into the overlying water was observed during laboratory flume experiments by Huettel et al. (1998), which demonstrated the build up of nutrients, iron and manganese in pore water of siliceous sandy sediments, while fluxes of these solutes to the overlying water were undetectable. These fluxes increased significantly after the construction of sand mounds on the originally-smooth sediment surface. Interestingly, only the fluxes of some of the nutrient species (nitrate and silicate) increased, while others (ammonium and phosphate) remained insignificant. Huettel et al. (1998) explained the fluxes of nitrate and silica as the outcome of pore water advection generated by low-pressure areas down-current from the sediment surface mounds (Ziebis et al. 1996; Huettel et al. 1998; Huettel and Webster 2001), but did not attempt to explain the lack of fluxes in ammonium and phosphate.

Another notable attempt at recording nutrient fluxes out of permeable sediments took place during in-situ incubations of organic-poor, siliceous, shelf sediments of the South Atlantic Bight (SAB) (Marinelli et al. 1998) using a free-vehicle benthic stirred chamber instrument (Jahnke and Christiansen 1989). The recorded fluxes were

infrequent, and, when they were detectable, were minor in magnitude. Closed incubations of sediment from the same site recorded nutrient build-up in pore water, suggesting that nutrients were generated in the sediments during the in-situ incubations but the anticipated fluxes from sediments into the overlying water were not observed.

Janssen et al. (2005a; 2005b) used an autonomous stirred benthic chamber system on sediments of the German Bight to record nutrient fluxes. These organic-poor siliceous sediments (similar to SAB sediments) showed on average a significant release of nutrients to the overlying water, but the range of measured fluxes spanned both release from and uptake by sediments, as in the case of the SAB sediments.

All of the observations and measurements described above are similar, in that they record organic-poor permeable sediments as both sources and sinks of nutrients over relatively short time scales (hours-days). The approach used to explain the SAB study results treated the instances of nutrient release from the sediments as the anticipated scenario (based on past literature, e.g., Rowe et al. 1975), and justified the instances of nutrient uptake as the outcome of microphytobenthic activity and general microbial demand (Marinelli et al. 1998; Nelson et al. 1999; Jahnke et al. 2000; Jahnke 2001). Another proposed explanation for variations in the direction of nutrient fluxes across the SWI involved shifting redox conditions and oxygen supply within the sediment during incubations (Janssen et al. 2005b).

The investigations described above are valuable, on the one hand, for providing observations that help constrain the magnitude and direction of fluxes across the SWI of permeable sediments. On the other hand, however, the authors can only speculate about their causes and controls. For this reason, and because of the more generally limited

understanding of permeable sediment biogeochemistry, important progress can be made by the manipulation of sediments in the laboratory using organic enrichment or nutrient addition experiments. Such experiments may help identify the metabolic pathways that permeable sediment microbial communities are capable of and may also constrain the rates at which their metabolic activity occurs. For example, Rusch et al. (2006) carried out ship-board dissolved organic carbon (DOC) enrichment experiments with flow-through chambers packed with Middle Atlantic Bight (MAB) sediment columns. When supplying the sediments with sea water enriched in DOC, Rusch et al. (2006) observed rapid increases in dissolved inorganic carbon (DIC) production rates, with rates linearly proportional to the DOC concentrations added. The results indicate that permeable sediment microbiota can respond rapidly to material inputs that are presumably limiting their metabolism, prompting the authors to call these sediments "biocatalytical filters."

In another example, Rao (2006) carried out ^{15}N-labeled nitrate enrichment experiments with SAB sediment columns in flow-through reactors. By analyzing and comparing in-flowing and out-flowing water through the reactors, she recorded the uptake of nitrate as well as the production of N_2 in these sediments. These findings demonstrated N demand in SAB sediments as well as significant loss of N by denitrification. The results contradicted past field studies of SAB sediments, which interpreted the absence of nitrate from pore water as evidence for the insignificance of denitrification as a nitrogen sink (Marinelli et al. 1998).

Following the spirit of laboratory experimentation in the literature reviewed above, the investigations described later in this chapter involved the manipulation of reef-associated carbonate sediments with two goals. First, experiments conducted using a

specially constructed microcosm attempted to discern the role of sediment column permeability in POM processing and nutrient regeneration. The hypotheses that rates of solute transport, particle filtration, particle decomposition-nutrient remineralization and nutrient efflux from the sediments increase with permeability was tested by monitoring the degradation of added POM, and the subsequent release of nutrients to the overlying water during microcosm organic enrichment experiments. Second, sediment plug incubations assessed nutrient demand or release in surface sediment under oxic conditions, typical of well ventilated ocean waters, to test the hypothesis that permeable sediments are a sink for macronutrients with respect to water column productivity and to identify potential nutrient sinks.

4.2 Experimental methods

4.2.1 Study site and sediment characterization

Sediments used in this study were collected from the site of the Kilo Nalu Observatory (Swanson et al. 2006). The sharp shift of sedimentary settings in this area, from coral reefs to sand fields, suggested the close proximity of unconsolidated sediments that vary in permeability, but that are exposed to the same physical conditions, such as temperature and salinity, wave forcing, and even overlying water biogeochemistry. These similarities should increase the probability that differences amongst various types of sediment were due to sedimentary characteristics themselves and not variations in fundamental properties of the local environment.

A 6 m-long transect across the boundary between a sand field and a coral reef at the 10 m-deep site of the observatory was selected for an initial field survey. Sediment was collected from three locations along this transect: one in a reef sediment pocket, one in an adjacent sand field, and one at the boundary between the sand field and the reef. Surface sediment samples (0-20 cm) were collected by divers using buckets. A variety of geological, hydrological, and biogeochemical characteristics of these sediments were determined and used in choosing sediments for the experiments.

Basic sediment grain size distribution parameters were determined using the definitions in McManus (1988), based on cumulative grain size curves (Figure 4.1). In all these definitions, the notation ϕ_x indicates the grain size over which x % of the weight fraction of the total sample is coarser. All parameters are calculated on sizes in the ϕ scale (see Table 2.1 for definition and discussion). The median, M_d, was defined as the grain size over which 50 % of the weight fraction is coarser, i.e., ϕ_{50}. The graphic mean size, M_z, was defined as:

$$M_z = \frac{1}{3}(\phi_{16} + \phi_{50} + \phi_{84}) \tag{4.1}$$

Sorting, σ_1, a measure of the spread of the particle distribution, was defined as:

$$\sigma_1 = \frac{\phi_{84} + \phi_{16}}{4} + \frac{\phi_{95} + \phi_5}{6.6} \tag{4.2}$$

Skewness, Sk_1, a measure if the asymmetry of the distribution, is defined as:

$$Sk_1 = \frac{\phi_{16} + \phi_{84} - 2\phi_{50}}{2(\phi_{84} + \phi_{16})} + \frac{\phi_5 + \phi_{95} - 2\phi_{50}}{2(\phi_{95} + \phi_5)} \tag{4.3}$$

Porosity was determined gravimetrically, using a modification of the "wet-packed" method of Beard and Weyl (1973). Wet sediment was placed in a pre-weighed

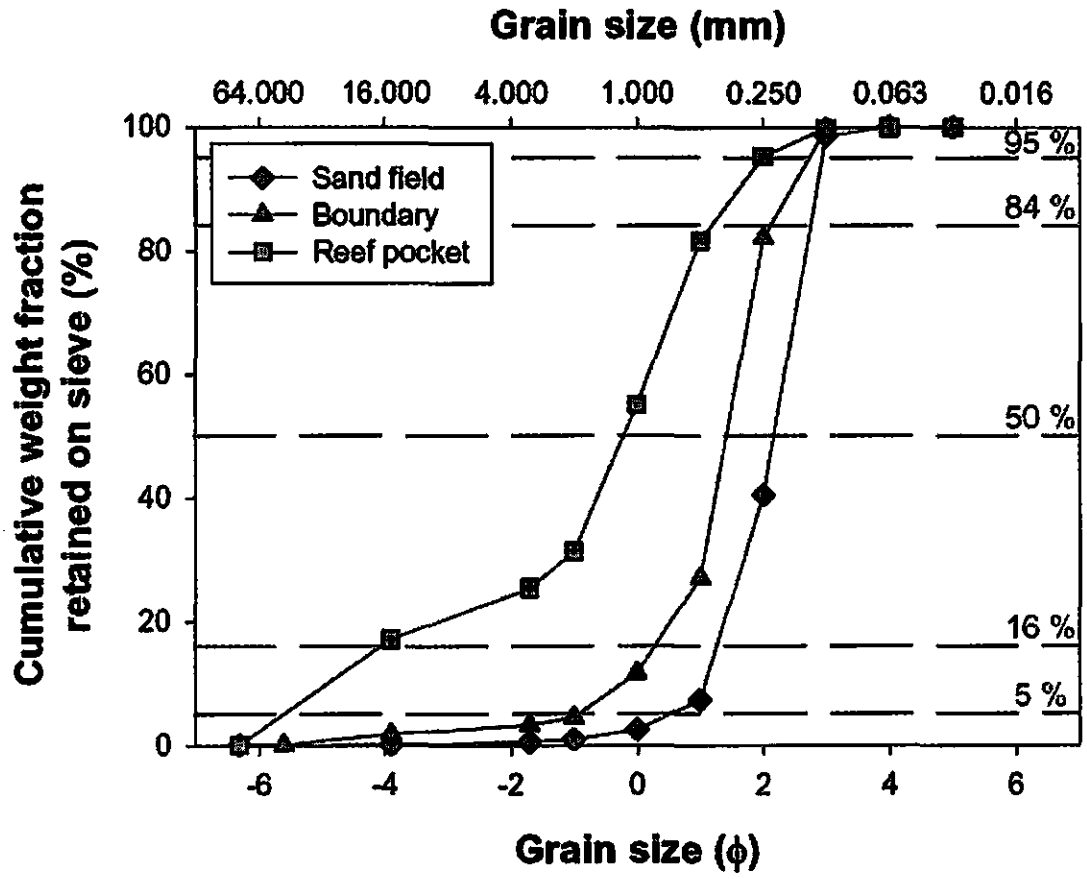

Figure 4.1 Cumulative weight fraction vs. grain size curves for the three sediment samples collected during the field site survey. Also shown are the lines for 5 %, 16 %, 50 %, 84 %, and 95 % weight fractions. The grain sizes at those particular weight fractions were used in the calculation of the basic size-distribution statistics used in describing the grain size composition of sediments (see text and Table 4.1 for definitions and values).

beaker and compacted by gentle tapping. Supernatant water was removed with a pipette, and the sediment surface height was marked on the beaker exterior. The weight of the wet sediment (W_{wet}) was measured, the sediment was dried for 72 h at 60 °C, and the dry sediment weight (W_{dry}) was obtained. The beaker was emptied, washed with soap, dried, filled with de-ionized water (DIW) to the marked line, and weighed to obtain the amount of DIW (W_{DIW}). Porosity was defined as:

$$\varphi = \frac{(W_{wet} - W_{dry}) \cdot \rho_{DIW}}{W_{DIW} \cdot \rho_{DIW}} \qquad 4.4$$

where the density of DIW, $\rho_{DIW} = 1.00\ g \cdot mL^{-1}$.

The permeability was determined using the falling head method, with1 m-deep sediment columns (Burmister 1955; Klute and Dirksen 1986; Rocha et al. 2005). The loading of sediment columns and the execution of permeability measurements are described in detail in section *3.3.2.2*.

Thermogravimetry, i.e., the weight lost during ignition at 550 °C, was used as a simple and affordable total organic carbon (TOC) proxy (Kristensen 1990). Samples were dried at 60 °C in a drying oven for 48-72 h, and combusted in clean porcelain vials for 4 h at 550 °C. The weight fraction of TOC in the sample was calculated as the ratio of the weight lost after combustion over the total sample weight before combustion. It is noteworthy that this method is only used as a proxy and as a means of comparing these three sediment samples with each other. This particular method, when employed on carbonate sediments, is likely to be sensitive to the decomposition of high-magnesium calcite (at approximately 400 °C), although no appropriate data exist for the interference of calcite decomposition with this TOC analytical technique (King et al. 1998). The

results are comparable only if the content of high-magnesium calcite is similar in all the samples (Froelich 1980), which is very likely the case in this application.

Sedimentary cell counts were obtained microscopically using the method of Wild et al. (2006), as modified by A. Rusch et al. (in preparation). Duplicate 2-g wet sediment sub-samples were weighed in serum bottles and then covered with 3 ml of a solution of 2 % formaldehyde and 2 % acetic acid in twice-filtered (0.2 μm) Waikiki Aquarium (Honolulu, Hawai'i) seawater (FSW). The serum bottles were sealed and stored until cell extraction. The cell extraction process started by sonication of a fixed sample for 5 seconds, followed by a pause of 10 s, and this was repeated four times. The supernatant was removed and stored in a beaker. The remaining sediment in the serum vial was washed with 3 ml of a 2 % acetic acid solution, the supernatant was removed, and this was repeated six times. The sonication-washing procedure was repeated four times yielding approximately 100 mL of sediment cell extract. The DNA stain DAPI was added to 1-mL aliquots of the extract at a DAPI concentration of 2 $\mu g \cdot mL^{-1}$, and the samples were allowed to incubate for 10 min, at which point they were filtered onto 0.2 μm black polycarbonate filters (Millipore, Bedford, Massachusetts, U.S.A.), and the cells enumerated using an epifluorescence microscope (Olympus America Inc., Melville, New York, U.S.A.).

The three sediment types are compared in Table 4.1. Gradients are observed in all measured parameters, with boundary sediment values always intermediate between those of the two end-members. Compared to the sand field sediments, the reef pocket sediments were coarser, more poorly sorted and more permeable, and also contained slightly less TOC and higher cell abundances. Despite the large difference between end-

Table 4.1 Characteristics of sediments collected at three locations along a 6-m transect at the 10 m site of the Kilo Nalu Observatory. The transect was perpendicular to the direction of the sand-field/coral-reef boundary. Sediment was collected from the sand field, a reef sediment pocket, and from the boundary between the sand field and the reef.

Sedimentary parameter	Sand field	Boundary	Reef pocket
Median M_d (=ϕ_{50}), ϕ (mm)	2.16 (0.22)	1.42 (0.37)	-0.21 (1.16)
Graphic mean M_z, ϕ (mm)	2.06 (0.24)	1.27 (0.41)	-1.03 (2.04)
Sorting σ_I	0.73	1.01	2.45
Class (McManus 1988 scale)	Moderate	Poor	Very poor
Skewness Sk_I	-0.28	-0.26	-0.44
Class (McManus 1988 scale)	Negative	Negative	Very negative
Porosity φ	0.54	0.48	0.39
Permeability k, m^2	3.9×10^{-11}	Not measured	5.4×10^{-11}
Loss-on-ignition, g g_{dry}^{-1} (%)	3.45 ± 0.02	3.19 ± 0.20	3.06 ± 0.06
Microbial abundance, cells g_{wet}^{-1}	5.6 (± 4.0) $\times10^7$	7.1 (± 5.0) $\times10^7$	1.3 (± 0.8) $\times10^8$

member M_z and M_d values, the permeabilities of the two sediments are relatively similar. This is probably due to the very poor sorting of the reef pocket sediment, which is suggestive of the presence of fine-grained particles that block pore water channels between larger grains (see extensive discussion on permeability-grain distribution relationships in Section *2.2.1*). Sand-field sediments were included in all investigations of this study because of the on-going in situ characterization and experimentation at this location (e.g., Hebert et al. 2007). For the study of permeability effects on material exchange across the SWI, experiments with sand field sediments ($k = 3.9\times10^{-11}$ m^2) were complemented by those using reef pocket sediments ($k = 5.4\times10^{-11}$ m^2), as well as reef-pocket sediment that had been wet-sieved through a 250 μm sieve to remove the fine fraction of the sediments.

4.2.2 Experimental procedures

4.2.2.1 Microcosm organic enrichment experiments

Microcosm experiments were conducted using the procedures described in detail in Chapter 3 (Section *3.3*). Three microcosm experiments took place using sand field sediments, reef pocket sediments, and sieved reef pocket sediments (> 250 μm). These sediments were collected by divers using buckets and kept under aerated seawater until use or in-between processing (12-72 hours). Before loading the microcosm, each sediment type was transferred 2-3 times into separate buckets containing FSW (see Section *3.2.3.3*), with the purpose of rinsing this sediment from nutrient- and reductant-rich pore water and very fine suspended particulates. In addition, any sediment particles greater than 1.5 cm (ϕ = -3.9) were also removed to minimize heterogeneous sediment

packing during loading. Rinsing thus aided the effort to construct biogeochemically homogeneous sediment columns. Samples of all three sediment types were stored and analyzed for sedimentological properties, sedimentary cell abundances and TOC content.

The organic material used for microcosm enrichment was a culture of the marine chlorophyte *Dunaliella salina* (wild type) from the culture collection of the Center for Marine Microbial Ecology and Diversity (CMMED, University of Hawai'i). Use of these algae ensured a source of marine organic material of fairly constant particle size and elemental composition throughout the study. The algae were grown in batch culture with f/2 medium under constant light conditions (Guillard and Ryther 1962). Cultures were only used for experiments if the cells were mobile and in suspension. Each culture was sub-sampled at the time of enrichment for cell enumeration, particulate elemental composition (C, N, and P) analyses, and dissolved nutrient analyses. Dissolved nutrient analyses were performed to detect any unused nutrients from the growth medium that were added to the microcosm along with the algal cells at the time of enrichment. The algal cell abundance in the culture (cells·mL^{-1}) and culture C, N, and P content (μg·mL^{-1}), were used to calculate the C, N, and P content in each algal cell (pg·cell^{-1}) as shown below:

$$\text{Elemental content per cell} = (\text{culture elemental content} \div \text{cell abundance}) \times 10^6 \qquad 4.5$$

Organic enrichment of the microcosm took place several days after the start of the microcosm experiments. A known amount of overlying water (typically, 300 mL out of a total of 3100 mL) was removed from the microcosm from the sampling port lying 10 cm above the SWI and kept in a beaker. This volume was replaced with the same volume of

a culture of *D. salina*, so as to produce an algal concentration of 5.5-7.0×10^4 cells·mL^{-1} in the overlying water (a culture dilution of 10.3 times or 9.7 %). This concentration range was estimated to keep the amount of organic material added as low as possible, while yielding an adequate phosphate signal if all cells were remineralized and released as phosphate into the overlying water or pore water.

Conservative tracer experiments and organic enrichment took place while pumping with an oscillation height, h, of 8.5 cm, and frequency, f of 2 min^{-1}. Before enrichment, conservative tracer transport experiments were conducted to assess enhanced solute exchange between the overlying water and the sediment (Section *3.3.2.4*). In addition, overlying water and pore water samples were collected for oxygen and nutrient analysis (approximately 4.5 mL per sample). Samples for cell counts were collected from the overlying water and the two shallowest pore water depths (typically, 5 and 10 cm). Immediately following enrichment, sampling of the overlying water and pore water from the top 10 cm for oxygen, nutrients and cell counts continued every 6-8 h, until 3-4 d after enrichment, when experiments were terminated. Immediately before dismantling the microcosm, samples were collected from all sampling ports for oxygen and nutrient analyses, as well as for pore water cell counts. The sediment column was sliced at 1-cm intervals between 0-5 cm, and at 10-cm to 20-cm intervals between 5-100 cm. Sediment samples were collected for algal counts (1-15 cm), as well as for cell counts and TOC content (whole column), with additional samples frozen at -20 °C or oven-dried at 60 °C for future use.

Bench-top control experiments took place to constrain the physiological response of the *Dunaliella* culture to mixing and dilution with overlying water. The overlying

water retrieved from the microcosm prior to enrichment was mixed with the algal culture to a dilution ratio identical to that of the enriched overlying water of the microcosm (1:10.3 or 9.7 %). The mixture was incubated in clean, 25-mL flasks in the dark (n = 2) for the remainder of the microcosm experiment. Additional treatments included dark incubations of unamended overlying water (n = 2), as well as light incubations of the culture-overlying water mixture (n = 2). Incubations were sampled for cell counts simultaneously with microcosm sampling throughout the experiment. At dismantling, in addition to samples for cell counts, incubation aliquots were filtered (0.2-μm) for dissolved nutrient analyses.

The number of algal cells degraded in the sediment was calculated by subtracting the number of cells found in the sediment at the end of the experiment, t_f, from the number of cells lost to the sediments from the overlying water over the same time period. The latter number was calculated by correcting the number of cells in the overlying water at t=0 for cell loss due to degradation in the overlying water up to t_f, using the cell loss due to degradation the same time period (i.e., to t_f) in the physiological control experiments (as in Huettel and Rusch 2000):

Number of algal cells lost to the sediments (t_f) =

number of cells in the overlying water (t=0) 4.6

× (1-fraction lost in the overlying water (t_f)

Number of algal cells degraded in sediments(t_f)

= number of algal cells lost to the sediments (t_f) 4.7

- number of cells found in sediments (t_f)

Cell numbers were converted to amounts of C, N and P (μmol) by multiplying by the elemental content per cell (pg·cell^{-1}), as follows:

$$\begin{aligned} &\text{Bio-element amount} \\ &= (\text{number of cells} \times \text{elemental content per cell}) \\ &\div (\text{elemental atomic weight} \times 10^6) \end{aligned} \qquad 4.8$$

The amount of N and P in cells degraded in sediment (Eq. 4.7) was compared to the concentration (μmol·L^{-1}) of the dissolved inorganic nutrients (DIN = NO_3^- + NO_2^- + NH_4^+, PO_4^{3-}) in overlying water measured throughout the experiment, to compare the amount of N and P entering the sediment in algal cells with the amount being released in the overlying water as inorganic nutrients.

4.2.2.2 Nutrient uptake experiments

Nutrient addition experiments were conducted to assess nutrient limitation and uptake in sediments of the sand field at Kilo Nalu. Particular attention was paid to sediments located at the SWI, which experience the most dynamic conditions of the whole sedimentary column. They lie at the focus of material exchange between overlying water and sediments, and are also subject to light-dark variations that have been shown to play a role in permeable sediment biogeochemistry (e.g., Jahnke et al. 2000; e.g., Jahnke 2001). Narrowing the focus of these experiments to surface sediments permitted the examination of the effects of light on nutrient dynamics, a factor not tested during the microcosm experiments. Moreover, nitrogen stable isotope additions were used to relate

the sequestration of nitrogen in nutrients to two major suggested sinks for permeable sediments: the sediments themselves, through biotic uptake (Marinelli et al. 1998; Nelson et al. 1999; Jahnke et al. 2000), and N_2 (through microbial denitrification: Rao 2006).

The experimental approach used was the thin-plug, open incubation method (Figure 4.2), adapted from Aller and Mackin (1989). This method involved exposing a thin layer of sediment to a well-mixed reservoir of water, and determining solute concentrations in the reservoir water and pore water at various time points. Changes in these concentrations are dictated by production or consumption rates, and by physical solute exchange between the reservoir and the sediment plug. Solute exchange in fine-grained sediment plugs is dictated by molecular diffusion as well as the geometry of the plugs (Aller and Mackin 1989). In permeable sediment plugs, this exchange will be rapid, allowing production or consumption processes to dominate changes in concentration with time. In this respect, the plug incubation method as applied to permeable sediments is very similar to water column incubation techniques (e.g., Eppley et al. 1969).

Surface sediment (0-1 cm) from the sand field at the 10 m node of Kilo Nalu was collected by divers by passing 50-mL plastic tubes horizontally through the sediment, so that half of the tube diameter (= 2 cm) was immersed in the sediment. The sediment collected in four tubes (approximate total volume of 200 mL) was combined, homogenized with a spatula, and rinsed with FSW three times, and then loaded in acid-cleaned Petri-dish caps, 5 cm in diameter and 3 mm in height, to form thin sediment plugs with an area of 19.63 cm^2, and a maximum volume of 5.89 cm^3. The sediment plugs were distributed in groups of 2-3 in acid-washed plastic containers capable of

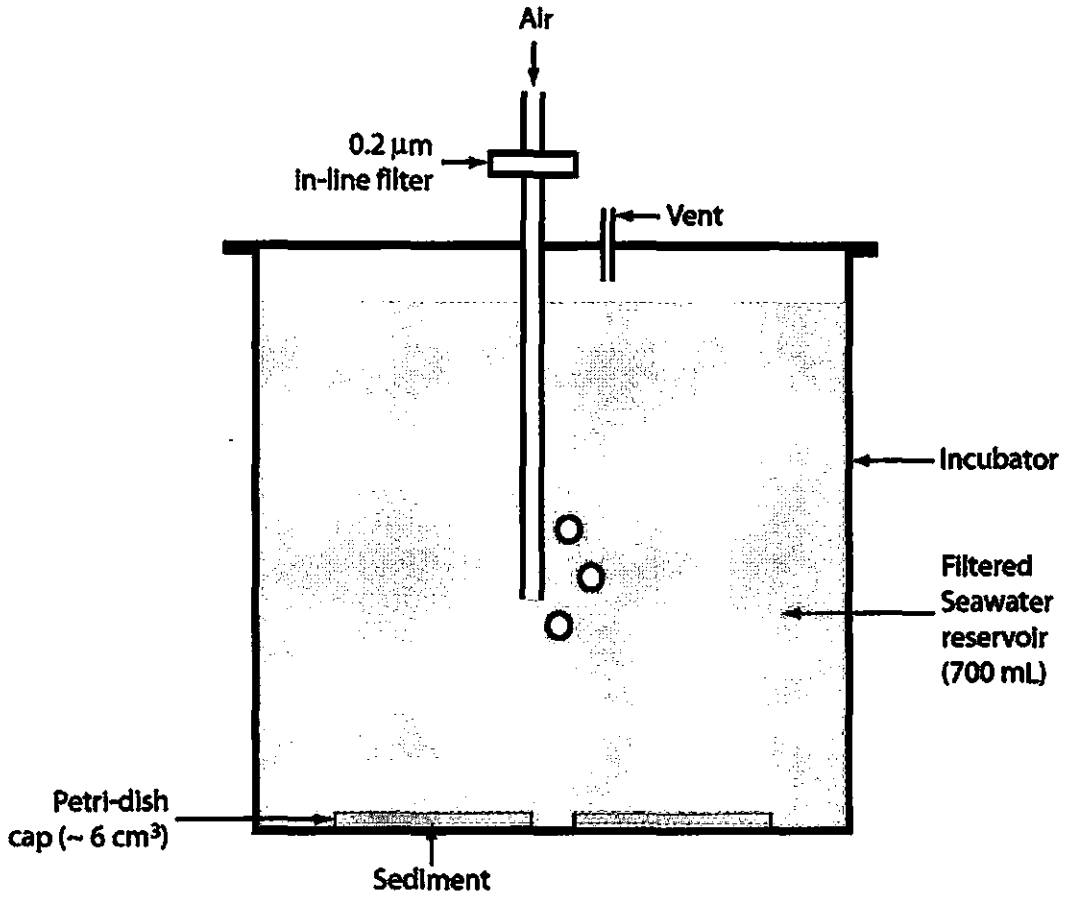

Figure 4.2 The thin-plug incubator used in the nutrient enrichment experiments, as it was adapted from Aller and Mackin (1989). The Petri-dish caps used to create the sediment plugs measured 3 mm in height and 5 cm in diameter, with a maximum capacity of approximately 6 cm^3.

holding 900 mL of water. Each container was filled with 700 mL of FSW or nutrient-enriched FSW at a slow rate using a syringe, so as not to disturb the plug surfaces. The containers were sealed with acid-washed lids, which incorporated tubing connected to aerators. The aerators pumped air into the water reservoirs through 0.2 μm filters at a gentle and constant rate. This pumping helped maintain high oxygen concentrations throughout the experiments (monitored using a Clark-type oxygen probe) and mixed the reservoir water rapidly (tested by conservative tracer mixing between plug pore water and overlying water during a preliminary experiment). All containers were incubated under two light treatments: in constant darkness, and under a 12-h light-12-h-dark cycle. Light was provided by a bank of daylight fluorescent bulbs (also used by Cassar et al. 2002), situated approximately 50 cm above the containers. The containers incubated in the dark were covered at all times, except during each sampling session (a total of 3 minutes).

Five different treatments, set up with three different nutrient media (Table 4.2), were run under each light treatment (Table 4.3). Nitrate and phosphate uptake was tested simultaneously in an attempt to obtain N-uptake:P-uptake ratios that might indicate the fate of these nutrients. The simultaneous use of these two nutrients is also supported by the high probability that they are supplied simultaneously by common pollution sources in shallow water settings at the Hawaiian Islands. Specifically, reported concentrations of near-shore nitrate inputs vary from 10^1-10^2 $\mu mol \cdot L^{-1}$ in the case of stream out-flows and land run-off (Hoover 2002) to 10^3 $\mu mol \cdot L^{-1}$ in the case of sewage outfalls (Dollar 1986). As nitrate concentrations in coastal surface seawater on O'ahu rarely exceed 3 $\mu mol \cdot L^{-1}$ (Taguchi and Laws 1987; Kinzie et al. 2001, in Hoover 2002), the nitrate enrichment level was set at the lower limits of input from external sources (10^1 $\mu mol \cdot L^{-1}$), while

Table 4.2 Nutrient media used during the nutrient uptake experiments.

Medium name	NO_3^- source	Initial $[NO_3^-]$ ($\mu mol \cdot L^{-1}$)	$\delta^{15}N\text{-}NO_3^-$	PO_4^{3-} source	Initial $[PO_4^{3-}]$ ($\mu mol \cdot L^{-1}$)	Initial $[NO_3^-] \div [PO_4^{3-}]$
Ambient	FSW	7.6 ± 0.1	1.7	FSW	0.54 ± 0.02	14.2
Regular	KNO_3	17.5 ± 0.1	7.5	$NaH_2PO_4.H_2O$	1.17 ± 0.06	15.0
Labeled	$K^{15}NO_3$	17.7 ± 0.3	3.65×10^5	$NaH_2PO_4.H_2O$	1.14 ± 0.00	15.6

phosphate enrichment levels were adjusted so that the starting ratio of nitrate to phosphate was close to the Redfield ratio (16:1).

Fluxes of nutrients in each container were calculated by obtaining the slope, b, of the linear phase of concentration-vs.-time relationships using a linear regression ($y = a + bt$). Each slope depended on the total sediment weight, wt_{sed}, present in the plugs of each container. Because this weight is not identical between containers, the slope, b ($\mu mol \cdot L^{-1} \cdot d^{-1}$), was normalized ($b_{norm}$) by multiplying it with a normalization factor:

$$b_{norm} = b \times \frac{\overline{wt}_{plug}}{\left(\frac{wt_{sed}}{n_{plugs}}\right)} \qquad 4.9$$

where n_{plugs} is the number of plugs in that container, and $\overline{wt}_{plug}$ is the average weight of all the plugs in all containers. The flux, Fw ($\mu mol \cdot g^{-1} \cdot d^{-1}$), in relation to the plug sediment weight, wt_{sed} (g), was calculated as follows:

Table 4.3 Nutrient enrichment experimental treatments. See text for justification and details.

Code	Treatment description	Light condition	Sediment	Replicates	No. of plugs	Nutrient medium
D1&L1-SW	Un-enriched seawater control	Dark/Light-dark	None	1	None	Ambient
D1&L1-14N	Enriched seawater control ($^{14}NO_3^-$)	Dark/Light-dark	None	1	None	Regular
D1&L1-15N	Enriched seawater control ($^{15}NO_3^-$)	Dark/Light-dark	None	1	None	Labeled
D2	Low nutrient level uptake	Dark	Live	1	3	Ambient
D3	Abiotic nutrient uptake	Dark	Autoclaved	1	3	Labeled
D4	Sediment incorporation of NO_3^-	Dark	Live	2	6	Labeled
D5	Loss of NO_3^- by denitrification	Dark	Live	2	6	Regular
L2	Low nutrient level uptake	Light-dark	Live	1	6	Ambient
L3	Abiotic nutrient uptake	Light-dark	Autoclaved	1	2	Labeled
L4	Sediment incorporation of DIN	Light-dark	Live	1	2	Labeled
L5	Loss of DIN by denitrification	Light-dark	Live	1	2	Regular

$$Fw = \frac{\mathbf{b}_{norm} \times V_{OW}}{wt_{sed}} \qquad 4.10$$

where V_{OW} (L) is the volume of the overlying water. The flux, Fa (mmol·m^{-2}·d^{-1}), in relation to the area of the plugs, A_{plugs}, was also calculated:

$$Fa = \frac{\mathbf{b}_{norm} \times V_{OW}}{10^3 \times A_{plugs}} \qquad 4.11$$

The stable isotope of nitrogen, ^{15}N, was the tool used to test the role of two potential major sinks for NO_3^-, sedimentary incorporation and denitrification. The content of ^{15}N in a sample was measured and reported as the value of $\delta^{15}N$:

$$\delta^{15}\mathrm{N} = \left(\frac{R_{sample}}{R_{air}} - 1 \right) \times 10^3 \qquad 4.12$$

where $R = \frac{^{15}\mathrm{N}}{^{14}\mathrm{N}}$ (the molar ratio), and $R_{air} = 1 \div 272$ (Kendall 1998).

Sedimentary incorporation or immobilization of NO_3^- was tested by the addition of a known, high amount of $^{15}NO_3^-$ in the water reservoir and tracing its incorporation into the sediment (treatments D4 and L4, Table 4.3). This mass-balance approach required the use of high levels of $^{15}NO_3^-$ (Labeled medium in Table 4.2) to achieve a significant signal of $\delta^{15}N$ in sediments. Two major sources of ^{15}N were assumed to exist in each container at the beginning of the experiment: sediment ^{15}N and $^{15}NO_3^-$. At the end of the experiment, any remaining NO_3^- was assumed to exclusively include ^{15}N, which is a safe assumption based on the very likely preferential uptake of $^{14}NO_3^-$ early in the experiment (e.g., Sigman and Casciotti 2001). The weight of ^{15}N in sediment, Wt_{15Nsed} (μg), was calculated using $\delta^{15}N_{sed}$ (determined by isotopic analysis) as follows:

$$Wt_{15Nsed} = \frac{R_{sed} \times r_{AW} \times Wt_{Nsed}}{1 + (R_{sed} \times r_{AW})} \quad 4.13$$

where $R_{sed} = \frac{^{15}N_{sed}}{^{14}N_{sed}}$ (can be obtained from a simple rearrangement of Eq. 4.12), r_{AW} (the atomic weight ratio of ^{15}N and ^{14}N) = $AW_{15N} \div AW_{14N}$ = 15.0001 ÷ 14.0031, and Wt_{Nsed} (the total weight of N in sediment) = $Wt_{15Nsed} + Wt_{14Nsed}$ (where Wt_{14Nsed} is the weight of ^{14}N in sediment). The weight of ^{15}N in dissolved NO_3^-, Wt_{15NO3} (μg), was similarly calculated:

$$Wt_{15NO3} = \frac{R_{NO3} \times r_{AW} \times Wt_{N-NO3}}{1 + (R_{NO3} \times r_{AW})} \quad 4.14$$

where R_{NO3} can be obtained from a simple rearrangement of Eq. 4.12 and the weight of N in NO_3^-, Wt_{N-NO3} (μg) is:

$$Wt_{N-NO3} = [NO_3^-] \times V_{OW} \times \left(\frac{R_{NO3} \times AW_{15N} + AW_{14N}}{1 + R_{NO3}} \right) \quad 4.15$$

where $[NO_3^-]$ ($\mu mol \cdot L^{-1}$) is the concentration of NO_3^- in the overlying water, and V_{OW} (L) is the volume of overlying water (0.7 L at t_0). The total weight of ^{15}N in the incubator, Wt_{15Ntot} (μg), was defined as:

$$Wt_{15Ntot} = Wt_{15Nsed} + Wt_{15NO3} \quad 4.16$$

The values of Wt_{15Nsed}, Wt_{15NO3}, and Wt_{15Ntot} were calculated at the beginning (t_0) and end (tf) of the experiment for each treatment, and were used to calculate the final distribution (at t_f) of the Wt_{15NO3}, added at t_0, as follows:

$$\Delta^{15}N_{NO3} = \frac{Wt_{15NO3}(t_f)}{Wt_{15NO3}(t = 0)} \times 100 \quad 4.17$$

$$\Delta^{15}N_{sed} = \frac{Wt_{15Nsed}(t_f) - Wt_{15Nsed}(t=0)}{Wt_{15NO3}(t=0)} \times 100 \quad 4.18$$

$$^{15}N_{missing} = \frac{Wt_{15Ntot}(t_f) - Wt_{15Ntot}(t=0)}{Wt_{15Ntot}(t=0)} \times 100 \quad 4.19$$

$$\Rightarrow \Delta^{15}N_{NO3} + \Delta^{15}N_{sed} + {}^{15}N_{missing} = 100 \quad 4.20$$

where $\Delta^{15}N_{NO3}$, $\Delta^{15}N_{sed}$, $^{15}N_{missing}$, are expressed as a fraction (%).

A simplified version of the nitrogen cycle in marine sediments is given in Figure 4.3 (modified from Lehmann et al. 2004). Calculated values of $\Delta^{15}N_{sed} > 0$ were considered to be evidence of biotic uptake of NO_3^- by benthic microbes (Figure 4.3). Values of $^{15}N_{missing} > 0$ were considered as evidence of N loss from the system via catabolic reactions, e.g., denitrification (Figure 4.3).

Evidence for these two processes was also tested by Rayleigh fractionation, i.e., the change in the fraction of $^{15}N_{NO3^-}$ with time (treatments D5 and L5, Table 4.3). This fractionation is an outcome of the preferential uptake of the lighter $^{14}NO_3^-$ by microbiota and especially denitrifiers (e.g., Sigman and Casciotti 2001). The detection of the small fractionation-induced change in $\delta^{15}N$ in near-pure $^{15}NO_3^-$ is analytically impossible at present, due to the enormous $\delta^{15}N$ signal of near-pure $^{15}NO_3^-$ (e.g., Labeled medium, Table 4.2). Instead, non-labeled ("regular") KNO_3 was used, whose $\delta^{15}N$ value (= 7.5 ‰) provided a suitably low background for fractionation detection (Table 4.2). Samples were collected at daily time-points for $\delta^{15}N_{NO3^-}$ analysis from the treatments enriched with the regular medium (D5 and L5, Table 4.2). The $\delta^{15}N_{NO3^-}$ values were used to calculate the ratio $R = \frac{^{15}N_{NO3}}{^{14}N_{NO3}}$ at each time point which was then divided by R_0, the value of R at t_0,

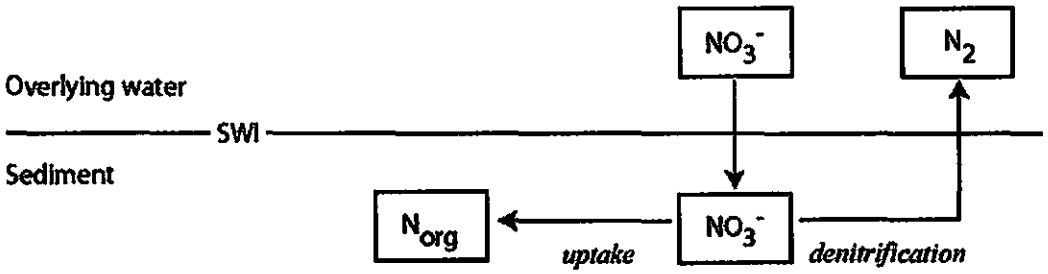

Figure 4.3 A schematic illustrating the experimental approach of the sediment plug incubation experiments (modified from Lehmann et al. 2004). During these experiments, NO_3^- from the overlying water comes in contact with the sediment grains and the associated microbiota, whose activity will determine whether N in NO_3^- will be stored on/in the sediment grains (*uptake*) or will be lost as N_2 (*denitrification*).

and plotted against $f^* = \frac{[NO_3^-]_t}{[NO_3^-]_{t0}}$, the fraction of the starting NO_3^- concentration, $[NO_3^-]_{t0}$, remaining in the overlying water at that particular time-point t, $[NO_3^-]_t$ (Fogel and Cifuentes 1993). The curve was fitted with the relationship:

$$\frac{R}{R_0} = f^{*(\alpha-1)} \qquad 4.21$$

and used to obtain the isotope fractionation effect:

$$\epsilon = (\alpha-1)\times 10^3 \qquad 4.22$$

The calculated ϵ values were compared with published values for nitrogen cycle processes, especially NO_3^- assimilation (ϵ = 4-6 ‰) and sedimentary denitrification (ϵ = 0 ‰) (Fogel and Cifuentes 1993; Sigman and Casciotti 2001; Lehmann et al. 2004).

In addition to nutrient-enriched FSW, sediment plugs were incubated in the presence of non-enriched FSW (treatments D2 and L2), which was analyzed for ambient nutrient concentrations, previously reported to be non-negligible (Atkinson et al. 1995). The purpose of this treatment was to test potential generation of nutrients by decomposition of sedimentary organic matter, which appears to be abundant (see loss-on-ignition TOC proxy, Table 4.1). Control treatments consisted of non-enriched (treatments D1-SW and L1-SW) and nutrient-enriched FSW (treatments D1-14N, L1-14N, D1-15N, and L1-15N) in the absence of sediments.

The final treatment consisted of sediment autoclaved at 121 °C for 15 min (treatments D3 and L3), in an attempt to record abiotic sediment-overlying water nutrient exchange due to physical processes such as adsorption. Autoclaving was used as an alternative to HgCl (e.g., Rasheed et al. 2005) in an attempt to employ "green chemistry."

The release of substantial nutrients, presumably due to cell dissociation, after autoclaving was treated by substantial rinsing with FSW before sediment plug formation. The application of the results from this treatment is questionable, due to the complexity of the texture and composition of carbonate sediment grains such as these (Wild et al. 2006). This holds for other methods attempting to remove biological activity while retaining the mineralogical and biogenic matrices of the sediment. For example, the application of HgCl to organic matter-rich sediments has side-effects on the organic matter present (Liu et al. 2006), while drying at high temperatures disrupts the sedimentary fabric enough to render it an artificial control (Rasheed et al. 2005). Until a suitable solution arises, slower physically-driven processes may be effectively ignored in the case where biological uptake rates are rapid.

4.2.3 Analytical methods

4.2.3.1 Solute analyses

Bromide and nutrients were analyzed using conventional spectrophotometric techniques adapted for small-volume samples, while oxygen was measured using a polarographic Clark-type electrode. These analytical methods are described in detail in Section *3.3.2.5*.

4.2.3.2 Particulate elemental analyses

Total organic carbon (TOC) was measured by thermogravimetry (Section *4.2.1*). Particulate carbon (PC) and nitrogen (PC) content of the *Dunaliella* culture were measured at the Hawaii Ocean Timeseries facility of the University of Hawai'i using a

Carlo Erba NC 2500 Elemental Analyzer. Particulate phosphorus (PP) content of the *Dunaliella* culture was measured by the Aspila method: samples were filtered through combusted, acid-washed, 25-mm GF/F filters, dried at 60 °C for 72 h, and combusted at 550 °C for 4 h (Aspila et al. 1976), to convert organic P to phosphate. The combusted filters were shaken for 16 h in 1 mol·L^{-1} HCl to extract the phosphate. The supernatant was filtered (0.45 μm) and the filtrate was analyzed for phosphate by spectrophotometry (Koroleff 1976), after neutralizing the acid to pH = 1 using a 12 mol·L^{-1} NaOH solution.

4.2.3.3 Cell counts

Cell counts of culture samples and water samples from microcosm experiments and control experiments, were obtained by flow cytometry using an EPICS ALTRA flow cytometer (Beckman Coulter, Fullerton, California, U.S.A.; Monger and Landry 1993). The combined sampling and analytical standard error was ± 15 %, based on 5 sets of duplicate samples. The size of live culture *Dunaliella* cells was determined by microscopy (> 100 cells; Verity et al. 1992) and by the electrical sensing zone (ESZ) method (> 1000 cells, with a Multisizer 3 Coulter counter, Beckman Coulter, Fullerton, California, U.S.A.).

Surface sediment samples (0-15 cm, typically 4-5 intervals) for algal cell enumeration were suspended in 25-40 mL of FSW and sequentially sieved through 100 μm and 40 μm BD Falcon nylon cell strainers (BD Biosciences, San Jose, California, U.S.A.). The filtrate was stained with DAPI (for DNA staining) and proflavin (for cell membrane staining) and filtered onto 1-μm black polycarbonate filters. The filters were mounted onto glass slides using mounting oil and cover slips, and viewed under an

epifluorescent microscope (Olympus BX51, Olympus America Inc., Melville, New York, U.S.A.) under a blue filter set (excitation: 460-490 nm, emission: 520 nm) at a magnification of 400 times. The dimensions of the field of view were determined using a stage micrometer calibration plate prior to each microscopy session.

4.2.3.4 Stable nitrogen isotope analyses

Bulk stable isotope analysis was performed using an on-line carbon-nitrogen analyzer coupled with an isotope ratio mass spectrometer (Finnigan ConFlo II/Delta-Plus, SOEST Stable Isotope Laboratory). Isotope values were reported in standard δ-notation relative to the atmospheric N_2 standard (see Eq. 4.12). To ensure accuracy, glycine and ground shrimp reference samples for which the $\delta^{15}N$ values had previously been well-characterized, were run along with the sediment samples. Precision was ≤ 0.2 ‰ for samples with $\delta^{15}N < 100$ ‰, and was ≤ 2.5 ‰ for samples with $\delta^{15}N \geq 500$ ‰. The standard deviation of replicate samples was generally ≤ 0.2 ‰.

The denitrifier method was used for the determination of $\delta^{15}N_{NO3^-}$ (Sigman et al. 2001; Casciotti et al. 2002). The samples were added to a culture of a strain of bacterial denitrifier that quantitatively converts NO_3^- and NO_2^- to N_2O, because it lacks nitrous oxide reductase activity. The product, N_2O, was extracted, purified and analyzed by continuous flow isotope ratio mass spectrometry (SOEST Stable Isotope Facility). The analytical precision is ± 0.4 ‰ (Dore et al. 1998).

4.3 Results and discussion

4.3.1 Microcosm organic enrichment experiments

Three organic enrichment experiments were performed with the permeable sediment microcosm. The physical characteristics of these sediments are shown in Table 4.4. All experiments were completed within 4-5 days of enrichment.

4.3.1.1 Solute transport

Exp. 12 was interrupted immediately before enrichment by a power failure due to an earthquake (October 15, 2006). Pumping ceased for 20 h, and – more importantly – the temperature rose by 4-5 °C over the same period of time. Despite this interruption, the experiment was completed due to the time and energy already invested in its planning and execution. Evidence from a variety of indicators suggests that the hydraulics of the column were adversely affected by the growth of a biofilm at the SWI. The results of conservative tracer experiments (Table 4.5) indicate that the solute enhancement factor, ε,

Table 4.4 Physical characteristics of the sediments used in the microcosm organic enrichment experiments.

Exp. No. – Sediment type	Grain size (mm)		σ_I	φ	k^a (m^2)
	Median	Mean			
11 – Sand field sediment	0.23	0.24	0.78	0.51	4.3×10^{-11}
12 – Reef pocket sediment	0.81	0.82	1.12	0.49	6.0×10^{-11}
13 – Sieved reef pocket sediment	0.83	0.85	1.08	0.47	1.7×10^{-10}

for Exp. 12 was lower than expected from the permeability, k_A, signifying a substantial disruption of the hydraulic operation of the column. In addition, the added culture of *Dunaliella* appeared to accumulate at the SWI, and this was verified by microscopic inspection of slides of sediment suspensions: Exp. 12 surface sediments (0-1.6 cm) contained high numbers of chlorophyll-containing cells partly concealed by mucous films (Figure 4.4). Slides of sediment suspensions from Exp. 11 and 13 revealed no such mucous films, and, while chlorophyll-containing cells abounded (e.g., centric and pennate diatoms, chlorophytes other than *Dunaliella*, and cyanobacteria) no *Dunaliella* cells (Figure 4.4). Due to the power failure and the effects described above, the data from Exp. 12 were not used further in this study.

Table 4.5 Results of conservative tracer experiments conducted during the three microcosm experiments (described in detail in Section *3.3.3.2*), where k_A (m^2) are sediment column permeabilities, ε are model-generated transport enhancement factors, and z_{layer} (mm) is the depth of the high-ε sediment surface layer. All measurements took place with pumping oscillation height, h, of 8.5 cm, and frequency, f, of 2 min^{-1}.

Microcosm Exp.	Tracer Exp. #	k_A (m^2)	z_{layer} (mm)	ε (log)
11	11-3	4.3×10^{-11}	75	1.2-2.0
12	12-1	6.0×10^{-11}	10	1.1-1.7
13	13-1	1.7×10^{-10}	55	2.1-2.6
13	13-2[a]	1.7×10^{-10}	-	1.8

[a] Tracer experiment 13-2 was conducted after the addition of the *Dunaliella* culture to the overlying water of the microcosm.

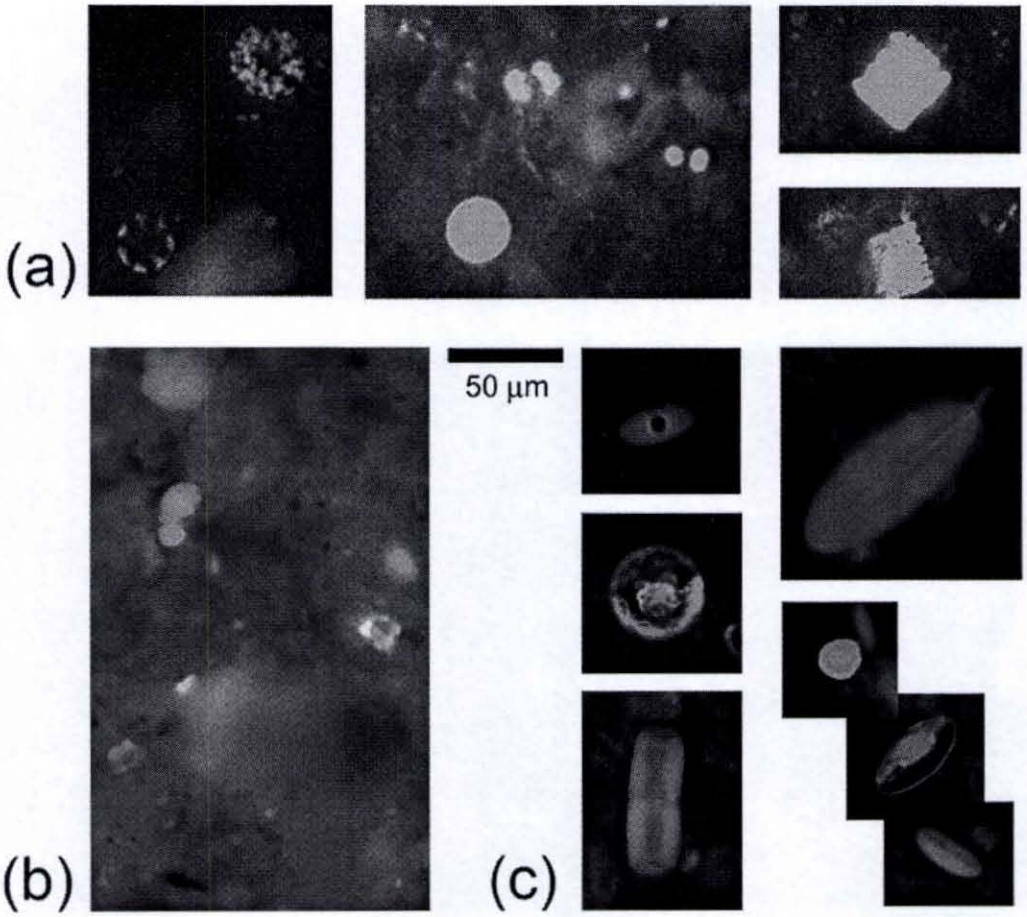

Figure 4.4 Selected microscope views of sediment suspension slides prepared with surface sediment samples (0-2 cm) from: (a) Exp. 11; (b) Exp. 12; and (c) Exp. 13. Chlorophyll-containing cells appear white in grey exposure and represent centric and pennate diatoms, and chlorophytes. The cloudy material covering the view in the slide from Exp. 12 (b) is biofilm and can be seen to cover numerous chlorophyll-containing cells < 15 µm in length, presumably *Dunaliella* retained in the biofilm that appeared following the disruption of the experiment by power failure.

Solute enhancement factors, ε, for Exp. 13 are greater than those for Exp. 11, as predicted by the higher permeability, k_A, of the sediment column (Table 4.5). It is interesting to note that Tracer Exp. 13-2 conducted after the *Dunaliella* culture enrichment yielded a lower ε value than tracer experiments before enrichment. A likely explanation for this is reduced hydraulic conductivity due to the transfer and trapping of the silt-sized *Dunaliella* cells from the overlying water into the sediment, and the development of microbial biofilms during their degradation.

4.3.1.2 Particle removal

The results of culture composition analyses at the time of addition to the microcosm are shown in Table 4.6. Elemental content and element ratios of *Dunaliella* cells were fairly similar between experiments, and also compared favorably with published values for *Dunaliella tertiolecta* (Verity et al. 1992). Although the particulate fraction constituted the majority of the input of nitrogen and phosphorus in both experiments, the two cultures differed substantially in dissolved nitrate content. This was because of different dissolved nitrate concentrations in the f/2 media used in each batch culture (S. Brown, personal communication).

Algal cell concentrations decreased dramatically during the first 24 h in the overlying water of the microcosm in both Exp. 11 and Exp. 13 (Figure 4.5). Approximately 99 % of the cells in the overlying water of the microcosm were lost within $t = 2$ d of enrichment. Measurable algal cell concentration decreases were also detected in the physiological control experiments (Figure 4.5), with 73 % and 60 % of the original number of cells lost by t_f in Exp. 11 and Exp. 13 respectively. Inspection of

Table 4.6 *Dunaliella* culture composition for the two batches used in Exp. 11 and 13: algal cell abundance and size, particulate and dissolved components of the culture, and dilution fraction by addition to the overlying water of the microcosm. Cell size and C and N content for *D. tertiolecta* (Verity et al. 1992) are given for comparison.

Characterization	Parameter	Exp. 11	Exp. 13	*D. tertiolecta*
Abundance and size	Cell abundance, mL^{-1}	9.2×10^5	1.0×10^6	-
	Length, μm	9.5 ± 0.9		10.9 ± 1.7
	Breadth, μm	7.8 ± 1.3		8.9 ± 2.1
Particulate composition [a]	PC, $\mu mol \cdot L^{-1}$	3502 ± 277	3459 ± 769	-
	Cell C content, $pg \cdot cell^{-1}$	45.5 ± 3.6	50.2 ± 11.1	63.2 ± 1.6
	PN, $\mu mol \cdot L^{-1}$	499 ± 29	461 ± 103	-
	Cell N content, $pg \cdot cell^{-1}$	7.6 ± 0.4	7.8 ± 1.7	10.3 ± 0.3
	PP, $\mu mol \cdot L^{-1}$	20.9 ± 0.6	21.6 ± 1.0	-
	Cell P content, $pg \cdot cell^{-1}$	0.7 ± 0.02	0.8 ± 0.04	ND [a]
	C:N, molar	7.0:1	7.5:1	7.2:1
	C:N:P, molar	168:24:1	160:21:1	ND [a]
Dissolved composition	DIN [b], $\mu mol \cdot L^{-1}$	62.0	361.9 ± 3.2	-
	PO_4^{3-}, $\mu mol \cdot L^{-1}$	3.4	2.20 ± 0.02	-
Dilution	Volume fraction in overlying water (%)	8.59	9.97	-

[a] Eq. 4.5.

[a] ND – Not determined.

[b] DIN is the sum of NO_3^-, NO_2^- and NH_4^+ concentrations.

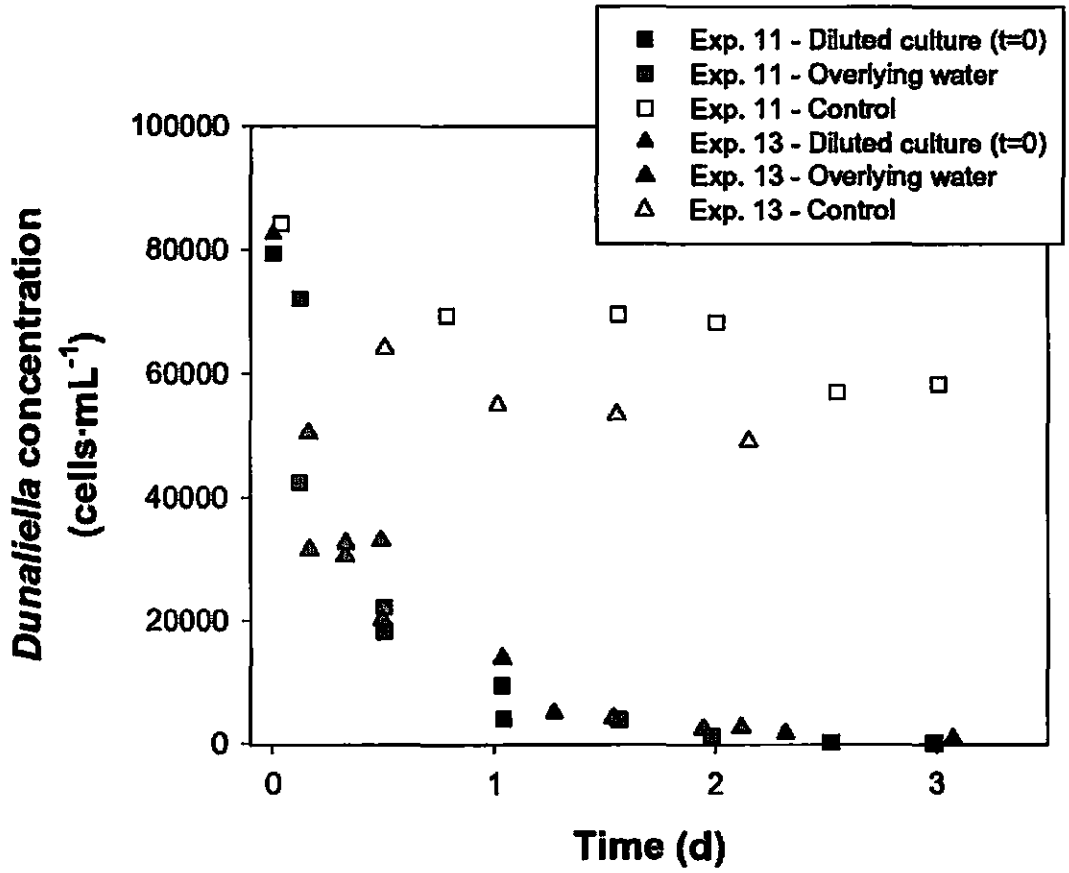

Figure 4.5 Algal concentration changes with time during Exp. 11 (squares) and Exp. 13 (triangles). Starting values calculated from culture concentrations multiplied by volume fractions during addition to the microcosm are shown by solid symbols. The log-transformed slopes of the two microcosm overlying water concentration vs. time relationships were found to be significantly different ($F_{1,19} = 27.1$, $p < 0.0001$) (Lowry 2007).

slides prepared from surface sediment (0-15 cm) sample suspensions revealed no *Dunaliella* cells in sediments at any depth at the termination of the experiments.

A mass balance calculation was performed to estimate the maximum numbers of cells lost to the sediment column (Eq. 4.6) during the two experiments. Since the vast majority of cells (99 %) was lost from the overlying water column within 2 d of addition, the sampling points closest to $t = 2$ d, $t_{99\%} = 1.98$ d and $t_{99\%} = 2.32$ d, were used for Exp. 11 and 13 respectively, instead of t_f. The numbers of cells lost to the sediments were converted to amounts C, N and P (Eq. 4.8) using the measured elemental contents of cells (Table 4.6). The C, N and P values were divided by $t_{99\%}$ to estimate a maximum flux rate of each element to the sediment. Moreover, since no cells were found in the sediments at t_f in either experiment, the number of cells degraded in the sediments equaled the number of cells lost to the sediments. Therefore, the C, N and P values in these cells were divided by t_f (5.7 d and 3.1 d for Exp. 11 and 13 respectively) to calculate a minimum rate of degradation for each element.

The results of these calculations are shown in Table 4.7. Although the initial algal cell concentrations were similar in both experiments, fluxes in Exp. 11 ($k_A = 4.3\times10^{-11}$ m^2) were higher than in Exp. 13 ($k_A = 1.7\times10^{-10}$ m^2). A similar result is obtained by a statistical comparison of the log-transformed slopes of the concentration-curves of the cells in overlying water ($F_{1,19} = 27.1$, $p < 0.0001$, $n = 27$, Figure 4.5). The trend of particle filtration rate with permeability is inverse from the one expected, i.e., higher permeability was predicted to allow deeper penetration of the cells, and consequently greater flux into the sediment (Huettel and Rusch 2000). However, shallower penetration of the cells in sediments of lower permeability may be counterbalanced by greater

Table 4.7 Maximum elemental fluxes of algal cells to the sediment column and sediment surface, minimum degradation rates and missing amounts of the supplied elements. Elemental fluxes were calculated using the C:N:P ratios measured for each culture (168:24:1 and 160:21:1 for Exp. 11 and Exp. 13 respectively, Table 4.6).

Rate	Parameter	Exp. 11	Exp. 13
Maximum flux ($mg \cdot m^{-2} \cdot d^{-1}$)	$t_{99\%}$ [a] (d)	1.98	2.32
	C	1034 ± 82	631 ± 140
	N	173 ± 9	98 ± 21
	P	16 ± 0.5	10 ± 0.5
Minimum degradation rate ($mg \cdot m^{-2} \cdot d^{-1}$)	t_f [b] (d)	5.66	3.09
	C	363 ± 29	433 ± 96
	N	61 ± 3	67 ± 14
	P	6 ± 0.2	7 ± 0.3
Missing bio-element amount [c] (mg, μmol)	C	9.5 ± 0.75, 790 ± 60	6.8 ± 1.5, 560 ± 125
	N	1.6 ± 0.08, 113 ± 6.0	1.1 ± 0.23, 75 ± 16
	P	0.15 ± 0.004, 4.7 ± 0.1	0.11 ± 0.005, 3.5 ± 0.2

[a] The time taken for the overlying water algal cell concentrations to reach 1 % of the initial concentration (at the time-point of enrichment, t=0).

[b] The time period between enrichment (t=0) and dismantling (t_f) of the experiment.

[b] Eq. 4.8.

trapping efficiency due to narrower interstitial spaces. Narrower corridors for trapping may also translate to greater grain surface area per unit volume of bulk sediment, thus increasing the possibility of contact between cells and sediment. One reason this was not obvious in analogous experiments conducted by Huettel and Rusch (2000) is that they either used commercially available sand or natural sediment that was aged for 7 months in a cold room. While their intention was to reduce algal biomass and chlorophyll, it is possible that biogenic matrices and additional organic material also degraded, reducing the adhesive or trapping ability of the natural sediment.

4.3.1.3 Particle decomposition-nutrient regeneration and nutrient efflux

Despite differences in flux rates, the minimum degradation rates are fairly similar between the two experiments. This, in part, is an artifact of the different t_f between the two experiments (5.7 d and 3.1 d for Exp. 11 and 13 respectively): a higher flux is counterbalanced by a longer incubation period for Exp. 11, relative to Exp. 13 (Table 4.7). However, this is also in concordance with recent reports that microbial abundances in permeable sediments, and especially reef-associated sands, do not differ substantially from those in finer-grained sediments (Wild et al. 2006; A. Rusch, personal communication). Even though no conclusive statements can be made about the effect of permeability on the observed degradation rates, it can be concluded that the permeable sediments used in these experiments are highly reactive and capable of responding rapidly to inputs of organic material.

Nutrients (primarily NO_3^- and PO_4^{3-}) supplied with the culture during organic enrichment caused an increase in nutrient concentrations in the overlying water at the

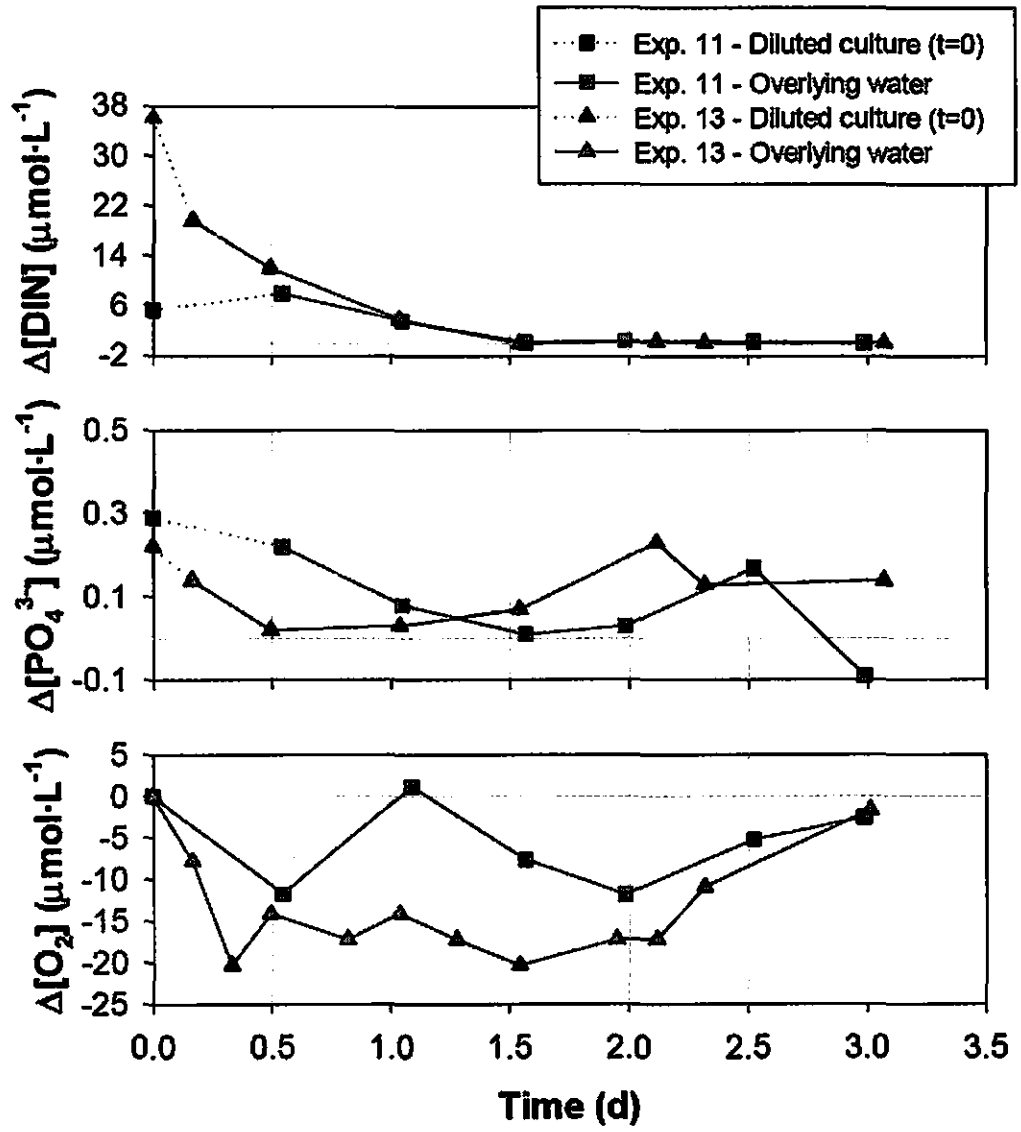

Figure 4.6 Concentrations of DIN, phosphate, and oxygen ($\mu mol \cdot L^{-1}$) in the overlying water after enrichment (t_0). Concentrations of DIN are the sum of the concentrations of NO_3^-, NO_2^-, and NH_4^+ concentrations (dominated by NO_3^-). Concentrations are given as the difference from the average concentration before the time of enrichment, ($\Delta[X] = [X]_t$ – average $[X]_{t<0\,d}$).

time-point of enrichment, t_0 (Figure 4.6). The initial concentrations of dissolved nutrients in the overlying water are explained by the dilution of nutrients added with the culture media upon addition to the microcosm (see Table 4.6 for relevant values). These concentrations decreased immediately after culture addition (Figure 4.6). In both experiments, both DIN and PO_4^{3-} are depleted from the overlying water between t_0 and t = 1.5 d. Time-integrated fluxes of DIN and PO_4^{3-} (mmol·m^{-2}·d^{-1}) were calculated by dividing the amount of DIN or PO_4^{3-} lost from the overlying water by the time of depletion, and multiplying by $10^4 \div A_{colA}$, where A_{colA} = 46.3 cm^2 is the cross-sectional area of Column A. The calculated fluxes are shown in Table 4.8. The slower fluxes in Exp. 11 relative to Exp. 13 are predicted by the difference in enhanced solute transport

Table 4.8 Time-integrated fluxes of DIN and PO_4^{3-}, added with the algal culture at the beginning of the experiments, and elemental fluxes of cumulative N and P added with the culture, being the sum of dissolved inorganic nutrients and elements contained in algal cells (converted to mmol·m^{-2}·d^{-1} from Table 4.7).

	Flux into the sediment (mmol·m^{-2}·d^{-1})	
Dissolved nutrient	**Exp. 11**	**Exp. 13**
DIN	3.4	8.0
PO_4^{3-}	0.095	0.175
DIN + N in algae	15.7	15.0
PO_4^{3-} + P in algae	0.610	0.500

coefficients, ε, between the two experiments (measured by the conservative tracer experiments, Table 4.5), which in turn are affected by the sediment column permeabilities, k_A, of 4.3×10^{-11} and 1.7×10^{-10} m^2 for Exp. 11 and 13 respectively (Table 4.5).

Secondary peaks in PO_4^{3-} concentration were observed after 2.0-2.5 d. The secondary peaks were preceded by periods of detectably reduced O_2 concentrations in the overlying water (Figure 4.6). It is very likely that the organic material supply and reduced exchange (e.g., as shown by Tracer Exp. 13-2, Table 4.5) during this time period may have induced shallower anoxia in the sediment column. This in turn could have mobilized phosphate from the oxidized phases in which it was bound (e.g., ferrous oxyhydroxides, Ogrinc and Faganeli 2006) into the pore water, which was then transferred to the overlying water by enhanced transport.

Inorganic nutrient levels in pore water at z = 5 cm (the shallowest depth at which pore water was sampled and analyzed) remained at the detection limit throughout the enrichment period. Moreover, the predicted nutrient release into the overlying water was not observed in either of the two experiments, as indicated by a comparison of the missing amounts of N and P (Table 4.7), produced by the degradation of algal cells in the sediments, with the observed overlying water nutrient concentrations during the time period following enrichment (Figure 4.6). The maximum level of the anticipated nutrient concentrations was calculated by considering overlying water volumes of 3.1 L and 2.9 L for Exp. 11 and Exp. 13 respectively. When the missing N and P amounts in Table 4.7 are divided by the overlying water volumes, nutrient concentrations of 20-41 $\mu mol \cdot L^{-1}$ for DIN and 1.1-1.7 $\mu mol \cdot L^{-1}$ for PO_4^{3-} should be observed, assuming the release of all the

remineralized N and P in the trapped and degraded algal cells into the overlying water. In addition, the total flux of total N and total P due to the culture addition (the sum of algal elemental contents and dissolved inorganic nutrients) is shown in Table 4.8, and is representative of the rates of disappearance of culture N and P 24-36 h after t_0. Dark incubations of the algal cell-overlying water mixture did yield nutrient increases of the order of 30 $\mu mol \cdot L^{-1}$ for DIN and 0.7 $\mu mol \cdot L^{-1}$ for PO_4^{3-}.

Therefore, it is apparent that the regenerated nutrients are sequestered into an unaccounted pool of dissolved or particulate matter. It is possible that dissolved organic nitrogen (DON) and dissolved organic phosphorus (DOP) could be generated during degradation. From what is known already about the participation of DON in N-cycling in sediments, the generation of DON is unlikely due to its rapid remineralization or uptake (see discussion in Burdige 2006, p. 463-464). The role of DOP cannot be dismissed as readily due to a lack of understanding of its role in P-cycling in marine sediments (Ruttenberg 2003).

An alternative sink for the removed N and P could be benthic microbiota (Marinelli et al. 1998; Nelson et al. 1999; Jahnke et al. 2000). The analysis for sedimentary TOC did not reveal a difference between sediments sampled during the column assembly and surficial sediments (1-cm layers between 0-5 cm) sampled at t_f during dismantling, with the TOC weight fraction at 3.50 % ± 0.15 %. I performed a calculation to determine whether the missing amounts of C, N, and P (Table 4.7) could be detected by analyzing sediment before and after enrichment. I calculated the weight of dry sediment of the 0-1 cm-depth slice of the microcosm sediment column, W_{dry} (g, Eq. 4.4), with the following equation:

$$W_{dry} = \rho_{wet} \times V_{slice} - \rho_{SW} \times V_{slice} \times \varphi \quad 4.23$$

where ρ_{wet} ($g \cdot cm^{-3}$) is the wet sediment density (1.86 $g \cdot cm^{-3}$ and 1.82 $g \cdot cm^{-3}$ for Exp. 11 and 13 respectively), V_{slice} is the volume of the 0-1 cm slice ($V_{slice} = A_{colA} \times 1 = 46.3\ cm^3$), ρ_{SW} ($g \cdot cm^{-3}$) is the density of the seawater used in the experiments (1.026 $g \cdot cm^{-3}$) and φ is the porosity (0.51 and 0.47 for Exp. 11 and 13 respectively). The sediment slice between 0-1 cm depth was chosen as a "best analytical case" scenario for analytical purposes, i.e., the case where the elemental amount would be concentrated in the smallest volume of sediment sampled at the end of the experiment (i.e., 1-cm thick slices). I also assumed that, based on the "best analytical case" scenario, all of the missing amounts of C, N, and P (Table 4.7), accumulated in this slice. The missing amounts of C, N, and P, from Table 4.7 were converted to g and divided by W_{dry} to yield weight fractions of change in C, N, and P respectively.

The values of the parameters used above as well as the results of the calculations are listed in Table 4.9. The weight fraction changes in C, N, and P, in the unrealistic "best analytical case" scenario are orders of magnitude lower than typical precisions of the analytical methods needed to detect these changes (see Table 4.9 for typical values). The outcome of the calculations in Table 4.9 is in sharp contrast with the very large changes that would be anticipated if the missing C, N, and P, entered the dissolved phase as inorganic nutrients (discussed earlier in this section). The contrast between solid and dissolved phase changes as a result of early diagenesis in sediments, as demonstrated by these calculations, is a reminder of the reason pore water solute composition is observed instead of organic geochemical parameters to describe the on-going diagenetic processes in a certain setting (Burdige 2006, p. 253).

Table 4.9 Calculations of change in the weight fraction of C, N, and P, in the top 0-1 cm slice of the sediment column, in the "best analytical case" scenario where all of the missing amount of C, N, and P, accumulates in this particular sediment slice.

Parameter		Exp. 11	Exp. 13
ρ_{wet} (g·cm^{-3})		1.86	1.82
V_{slice} (cm^3)		46.3	
ρ_{SW} (g·mL^{-1})		1.026	
φ [a] (-)		0.51	0.47
W_{dry} (g)		61.89	61.94
Missing amount [b] (mg)	C	9.5	6.8
	N	1.6	1.1
	P	0.15	0.11
Change in weight fraction (%)	C	0.015	0.011
	N	0.0026	0.0018
	P	0.0002	0.0002
Analytical precision [c] (%)	C	1.2, 0.3	
	N	1.5, 0.4	
	P	1.95, 10.24, 1.47	

[a] Porosity φ from Table 4.4.

[b] Missing amounts of C, N, and P, from Table 4.7.

[c] Analytical precision is reported as weight fraction of element over the total weight of the sample (%).

Sources: Organic C, 1.2 % (King et al. 1998) and 0.3 % (Chapter 6); total N, 1.5 % (King et al. 1998) and 0.4 % (Chapter 6); total P, 1.95 %, organic P, 10.24 %, and total inorganic P, 1.47 % (Ruttenberg 1992).

In summary, the last stage of the nutrient regeneration hypothesis, stating that nutrient efflux from the sediments into the overlying water increases with increasing permeability, could not be tested, since both Exp. 11 and Exp. 13 did not demonstrate nutrient accumulation in the overlying water, especially of a magnitude analogous to the input. Instead, N, and P, added as inorganic dissolved nutrients along with the more substantial N, and P pools in algal cells (Table 4.6) were taken up rapidly (Figure 4.6),along with the added algal cells (Figure 4.5). The fate of the missing amounts of C, N, and P, could not be determined due to the analytical reasons described previously. I propose that, while the results of Exp. 11 and 13 demonstrate that permeable carbonate sediments can respire large amounts of organic material at fairly rapid rates, permeable carbonate sediments also retain any re-mineralized nutrients through microbenthic processes, as proposed previously (e.g., Marinelli et al. 1998; Nelson et al. 1999; Jahnke et al. 2000). The microbenthic processes implicated in this uptake are further explored with the nutrient enrichment experiments discussed in the following section.

4.3.2 Nutrient uptake experiments

4.3.2.1 Sedimentary nutrient uptake rates

The lack of nutrient accumulation in the overlying water, despite a very high input of organic material during the microcosm enrichment experiments, suggests that Kilo Nalu sediments may be nutrient-limited and that they may have the capacity to take up substantial amounts of nutrients when available. The sediment plug experiments aimed at quantifying the capability of surface sediments from the Kilo Nalu sand field to take nutrients up from the surrounding seawater. The concentration-vs.-time curves of NO_3^-

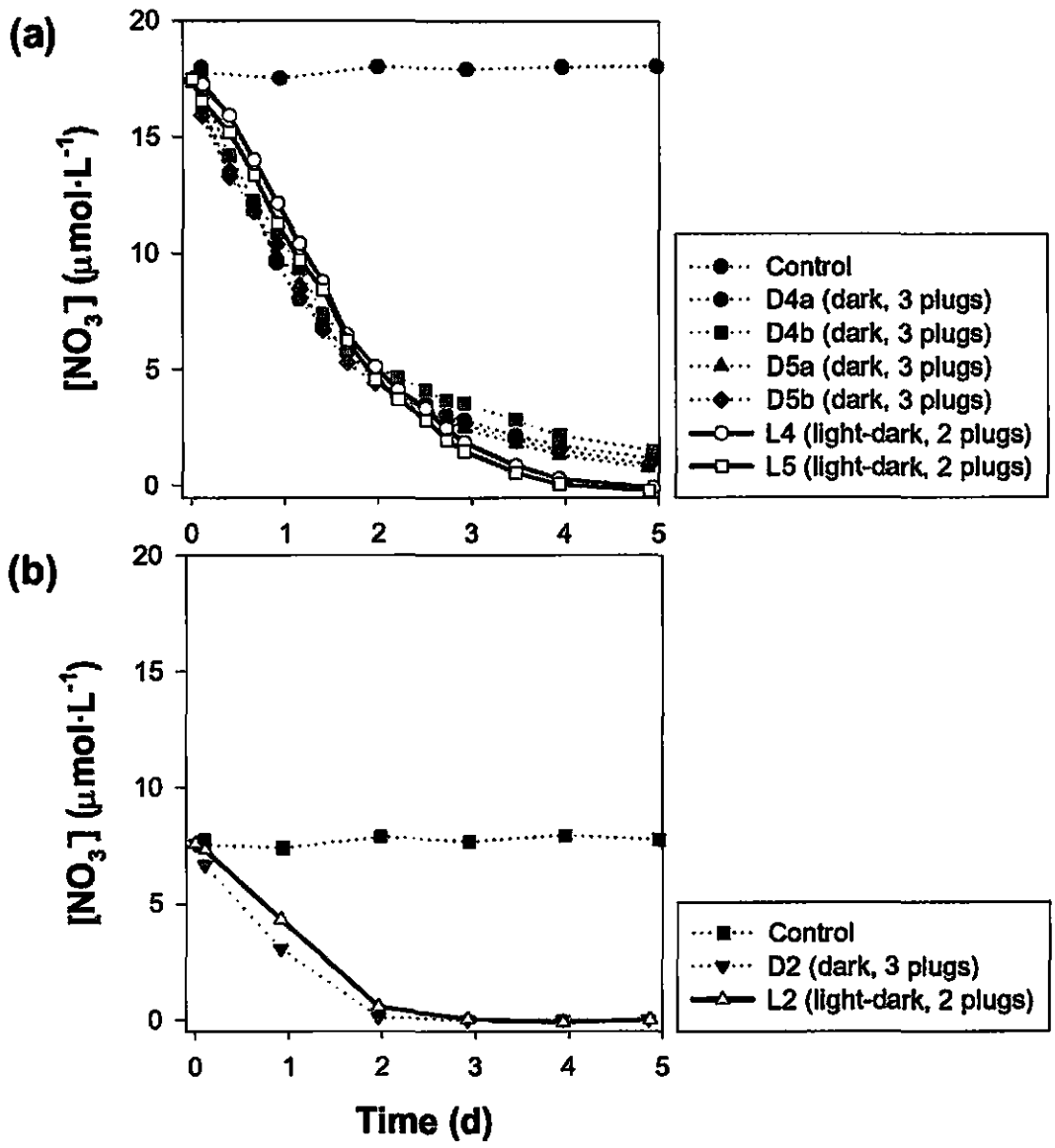

Figure 4.7 Nitrate concentration changes vs. time during sediment plug nutrient uptake experiments (Table 4.3): (a) Results for incubations with high nutrient-level media (regular and labeled, Table 4.2); (b) Results of incubation with low-level nutrient media (FSW, Table 4.2).

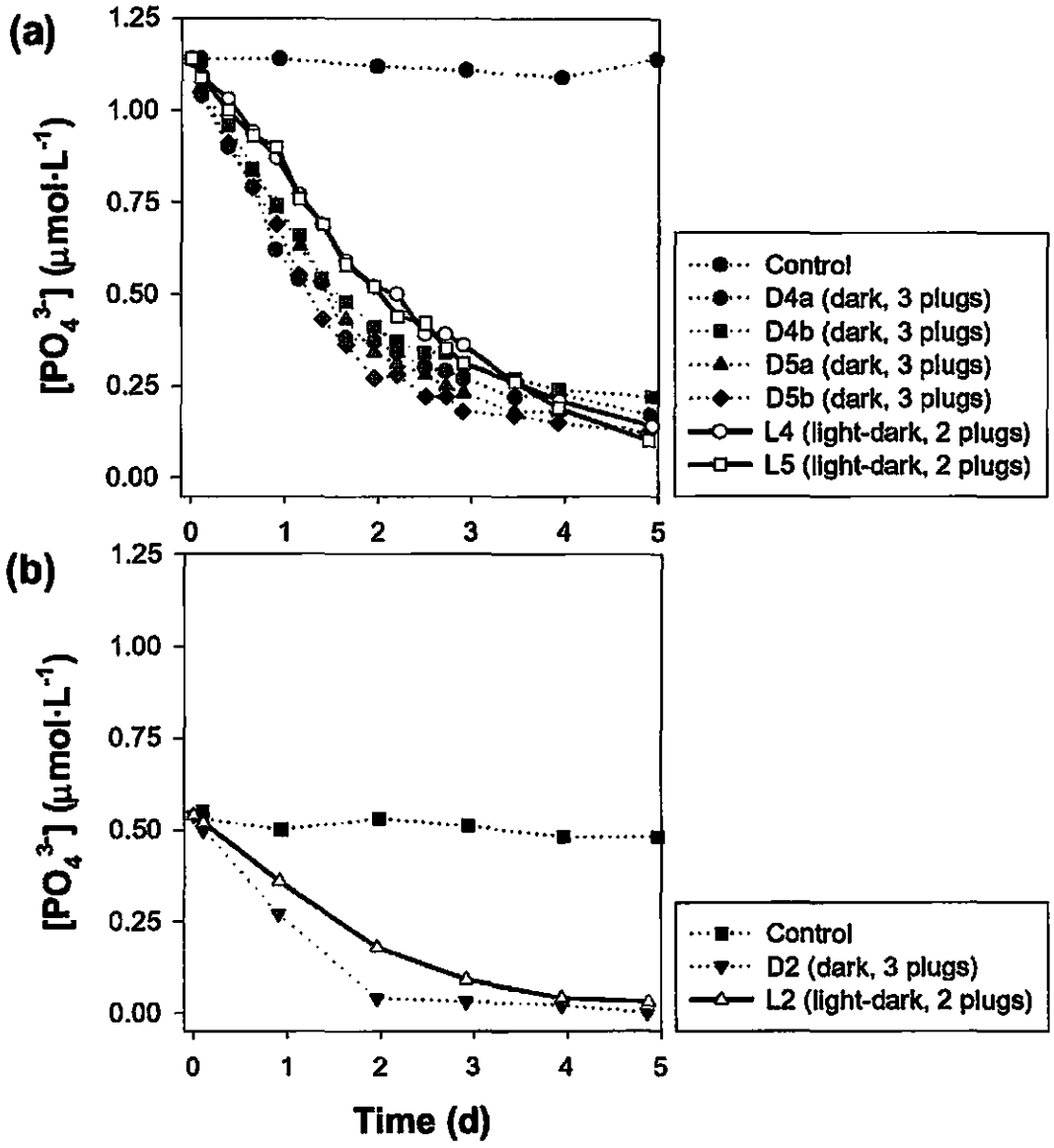

Figure 4.8 Phosphate concentration changes vs. time during sediment plug nutrient uptake experiments (Table 4.3): (a) Results for incubations with high nutrient-level media (regular and labeled, Table 4.2); (b) Results of incubation with low-level nutrient media (FSW, Table 4.2).

and PO_4^{3-} (Figure 4.7 and Figure 4.8, respectively) demonstrate active sediment nutrient uptake. In contrast, the concentrations of NO_2^- and NH_4^+ stayed at detection limit levels (0.14 $\mu mol \cdot L^{-1}$ and 0.03 $\mu mol \cdot L^{-1}$, respectively) or below throughout the incubation period. The rapid decline in nutrient concentrations, especially during the first two days of incubation, is indicative of nutrient limitation in the reef-associated carbonate permeable sediments.

Model fits of the concentration-time curves were performed with the linear decay model on the linear phase of the curves, as initially planned, as well as with an exponential decay model which traces concentrations throughout the duration of the experiment. The parameters used to calculate sediment uptake fluxes from the linear decay model fits are shown in Table 4.10. The results of the calculations are shown in Table 4.11 and in Figure 4.9. Treatments using regular and labeled media (Table 4.3) yield very similar fluxes, suggesting that the isotopic composition of NO_3^- does not affect net fluxes, and are therefore grouped together in the summary plots based on the treatment photoperiod (Figure 4.9).

Sediment uptake fluxes under alternating light-dark photoperiods (L2, L4 and L5) are greater than those under constant dark (D2, D4 and D5). This effect is more pronounced for NO_3^- than for PO_4^{3-}, and this leads to a large difference in the NO_3^- to PO_4^{3-} uptake ratios between treatments with the two light treatments. The uptake ratios are greater for incubations under the light-dark cycle (20.1 ± 0.7) than under constant dark conditions (15.8 ± 1.2). The higher ratios are mostly driven by differences in NO_3^- uptake between the two light-treatment incubations (compare NO_3^- and PO_4^{3-} fluxes in Table 4.11). One would expect photosynthesizers to control uptake under light conditions

Table 4.10 Fits of concentration-time curves from nutrient uptake experiments (Figure 4.7, Figure 4.8), using two models: an exponential decay model (performed on the entire concentration vs. time curve), and a linear extinction model (performed on the initial, linear portions of the curves).

			$[NO_3^-]$ ($\mu mol \cdot L^{-1}$)			$[PO_4^{3-}]$ ($\mu mol \cdot L^{-1}$)		
Model	**Treatment**	**n**	**a**	**b**	r^2	**a**	**b**	r^2
Exponential decay $y(t)=ae^{-bt}$	D2	7	7.63	1.20	0.99	0.55	0.95	0.99
	L2	7	7.94	0.93	0.98	0.55	0.57	0.99
	D4a	16	17.46	0.65	1.00	1.09	0.52	0.97
	D4b	16	17.75	0.58	0.99	1.12	0.46	0.99
	D5a	16	17.27	0.64	1.00	1.15	0.55	0.99
	D5b	16	17.09	0.64	0.99	1.16	0.64	0.99
	L4	16	19.29	0.64	0.97	1.18	0.41	0.99
	L5	16	18.45	0.66	0.97	1.22	0.44	0.99
Linear decay $y(t)=a+bt$	D2	4	7.14	-3.74	0.98	0.53	-0.25	0.99
	L2	4	7.64	-3.60	1.00	0.54	-0.18	1.00
	D4a	8	16.80	-7.17	0.98	1.09	-0.44	0.97
	D4b	8	17.24	-6.90	0.99	1.10	-0.40	0.99
	D5a	8	16.50	-6.76	0.99	1.12	-0.42	0.99
	D5b	8	16.43	-6.84	1.00	1.12	-0.48	0.99
	L4	9	18.06	-6.67	0.99	1.14	-0.32	1.00
	L5	9	17.22	-6.41	0.99	1.15	-0.33	0.99

Table 4.11 Fluxes of nitrate (F_{NO3-}) and phosphate (F_{PO43-}): *Fw* ($\mu mol \cdot g^{-1} \cdot d^{-1}$, Eq. 4.10) in relation to plug sediment weight, wt_{sed} (g), and *Fa* ($mmol \cdot m^{-2} \cdot d^{-1}$, Eq. 4.11) in relation to plug area, A_{plugs}. For each flux, the linear slope, b (from Table 4.10), was normalized with the normalization factor (Eq. 4.9), where $\overline{wt}_{plug}$ = 11.41 g (± 0.27 g). Flux ratios are also given (ratio values were the same, whether using *Fw* or *Fa*,). Negative *F* values indicate fluxes into the sediment. See Figure 4.9 for plots of the data.

Treatment	n_{plugs}	Normalization factor	wt_{sed} (g)	A_{plugs} (m^2)	*Fw* ($\mu mol \cdot g^{-1} \cdot d^{-1}$)		*Fa* ($mmol \cdot m^{-2} \cdot d^{-1}$)		$F_{NO3-} \div F_{PO43-}$
					Fw_{NO3-}	Fw_{PO43-}	Fa_{NO3-}	Fa_{PO43-}	
D2	3	1.01	34.07	0.00589	-0.08	-0.005	-0.45	-0.030	15.0
L2	2	0.99	23.01	0.00393	-0.11	-0.005	-0.64	-0.032	20.0
D4a	3	1.04	32.83	0.00589	-0.15	-0.009	-0.89	-0.055	16.3
D4b	3	0.97	35.15	0.00589	-0.14	-0.008	-0.80	-0.046	17.3
D5a	3	0.98	35.07	0.00589	-0.13	-0.008	-0.78	-0.049	16.1
D5b	3	1.00	34.16	0.00589	-0.14	-0.010	-0.81	-0.057	14.3
		Dark average			*-0.14*	*-0.009*	*-0.82*	*-0.052*	*16.0*
L4	2	1.02	22.30	0.00393	-0.21	-0.010	-1.22	-0.058	20.8
L5	2	0.99	23.13	0.00393	-0.19	-0.010	-1.13	-0.058	19.4
		Light-Dark average			*-0.20*	*-0.010*	*-1.17*	*-0.058*	*20.1*

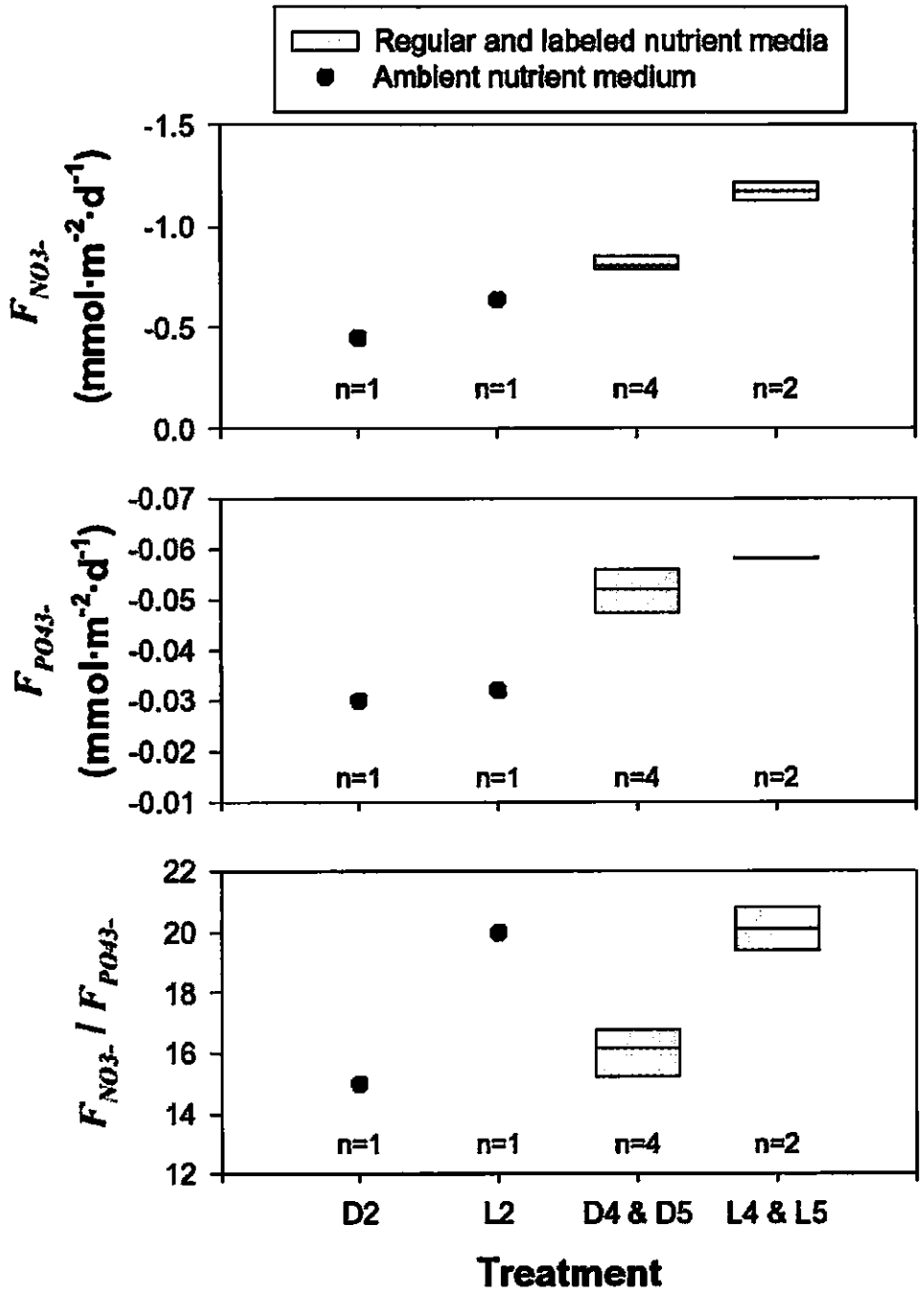

Figure 4.9 Fluxes and flux ratios from Table 4.11, grouped by initial nutrient levels (see Table 4.2) and by light treatment (D = dark, L = light-dark, Table 4.3). See Table 4.11.

and thus drive the uptake ratio towards the Redfield value 16. However, in this case the treatments exposed to constant darkness yield Redfield-like uptake ratios, while the treatments exposed to alternating light and dark conditions show higher-than-Redfield uptake ratios. It has been known that N- and P-rich bacteria could have N:P ratios significantly lower than 16 (Sterner and Elser 2002, p. 206), while many photosynthesizers including cyanobacteria can exhibit dramatic stoichiometric plasticity (e.g., White et al. 2007). The likely occurrence of photosynthesis in surficial Kilo Nalu sediments (due to ample photosynthetically available radiation, PAR, at 10 m depth) may cause changes in redox conditions in grain surface biofilms induced by the production of oxygen. Redox conditions dictate the phase and mobility of metabolically important species such as Fe and P, whose biogeochemistry is closely connected (Ruttenberg 2001), and may consequently drive stoichiometric balance and demand in microbial communities in carbonate reef permeable sediments.

4.3.2.2 Sedimentary nutrient incorporation

The results of the enrichment incubations with Labeled medium (Table 4.12) support the hypothesis that incorporation of nutrients in sediments is an important nutrient sink. The majority (61-66 %) of the added ^{15}N was found in the sediments in incubations conducted in the dark. Sediments treated to light-dark oscillations (L4) still contained more than half of the added ^{15}N at the time of experimental dismantling, but this fraction (52 %) is substantially lower than that retained in dark incubations. The rapid uptake of NO_3^- and its exhaustion from the overlying water in this incubation indicate that some of the ^{15}N may have been remobilized after 4 d when NO_3^- reached

Table 4.12 Mass balance calculations for the plug incubations using Labeled medium (Table 4.2). Wt_{15Nsed} (the amount of ^{15}N in sediment), Wt_{15NO3} (the amount of ^{15}N in NO_3^-), and Wt_{15Ntot} (the amount of total ^{15}N in the incubator), are all given in μg at the beginning (t_0) and at the end (t_f) of the experiment (see Eq. 4.13, 4.14, and 4.16). Also shown are the fractions (%) of the ^{15}N added as NO_3^- at t_0 found at t_f in NO_3^- ($\Delta^{15}N_{NO3}$, Eq. 4.17), in the sediment ($\Delta^{15}N_{sed}$, Eq. 4.18), or missing ($^{15}N_{missing}$, Eq. 4.19).

Treatment		$Wt(t_0)$ (μg)			$Wt(t_f)$ (μg)			(%)		
Code	**Light condition**	Wt_{15NO3}	Wt_{15Nsed}	Wt_{15Ntot}	Wt_{15NO3}	Wt_{15Nsed}	Wt_{15Ntot}	$\Delta^{15}N_{NO3}$	$\Delta^{15}N_{sed}$	$^{15}N_{missing}$
D4a	Dark	97.9	27.1	125.0	11.3	92.0	103.3	12	66	22
D4b	Dark	101.7	29.4	131.1	14.5	91.0	105.5	14	61	25
L4	Light-dark	104.0	18.6	122.6	0.0	72.9	72.9	0	52	48

very low levels. Regardless, the fraction of added ^{15}N that was recovered as part of the sediment was high, supporting the role of surface sediments as sites of N storage. This is also supported by the fact that the sedimentary weight fraction of N at Kilo Nalu sediments was repeatedly measured during this study and found to be on average 0.03 ‰, which is an order of magnitude greater than values reported in other permeable sediment settings such as the SAB (Marinelli et al. 1998).

4.3.2.3 Sedimentary denitrification

Another significant finding from the labeled medium incubations (Section *4.3.2.2*) is the magnitude of the ^{15}N fraction that cannot be found in the sediments and cannot be accounted for by the negligible overlying water concentrations of NO_2^- or NH_4^+ (at or below their detection limit). The substantial amount of added ^{15}N not found in the sediments or the overlying water at t_f, could be explained by the other proposed major sink for NO_3^- in permeable sediments, denitrification (Rao 2006). The role of denitrification in the removal of N was tested with treatments D5a, D5b, and L5. Plots of $R \div R_0$ vs. f^*, fitted with Eq. 4.21, are shown in Figure 4.10. The sample values are compared to those reported for isotopic fractionation by NO_3^- assimilation (ϵ = 4-6 ‰) and by sedimentary denitrification (ϵ = 0 ‰) (Sigman and Casciotti 2001; Lehmann et al. 2004). There is a significant difference between fractionation effects during sedimentary denitrification and water column denitrification (ϵ = 13-28 ‰) (Lehmann et al. 2004), the reason being that NO_3^- is physically transported to reactive micro-sites in sediments by diffusive processes (which do not fractionate NO_3^-), and upon arrival it is

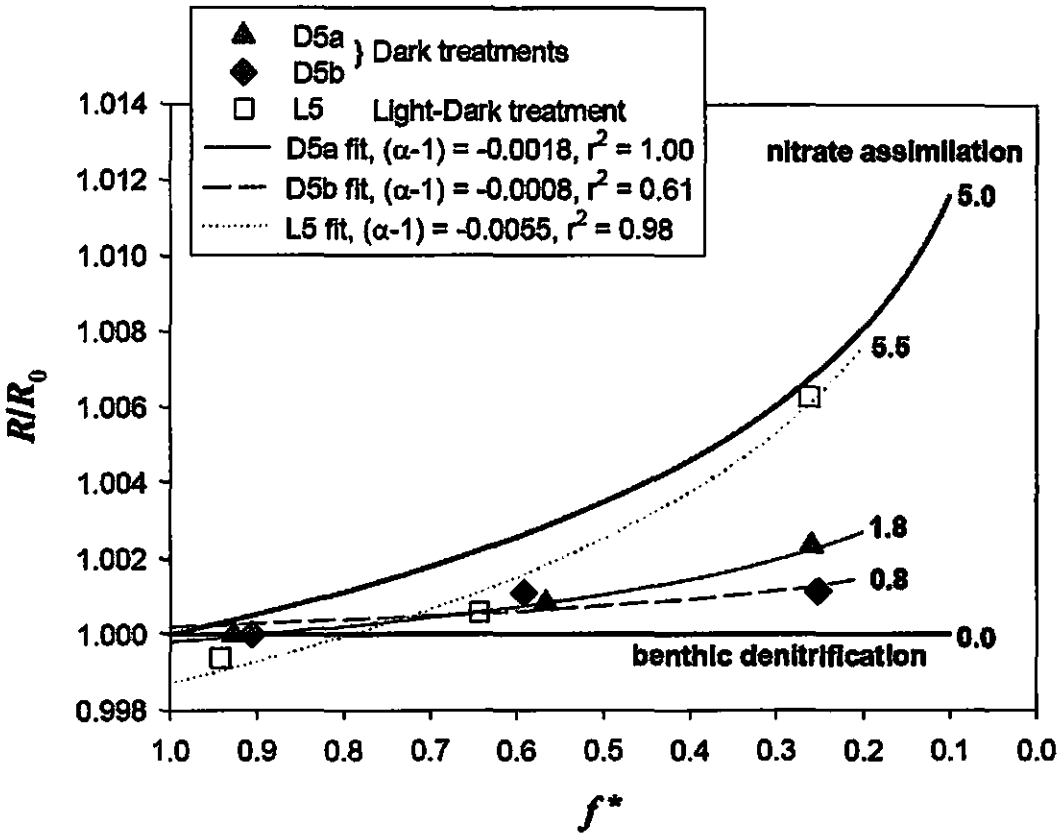

Figure 4.10 Plots of $R \div R_0$ vs. f^* (see Eq. 4.21-4.22 for definitions) for the three treatments with regular enrichment medium (D5a and D5b – dark; L5 – light-dark). The plots are fitted with Eq. 4.21. The data at $f^* = 0.26$ correspond to t = 2 d of the incubations (Figure 4.7). Black, thick solid curves show trends for nitrate assimilation and sedimentary denitrification (Sigman and Casciotti 2001; Lehmann et al. 2004). Bold numbers indicate the value of ϵ for each curve as calculated with Eq. 4.22.

completely consumed resulting in no discernible change in $\delta^{15}N_{NO3}$. (Bender 1990; Brandes and Devol 1997; Lehmann et al. 2004). The resultant $\in$ values for D5a, D5b, and L5 are 1.8‰, 0.8 ‰, and 5.5 ‰ respectively. While the value for incubation in the light-dark cycle (L5) is within the range indicative of NO_3^- assimilation, the values for incubation in the dark (D5) are indicative of a combined effect of NO_3^- assimilation and sedimentary denitrification.

An estimate of the time-integrated denitrification rate, F_{denit} (mmol·m^{-2}·d^{-1}), in the plug incubation experiments was calculated as follows:

$$F_{denit} = \frac{V_{OW} \times \frac{[NO_3^-]_{t0}}{1000} \times \frac{^{15}N_{missing}}{100}}{t_f \times A_{plugs}} \qquad 4.24$$

where V_{OW} (L) is the volume of overlying water, $[NO_3^-]_{t0}$ (μmol·L^{-1}) is the concentration of nitrate in the overlying water at t_0, $^{15}N_{missing}$ (%) is the fraction of the ^{15}N added as NO_3^- at t_0 and missing at t_f (d), which is the duration of the experiment, and A_{plugs} (m2) is the area of the sediment plugs. The assumption made in the calculation of Eq. 4.24 is that $^{15}N_{missing}$ is representative of all the N that is missing, and it is quite reasonable considering that approximately 60 % of NO_3^- at t_0 was $^{15}NO_3^-$. The results are shown in Table 4.13, along with data from the literature. The denitrification rate estimates from the plug incubation experiments are comparable to those from other permeable sediments, both carbonate reef sediments and silicate shelf (relict) sediments. Even though a variety of incubation methods are used to quantify N loss from the sediments by denitrification, the areal denitrification rate estimates for permeable sediments from different locations and settings (Table 4.13) generally vary between 10^{-2} and 10^{0} mmol·m^{-2}·d^{-1}.

Table 4.13 Estimates of denitrification rates, F_{denit} (mmol·m^{-2}·d^{-1}) from the plug incubation experiments (this study), and from incubations reported in the literature. Depths of integration (cm) indicate the thickness of the sediment column on which the experimental measurements were performed. All incubations were performed in the dark, except the 12 h Light:12 h Dark plug incubations of Kilo Nalu sediment (this study) which are marked L:D.

Location	F_{denit} (mmol·m^{-2}·d^{-1})	Incubation method	Depth of integration (cm)	Source
Carbonate reef permeable sediments				
Kilo Nalu	0.09-0.10	Plug	0.3	This study
Kilo Nalu (L:D)	0.20	Plug	0.3	This study
Ishigaki Island	0.04-0.16	Closed core	15	Miyajima et al. (2001)
Great Barrier Reef	0.003-0.32	Aerobic slurry	2	Capone et al. (1992)
Silicate shelf permeable sediments				
South Atlantic Bight	0.27-0.58	Flow-through reactor	8 to 32	Rao et al. (2007)
South Atlantic Bight	0.023-0.034	Closed core	15 to 18	Vance-Harris and Ingall (2005)
Mid-Atlantic Bight	1.7	Benthic chamber	8	Laursen and Seitzinger (2002)
North Sea	0.13-0.32	Open core	5	Lohse et al. (1996)

4.3.3 Permeable carbonate reef sediments and nutrient dynamics

4.3.3.1 Particle and nutrient uptake

The experiments performed in this study indicated that carbonate reef permeable sediments rapidly take up the important macronutrients N and P, whether they are in the dissolved form or originally in trapped particles which are degraded. Algal cells, which were added to the microcosm overlying water at initial cell concentrations upwards of 8×10^4 mL^{-1}, could not be found 3 d to 5 d after addition either in the overlying water or in the sediment. The macronutrients contained in the algal cells were not seen to emerge as dissolved inorganic nutrients, either in pore water or in overlying water, suggesting that remineralization resulted either in sedimentary retention of these nutrients or, in the case of N, to their loss in the gas phase.

The fluxes calculated from the data of the two experiment sets were compared to examine the likelihood that the total N and P (both particulate and dissolved) added during the microcosm enrichment experiments could be retained in the solid phase of surface permeable sediments and not give a dissolved inorganic nutrient signal in the pore water. In other words, the calculation was ultimately meant to test the capability of surficial permeable sediments to fully exploit the absorbed and regenerated nutrients. An extreme scenario was simulated, during which the total N and P in algae are not only instantaneously remineralized after trapping, but the generated dissolved nutrients are released immediately into the pore water. The scenario is extreme in that the trapping and degradation of cells would most likely happen on and in grain-surface biofilms generated by sedimentary microbes (Huettel and Rusch 2000) gradually and not instantaneously, at

rates higher than the calculated minimum mineralization rates for the microcosm experiments (Table 4.7). Moreover, the microbial biofilms are likely to retard the release of any generated solutes to the pore water (Hannides et al. 2005), thus allowing their further exploitation. Finally, as the plug incubation experiments have shown (

Table 4.12), in the case of N, most of the available amount (approximately 75 %) is likely to be assimilated into the sediment. Therefore, the outlined situation is meant to illustrate the capability of enhanced transport to distribute regenerated nutrients had they been available for transport.

The flux of DIN + N in algae ($mmol \cdot m^{-2} \cdot d^{-1}$) from microcosm enrichment Exp. 11 (Table 4.8) represents the supply rate of total N to the microcosm sediment column of Kilo Nalu sand field sediment. The average NO_3^- flux, Fa_{NO3^-} ($mmol \cdot m^{-2} \cdot d^{-1}$), from the plug incubation experiments under dark conditions (Table 4.11), is assumed to represent an average zeroth-order uptake rate of remineralized N by surficial Kilo Nalu sand field sediment. The ratio of the two fluxes was calculated and multiplied by 3 mm to generate the depth of the microcosm surface sediment column, $z_N = 57$ mm, down to which the regenerated DIN should be transported to counterbalance supply rate and uptake rate. A similar calculation, performed using PO_4^{3-} + P in algae ($mmol \cdot m^{-2} \cdot d^{-1}$) from Exp. 11 (Table 4.8) and Fa_{PO43-} ($mmol \cdot m^{-2} \cdot d^{-1}$) from plug incubation experiments under dark conditions (Table 4.11), yielded a depth of the microcosm surface sediment column, z_P = 35 mm, down to which the regenerated PO_4^{3-} should be transported to counterbalance supply rate and uptake rate. The Einstein-Smoluchowski relation (Eq. 3.15; Boudreau 1997, p. 101-102) was used to calculate the enhanced transport coefficient, ε, necessary

to transport a solute a distance of z_N and z_P within t = 0.25 d (or 6 h), the average time between microcosm sampling points:

$$\varepsilon = \frac{z_N^{\,2}}{2tD_0\varphi} \qquad 4.25$$

where $D_s = \varepsilon D_0 \div \theta^2 = \varepsilon D_0 \varphi$ (see section *3.2.3.2*), D_0 = 153 $mm^2 \cdot d^{-1}$ for DIN and D_0 = 49 $mm^2 \cdot d^{-1}$ for PO_4^{3-} (Boudreau 1997, p. 115-116) and φ = 0.51 (Table 4.4). The resulting values of $\log(\varepsilon)$ = 1.92 for DIN and $\log(\varepsilon)$ = 1.39 for PO_4^{3-} are within the range of values obtained during solute Tracer Exp. 11-1 (Table 4.5). The calculation results demonstrate the high probability that – even in the extreme scenario of instantaneous mineralization of algal macronutrients and their release as dissolved inorganic nutrients into pore water – Kilo Nalu sand field sediments would have the capability to absorb the dissolved nutrients back into the solid phase at such a rate as to prevent their accumulation in the pore water. The dissolved-nutrient uptake rates measured for carbonate reef sediments with the plug incubation experiments are capable of removing from solution any dissolved nutrients regenerated during the degradation of algal cells in the culture added to the microcosm during enrichment experiments.

4.3.3.2 Nitrogen retention

The use of the stable isotope ^{15}N during nutrient addition experiments revealed that a large fraction (75 %) of the NO_3^- removed from the overlying water was retained in the sediment (Table 4.12). The fractionation effects calculated from $\delta^{15}N_{NO3-}$, while it was being removed from the overlying water, bore a strong signal of nitrate assimilation (Figure 4.10). While treatments under dark conditions indicated a combination of nitrate

assimilation and benthic denitrification as removal mechanisms (Bender 1990; Brandes and Devol 1997; Sigman and Casciotti 2001), the incubations under light-dark oscillations (which simulate light conditions experienced by surface sediments more accurately than constant-dark incubations) yielded higher nutrient uptake rates than constant-dark incubations (Figure 4.9), as well as $\delta^{15}N_{NO3^-}$ fractionation effects that are clearly representative of NO_3^- assimilation (Figure 4.10).

The evidence for NO_3^- assimilation in all treatments, regardless of light conditions, suggests a strong retaining mechanism for N in carbonate reef permeable sediments, which may explain the high N content of these sediments (0.03 %), relative to silicate permeable sediments (0.005-0.008 %, Marinelli et al. 1998; Rao et al. 2007). Significant assimilatory uptake and retention of N by carbonate reef sedimentary microbiota has also been reported in Ishigaki Bay (Miyajima et al. 2001), suggesting that carbonate reef sediments may be similar to finer-grained sediments that show similar N retention properties when offered additional DIN (Veuger et al. 2007).

The reason for the ability to retain nutrients may be microbial abundances, which are now recognized to be higher than those predicted by the grain size distribution of permeable sediments (Table 4.1; Wild et al. 2006; Sørensen et al. 2007). Active and high assimilation rates could be attributed to heterotrophic bacteria and archaea as well as benthic microalgae, such as cyanobacteria (Zehr and Ward 2002), which were observed with epifluorescence microscopy in slides of sedimentary suspensions (Figure 4.4). The clear signal of nitrate assimilation in the light-dark treatments (from the fractionation effect results, Figure 4.10) points to a photosensitive response to nutrient uptake and, very likely, C fixation (Sterner and Elser 2002, p. 97-102), and underlines the role

microphytobenthos may play in nutrient dynamics and organic matter cycling in permeable sediments (Jahnke et al. 2000).

4.3.3.3 Nitrogen loss – denitrification

The occurrence of denitrification under the plug incubation experimental conditions (well-oxygenated overlying water exchanging rapidly with pore water) is startling but in accordance with previous reports of denitrification under similar conditions, both in the water column (e.g., Lehmann et al. 2005) and in permeable sediments (e.g., Rao 2006; Rao et al. 2007). Recent findings in sedimentary N-cycling allow the diversification of the overly simplified direct path from NO_3^- to N_2 in Figure 4.3 to multiple possible pathways. For example, a recent review of the marine nitrogen cycle (Brandes et al. 2007) highlights six processes that could potentially contribute to the conversion of NO_3^- to N_2 (Figure 4.11, Table 4.14).

The experiments conducted in this study were not designed to distinguish between different denitrifying pathways and their contribution to overall N loss. It is likely that a combination of the processes known to occur in sediments is taking place and contributing to N loss. The anoxic and suboxic microniches necessary for canonical denitrification, anammox and OLAND to take place could be readily provided by the complex landscape of biogenic carbonate reef sediments grains (Wild et al. 2006). Microzones filled with mucous biofilms within depressions and crevasses on the grain surface, hosting numerous microbes sheltered by grazing (Weise and Rheinheimer 1977), are likely sites of intense O_2 and NO_3^- gradients (Jahnke 1985) and subsequent interacting transformations of N. Clearly, there are benefits to be gained by interrogating individual

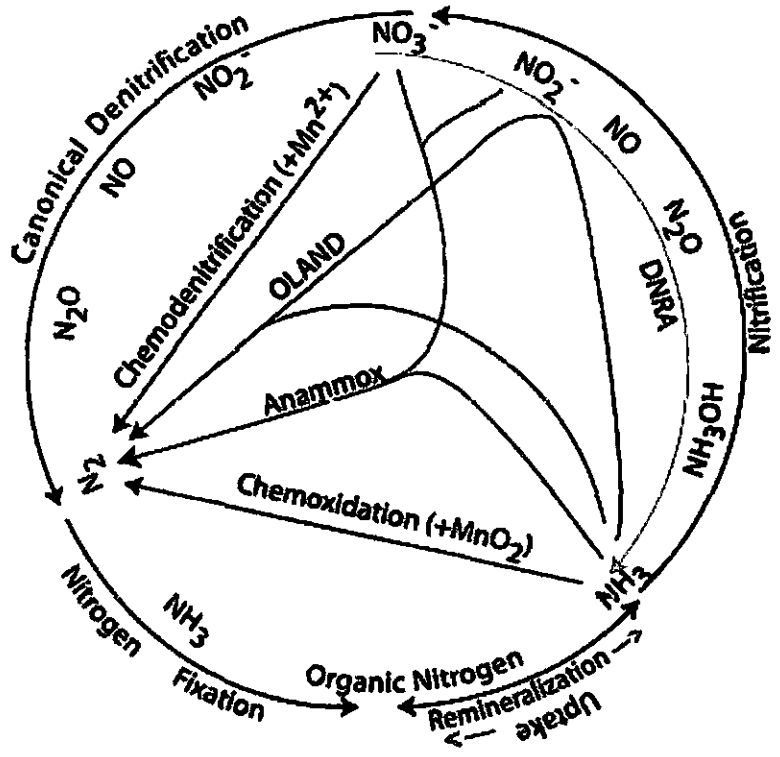

Figure 4.11 A schematic of processes implicated in marine nitrogen cycling (Brandes et al. 2007). This schematic identifies 6 processes that may ultimately convert N in NO_3^- to N_2: while canonical denitrification, and chemodenitrification can convert N in NO_3^- directly into N_2, anaerobic ammonia oxidation (anammox), oxygen-limited autotrophic nitrification-denitrification (OLAND), and chemooxidation require the partial conversion of NO_3^- to one or more intermediate products of dissimilatory nitrate reduction to ammonium (DNRA). A seventh process, which is not drawn by the authors (for clarity), is assimilatory nitrate reduction to ammonium (ANRA) by photosynthesizers and various bacterial strains (Zehr and Ward 2002; Brandes et al. 2007), during which NO_3^- generally follows the transformations of DNRA to NH_4^+.

Table 4.14 Formulas representative of the reactions shown in Figure 4.11 that are implicated in loss of N, originally contained in NO_3^-, as N_2. Canonical denitrification and chemodenitrification convert N in NO_3^- directly into N_2, while anaerobic ammonia oxidation (anammox), oxygen-limited autotrophic nitrification-denitrification (OLAND), and chemooxidation require the partial conversion of NO_3^- to one or more intermediate products of dissimilatory nitrate reduction to ammonium (DNRA, Figure 4.11). NO_3^- and N_2 are marked in bold, while intermediate products of DNRA are underlined.

Canonical denitrification (Van Cappellen and Wang 1995)

$$(CH_2O)x(NH_3)y(H_3PO_4)z + ((4x+3y)\div 5))\mathbf{NO_3^-} \rightarrow ((2x+4y)\div 5))\mathbf{N_2} + ((x-3y+10z)\div 5))CO_2 + ((4x+3y-10z)\div 5))HCO_3^- + zPO_4^{2-} + ((3x+6y+10z)\div 5))H_2O$$

Chemodenitrification (Luther et al. 1997; 1998)

$$15MnO + 6H\mathbf{NO_3^-} \rightarrow 15MnO_2 + 3\mathbf{N_2} + 3H_2O$$

Anaerobic ammonia oxidation (Anammox) (Brandes et al. 2007)

$$\underline{NH_4^+} + 1.32\underline{NO_2^-} + 0.066HCO_3^- + 0.13H^+ \rightarrow 0.26\mathbf{NO_3^-} + 1.02\mathbf{N_2} + 0.066CH_2O_{0.5}N_{0.15} + 2.03H_2O$$

Oxygen-limited autotrophic nitrification-denitrification (OLAND) (Brandes et al. 2007)

$$2\underline{NH_4^+} + 1.5O_2 \rightarrow \mathbf{N_2} + 3H_2O + 2H^+$$

Chemooxidation (Luther et al. 1997; 1998)

$$15MnO_2 + 10\underline{NH_3} \rightarrow 15MnO + 5\mathbf{N_2} + 15H_2O$$

grains from carbonate reef sediments to elucidate their microbial demography. Techniques of in-situ microbial observation from other fields of study, such as bio-reactor technology (e.g., Neef et al. 1996), may be combined with the use of conventional microscopy techniques (e.g., Reid et al. 2000; Wild et al. 2006) and increasingly reliable microelectrodes (e.g., Schulz and de Beer 2002) to investigate micro- and sub-microniches on grain surfaces and their metabolic and biogeochemical capabilities.

Apart from NO_3^- and suboxic conditions, canonical denitrification also requires the presence of N-rich organic matter which fuels it. The availability of sedimentary organic matter in Kilo Nalu sand could not be ascertained, because of analytical issues surrounding the measurement of organic carbon in carbonate grains (e.g., Ingalls et al. 2004). High-magnesium calcite interferes with thermogravimetry, which gave TOC weight fractions in Kilo Nalu sand field sediments of 3.50 % ± 0.15 %. However, the magnitude of the TOC fraction, as well as the characteristic smell routinely accompanying the drying of sediment samples from this location, hint at a high organic matter content of carbonate sediments. The N weight fraction of the sediment plug samples at t_0 was 0.030 %, which is approximately 6 times greater than that reported for silicate sediments of the SAB (Marinelli et al. 1998), and supports the hypothesis that carbonate reef sediments are richer in organic material than silicate relict sediments of the continental shelf. Based on the stoichiometry of canonical denitrification (Table 4.14), and the amount of missing N from treatments D4a, D4b, and L4 (Table 4.12), the amount of organic material needed to account for the missing NO_3^-, assuming it was all lost during canonical denitrification, can be estimated with the following equation:

$$4x + 3y = 5\left(V_{OW} \times \frac{[NO_3^-]_{t0}}{1000} \times \frac{^{15}N_{missing}}{100} \right) \quad 4.26$$

where x is μmol of organic C (TOC), y is μmol of organic N (N_{org}), V_{OW} (L) is the volume of overlying water, $[NO_3^-]_{t0}$ (μmol·L^{-1}) is the concentration of nitrate in the overlying water at t_0, and $^{15}N_{missing}$ (%) is the fraction of the ^{15}N added as NO_3^- at t_0 and missing at the end of the experiment (t_f). Maximum possible values for x and y can be estimated by setting y and x at 0 respectively, and the corresponding weights converted to C and N weight fraction (%) in the sediment, by dividing by the sedimentary weight of the plugs in each treatment. The results are shown in Table 4.15, and illustrate the minute amounts of TOC and N_{org} needed to drive the measured loss of N by canonical

Table 4.15 Maximum amounts of organic C (TOC) and organic N (N_{org}) needed to drive the loss of the N missing at the end point, t_f, of plug incubations D4a, D4b, and L4, by canonical denitrification. Maximum amounts were converted to weight fractions (%) of the total sediment weight of the plugs in each treatment. See text for more details on the performed calculations.

	N missing	Max. amount (μmol)		Weight fraction (%)	
Treatment	at t_f (μmol)	x (TOC)	y (N_{org})	TOC	N_{org}
D4a	0.0025	0.0031	0.0042	1.2×10^{-9}	1.3×10^{-9}
D4b	0.0030	0.0037	0.0050	1.3×10^{-9}	1.5×10^{-9}
L4	0.0058	0.0072	0.0096	3.9×10^{-9}	4.5×10^{-9}

denitrification, suggesting that canonical denitrification during the sedimentary plug incubations is more likely to be controlled by NO_3^- supply or by unsuitable O_2 concentrations than by organic matter availability.

The evidence for N-dynamics in the incubations under light-dark oscillations (L4 and L5) is quite intriguing and deserves further scrutiny, in view of the following observations:

a) Nutrient uptake rates are higher under light-dark oscillation conditions than under constant dark conditions (Table 4.11, Figure 4.9).

b) Fractionation effects under light-dark oscillation conditions were typical of NO_3^- assimilation, in contrast to effects of incubations in the dark which suggest a mix of benthic denitrification and NO_3^- assimilation (Figure 4.10).

c) N-mass-balance calculations indicate that not only a significant fraction of the removed NO_3^- is probably lost from the incubator, but that this fraction is actually even greater than that for the light-dark incubations (Table 4.12-Table 4.13).

A possible explanation for the combined observations listed above is that the periodic light availability stimulated microbenthic photosynthetic activity by microbenthic photosynthesizers, such as diatoms, chlorophytes and cyanobacteria (observed repeatedly in sedimentary suspensions under an epifluorescent microscope; section *4.3.1.1*). Photosynthetic activity could not only drive high rates of NO_3^- assimilation, but could also provide a localized source of O_2 within grain surface biofilms. A point source of O_2 may enlarge the portion of grain biofilms occupied by oxic-anoxic interfaces, which are the niche for nitrification-denitrification (Zehr and Ward 2002; Rao 2006), and may consequently accelerate N loss from the system by providing the intermediate species

which participate in the reactions in Table 4.14. In other words, it is proposed that in the presence of light-dark oscillations, which are the norm for surface sediments in shelf and reef environments (e.g., Jahnke 2001), nitrogen recycling may be accelerated, may become spatially complex, and may result in enhanced loss of N.

4.3.3.4 Phosphorus dynamics in carbonate reef permeable sediments

The nature of P cycling in permeable sediments remains relatively unknown. Study of the transformations of P in realistic conditions, i.e., the dynamic physical transport regime which characterizes permeable sediments, is hindered due to the redox variations caused by changes in the availability of O_2. Oxygen presence dictates the form, and consequently the phase, of other elements such as Fe which may interact with P, depending on the redox state (e.g., Slomp et al. 1996; Ruttenberg 2003).

In the case of the plug incubation experiments conducted during this study, ratios of uptake rates of NO_3^- and PO_4^{3-} fluctuated between Redfield levels of 16 up to 20, and are within the range generally proposed for the relatively plastic stoichiometric demands of both microbial heterotrophs and autotrophs (e.g., Sterner and Elser 2002, p. 206; White et al. 2007). As in the case of NO_3^-, uptake rates of PO_4^{3-} differed with experimental light conditions (Table 4.11, Figure 4.9). If, indeed, the reason for the difference in uptake rate ratios between the two light conditions is the occurrence of photosynthesis, there are two aspects of the microbiology of these sediments that deserve further study. The first aspect is the examination of autotrophic and heterotrophic functions of the microbial communities, and specifically their nutritional and metabolic demands, e.g., as manifested by elemental stoichiometry (Sterner and Elser 2002, p. 206).

It should be noted that the photosynthesizers observed in sediments incubated in the microcosm (Figure 4.4) persisted for long time periods of days-to-weeks in the absence of light, presumably in a heterotrophic mode as has been observed in past studies (White 1974). Therefore, chlorophyll-containing cells should be treated as facultative autotrophs in nutritional assays. The second aspect of carbonate reef sediment microbiology that warrants more attention is possible changes in redox conditions in biofilms on grain surfaces and microstructures, as they are induced by the production of O_2. Redox states are significant, since they are likely to determine whether PO_4^{3-} remains bound to Fe-oxyhydroxides or whether it is allowed to freely diffuse away from binding sites.

The case of carbonate reef permeable sediments presents an additional complication in the study of P dynamics, in the form of abundant $CaCO_3$, which may cause a significant fraction of P to be bound to Ca (Ogrinc and Faganeli 2006). Constraining the rate and contribution of this process to total PO_4^{3-} removal from solution onto the sediment surface has been a particularly difficult task, due to the high microbial abundances which characterize biogenic carbonate sediments (Table 4.1; Wild et al. 2006; Sørensen et al. 2007). Disabling microbial uptake to study PO_4^{3-} removal has been attempted with the addition of poisons, such as $HgCl_2$ (Rasheed et al. 2005), and with autoclaving (this study, section *4.2.2.2*; Rusch et al., in preparation), while desiccation of the sediment at low heat (80-100 °C) followed by re-hydration was also considered. All of the methods mentioned are problematic in that they cause effects beyond the desired disruption of microbial activity. The addition of poisons can cause the release of organic material from poisoned cells (e.g., Liu et al. 2006). Autoclaving causes cell lysis and the subsequent release of large amounts of nutrients which supersaturate the sediment

surfaces and are released slowly into solution (A. Rusch, personal communication; personal observations), while desiccation may have a similar effect and may also disrupt biofilms and sedimentary fabric at large. It is possible that active microbial uptake of PO_4^{3-} and passive adsorption onto organic and inorganic matrices cannot be separated (as suggested by the results of the uptake experiments by Rasheed et al. 2005), since the sedimentary framework which includes biofilms is an outcome of the biotic activities of the particular habitat, thus permitting the treatment of net PO_4^{3-} uptake as an integral phenomenon of a specific carbonate reef permeable sediment habitat at a particular time.

4.4 Conclusions

The experiments described in Chapter 4 demonstrate that reef-associated, carbonate permeable sediments are the site of rapid organic matter processing and nutrient cycling. Sediments from the Kilo Nalu Observatory site at the south shore of O'ahu, incubated in a specially constructed microcosm under enhanced transport conditions, rapidly sequestered a culture of algal cells and dissolved nutrients which was added to the overlying water and did not return any remineralized nutrients back to the water column. Nutrient enrichment experiments, conducted with plugs of surface sediment from the same site demonstrated high uptake rates and strong retention of nitrogen. A significant portion of the removed nitrogen could not be accounted for at the end of the incubations, and isotope fractionation data suggest that it was lost due to benthic denitrification. The experimental design indicates that the potential for denitrification is very high in surface sediments, which host both heterotrophic and autotrophic microbial communities. Differences in uptake rates and N uptake processes

with different light treatments suggest that microbenthic photosynthetic activity has an impact on the biogeochemical functioning of carbonate reef permeable sediments. The observed lack of nutrient fluxes to the overlying water following algal particle sequestration and degradation, along with the demonstrated strong retention of nutrients in thin surface sediment plugs, suggest that carbonate reef permeable sediments are the site of very fast particulate organic matter trapping and decomposition, of nutrient remineralization, and of retention of the regenerated nutrients which may support benthic instead of planktonic productivity.

4.5 References

Aller, R. C. and J. E. Mackin (1989) Open-incubation, diffusion methods for measuring solute reaction rates in sediments. Journal of Marine Research, 47: 411-440.

Aspila, K. I., H. Agemian and A. S. Y. Chau (1976) A semi-automated method for the determination of inorganic, organic and total phosphate in sediments. Analyst, 101: 187-197.

Atkinson, M. J., B. Carlson and G. L. Crow (1995) Coral growth in high-nutrient, low-pH seawater: A case study of corals cultured at the Waikiki Aquarium, Honolulu, Hawai'i. Coral Reefs, 14: 215-223.

Bacon, M. P., R. A. Belastock and M. H. Bothner (1994) ^{210}Pb balance and implications for particle transport on the continental shelf, U.S. Middle Atlantic Bight. Deep-Sea Research II, 41: 511-535.

Beard, D. C. and P. K. Weyl (1973) Influence of texture on porosity and permeability of unconsolidated sand. American Association of Petroleum Geologists Bulletin, 52: 349-369.

Bender, M. L. (1990) The $\delta^{18}O$ of dissolved O_2 in seawater: a unique tracer of circulation and respiration in the deep sea. Journal of Geophysical Research - Oceans, 95: 22243-22252.

Berner, R. A. (1980) Early diagenesis. Princeton University Press, Princeton, New Jersey, U.S.A., pp. 241.

Boudreau, B. P. (1997) Diagenetic models and their implementation. Springer, Berlin, Germany, pp. 414.

Boudreau, B. P., M. Huettel, S. Forster, R. A. Jahnke, A. McLachlan, J. J. Middelburg, P. Nielsen, F. J. Sansone, G. L. Taghon, W. Van Raaphorst, I. T. Webster, J. M. Weslawski, P. Wiberg and B. Sundby (2001) Permeable marine sediments: overturning an old paradigm. Eos, Transactions of the American Geophysical Union, 82: 133, 135-136.

Brandes, J. A. and A. H. Devol (1997) Isotopic fractionation of oxygen and nitrogen in coastal marine sediments. Geochimica et Cosmochimica Acta, 61: 1793-1801.

Brandes, J. A., A. H. Devol and C. Deutsch (2007) New developments in the marine nitrogen cycle. Chemical Reviews, 107: 577-589.

Burdige, D. J. (2006) Geochemistry of marine sediments. Princeton University Press, Princeton, New Jersey, U.S.A., pp. 609.

Burmister, D. M. (1955) Principles of permeability testing of soils, p. 3-20. *In* Barber, E. S. [ed.], Symposium on permeability of soils. ASTM Special Technical Publication No. 163. American Society for Testing Materials, Philadelphia, Pennsylvania, U.S.A.

Capone, D. G., S. E. Dunham, S. G. Horrigan and L. E. Duguay (1992) Microbial nitrogen transformations in unconsolidated coral reef sediments. Marine Ecology Progress Series, 80: 75-88.

Casciotti, K. L., D. M. Sigman, M. G. Hastings, J. K. Böhlke and A. Hilkert (2002) Measurement of the oxygen isotopic composition of nitrate in seawater and freshwater using the denitrifier method. Analytical Chemistry, 74.

Cassar, N., E. A. Laws, B. N. Popp and R. R. Bidigare (2002) Sources of inorganic carbon for photosynthesis in a strain of *Phaeodactylum tricornutum*. Limnology and Oceanography, 47: 1192-1197.

Dollar, S. J. (1986) Response of benthic ecosystems to deep ocean sewage outfalls in Hawai'i: nutrient fluxes at the sediment-water interface. Ph. D. Dissertation, University of Hawai'i, pp. 217.

Dore, J. E., B. N. Popp, D. M. Karl and F. J. Sansone (1998) A large source of atmospheric nitrous oxide from subtropical North Pacific surface waters. Nature, 395: 63-66.

Emery, K. O. (1968) Relict sediments on continental shelves of the world. American Association of Petroleum Geologists Bulletin, 52: 445-464.

Eppley, R. W., J. N. Rogers and J. J. McCarthy (1969) Half-saturation constants for uptake of nitrate and ammonium by marine phytoplankton. Limnology and Oceanography, 14: 912-920.

Falter, J. L. and F. J. Sansone (2000) Hydraulic control of pore water geochemistry within the oxic-suboxic zone of a permeable sediment. Limnology and Oceanography, 45: 550-557.

Fogel, M. and L. A. Cifuentes (1993) Isotope fractionation during primary production, p. 73-98. *In* Engel, M. H. and S. A. Macko [eds.], Organic Geochemistry. Plenum Press, New York, New York, U.S.A.

Froelich, P. N. (1980) Analysis of organic carbon in marine sediments. Limnology and Oceanography, 25: 564-572.

Guillard, R. R. L. and J. H. Ryther (1962) Studies of marine planktonic diatoms. I. *Cyclotella nana* Hustedt and *Detonula confervacea* Cleve. Canadian Journal of Microbiology, 8: 229-239.

Hannides, A. K., S. M. Dunn and R. C. Aller (2005) Diffusion of organic and inorganic solutes through macrofaunal mucus secretions and tube linings in marine sediments. Journal of Marine Research, 63: 957-981.

Hebert, A. B., F. J. Sansone and G. R. Pawlak (2007) Tracer dispersal in sandy sediment porewater under enhanced physical forcing. Continental Shelf Research, 27: 2278-2287.

Hoover, D. J. (2002) Fluvial nitrogen and phosphorus in Hawai'i: Storm runoff, land use, and impacts on coastal waters. Ph. D. Dissertation, University of Hawai'i, pp. 437.

Hopkinson, C. S. J. (1987) Nutrient regeneration in shallow-water sediments of the estuarine plume region of the nearshore Georgia Bight, USA. Marine Biology, 94: 127-142.

Huettel, M., W. Ziebis, S. Forster and G. W. Luther III (1998) Advective transport affecting metal and nutrient distributions and interfacial fluxes in permeable sediments. Geochimica et Cosmochimica Acta, 62: 613-631.

Huettel, M. and A. Rusch (2000) Transport and degradation of phytoplankton in permeable sediment. Limnology and Oceanography, 45: 534-549.

Huettel, M. and I. T. Webster (2001) Porewater flow in permeable sediments, p. 144-179. *In* Boudreau, B. P. and B. B. Jørgensen [eds.], The Benthic Boundary Layer. Oxford University Press, New York, New York, U.S.A.

Ingalls, A. E., R. C. Aller, C. Lee and S. G. Wakeham (2004) Organic matter diagenesis in shallow water carbonate sediments. Geochimica et Cosmochimica Acta, 68: 4363-4379.

Jahnke, R. A. (1985) A model of microenvironments in deep-sea sediments: formation and effects on porewater profiles. Limnology and Oceanography, 30: 956-965.

Jahnke, R. A. and M. B. Christiansen (1989) A free-vehicle benthic chamber instrument for sea floor studies. Deep-Sea Research, 36: 625-637.

Jahnke, R. A., J. R. Nelson, R. L. Marinelli and J. E. Eckman (2000) Benthic flux of biogenic elements on the Southeastern US continental shelf: influence of pore water advective transport and benthic microalgae. Continental Shelf Research, 20: 109-127.

Jahnke, R. A. (2001) Constraining organic matter cycling with benthic fluxes, p. 302-319. *In* Boudreau, B. P. and B. B. Jørgensen [eds.], The Benthic Boundary Layer. Oxford University Press, New York, New York, U.S.A.

Janssen, F., P. Faerber, M. Huettel, V. Meyer and U. Witte (2005a) Pore-water advection and solute fluxes in permeable marine sediments (I): Calibration and performance of the novel benthic chamber system *Sandy*. Limnology and Oceanography, 50: 768-778.

Janssen, F., M. Huettel and U. Witte (2005b) Pore-water advection and solute fluxes in permeable marine sediments (II): Benthic respiration at three sandy sites with different permeabilities (German Bight, North Sea). Limnology and Oceanography, 50: 779-792.

Jenkins, C. J., A. J. Kettner, C. Moore and G. Sharman (2003) goSEABED World Seabed Data Browser. University of Colorado Institute of Arctic and Alpine Research, Boulder, Colorado, U.S.A.

Jørgensen, B. B. (1983) Processes at the sediment-water interface, p. 477-509. *In* Bolin, B. and R. B. Cook [eds.], The major biogeochemical cycles and their interactions. John Wiley and Sons, Chichester, U. K.

Kendall, C. (1998) Tracing nitrogen sources and cycling in catchments, p. 519-576. *In* Kendall, C. and J. J. McDonnell [eds.], Isotope tracers in catchment hydrology. Elsevier Science, Amsterdam, Netherlands.

King, P., H. Kennedy, P. P. Newton, T. D. Jickells, T. Brand, S. Calvert, G. Cauwet, H. Etcheber, B. Head, A. Khripounoff, B. Manighetti and J. C. Miquel (1998) Analysis of total and organic carbon and total nitrogen in settling oceanic particles and a marine sediment: an interlaboratory comparison. Marine Chemistry, 60: 203-216.

Klute, A. and C. Dirksen (1986) Hydraulic conductivity and diffusivity: laboratory methods, p. 687-734. *In* Klute, A. [ed.], Methods of soil analysis, Part 1: Physical and mineralogical methods. American Society of Agronomy - Soil Science Society of America, Madison, Wisconsin, U.S.A.

Koroleff, F. (1976) Determination of phosphate, p. 117-122. *In* Grasshoff, K. [ed.], Methods of seawater analysis. Verlag-Chemie, Weinheim, Germany.

Kristensen, E. (1990) Characterization of biogenic organic matter by stepwise thermogravimetry (STG). Biogeochemistry, 9: 135-159.

Lalli, C. M. and T. R. Parsons (1997) Biological oceanography: an introduction. Butterworth-Heinemann, Oxford, U.K., pp. 314.

Laursen, A. E. and S. P. Seitzinger (2002) The role of denitrification in nitrogen removal and carbon mineralization in Mid-Atlantic Bight sediments. Continental Shelf Research, 22: 1397-1416.

Lehmann, M. F., D. M. Sigman and W. M. Berelson (2004) Coupling the $^{15}N/^{14}N$ and $^{18}O/^{16}O$ of nitrate as a constraint on benthic nitrogen cycling. Marine Chemistry, 88: 1-20.

Lehmann, M. F., D. M. Sigman, D. C. McCorkle, B. G. Brunelle, S. Hoffman, M. Kienast, G. Cane and J. Clement (2005) Origin of the deep Bering Sea nitrate

deficit: Constraints from the nitrogen and oxygen isotopic composition of water column nitrate and benthic nitrate fluxes. Global Biogeochemical Cycles, 19: GB4005, doi: 10.1029/2005GB002508.

Liu, Z., C. Lee and S. G. Wakeham (2006) Effects of mercuric chloride and protease inhibitors on degradation of particulate organic matter from the diatom *Thalassiosira pseudonana*. Organic Geochemistry, 37: 1003-1018.

Lohse, L., H. T. Kloosterhuis, W. Van Raaphorst and W. Helder (1996) Denitrification rates as measured by the isotope pairing method and by the acetylene inhibition technique in continental shelf sediments of the North Sea. Marine Ecology Progress Series, 132: 169-179.

Lowry, R. (2007) VassarStats, faculty.vassar.edu/lowry/VassarStats.html. Vassar College, Poughkeepsie, New York, USA.

Luther, G. W., B. Sundby, B. L. Lewis, P. J. Brendel and N. Silverberg (1997) Interactions of manganese with the nitrogen cycle: Alternative pathways to dinitrogen. Geochimica et Cosmochimica Acta, 61: 4043-4052.

Luther, G. W., P. J. Brendel, B. L. Lewis, B. Sundby, L. Lefrancois, N. Silverberg and D. B. Nuzzio (1998) Simultaneous measurement of O_2, Mn, Fe, I-, and S(-II) in marine pore waters with a solid-state voltammetric microelectrode. Limnology and Oceanography, 43: 325-333.

Marinelli, R. L., R. A. Jahnke, D. B. Craven, J. R. Nelson and J. E. Eckman (1998) Sediment nutrient dynamics on the South Atlantic Bight continental shelf. Limnology and Oceanography, 43: 1305-1320.

McManus, J. (1988) Grain size determination and interpretation, p. 63-85. *In* Tucker, M. [ed.], Techniques in sedimentology. Blackwell Scientific Publications, Oxford, U.K.

Miyajima, T., M. Suzumura, Y. Umezawa and I. Koike (2001) Microbiological nitrogen transformation in carbonate sediments of a coral-reef lagoon and associated seagrass beds. Marine Ecology Progress Series, 217: 273-286.

Monger, B. C. and M. R. Landry (1993) Flow cytometric analysis of marine bacteria with Hoechst 33342. Applied and Environmental Microbiology, 59: 905-911.

Neef, A., A. Zaglauer, H. Meier, R. Amann, H. Lemmer and K.-H. Schleifer (1996) Population analysis in a denitrifying sand filter: conventional and in situ

identification of *Paracoccus* spp. in methanol-fed biofilms. Applied and Environmental Microbiology, 62: 4329-4339.

Nelson, J. R., J. E. Eckman, C. Y. Robertson, R. L. Marinelli and R. A. Jahnke (1999) Benthic microalgal biomass and irradiance at the sea floor on the continental shelf of the South Atlantic Bight: Spatial and temporal variability and storm effects. Continental Shelf Research, 19: 477-505.

Nixon, S. W., J. R. Kelly, B. N. Furnas, C. A. Oviatt and S. S. Hale (1980) Phosphorus regeneration and the metabolism of coastal marine bottom communities, p. 219-242. *In* Tenore, K. R. and B. C. Coull [eds.], Marine benthic dynamics. University of South Carolina Press, Georgetown, South Carolina, U.S.A.

Ogrinc, N. and J. Faganeli (2006) Phosphorus regeneration and burial in near-shore marine sediments (the Gulf of Trieste, northern Adriatic Sea). Estuarine, Coastal and Shelf Science, 67: 579-588.

Precht, E. and M. Huettel (2003) Advective pore-water exchange driven by surface gravity waves and its ecological implications. Limnology and Oceanography, 48: 1674–1684.

Precht, E., U. Franke, L. Polerecky and M. Huettel (2004) Oxygen dynamics in permeable sediments with wave-driven pore water exchange. Limnology and Oceanography, 49: 693–705.

Rao, A. M. F. (2006) Carbon and nitrogen cycling in permeable continental shelf sediments and porewater solute exchange across the sediment-water interface. Ph.D. Dissertation, Georgia Institute of Technology, pp. 228.

Rao, A. M. F., M. J. McCarthy, W. S. Gardner and R. A. Jahnke (2007) Respiration and denitrification in permeable continental shelf deposits on the South Atlantic Bight: Rates of carbon and nitrogen cycling from sediment column experiments. Continental Shelf Research, 27: 1801-1819.

Rasheed, M. Y. M., S. A. Al-Rousan and M. I. Badran (2005) Phosphate enrichment in the northern Gulf of Aqaba: regulation by carbonate sediments and impact on nitrogen elevation. Chemistry and Ecology, 21: 199-208.

Reid, R. P., P. T. Visscher, A. W. Decho, J. F. Stolz, B. M. Beboutk, C. Dupraz, I. G. Macintyre, H. W. Paerl, J. L. Pinckney, L. Prufert-Beboutk, T. F. Steppe and D. J. DesMarais (2000) The role ofmicrobes in accretion, lamination and early lithifcation of modern marine stromatolites. Nature, 406: 989-992.

Reimers, C., C. Friedrichs, B. Bebout, P. Howd, M. Huettel, R. Jahnke, P. MacCready, K. Ruttenberg, L. Sanford and J. Trowbridge (2004a) Coastal Benthic Exchange Dynamics. Report TR-04-01, Skidaway Institute of Oceanography, pp. 92.

Reimers, C. E., H. A. Stecher III, G. L. Taghon, C. M. Fuller, M. Huettel, A. Rusch, N. Ryckelynck and C. Wild (2004b) In situ measurements of advective solute transport in permeable shelf sands. Continental Shelf Research, 24: 183-201.

Riedl, R. J., N. Huang and R. Machan (1972) The subtidal pump: a mechanism of interstitial water exchange by wave action. Marine Biology, 13: 210-221.

Rocha, C., S. Forster, E. Koning and E. Epping (2005) High-resolution permeability determination and two-dimensional porewater flow in sandy sediments. Limnology and Oceanography Methods, 3: 10-23.

Rowe, G. T., C. H. Clifford, K. L. J. Smith and P. L. Hamilton (1975) Benthic nutrient regeneration and its coupling to primary productivity in coastal waters. Nature, 255: 215-217.

Rowe, G. T., C. H. Clifford and K. L. J. Smith (1977) Nutrient regeneration in sediments off Cap Blanc, Spanish Sahara. Deep- Sea Research, 25: 57-63.

Rusch, A., M. Huettel and S. Forster (2000) Particulate organic matter in permeable marine sands - dynamics in time and depth. Estuarine, Coastal and Shelf Science, 51: 399-414.

Rusch, A. and M. Huettel (2000) Advective particle transport into permeable sediments - evidence from experiments in an intertidal sandflat. Limnology and Oceanography, 45: 525-533.

Rusch, A., S. Forster and M. Huettel (2001) Bacteria, diatoms and detritus in an intertidal sandflat subject to advective transport across the water-sediment interface. Biogeochemistry, 55: 1-27.

Rusch, A., M. Huettel, C. Wild and C. E. Reimers (2006) Benthic oxygen consumption and organic matter turnover in organic-poor, permeable shelf sands. Aquatic Geochemistry, 12: 1-19.

Ruttenberg, K. C. (1992) Development of a sequential extraction method for different forms of phosphorous in marine sediments. Limnology and Oceanography, 37: 1460-1482.

Ruttenberg, K. C. (2001) Phosphorus cycle, p. 2149-2162. *In* Steele, J. H., K. K. Turekian and S. A. Thorpe [eds.], Encyclopedia of Ocean Sciences, Vol. 4. Academic Press, London, U.K.

Ruttenberg, K. C. (2003) The global phosphorus cycle, p. 585-643. *In* Schlesinger, W. C. [ed.], Treatise on Geochemistry, Vol. 8. Elsevier, Amsterdam, Netherlands.

Ryther, J. H. (1969) Photosynthesis and fish production in the sea. Science, 166: 72-76.

Schulz, H. and D. de Beer (2002) Uptake rates of oxygen and sulfide measured with individual *Thiomargarita namibiensis* cells by using microelectrodes. Applied and Environmental Microbiology, 68: 5746-5749.

Shum, K. T. (1992) Wave-induced advective transport below a rippled water-sediment interface. Journal of Geophysical Research, 97: 789-808.

Sigman, D. M. and K. L. Casciotti (2001) Nitrogen isotopes in the ocean, p. 1884-1894. *In* Steele, J. H., K. K. Turekian and S. A. Thorpe [eds.], Encyclopedia of Ocean Sciences. Academic Press, London, U.K.

Sigman, D. M., K. L. Casciotti, M. Andreani, C. Barford, M. Galanter and J. K. Böhlke (2001) A bacterial method for the nitrogen isotopic analysis of nitrate in seawater and freshwater. Analytical Chemistry, 73: 4145-4153.

Slomp, C. P., E. H. G. Epping, W. Helder and W. Van Raaphorst (1996) A key role for iron-bound phosphorus in authigenic apatite formation in North Atlantic continental platform sediments. Journal of Marine Research, 54: 1179-1205.

Sørensen, K. B., B. Glazer, A. Hannides and E. Gaidos (2007) Spatial structure of the microbial community in sandy carbonate sediment. Marine Ecology Progress Series: in press.

Sterner, R. W. and J. J. Elser (2002) Ecological Stoichiometry. Princeton University Press, Princeton, New Jersey, U.S.A., pp. 439.

Swanson, M., J. Sevadjian, F. Sansone, G. Pawlak, A. Hebert, M. McManus, E. de Carlo, T. Stanton, J. Shacat, K. Millikan, B. McLaughlin, J. Wells, A. Hanson and R. H. Byrne (2006) The Kilo Nalu cabled observatory, Oahu, Hawaii: A flexible platform for integrated physical and biogeochemical adaptive sampling and experimentation. Eos, Transactions of the American Geophysical Union, December 8th-12th, 2003, 87(52), Fall Meeting Supplement, Abstract OS31C-1657.

Taguchi, S. and E. A. Laws (1987) Patterns and causes of temporal variability in the physiological condition of the phytoplankton community in Kaneohe Bay, Hawaii. Journal of Plankton Research, 9: 1143-1157.

Van Cappellen, P. and Y. Wang (1995) Metal cycling in surface sediments: modeling the interplay of transport and reaction, p. 21-64. *In* Allen, H. M. [ed.], Metal contaminated aquatic sediments. Ann Arbor Press, Chelsea, Michigan, U.S.A.

Vance-Harris, C. and E. Ingall (2005) Denitrification pathways and rates in the sandy sediments of the Georgia continental shelf, USA. Geochemical Transactions, 6: 12-18.

Verity, P. G., C. Y. Robertson, C. R. Tronzo, M. G. Andrews, J. R. Nelson and M. E. Sieracki (1992) Relationships between cell volume and the carbon and nitrogen content of marine photosynthetic nanoplankton. Limnology and Oceanography, 37: 1434-1446.

Veuger, B., B. D. Eyre, D. Maher and J. J. Middelburg (2007) Nitrogen incorporation and retention by bacteria, algae, and fauna in a subtropical intertidal sediment: an in situ ^{15}N-labeling study. Limnology and Oceanography, 52: 1930-1942.

Webb, J. E. and J. Theodor (1968) Irrigation of marine submerged sands through wave action. Nature, 220: 682-683.

Webb, J. E. and J. L. Theodor (1972) Wave-induced circulation in submerged sands. Journal of the Marine Biological Association of the United Kingdom, 52: 903-914.

Webster, I. T. and J. H. Taylor (1992) Rotational dispersion in porous media due to fluctuating flows. Water Resources Research, 28: 109-119.

Weise, W. and G. Rheinheimer (1977) Scanning electron microscopy and epifluorescence investigation of bacterial colonization of marine sand sediments. Microbial Ecology, 4: 175-188.

White, A. W. (1974) Growth of the two facultatively heterotrophic marine centric diatoms. Journal of Phycology, 10: 292–300.

White, A. W., F. G. Prahl, R. Letelier and B. N. Popp (2007) Summer surface waters in the Gulf of California: prime habitat for biological N_2 fixation. Global Biogeochemical Cycles, 21: GB2017, doi:10.1029/2006GB002779.

Wild, C., C. Laforsch and M. Huettel (2006) Detection and enumeration of microbial cells within highly porous calcareous reef sands. Marine and Freshwater Research, 57: 415-420.

Zehr, J. P. and B. B. Ward (2002) Nitrogen cycling in the ocean: new perspectives on processes and paradigms. Applied and Environmental Microbiology, 68: 1015-1024.

Ziebis, W., M. Huettel and S. Forster (1996) Impact of biogenic sediment topography on oxygen fluxes in permeable seabeds. Marine Ecology Progress Series, 140: 227-237.

Chapter 5 – Introduction to large organic falls on the deep sea floor: their quality, processing, and impact on sediment biogeochemistry

5.1 Large organic particles: diverse fuel for the deep sea floor

The deep sea floor relies for the most part on the supply of photosynthetically-derived organic material from the euphotic zone (Figure 5.1). This supply is the result of gravitational settling of particulate organic matter (POM) (Alldredge and Silver 1988; Wakeham and Lee 1993; Alldredge 2000; Volkman and Tanoue 2002). It is often assumed that, while settling, the labile (more nutritional and enzymatically degradable) component of POM is consumed, leaving behind the refractory (degradation-resistant) component to reach the deep sea floor biota (e.g., Wirsen and Jannasch 1976; Wakeham and Lee 1993). This assumption is supported by studies that show alteration of the biochemical composition of sinking particles with depth (e.g., Lee et al. 2004). As a result, deep sea floor faunal communities were thought to rely, in part, on the conversion of this refractory material into microbial biomass, a more labile food source (Rowe and Deming 1985; Gage and Tyler 1991). Recent work with sediment trap time-series has established that deep sea benthic fauna may also benefit directly from episodic pulses of phytodetritus that could account for a substantial fraction of the annual material flux to the sea floor (Billett et al. 1983; Miller et al. 2000; Lampitt et al. 2001; Smith et al. 2002b).

The conceptual model of POM supply to the sea floor described above (Figure 5.1a) has, to a certain extent, diverted attention away from larger organic particles descending through the water column, and its impact on sedimentary biogeochemistry.

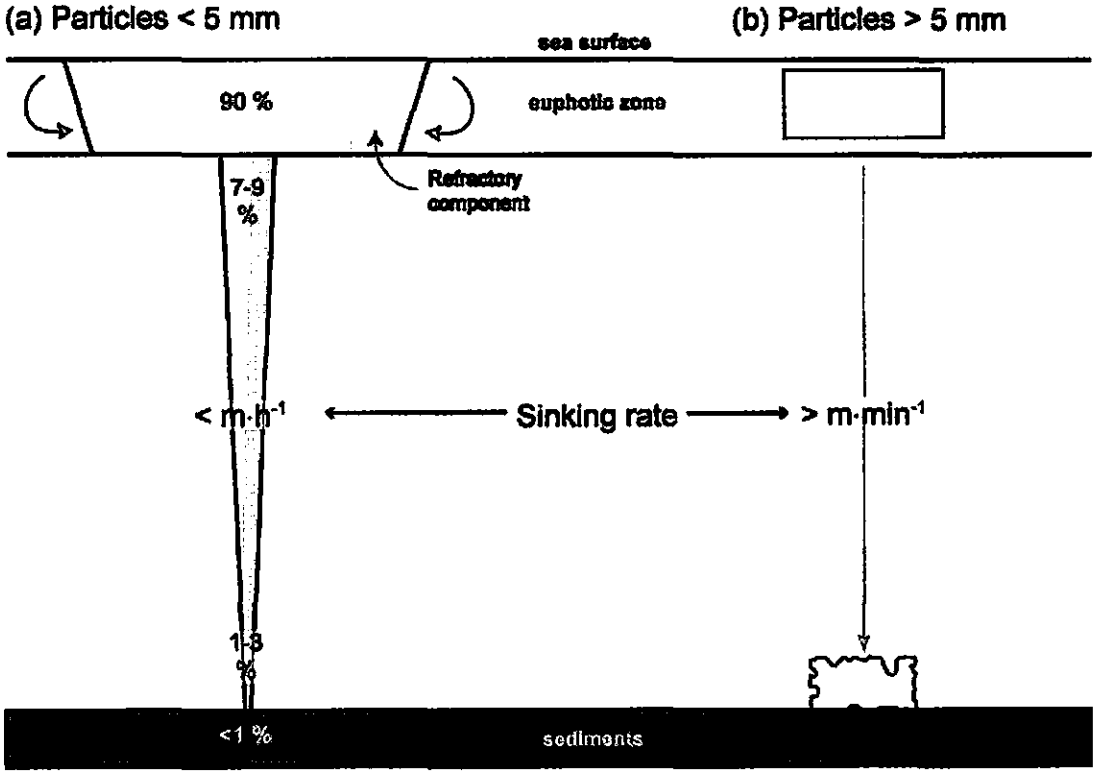

Figure 5.1 Schematic illustrating the trajectory from euphotic waters to the seafloor of two particle size classes: (a) small particles (< 5 mm) dominate the flux of POM from the euphotic zone to the sea floor world-wide (e.g., Alldredge and Silver 1988). Their slow sinking rates (< $m \cdot h^{-1}$) allow the alteration of their POM composition by preferential removal of labile over refractory material (e.g., Lee et al. 2004); (b) large particles (> 5mm, but typically bigger) occur in lower abundances (Sheldon et al. 1972), but bypass the POM composition alteration phase due to their rapid sinking rates (> $m \cdot min^{-1}$).

This is partly justified. While particles in the ocean exist in a continuum of sizes, from "colloids to whales" (Sieburth et al. 1978; Wakeham and Lee 1993), the number of particles varies inversely with size (Sheldon et al. 1972). Thus, researchers have assumed that the flux of sub-centimeter-sized particles (approximately 50 μm-5 mm) dominates bulk POM flux. Generally speaking, this appears to be valid for the deep sea (e.g., Romankevich 1978, p. 96-99; Alldredge and Silver 1988; Wakeham and Lee 1993; Smith and Demopoulos 2003; Lee et al. 2004). Despite the broad validity of this generalization, the flux of large organic particles to the deep sea floor cannot be ignored for numerous reasons.

Firstly, studies in the North Pacific have found that the organic matter flux due to large particles may be needed to balance benthic community respiration (Smith 1987; 1992; Smith et al. 1992a; Smith and Kaufmann 1999; Smith et al. 2002b). Organic fluxes measured by sediment traps underestimate benthic community demand for carbon by a substantial degree (e.g., Smith et al. 1992a), suggesting that much of the carbon flux to the sea floor was missed by sediment trap collections (Table 5.1 lists several examples of particles that could contribute to this discrepancy). More specifically, the hypothesis that animal carcasses could supply some of the missing carbon is supported by the common occurrence of highly mobile bentho-pelagic scavengers in most deep sea floor habitats (e.g., Dayton and Hessler 1972; Isaacs and Schwartzlose 1975; Smith 1985; Smith et al. 1992b; Priede and Merrett 1996; 1998).

A second reason why large organic particle flux cannot be ignored is the increased likelihood of delivering highly labile organic material to the sea floor. Larger particles have higher sinking rate, shorter water column transit times, and consequently

Table 5.1 Examples of large, passively-sinking organic particles whose flux cannot be detected by sediment trap techniques.

Carbon source	Selected references
Fish	Dayton and Hessler (1972), Jannasch (1978), Smith (1983; 1985; 1986)
Marine mammals (e.g., cetaceans)	Smith et al. (1989; 1998; 2002a), Smith and Baco (2003), Kemp et al. (2006)
Invertebrates (e.g., medusae)	Billett et al. (2006)
Discarded body parts (e.g., larvacean houses)	Robison et al. (2005)
Macrophytes (e.g., seagrasses, kelp, land plants)	Wolff (1979), Smith (1983), Vetter (1994), Vetter and Dayton (1998; 1999)
Wood	Turner (1973), Wolff (1979), Distel et al. (2000)

experience less degradation in the water column. Therefore, the proportion of mass lost in transit to the seafloor will be less for a large organic particle than for a small organic particle. Moreover, a greater fraction of labile material is likely to survive the water column transit if it is contained in a larger rather than a smaller particle. Consequently, rapid sinking rates probably result in minimal or no alteration of large particle POM composition. Therefore, the short sinking time experienced by large particles creates a

shunt between euphotic waters and the sea floor, and allows the transfer of organic material with nearly the original degree of lability from more productive surface waters to the deep sea.

Finally, large particle fluxes are important because they are extremely localized. For example, several independent calculations suggested that the surface-to-sea-floor carbon flux due to dead whales is approximately 1-2 % of the flux measured by sediment traps over ocean basin scales (Jelmert and Oppen-Berntsen 1996; Smith and Baco 2003; Smith 2007). However, these whale carcasses do not deposit themselves as a veneer of organic matter (Smith 2007). Instead, they are deposited as massive parcels of organic-rich compounds (Butman et al. 1996). Recent examples of large organic particles significantly contributing to localized POM flux to the sea floor (depths of 400-2900 m) include kelp debris in Carmel Submarine Canyon (Harrold et al. 1998), and larvacean houses in Monterey Canyon (Robison et al. 2005), both off the coast of California.

Because of these reasons, the arrival of POM as large particle falls on the sea floor causes a cascade of ecological and biogeochemical changes in the benthic ecosystem that deserve further study (e.g., Butman et al. 1995; Smith et al. 1998; Smith and Baco 2003). At the time and location of their arrival, large particle falls challenge the conventional simplified picture of both POM flux to the deep sea floor and POM processing by benthic communities. In the following section, I provide an introduction to these large particle falls. I discuss: (a) definitions used over time, (b) various types of large falls that have been identified and studied, (c) their processing by benthic communities, and (d) their impact on sedimentary biogeochemistry.

5.2 Defining large organic particle falls

Because of the great variety of large organic particle falls, numerous terms have been used in describing them. A brief discussion of these definitions is warranted, to select one for use in this dissertation. Table 5.2 lists definitions that have been used in the past to collectively describe various types of large POM supplied to the sea floor. Detritus is defined as "non-living" (Odum and de la Cruz 1963), and its use to describe sinking POM is controversial, since many particles are populated by living organisms that are transported along with the sinking material through the water column (see review and discussion by Silver and Gowing 1991). The use of the term "food" implies an almost exclusive focus on the exploitation of POM by scavenging fauna. This restricts the scope of the investigation to the earlier stages of large POM processing on the sea floor, and excludes microbial processing that drives early diagenesis. The use of the word "solid" to describe POM of a certain size is curious, to say the least. A significant fraction of organic material in particles is in the form of colloids or solutes enclosed in intra- or inter-cellular space (Alldredge and Silver 1988; Alldredge 2000).

Clearly, the most appropriate term is "large organic falls" (Smith 1983). The employment of a commonly understood descriptor of size ("large") moderates the impulse to quantify what the exact size cut-off is between "large" and "small" sinking POM. This value can be constrained using the definition of a scavenger's "food" as "particles ... larger than a single 'bite'" (C.R. Smith, personal communication). Considering that almost all bentho-pelagic scavengers studied are classified as megafauna (> 3 cm in length), "large" could mean at least several centimeters long. Finally, the term "Massive organic matter" (MOM), used (but not defined) by Hannides et al. (2005;

2006), should be viewed as an attempt to formulate organic matter contained in "large falls" in terms of POM (the largest fraction), and specifically as a subset of POM. For the purposes of this dissertation, the particles will be referred to as large organic falls (LOF), whereas the organic matter contained therein will be referred to as MOM.

Table 5.2 Common definitions used to collectively describe large POM.

Definition	Large POM type	References
Food falls; detrital food	Dead nekton (crustaceans, cephalopods, fish and mammals)	Dayton and Hessler (1972); Stockton and DeLaca (1982)
Solid organic materials	Fish tissue, seaweed, wood, paper, chitin, gels	Wirsen and Jannasch (1976)
Large organic falls	Nekton, macrophytes	Smith (1983; 1986)
Massive organic matter falls	Fish and mammal carcasses, macrophytes, wood	Hannides et al. (2005; 2006)

5.3 LOF processing: metazoa versus microbes, and the role of quality

Upon LOF arrival at the sea floor, a competition ensues between metazoa and microbes, in the processing of the majority of MOM. The rate of processing is dictated by various physical (e.g., mass, surface area to volume ratio, material hardness or toughness)

or biogeochemical (e.g., elemental composition, major compounds present, their reactivity, etc.) characteristics of both LOF and MOM. All these characteristics collectively describe the quality of a fall (see Chapter 6 for more discussion).

Processing of LOF on the deep sea floor can be divided into two main stages of biotic activity. The first stage is the direct retrieval of MOM from LOF themselves. In the case of metazoa, this is achieved with ingestion of LOF material, and in the case of microbes, with the colonization of the exposed surfaces of LOF. The second stage is the reworking of POM derived from the first stage, and this typically takes place in the surrounding sediments. In this section, I briefly review what is known about the first stage of LOF processing, i.e., the direct interaction of metazoa and microbes with LOF. The second stage of LOF processing is discussed in Section *5.4*.

Experimentation with implanted animal carcass and kelp LOF demonstrated repeatedly that metazoan scavenging is the first step in LOF processing in the deep sea (Isaacs and Schwartzlose 1975; Stockton and DeLaca 1982; Smith 1983; 1985; 1986; Smith et al. 1998; Smith et al. 2002a; Kemp et al. 2006). Metazoa, such as fish, crustaceans, and mollusks (Hargrave et al. 1995; Tamburri and Barry 1999; Smith et al. 2002a; Kemp et al. 2006), remove portions of animal carcasses with their mouths and, although they may lose some fragments to the surrounding environment, they ingest most of the material (C. R. Smith, personal communication). Scavengers have been observed to process LOF rapidly (Isaacs and Schwartzlose 1975; Hargrave et al. 1994; Hargrave et al. 1995; Tamburri and Barry 1999; Smith et al. 2002a), and to assimilate the vast majority of ingested MOM (Hargrave et al. 1995). In the case of fish scavengers, such

findings are in agreement with high absorption rates (> 90 %) of lipids and proteins by both deep- and shallow-water fish (Drazen et al. 2007).

In contrast to animal carcass LOF, woody LOF are characterized by structural hardness, refractory compounds (e.g., cellulose and lignin), and very high C:N ratios (Browning 1963; Jones 1989; Parker and LeVan 1989). Consequently, specialized wood borers, particularly mollusks and crustaceans, have evolved to exploit these falls in the deep sea (Barnard 1961; Knudsen 1961; Turner 1973; Distel et al. 2000). Xylophagainid bivalves are obligate wood-borers, i.e., they colonize wood LOF as larvae and grow by excavating the wood using their shells, to form oblong cavities (Knudsen 1961; Distel and Roberts 1997). While excavating, they consume the wood shavings, which are stored in a large caecum and from there are transported to the stomach (Distel and Roberts 1997). There is no direct evidence for assimilation of wood as part of the xylophagainid diet, but such a prospect is supported by the active ingestion of wood shavings by xylophagainids. Findings from study of the related group of shallow-water, wood-boring bivalves, the Teredinidae, also support the case for wood assimilation: symbionts discovered in the teredinid gills are capable of digesting cellulose and fixing nitrogen, and could thus complement the carbon-rich, nitrogen-poor diet that is wood (Popham and Dickson 1973; Waterbury et al. 1983). Such symbionts have also been observed in xylophagainids (Distel and Roberts 1997), but their role in the metazoan nutrition and assimilation efficiency is not yet known. Finally, at an advanced stage of wood LOF processing, wood borers nearly completely excavate the structure of the fall, resulting in its mechanical instability and collapse (Turner 1973; 1978).

The activity of metazoa on macroalgae and seagrasses interpolates those on animal matter and wood. Macroalgae and seagrasses are carbohydrate-rich LOF that differ from wood in that they do not contain lignin, the macromolecule responsible for wood's hardness (de Leeuw and Largeau 1993). Macroalgae also contain more nitrogen and are generally a more labile organic matter source than seagrasses (Tenore 1977; Tenore and Hanson 1980; Tenore 1983). Rapid processing of these LOF by crustacean and echinoderm scavengers results in high productivity and sustains metazoan populations that prey on the LOF scavengers (Vetter 1994; Vetter 1998; Vetter and Dayton 1999). Borers are also known to colonize and grow on the more vascular parts of macroalgae and seagrasses, e.g., holdfasts (Wolff 1979).

While, in the case of carcass LOF, scavenging occurs at rates high enough to dominate direct LOF processing, there are several examples of other LOF types whose surfaces are initially colonized by microbes who dominate the initial processing stage. Wood fragments are colonized by dense microbial populations shortly after arrival to the sea floor (Wirsen and Jannasch 1976). Macroalgal and seagrass detritus is subject to colonization by sulfide-oxidizing *Beggiatoa* (Vetter 1998), which thrives on sulfide generated by the remineralization of organic sulfur contained in kelp tissue as well as by anaerobic sulfate reduction (ZoBell 1971; Smith 1983). Actually, in the case of the California Borderland Basins, microbes successfully out-compete metazoa in the initial colonization and degradation of kelp detritus (Smith 1983). Most notably, lipid-rich whale bones, when they are stripped of flesh by scavengers, are colonized by sulfate reducing microbes, which anaerobically degrade the lipids (Deming et al. 1997; Smith and Baco 2003). Also, the surfaces of bones as well as any remaining tissue surrounding

the skeleton can be the site of thick microbial mat formation (Smith and Baco 2003; Smith 2007; Treude et al., in preparation).

The first stage of LOF processing can be the result of synergistic activities between metazoa and microbes. The decomposition of whale bone lipids yields two examples of such synergy. Sulfide generated during sulfate reduction during lipid decomposition (Deming et al. 1997) supports metazoa, e.g., the mussel *Idas washingtonia*, vesicomyid clams, and vestimentiferan worms, that harbor chemosynthetic-autotrophic endosymbionts (see Smith and Baco 2003 for review). Other bone-colonizing metazoa, e.g., the "zombie worms" *Osedax*, harbor chemoorganotrophic symbionts, i.e., heterotrophic bacteria that digest complex organic molecules (Rouse et al. 2004; Glover et al. 2005; Goffredi et al. 2005; 2007).

Another case of synergistic LOF processing is driven by LOF fragmentation. Fragmentation of LOF, mediated by metazoan scavenging, increases the surface-area-to-volume-ratio of the particles present. Since microbial colonization of detrital material may be largely correlated with the surface area available (e.g., DeFlaun and Mayer 1983; Findlay et al. 1992), it is likely that fragmentation substantially increases the accessibility of MOM to microbes. Wirsen and Jannasch (1976) deployed various types of organic material to the deep sea (see Table 5.2), in special packages with openings of 13 mm (to allow access to animals). They observed higher degradation in these packages than in "closed" packages (with openings < 1 mm), but it is not clear whether this was true of all the materials they used, or which metazoa may have been responsible. In a more focused study, Harrison (1977) observed enhanced mineralization rates of seagrass (*Zostera*) carbon during fragmentation of seagrass leaves by amphipods (*Gammarus*) during

experiments in non-sterile seawater. Harrison (1977) suggested that simple fragmentation of seagrass by amphipods without gut passage contributed significantly to the enhanced mineralization of seagrass POM, but this was not easy to prove from his data. The main relevant point from the studies mentioned above is that fragmentation of LOF material, whether it is accompanied by ingestion or not, is likely to accelerate the processing of the fragmented material due to increased surface area availability for microbial colonization.

The degree of digestion of ingested MOM by scavengers was questioned by Wirsen and Jannasch (1976). Many studies have shown that assimilation of ingested MOM from carcass LOF is very high among the metazoa that process LOF and that these metazoa appear to leave little for the surrounding community in the form of feces (Priede et al. 1991; Hargrave et al. 1995; Drazen et al. 2007). In conclusion, during the first stage of exploitation of carcass LOF on the deep sea floor, the vast majority of MOM is consumed and assimilated by metazoan scavengers (Hargrave et al. 1995), whereas in the case of woody LOF this is unlikely (Distel and Roberts 1997).

5.4 Effects of MOM processing on sedimentary biogeochemistry: the generation of biogenic reducing habitats

The second stage of LOF exploitation is the sedimentary processing of POM derived from the direct interaction of biota with the falls. In view of the conclusion of the previous section, it is interesting to contemplate the origin of this POM. In the case of wood, a large fraction of the ingested material is passed through the gut unprocessed (Distel and Roberts 1997). In the case of carcasses, however, high assimilation of labile MOM and consequently low loss through defecation may lead to the dominant source of

MOM to surrounding sediments being the fragments of MOM lost during scavenger feeding. This fragmentation and loss during feeding was first described in the zooplankton literature (Conover 1966a; 1966b), and is more commonly referred to as sloppy feeding (e.g., Møller 2007). It has not been well studied in scavenging metazoa, but its occurrence is evident when video of scavenger activity is carefully inspected: strands of MOM can be seen to emanate from sites of scavenger activity and to drift across the field of view (personal observations). Sloppy feeding has recently been evoked to explain enzymatic activity patterns in sediments surrounding fish LOF (Sauter et al. 2006), so it is likely that further investigation of this phenomenon during LOF scavenging will follow. Since assimilation efficiencies for macroalgal, seagrass, and woody feeders are probably lower than those for animal carcasses (e.g., Tenore 1983), one would expect the importance of defecated material to be higher for plant materials and especially high in the case of wood LOF processed by wood-borers.

The dispersal of MOM to surrounding sediments leads to another opportunity for microbes and metazoa to compete or collaborate for further MOM degradation. In the case of whale falls, the arrival and processing activities of mobile scavengers is only the first stage of an ecological succession, and is followed by at least two more stages (Smith et al. 1998; Smith and Baco 2003):

a) The organic enrichment stage, during which mat-forming microbes and sedimentary macrofauna colonize the surrounding sediments and exploit the MOM fallout dispersed by scavengers;

b) The sulfophilic stage, during which sulfide tolerant or sulfophilic microbes occur as symbionts in metazoans either in sediments or in bones (Smith et al. 1989; Deming et al. 1997).

These latter stages have a major effect on the biogeochemical character of the sediments. The sulfophilic stage, in particular, has attracted much attention due to its ecological implications: the whale fall site becomes in essence a biogenic chemosynthetic habitat (Smith et al. 1989; Bennett et al. 1994; Deming et al. 1997; Smith and Baco 2003). Moreover, in the case of the Southern California Borderland Basins region, there are areas of presumed frequent whale fall occurrence (underlying major whale migration routes) which may connect with regions containing hydrothermal vents and cold seeps (Smith and Baco 2003). This observation led to the stepping stone hypothesis, which suggests that falls provide intermediary chemosynthetic habitats between vent and seep fields, thereby facilitating the dispersal of species dependent on chemoautotrophic production between these fields (Smith et al. 1989). Evidence in favor of this hypothesis includes the occurrence of certain groups of organisms, such as vesicomyid clams and various mussel species, in association with whale and wood falls, vents and seeps (Baco et al. 1999; Distel et al. 2000; Baco-Taylor 2002).

A major sulfide generation site of a whale fall is considered to be the whale bones, where sulfate reduction is fueled by bone lipids (Deming et al. 1997). The presence of many chemosynthetic-symbiont-bearing metazoa living in sediments adjacent to bones (Smith and Baco 2003) raises the question of the role of surrounding sediments in processing MOM from sloppy feeding and generating sulfidic conditions. The answer may involve a progression of events based on the Pearson and Rosenberg (1978) organic

enrichment model: scavenger-driven dispersal of MOM leads to sedimentary organic enrichment and decomposition, and subsequent sulfide build up in the region of a fall. Whether MOM decomposition is aerobic or anaerobic will depend on the rate of decomposition and if it is fast enough to sequentially exhaust the available electron acceptors in order of energetic yield (Froelich et al. 1979). From the moment oxygen is exhausted, sulfate reducers (which are obligate anaerobes) can metabolize, compete with other anaerobes for POM, multiply, and generate sulfide through dissimilatory sulfate reduction (Madigan et al. 2000, p. 498, 608). If the sediments are fine-grained, molecular diffusion may be adequately slow to inhibit oxygen penetration, and simultaneously allow appreciable build-up of sulfide in pore water and subsequent flux into the overlying water.

Organic matter supply rates and decomposition rates must be fairly high for sedimentary dissimilatory sulfate reduction to generate appreciable build-up of sulfide in pore waters (Westrich and Berner 1984). Decomposition rates will be greatly influenced by the lability of organic material (e.g., Lyons and Gaudette 1979), i.e., by the ability of microbial enzymes to digest it and absorb it through the cell wall for further processing. The diversity of biochemical compounds and elemental composition of LOF (Table 6.1) indicates that microbial POM decomposition rates will vary substantially in sediments adjacent to LOF. Specifically, decomposition rates should increase with decreasing POM carbon:nitrogen (C:N) ratios, which are commonly considered an indicator of labile material (e.g., Soetaert et al. 1996). High C:N ratios could be due to nitrogen-poor POM, or refractory structural compounds, e.g., cellulose and lignin, and may result in slow decomposition rates. In the case where high C:N ratios coincide with high total organic

carbon (TOC) content, it is possible that decomposition may be slow enough to allow oxygen to be replenished and to prevent sulfidic conditions in the sediment. The study of LOF exploitation and its impact on the biogeochemistry of adjacent sediments thus offers itself to the testing of some of these dynamic scenaria in early diagenesis. The relationships between parameters such as LOF scavenger processing rates, MOM quality, organic enrichment in adjacent sediments, and pore water sulfide content are of particular importance in gauging the development and duration of biogenic reducing habitats.

5.5 Past findings and present goals

Previous attempts to collect evidence for sedimentary organic enrichment and elevated concentrations of pore water sulfide surrounding whale falls have been inconclusive or conflicting. Smith et al. (1998) measured sedimentary TOC and total nitrogen (TN) at various distances away from a whale fall in Santa Catalina Basin. Their data did not reveal any enrichment near the fall or any trend with distance (Table 5.2).

Pore water data generated during the same cruise show very low total dissolved sulfide (ΣH_2S) concentrations (< 10 $\mu mol \cdot L^{-1}$) in these sediments, essentially indistinguishable from those in one background core at the same site (Figure 5.3; Smith et al. 1998). However, the age of that whale fall at the time of sampling was 35 ± 12 years (based on radioisotope disequilibria; Schuller et al. 2004), well after the initial mobile megafaunal scavenger stage, and clearly past the organic enrichment stage. Unpublished data collected on a much younger whale fall (1.5-18 months old), reveal

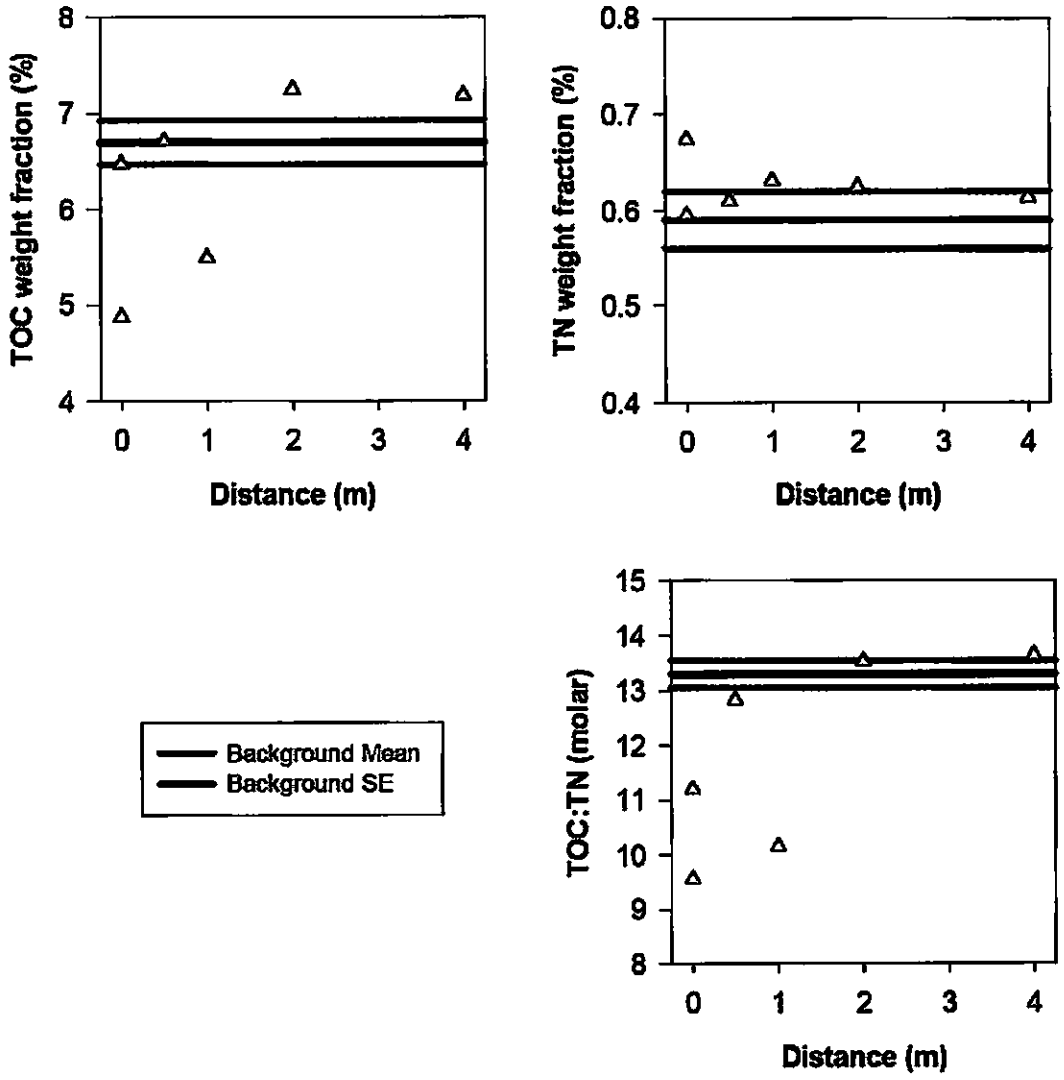

Figure 5.2 Weight fractions of TOC and TN (%), and molar ratio of TOC:TN, plotted against distance from a 35 year-old whale fall in Santa Catalina Basin (data from Smith et al. 1998). The background mean and standard error (SE) were calculated from sediment samples (n=2) collected 100 m away from this whale fall.

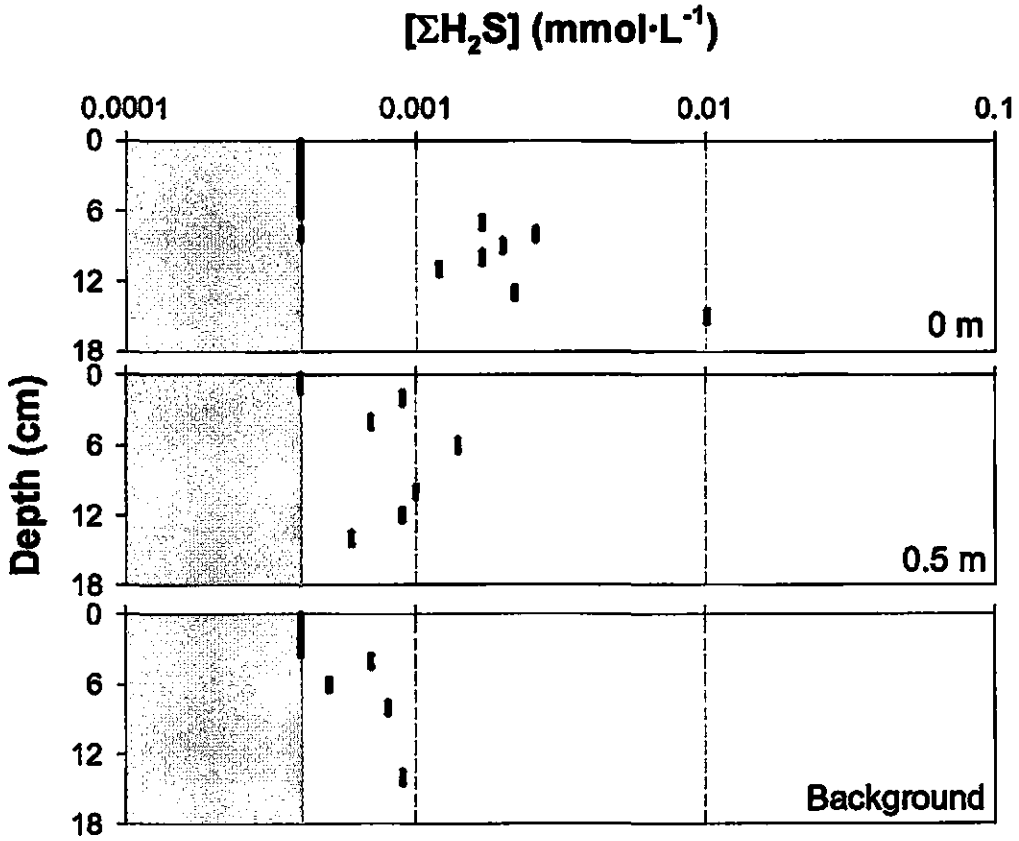

Figure 5.3 Total dissolved sulfide (ΣH_2S) concentrations down-core in sediments away from a 35 ± 12 year-old whale fall in Santa Catalina Basin (data from Smith et al. 1998). Black vertical lines indicate the depth range of each sediment sample. The grey region indicates the detection limit of the analysis.

TOC content two times greater than background in sediments adjacent to a whale fall in Santa Cruz Basin (C. R. Smith, unpublished data), while sulfide levels exceeded background levels by three orders of magnitude (Figure 5.4; M. E. Torres and C. R. Smith, unpublished data).

To better constrain the occurrence, development rate, and duration of biogenic reducing habitats, it would be beneficial to record sedimentary organic matter content and pore water sulfide in LOF of different quality and exploitation stage. In Chapter 6, I use a data set of TOC, TN, and ΣH_2S, collected from three types of falls (whales, kelp and wood parcels) located in the California Borderland Basins region, to explore similarities and differences in levels of organic enrichment and sulfide with fall type and age. In Chapter 7, I present a model of fall processing by the deep sea floor communities. The model incorporates scavenger processing, dispersal of fragmented material, and decomposition during early diagenesis. The model is used to predict the ability of organic matter released by metazoa at each fall to generate a reducing habitat, based on the fall type, fall size, metazoan processing rates, and MOM decomposition rates during early diagenesis. The combination of biogeochemical observations and mathematical calculations may allow an improved description of LOF as sources of POM and agents of biogeochemical change on the deep sea floor.

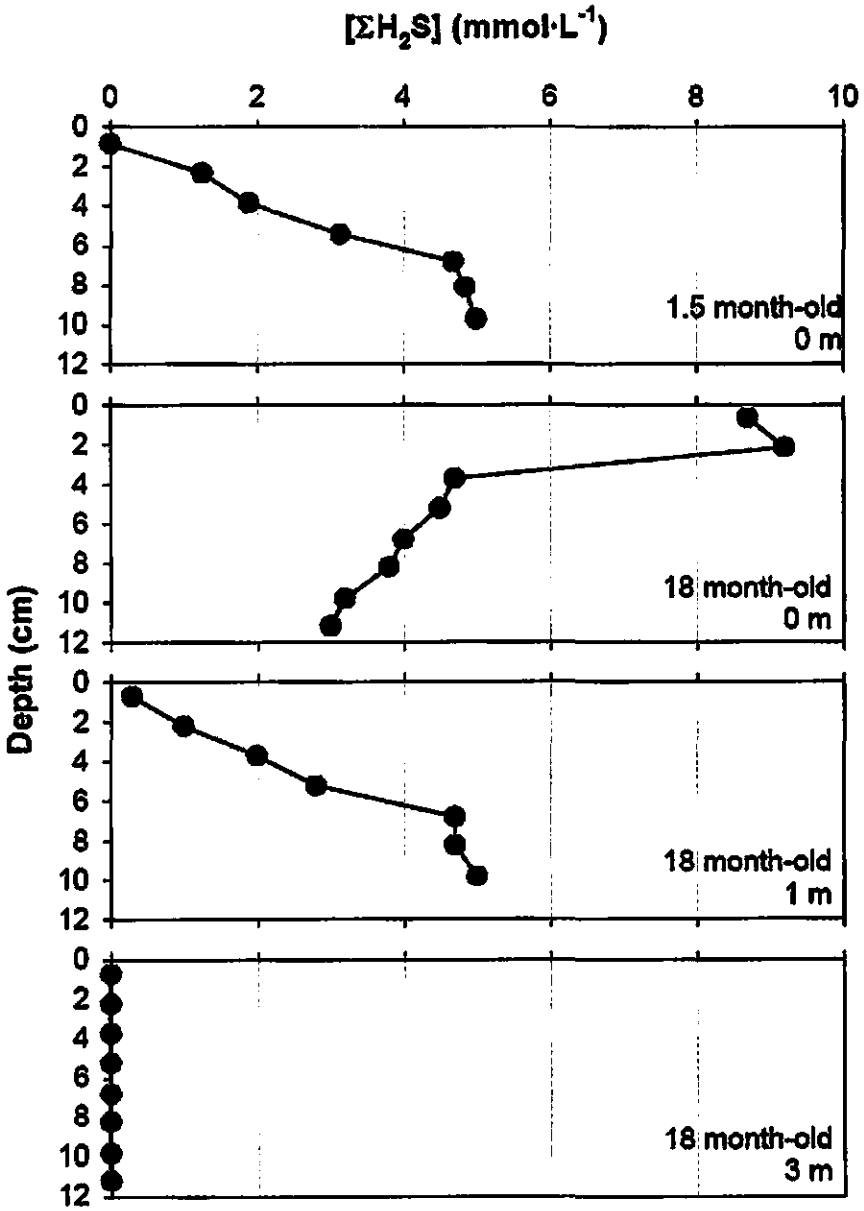

Figure 5.4 Total dissolved sulfide (ΣH_2S) concentrations down-core in sediments associated with an experimental whale fall in Santa Cruz Basin. Sediments were sampled at 1.5 and 18 months after the fall event. At 18 months, sediments were also collected 1 and 3 m away from the whale fall (M. E. Torres and C. R. Smith, unpublished data from two R/V Alvin dives in 1998 and 1999).

5.6 References

Alldredge, A. L. and M. W. Silver (1988) Characteristics, dynamics and significance of marine snow. Progress in Oceanography, 20: 41-82.

Alldredge, A. L. (2000) Interstitial dissolved organic carbon (DOC) concentrations within sinking marine aggregates and their potential contribution to carbon flux. Limnology and Oceanography, 45: 1245-1253.

Baco-Taylor, A. R. (2002) Food-web structure, succession and phylogenetics on deep-sea whale skeletons. Ph.D. Dissertation, University of Hawai'i, pp. 275.

Baco, A. R., C. R. Smith, A. S. Peek, G. K. Roderick and R. C. Vrijenhoek (1999) The phylogenetic relationships of whale-fall vesicomyid clams based on mitochondrial COI DNA sequences. Marine Ecology Progress Series, 182: 137-147.

Barnard, J. L. (1961) Gammaridean Amphipoda from depths of 400 to 6000 meters. Galathea Report, 5: 23-128.

Bennett, B. A., C. R. Smith, B. Glaser and H. L. Maybaum (1994) Faunal community structure of a chemoautotrophic assemblage on whale bones in the deep northeast Pacific Ocean. Marine Ecology Progress Series, 108: 205-223.

Billett, D. S. M., R. S. Lampitt, A. L. Rice and R. F. C. Mantoura (1983) Seasonal sedimentation of phytoplankton to the deep-sea benthos. Nature, 302: 520-522.

Billett, D. S. M., B. J. Bett, C. L. Jacobs, I. P. Rouse and B. D. Wigham (2006) Mass deposition of jellyfish in the deep Arabian Sea. Limnology and Oceanography, 51: 2077-2083.

Browning, B. L. (1963) The composition and chemical reactions of wood, p. 57-101. *In* Browning, B. L. [ed.], The chemistry of wood. Wiley Interscience, New York, New York, U.S.A.

Butman, C. A., J. T. Carlton and S. R. Palumbi (1995) Whaling effects on deep-sea biodiversity. Conservation Biology, 9: 462-464.

Butman, C. A., J. T. Carlton and S. R. Palumbi (1996) Whales don't fall like snow: reply to Jelmert. Conservation Biology, 10: 655-656.

Conover, R. J. (1966a) Assimilation of organic matter by zooplankton. Limnology and Oceanography, 11: 338-345.

Conover, R. J. (1966b) Factors affecting the assimilation of organic matter by zooplankton and the question of superfluous feeding. Limnology and Oceanography, 11: 346-354.

Dayton, P. K. and R. R. Hessler (1972) Role of biological disturbance in maintaining diversity in the deep sea. Deep-Sea Research, 19: 199-208.

de Leeuw, J. W. and C. Largeau (1993) A review of macromolecular organic compounds that comprise living organisms and their role in kerogen, coal, and petroleum formation, p. 23-72. *In* Engel, M. H. and S. A. Macko [eds.], Organic Geochemistry. Plenum Press, New York, New York, U.S.A.

DeFlaun, M. F. and L. M. Mayer (1983) Relationships between bacteria and grain surfaces in intertidal sediments. Limnology and Oceanography, 28: 873-881.

Deming, J. W., A. L. Reysenbach, S. A. Macko and C. R. Smith (1997) Evidence for the microbial basis of a chemoautotrophic community at a whale fall on the deep seafloor: bone-colonizing bacteria and invertebrate endosymbionts. Microscopy Research and Technique, 37: 162-170.

Distel, D. L. and S. J. Roberts (1997) Bacterial endosymbionts in the gills of the deep-sea wood-boring bivalves *Xylophaga atlantica* and *Xylophaga washingtona*. Biological Bulletin, 192: 253-261.

Distel, D. L., A. R. Baco, E. Chuang, W. Morrill, C. Cavanaugh and C. R. Smith (2000) Do mussels take wooden steps to deep-sea vents? Nature, 403: 725-726.

Drazen, J. C., K. R. Reisenbichler and B. H. Robison (2007) A comparison of absorption and assimilation efficiencies between four species of shallow- and deep-living fishes. Marine Biology, 151: 1551-1558.

Findlay, R. H., S. L. Kim and C. A. Butman (1992) Colonization of freshly deposited barite and silica sediments by marine microorganisms in a laboratory flume flow. Marine Ecology Progress Series, 90: 73-88.

Froelich, P. N., G. P. Klinkhammer, M. L. Bender, N. A. Luedtke, G. R. Heath, D. Cullen, P. Dauphin, D. Hammond, B. Hartman and V. Maynard (1979) Early oxidation of organic matter in pelagic sediments of the eastern equatorial Atlantic: suboxic diagenesis. Geochimica et Cosmochimica Acta, 43: 1075-1090.

Gage, J. D. and P. A. Tyler (1991) Deep-sea biology. Cambridge University Press, Cambridge, U.K., pp. 504.

Glover, A. G., B. Källström, C. R. Smith and T. G. Dahlgren (2005) World-wide whale worms? A new species of *Osedax* from the shallow north Atlantic. Proceedings of the Royal Society B, 272: 2597-2592.

Goffredi, S. K., V. J. Orphan, G. W. Rouse, L. Jahnke, T. Embaye, K. Turk, R. Lee and R. C. Vrijenhoek (2005) Evolutionary innovation: a bone-eating marine symbiosis. Environmental Microbiology, 7: 1369-1378.

Goffredi, S. K., S. B. Johnson and R. C. Vrijenhoek (2007) Genetic diversity and potential function of microbial symbionts associated with newly discovered species of *Osedax* polychaete worms. Applied and Environmental Microbiology, 73: 2314-2323.

Hannides, A. K., C. R. Smith and A. R. Baco-Taylor (2005) Massive organic matter fall processing and organic enrichment in deep sea sediments: the role of fall type. Eos, Transactions of the American Geophysical Union, December 5th-9th, 2005, 86(52), Fall Meeting Supplement, Abstract B21A-1017.

Hannides, A. K., C. R. Smith, T. Treude, A. Boetius and F. Wenzhöfer (2006) Massive organic matter falls in the deep sea: interactions among organic matter quality, biogeochemical processes, and microbe-versus-metazoan competition. Eos, Transactions of the American Geophysical Union, February 20th-24th, 2006, 87(36), Ocean Sciences Meeting Supplement, Abstract 15F-05.

Hargrave, B. T., N. J. Prouse, G. A. Phillips and P. J. Cranford (1994) Meal size and sustenance time in the deep-sea amphipod *Eurythenes gryllus* collected from the Arctic Ocean. Deep- Sea Research I, 41: 1489-1508.

Hargrave, B. T., G. A. Phillips, N. J. Prouse and P. J. Cranford (1995) Rapid digestion and assimilation of bait by the deep-sea amphipod *Eurythenes gryllus*. Deep- Sea Research I, 42: 1905-1921.

Harrison, P. G. (1977) Decomposition of macrophyte detritus in seawater: effects of grazing by amphipods. Oikos, 28: 165-169.

Harrold, C., K. Light and S. Lisin (1998) Organic enrichment of submarine-canyon and continental-shelf benthic communities by macroalgal drift imported from nearshore kelp forests. Limnology and Oceanography, 43: 669-678.

Isaacs, J. D. and R. A. Schwartzlose (1975) Active animals of the deep-sea floor. Scientific American, 233: 85-91.

Jannasch, H. W. (1978) Experiments in deep-sea microbiology. Oceanus, 21: 50-57.

Jelmert, A. and D. O. Oppen-Berntsen (1996) Whaling and deep-sea biodiversity. Conservation Biology, 10: 653-654.

Jones, T. H. [ed.] (1989) The encyclopedia of wood, revised. Sterling Publishing Co., New York, New York, U.S.A., pp. 464.

Kemp, K. M., A. J. Jamieson, P. M. Bagley, H. McGrath, D. M. Bailey, M. A. Collins and I. G. Priede (2006) Consumption of a large bathyal food fall, a six month study in the north-east Atlantic. Marine Ecology Progress Series, 310: 65-76.

Knudsen, J. (1961) The bathyal and abyssal *Xylophaga* (Pholadidae, Bivalvia). Galathea Report, 5: 163-209.

Lampitt, R. S., B. J. Bett, K. Kiriakoulakis, E. E. Popova, O. Ragueneau, A. Vangriesheim and G. A. Wolff (2001) Material supply to the abyssal seafloor in the northeast Atlantic. Progress in Oceanography, 50: 27-63.

Lee, C., S. G. Wakeham and C. Arnosti (2004) Particulate organic matter in the sea: the composition conundrum. Ambio, 33: 565-575.

Lyons, W. B. and H. E. Gaudette (1979) Sulfate reduction and the nature of organic matter in estuarine sediments. Organic Geochemistry, 1: 151-155.

Madigan, M. T., J. M. Martinko and J. Parker (2000) Brock biology of microorganisms, 9th Edition. Prentice-Hall, Upper Saddle River, New Jersey, U.S.A., pp. 991.

Miller, R. J., C. R. Smith, D. J. DeMaster and W. L. Fornes (2000) Feeding selectivity and rapid particle processing by deep-sea megafaunal deposit feeders: a ^{234}Th tracer approach. Journal of Marine Research, 58: 653-673.

Møller, E. F. (2007) Production of dissolved organic carbon by sloppy feeding in the copepods *Acartia tonsa*, *Centropages typicus*, and *Temora longicornis*. Limnology and Oceanography, 52: 79-84.

Odum, E. P. and A. A. de la Cruz (1963) Detritus as a major component of ecosystems. American Institute Biological Sciences Bulletin, 13: 39-40.

Parker, W. J. and S. L. LeVan (1989) Kinetic properties of the components of Douglas-fir and the heat of combustion of their volatile pyrolysis products. Wood and Fiber Science, 21: 289-305.

Pearson, T. H. and R. Rosenberg (1978) Macrobenthic succession in relation to organic enrichment and pollution of the marine environment. Oceanography and Marine Biology: an Annual Review, 16: 229-311.

Popham, J. D. and M. R. Dickson (1973) Bacterial associations in the teredo *Bankia australis* (Lamellibranchia, Mollusca). Marine Biology, 19: 338-340.

Priede, I. G., P. M. Bagley, J. D. Armstrong, K. L. J. Smith and N. R. Merrett (1991) Direct measurement of active dispersal of food-falls by deep-sea demersal fishes. Nature, 351: 647-649.

Priede, I. G. and N. R. Merrett (1996) Estimation of abundance of abyssal demersal fishes: a comparison of data from trawls and baited cameras. Journal of Fish Biology, 49 (Suppl. A): 207-216.

Priede, I. G. and N. R. Merrett (1998) The relationship between numbers of fish attracted to baited cameras and population density: Studies on demersal grenadiers *Coryphaenoides* (*Nematonurus*) *armatus* in the abyssal NE Atlantic Ocean. Fisheries Research, 36: 133-137.

Robison, B. H., K. R. Reisenbichler and R. E. Sherlock (2005) Giant larvacean houses: rapid carbon transport to the deep sea floor. Science, 308: 1609 - 1611.

Romankevich, E. A. (1978) Geochemistry of organic matter in the ocean. Springer - Verlag, Berlin, Germany, pp. 334.

Rouse, G. W., S. K. Goffredi and R. C. Vrijenhoek (2004) *Osedax*: Bone-eating marine worms with dwarf males. Science, 305: 668-671.

Rowe, G. T. and J. W. Deming (1985) The role of bacteria in the turnover of organic carbon in deep-sea sediments. Journal of Marine Research, 43: 925-950.

Sauter, E. J., O. Sachs, I. Schewe and T. Soltwedel (2006) Impact of large food-falls on spatial and temporal patterns of dissolved oxygen in the upper sediment layers. 11th International Deep-Sea Biology Symposium, Southampton, U.K., July 9th-14th, 2006, Book of abstracts, p. 159.

Schuller, D., D. Kadko and C. R. Smith (2004) Use of $^{210}Pb/^{226}Ra$ disequilibria in the dating of deep-sea whale falls. Earth and Planetary Science Letters, 218: 277-289.

Sheldon, R. W., A. Prakash and W. H. J. Sutcliffe (1972) The size distribution of particles in the ocean. Limnology and Oceanography, 17: 327-340.

Sieburth, J. M., V. Smetacek and J. Lenz (1978) Pelagic ecosystem structure: heterotrophic compartments of the plankton and their relationship to plankton size fractions. Limnology and Oceanography, 23: 1256-1263.

Silver, M. W. and M. M. Gowing (1991) The "particle" flux: origins and biological components. Progress in Oceanography, 26: 75-113.

Smith, C. R. (1983) Enrichment, disturbance and deep-sea community structure: the significance of large organic falls to bathyal benthos in Santa Catalina Basin. Ph.D. Dissertation, University of California San Diego, pp. 310.

Smith, C. R. (1985) Food for the deep sea: utilization, dispersal, and flux of nekton falls at the Santa Catalina basin floor. Deep-Sea Research, 32: 417-442.

Smith, C. R. (1986) Nekton falls, low-intensity disturbance and community structure of infaunal benthos in the deep sea. Journal of Marine Research, 44: 567-600.

Smith, C. R., H. Kukert, R. A. Wheatcroft, P. A. Jumars and J. W. Deming (1989) Vent fauna on whale remains. Nature, 341: 27-28.

Smith, C. R., H. L. Maybaum, A. R. Baco, R. H. Pope, S. H. Carpenter, P. L. Yager, S. A. Macko and J. W. Deming (1998) Sediment community structure around a whale skeleton in the deep Northeast Pacific: Macrofaunal, microbial and bioturbation effects. Deep-Sea Research II, 45: 335-364.

Smith, C. R., A. R. Baco and A. G. Glover (2002a) Faunal succession on replicate deep-sea whale falls: time scales and vent-seep affinities. Cahiers de Biologie Marine, 43: 293-297.

Smith, C. R. and A. W. J. Demopoulos (2003) The deep Pacific ocean floor, p. 179-218. *In* Tyler, P. A. [ed.], Ecosystems of the world, Vol. 28: Ecosystems of the deep ocean. Elsevier, Amsterdam, Netherlands.

Smith, C. R. and A. R. Baco (2003) Ecology of whale falls at the deep-sea floor. Oceanography and Marine Biology: an Annual Review, 41: 311-354.

Smith, C. R. (2007) Bigger is better: the role of whales as detritus in marine ecosystems, p. 286-302. *In* Estes, J. A., D. P. DeMaster, D. F. Doak, T. M. Williams and R. L. Brownell Jr. [eds.], Whales, whaling, and ocean ecosystems. University of California Press, Berkeley, California, U.S.A.

Smith, K. L. (1987) Food energy supply and demand: a discrepancy between particulate organic carbon flux and sediment community oxygen consumption in the deep ocean. Limnology and Oceanography, 32: 201-220.

Smith, K. L., R. J. Baldwin and P. M. Williams (1992a) Reconciling particulate organic carbon flux and sediment community oxygen consumption in the deep North Pacific. Nature, 359: 313-316.

Smith, K. L., R. S. Kaufmann, J. L. Edelman and R. J. Baldwin (1992b) Abyssopelagic fauna in the central North Pacific: comparison of acoustic detection and trawl and bated trap collections to 5800 m. Deep-Sea Research, 39: 659-685.

Smith, K. L. (1992) Benthic boundary layer communities and carbon cycling at abyssal depths in the central North Pacific. Limnology and Oceanography, 37: 1034-1056.

Smith, K. L. and R. S. Kaufmann (1999) Long-term discrepancy between food supply and demand in the deep eastern north Pacific. Science, 284: 1174-1177.

Smith, K. L., R. J. Baldwin, D. M. Karl and A. Boetius (2002b) Benthic community responses to pulses in pelagic food supply: North Pacific Subtropical Gyre. Deep-Sea Research I, 49: 971-990.

Soetaert, K., P. M. J. Herman and J. J. Middelburg (1996) A model of early diagenetic processes from the shelf to abyssal depths. Geochimica et Cosmochimica Acta, 60: 1019-1040.

Stockton, W. L. and T. E. DeLaca (1982) Food falls in the deep sea: occurrence, quality and significance. Deep- Sea Research, 29: 157-169.

Tamburri, M. N. and J. P. Barry (1999) Adaptations for scavenging by three diverse bathyal species, *Eptatretus stouti, Neptunea amianta, Orchomene obtusus*. Deep-Sea Research I, 46: 2079-2093.

Tenore, K. R. (1977) Utilization of aged detritus derived from different sources by the polychaete *Capitella capitata*. Marine Biology, 44: 51-55.

Tenore, K. R. and R. B. Hanson (1980) Availability of detritus of different types and ages to a polychaete macroconsumer, *Capitella capitata*. Limnology and Oceanography, 25: 553-558.

Tenore, K. R. (1983) What controls the availability to animals of detritus derived from vascular plants: organic nitrogen enrichment or caloric availability? Marine Ecology Progress Series, 10: 307-309.

Turner, R. D. (1973) Wood-boring bivalves, opportunistic species in the deep sea. Science, 180: 1377-1379.

Turner, R. D. (1978) Wood, mollusks, and deep-sea food chains. Bulletin of the American Malacological Union, 1977: 13-19.

Vetter, E. W. (1994) Hotspots of benthic production. Nature, 372: 47.

Vetter, E. W. and P. K. Dayton (1998) Macrofaunal communities within and adjacent to a detritus-rich submarine canyon system. Deep-Sea Research II, 45: 25-54.

Vetter, E. W. (1998) Population dynamics of a dense assemblage of marine detritivores. Journal of Experimental Marine Biology and Ecology, 226: 131-161.

Vetter, E. W. and P. K. Dayton (1999) Organic enrichment by macrophyte detritus, and abundance patterns of megafaunal populations in submarine canyons. Marine Ecology Progress Series, 186: 137-148.

Volkman, J. K. and E. Tanoue (2002) Chemical and biological studies of particulate organic matter in the ocean. Journal of Oceanography, 58: 265-279.

Wakeham, S. G. and C. Lee (1993) Production, transport, and alteration of particulate organic matter in the marine water column, p. 145-169. *In* Engel, M. H. and S. A. Macko [eds.], Organic Geochemistry. Plenum Press, New York, New York, U.S.A.

Waterbury, J. B., C. B. Calloway and R. D. Turner (1983) A cellulolytic-nitrogen fixing bacterium cultured from the Gland of Deshayes in shipworms (Bivalvia: Teredinidae). Science, 221: 1401-1403.

Westrich, J. T. and R. A. Berner (1984) The role of sedimentary organic matter in bacterial sulfate reduction: the *G* model tested. Limnology and Oceanography, 29: 236-249.

Wirsen, C. O. and H. W. Jannasch (1976) Decomposition of solid organic materials in the deep sea. Environmental Science and Technology, 10: 880-886.

Wolff, T. (1979) Macrofaunal utilization of plant remains in the deep sea. Sarsia, 64: 117-136.

ZoBell, C. E. (1971) Drift seaweeds on San Diego County beaches, p. 269-314. *In* North, W. J. [ed.], The biology of giant kelp beds (*Macrocystis*) in California, Beihefte zur Nova Hedwigia, Heft 32. Verlag von J. Cramer, Lehre, Germany.

Chapter 6 – Large organic falls in the deep sea: the role of fall quality on sedimentary biogeochemical processes

6.1 Introduction

Deep-sea marine sediment communities often appear to be food limited, and to rely on photosynthetically-derived organic material sinking from the euphotic zone for their energy requirements (Gage and Tyler 1991). Respiratory balance studies of benthic communities indicate that sinking fluxes estimated from sediment trap collections can underestimate benthic demand for carbon by substantial amounts (Smith 1987; 1992; Smith et al. 1992a; Smith and Kaufmann 1999; Smith et al. 2002b). This finding suggests the presence of an unaccounted source of organic matter supply to deep-sea communities, which, coupled with the common occurrence of highly mobile bentho-pelagic scavengers in the same setting, provides compelling evidence for the hypothesis that large organic falls are frequent and may supply part of the missing carbon flux (Dayton and Hessler 1972; Isaacs and Schwartzlose 1975; Smith 1985; Smith et al. 1992b; Priede and Merrett 1996; 1998).

6.1.1 The quality of large organic falls

Large organic falls (LOF) are massive parcels of organic-rich compounds, larger in size than the amount handled in an instant by an individual that is exploiting them (Smith 1983; 1986). Such sizes imply fairly fast sinking rates, higher than those of the fine (approximately 50 μm-5 mm) particles that dominate the flux of particulate organic matter (POM) from the ocean's surface to the sea floor (Alldredge and Silver 1988). The

fast sinking rates result in short water-column transit times and minimum alteration of the material's biochemical composition, unlike the case of slow-sinking fine particles (see review by Wakeham and Lee 1993). Thus, this rapid shunt from productive surface waters to the deep sea floor allows the full range of LOF characteristics to be transported to the deep sea benthic regime essentially unaltered.

The rapid delivery of organic matter by LOF to the sea floor has important implications for the deep-sea floor communities and sedimentary biogeochemistry. The physical and biochemical characteristics of LOF will determine the rate in which the organic material will reach the sedimentary community and its state upon arrival. Organic material contained in LOF, hereby referred to as massive organic matter (MOM), constitutes a very large amount supplied instantaneously to a relatively small area of the sea floor (Butman et al. 1996; Smith 2007). However, it remains relatively inaccessible to the sedimentary community until metazoa arrive and start to process it (Chapter 5, section *5.3*). Experimentation with implanted animal carcass and kelp LOF demonstrated repeatedly that metazoan scavenging is the first step in the processing of a fall's organic matter in the deep sea (Isaacs and Schwartzlose 1975; Smith 1983; 1985; 1986; Smith et al. 1998; Smith et al. 2002a; Kemp et al. 2006).

During scavenger processing, fish, crustaceans, and mollusks actively seek, find, and consume MOM at fairly rapid rates (Hargrave et al. 1995; Tamburri and Barry 1999; Smith et al. 2002a; Kemp et al. 2006). Sediments ultimately receive a portion of this MOM as scavenger feces or primarily as uneaten particles during sloppy feeding, with potentially substantial organic enrichment in the surrounding sediments as a result (Smith and Baco 2003; C.R. Smith, personal communication). In the case of wood LOF, the

hardness and refractory nature of the material require specialist wood-boring metazoa, such as the bivalve subfamily *Xylophagainae*, to exploit this source of MOM (Knudsen 1961; Distel and Roberts 1997; Distel et al. 2000). These obligatory wood-borers settle on the wood LOF as larvae and grow by excavating the wood with their shells and consuming the wood shavings (Turner 1973; 1978; Distel and Roberts 1997). Further details of their nutrition, such as assimilation efficiency, and the nitrogen source used to complement their otherwise carbon-rich, nitrogen-poor wood diet, are not known. Therefore, although it is known that they process and ingest most of the wood LOF, it is not known how much of this MOM is supplied to the surrounding sediments and in what condition.

This brief comparison between processing of animal or macroalgal LOF and processing of wood LOF by metazoa illustrates the point that the large variety in fall characteristics implies an equally large variety of exploitation strategies of falls by benthic and bentho-pelagic metazoa. This variety of strategies translates into varying rates and intensities of organic matter supply to the surrounding sediments. For example, scavengers in the deep sea will locate and start processing a suitable LOF (animal carcasses, macroalgae) rapidly (i.e., within hours; e.g., Dayton and Hessler 1972; Smith 1983; Priede and Merrett 1996; Kemp et al. 2006). Wood-borers, on the other hand, settle as larvae and process a wood LOF gradually as they grow (Turner 1973; 1978). The former case leads to the generation of labile fragmented MOM at high rates, while the latter to refractory fragmented MOM at slow rates.

Ultimately, the processing rate of LOF by benthic or bentho-pelagic biota is dictated by various physical (e.g., size, surface area to volume ratio, material hardness or

toughness) and biogeochemical (e.g., elemental composition, major compounds present, their reactivity etc.) characteristics of the fall. All of these characteristics collectively describe the quality of a fall. Table 6.1 summarizes differences in various physical and biogeochemical characteristics between three types of large organic falls investigated in this study: whale carcasses, kelp, and wood. Key differences in the major constituent compounds (lipids and proteins versus cellulose and lignin) and in the structural hardness or toughness (elastic modulus) of each fall correspond to the existence of a mobile bentho-pelagic scavenger stage (Chapter 5, Section *5.3*). This stage is present if the fall is palatable and labile (and consequently nutritional) and if it can be directly ingested by mouth. This is obviously the case for whale and kelp LOF (Wolff 1979; Smith 1983; Vetter 1994; Smith et al. 1998; Vetter and Dayton 1998; 1999; Smith et al. 2002a; Smith and Baco 2003), but not for wood LOF. Because of its unpalatability and hardness, wood in the deep sea is preferentially colonized by specialist wood-boring bivalves, and occasionally amphipods (Barnard 1961; Knudsen 1961; Turner 1973).

The difference in major macromolecules is reflected in the elemental composition of a fall. For example, the carbon:nitrogen ratio (C:N) is directly related to the fraction of carbohydrate and inversely related to the fraction of protein in the fall material. This difference also reflects the degradation rates of MOM, which are in part controlled by the need to secure N from alternative sources. It is important to point out that high C:N ratios are not simply an outcome of variation in N content, but its combined effect with C content, and that, in the case of the falls studied here, the most C-rich fall type, wood, is also the most N-poor. Therefore, an otherwise C-rich food source such as wood is also nutritionally imbalanced and may persist longer in an unprocessed phase on the sea floor.

Table 6.1 Physical and chemical characteristics of the large organic falls investigated during this study, focusing on species occurring in the California Borderland Basins region: blue (*Balaenoptera musculus*), gray (*Eschrichtius robustus*) and humpback (*Megaptera novaeangliae*) whales, the Californian giant kelp (*Macrocystis pyrifera*), and the Douglas fir (*Pseudotsuga menziesii*) of the Pacific North American coastal forests.

Characteristic	Whales	Kelp	Wood
Size, m	4-29 [a]	0.05-3.5 [b]	0.05-50 [c]
Weight, kg	5×10^{2}-1.6×10^{5} [d]	2×10^{-1}-2×10^{3} [b]	2×10^{-3}-2×10^{4} [e]
Surface area to volume ratio, m^{-1}	1-16 [f]	1800-5400 [g]	4-1400 [e]
Bulk density, $g\cdot cm^{-3}$	1.01-1.05 [h]	1.03-1.05 [i]	0.45-0.48 [j]
Elastic modulus, 10^{6} Pa	0.05-1.5 [k]	1-100 [l]	10800-13400 [j]
Fall sea floor surface area, m^{2}	2-105 [m]	0.01-10 [b]	10^{-4}-50 [e]
Water weight fraction, %	51-43 [n]	86-88 [o]	28-32 [p]
Organic C weight fraction, %	27.4-32.7 [n]	3.1-3.6 [o]	33-35 [p]
(dry weight fraction, %)	(56.3-57.7) [n]	(22-30) [o]	(48.9) [p]
N content, % weight	2.6-2.3 [n]	0.1-0.4 [o]	0.14 [p]
(dry weight fraction, %)	(5.3-4.1) [n]	(1.1-1.7) [o]	(0.2) [p]
C:N, molar	12.4-16.4 [n]	30(17-40):1 [o]	250 [p]
Major macromolecules	Lipids, proteins, apatite, collagen [n]	Carbohydrates, protein, fiber [o]	Cellulose, lignin, xylans [p]
Microbial decomposition rate, d^{-1}	N.A. [q]	0.030-0.032 [r]	0.035-0.0003 [r]

[a] From Evans (1987) and Woodward et al. (2006). Minimum lengths are those of newborn *E. robustus* and *M. novaeangliae*. Maximum length is that reported for *B. musculus*;

[b] Based on observations on fall surface area by Smith (1983) and Smith and Hamilton (1983). Size was calculated assuming approximately circular patch shape. Weight was calculated by assuming a patch height of 0.10 m and multiplying by a *M. pyrifera* packing density of 264 $kg \cdot m^{-3}$ (Hart et al. 1978);

[c] Based on reports from the Galathea expedition (Bruun 1959; Knudsen 1961), and on the minimum height of adult Douglas fir trees (Franklin and Spies 1991) reported to drift over open ocean waters in the Pacific Ocean (Maser and Sedell 1994);

[d] Maximum weight for blue whale at maturity is 150 metric tons (Evans 1987). Minimum weight calculated for gray whale using a length at birth of 4 m (Evans 1987) with Lockyer's formula and constants – particular to this species – determined by Woodward et al. (2006): Weight (metric tons) = $0.0054 \times \text{Length (m)}^{3.28}$;

[e] Minimum weight value from measurements on the Galathea expedition (Bruun 1959). Maximum weight value was calculated for minimum-sized adult Douglas fir trees, using their volume and wood density. Volume (V) was estimated assuming a cylinder geometry, a radius (r) of 0.5 m, and a height (h) of 50 m (Franklin and Spies 1991), using $V = h\pi r^2$. Wood density (see footnote j) was converted to $kg \cdot m^{-3}$ by multiplying by 1000. Surface areas and volumes for large wood falls were calculated using the same morphometric values for adult Douglas-fir trees above, using the formula for a cylinder's surface area, A, where $A = 2h\pi r + 2\pi r^2$, and yielding SA/V of approximately 4 m^{-1}. For small wood particles, photos of the samples of the Galathea expedition were inspected (Bruun 1959) and two shapes were selected for calculation: rectangular-cubic chips of a height to width to length ratio of 1:2:10, which yield an SA/V value of 1300 m^{-1} at the minimum height value of 2 mm; and toothpick-like, cylindrical splinters with a radius to length ratio of approximately 30, which yield an SA/V value of 1370 m^{-1}. The same morphometric information was used to calculate fall surface area by multiplying height with diameter ($=2r$);

[f] Ratio = SA/V. Surface area, SA (m^2), was calculated using the Meeh equation with coefficients for cetaceans as determined by Fish (1993) (in Woodward et al. 2006): $SA = 0.08M^{0.65}$, where M is the

weight in kg. Volume, V (m^3), calculated by assuming neutral buoyancy and sea water density, ρ_{sw} = 1025 $kg \cdot m^{-3}$, therefore $V = M / \rho_{sw}$. The ratio was determined using the minimum and maximum values of M as defined in the table (10^2 and 10^5 kg respectively);

[g] Calculated using surface area per unit mass values of 1.7-5.1 $m^2 \cdot kg^{-1}$ (Wing and Clendenning 1971) and a density of 1050 $kg \cdot m^{-3}$ (Gaylord and Denny 1997);

[h] Range of estimates for seals (Watanabe et al. 2006) and sperm whales (*Physeter macrocephalus*; Miller et al. 2004);

[i] Gaylord and Denny (1997), Gaylord et al. (2001);

[j] For green and dry wood from the coastal population of the northwestern American range of the species (Jones 1989). Elastic modulus values of $1.56\text{-}1.95 \times 10^6$ $lbf \cdot in^{-2}$ were converted to Pascals by multiplying by 6.894757×10^3;

[k] Measured for blubber, connective tissue and acoustic fat tissues of the head of Cuvier's beaked whale (*Ziphius cavirostris*) (Soldevilla et al. 2005);

[l] Denny and Gaylord (2002);

[m] A whale fall's surface area is assumed to be the horizontal cross section of a whale. A whale's shape was assumed to be a prolate ellipse, whose short radius, r, was calculated using the length-to-diameter ratios reported in Woodward et al. (2006) and the lengths, L, reported earlier in the table (see footnote a). The area was calculated by the formula $\pi(L/2)r$;

[n] Whale body composition was calculated by combining information on morphometry-size-body part relationships and compound contribution to different body parts. Based on the morphometry relationships of Smith and Pace (1971), the contribution of the three dominant body components of baleen whales was calculated as a function of size, from 10-160 tons. In this size range, skeleton, blubber, and tissue with internal organs contribute 14.5-15.6 %, 19.0-34.7 %, and 64.7-47.0 % respectively. Note that the contribution of blubber increases with size at the expense of tissue and internal organs and, consequently, water and total nitrogen content.

Approximately 30 % of the skeleton consists of bone (based on dry, fat-free bone contribution to total whale weight; Robineau and de Buffrénil 1993). Bone mostly consists of hydroxyapatite,

$Ca_5(PO4)_3OH$ (60-70 %) with the remainder 30-40 % consisting of the protein collagen (Sterner and Elser 2002). Water contributes to 10 % of skeletal weight, with the remaining 60 % attributed to fat (Ichihara 1968). Tissue and internal organs consist of 70 % water, 21 % protein, 8 % fat and 1 % ash, while blubber contains 62 % fat, 24 % water, 13 % protein, and 1 % ash (Ichihara 1968). The following elemental contributions are considered for these compounds: protein, including collagen, consists of 47 % C and of 14.6 % N (based on protein amino acid chemical composition); fatty acids contain no N or P and are made up almost exclusively of C and H, carbon contributing on average 75 % of total weight (de Leeuw and Largeau 1993; Sterner and Elser 2002). The total body elemental composition was calculated for the weight range reported in the table by scaling the contribution of each body component at each body weight;

[o] The values reported in the table are a combination of independent measurements – if available – in studies mentioned below, as well as of calculations based on the chemical composition of *M.* pyrifera from the same studies. Kelp is mostly water (North 1971; Hart et al. 1978; Castro-González et al. 1994). The composition of the organic material is assumed to be 45 % carbohydrates (5 % of which is crude fiber), and 15 % protein by dry weight (North 1971; Hart et al. 1978; Castro-González et al. 1994). Since the majority of the carbohydrates (two-thirds of the weight) are alginic acids, carbohydrate elemental composition is based on the dimer formula of alginic acids, $C_{12}H_{16}O_{12}$ (North 1971), hence they contribute 16.4 % of carbon to the total dry weight. Fiber is assumed to be structural carbohydrates, and thus contributes 2.8 % of carbon to the total dry weight. Amino acid-based protein consists of 47.0 % C and 14.6 % N, therefore it contributes 7 % of C and 1 % of N to the total dry weight of kelp. In total, dry weight of kelp consists of 26.2 % of C and 1 % of N values falling well within independent measurements from the studies mentioned above. It should be noted that the 2 % range in kelp water content estimates translates as a 14-17 % error in kelp solids estimates, e.g., the 26.2 % C estimate translates into 22-30 %. The molar ratio from this calculation is 30, and is enveloped symmetrically by the estimates of 17:1 to 40:1 in a personal communication of North to Jackson (1977);

[p] Water content of wood is reported in the case of saturation, i.e., 100 % relative humidity (Browning 1963b). Percent content of carbon and nitrogen is typically measured on oven-dried wood, therefore percent carbon and nitrogen content in water-saturated wood had to be calculated by considering this

water content range. The chemical composition of the solids of *P. meziesii*, is as follows: cellulose (glucan) - 36.5 %; mannan - 12.3 %; arabinan - 0.4 %; galactan - 3.6 %; xylan - 3.5 %; lignin - 29.8 %; acetyl - 0.8 %; uronic anhydride - 1.3 %; and extractives - 8.4 % (Parker and LeVan 1989). Calculation of carbon was based on this composition and the following chemical formulas: cellulose (glucan) - $C_8H_{14}O_5$; mannan - $C_8H_{13}O_5$; arabinan - $C_{15}H_{24}O_{12}$; galactan - $C_6H_{11}O_6$; xylan - $C_7H_{12}O_4$; lignin - $C_{10}H_{12}O_3$; acetyl – C_2H_3O; and uronic anhydride - $C_6H_{10}O_7$ (de Leeuw and Largeau 1993). Extractives were assumed to consist of 50 % carbon (Parker and LeVan 1989). The atomic weights of 12.01, 1.01, and 16.00 were used for C, H, and O respectively. The N content of 0.2 % dry weight is consistently reported for various woods (Woods 1952, in Browning 1963a) and also supported by numerous reports on the protein content of wood (< 1 % of solids; e.g., Browning 1963a; Jones 1989; Parker and LeVan 1989; de Leeuw and Largeau 1993).

[q] Not available;

[r] From Enríquez et al. (1993). Values for kelp refer to *M. integrifolia* degradation. Values for wood refer to all types of wood reported upon, including twigs and branches.

Although kelp falls lie between whale and wood falls in many respects, they differ markedly in their surface-area-to-volume ratio. This indicator represents the amount of a fall that is accessible directly from its surface, which is where organisms (both faunal and microbial) interact with the fall material and process it. The very high surface-area-to-volume ratio of kelp falls facilitates faster fragmentation than in the case of the other two types, as well as extensive colonization and degradation by microbes (Smith 1983; Vetter 1998)

6.1.2 Impacts of LOF on sedimentary biogeochemistry

The effects of sedimentary organic enrichment around falls may be similar to those described for coastal settings by the Pearson and Rosenberg (1978) model. Indeed,

the ecological succession of benthic fauna at whale falls in the California Borderland Basins corroborates this assertion. The scavenger stage, described in the previous section, is followed by an organic enrichment stage, during which dense assemblages of rapidly-recruited, opportunistic benthic macrofauna develop (Smith et al. 1998; Smith and Baco 2003). Finally, when the bones of the whale become exposed (after 1.5-2 years), assemblages relying on bone-lipid exploitation appear, and they include a chemoautotrophic symbiont-containing contingent which relies on oxidation of sulfide generated during sulfate reduction in the bone (Smith et al. 1989; Deming et al. 1997). This period of high chemosynthetic taxon abundance is termed the sulfophilic ecological succession stage and renders the whale fall a biogenic reducing habitat (Bennett et al. 1994; Smith et al. 1998; Smith and Baco 2003). The role of sediments in the development of such biogenic reducing habitats, and the existence, magnitude, and duration of sedimentary sulfide that may sustain them, are not known. In the case of whale falls, both faunal and microbial sediment dwellers that exploit sulfide chemosynthetically have been reported (Smith et al. 1989), although the focus has been on skeleton-inhabiting chemosynthetic symbiont-containing fauna (e.g., Smith et al. 1989; Smith et al. 1998; Smith et al. 2002a).

The build-up of sulfide in sediment pore water occurs where the rates of POM supply and POM decomposition (by anaerobic dissimilatory sulfate reduction) exceed the rate of re-supply of oxygen by diffusion (Chapter 5, Section *5.4*; Westrich and Berner 1984). The quality of MOM, for both metazoa and microbes, will affect the rise of sulfide. In the case of metazoa, high-quality LOF will be more palatable, will be processed faster, and will result in higher MOM accumulation rates in the sediment. In

turn, sedimentary microbiota will decompose labile MOM faster (Lyons and Gaudette 1979), simultaneously counter-acting MOM accumulation in the sediments as well as oxygen re-supply, thus giving rise to moderate organic enrichment and sulfidic conditions respectively. For example, two of the three LOF investigated in this study, whale and kelp falls, would likely generate high MOM accumulation rates and sedimentary decomposition rates because of their high quality, as indicated by low C:N ratios and nutritional structural macromolecules (Table 6.1). On the other hand, low-quality LOF such as wood (indicated by very high C:N ratios and refractory structural macromolecules) may result in a combination of relatively low MOM accumulation rates but also slow sedimentary microbial decomposition rates. The end result will be substantial organic enrichment of sediments surrounding wood falls (because of the high organic carbon content of wood MOM), as well as modest sulfide build-up, if at all present.

A comparison of LOF of different quality and known age using a time-series sampling strategy would be appropriate to test these predictions. Past findings illustrate the importance of knowing the age of a fall and the particular stage of processing. Smith et al. (1998) measured sedimentary total organic carbon (TOC) and total nitrogen (TN), as well as pore water sulfide (ΣH_2S), in sediments associated with a whale fall in Santa Catalina Basin. They observed neither organic enrichment nor sulfidic conditions in the sediment (Figures 5.2 and 5.3). This whale fall was later dated at 35 ± 12 years using radioisotope disequilibria on the whale bones (Schuller et al. 2004). Presumably, this fall had progressed beyond the stage of organic enrichment and sulfide generation in surrounding sediments. This finding constrained estimates of the duration of

biogeochemical impacts of LOF on sediments. The same measurements performed on a much younger (1.5-18 months old) experimental whale fall in Santa Cruz basin were more illuminating of the shorter time-scales of impact duration. The results showed a doubling of sedimentary TOC and increases of 3 orders of magnitude in pore water sulfide in sediments adjacent to the fall (Figure 5.4; M. E. Torres and C. R. Smith, unpublished data). Further monitoring of this fall would allow constraining of fall effects on sedimentary biogeochemistry and the development and maintenance of biogenic reducing habitats.

6.1.3 Study objectives

The following objectives were addressed with this study:

a) to test whether LOF quality affects organic enrichment and sulfide generation, and

b) to predict the development, magnitude and duration of biogenic reducing conditions in LOF-associated sediments in relation to fall type or quality.

The comparison of the three LOF types and their quality (section *6.1.1*), and the available biogeochemical data (section *6.1.2*), suggest that there are strong relationships between sedimentary biogeochemistry and the quality and age of a fall. Probable relationships between LOF type, organic enrichment, sulfidic conditions, and fall age can be hypothesized (Figure 6.1).

It is predicted that whale and kelp LOF are processed quickly by scavengers over weeks to months (Smith 1983; Smith and Baco 2003), resulting in high MOM supply rates to the sediments.

Because of its high lability, whale MOM is predicted to decompose at accelerated rates resulting in modest organic enrichment and high sulfide content. Kelp MOM is predicted to show a similar trajectory as whale MOM, despite its moderate lability, because of a faster scavenger processing rate due to its high surface-area-to-volume ratio.

In contrast, sediments associated with wood LOF are predicted to experience a slow supply of refractory organic material, which accumulates to substantial concentrations and decomposes slowly and, therefore, aerobically.

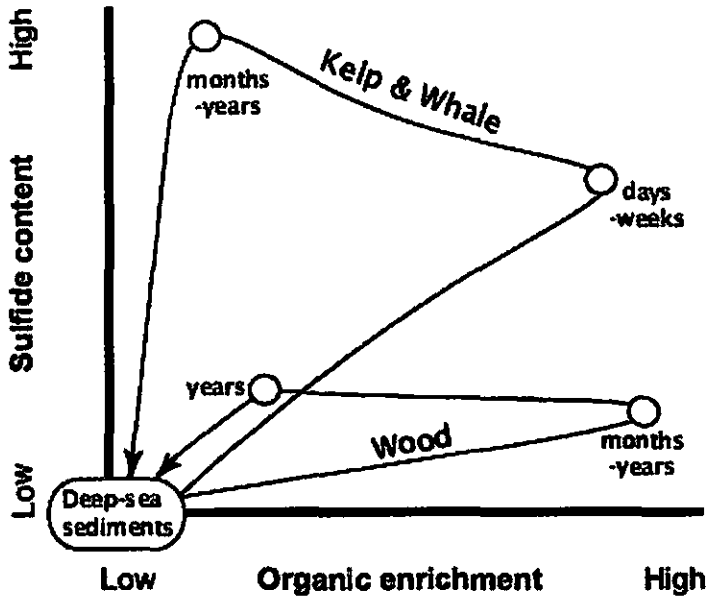

Figure 6.1 Hypothetical temporal progression of biogeochemical conditions of surface sediments (0-1 cm) associated with three LOF types.

The objectives and predictions of this study were addressed with a survey of sediments surrounding natural and artificial LOF (whale, kelp and wood) in the California Borderland Basins region. Organic enrichment and sulfidic conditions for each fall type and age were compared to construct a prospective timeline of biogenic reducing conditions in LOF-associated sediments.

6.2 Study sites and methods

6.2.1 Study sites: natural and experimental implantations

This study was undertaken as a component of a multi-year research project focusing on succession of chemoautotrophic communities at large falls and their affinity to chemoautotrophic communities of seeps and vents. One of the goals of this project is to compare whale fall ecology and biogeochemistry with those of other common LOF (Smith, personal communication). To achieve this goal, experimental implantations of kelp and wood parcels were carried out around known and well-studied whale falls in the California Borderland Basins region (Figure 6.2, Table 6.2).

The troughs, basins and ridges that characterize the California Borderland Basins region have been relatively well studied, due to their proximity to large urban centers and the economic significance of their natural resources (see reviews by Emery 1960; Dailey et al. 1993). The seafloor habitat of the two main study sites, the Santa Cruz and Santa Catalina Basins, is characterized by adequate bottom water oxygen concentrations, e.g., reported at 18 and 36 $\mu mol \cdot L^{-1}$ respectively by Emery (1960, p. 108), unlike inner basins such as the Santa Barbara Basin which may be anoxic. Even though the sedimentation

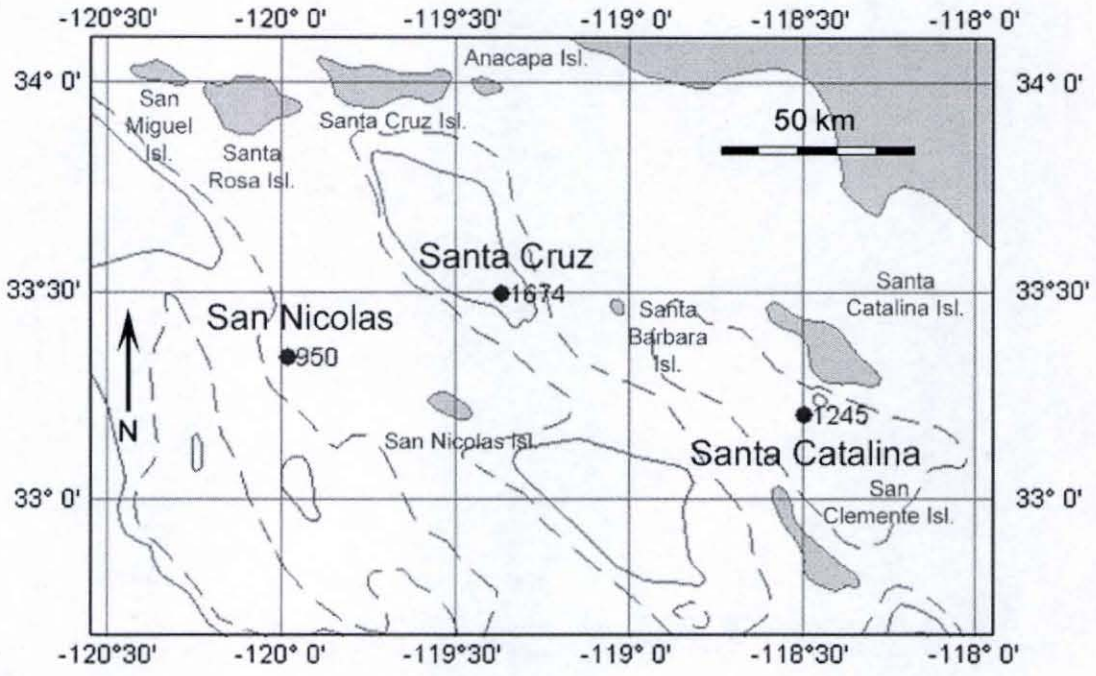

Figure 6.2 Sites of studied large organic falls in the California Borderland basins (numbers indicate site depth). Depth contours of 1000 m (dashed lines) and 1500 m (solid lines) are also shown. The site identified as "San Nicolas" is actually on the Santa Rosa-Cortes Ridge (Emery 1960, Chart 1).

Table 6.2 Large organic falls (LOF) sampled in this study. The Santa Catalina Basin and San Nicolas whale falls are natural, whereas all the other falls are experimental.

Fall type	Region [a]	Exp. CRS #	Age (y) at sampling	Latitude (N)	Longitude (W)	Depth (m)	Mass (kg)
Whale	SCrB	-	4.5	33° 29.61'	119° 22.03'	1674	24,300 [c]
	SCB	-	49.4 ± 12.4 [b]	33° 11.72'	118° 29.48'	1244	57,500 [c]
	SN	-	75.2 ± 18.4 [b]	33° 20.35'	119° 58.89'	951	40,000 [c]
Kelp	SCrB	806	0.25	33° 29.68'	119° 22.03'	1675	100 [e]
	SCrB	799	0.5	33° 29.61'	119° 22.06'	1674	100 [e]
	SCB	804	0.25	33° 12.35'	118° 29.46'	1244	100 [e]
	SCB	803	0.5	33° 12.32'	118° 29.54'	1245	100 [e]
Wood	SCrB	800	0.5	33° 29.66'	119° 22.06'	1674	85 [f]
	SCrB	397	3.0	33° 29.61'	119° 21.74'	1672	85 [f]
	SCB	801	0.5	33° 12.32'	118° 29.55'	1244	85 [f]
	SCB	398	3.0	33° 11.75'	118° 29.33'	1244	85 [f]

[a] Abbreviations: SCrB – Santa Cruz Basin, SCB – Santa Catalina Basin, SN – San Nicolas Slope.

[b] Estimated using radioisotope disequilibria (Schuller et al. 2004).

[c] Calculated anew based on the reported lengths in Smith and Baco (2003), 13 m and 21 m for the SCrB and SCB whale falls respectively. Weights were calculated using Lockyer's formula, Mass (tons) = a×Length (m)^b, and species-specific constants determined by Woodward et al. (2006): for the SCrB whale fall (*E. robustus*), a = 0.0054 and b = 3.28, and for the SCB whale fall (*B. musculus*), a = 0.0029 and b = 3.25.

[e] Reported in Smith and Baco (2003).

[e] Kelp parcels were weighed onboard during parcel preparation.

[f] Wood parcel weights were estimated by multiplying the total volume of the 22 wooden plank (240 cm × 9.0 cm × 3.8 cm × 22 planks = 182000 cm^3) by the density of wood (0.465 $g \cdot cm^{-3}$; Table 6.1).

---

rates of organic carbon in the basins are relatively low, 1.2 and 1.3 $mg \cdot cm^{-2} \cdot y^{-1}$ respectively (Emery 1960; Schwalbach and Gorsline 1985; Eganhouse and Venkatesan 1993), the weight fraction of organic carbon in sediments is fairly high and constant with sediment depth, ranging between 4 and 10 %, because of relatively low dilution from terrestrial sources of detritus (Emery 1960; Schwalbach and Gorsline 1985; Shaw et al. 1990). Reimers (1987) and Reimers and Smith (1986) have shown that in Santa Catalina Basin the vast majority of organic carbon remineralization in basin sediments takes place within the top few mm of the sediment column. The conclusion that is drawn from this is that the majority of the deposited organic carbon must be fairly refractory and escapes degradation at a relatively shallow depth. As a consequence, early diagenesis in basins of the region with adequate bottom water oxygen concentrations (> 16 $\mu mol \cdot L^{-1}$) is dominated by aerobic degradation as well as suboxic processes, such as nitrate, iron and manganese reduction (Shaw et al. 1990; Eganhouse and Venkatesan 1993). Sulfate reduction plays a relatively minor role as is evident from dissolved sulfate pore water profiles, which remain constant at bottom water concentrations down to at least 1 m (Berelson et al. 1987).

The positions of LOF relative to each other in the sites in Santa Cruz and Santa Catalina Basins are shown in Figure 6.3 (a) and (b) respectively. Two of the three whale

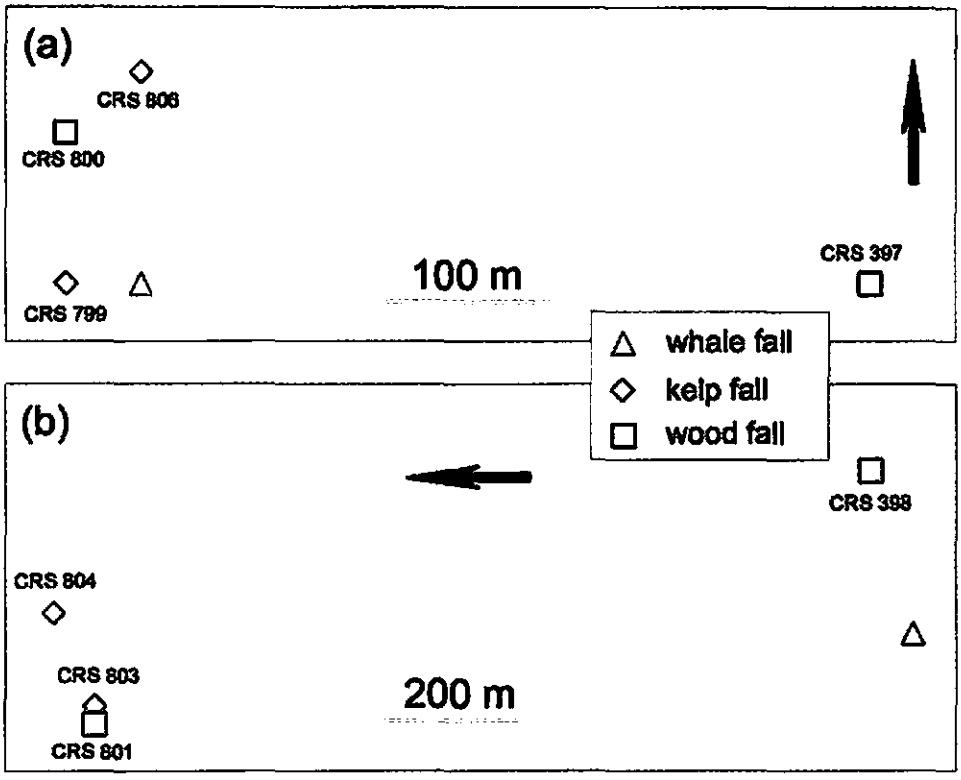

Figure 6.3 Large organic fall site charts showing the distance between all the falls at each site: (a) Santa Cruz Basin site (average depth = 1674 m), and (b) Santa Catalina Basin (average depth = 1245 m). CRS codes refer to implantation experiments (see Table 6.2 for more details). The arrows point towards the north.

falls visited in this study were natural. The Santa Catalina Basin whale fall was the first one to be discovered, in 1987 (Smith et al. 1989). It was associated with a 21-m balaenopterid skeleton, and has been the object of extensive ecological and biogeochemical studies (Allison et al. 1991; Bennett et al. 1994; Deming et al. 1997; Feldman et al. 1998; Smith et al. 1998; Smith and Baco 2003). The whale skeleton on the continental slope off San Nicolas Island was discovered by the United States Navy in 1993, and has been sampled for community composition studies (Baco et al. 1999; Baco-Taylor 2002; Baco and Smith 2003). Both of these skeletons have been dated with a radioisotope disequilibrium method, and in 2002 they were found to be 49.4 ± 12.4 and 75.2 ± 18.4 years-old respectively (Schuller et al. 2004). The third whale fall, in Santa Cruz Basin, was experimentally implanted in April of 1998 using a 13-m carcass of a mature gray whale, which died of natural causes, and has been visited on multiple occasions (1.5 months - 6.5 years; Baco-Taylor 2002).

Kelp and wood implantations were conducted in the vicinity of the two youngest whale falls in Santa Cruz and Santa Catalina Basins (Figure 6.3). Kelp parcels were deployed in late April-early May 2002 (CRS 799 and 803) and July 2002 (CRS 804 and 806) (Table 6.2). Wood parcels were deployed in October 1999 (CRS 397 and 398) and late April-early May 2002 (CRS 800 and 801) (Table 6.2, Smith et al. in preparation). All deployments took place from the R/V Sproul, except the October 1999 deployment, which was conducted from the R/V Atlantis II. To make a kelp parcel, several freshly collected California giant kelp, *Macrocystis Pyrifera*, including holdfasts were placed in a 10 cm-mesh nylon net bag to bring the total weight to approximately 100 kg. Wood parcels consisted of 22 commercially available untreated Douglas fir (*P. menziesii*)

planks (244 cm × 9.0 cm × 3.8 cm), nailed together to form an 85 kg, 2.40 m-long block. Because the retrieval of wood implantations has been problematic in the past due to borers' activity (e.g., Turner 1973), smaller pieces of plank approximately 30 cm long were placed in 5-cm-mesh nylon net bags and attached to the main block to allow their easy retrieval for ship-board examination and sampling. Both types of parcels were outfitted with heavy metal ballast, an acoustic transponder and a glass float to allow easier visual relocation (Smith et al. in preparation).

6.2.2 Sampling and chemical analyses

Samples were collected by the ROV Tiburon operated from the carrier vessel R/V Western Flyer during a cruise on October 2002. Plastic tubing sections 30 cm-long and 7 cm in diameter were used to collect replicate sediment cores at various distances from each fall. In most cases, these cores were collected along one or more transects running outwards from randomly selected points adjacent to the fall. Occasionally, lost or damaged cores were replaced with new ones taken on a random heading at the appropriate distance from the fall to avoid re-sampling previously disturbed sediments. Cores were always collected at the sediment-fall interface, defined as the location where the fall stopped covering the seafloor directly, and designated as the distance of 0 m. In the case of the whale falls, additional cores were taken at 1, 2-3, and 9 m, with the exception of the Santa Catalina Basin whale fall, which was only sampled at 0 m on this particular cruise (Smith et al. 1998). These distances were selected because they envelope previously observed zones of whale-fall biogeochemical influence (Smith et al. 1998; Baco-Taylor 2002; Smith et al. 2002a; Smith and Baco 2003). In the case of kelp and

wood, the selected transect distances away from the fall were shorter, because of the smaller expected biogeochemical footprint, and extended to 1.5-2 m.

With the exception of the Santa Cruz Basin whale fall, cores for pore water sulfide were only taken from the immediate vicinity of each fall (0 m). This was done in part due to logistical constrains with regards to the processing time required for sample extraction and collection. Prioritization of core collection also took into account the smaller expected footprint of the smaller falls (kelp and wood), but also the lack of previous evidence of sulfidic sediments around the older whale falls. In the case of the Santa Cruz Basin whale fall, extensive microbial mats covering the bones and adjacent sediment verified that the fall community had entered the sulfophilic stage and that this study was an excellent opportunity to conduct a spatial assessment of sulfide presence. For this reason, additional cores were collected at 1, 3 and 9 m from the whale fall. Background cores were collected at random locations at distances of approximately 100 m from the nearest known LOF.

After each dive, cores were brought on deck and distributed to various stations, where they were sampled by other investigators for macrofauna-, meiofauna- and microbial-related analyses, and also for pore water sulfide, TOC and TN analyses. An inventory of the cores from the 2002 cruise used for this study is listed in Table 6.3.

An additional cruise on the R/V Western Flyer in 2004 provided the opportunity to collect and analyze sediment pore water for ΣH_2S, and to obtain supplementary fall age-related information on ΣH_2S concentrations. The falls sampled during the 2004 cruise were the Santa Cruz Basin whale fall and Santa Catalina Basin wood fall CRS 800, which were 5.8 years old and 1.83 years old respectively at that point (Table 6.2).

Table 6.3 Inventory of cores collected for chemical analyses during the 2002 cruise.

Location	Fall type	Exp. CRS #	Age (y) at sampling	Distance (m)	No. of cores TOC&TN	No. of cores $[\Sigma H_2S]$
Santa Cruz Basin	Whale	-	4.5	0.1	5	3
				1	5	2
				3	5	2
				9	5	1
	Kelp	806	0.25	0.1	-	1
				0.5	-	1
				1	-	-
		799	0.5	0.1	2	2
				1	2	-
				1.5	2	-
	Wood	800	0.5	0.1	3	2
				1	1	-
				1.5	2	-
				2	1	-
		397	3	0.1	2	2
				1	2	-
				1.5	2	-
				2	2	-
				4	2	-
	Background	-	-	100	5[a]	2
Santa Catalina Basin	Whale	-	49	0.1	-	2
	Kelp	804	0.25	0.1	2	2
				1	2	-
				1.5	2	-
		803	0.5	0.1	2	2
				0.5	2	-
				1	2	-
				2	1	-
	Wood	801	0.5	0.1	5	2
				1	2	-
				1.5	2	-
				2	1	-
		398	3	0.1	3	2
				1	2	-
				1.5	2	-
				2	2	-
	Background	-	-	100[b]	3	-
San Nicolas slope	Whale	-	75	0.1	3	2
				1	2	-
				2	2	-
				9	2	-

[a] One core is 100 m away from the whale fall and three cores are 100 m away from wood fall CRS 397.
[b] Distance of 100 m from whale fall.

6.2.2.1 TOC and TN

For logistical reasons, only surface sediment (0-1 cm) was analyzed for TOC and TN analysis. After sampling, the sediment was stored at -40° C. Processing and analysis took place with the methods of Verardo et al. (1990) using a Perkin-Elmer 2400 CHN Elemental Analyzer. Inorganic carbon was removed by acidification with repeated additions of sulfurous acid (volume fraction of 8 %) until no effervescence was observed. Standards were made with acetanilide. Blanks consisted of both unacidified and acidified cups (both giving minor signals of TOC and TN). The limit of detection of this method was 1 μg and 1.2 μg for C and N respectively, while the precision was 0.3 % and 0.4 % for C and N respectively.

6.2.2.2 Sulfide

Cores for sulfide sampling were immediately placed in a glove bag, which was flushed and filled with nitrogen three times before being sealed, and sliced in 1-3 cm intervals. Sediment from each interval was transferred into 50-mL syringes, whose internal tip end was fitted with a fine-diameter (10-μm) Nytex screen. Polycarbonate 0.2-μm in-line filters were attached onto the syringes, and gradual and modest pressure was applied on the syringe pistons using a press to extract the pore water (see discussion on effects of pressure by Jahnke 1988). The first milliliter of filtered pore water obtained from each sample was discarded and the second was transferred into a scintillation vial that contained 0.5 mL of 0.05 $mol \cdot L^{-1}$ zinc acetate. Samples thus fixed are stable for several weeks (Cline 1969).

In the laboratory, all samples were analyzed for dissolved sulfide using the colorimetric method of Cline (1969). This method determines the concentration of all species of dissolved sulfide, i.e., total dissolved sulfide, ΣH_2S ($H_2S + HS^- + S^{2-}$). Fifty microliters of a diamine reagent (made by adding 4 g of ferric chloride and 1.6 g of N,N-dimethyl-p-phenylene diamine sulfate to 100 mL of 6 $mol \cdot L^{-1}$ HCl) were added to each sample. After 20 min, 2 mL of DIW were added and the sample was allowed to sit for another 15 min. The sample absorbance at 670 nm was measured using a spectrophotometer. Standards were made by diluting 0.12 g of sodium sulfide nonnahydrate in 100 mL of DIW (previously deareated with N_2). The resulting 5 $mmol \cdot L^{-1}$ solution was diluted further to generate standards in the range of 50-500 $\mu mol \cdot L^{-1}$. Due to the high concentrations expected in a number of cores, samples were diluted *a priori* and analyzed. If concentrations were very low, these samples were re-run at a lower degree of dilution to corroborate the values obtained. The limit of detection was 2 $\mu mol \cdot L^{-1}$, and the precision was 1.9 %.

6.3 Results

6.3.1 Qualitative observations

All background core sediments were light-colored and cohesive, exhibiting little variation in appearance and texture with depth, except for a surface highly fluidized layer a few millimeters thick. Sediment proximal to the Santa Cruz basin whale fall was black, suggesting a high content of iron monosulfides. The surface layer down to 3 to 4 cm was relatively fluidized and contained a high number of large particles (> 1 cm), probably

molluscan shells, while deeper sediment was more cohesive. Tissue fragments and mucous masses were also a common component of the sediment down to several centimeters and, together with shell fragments, added a high level of heterogeneity to the sediment fabric. Evidence of the above was lacking as one moved away from the Santa Cruz basin whale fall, and also at the other two whale falls. Sediments were more oxidized and more cohesive at these locations, while at the Santa Catalina whale fall whole and fragmented clam shells were present at or near the sediment surface.

Many cores adjacent to kelp falls exhibited a varve-like pattern in sediment color, in which millimeter-to-sub-centimeter thick layers of black sediment were interspersed with lighter-color sediment. This may suggest sub-surface burial of kelp matter at locations which constitute sites of intense reduction, surrounded by less reduced sediment. This heterogeneity may not be detected by the sampling technique, especially at thicker layers. Most wood fall cores were light-colored and presumably fairly oxidized, while only one at a 3 year-old fall included a black (presumably sulfidic) sediment layer.

6.3.2 TOC and TN

The results of the TOC and TN analyses are shown in Table 6.4 and Figure 6.4-Figure 6.10. Background values show enough broad variation to match, in most cases, the range for values measured along transects away from all falls (Table 6.4). Exceptions to this are almost always samples adjacent to the falls (0 m).

6.3.2.1 Whale falls

Values of TOC and TN content away from the 4.5 year-old whale fall in Santa Cruz Basin follow two trends (Figure 6.5). In three of the four transects (Transects 1, 4,

Table 6.4 Background levels of TOC and TN content, and TOC:TN ratio in surface sediments (0-1 cm) of Santa Cruz and Santa Catalina Basins. Values of individual samples, as well as mean and standard error (SE) for every basin are shown. Previously measured values at 100 m from the Santa Catalina whale fall (Smith et al. 1998) are also reported for comparison.

Location	Weight fraction of TOC (%)	Weight fraction of TN (%)	TOC:TN (molar)
Santa Cruz Basin	6.7	0.55	14.3
	7.4	0.63	13.7
	7.2	0.60	14.0
	7.3	0.63	13.6
	7.0	0.58	14.0
Mean ± SE	*7.1 ± 0.06*	*0.60 ± 0.01*	*13.9 ± 0.06*
Santa Catalina Basin	6.5	0.52	14.6
	6.8	0.56	14.2
	7.1	0.57	14.7
Mean ± SE	*6.8 ± 0.11*	*0.55 ± 0.01*	*14.5 ± 0.9*
Santa Catalina Basin, 1988 (Smith et al. 1998)	7.1	0.65	12.7
	6.3	0.60	12.2

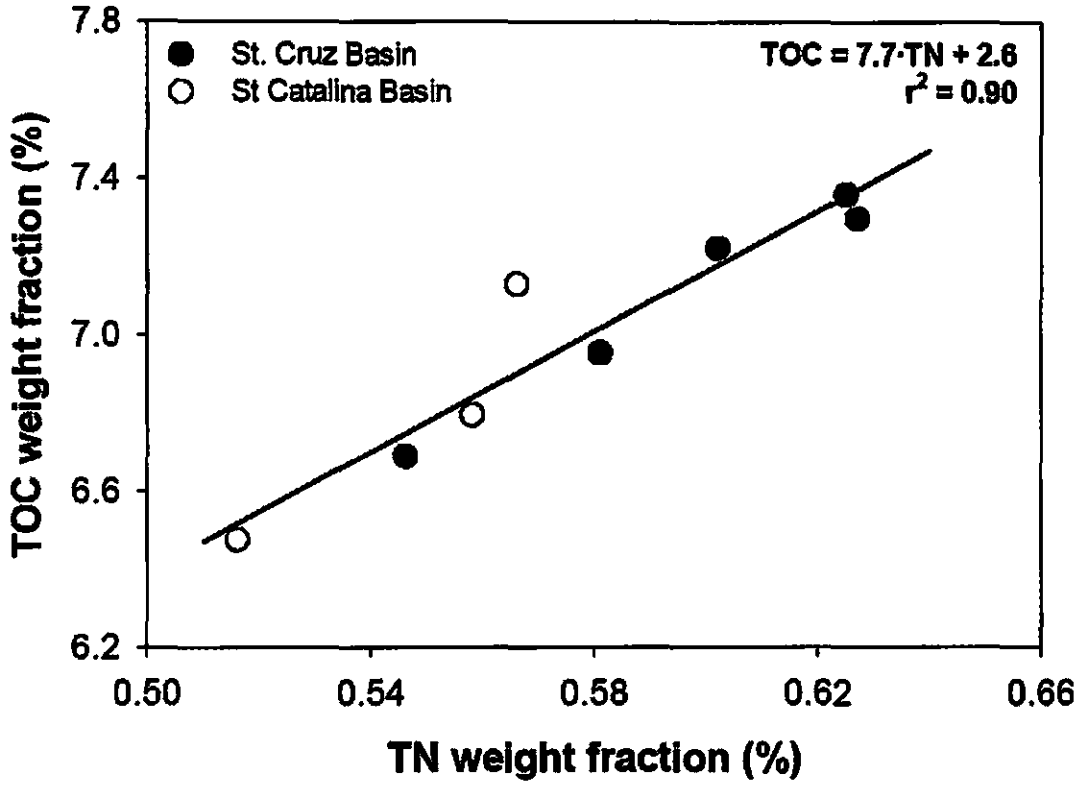

Figure 6.4 TOC and TN content in background sediments of Santa Cruz and Santa Catalina Basins (Table 6.4).

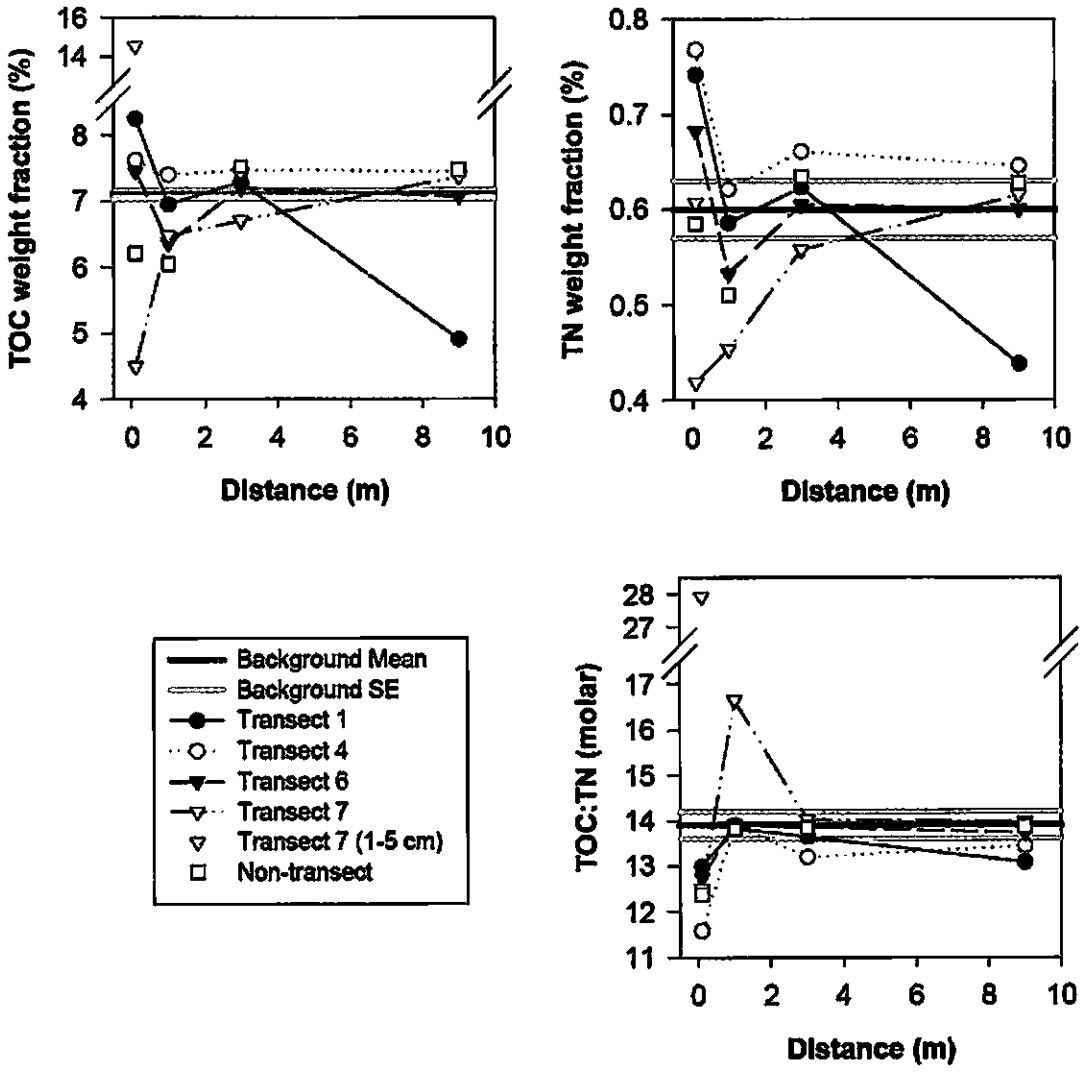

Figure 6.5 TOC and TN content, and TOC:TN molar ratio at isolated distances away from a 4.5 year-old whale fall in Santa Cruz Basin. The background mean and standard error (SE) were calculated from sediment samples (n=4) collected 100 m away from any known LOF at this site.

and 6), values are elevated at 0 m, drop to a minimum at 1 m, and reach background levels beyond this point. In the fourth transect (Transect 7), values are at a minimum at 0 m and reach background levels at 3 m. When plotted against distance, the molar ratio of the two measured parameters, TOC:TN, reveals a distinct elemental signature only at the samples 0 m from the fall, while background level signatures are indicated at almost all remaining samples. All four transects are characterized by TOC:TN minima occurring at 0 m.

The trend away from the 75 year-old San Nicolas slope whale fall (Figure 6.6) mimics that of the dominant trend in the Santa Cruz Basin whale fall. Values of TOC and TN content are elevated at 0 m, drop to a minimum at 1 m, and increase slightly beyond this distance. The ratio of TOC:TN is lowest at 0 m and levels off at 1 m. One notable aspect of these data is the high value of TOC content at this location. Although true background samples were not collected, the samples 9 m away from the fall, which are at most mildly affected by the fall presence, have values of TOC content in the region of 8.5-9.0 %.

6.3.2.2 Kelp falls

Sediments adjacent to kelp falls show distinct enrichment in TOC and TN (Figure 6.7-Figure 6.8). This is most evident in the case of the 3 month-old kelp fall in Santa Catalina Basin (Figure 6.8), where both TOC and TN content are substantially elevated above background in surface sediments adjacent to the fall (0 m) and reach background or lower levels beyond that.

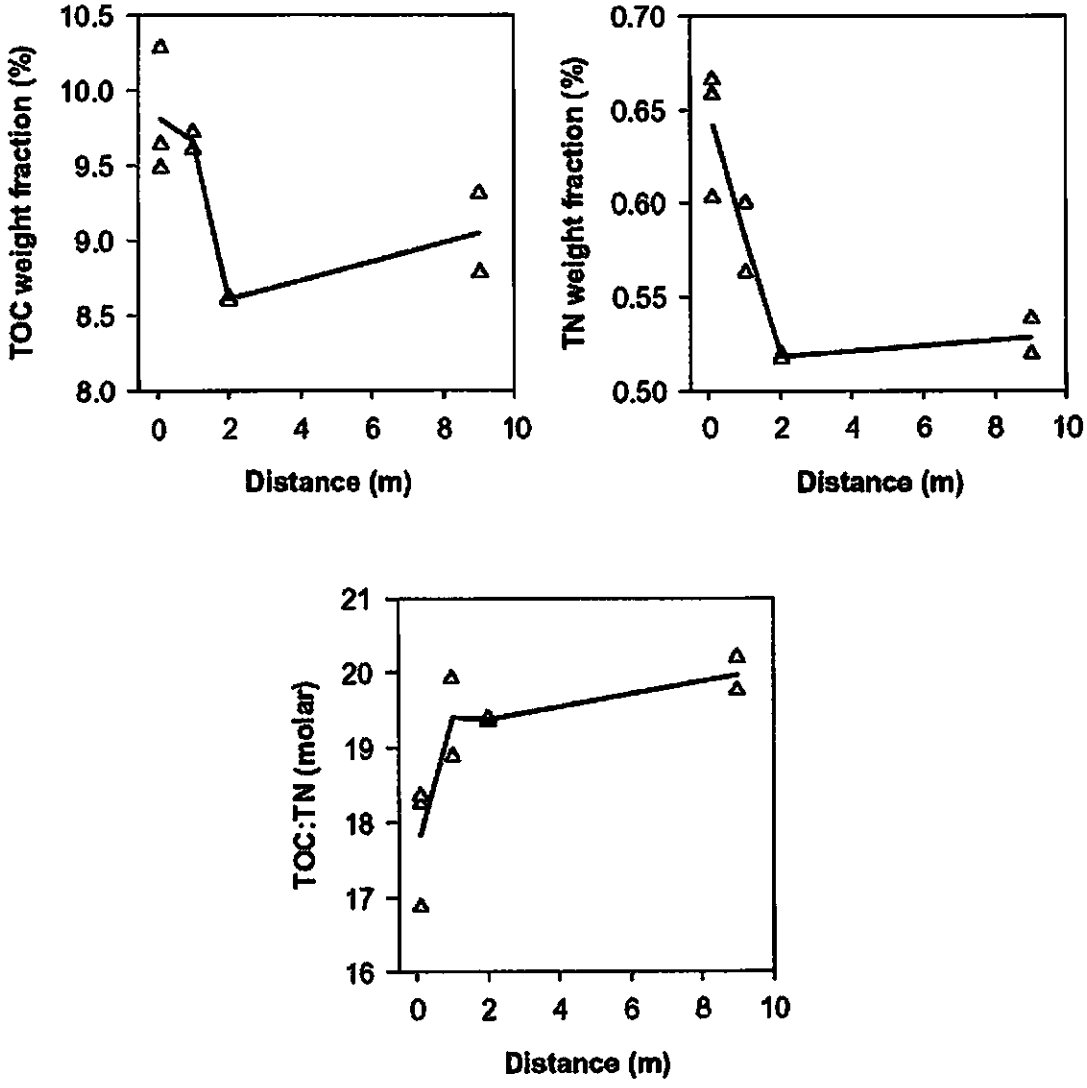

Figure 6.6 TOC and TN content, and TOC:TN molar ratio at isolated distances away from a 75 year-old whale fall on the San Nicolas slope. The cores were collected on a single transect during one dive. The black lines link the average values of each parameter at each distance from the fall along this transect. No background levels are available from this fall.

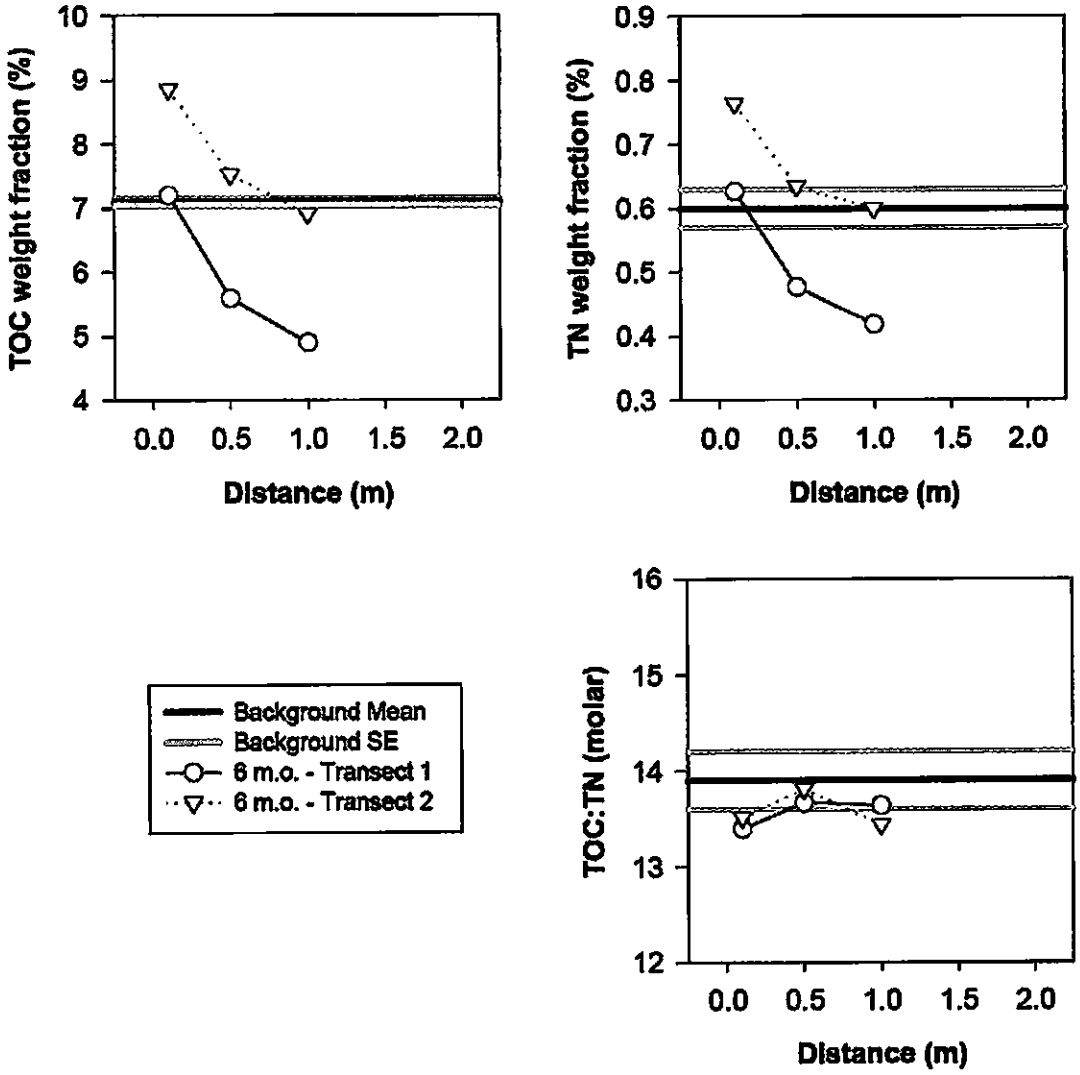

Figure 6.7 TOC and TN content, and TOC:TN molar ratio at isolated distances away from a 6 month-old kelp fall, CRS 799, in Santa Cruz Basin. The background mean and standard error (SE) were calculated from sediment samples (n=4) collected 100 m away from any known LOF at this site.

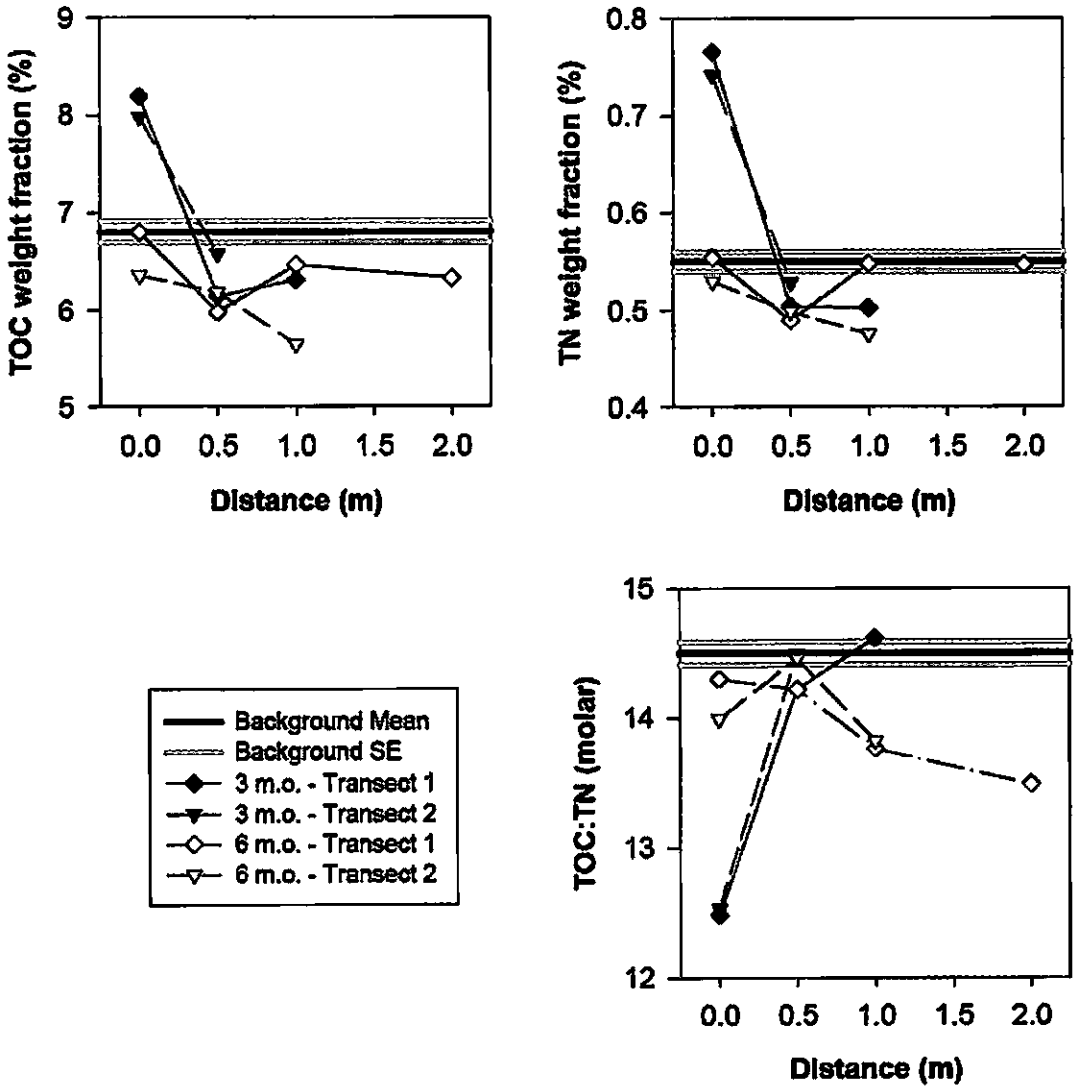

Figure 6.8 TOC and TN content, and TOC:TN molar ratio at isolated distances away from a 3 month-old kelp fall, CRS 804, and a 6 month-old kelp fall, CRS 803, in Santa Catalina Basin. The background mean and standard error (SE) were calculated from sediment samples (n=3) collected 100 m away from any known LOF at this site.

The data from sediments adjacent to 6 month-old kelp falls show interesting patterns. Although both transects away from a 6 month-old fall in Santa Cruz Basin show the same trend in TOC and TN content (maximum values at 0 m), their values are significantly offset relative to background value ranges (Figure 6.7). There is good agreement between one of these two transects (Transect 1) and the two transects from the 6 month-old kelp fall in Santa Catalina Basin (Figure 6.8), which all indicate enrichment in carbon close to the falls.

The trends in TOC:TN indicate a distinct signal in the case of the sediments adjacent to the 3 month-old fall in Santa Catalina Basin (Figure 6.8), presumably due to the presence of N-enriched organic matter from the kelp fall. Another notable trend in TOC:TN is the low values registered up to 2 m from the 6 month-old kelp falls at the same location (Figure 6.8). These low values are driven by TOC depletion coupled with background levels of TN in those samples.

6.3.2.3 Wood falls

Of all treatments, sediments adjacent to 3 year-old wood falls in both basins show, by far, the most dramatic deviations from background TOC content (Figure 6.9-Figure 6.10). Sediments adjacent to 3 year-old wood falls (distance of 0 m) contain 4 times the TOC present in background sediments, while 0.5 year-old wood falls show only mild enrichment above background. The values of % TN hover around those of background sediments except in the case of sediments adjacent to 3 year-old wood falls, which generally have 0.25-0.5 times the TN content of background sediments. The majority of samples maintain background TOC:TN values. The exception is sediments at

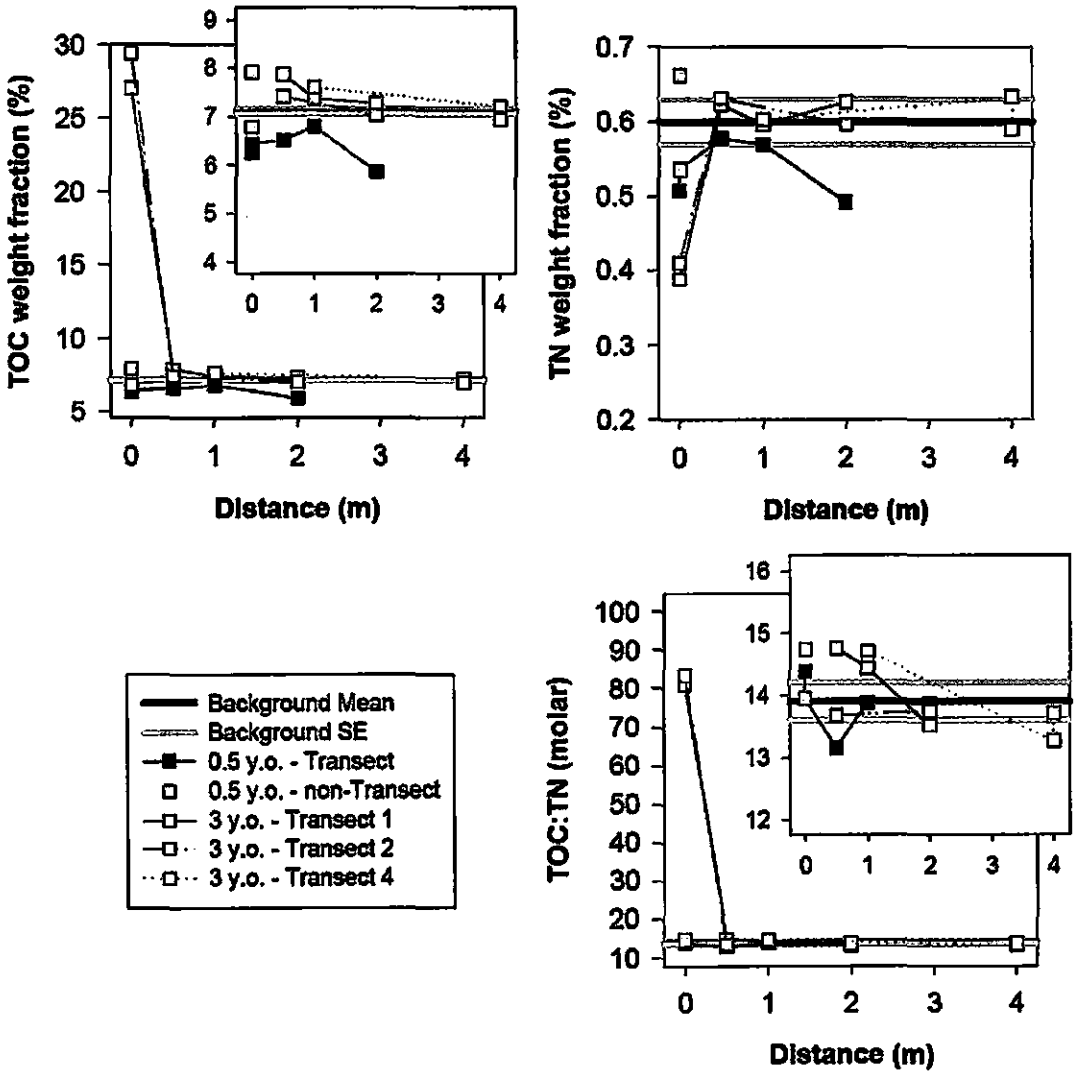

Figure 6.9 TOC and TN content, and TOC:TN molar ratio, at isolated distances away from a 6 month-old wood fall, CRS 800, and a 3 year-old wood fall, CRS 397, in Santa Cruz Basin. The background mean and standard error (SE) were calculated from sediment samples (n=4) collected 100 m away from any known LOF at this site. Insets are plots that exclude data at 0 m from the 3-year-old fall (n=2).

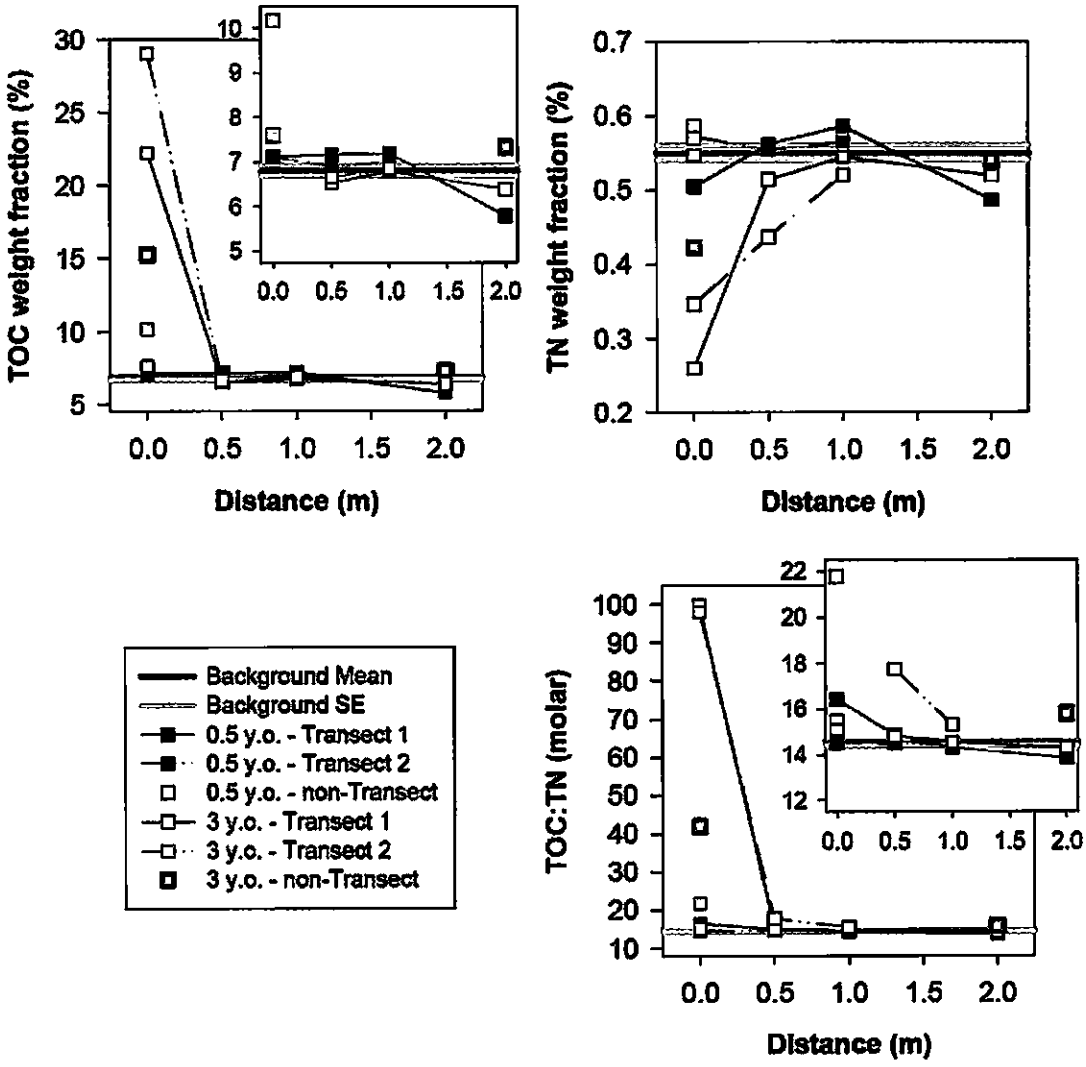

Figure 6.10 TOC and TN content, and TOC:TN molar ratio at isolated distances away from a 6 month-old wood fall , CRS 801, and a 3 year-old wood fall, CRS 398 in Santa Catalina Basin. The background mean and standard error (SE) were calculated from sediment samples (n=3) collected 100 m away from any known LOF at this site. Insets are plots that exclude data at 0 m from the 3-year-old fall (n=3).

0 m sediments from 3 year-old falls which are characterized by TOC:TN values that are very high for marine sediments, 4-5 times those of background.

6.3.3 Sulfide

6.3.3.1 Whale falls

The pore water ΣH_2S concentration profiles observed in sediments adjacent to the 4.5-year-old Santa Cruz whale fall (0 m) revealed high heterogeneity, varying by three orders of magnitude at the surface while converging to values of 1-10 $mmol \cdot L^{-1}$ at depth (< 11 cm, Figure 6.11). The profiles obtained at the same whale fall 1.3 years later (i.e., at a fall age of 5.8 years, Figure 6.12) show that pore water sulfide levels slightly decreased during this time period, while the high heterogeneity between profiles is maintained. The 49-year-old Santa Catalina Basin whale fall showed slight enrichment in pore water sulfide over previously reported background values (Smith et al. 1998), especially at depth (Figure 6.13), while the 75-year-old San Nicolas slope whale fall displayed a more characteristic profile: undetectable levels at the surface and increase in concentration with depth. It is possible that background sediment at this shallower site (950 m) does sustain some degree of sulfate reduction by increased POM supply from the euphotic zone.

6.3.3.2 Kelp falls

Sulfidic conditions were pronounced at 3-month-old kelp fall-associated sediments, while at 6-month-old fall-associated sediments the levels return to those of background sediments (Figure 6.14 Figure 6.15). The depth profile was unusual in that it

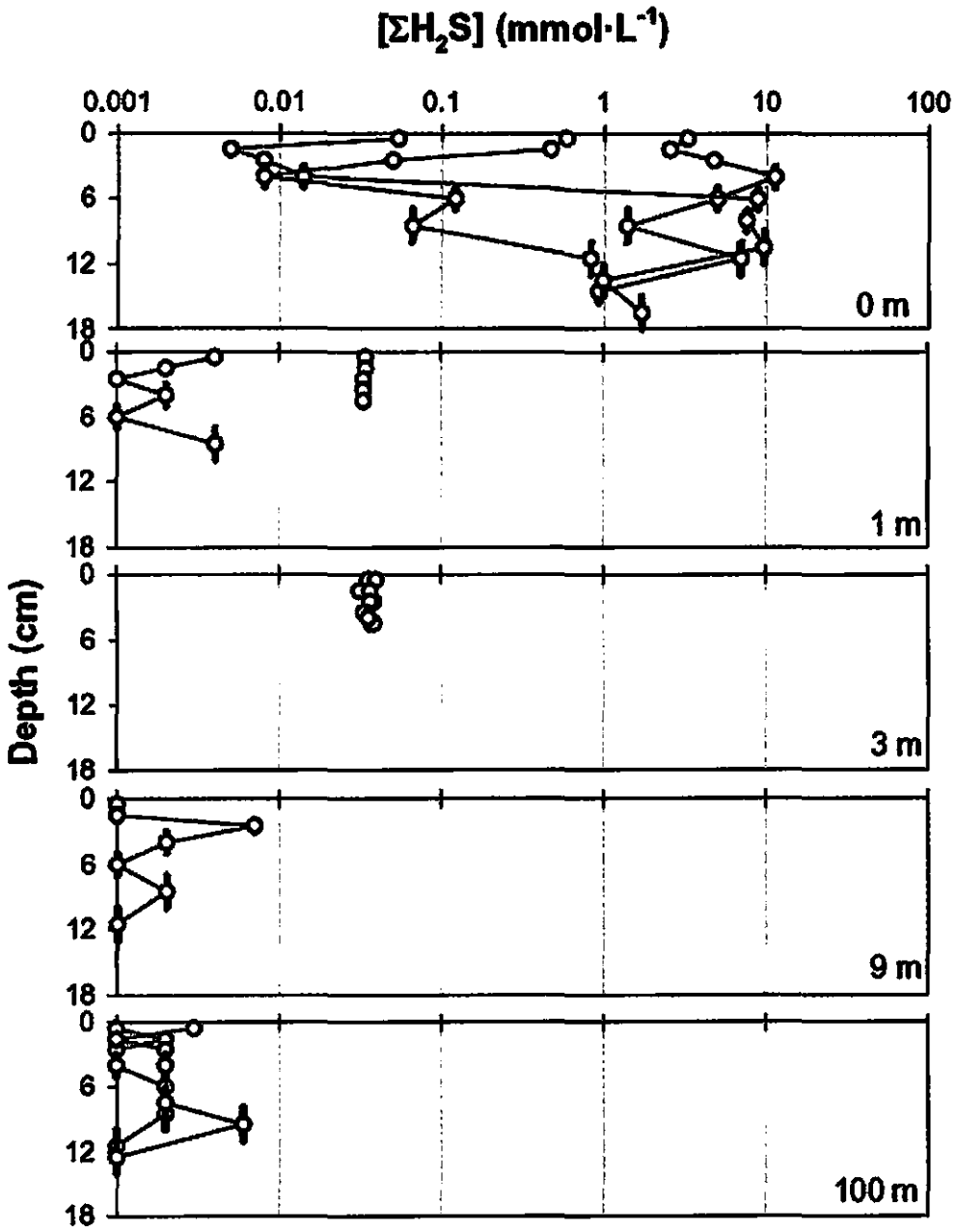

Figure 6.11 Total dissolved sulfide concentrations in pore water from cores associated with a 4.5 year-old whale fall in Santa Cruz Basin. Cores were taken at 0 (n=3), 1 (n=2), 3 (n=2), 9 (n=1), and 100 (n=2) m (background) away from the fall. Black vertical lines indicate the depth range of each sediment sample.

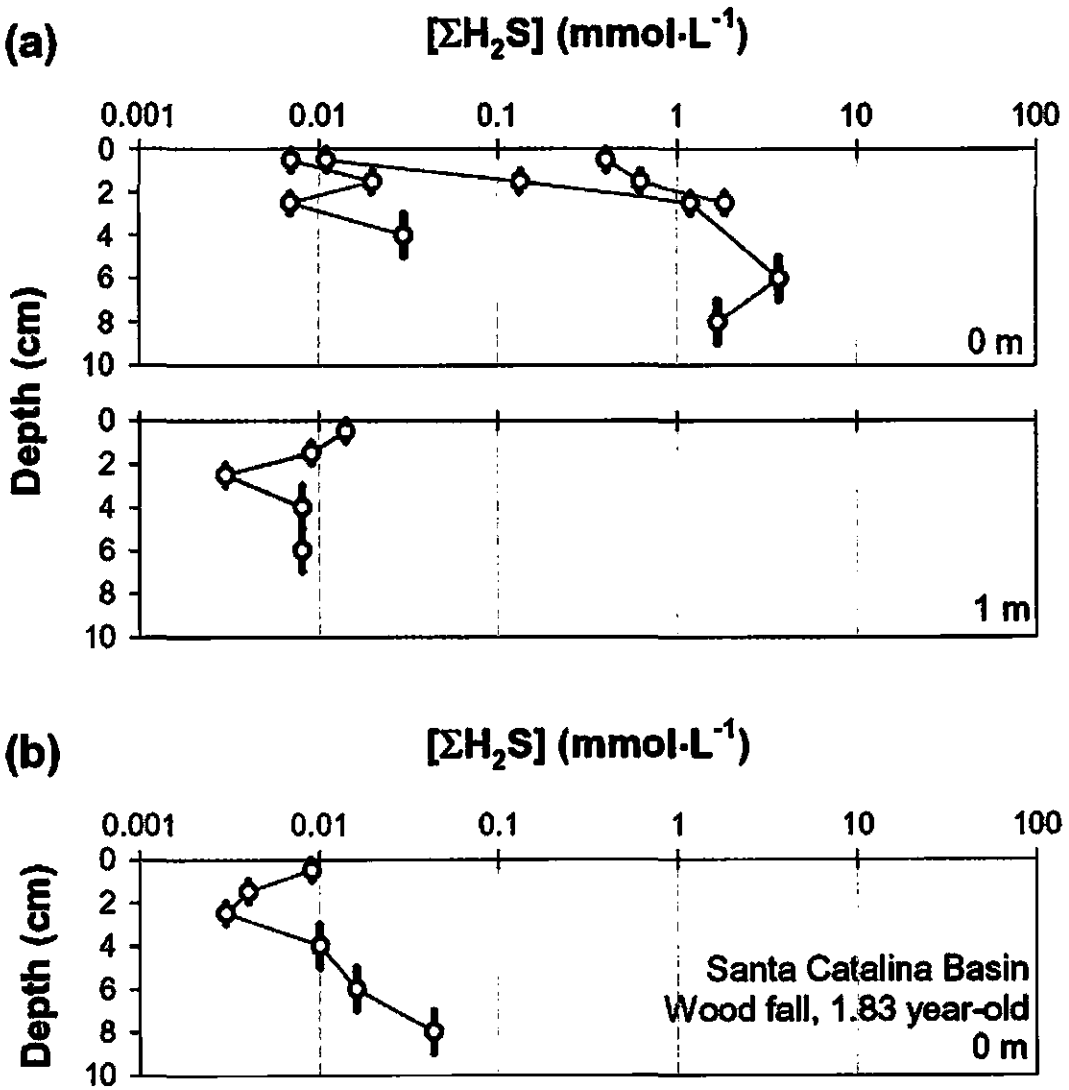

Figure 6.12 Pore water ΣH_2S in cores collected in February 2004: (a) at 0 m (n=3) and 1 m (n=1) away from the 5.8 year-old Santa Cruz Basin whale fall; (b) at 0 m away from the 1.83 year-old wood fall, CRS 800, in Santa Catalina Basin (n=1).

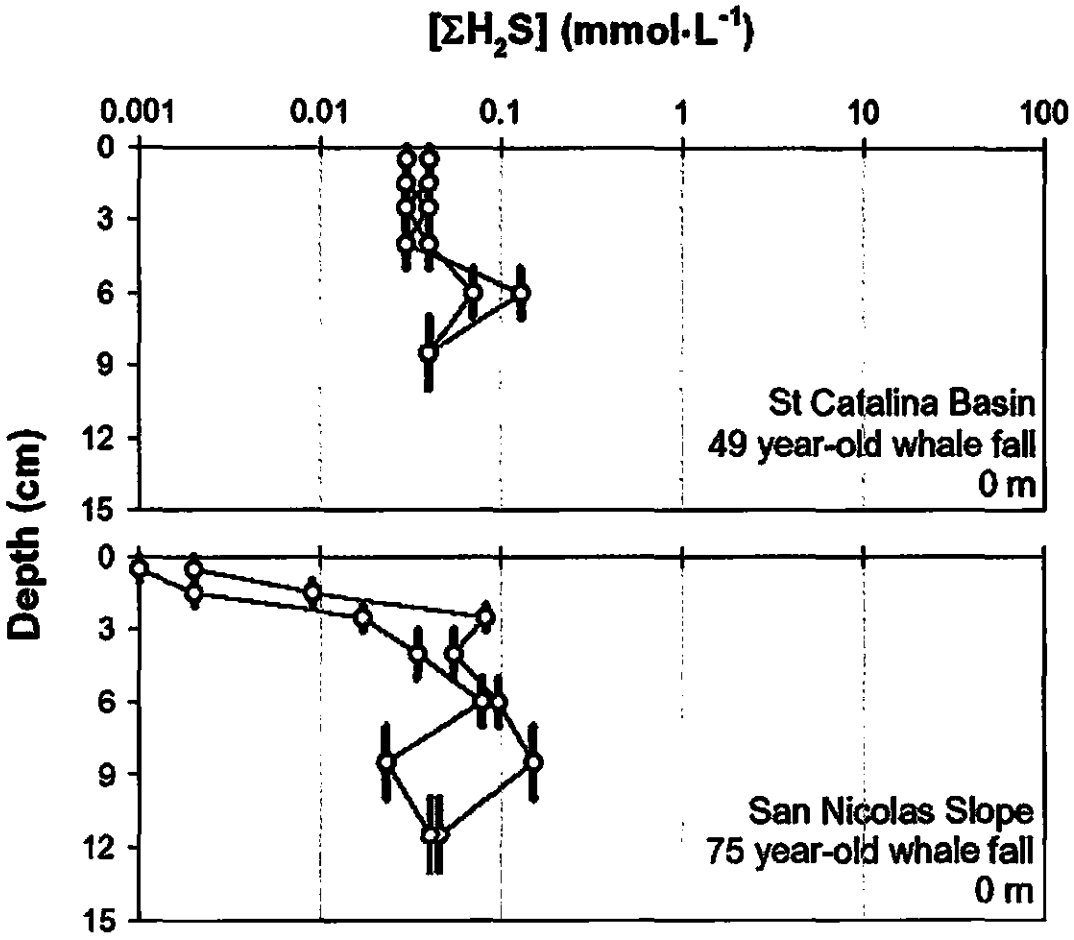

Figure 6.13 Total dissolved sulfide concentrations in pore water of sediments adjacent (0 m) to a 49 year-old whale fall in Santa Catalina Basin, and a 75 year-old whale fall on the San Nicolas slope. Black vertical lines indicate the depth range of each sediment sample.

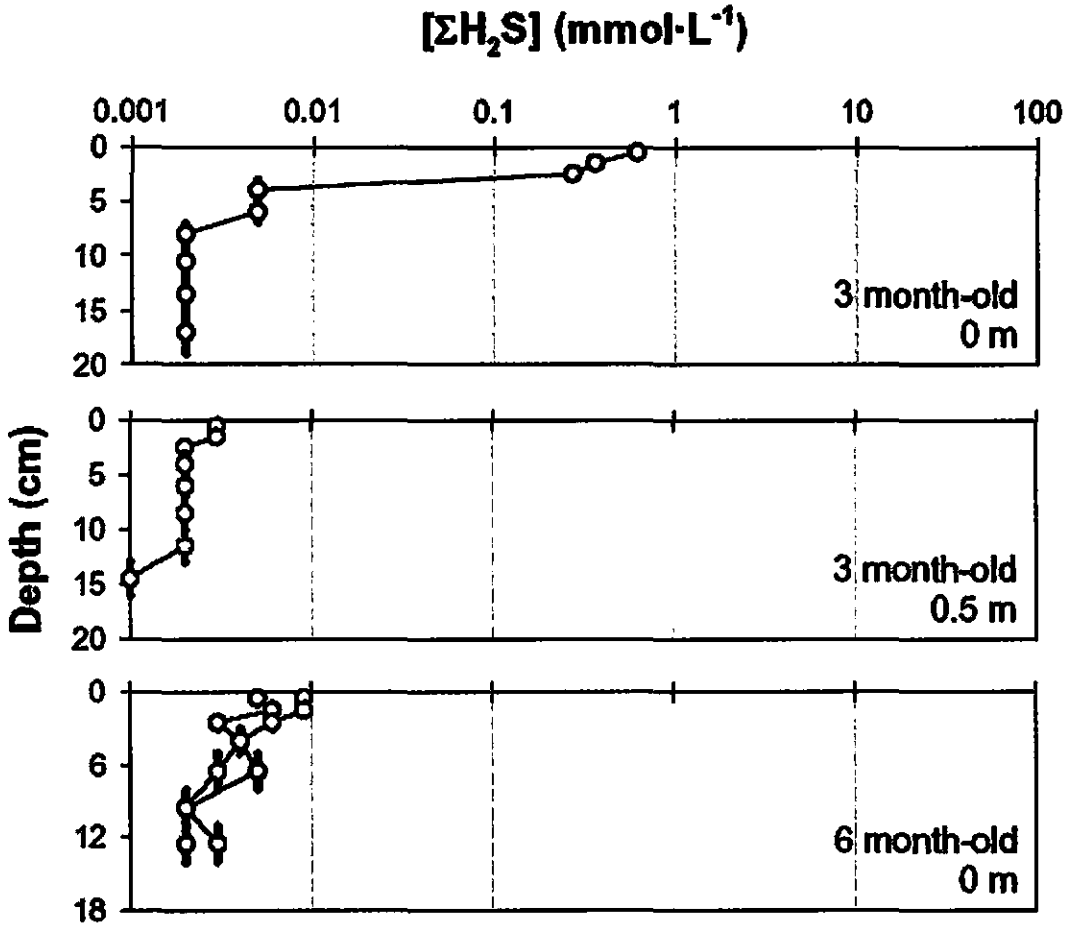

Figure 6.14 Total dissolved sulfide concentrations in pore water from cores associated with two kelp falls in Santa Cruz Basin: a 3 month-old kelp fall, CRS 806 (at 0 and 0.5 m from the fall), and a 6-month old kelp fall, CRS 799 (at 0 m from the fall).Black vertical lines indicate the depth range of each sediment sample.

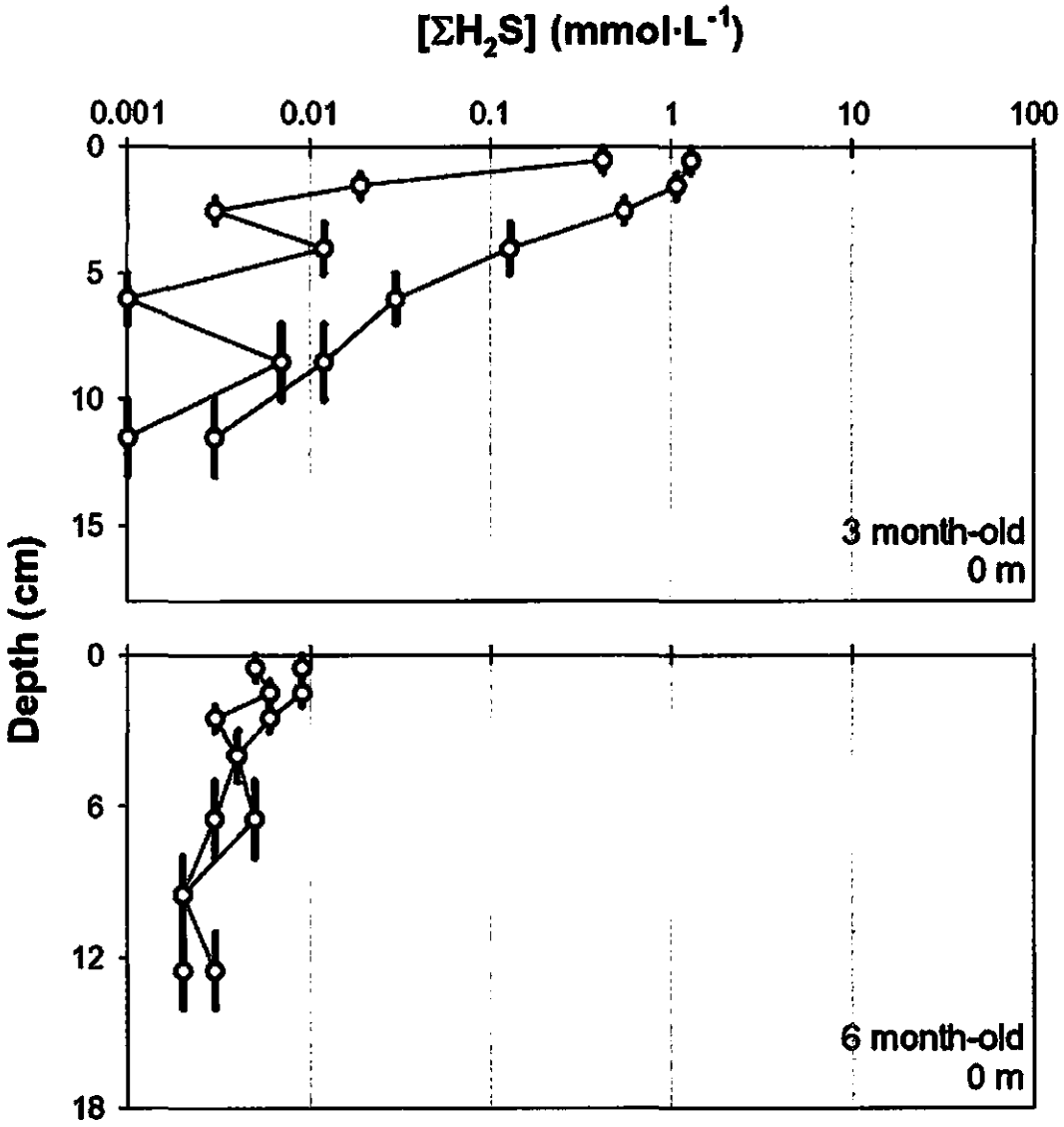

Figure 6.15 Total dissolved sulfide concentrations in pore water from cores adjacent to two kelp falls in Santa Catalina Basin: a 3 month-old kelp fall, CRS 804 (n=2), and a 6-month old kelp fall, CRS 803 (n=2). Black vertical lines indicate the depth range of each sediment sample.

was highest at the surface and decreases logarithmically to depth. This shape was evident in both 3- and 6-month-old fall sediments, albeit at a different magnitude.

6.3.3.3 Wood falls

Wood falls generated very modest sulfidic conditions in surrounding sediments, specifically at 3 years after the fall event (Figure 6.16). The rise in [ΣH_2S] was on the order of 1-1.5 orders of magnitude and displays the highest concentration at the surface.

6.4 Discussion

6.4.1 General patterns

Background sediments from Santa Cruz and Santa Catalina Basins are characterized by high TOC and TN content (Table 6.4, Figure 6.4) relative to their depth (Figure 6.2), and very low pore water sulfide concentrations (e.g., at 100 m in Figure 6.11), and this is consistent with previous measurements from this well-studied region (Emery 1960, p. 250; Eganhouse and Venkatesan 1993; Smith et al. 1998). The linearity between TOC and TN in background sediments is startling (Figure 6.4), and is suggestive of a homogenized pool of organic matter (Hedges et al. 1986; Ruttenberg and Goñi 1997). The positive TOC intercept suggests that the homogenized organic matter pool consists of a nitrogen-depleted organic matter component (TOC:TN = ∞) which is mixed with one or more nitrogen-rich organic matter pools (Hedges et al. 1986; Ruttenberg and Goñi 1997).

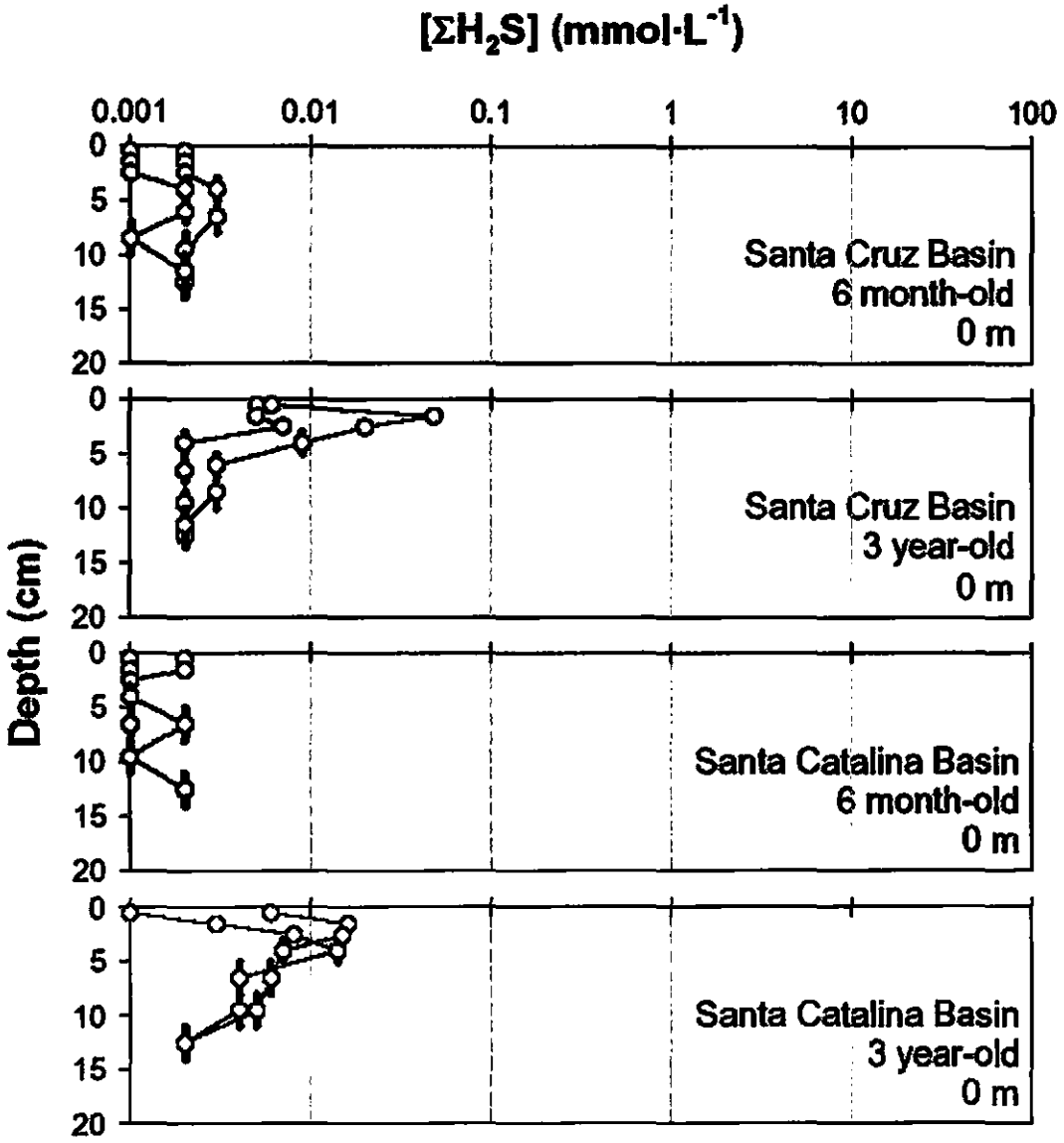

Figure 6.16 Total dissolved sulfide concentrations in pore water from cores adjacent to four wood falls in Santa Cruz Basin (6-month old CRS 800, and 3 year-old CRS 397) and Santa Catalina Basin (6 month-old CRS 801, and 3-year old CRS 398). Black vertical lines indicate the depth range of each sediment sample.

The falls implanted naturally or experimentally at the study sites (Table 6.2) provide a substantial amount of organic material to the area of the sea floor upon which they settle. A comparison of organic carbon (OC) supply via background accumulation and by LOF processing indicates that the OC instantaneously provided by a fall event would take centuries to millennia to be provided by background accumulation (Table 6.5).

Table 6.5 Comparison between organic carbon (OC) supply to the sea floor via background accumulation and via instantaneous deposition of large organic falls.

Basin	OC accumulation rate ($kg \cdot m^{-2} \cdot y^{-1}$)	Fall type	Fall mass [b] (kg)	Fall surface area (m^2)	Year equivalents of OC supply (y) [f]
SCrB	0.012 [a]	Whale	24,300	23.54 [c]	24,700
		Kelp	100	0.09 [d]	3,100
		Wood	85	1.09 [e]	3,200
SCB	0.013 [a]	Whale	57,500	27.18 [c]	49,000
		Kelp	100	0.09 [d]	2,900
		Wood	85	1.09 [e]	2,900

[a] In Eganhouse and Venkatesan (1993), originally from Emery (1960).

[b] See Table 6.2 for more information.

[c] Whale fall areas were calculated assuming the falls were prolate ellipses whose Area = $\pi \times s_1 \times s_2$, where s_1 is the long radius and s_2 is the short radius. The short radius, s_2 (= Diameter ÷ 2), was calculated from the

long radius, s_1, (= Length ÷ 2) using whale fall lengths of 13 m and 21 m for the SCrB and SCB whale falls respectively, and Length ÷ Diameter ratios of 5.64 and 6.37 respectively (Woodward et al. 2006).

[d] Kelp fall areas were estimated from visuals to occupy approximately a 30 cm × 30 cm area (personal observations; A. Bernardino, personal communication).

[e] Wood fall areas were estimated from the dimensions of the prepared wood packages (section *6.2.1*). Because the packages were asymmetric, they were assumed to lie on the side which covered the largest area of the seafloor, for the purposes of this exercise. The dimensions were 5 planks × 0.09 m × 2.44 m.

[f] The amount of OC deposited instantaneously by each fall was estimated by multiplying the mass of each fall by the average wet weight fraction of carbon of each fall type: 28.7 % for the SCrB whale fall, 30.2 % for the SCB whale fall, 3.36 % for the kelp falls, and 48.9 % for the wood falls. The OC provided by each fall was subsequently divided by the surface area of the sea floor, yielding kg·m-2, which in turn were divided by the background OC accumulation rate to yield the year equivalent.

All three LOF types investigated in this study impacted the biogeochemical conditions of surrounding sediments. The impact was strongest in sediments adjacent to the falls (0 m), and varied with age. The greatest organic enrichment signal was seen in 3-year-old wood fall, followed by 6-month-old wood fall, and 3-month-old kelp fall and 4.5-year-old whale fall. Sulfide concentrations were highest in the 4.5-year-old whale fall, followed by those in the 3-month-old kelp falls, and the 3-year-old wood falls. These patterns are discussed in detail in the following sections.

6.4.2 TOC and TN content and organic matter sources

Visual inspection of the TOC and TN content data around the investigated falls indicates that any evidence of an enrichment effect is restricted to the sediments adjacent to the falls (Figure 6.17). Further inspection revealed that the vast majority of the

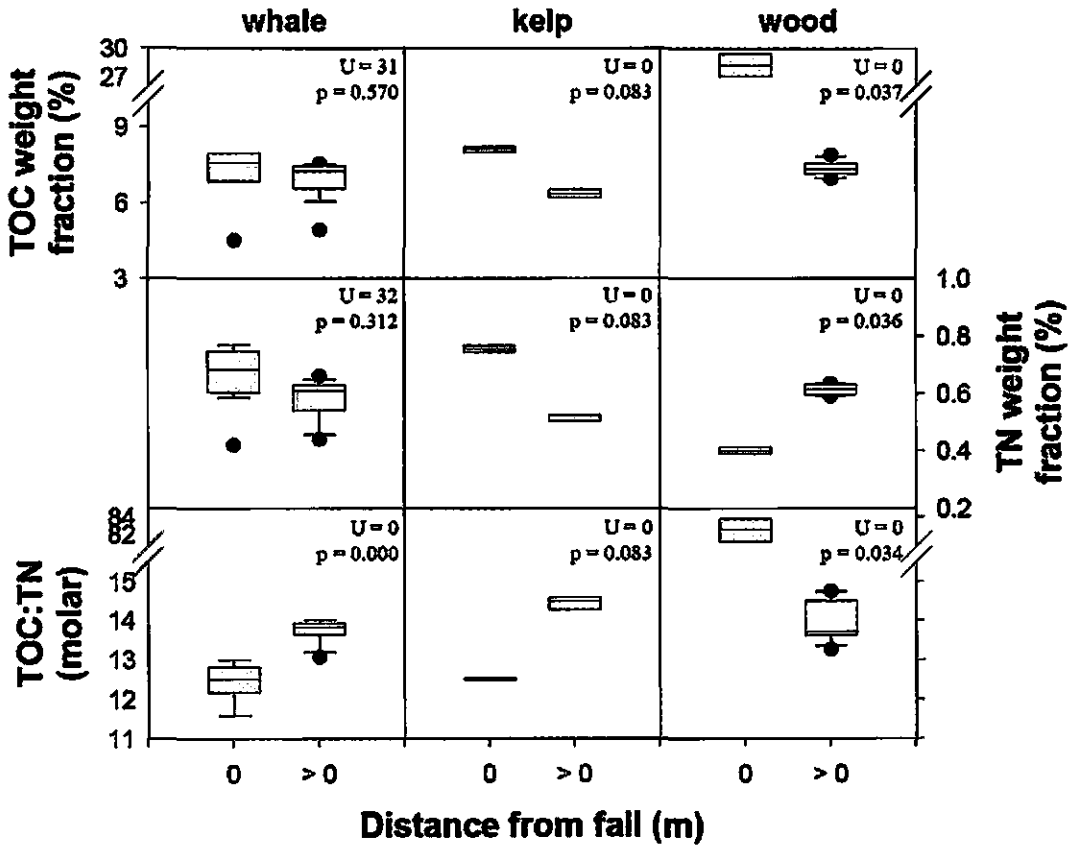

Figure 6.17 Comparison of data from selected falls showing evidence of organic enrichment: *left column* – comparison of pooled data from 0 m (n=5) and 1-9 m (n=15) away from the 4.5-year-old Santa Cruz Basin whale fall (Figure 6.5); *middle column* – comparison of pooled data from 0 m (n=2) and 0.5-2 m (n=3) away from a 3-month-old kelp fall (CRS 804) in Santa Catalina Basin (Figure 6.8); *right column* – comparison of pooled data from 0 m (n=2) and 0.5-4 m (n=8) away from a 3-year-old wood fall (CRS 397) in Santa Cruz Basin (Figure 6.9). The U and p values of the Mann-Whitney statistical comparison test are shown on the top right corner of each plot.

samples, including most sediments 0 m from the falls, contained TOC and TN in proportions comparable to those of background sediment (Figure 6.18). The linear relationship between these two parameters in sediments falls between the C and N signatures of these three common LOF in this region, and the Redfield ratio. This suggests that at least one of the nitrogen-rich sources of organic material commonly reaching these sediments could be marine algal material from the euphotic zone.

6.4.2.1 High TOC enrichment by wood falls – a "sawdust" supply

One exception to the linear relationship outlined in Figure 6.18 was sediment adjacent to 3-year-old wood falls (TOC = 15-27 %, TN = 0.26-0.42 %). It should be noted that, in the case of wood LOF, organic enrichment, in the form of enhanced TOC content, already becomes evident at the 6-month-old falls (TOC up to 10 % in CRS 801, Figure 6.10). The 3 year-old wood fall samples lie on an approximately linear trajectory connecting background sediment values and wood LOF values since, concurrently with TOC enrichment, the TN content of these samples declines down to 0.5 times of the background levels (see CRS 398, Figure 6.10). While weighing these samples for the CHN analysis, it was observed that they were significantly less dense than all other samples. This observation and the TOC content values indicate that a good portion of the wood LOF material may be delivered to the sediment retaining its original characteristics, such as low density and high C:N ratio (Table 6.1); i.e., it is relatively unaltered by the wood borers.

From a biochemical aspect, relatively passive processing of wood LOF by wood borers is supported by observations of the digestive storing and processing of wood chips

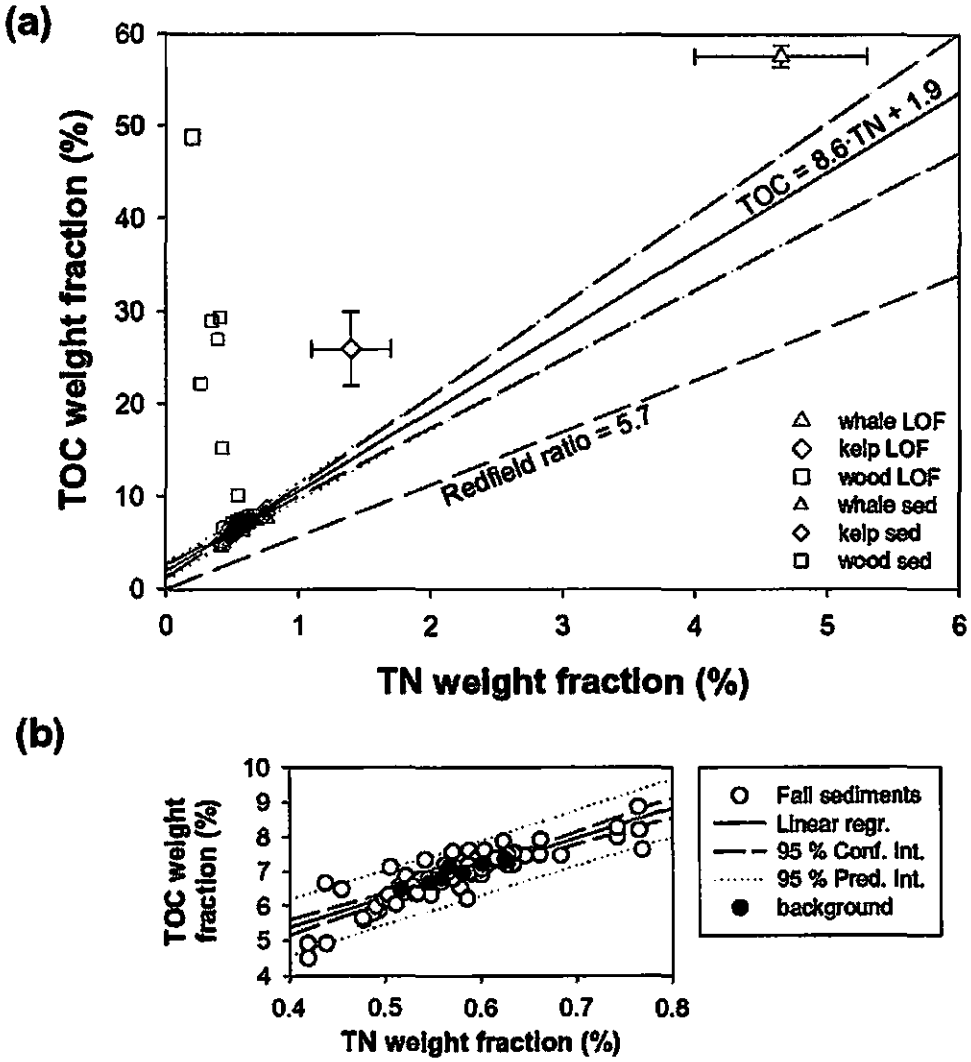

Figure 6.18 (a) Comparison of source (whale, kelp and wood LOF) C and N content (closed symbols; from Table 6.1) with TOC and TN content of sediments (open symbols). The linear regression between TOC and TN content of sedimentary samples (excluding sediment samples adjacent to 3-year old wood falls; see text for explanation) is also shown with (95 % Confidence Interval) (Figure 6.4). The Redfield ratio for weight fractions is shown for comparison. (b) Plot of all the sediment samples excluding the 3 year-old wood fall 0-m samples (n=6).

by wood-boring bivalves (Distel and Roberts 1997). This case can be tested using a conservative mixing model between two end-members: wood and sediment TOC. Let w be the weight fraction of wood in a sample, and consequently 1-w be the weight fraction of sediment. It follows that:

$$TOC_{sample} = w \cdot TOC_w + (1-w) \cdot TOC_{sed} \quad 6.1$$

where the TOC value for wood, TOC_w, is 48.9 (Table 6.1), and the TOC value of background sediment, TOC_{sed}, is 7.1 and 6.8 for Santa Cruz and Santa Catalina Basins respectively (averages from Table 6.4). Solving Eq. 6.1 for w yields:

$$w = (TOC_{sample} - TOC_{sed}) \div (TOC_w - TOC_{sed}) \quad 6.2$$

Provided that 0.2 % of wood weight is TN (Table 6.1), one may test the extent of conservative end-member mixing at the wood-fall sediment boundary by inspecting the ability of w to predict the amount of TN in the sample ($TN_{sample\text{-}pred}$), which is calculated as follows:

$$TN_{sample\text{-}pred} = w \cdot TN_w + (1-w) \cdot TN_{sed} \quad 6.3$$

The TN content of background sediment, $\%TN_{sed}$, is 0.60 and 0.55 for Santa Cruz and Santa Catalina Basins, respectively (Table 6.4). The results of these calculations are shown in Figure 6.19. The predictions of the model agree relatively well with the measurements and support the hypothesis that ingestion and digestive processing by wood borers does not alter the C:N ratio of ingested wood substantially before release to the surrounding sediments. This has important implications for sedimentary microbial decomposition of wood MOM released by the primary processors. It reinforces the expectation that wood LOF processing will result in fairly refractory woody material of

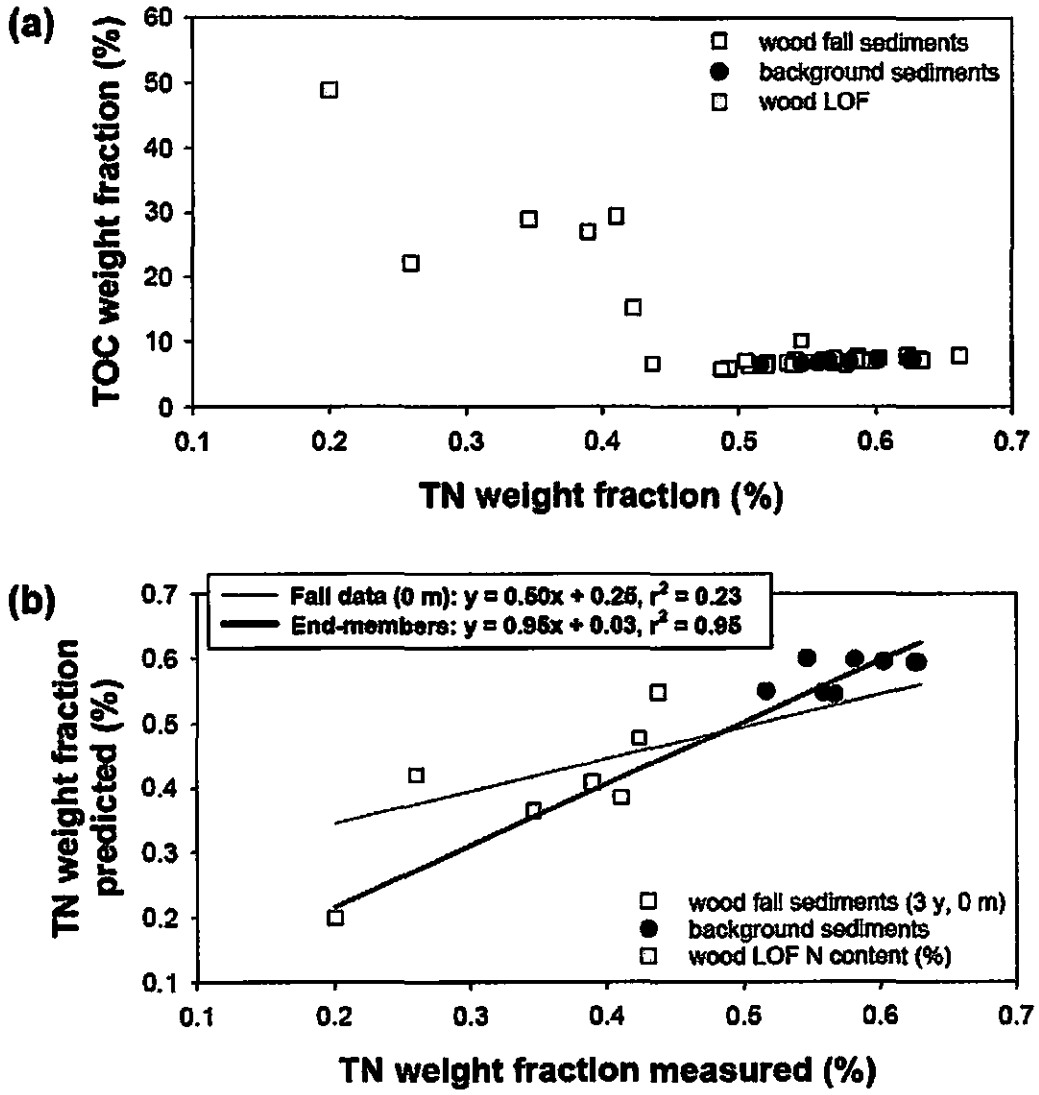

Figure 6.19 (a) TOC and TN content in wood fall-associated sediments, compared with background sediment values and wood LOF (Table 6.1); (b) Predicted TN content in sediments adjacent to 3 year-old wood falls by a conservative, two-end-member mixing model between background sediments and wood, plotted versus TN content measured. The end-members linear regression was performed on a fit of just the background values and wood. The two slopes are not significantly different (comparison of slope test, $F_s = 0.048 < F_{0.05} = 4.84$, n=11) (Sokal and Rohlf 1995, p. 498).

high C:N being supplied to the sediments and actually accumulating due to slow decomposition rates.

6.4.2.2 Whale fall enrichment effects in time and space

Sediments associated with the Santa Cruz Basin 4.5 year-old whale fall overall showed evidence of an organic enrichment effect in the form of above-background TOC and TN content in samples adjacent to the fall (0 m; Figure 6.17). The highly sulfidic nature of sediments at this distance (Figure 6.11) corroborates the hypothesis of high organic matter supply rates in the past. However, the trends of TOC and TN content with distance were not unequivocal (Figure 6.5). In three of the four transects, sediments at 0 m from the fall were enriched in TOC and TN while in the fourth they were depleted. Non-transect samples reflected this variability. The distribution of TOC:TN values with distance away from this fall indicates that the slight enrichment of sediments next to the fall (0 m) is greater in nitrogen relative to carbon.

These data suggest that at 4.5 years after the fall event, sediments adjacent to the fall were experiencing high anaerobic decomposition rates sustained by remnants of MOM from the whale carcass. The slight enrichment in TOC and TN may be due in part to material stored in living epifaunal and infaunal biomass, which was distinctly greater in sediments adjacent to the fall (0 m) than further away (Smith et al. 2002a; Smith and Bernardino, unpublished data). The lower-than-background TOC:TN ratio can be explained by preferential degradation of certain components of the whale MOM, such as carbon-rich lipids and short-chain glycoproteins, leaving behind greater fractions of long-chain, nitrogen-rich compounds, such as the protein collagen (see Table 6.1, footnote n).

Collagen forms fibers in blubber (Wainwright 1995) and is also abundant in bone (Sterner and Elser 2002), where it could be protected from degradation by the hydroxyapatite matrix. Another potential contributor to the phenomenon of enhanced nitrogen enrichment relative to carbon is the build-up of microbial abundances close to the fall, fueled by MOM. Marine bacteria are characterized by low C:N ratios (4.5-7, Goldman and Dennett 2000), and could constitute a detectable fraction of TN if their abundances grow to an appreciable size relative to background sediments, in proportion to the growth of macrofaunal biomass (Smith et al. 2002a). Ultimately, due to the relatively high background concentrations of TOC and TN, organic enrichment is not as evident from these measurements as it is from proxies of organic matter decomposition such as pore water sulfide (see next section).

The TOC and TN content of the sediments associated with the 75 year-old San Nicolas whale fall are highest next to the fall (0 m), and reach a minimum at 1 m (Figure 6.6), in a pattern similar to that of the 4.5 year-old Santa Cruz whale fall (Figure 6.5). It is startling to see a pattern of apparent enrichment close to a 75 year-old whale fall, as illustrated by both TOC and TN. However, the background TOC content is higher than anticipated for this region of the California Borderland Basins, and is more typical of the nearby basins (Emery 1960, p. 250). While there are no literature values for this particular region, TOC content of 5 % was reported by Schwalbach and Gorsline (1985) in regions landward from this ridge. Although analytical errors are possible, the inter-comparison of data from this study with others for background sediments (Table 6.4; Smith et al. 1998) and whale fall-associated sediments (T. Treude et al., in preparation; section *6.4.3*) suggests that such an explanation is not likely. Instead, it is possible that

organic material from the skeleton, which is still visible, may be sustaining microbial activity that is adequate to maintain TOC and TN next to the fall at levels higher than background values.

The trends in surface sediment TOC and TN content with distance at these two whale falls are not comparable with the pattern reported by Smith et al (1998) for the Santa Catalina Basin whale fall, which was 35 years-old at the time of that study (see Figure 5.2). However, all three whale falls yield TOC:TN ratios lower than background values in sediments adjacent to the falls. The difference is that in the Santa Cruz Basin whale fall (Figure 6.5) and the 75 year-old San Nicolas Slope whale fall (Figure 6.6), higher-than-background TN values clearly drive the TOC:TN ratio to below-background levels, whereas in the 35 year-old Santa Catalina Basin whale fall (Figure 5.2; Smith et al. 1998) the low TOC values drive the TOC:TN ratio below the background levels. However, with the present data and observations, it is impossible to completely explain the discrepancy in TOC and TN content between the three whale fall-impacted sedimentary settings.

6.4.2.3 Rapid enrichment rates at kelp falls

Kelp falls generate substantial enrichment of sediments in TOC and TN between several weeks to 3 months after the fall event, and this enrichment appears to dissipate after 6 months (Figure 6.8). The TOC:TN signatures of kelp fall-associated sediments appear to be on the lower end of background values or below them. This may be due to preferential degradation of the abundant short-chain carbohydrates (North 1971; ZoBell 1971; Hart et al. 1978) relative to proteins and fiber (Table 6.1, footnote o). It is also

likely that rapid microbial colonization and growth on kelp MOM, which has been reported in the past (e.g., ZoBell 1971; e.g., Harrold et al. 1998), may have contributed to the retention and accumulation of TN in these sediments, a fairly common occurrence with high C:N detritus (e.g., Newell 1965).

6.4.3 Free dissolved sulfide in LOF sediments: Biogenic reducing habitats

The LOF types investigated in this study all give rise to sulfidic conditions at certain ages. These sulfidic conditions, in the case of whale falls, are certainly the outcome of sulfate reduction during organic matter decomposition (Treude et al. 2006). In the case of kelp, which contains an appreciable amount of organic sulfur (ZoBell 1971), it is possible that some of the sulfide can be generated by the dissociation of this organic sulfur under anoxic conditions. This amount, however, is likely too small (up to a dry weight fraction of 1.25 %) to contribute significantly to the observed profiles relative to sulfate reduction-generated sulfide (ZoBell 1971).

High between-transect heterogeneity characterizes the whale-fall dissolved sulfide profiles. Such heterogeneity has been observed before in other reducing habitats (e.g., Arvidson et al. 2004). In the case of LOF, heterogeneity may be caused by patchiness in MOM distribution induced by mobile benthopelagic scavengers, and complicates the comparison of patterns in sulfidic conditions among different LOF types. Averaging replicate profiles has aided the clearer visualization of such variable sulfide profiles at cold seeps (e.g., Cordes et al. 2005). The ΣH_2S profiles from cores adjacent to the 4.5 year-old Santa Cruz whale fall were averaged and compared with similarly averaged cores from 3 month-old kelp falls and 3 year-old wood falls (Figure 6.20). The whale fall

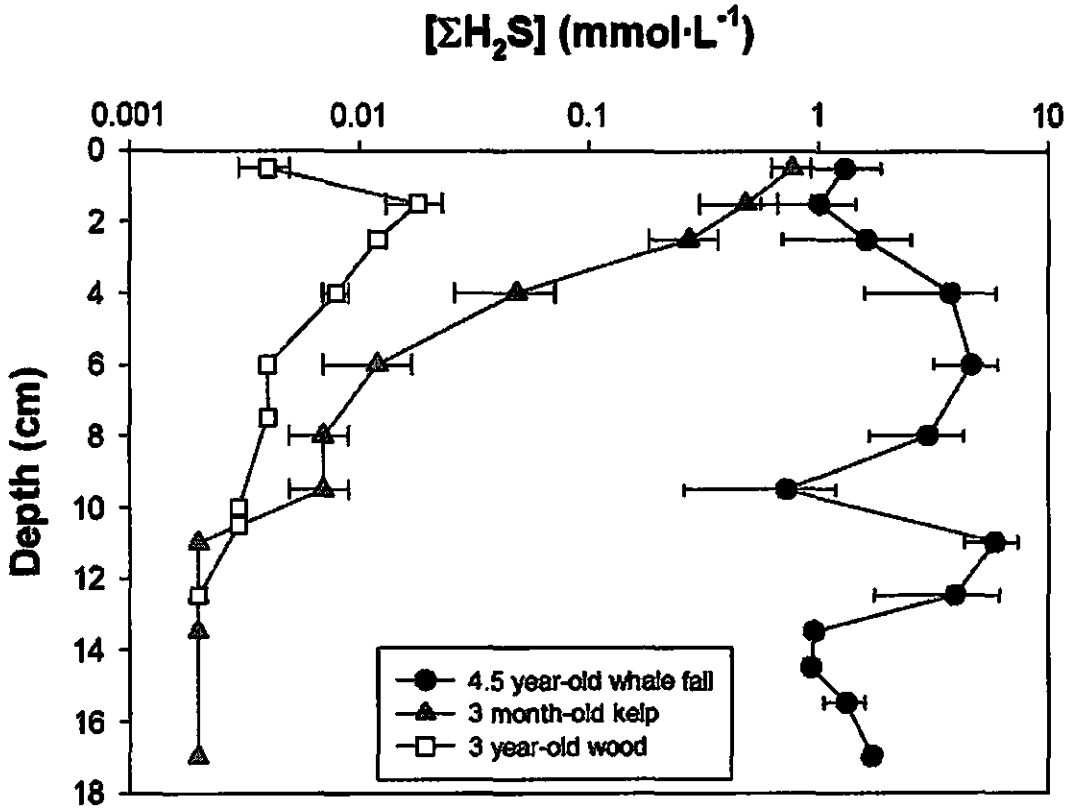

Figure 6.20 A comparison of averaged pore water ΣH_2S profiles with depth at the three types of falls where sulfidic conditions developed: the 4.5 year-old Santa Cruz Basin whale fall (n=3); the 3 month-old kelp falls CRS 804 and CRS 806 from Santa Catalina Basin and Santa Cruz Basin respectively (n=3); and the 3 year-old wood falls CRS 397 and CRS 398 from Santa Cruz Basin and Santa Catalina Basin respectively (n=4). The horizontal error bars indicate the standard error.

[ΣH_2S] profile differs significantly from kelp and wood fall profiles. Keeping in mind that background sediments do not contain any sulfide, it appears that in the case of the whale fall there is a source of sulfide below the sediment-water interface (SWI), but in the case of kelp and wood falls, the source of sulfide appears to be within 2 cm of the SWI. Sulfate reduction in the deep sediments of the California Borderland Basins region is probably driven by the addition of labile POM (e.g., Jackson et al. 1989). Since the MOM fragments, discarded by metazoa by defecation or sloppy feeding, would be expected to settle on the SWI of a relatively non-bioturbated sediment (Smith et al. 1998), the site of maximum decomposition (and, subsequently, sulfide generation) should be at the SWI or right below it. The profiles of ΣH_2S at kelp and wood falls are consistent with this hypothesis.

The distribution of ΣH_2S in whale fall-associated sediments is more puzzling. The deep bulge of pore water ΣH_2S suggests that MOM has been entrained well below the SWI, where it is decomposing in part by sulfate reduction. Data collected at this whale fall in February of 2004 (R/V Western Flyer cruise), when the fall was 5.8 years-old, provided useful information for a more definitive interpretation of this pattern. Samples were taken down-core at 0 m, 1 m, and 3 m from this whale fall, and analyzed for TOC and TN (Treude et al., in preparation). The TOC content profile of the core collected at 0 m is shown in Figure 6.21, and reveals a sub-surface pool of organic carbon. The surface values at the two fall ages compare favorably. The TOC vs. depth profile also explains the high value obtained on the sole sub-surface sample analyzed for TOC and TN during this study (see Figure 6.5, Transect 7, 1-5 cm sample). The TOC:TN values down-core range from 10-27 (Treude et al. in preparation), in agreement with the original source

material (Table 6.1), as well as being consistent with preferential nitrogen degradation. The sub-surface accumulation of TOC was only observed at 0 m, while 1 m and 3 m cores exhibited constant values from surface to 10 cm depth (weight fraction of 5.4 % ± 0.2 %, Treude et al., in preparation), suggesting that the TOC pool observed at 0 m presumably originated from the whale fall. Surface sediment TOC content at 1 and 3 m away from the 5.8 year-old whale fall is similar in magnitude to that observed 1.3 years earlier at the same distances (Figure 6.5).

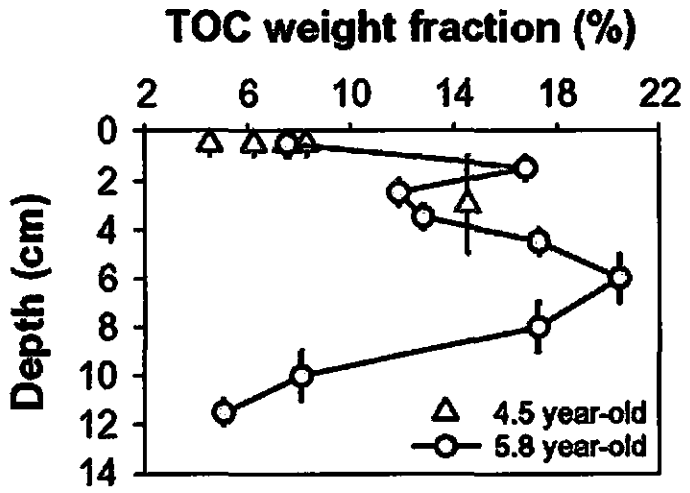

Figure 6.21 TOC content in sediments adjacent (0 m) to a Santa Cruz Basin whale fall 5.8 years after the fall event (T. Treude, unpublished data), and 4.5 years after the fall event (this study; Figure 6.5). Vertical lines indicate the depth range of each sediment sample.

The presence of this sub-surface organic carbon pool is significant. Based on the size of the St. Cruz Basin whale fall (Table 6.2), and the characteristics of whale LOF (Table 6.1), it is estimated that this experimental whale fall supplied approximately 7000 kg to the sea floor. Assuming the TOC profile with depth (Figure 6.21) is characteristic of a ring of sediment around this whale fall as wide as the corer used to sample these sediments (7 cm), the amount of TOC contained in this ring is 34 kg, 5.8 years after the fall event. This equals as much as 0.49 % of the original carbon content of the whale fall, or 0.63 % of the soft tissue of the carcass.

The origin of this deep pool of TOC can only be speculated. Perhaps it is an accumulation-induced phenomenon, a result of high MOM deposition rates in a narrow ring around the whale fall. The soft tissue of this particular whale carcass (85 % of total weight, or 30,000 kg; Table 6.1, footnote n) was estimated to have been removed by 1.5 years, allowing for enough material to escape metazoan assimilation and be deposited at high rates in a small area around this whale fall. It is also possible that large metazoan scavengers at this location, e.g., hagfish (primarily *Eptatretus deani*, Smith et al. 2002a), may mix MOM fragments with the sediment during LOF processing (C.R. Smith, personal communication). The presence of whale material, such as soft tissue fragments, in cores adjacent to this whale fall was actually witnessed during slicing of the cores for pore water extraction (personal observations, section *6.3.1*). Regardless of its origin, this pool of TOC appears to be utilized primarily by microbial populations, based on the sulfidic character of the sediments which excludes any aerobic metazoans.

This is in contrast to the organic enrichment opportunist stage, during which benthic metazoa take advantage of MOM in sediment to rapidly recruit and grow around whale falls. This stage was observed to last less than 2 years in a smaller whale carcass in the San Diego Trough (Smith and Baco 2003). At the point of sampling (4.5 and 5.8 y), there were no large metazoan scavengers observed, and benthic macrofauna was limited to small infaunal species inhabiting the top few centimeters of sediment (A. Bernardino, personal communication). The processes responsible for burial of this MOM in deeper sediments ultimately place this organic material out of reach for most metazoa and allow anaerobic microbes to exploit it.

Finally, the profile of TOC content with depth next to the St. Cruz whale fall (Figure 6.21; Treude et al. in preparation) suggests that surface sediment sampling may not be adequate to characterize organic enrichment patterns in LOF-associated sediments. Surface sediment was sampled to maximize lateral coverage of LOF-associated sediments. It may be equally important to recognize where depth profiles should be taken instead of just surficial lateral samples.

The whale fall-associated ΣH_2S profiles from 2004, when the whale fall was 5.8 years old, indicate that levels decreased slightly since 2002, but remained of the same order of magnitude (compare Figure 6.12 with Figure 6.11). Moreover, the three profiles collected in 2004 differ from each other in magnitude and curvature (Figure 6.12), a feature also present in the 2002 profiles (Figure 6.11), which suggests that heterogeneity in sulfidic conditions is the rule and not the exception in whale fall-associated sediments. The 1.83 year-old wood fall ΣH_2S profile resembled 3 year-old fall profiles (Figure 6.16),

and indicates that slightly sulfidic conditions arise in wood-fall impacted sediments approximately 1.5 y after the fall event.

The dissolved sulfide (ΣH_2S) data obtained during the two cruises allow the discernment of trends of sulfidic conditions with age for each fall type (Figure 6.22). The best fits of the Gaussian peak model give high values of [ΣH_2S] at fall ages of 0 y in the case of whale and kelp falls (3.82 mmol·L^{-1} and 0.072 mmol·L^{-1} respectively). In practice, values of [ΣH_2S] at fall age of 0 y lie below 0.01 mmol·L^{-1} as with background pore water levels (Figure 6.11). The fact that best fits yield a much higher intercept is strongly suggestive of the rise of sulfidic conditions within days to weeks of the fall events. On the contrary, the best fit of the model on wood fall data yields an intercept below detection, and this is consistent with only mild sulfidic conditions arising over a period of several months after a wood fall event.

Significant differences were observed in organic enrichment and sulfidic conditions between the three types of LOF investigated in this study (Figure 6.23). Whale fall-associated sediments are rich in sulfide years after the fall event, while they sustain marginal enrichment in organic material at the surface. The sub-surface reducing layers are probably sustained by substantial organic enrichment at depth (below 1 cm; Figure 6.21, Treude et al. in preparation). Kelp fall-associated sediments are characterized by ephemeral sulfide and organic matter peaks lasting weeks to a few months and appear to return to background values within half a year from the fall event. The rapid generation of reducing conditions in sediments associated with whale falls and kelp falls is an indicator of the lability of MOM released during LOF processing. Wood falls are distinct from the other two fall types, in that their processing yields high sedimentary enrichment

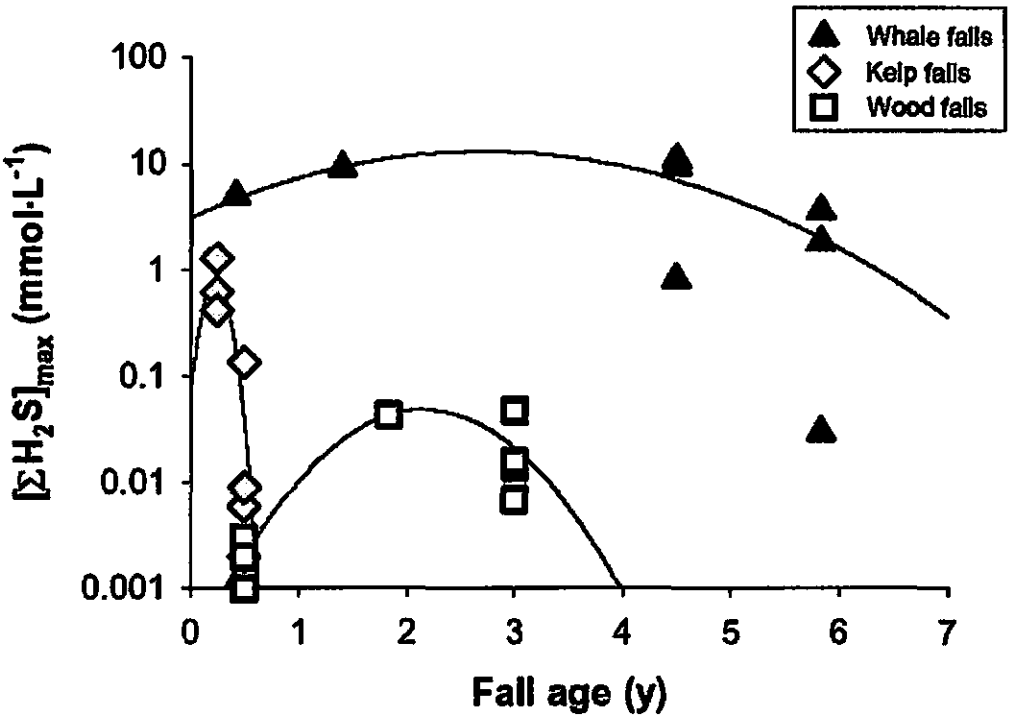

Figure 6.22 Maximum detected concentrations of dissolved sulfide (ΣH_2S) plotted against age for the three fall types investigated in this study: the 24,300-kg Santa Cruz Basin whale fall, four 100-kg kelp falls in Santa Cruz Basin and Santa Catalina Basin, and four 85-kg wood falls in Santa Cruz Basin and Santa Catalina Basin. The samples for the whale fall at 0.125 y and 1.5 y were collected by M.E. Torres (Figure 5.4; M.E. Torres and C.R. Smith, unpublished data). The three concentration-time curves were fitted with a three-parameter Gaussian peak model using the statistical package SPSS:

$$[\Sigma H_2S] = ae^{\left[-0.5\left(\frac{age-age_0}{b}\right)^2\right]}$$

The model curves are simply intended to highlight the parabolic nature of the ΣH_2S trend with fall age (see text for more details).

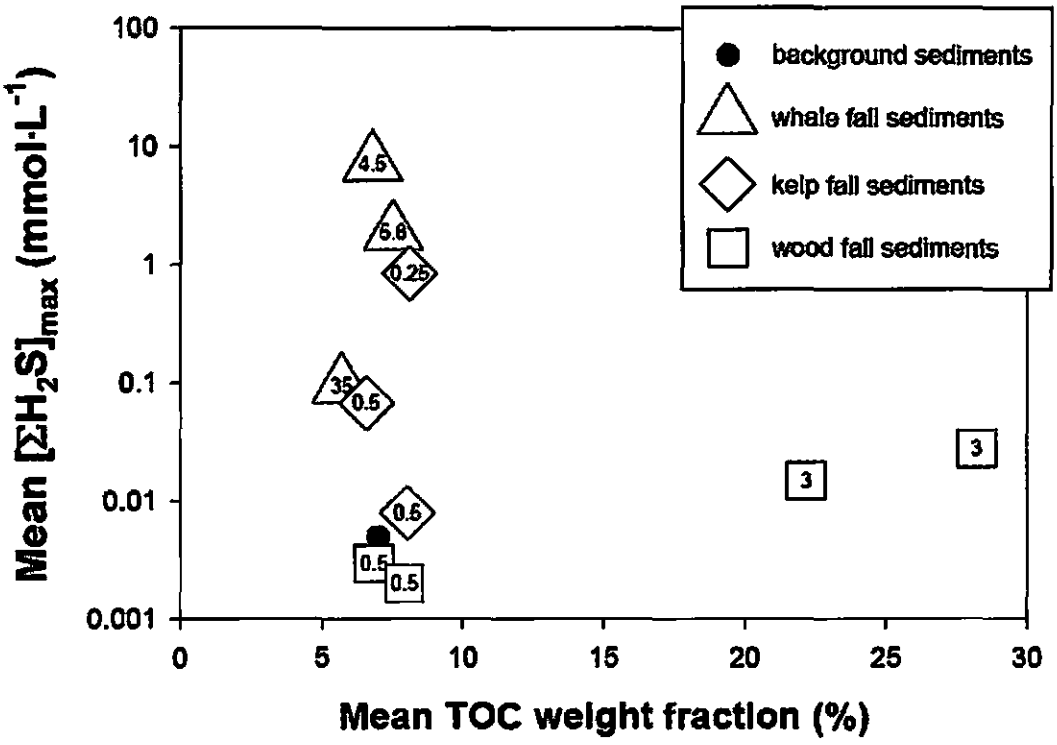

Figure 6.23 Age-specific relationships between organic enrichment and sulfide content for LOF-associated sediments in the California Borderland Basins. Age is shown in years within symbols. Mean TOC weight fraction (%) and mean maximum [ΣH_2S] are shown without error bars for clarity. Data from this study were supplemented with data for the 35 year-old Santa Catalina Basin whale fall (Smith et al. 1998). Compare with Figure 6.1.

in relatively unaltered wood MOM of very high TOC:TN. The refractory nature of wood MOM allows its accumulation to a high degree and does not generate appreciable reducing conditions in sediment pore water.

6.5 Conclusions

The studied large organic falls provided a small area of the deep sea floor with a very high amount of organic material over a very short period of time. Sedimentary organic enrichment following their processing did not necessarily lead to a sedimentary redox shift from oxic-anoxic conditions to anoxic-sulfidic conditions. The relatively labile organic material generated by the processing of whale falls and kelp falls generated substantial pore water sulfide levels in impacted sediment. In contrast, wood derived material input did not result in sulfidic conditions, despite generating very high organic enrichment in impacted sediments, due to its refractory nature.

The comparison of the concentration-time curves in Figure 6.22 is limited to the particular sizes of these falls. For example, when a 24,300 kg whale fall is compared with a 100 kg kelp fall, it is evident that the amounts of organic material processed in each case differ substantially and the size of the fall should be taken into consideration. When comparing different fall types, this concern is curbed to a certain degree by inherent limits in the possible size ranges of types (Table 6.1). The question persists, however, when comparing different falls of the same type. Such differences in size are certainly possible in all three cases and should be investigated.

The conclusions drawn from this study rely on data sets of limited temporal and spatial extent. The surface-sediment signatures of TOC and TN content do not

necessarily reflect the enrichment levels of sediment adjacent to the falls. The data sets used in this study are also limited by the size of the sampled falls. The size of a LOF is proportional to the MOM eventually released to sedimentary communities and is probably a controlling factor in the development of biogenic reducing habitats. Logistical limitations (e.g., remoteness of study sites, availability of certain LOF types, funding) restrict our ability to carry out experiments to test further the effects of LOF size and quality on the development of biogenic reducing conditions in surrounding sediments. The use of mathematical models, parameterized using the available data, would provide useful insights into directing future opportunities for experimentation. Such insights may include the recognition of factors that need to be better constrained, as well as specific fall ages that may be critical in the development of biogenic reducing conditions in deep sea sediments.

6.6 References

Alldredge, A. L. and M. W. Silver (1988) Characteristics, dynamics and significance of marine snow. Progress in Oceanography, 20: 41-82.

Allison, P. A., C. R. Smith, H. Kukert, J. W. Deming and B. A. Bennett (1991) Deep-water taphonomy of vertebrate carcasses: a whale skeleton in the bathyal Santa Catalina Basin. Paleobiology, 17: 78-89.

Arvidson, R. S., J. W. Morse and S. B. Joye (2004) The sulfur biogeochemistry of chemosynthetic cold seep communities, Gulf of Mexico, USA. Marine Chemistry, 87: 97-119.

Baco-Taylor, A. R. (2002) Food-web structure, succession and phylogenetics on deep-sea whale skeletons. Ph.D. Dissertation, University of Hawai'i, pp. 275.

Baco, A. R., C. R. Smith, A. S. Peek, G. K. Roderick and R. C. Vrijenhoek (1999) The phylogenetic relationships of whale-fall vesicomyid clams based on mitochondrial COI DNA sequences. Marine Ecology Progress Series, 182: 137-147.

Baco, A. R. and C. R. Smith (2003) High species richness in deep-sea chemoautotrophic whale skeleton communities. Marine Ecology Progress Series, 260: 109-114.

Barnard, J. L. (1961) Gammaridean Amphipoda from depths of 400 to 6000 meters. Galathea Report, 5: 23-128.

Bennett, B. A., C. R. Smith, B. Glaser and H. L. Maybaum (1994) Faunal community structure of a chemoautotrophic assemblage on whale bones in the deep northeast Pacific Ocean. Marine Ecology Progress Series, 108: 205-223.

Berelson, W. M., D. E. Hammond and K. S. Johnson (1987) Benthic fluxes and the cycling of biogenic silica and carbon in two southern California borderland basins. Geochimica et Cosmochimica Acta, 51: 1345-1363.

Browning, B. L. (1963a) The composition and chemical reactions of wood, p. 57-101. *In* Browning, B. L. [ed.], The chemistry of wood. Wiley Interscience, New York, New York, U.S.A.

Browning, B. L. (1963b) The wood-water relationship, p. 405-439. *In* Browning, B. L. [ed.], The chemistry of wood. Wiley Interscience, New York, New York, U.S.A.

Bruun, A. F. (1959) General introduction to the reports and list of deep-sea stations. Galathea Report, 1: 7-48.

Butman, C. A., J. T. Carlton and S. R. Palumbi (1996) Whales don't fall like snow: reply to Jelmert. Conservation Biology, 10: 655-656.

Castro-González, M. I., S. Carrillo-Domínguez and F. Pérez-Gil (1994) Chemical composition of *Macrocystis pyrifera* (Giant sargazo) collected in summer and winter and its possible use in animal feeding. Ciencias Marinas, 20: 33-40.

Cline, J. D. (1969) Spectrophotometric determination of hydrogen sulfide in natural waters. Limnology and Oceanography, 14: 454-458.

Cordes, E. E., M. A. Arthur, K. Shea, R. S. Arvidson and C. R. Fisher (2005) Modeling the mutualistic interactions between tubeworms and microbial consortia. PLoS Biology, 3: 497-506.

Dailey, M. D., D. J. Reish and A. J. W. [eds.] (1993) Ecology of the Southern California Bight, University of California Press, Berkeley, California, U.S.A., pp. 926.

Dayton, P. K. and R. R. Hessler (1972) Role of biological disturbance in maintaining diversity in the deep sea. Deep-Sea Research, 19: 199-208.

de Leeuw, J. W. and C. Largeau (1993) A review of macromolecular organic compounds that comprise living organisms and their role in kerogen, coal, and petroleum formation, p. 23-72. *In* Engel, M. H. and S. A. Macko [eds.], Organic Geochemistry. Plenum Press, New York, New York, U.S.A.

Deming, J. W., A. L. Reysenbach, S. A. Macko and C. R. Smith (1997) Evidence for the microbial basis of a chemoautotrophic community at a whale fall on the deep seafloor: bone-colonizing bacteria and invertebrate endosymbionts. Microscopy Research and Technique, 37: 162-170.

Denny, M. W. and B. Gaylord (2002) The mechanics of wave-swept algae. Journal of Experimental Biology, 205: 1355-1362.

Distel, D. L. and S. J. Roberts (1997) Bacterial endosymbionts in the gills of the deep-sea wood-boring bivalves *Xylophaga atlantica* and *Xylophaga washingtona.* Biological Bulletin, 192: 253-261.

Distel, D. L., A. R. Baco, E. Chuang, W. Morrill, C. Cavanaugh and C. R. Smith (2000) Do mussels take wooden steps to deep-sea vents? Nature, 403: 725-726.

Eganhouse, R. P. and M. I. Venkatesan (1993) Chemical oceanography and geochemistry, p. 71-189. *In* Dailey, M. D., D. J. Reish and A. J. W. [eds.], Ecology of the Southern California Bight. University of California Press, Berkeley, California, U.S.A.

Emery, K. O. (1960) The sea off southern California. John Wiley and sons, New York, New York, U.S.A., pp. 366.

Enríquez, S., C. M. Duarte and K. Sand-Jensen (1993) Patterns in decomposition rates among photosynthetic organisms: the importance of detritus C:N:P content. Oecologia, 94: 457-471.

Evans, P. G. H. (1987) The natural history of whales and dolphins. Facts on File, New York, New York, U.S.A., pp. 343.

Feldman, R. A., T. M. Shank, M. B. Black, A. R. Baco, C. R. Smith and R. C. Vrijenhoek (1998) Vestimentiferan on a Whale Fall. Biological Bulletin, 194: 116-119.

Fish, F. E. (1993) Power output and propulsive efficiency of swimming bottlenose dolphins (*Tursiops truncatus*). Journal of Experimental Biology, 185: 179-193.

Franklin, J. F. and T. A. Spies (1991) Composition, function, and structure of old growth Douglas-fir forests, p. 71-80. *In* Ruggiero, L. F., K. B. Aubry, A. B. Carey and M. H. Huff [eds.], Wildlife and vegetation of unmanaged Douglas-fir forests, General Technical Report PNW-GTR-285. U.S. Department of Agriculture, Forest Service, Pacific Northwest Research Station, Portland, Oregon, U.S.A.

Gage, J. D. and P. A. Tyler (1991) Deep-sea biology. Cambridge University Press, Cambridge, U.K., pp. 504.

Gaylord, B. and M. W. Denny (1997) Flow and flexibility. I. Effects of size, shape and stiffness in determining wave forces on the stipitate kelps *Eisenia arborea* and *Pterygophora californica*. Journal of Experimental Biology, 200: 3141-3164.

Gaylord, B., B. B. Hale and M. W. Denny (2001) Consequences of transient fluid forces for compliant benthic organisms. Journal of Experimental Biology, 204: 1347-1360.

Goldman, J. C. and M. R. Dennett (2000) Growth of marine bacteria in batch and continuous culture under carbon and nitrogen limitation. Limnology and Oceanography, 45: 789-800.

Hargrave, B. T., G. A. Phillips, N. J. Prouse and P. J. Cranford (1995) Rapid digestion and assimilation of bait by the deep-sea amphipod *Eurythenes gryllus*. Deep- Sea Research I, 42: 1905-1921.

Harrold, C., K. Light and S. Lisin (1998) Organic enrichment of submarine-canyon and continental-shelf benthic communities by macroalgal drift imported from nearshore kelp forests. Limnology and Oceanography, 43: 669-678.

Hart, M. R., D. de Fremery, C. K. Lyon and G. O. Kohler (1978) Dewatering kelp for fuel, feed, and food uses: process description and material balances. Transactions of the American Society of Agricultural Engineers, 21: 186-190,196.

Hedges, J. I., W. A. Clark, P. D. Quay, J. E. Richey, A. H. Devol and U. d. M. Santos (1986) Compositions and fluxes of particulate organic matter in the Amazon River. Limnology and Oceanography, 31: 717-738.

Ichihara, T. (1968) Whale products, p. 220-240. *In* Matthews, L. H. [ed.], The whale. Simon and Schuster, New York, New York, U.S.A.

Isaacs, J. D. and R. A. Schwartzlose (1975) Active animals of the deep-sea floor. Scientific American, 233: 85-91.

Jackson, G. A. (1977) Nutrients and production of giant kelp, *Macrocystis pyrifera*, off southern California. Limnology and Oceanography, 22: 979-955.

Jackson, G. A., F. Azam, A. F. Carlucci, R. W. Eppley and P. M. Williams (1989) Elemental cycling and fluxes off southern California. Eos Transactions of the American Geophysical Union, 70: 146-149, 154-155.

Jahnke, R. A. (1988) A simple, reliable, and inexpensive pore-water sampler. Limnology and Oceanography, 33: 483-487.

Jones, T. H. [ed.] (1989) The encyclopedia of wood, revised. Sterling Publishing Co., New York, New York, U.S.A., pp. 464.

Kemp, K. M., A. J. Jamieson, P. M. Bagley, H. McGrath, D. M. Bailey, M. A. Collins and I. G. Priede (2006) Consumption of a large bathyal food fall, a six month study in the north-east Atlantic. Marine Ecology Progress Series, 310: 65-76.

Knudsen, J. (1961) The bathyal and abyssal *Xylophaga* (Pholadidae, Bivalvia). Galathea Report, 5: 163-209.

Lyons, W. B. and H. E. Gaudette (1979) Sulfate reduction and the nature of organic matter in estuarine sediments. Organic Geochemistry, 1: 151-155.

Maser, C. and J. R. Sedell (1994) From the forest to the sea: the ecology of wood in streams, rivers, estuaries, and oceans. St. Lucie Press, Delray Beach, Florida, U.S.A., pp. 200.

Miller, P. J. O., M. P. Johnson, P. L. Tyack and E. A. Terray (2004) Swimming gaits, passive drag and buoyancy of diving sperm whales *Physeter macrocephalus*. Journal of Experimental Biology, 207: 1953-1967.

Newell, R. (1965) The role of detritus in the nutrition of two marine deposit feeders, the prosobranch *Hydrobia ulvae* and the bivalve *Macoma balthica*. Proceedings of the Zoological Society of London, 144: 25-45.

North, W. J. (1971) Introduction and background, p. 1-97. *In* North, W. J. [ed.], The biology of giant kelp beds (*Macrocystis*) in California, Beihefte zur Nova Hedwigia, Heft 32. Verlag von J. Cramer, Lehre, Germany.

Parker, W. J. and S. L. LeVan (1989) Kinetic properties of the components of Douglas-fir and the heat of combustion of their volatile pyrolysis products. Wood and Fiber Science, 21: 289-305.

Pearson, T. H. and R. Rosenberg (1978) Macrobenthic succession in relation to organic enrichment and pollution of the marine environment. Oceanography and Marine Biology: an Annual Review, 16: 229-311.

Priede, I. G. and N. R. Merrett (1996) Estimation of abundance of abyssal demersal fishes: a comparison of data from trawls and baited cameras. Journal of Fish Biology, 49 (Suppl. A): 207-216.

Priede, I. G. and N. R. Merrett (1998) The relationship between numbers of fish attracted to baited cameras and population density: Studies on demersal grenadiers *Coryphaenoides* (*Nematonurus*) *armatus* in the abyssal NE Atlantic Ocean. Fisheries Research, 36: 133-137.

Reimers, C. E. and K. L. J. Smith (1986) Reconciling measured and predicted fluxes of oxygen across the deep sea sediment-water interface. Limnology and Oceanography, 31: 305-318.

Reimers, C. E. (1987) An in situ microprofiling instrument for measuring interfacial pore water gradients: Methods and oxygen profiles from the North Pacific Ocean. Deep-Sea Research, 34: 2019-2035.

Robineau, D. and V. de Buffrénil (1993) Nouvelles données sur la masse du squelette chez le grands cétacés (Mammalia, Cetacea). Canadian Journal of Zoology, 71: 828-834.

Ruttenberg, K. C. and M. A. Goñi (1997) Phosphorus distribution, C:N:P ratios, and $\delta^{13}C_{OC}$ in arctic, temperate, and tropical coastal sediments: tools for characterizing bulk sedimentary organic matter. Marine Geology, 139: 123-145.

Schuller, D., D. Kadko and C. R. Smith (2004) Use of $^{210}Pb/^{226}Ra$ disequilibria in the dating of deep-sea whale falls. Earth and Planetary Science Letters, 218: 277-289.

Schwalbach, J. R. and D. S. Gorsline (1985) Holocene sediment budgets for the basins of the California Continental Borderland. Journal of Sedimentary Petrology, 55: 829-842.

Shaw, T. J., J. M. Gieskes and R. A. Jahnke (1990) Early diagenesis in differing depositional environments: the response of transition metals in pore water. Geochimica et Cosmochimica Acta, 54: 1233-1246.

Smith, A. H. and N. Pace (1971) Differential component and organ size relationship among whales. Environmental Physiology, 1: 122-136.

Smith, C. R. (1983) Enrichment, disturbance and deep-sea community structure: the significance of large organic falls to bathyal benthos in Santa Catalina Basin. Ph.D. Dissertation, University of California San Diego, pp. 310.

Smith, C. R. and S. C. Hamilton (1983) Epibenthic megafauna of a bathyal basin off southern California: patterns of abundance, biomass, and dispersion. Deep- Sea Research, 30: 907-928.

Smith, C. R. (1985) Food for the deep sea: utilization, dispersal, and flux of nekton falls at the Santa Catalina basin floor. Deep-Sea Research, 32: 417-442.

Smith, C. R. (1986) Nekton falls, low-intensity disturbance and community structure of infaunal benthos in the deep sea. Journal of Marine Research, 44: 567-600.

Smith, C. R., H. Kukert, R. A. Wheatcroft, P. A. Jumars and J. W. Deming (1989) Vent fauna on whale remains. Nature, 341: 27-28.

Smith, C. R., H. L. Maybaum, A. R. Baco, R. H. Pope, S. H. Carpenter, P. L. Yager, S. A. Macko and J. W. Deming (1998) Sediment community structure around a whale skeleton in the deep Northeast Pacific: Macrofaunal, microbial and bioturbation effects. Deep-Sea Research II, 45: 335-364.

Smith, C. R., A. R. Baco and A. G. Glover (2002a) Faunal succession on replicate deep-sea whale falls: time scales and vent-seep affinities. Cahiers de Biologie Marine, 43: 293-297.

Smith, C. R. and A. R. Baco (2003) Ecology of whale falls at the deep-sea floor. Oceanography and Marine Biology: an Annual Review, 41: 311-354.

Smith, C. R. (2007) Bigger is better: the role of whales as detritus in marine ecosystems, p. 286-302. *In* Estes, J. A., D. P. DeMaster, D. F. Doak, T. M. Williams and R. L.

Brownell Jr. [eds.], Whales, whaling, and ocean ecosystems. University of California Press, Berkeley, California, U.S.A.

Smith, K. L. (1987) Food energy supply and demand: a discrepancy between particulate organic carbon flux and sediment community oxygen consumption in the deep ocean. Limnology and Oceanography, 32: 201-220.

Smith, K. L., R. J. Baldwin and P. M. Williams (1992a) Reconciling particulate organic carbon flux and sediment community oxygen consumption in the deep North Pacific. Nature, 359: 313-316.

Smith, K. L., R. S. Kaufmann, J. L. Edelman and R. J. Baldwin (1992b) Abyssopelagic fauna in the central North Pacific: comparison of acoustic detection and trawl and bated trap collections to 5800 m. Deep-Sea Research, 39: 659-685.

Smith, K. L. (1992) Benthic boundary layer communities and carbon cycling at abyssal depths in the central North Pacific. Limnology and Oceanography, 37: 1034-1056.

Smith, K. L. and R. S. Kaufmann (1999) Long-term discrepancy between food supply and demand in the deep eastern north Pacific. Science, 284: 1174-1177.

Smith, K. L., R. J. Baldwin, D. M. Karl and A. Boetius (2002b) Benthic community responses to pulses in pelagic food supply: North Pacific Subtropical Gyre. Deep-Sea Research I, 49: 971-990.

Sokal, R. R. and F. J. Rohlf (1995) Biometry, 3rd edition. W. H. Freeman and Co, New York, New York, U.S.A., pp. 887.

Soldevilla, M. S., M. F. McKenna, S. M. Wiggins, R. E. Shadwick, T. W. Cranford and J. A. Hildebrand (2005) Cuvier's beaked whale (*Ziphius cavirostris*) head tissues: physical properties and CT imaging. Journal of Experimental Biology, 208: 2319-2332.

Sterner, R. W. and J. J. Elser (2002) Ecological Stoichiometry. Princeton University Press, Princeton, New Jersey, U.S.A., pp. 439.

Tamburri, M. N. and J. P. Barry (1999) Adaptations for scavenging by three diverse bathyal species, *Eptatretus stouti, Neptunea amianta, Orchomene obtusus*. Deep-Sea Research I, 46: 2079-2093.

Treude, T., C. R. Smith, W. Ziebis, F. Wenzhöfer, A. K. Hannides and A. Boetius (2006) A comparison of whale-fall, seep and vent habitats at the deep-sea floor: sulfide fluxes, persistence times and global distributions. Eos, Transactions of the American Geophysical Union, February 20th-24th, 2006, 87(36), Ocean Sciences Meeting Supplement, Abstract 11E-04.

Turner, R. D. (1973) Wood-boring bivalves, opportunistic species in the deep sea. Science, 180: 1377-1379.

Turner, R. D. (1978) Wood, mollusks, and deep-sea food chains. Bulletin of the American Malacological Union, 1977: 13-19.

Verardo, D. J., P. N. Froehlich and A. McIntyre (1990) Determination of organic carbon and nitrogen in marine sediments using the Carlo Erba NA-1500 Analyser. Deep-Sea Research I, 37: 157-165.

Vetter, E. W. (1994) Hotspots of benthic production. Nature, 372: 47.

Vetter, E. W. and P. K. Dayton (1998) Macrofaunal communities within and adjacent to a detritus-rich submarine canyon system. Deep-Sea Research II, 45: 25-54.

Vetter, E. W. (1998) Population dynamics of a dense assemblage of marine detritivores. Journal of Experimental Marine Biology and Ecology, 226: 131-161.

Vetter, E. W. and P. K. Dayton (1999) Organic enrichment by macrophyte detritus, and abundance patterns of megafaunal populations in submarine canyons. Marine Ecology Progress Series, 186: 137-148.

Wainwright, S. A. (1995) What can we learn from soft biomaterials and structures, p. 1-12. *In* Sarikaya, M. and I. A. Aksay [eds.], Biomimetics. American Institute of Physics, Woodbury, New York, U.S.A.

Wakeham, S. G. and C. Lee (1993) Production, transport, and alteration of particulate organic matter in the marine water column, p. 145-169. *In* Engel, M. H. and S. A. Macko [eds.], Organic Geochemistry. Plenum Press, New York, New York, U.S.A.

Watanabe, Y., E. A. Baranov, K. Sato, Y. Naito and N. Miyazaki (2006) Body density affects stroke patterns in Baikal seals. Journal of Experimental Biology, 209: 3269-3280.

Westrich, J. T. and R. A. Berner (1984) The role of sedimentary organic matter in bacterial sulfate reduction: the *G* model tested. Limnology and Oceanography, 29: 236-249.

Wing, B. L. and K. A. Clendenning (1971) Kelp surfaces and associated invertebrates, p. 320-341. *In* North, W. J. [ed.], The biology of giant kelp beds (*Macrocystis*) in California, Beihefte zur Nova Hedwigia, Heft 32. Verlag von J. Cramer, Lehre, Germany.

Wolff, T. (1979) Macrofaunal utilization of plant remains in the deep sea. Sarsia, 64: 117-136.

Woodward, R. L., J. P. Winn and F. E. Fish (2006) Morphological specializations of baleen whales associated with hydrodynamic performance and ecological niche. Journal of Morphology, 267: 1284-1294.

ZoBell, C. E. (1971) Drift seaweeds on San Diego County beaches, p. 269-314. *In* North, W. J. [ed.], The biology of giant kelp beds (*Macrocystis*) in California, Beihefte zur Nova Hedwigia, Heft 32. Verlag von J. Cramer, Lehre, Germany.

Chapter 7 – Modeling large organic fall processing by deep sea communities

7.1 Introduction

Large organic falls (LOF) consist of massive packages of organic matter that reach the seafloor and cannot be ingested whole by benthic infauna or epifauna. The organic material in these falls (massive organic matter, MOM) is instead processed by organisms during two stages of biotic activity: (a) the fragmentation, ingestion, and digestive processing of MOM by benthopelagic metazoa (Section *5.3*), and (b) and the sedimentary microbial processing of particulate organic matter (POM) derived from the first stage (Section *5.4*). A third stage, physical dispersal, is responsible for distributing the material generated during metazoan processing of the fall, i.e., biotic stage (a), to the sea floor sedimentary microbial communities, i.e., biotic stage (b).

If LOF occur in the deep sea, where background POM flux to the sea floor is relatively low, e.g., < 10 $g \cdot m^{-2} \cdot y^{-1}$ (e.g., Honjo et al. 1995; Berelson et al. 1997), they may cause substantial increases in the organic material supply rates to the sediments, followed by accelerated degradation rates, which may instigate a shift in sedimentary redox conditions, from oxic-suboxic to anoxic. The generation of sedimentary reducing conditions during LOF processing is important because of its potential role in sustaining biogenic chemosynthetic habitats in deep-sea sediments (Smith and Baco 2003; Aguilera et al. 2005). The shift in sedimentary redox conditions and the generation of reducing conditions in some types of LOF (e.g., whale falls) but not in others (e.g., wood falls) (Chapter 6) may reflect differences in several factors. These factors include LOF quality

(Table 6.1), LOF processing rates, MOM supply rates to surrounding sediments, and MOM degradation rates during early diagenesis.

Observational and experimental studies have provided some insight into both stages of LOF processing and their impacts on the surrounding benthopelagic and benthic communities (see Chapters 5 and 6). However, logistical limitations, e.g., remoteness of study sites, availability of certain LOF types, funding, etc., restrict our ability to carry out experiments to test further the effects of these factors on the development of biogenic reducing conditions in surrounding sediments. The use of mathematical models, parameterized using any available data, may provide useful insights to direct future opportunities for experimentation.

In this chapter, I explore the anatomy of a model of fall processing by deep sea floor communities. The proposed model incorporates metazoan processing and dispersal of fragmented material. I use two specific falls from the California Borderland Basins region as case studies to develop the proposed modeling concept. The availability of data from the case studies regarding the characteristics of the falls, processing rates, and impact of fall processing on monitored parameters permitted the assessment of the model output. I further discuss linking my model output to multi-component reaction transport models in order to study the development of biogenic reducing habitats as a result of LOF processing by metazoa during early diagenesis.

7.2 Model overview

The processing of LOF on the sea floor can be divided into three stages. The first stage is the fragmentation stage, during which metazoa attack the fall directly and process

the material by fragmentation, ingestion, absorption, and defecation. The second stage, referred to as the dispersal stage, describes the supply of unprocessed fragments and metazoan feces to the surrounding sediments. The final stage of the fall, the early diagenesis stage, involves the degradation of the supplied organic material by the sedimentary community.

The model addresses the first two stages of LOF processing, i.e., fragmentation and dispersal, which correspond to two homonymous model modules. The fragmentation module consisted of a box model tracing the passage of material from the fall to the pool of material available for dispersal. The dispersal module calculated the distribution of this material in the surrounding sediments using an area-averaged supply term, inspired from the seed dispersal literature.

Two case studies from the Santa Cruz Basin, California Borderland Basins region were used in this chapter to develop, test and evaluate this model. The first case study was based on a 13-m gray whale (*Eschrichtius robustus*) carcass, experimentally implanted by C. R. Smith and collaborators in April of 1998 (Smith and Baco 2003). The second case study involved 120-kg wood parcels deployed by C. R. Smith and collaborators in October 1999 and late April-early May 2002.

Details about whale and wood falls and their characteristics as they pertain to this modeling effort are presented in Table 7.1. The two fall types provide contrasting points along a continuum of fall size, quality, and processing rate. The soft tissue of whale falls is supplied in greater amounts, is more labile, and is consequently processed at faster rates than wood falls, which generally consist of very refractory material, only used directly by specialist metazoa and microbes, which accounts for slower processing rates

(see Chapter 5 for an extensive discussion of these fall types). The modeling concept proposed in this chapter may eventually be used to investigate the role of fall size, quality, and processing rate, on redox shifts in surrounding sediments and the generation of biogenic reducing habitats.

7.3 Methods

7.3.1 Whale fall fragmentation

7.3.1.1 Whale fall fragmentation model

The whale fall fragmentation model is shown in Figure 7.1. It was implemented in MATLAB (Mathworks Inc., Natick, Massachusetts, U.S.A.), a computation, visualization, and programming software package (see Appendix E). The initial conditions and flux values used are discussed in the following paragraphs.

7.3.1.2 Whale fall scavenging

Scavenging of a whale fall by bentho-pelagic scavengers was assumed to begin within minutes to hours of carcass arrival, and this assumption was based on a number of observations using baited camera studies (Dayton and Hessler 1972; Smith 1985; Priede et al. 1990; Priede et al. 1991). One single scavenging rate was used to represent the activity of all scavenging species. The scavenging rate, F_{SC} (kg·d^{-1}), has been shown to be related to the initial carcass weight, M_{cet} (kg), at the time of the fall arrival to the sea floor, t_0 ($t = 0$), by the following relationship (Smith and Baco 2003):

$$F_{SC} = 4.993 \times \ln(M_{cet}(t_0)) + 1.5996 \qquad 7.1$$

Table 7.1 Geometric and biochemical characteristics of the two LOF used as case studies in this chapter. The whale fall is from a carcass of a subadult gray whale, *Eschrichtius robustus*, in Santa Cruz Basin, while the wood fall consists of a parcel of untreated planks of Douglas fir, *Pseudotsuga menziesii*. Available tissue indicates the total tissue available to metazoa during the processing stage of the fall. Parameter symbols for the whale fall and wood fall are distinguished in the text with the subscripts *cet* and *wood* respectively.

Parameter, symbol (units)	**Whale fall**	**Wood parcel**
Weight, M (kg)	24300 [a]	120 [b]
Length, l (m)	13	2.4 [c]
Volume, V (m^3)	34.0 [d]	0.18 [c]
Available wet tissue, Wt (kg)	20680 [e]	120 [b]
Bulk density, ρ ($kg \cdot m^{-3}$)	1030 [d]	670 [b]
Water content, *WtH20* (kg, % of Wt)	11831, 57 [f]	36, 30 [g]
Carbon content, *WtC* (kg, % of Wt)	5394, 26 [f]	41, 34 [g]
Nitrogen content, *WtN* (kg, % of Wt)	567, 2.7 [f]	0.17, 0.14 [g]
Phosphorus content, *WtP* (kg, % of Wt)	25, 0.12 [f]	0.006, 0.005 [g]
Elemental molar ratio, C:N:P (-)	555:50:1 [f]	4860:20:1 [g]

[a] The weight, M_{cet} (kg), of the Santa Cruz whale fall carcass at the time of implantation has been reported as 35000 kg (Smith et al. 2002; Smith and Baco 2003; Chapter 6). In this chapter, it is calculated using the length, l (= 13 m) reported by Smith et al. (2002), and Lockyer's equation with coefficients from Woodward et al. (2006) for gray whales: $M_{cet} = 0.0054 \times l^{3.28}$ (M_{cet} is given in metric tons, which are converted to kg by multiplying by 1000).

[b] The total weight of the wood fall is estimated for a wet parcel under conditions of 100 % humidity using a density of 670 $kg \cdot m^{-3}$ (Browning 1963b; Jones 1989), and the volume of the wood parcel calculated in footnote c. Compare to a density of 465 $kg \cdot m^{-3}$ for green and dry wood (Jones 1989) which results to a total parcel weight of 85 kg.

[c] The wood fall parcel consisted of 22 planks of Douglas fir wood, each measuring 2.4 m × 0.09 m × 0.04 m, and arranged in sets of five. The volume of the parcel, V_{wood} (m^3), was calculated by multiplying the volume of each plank by 22 planks, i.e., $V_{wood} = 22 \times 2.4\ m \times 0.09\ m \times 0.04\ m$.

[d] The whale fall volume, V_{cet} (m^3), calculated by assuming neutral buoyancy and a density, $\rho_{cet} = 1030$ $kg \cdot m^{-3}$, therefore $V_{cet} = M_{cet} / \rho_{sw}$. The density, ρ_{cet} is the average of a range of estimates for seals (Watanabe et al. 2006) and sperm whales (*Physeter macrocephalus*; Miller et al. 2004).

[e] The whale fall tissue available for scavenging was calculated by multiplying M_{cet} by 0.85. Based on the morphometry relationships of Smith and Pace (1971), the skeleton of a whale in this particular size range constitutes 15 % of the total weight of the whale, M_{cet} (see footnote n of Table 6.1).

[f] Water, carbon, and nitrogen contributions to the available tissue, Wt_{cet}, were calculated using the weight fractions of blubber, muscle and internal organs to total weight, M_{cet}, and the distinct compositions of these body components (see footnote n of Table 6.1 for all the details). The atomic or molar C:N ratio of these components is 11.1. Phosphorus was assumed to be present in an atomic ratio N:P of 50, based on nitrogen and phosphorus composition of mammalian organs and organ systems by Elser et al. (1996).

[g] Water content of wood is reported in the case of saturation, i.e., 100 % relative humidity (Browning 1963b). Carbon, and nitrogen contributions to the available woody tissue, Wt_{wood}, were calculated using the chemical composition of the solids of *P. menziesii* in Parker and LeVan (1989) and additional reports on the protein content of wood (Browning 1963a; see footnote p of Table 6.1). Contribution of phosphorus was calculated by assuming a maximum ash content of wood equal to nitrogen, i.e., 0.2 % (e.g., Browning 1963a), and a phosphorus contribution to *Pseudotsuga* ash of 5 % (Ovington and Madgwick 1958).

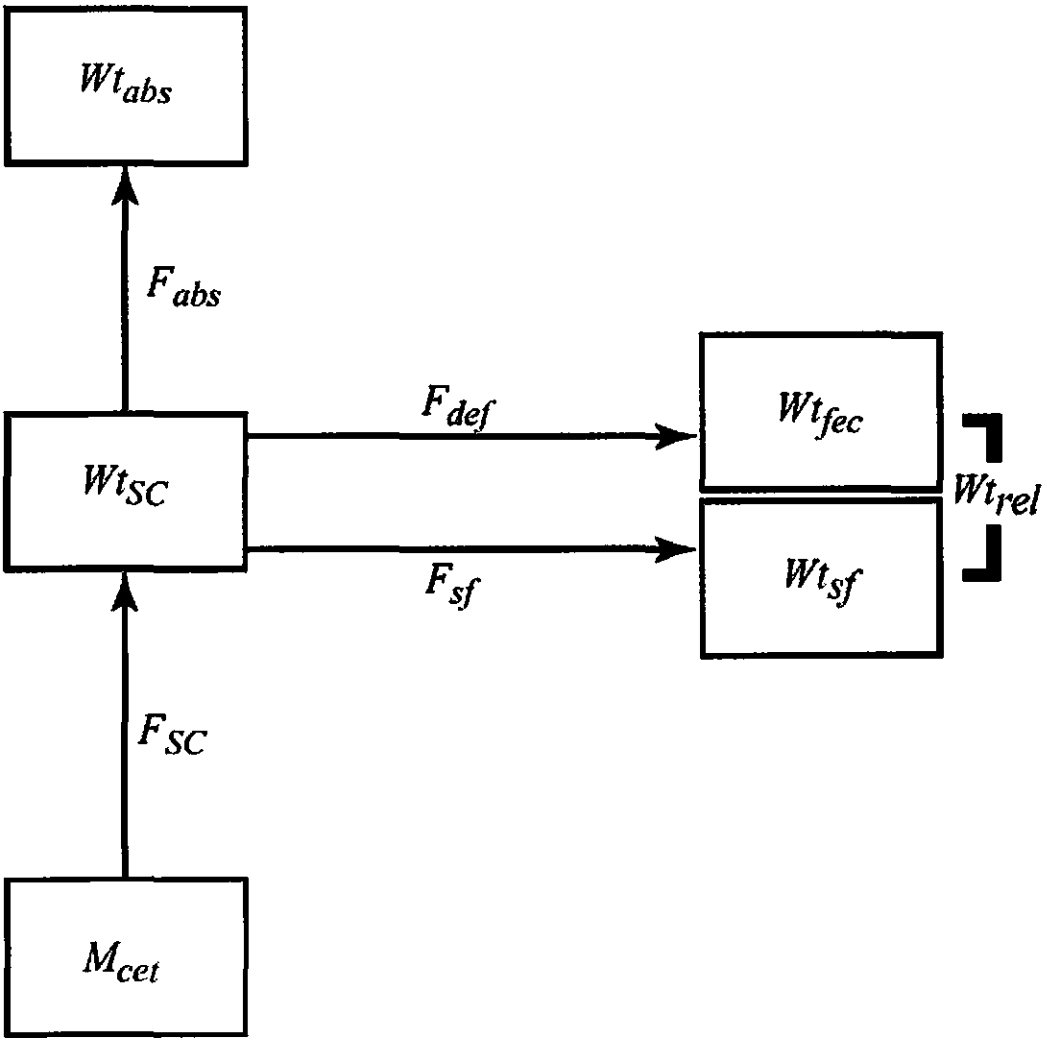

Figure 7.1 The whale fall fragmentation model: M_{cet} – whale fall mass, Wt_{SC} – scavenged mass, Wt_{abs} – scavenged mass absorbed by the scavenger, Wt_{fec} – scavenged mass defecated by the scavenger, Wt_{sf} – scavenged mass released by sloppy feeding, Wt_{rel} – total mass released for dispersal to sediments, F_{SC} – scavenging flux, F_{abs} – scavenger absorption flux, F_{def} – scavenger defecation flux, F_{sf} – sloppy feeding flux. Masses are calculated in kg, and fluxes in $kg \cdot d^{-1}$.

The scavenging rate, F_{SC}, is a time-averaged rate, in the sense that it was estimated using a carcass' initial soft tissue weight, $Wt_{cet}(t_0)$, divided by the time taken for the soft tissue to disappear, t_f (Smith and Baco 2003). It is possible that F_{SC} may vary during scavenging, perhaps in a Monod-type relationship with the remaining soft tissue. Since the dependency of F_{SC} on time or remaining soft tissue is not known, the simplest-case scenario was considered in this model, whereby F_{SC} is maintained constant (according to Eq. 7.1) throughout the duration of scavenging until the time point, t_f, when all of the soft tissue was removed ($M_{cet}(t_f) = M_{cet}(t_0) \times 0.15$). At that point, scavenging ceased:

$$M_{cet}(t_f)\ ,\ F_{SC} = 0$$

The fragmentation activity by the scavengers was assumed to lead to the production of two major types of fragments released to the surroundings: feces from the ingested material, Wt_{fec}, as well as uningested fragments escaping from the mouths of scavengers during removal from the fall, Wt_{sf} (a phenomenon referred to as "sloppy feeding," e.g., Møller 2007). Together, feces and uningested fragments constituted the total pool of material to be dispersed, Wt_{rel}:

$$Wt_{rel}(t) = Wt_{fec}(t) + Wt_{sf}(t) \qquad 7.2$$

$$F_{rel}(t) = F_{fec}(t) + F_{sf}(t). \qquad 7.3$$

The role of defecation and sloppy feeding in supply of dispersed material to the sediments is discussed in the next section, *7.3.1.3*.

7.3.1.3 Whale fall scavenger metabolic considerations

The proportion of ingested MOM that is released as feces (defined as the defecation component, DFC) depends on the absorption efficiency of the scavengers.

Moreover, it is important to know whether the major components of the whale's soft tissue, primarily glycolipids and proteins, are processed at a similar rate during digestion. Differences in these two components' elemental contents (especially in C and N) indicate potential variability in the elemental ratio of the released material, if the components are digested with different efficiencies, and the elemental ratio may affect the quality of the material, and consequently its degradation rate. There is a dearth of information on the absorption efficiencies of the scavengers relevant to this case study, mainly the hagfish *Eptatretus deani* and the sleeper shark, *Somniosus pacificus* (Smith et al. 2002). The absorption efficiency (defined as the proportion of the ingested material not lost as feces) of two deep-sea zoarcids, *Melanostigma pammelas* and *Lycodapus mandibularis*, was recently investigated by Drazen et al. (2007). It was found to be very high (87-90 %), while assimilation efficiency varied between 84-86.5 %. The feed used (krill meal, *Euphasia pacifica*) was rich in both lipids and protein, and this allowed the comparison of absorption efficiencies for these two components. The *M. pammelas* individuals fed multiple meals appeared to absorb protein and lipids equally.

Based on the results of Drazen et al. (2007), I assumed an absorption efficiency of 90 % of the ingested material. This assumption translated to a DFC (defecation component) value of 0.1. I also assumed an absorption efficiency of 90 % for both proteins and lipids, which constitute the vast majority of the ingested tissue (Table 6.1). This assumption means that the defecated material retains the elemental ratio value of the source. Finally, I assumed that defecation occurs after a relatively long gut passage time of 10 d (J. C. Drazen, personal communication). Based on these assumptions, the flux of defecated material, F_{def} (kg·d^{-1}), was expressed as follows:

$$F_{def}(t + 10) = (F_{SC}(t) - F_{sf}(t)) \times \text{DFC} \quad 7.4$$

where F_{SC} (kg·d^{-1}) is the scavenging rate, F_{sf} (kg·d^{-1}) is the sloppy feeding flux, and DFC is the defecation component. I also assumed that as soon as all the soft tissue is removed (i.e., at t_f), the scavengers depart, ending the supply of defecated material to the surrounding sediments:

$$M_{cet}(t_f) , F_{def} = 0.$$

It has been shown that MOM ingested by scavengers such as *Coryphaenoides* is rapidly dispersed over a much larger area than that of the LOF (Priede et al. 1990; Priede et al. 1991). However, the studies by Priede et al. (1990; 1991) used mackerel carcasses with weights of an average weight of 0.5 kg, much smaller than the estimated 24300 kg of the Santa Cruz whale carcass. It is possible that with a substantial food source still available, individual scavengers could pursue the strategy of suspending search activities for a different food source and continue feeding at this particular LOF (Dayton and Hessler 1972). Clearly, the effects of carcass size on the behavior of scavengers, while there is still a significant point source of nutrition, are not well known. Consequently, the model proposed here could only help constrain the contribution of defecation to MOM flux to the sediments immediately surrounding the falls. The amount of Wt_{fec} contributing to Wt_{rel} was bound at the lower end by the case where all feces are removed from the LOF area, as in Priede et al. (1991), i.e. (from Eq. 7.2):

$$Wt_{rel} = Wt_{sf}. \quad 7.5$$

$$F_{rel}(t) = F_{sf}(t). \quad 7.6$$

The upper boundary of the contribution of Wt_{fec} to Wt_{rel} was set by the case where all the feces are being released in the LOF area (Eq. 7.2).

7.3.1.4 The importance of sloppy feeding

Loss of MOM during sloppy feeding is evident from footage of scavengers feeding on the Santa Cruz whale fall, as strands of fat and tissue drifting originating from the immediate area of activity of the scavengers and drifting across the field of view (personal observations). In addition, sediment cores, collected several years after the fall event (4.5 y; Chapter 6) from the vicinity of the fall, included fragments of whale tissue and blubber, corroborating the importance of sloppy feeding. Because this MOM escapes ingestion and the substantial accompanying absorption, it could potentially contribute to a significant degree to MOM supply to the surrounding sediments.

The proportion of scavenged soft tissue, Wt_{SC}, which escapes scavenger digestion (hereon referred to as the sloppy feeding component, SFC), is unknown. I attempted to obtain an order-of-magnitude estimate of SFC by observing footage of scavenging from the whale carcass under study. It was impossible to quantify the volume of drifting strands of fat and tissue due to the lack of scale and their irregular, ever-changing shape as they cross the field of view. The best-guess estimate of a maximum limit on the value of SFC is 0.1 (10 %, C. R. Smith, personal communication). Instead of committing to a certain fraction, various degrees of SFC (between 0.01 % and 10 %) were tested, to compare this process' potential contribution to total material released from scavenger activity.

7.3.1.5 MOM carbon release rates

The rate of MOM release was calculated from the linear slope, F_{mat} (kg·d^{-1}), of the relationship between Wt_{rel} (kg) and t (d). Since F_{mat} represents soft wet tissue weight

released per unit time ($kg \cdot d^{-1}$), it was converted to the production rate of carbon available for dispersal, F_{matC} ($kg \cdot d^{-1}$), by multiplying F_{mat} by the weight fraction of C, $WtC_{cet} = 26$ % (Table 7.1):

$$F_{matC} = F_{mat} \times WtC_{cet}. \quad 7.7$$

Similarly, production rates of N and P (F_{matN} and F_{matP}, respectively) were calculated using the C:N:P value of 555:50:1 (Table 7.1), based on the assumptions discussed in section *7.3.1.3*) by multiplying F_{matC} with 50/555 and 1/555 respectively.

7.3.2 Wood fall fragmentation

7.3.2.1 Basic information on wood fall fragmentation

Wood falls in the case study area, as in most deep sea sites, are primarily exploited by bivalves of the genus *Xylophaga* (Turner 1973; Smith et al., in preparation). Individuals colonize wood LOF as larvae and excavate the wood using their shells, to form oblong cavities (Knudsen 1961; Distel and Roberts 1997). While excavating, they consume the wood shavings, which are stored in a large caecum and from there are transported to the stomach (Distel and Roberts 1997). Elemental analysis of sedimentary samples adjacent to 3 year-old wood falls in the California Borderland Basins (Chapter 6), along with a conservative mixing model calculation (Section *6.4.2.1*) indicated that the digestive processing of the ingested wood shavings does not result in a detectable change in elemental composition by the time the ingested material is released to the surrounding sediments. Therefore, wood fall processing by metazoa could be modeled purely as a fragmentation process (see Appendix F).

Wood fragmentation by wood borers is thought to occur during the first months to years after the fall event (Turner 1973; 1978). After settling as larvae, wood borers grow to a population biomass capable of sustaining predators and scavengers that feed on them, whereupon this specialized food web can collapse (Turner 1978). Wood fragmentation can thus be considered to end immediately or soon after predation begins, typically years after the fall event. At this point, it is not known whether re-colonization of wood LOF follows such predation events, or whether it continues throughout. It could be speculated that continuous or repeated colonization is likely, given that the substrate, i.e., the wood LOF, is not altered in any significant manner as a settling and feeding surface (personal observations). In this study, a time-averaged, continuous wood fall fragmentation rate was used to model the processing of a wood LOF in the California Borderland Basins region (Table 7.1).

7.3.2.2 Wood removal rates

The rate of wood fall fragmentation was constrained by measuring the volume of small blocks of Douglas fir (*Pseudotsuga menziesii*) wood, retrieved from two wood falls, one in Santa Cruz Basin (CRS 800) and one in Santa Catalina Basin (CRS 398; see Table 6.2 for more details). The wood blocks were retrieved from the sea floor at the ages of 1.9 y, 4.5 y, and 5.4 y after deposition. The volume of the wood blocks at the time of collection was measured with volume displacement, by immersing water-saturated wood samples were suspended from a fine string into a container filled with distilled water and measuring the displaced volume of water. The measured volume of water was subtracted from the envelope volume, V_l (cm^3), i.e. the geometric volume of the original wood

block, to yield the missing volume, $V_{i\text{-}missing}$ (cm^3). The volume of missing wood, $V_{T\text{-}missing}$ (m^3), from the sampled wood fall was calculated with the following equation:

$$V_{T-missing} = \frac{V_{wood} \times \Sigma V_{i-missing}}{\Sigma V_i} \qquad 7.8$$

where V_{wood} (m^3) is the total volume of the wood fall (0.18 m^3; Table 7.1), $\Sigma V_{i\text{-}missing}$ (cm^3) is the sum of all $V_{i\text{-}missing}$, and ΣV_i (cm^3) is the sum of all V_i (cm^3). The missing volume, $V_{T\text{-}missing}$ (m^3), was converted to a missing weight by multiplying by a bulk density, ρ_{wood}, of 670 $kg \cdot m^{-3}$ (Table 7.1). The missing weight corresponds to the cumulative weight of wood removed during the implantation period, Wt_{WR} (kg). The time-integrated removal rate of wood, F_{WR} ($kg \cdot d^{-1}$), was calculated by dividing Wt_{WR} (kg) by the age of the wood fall at the time of collection (d).

7.3.2.3 Wood borer metabolic considerations

To convert the removal rate of wood, F_{WR}, by wood borers to the rate of MOM release to the surrounding sediments, F_{mat}, one must consider the fraction of the removed material which is used by wood borers and their symbionts before release as feces. The absorption efficiency (defined in section *7.3.1.3* as the proportion of the ingested material not lost as feces) is currently not known for any wood-boring species, including the better studied Teredinidae (Gallager et al. 1981; Distel and Roberts 1997). Bioenergetic studies of other bivalves revealed great variation in absorption efficiency (from <10 % to >90 %), caused by variation in organic matter source and quality (see discussion in Grant and Bacher 1998). Estimates of the absorption efficiency of *Geukensia demissa* (one of a number of bivalves exhibiting cellulase activity, Brock and Kennedy 1992) when fed a

cellulose-rich diet ranged between 9 % and 14 % (Langdon and Newell 1990), and suggest that relatively refractory materials, such as wood, may be absorbed with efficiencies that are on the low end of the ranges reported for bivalve taxa.

Based on the taxonomically relevant bioenergetic information described above, I assumed an absorption efficiency of 10 %. Consequently, the value of the proportion of ingested MOM which is released as feces (the defecation component, DFC) was 0.9. The rate of wood MOM release to the surrounding sediments, F_{mat} (kg·d^{-1}), was defined as:

$$F_{mat} = F_{WR} \times \text{DFC} \qquad 7.9$$

As in the whale fall case study, F_{mat} was converted to the production rate of carbon available for dispersal, F_{matC} (kg·d^{-1}) using Eq. 7.7 and a weight fraction of C, WtC_{wood} = 34 % (Table 7.1). The rates of release of N and P, F_{matN} and F_{matP} respectively, were assumed to be proportional to that of C, F_{matC}, based on the C:N:P value of 4860:20:1 (Table 7.1).

7.3.3 Dispersal of whale MOM

7.3.3.1 Description of the whale LOF dispersal module

The purpose of this module was to model the distribution of MOM released from the fall during fragmentation to the surrounding sediments. The problem of modeling the tracking and settling of particles released from a point source has occupied the field of fish cage farming for some time. Efforts to model the settling and deposition of feces and uneaten food particles from fish cages (particle tracking models) indicated a number of elements that are needed for reliable predictions (e.g., Cromey et al. 1998; 2002):

a) Particle numbers and size-ranges, which can be determined by sampling water as close to the point of release as possible and analyzing the collected particles therein, e.g., by the electrical sensing zone (ESZ) method (using a Coulter counter).

b) Particle settling velocities, which can either be determined using settling cylinder measurements or can be calculated using a Stokes' model (McCave 1975; Eq. 2.5).

c) Current velocities, which are typically measured using current meters, and used to calculate turbulent dispersion coefficients, which are used in a three-dimensional random walk model (e.g., Allen 1982).

All this information could be combined in a three dimensional grid to calculate the time and place each particle will settle (see DEPOMOD by Cromey et al. 2002 for an example).

The information currently available on LOF, even from the better studied cases, was inadequate to allow the construction of a thorough particle dispersal model for LOF. Instead, the fields of botany and forestry provided an alternative route to follow in this modeling exercise. The distribution of feces and uneaten particles from a fall is analogous to a "seed shadow," which describes the dispersal of seeds by describing the density of seeds with distance from a source (Clark et al. 1999):

$$\text{seed shadow} = \text{fecundity} \times \text{dispersal kernel}$$

$$\left(\frac{\#}{\mathrm{m}^2 \cdot \mathrm{y}}\right) = \left(\frac{\#}{\mathrm{y}}\right) \times \left(\frac{1}{\mathrm{m}^2}\right) \qquad 7.10$$

In the case of C released from a LOF, the seed shadow was replaced by a supply rate, $F_{sedC}(r)$ ($\mathrm{mg \cdot cm^{-2} \cdot y^{-1}}$), which is a function of distance, r (cm), from the perimeter of the fall ($r = 0$). The fecundity was replaced by the production rate of C available for

dispersal, F_{matC} (Eq. 7.7), converted from units of $kg \cdot d^{-1}$ to units of $mg \cdot y^{-1}$ by multiplying by 3.65×10^8. The dispersal kernel, $DK(r)$ (cm^{-2}), describes the scatter of particles from the perimeter of the fall ($r = 0$), and is discussed extensively in the next section, *7.3.3.2.* Assuming radial symmetry, the final adapted equation becomes:

$$F_{sedC}(r) = F_{matC} \times DK(r). \qquad 7.11$$

7.3.3.2 The dispersal kernel around a whale fall

The dispersal kernel, *DK*, is in essence a "probability density," i.e., it is defined as the probability that a particle lands on an area of the seafloor at distance r from the perimeter of the fall ($r = 0$ cm). The r-dependent *DK* is the product of an area normalization factor, $N(r)$ (cm^{-2}), and a dimensionless density function, $\rho_f(r)$:

$$DK(r) = N(r) \times \rho_f(r) \qquad 7.12$$

To calculate the area normalization factor, $N(r)$, the seafloor area radiating away from the fall was divided into subunits, whose dimensions were realistic with regard to the observational methods used for data collection. Considering that the diameter of cores used to sample sediments during field investigations of this fall (and thus the horizontal resolution of data) was 7 cm (e.g., Chapter 6), this area was divided into rings of width, $r_w = 10$ cm. To calculate the area of each ring, I assumed that the Santa Cruz whale fall occupied an area of the seafloor in the form of a prolate ellipse, whose major axis, l_{cet1} (cm), is the length of the carcass, $l_{cet} = 1300$ cm (Table 7.1) and whose minor axis, $l_{cet2} = 230$ cm, was calculated using the ratio $l_{cet1} : l_{cet2} = 5.64$, determined for *E. robustus* by Woodward et al. (2006). The area, A (cm^2), of a ring i located between the distances $r = r_i$

and $r = r_f + r_w$ from the fall, i.e., from the ellipse's perimeter, is defined by the following generic formula:

$$A(r_f) = \pi \times r_w \times (s_{cet1} + s_{cet2} + 2r_f + r_w) \quad 7.13$$

where $s_{cet1} = l_{cet1} \div 2$ (cm), and $s_{cet1} = l_{cet2} \div 2$ (cm). The resulting relationship between r_f (cm) and A (cm^2) for this particular whale fall is:

$$A(r_f) = 63r_f + 2.4347\times10^4 \quad 7.14$$

and is shown in Figure 7.2. The consequent normalization factor, $N(r_f)$ (cm^{-2}) is:

$$N(r_f) = A(r_f)^{-1}. \quad 7.15$$

For the purposes of this model, I assumed the most common form of density function, ρ_f, used in seed shadows (Clark et al. 1999), the exponential:

$$\rho_f(r) = e^{-\alpha r} \quad 7.16$$

where α (cm^{-1}) is a distance coefficient, and r is distance.

The value of α determines the maximum distance, r_{max}, from the fall at which the fall TOC supply rate, F_{sedC}, is non-negligible. To determine α, one needs a sense of the distance over which F_{sedC} is non-negligible as well as a quantitative definition of "non-negligible." Observations and measurements from past studies at this fall have shown that differences in values of biological and geochemical sedimentary parameters from those of background sediments extended at least to a distance of 3 m from the perimeter of the fall, while at 9 m the values of these parameters were indistinguishable from background (Baco-Taylor 2002; Smith et al. 2002; Smith and Baco 2003; Treude et al., in preparation; Chapter 6). Based on this, I assumed that, in the case of the Santa Cruz

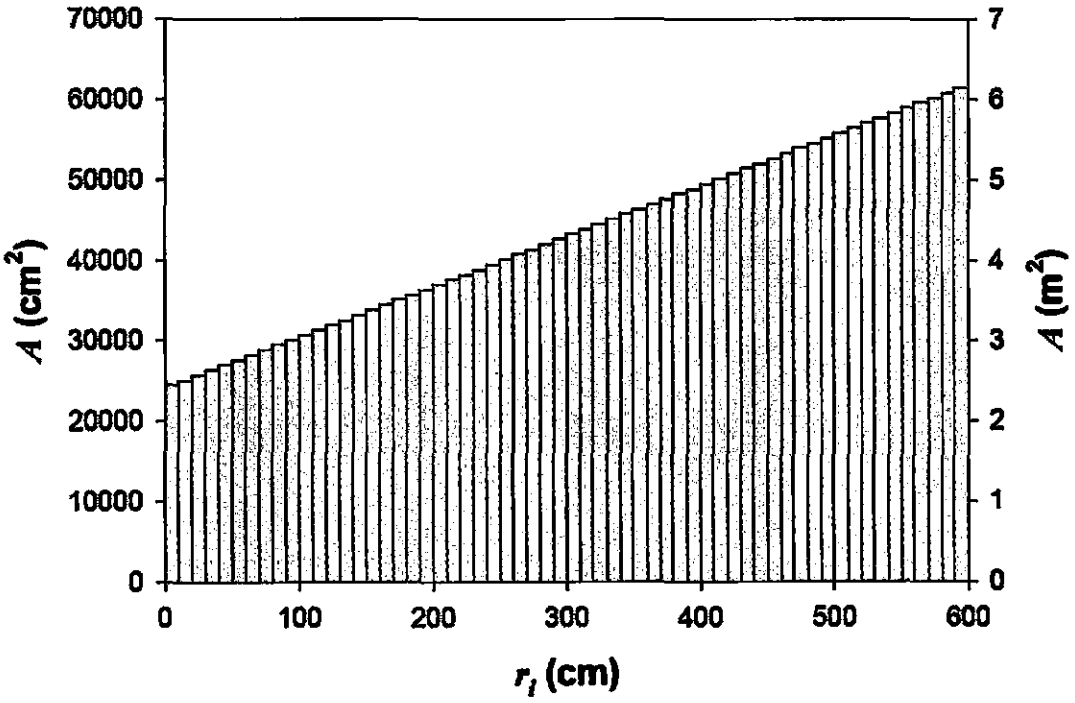

Figure 7.2 The variation of the area of 10 cm-wide areal rings, A (Eq. 7.14), with distance r_i (cm), away from the Santa Cruz whale fall (only the first 6 m shown).

whale fall, the maximum distance, r_{max}, at which F_{sedC} is non-negligible is 600 cm, i.e., the mid-point between 3 m and 9 m.

I defined as "non-negligible" the case where the TOC supply rate from the fall input, F_{sedC}, was more than 5 % the natural TOC sedimentation rate in Santa Cruz basin. The value of 5 % originates from frequently reported upper values of analytical precision for TOC measurements using a CHN auto-analyzer (e.g., King et al. 1998; Ingalls et al. 2004). Stated differently, "non-negligible" flux in this case is defined as that which was one standard deviation greater than the mean background flux. Using a reported value of natural TOC sedimentation rate in Santa Cruz Basin of 1.2 $mg \cdot cm^{-2} \cdot y^{-1}$ (Eganhouse and Venkatesan 1993), non-negligible F_{sedC} in this particular case should exceed 0.06 $mg \cdot cm^{-2} \cdot y^{-1}$.

An optimization process was used to find the value of α at which $F_{sedC}(600) >$ 0.06 $mg \cdot cm^{-2} \cdot y^{-1}$. An initial value of α was calculated by setting $\rho_f(r_{max}) \div \rho_f(0) = 0.001$ %, such that, when solved using Eq. 7.16, resulted in:

$$\alpha = -\frac{\ln\left(1 \times 10^{-5}\right)}{r_{max}}. \qquad 7.17$$

For r_{max} = 600 cm, the initial $\alpha = 1.92 \times 10^{-2}$ cm^{-1}. The optimization consisted of running the model with incremental values of α until F_{sedC} at 590-600 cm exceeds 0.06 $mg \cdot cm^{-2} \cdot y^{-1}$. After the optimization of α, the value of the density function for each areal ring, $\rho_f(r_i)$, was calculated as follows:

$$\rho_f(r_i) = \frac{\int_{r}^{r+r_w} e^{-\alpha r}\, dr}{\int_{0}^{r_{max}} e^{-\alpha r}\, dr}. \qquad 7.18$$

7.3.4 Dispersal of wood MOM

7.3.4.1 Description of the wood LOF dispersal module

The approach that was followed in the modeling of the dispersal of material released from the wood falls of the case study was similar to that used in the whale fall, i.e., the adaptation of the "seed shadow" concept to the particular problem of LOF (see discussion in section 7.3.3.1). The production rate of C, F_{matC}, available for dispersal (Table 7.3) is converted from units of $kg \cdot d^{-1}$ to units of $mg \cdot y^{-1}$ by multiplying by 3.65×10^8. The converted F_{matC}, is multiplied by a dispersal kernel, $DK(r)$ (cm^{-2}), to yield the supply rate of C to the sediments, $F_{sedC}(r)$ ($mg \cdot cm^{-2} \cdot y^{-1}$), which is a function of distance, r (cm), from the perimeter of the fall (Eq. 7.11). The dispersal kernel for a wood fall is different than that for a whale fall and is discussed in the next section.

7.3.4.2 The dispersal kernel around a wood fall

The wood falls under study occupy a rectangular area with length, $l_{wood1} = 240$ cm (Table 7.1), and width, $l_{cel} = 45$ cm. The area, A (cm^2), of a ring i located between the distances $r = r_l$ and $r = r_l + r_w$ from the fall, i.e., from the rectangle's perimeter, is defined by the following generic formula:

$$A(r_l) = 2r_w \times (l_{wood1} + l_{wood2} + 4r_l + 2r_w) \qquad 7.19$$

where $r_w = 10$ cm (see section *7.3.3.2* for a discussion on the value of r_w). The resulting relationship between r_l (cm) and A (cm^2) for this particular whale fall is:

$$A(r_l) = 80r_l + 6.1 \times 10^3. \qquad 7.20$$

The consequent normalization factor, $N(r_i)$ (cm^{-2}) is shown in Eq. 7.15.

The second step in the determination of the dispersal kernel is the parameterization of the density function, ρ_f (Eq. 7.16). The two parameters needed to define ρ_f are the maximum distance, r_{max}, at which the supply rate of TOC due to the fall, F_{sedC}, is non-negligible. A "non-negligible" F_{sedC} at the study area has been defined as that which exceeds 0.06 $mg \cdot cm^{-2} \cdot y^{-1}$ (section *7.3.3.2*). Based on observations of sedimentary TOC content away from wood falls at the study area (Chapter 6) as well as other biological indicators (Smith and Bernardino, unpublished data), the maximum distance, r_{max}, in this case was set at 50 cm. The small r_{max} value for the case study wood fall compared to that for the whale fall is due to the immobility of the wood borers as well as due to the relative sizes of the two types of falls. The optimization routine to determine the value of α at which $F_{sedC}(50) > 0.06$ $mg \cdot cm^{-2} \cdot y^{-1}$ was performed as in section *7.3.3.2*, after determining an initial value for $\alpha = 2.30 \times 10^{-1}$ cm^{-1} by applying r_{max} = 50 cm in Eq. 7.17.

7.4 Results and discussion

7.4.1 Fall fragmentation

7.4.1.1 Whale fall fragmentation

Two sets of runs of the whale fall fragmentation module were performed: one in which defecation contributed to the pool of released MOM during fragmentation, and one in which it did not (Eq. 7.2 and 7.5 respectively). In both sets, individual runs were

performed with SFC values ranging from 0.001 to 0.1, and iteration time steps of 0.25 d. The results are shown in Table 7.2 and Figure 7.3. The soft tissue of the Santa Cruz whale fall was completely removed by t_f = 397 d, which renders the importance of the assumption of a defecation lag of 10 d (Eq. 7.4) relatively minor.

The model results propose an upper limit of the amount of carbon generated during the fragmentation stage of this fall. The upper limit is set when the highest estimate of sloppy feeding generated material is assumed (SFC = 0.1), while all the feces are released in the vicinity of the LOF, and has a value of $Wt_{relC}(397)$ = 1010 kg and F_{matC} = 2.57 kg·d^{-1}. The lower limit of $Wt_{relC}(397)$ and F_{matC} can be constrained by referring to the limited data available. A calculation reported elsewhere in this dissertation (section *6.4.3*) showed that, based on a total organic carbon (TOC) profile obtained 5.8 years after the fall event, at least 34 kg of C from the carcass were still present in sediments adjacent to the fall. The supply rate, F_{matC}, of TOC needed to produce such a pool of TOC is 0.09 kg ·d^{-1}, (34 kg ÷ 397 d, where 397 d = t_f), assuming that the supplied TOC does not degrade. The "no degradation" assumption is unrealistic, judging by geochemical and biological evidence at this fall that is indicative of intense organic matter processing and decomposition in the sediments (Baco-Taylor 2002; Smith et al. 2002; Smith and Baco 2003; Treude et al., in preparation; Chapter 6). Therefore, a lower limit of F_{matC} = 0.09 kg·d^{-1} during the scavenging period is almost certainly an underestimate. The results of the fragmentation module runs in Table 7.2 indicate the scenaria of SFC = 0.001 and SFC = 0.005, both in the absence of defecation input, which would result in F_{matC} < 0.09 kg·d^{-1}. Using the relationship between F_{matC} and SFC from Figure 7.3, I estimated that, in the absence of defecation input, SFC should be ≥ 0.007 for F_{matC} to exceed 0.09 kg·d^{-1}.

Table 7.2 Results of runs of the whale fall fragmentation module at selected evenly-spaced SFC values (see Figure 7.3). For the two sets of runs (excluding and including the defecation contribution (Wt_{fec}), both the cumulative amount of carbon released by the completed fragmentation of the soft tissue of the fall ($Wt_{relC}(t_f)$, kg) and the production rate of carbon during the fragmentation stage (F_{matC}, kg·d^{-1}) are shown.

	Without Wt_{fec} input		**With Wt_{fec} input**	
SFC	**$Wt_{relC}(t_f)$ (kg)**	**F_{matC} (kg·d^{-1})**	**$Wt_{relC}(t_f)$ (kg)**	**F_{matC} (kg·d^{-1})**
0.001	5.4	0.0135	529	1.36
0.005	26.9	0.0676	548	1.41
0.01	53.8	0.135	573	1.47
0.05	269	0.676	766	1.96
0.1	538	1.35	1010	2.57

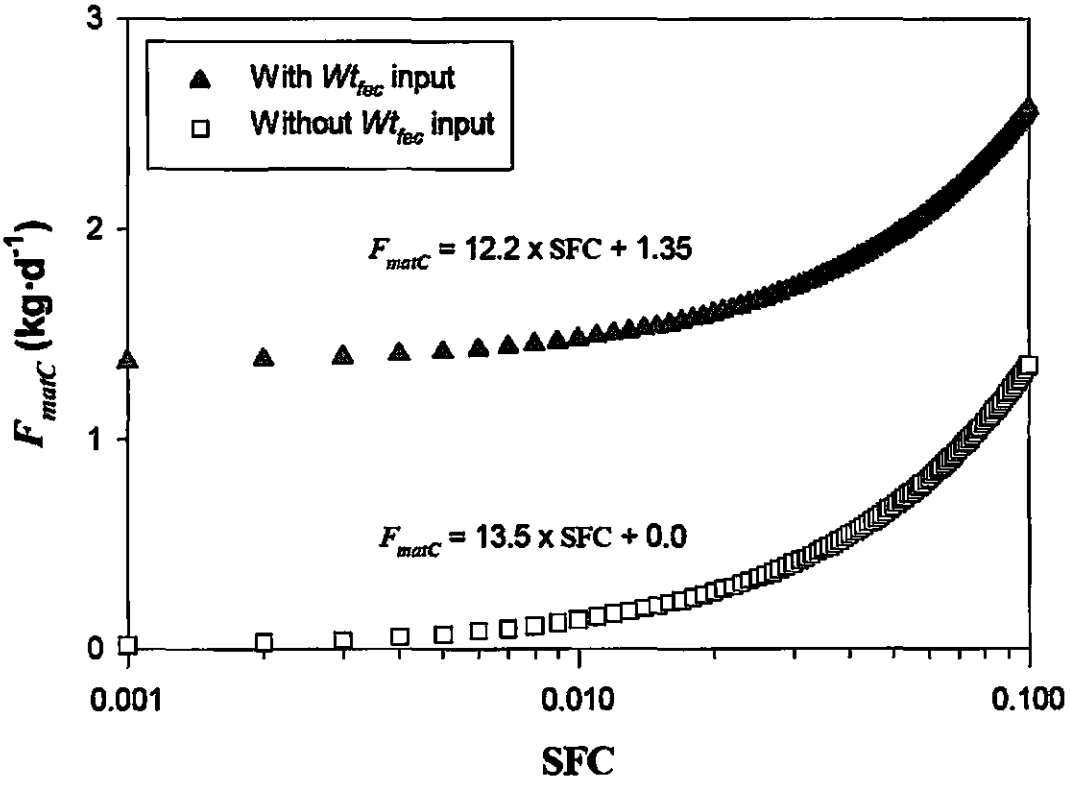

Figure 7.3 The modeled production rate of carbon during the fragmentation stage (F_{matC}, kg·d^{-1}) from the whale fall plotted against the sloppy feeding component (SFC). Each point on the plot represents the results of a single model run. The runs were performed in two sets: one including the contribution of defecation (Wt_{fec}) and one excluding the contribution of defecation (Eq. 7.2 and 7.5 respectively). Within each set, the sloppy feeding component (SFC) ranged from 0.001 to 0.1 in increments of 0.001, and is plotted against the modeled rate of carbon production by scavenging, F_{matC} (kg·d^{-1}) at the Santa Cruz whale fall. Equations indicate the linear relationships between the two parameters.

In summary, the results of the modeling calculations by the fragmentation module suggest that the processing of the Santa Cruz whale fall yields TOC generation rates, F_{matC}, by fall fragmentation in the range of 0.09-2.57 $kg \cdot d^{-1}$ for a period of 397 d after the fall event. Sloppy feeding alone may only generate such levels of TOC supply rate if the fraction of the processed material that escapes ingestion, SFC, is greater than 0.007. Using the reported value of background TOC sedimentation rate of 1.2 $mg \cdot cm^{-2} \cdot y^{-1}$ in Santa Cruz Basin (Eganhouse and Venkatesan 1993), I estimated that 0.09-2.57 $kg \cdot d^{-1}$ corresponds to the daily background TOC supply on an area of 2,700-78,200 m^2 of Santa Cruz Basin sea floor.

Critical parameters used in the fragmentation module are the scavenging rate, the sloppy feeding component, and the defecation component. The scavenging rate on a whale fall was calculated from a relationship published by Smith and Baco (2003) based on five observations. Clearly, more observations are needed but the calculated relationship constrains sufficiently the scavenging rate for the purposes of this study. The relative importance of sloppy feeding is a major unknown. The model presented in this chapter reveals that it can have a significant effect on the amount of the soft tissue of a whale fall which is dispersed to the sediments in the immediate vicinity of the fall.

Another unknown factor which needs further investigation is the behavior of individual scavengers in the presence of a whale fall weighing several tons. Some previous investigations suggest that scavengers may depart a LOF after feeding and dispersing the ingested material over great distances (Priede et al. 1991), while other studies (Smith 1985) suggest that scavengers may remain in the vicinity of LOF for several days. It should be noted that the LOF sizes used in these investigations were

much smaller than the whale fall used as a case study in this chapter. If scavengers, such as hagfish, which are attracted to a large whale fall, remain in the immediate vicinity of the fall for extensive periods of time (> 10 d), they may return some of the ingested material as feces. Because of the very high ingestion rates of soft tissue by scavengers (i.e., comparatively low SFC), the contribution of defecation to MOM release around a whale LOF can be dramatic (e.g., Figure 7.3). The question of the impact of defecation on organic matter input to sediments around a fall signifies the importance of individual behavior on a biogeochemical process.

7.4.1.2 Wood fall fragmentation

The results of measurements and calculations are shown in Table 7.3. The values of F_{WR} varied within an order of magnitude, between 0.011 kg·d^{-1} and 0.051 kg·d^{-1}, while the rate of C release, F_{matC}, ranged between 0.004 kg·d^{-1} and 0.017 kg·d^{-1}. If the F_{WR} values are divided into the weight of the tissue available for processing, Wt_{wood} (= 120 kg; Table 7.1), estimates for the time needed for the wood fall to disappear are obtained. The resulting estimates are 6.4 y for F_{WR} = 0.051 kg·d^{-1} (t = 1.9 y), and 29.9 y for F_{WR} = 0.011 kg·d^{-1} (t = 4.5 y). Based on personal observations of the status of the experimental wood falls, while the latter estimate is conceivably possible, the former estimate is very short and does not correspond to observations of other falls. A re-visitation of wood fall CRS 800, implanted in late April 2002, would serve as a test of the validity and reliability of the measurements of missing volume and of the resulting rates of exploitation of that fall.

Table 7.3 Results of measurements of wood volume removal from wood falls in the California Borderland Basins at three different fall ages. Fall CRS 800 was implanted in Santa Cruz Basin, while CRS 398 was implanted in Santa Catalina Basin. The following measurement related parameters are shown: n_i – number of blocks, $\Sigma V_{i\text{-}missing}$ (cm^3) – total missing volume, ΣV_i (cm^3) – total geometric volume. Also shown are, the results of the calculations of cumulative wood MOM released from the fall, Wt_{WR} (kg), the resulting wood removal rate, F_{WR} ($kg \cdot d^{-1}$), and the rate of wood MOM release to the surrounding sediments, F_{mat} ($kg \cdot d^{-1}$). For fall characteristics, see Table 7.1.

Fall	Age (y)	n_i	$\Sigma V_{i\text{-}missing}$ (cm^3)	ΣV_i (cm^3)	Wt_{WR} (kg)	F_{WR} ($kg \cdot d^{-1}$)	F_{matC} ($kg \cdot d^{-1}$)
CRS 800	1.9	9	1373	4684	35	0.051	0.017
CRS 398	4.5	6	912	5850	19	0.011	0.004
CRS 398	5.4	3	535	2808	23	0.012	0.004

Two major assumptions are implied in the calculation performed in the previous paragraph. The first assumption is that the whole wood parcel can be consumed and processed by wood borers. The infiltration of a wood parcel by growing wood borers results in the creation of a network of loosely connected, narrow sections of wood tissue. The network may be subject to partial, periodic collapse, and the consequent release of large fragments of wood onto the surrounding sediments, rendering the estimated wood fall lifetimes calculated above as underestimates.

The second assumption in the calculation of t_f is the continuity in wood-borer activity. As mentioned already (section *7.3.2.1*), it has been observed that wood-borer populations are subjected to predation to the extent of near extinction (Turner 1978). The occurrence of re-colonization of the wood fall following a predation event has not been investigated, but is quite likely, considering that the chemical and physical structure of the wood fall does not seem to be affected by predation events (Turner 1978). Therefore, the processing of a wood fall by specialist wood borers is less of a continuous function and more like a step-function or a series of delta-functions with time, and the lifetime of the wood falls of the case study is probably longer than estimated above. In summary, the wood fall fragmentation model does not account for the impacts of instability-driven partial fall collapse and of wood-borer-predator food-web effects on fall exploitation rates.

Finally, a comment is warranted on the assumption made regarding the absorption of ingested material by wood borers. Based on the bivalve bioenergetics literature and absorption efficiencies of 9-14 % reported for a refractory diet of cellulose-rich material (Langdon and Newell 1990), I assumed an absorption efficiency of 10 %. Wood borers of

the genus *Xylophaga* are known to be similar to their shallow-water wood-borer relatives, the Teredinidae, in that they actively consume wood shavings and harbor symbiotic microbes in their gills that may help with cellulose digestion and nitrogen fixation (Popham and Dickson 1973; Waterbury et al. 1983; Distel and Roberts 1997). It is possible that the absorption efficiency deviates greatly from the assumed value. A way to constrain the absorption efficiency of wood borers would be to estimate the C content of the biomass inhabiting an experimental parcel and compare it to the C content of the missing wood parcel. Thus, a minimum estimate can be obtained, since a significant fraction of the absorbed C could be lost during respiration.

7.4.2 Fall MOM dispersal

7.4.2.1 The sedimentary supply rate of TOC around a whale fall

The supply rate of TOC to the sea floor, $F_{sedC}(r)$ ($mg \cdot cm^{-2} \cdot y^{-1}$), was modeled for the ten scenaria simulated by the whale fragmentation module (Table 7.2), in the way discussed in section *7.3.3.1*. For brevity, detailed data of the calculations of DK(r) and $F_{sedC}(r)$ are shown only for the scenario where SFC = 0.01 and feces input is included (F_{matC} = 1.47 $kg \cdot d^{-1}$, Table 7.2), in Figure 7.4, Figure 7.5 and Table 7.4 (the optimized value of α in this case was 1.70×10^{-2} cm^{-1}). The results of the ten model runs are shown in Figure 7.6. Differences in model output between the different scenaria are depicted in Figure 7.7.

The estimated supply rates of TOC to the sea floor adjacent to the fall, $F_{sedC}(r_0)$, exceed background rates of 1.2 $mg \cdot cm^{-2} \cdot y^{-1}$ by 1 to 3.5 orders of magnitude (Figure 7.6, Table 7.5). A significant portion of the range in $F_{sedC}(r_0)$ (approximately 2 orders of

magnitude) emerges from the uncertainty in the contribution of sloppy feeding to the MOM release process. An examination of the relationship between the rate of carbon production by scavenging, F_{matC} (kg·d^{-1}) and the distance r (cm) at which F_{sedC} equals the background organic C supply rate (Figure 7.7), reveals a plateau above an F_{matC} value of approximately 0.5 kg·d^{-1}. In other words, while the TOC sedimentation rate values around the fall (F_{sedC}) may vary significantly, their impact does not extend beyond a distance of $r_{FsedC=bkg}$ = 420-440 cm (Table 7.5). It should be noted that the observed plateau in F_{matC} values is an outcome of using an exponential density function (Eq. 7.16) in the dispersal module.

The values of $r_{FsedC=bkg}$ are controlled to a large degree by the value of the maximum distance, r_{max}, from the fall at which the fall TOC supply rate is non-negligible (Eq. 7.16, 7.17). In the model proposed in this chapter, the value of r_{max} itself is set by the model user, and is based on biogeochemical (e.g., TOC content, sedimentary redox conditions) and ecological (e.g., macrofaunal abundances, microbial activities) information indicative of the extent of impact of a specific LOF on the surrounding sediments. That the model requires baseline information, such as sedimentary biogeochemical and ecological variations with distance away from the fall, could be perceived as a limitation of the model, because such data are not available for many falls during the fragmentation stage (Smith and Baco 2003). On the other hand, it may be possible to approximately assess the extent of impact by visual inspection of photographs or footage that may be more readily available than the information used in the Santa Cruz Basin case study.

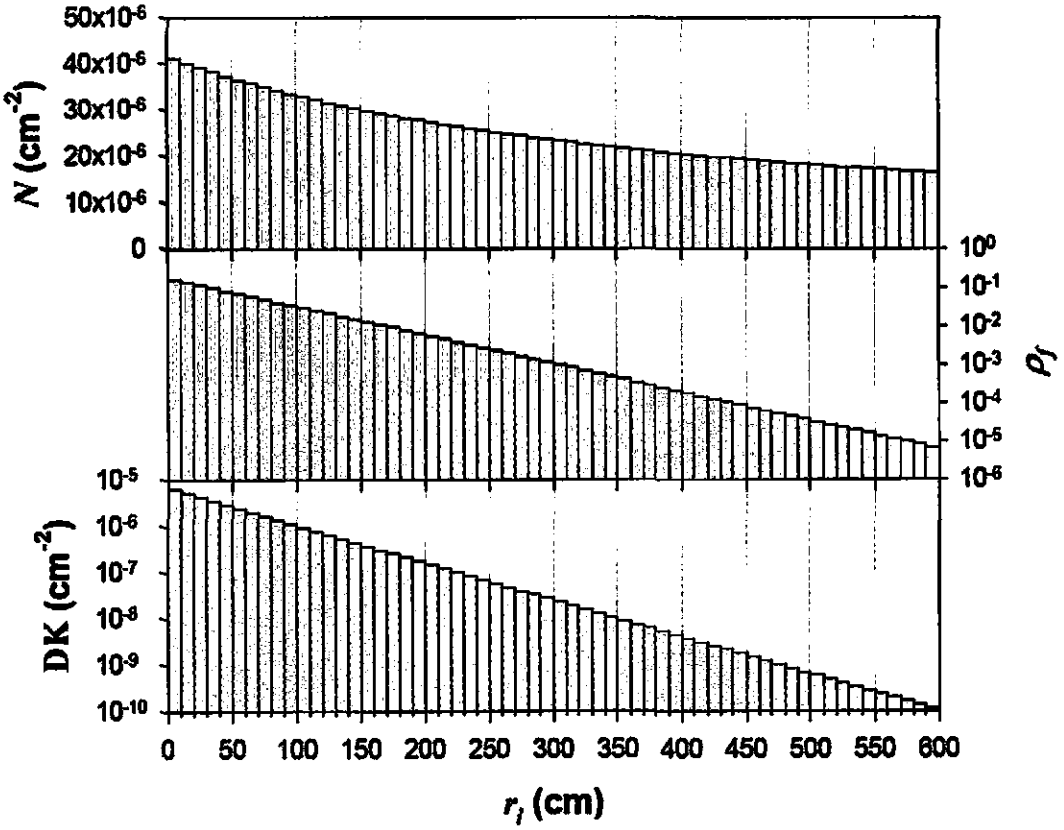

Figure 7.4 Values for dispersal components (Eq. 7.12) with distance, r_i (cm), calculated for the scenario where SFC = 0.01 and feces input is included (F_{matC} = 1.47 kg·d^{-1}, Table 7.2): *top* – the area normalization factor, N (= A^{-1}; cm^{-2}), *middle* - the dimensionless density function, ρ_f, *bottom* – the dispersal kernel, DK (cm^{-2}). Specific values of the parameters for selected areal rings are given in Table 7.4.

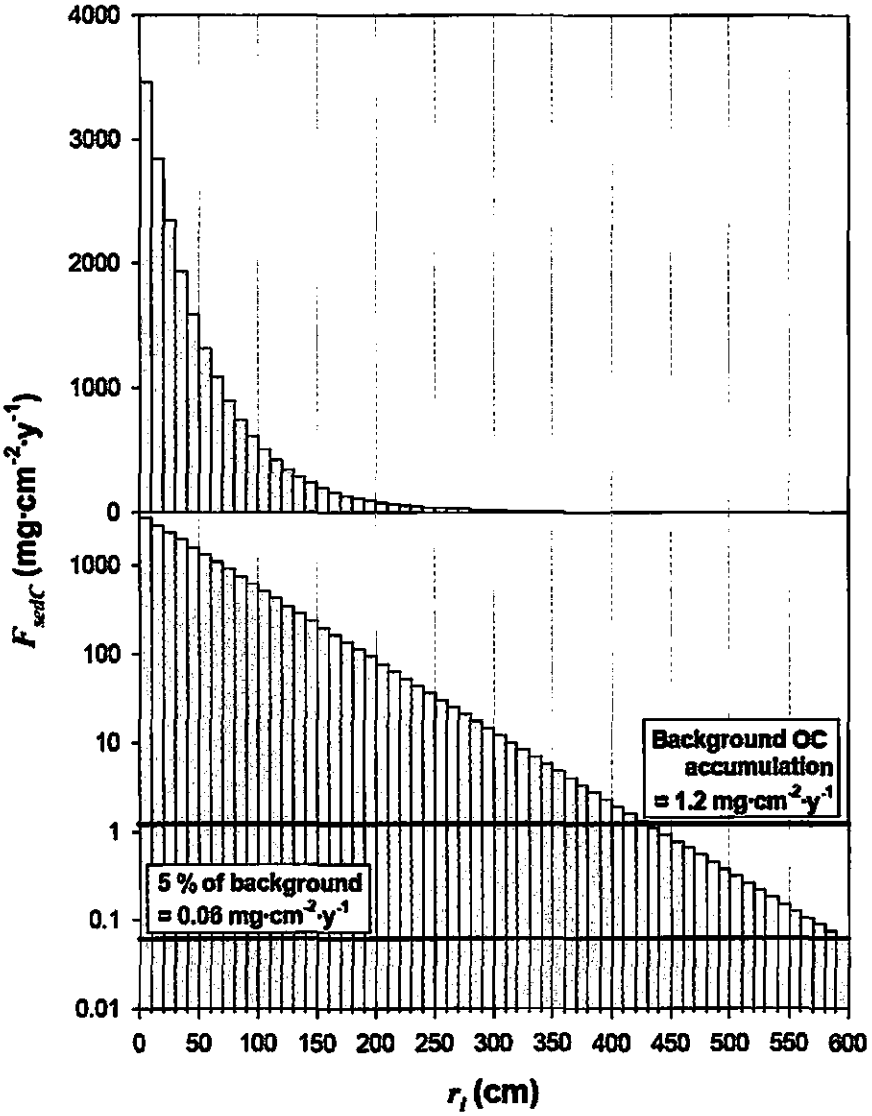

Figure 7.5 The modeled TOC sedimentation rate, F_{sedC}, in both normal (*top*) and log-normal (*bottom*) axis scales, with distance r_l (cm), for the scenario where SFC = 0.01 and feces input is included (F_{matC} = 1.47 kg·d^{-1}, Table 7.2). The value of background TOC accumulation rate, as well as 5 % of this value (defined as non-negligible), are also shown on the second plot. Exact values of F_{sedC}, as well as of other parameters, at select r_l are shown in Table 7.4.

Table 7.4 Calculated values of the area normalization factor, N (cm^{-2}), the dimensionless density function, ρ_f, the dispersal kernel, DK (cm^{-2}), and the TOC sedimentation rate, F_{sedC} ($mg \cdot cm^{-2} \cdot y^{-1}$), at select areal rings, r_i, away from the Santa Cruz whale fall. The model was run for the scenario where SFC = 0.01 and feces input is included (F_{matC} = 1.47 $kg \cdot d^{-1}$, Table 7.2).Complete plots of N, ρ_f, DK, and F_{sedC} against r are shown in Figure 7.4 and Figure 7.6.

r_i (cm)	$N(r_i)$ (cm^{-2})	$\rho_f(r_i)$ (-)	DK(r_i) (cm^{-2})	$F_{sedC}(r_i)$ ($mg \cdot cm^{-2} \cdot y^{-1}$)
0-10	4.11×10^{-5}	1.56×10^{-1}	6.42×10^{-6}	3460
50-60	3.64×10^{-5}	6.68×10^{-2}	2.43×10^{-6}	1310
100-110	3.26×10^{-5}	2.85×10^{-2}	9.32×10^{-7}	502.0
150-160	2.96×10^{-5}	1.22×10^{-2}	3.61×10^{-7}	194.3
200-210	2.71×10^{-5}	5.21×10^{-3}	1.41×10^{-7}	76.00
300-310	2.32×10^{-5}	9.51×10^{-4}	2.20×10^{-8}	11.80
400-410	2.02×10^{-5}	1.74×10^{-4}	3.51×10^{-9}	1.89
500-510	1.79×10^{-5}	3.17×10^{-5}	5.68×10^{-10}	0.31
590-600	1.63×10^{-5}	6.85×10^{-6}	1.12×10^{-10}	0.06

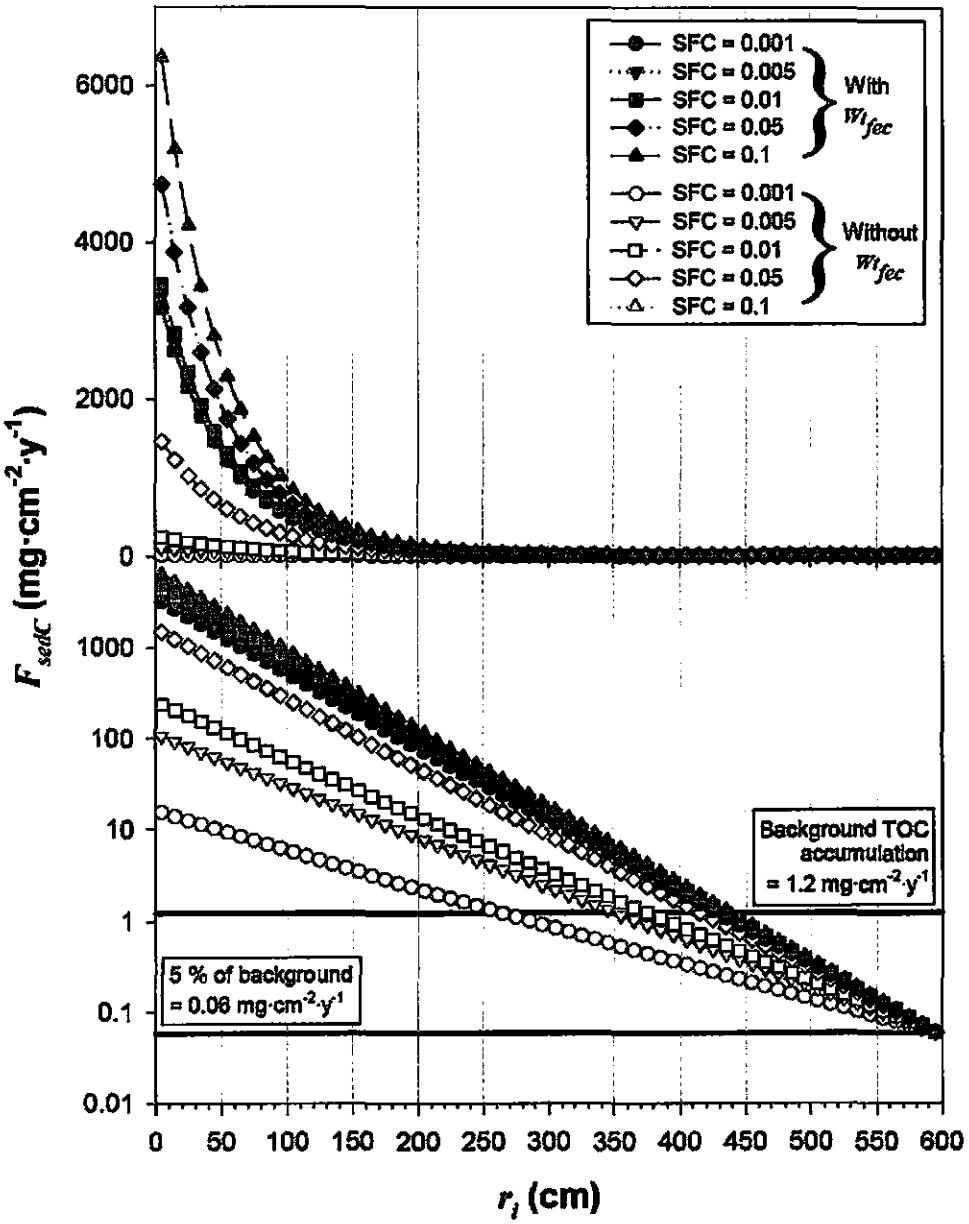

Figure 7.6 Modeled TOC sedimentation rate, F_{sedC} (mg·cm^{-2}·y^{-1}), with distance, r_l (cm), for 10 different fragmentation-release scenaria (Table 7.2), representing variation in sloppy feeding component, SFC, and the inclusion or exclusion of feces input, Wt_{fec} (closed and open symbols respectively). Results are shown in normal (*top*) and log-normal (*bottom*) ordinate scales.

Table 7.5 Results of dispersal module runs using the TOC release rates, F_{matC}, generated using the fragmentation module for 10 scenaria of variation in sloppy feeding component, SFC, and the inclusion or exclusion of feces input, Wt_{fec} (Table 7.2). Two parameters are extracted from the detailed plots in Figure 7.6: the TOC sedimentation rate at the areal ring adjacent to the fall, $F_{sedC}(0)$ (mg·cm^{-2}·y^{-1}), and the distance from the fall, $r_{FsedC=bkg}$ (cm), at which F_{sedC} equals the background TOC sedimentation rate, 1.2 mg·cm^{-2}·y^{-1}.

Wt_{fec} input	SFC	F_{matC} (kg·d^{-1})	α (cm^{-1})	$F_{sedC}(0)$ (mg·cm^{-2}·y^{-1})	$r_{FsedC=bkg}$ (cm)
	0.001	0.0135	7.83×10^{-3}	15.42	270
	0.005	0.0676	1.11×10^{-2}	106.8	350
Exclusion	0.01	0.135	1.25×10^{-2}	237.9	380
	0.05	0.676	1.55×10^{-2}	1460	420
	0.1	1.35	1.68×10^{-2}	3140	430
	0.001	1.36	1.69×10^{-2}	3180	430
	0.005	1.41	1.69×10^{-2}	3300	430
Inclusion	0.01	1.47	1.70×10^{-2}	3460	430
	0.05	1.96	1.75×10^{-2}	4730	430
	0.1	2.57	1.80×10^{-2}	6360	440

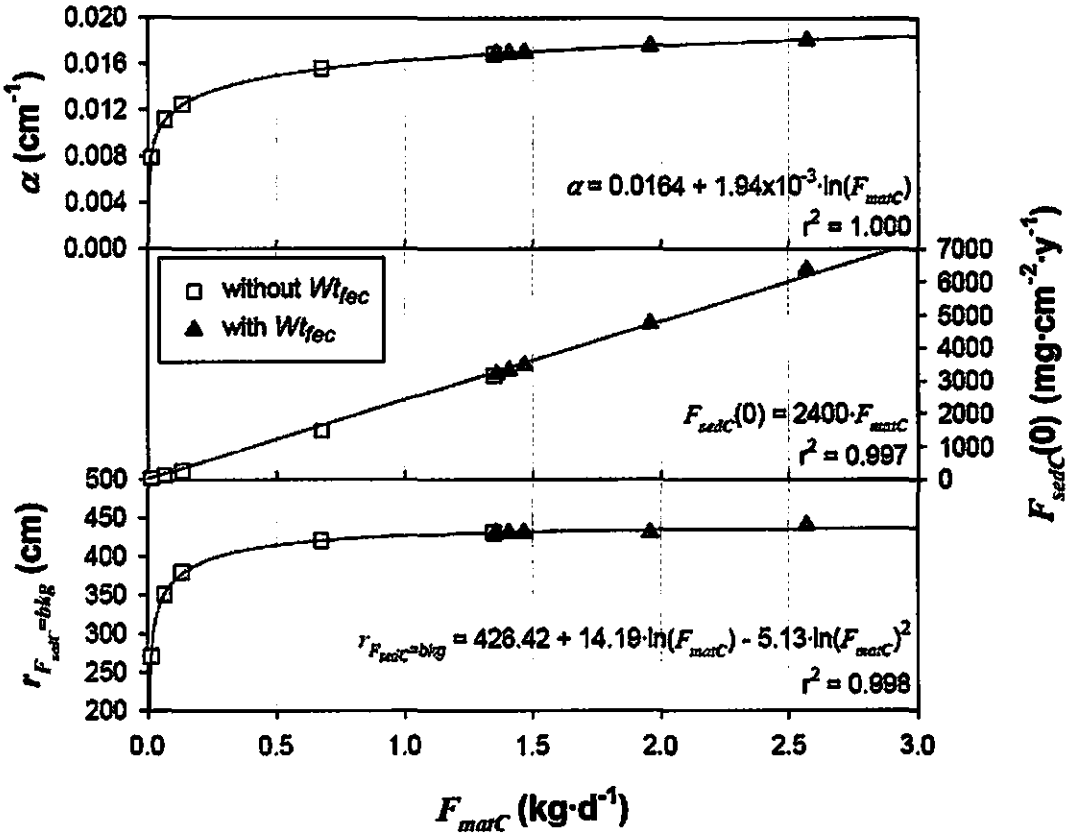

Figure 7.7 Plots of TOC release rate F_{matC} (kg·d^{-1}), against the distance coefficient α (cm^{-1}) (*top*), the TOC supply rate at the first areal ring next to the fall F_{sedC} (0) (mg·cm^{-2}·y^{-1}) (*middle*) and the distance from the fall, $r_{FsedC=bkg}$ (cm), at which F_{sedC} equals the background TOC sedimentation rate, 1.2 mg·cm^{-2}·y^{-1} (*bottom*). Model output for scenaria excluding defecation input (without Wt_{fec}) are shown with open symbols, while scenaria including defecation input (with Wt_{fec}) are shown with closed symbols. The equations of the best-fit relationships between the three pairs of data are also shown, along with correlation coefficients.

An implicit assumption of the model that needs consideration in the future is rotational symmetry. Although currents over the deep sea floor are not as strong as in shallower water, they are still measurable (e.g., Gardner et al. 1984) and can affect the geometry of dispersal around a point source such as an LOF. Specifically, most of the deposition in the presence of the current would be expected to occur down-stream from the fall, and consequently the impact zone of deposition would be wider in this direction than up-stream (Stockton and DeLaca 1982).

A related phenomenon not addressed by the dispersal module is the observed patchiness in measured biogeochemical parameters around the Santa Cruz whale fall, e.g., pore water sulfide concentrations (Figure 6.12), for several years after the fall event. What accounts for this patchiness is not known, but may be driven by biotic phenomena (e.g., scavenger behavior, macrobenthic opportunist aggregations and food web interactions, microbial colonization) as well as by abiotic processes (e.g., clustering of depositing particles due to current-induced eddy formation over the fall, injection of fall material into sediment at time point of impact). Although patchiness is ignored in the model presented here, as well as in other, more elaborate dispersal models (e.g., Allen 1982; Cromey et al. 2002), it is important to note its occurrence and its significance on corroborating model findings with data.

7.4.2.2 The sedimentary supply rate of TOC around a wood fall

The supply rate of TOC to the sea floor, $F_{sedC}(r_i)$ ($mg \cdot cm^{-2} \cdot y^{-1}$), was modeled for the low and high values of F_{WR} generated by the wood parcel fragmentation module (Table 7.3), 0.011 $kg \cdot d^{-1}$ and 0.51 $kg \cdot d^{-1}$, respectively. The optimized values of α were

1.88×10^{-1} cm^{-1} for $F_{WR} = 0.011$ $kg\cdot d^{-1}$ and 2.28×10^{-1} cm^{-1} for $F_{WR} = 0.051$ $kg\cdot d^{-1}$. The results of the two model runs are shown in Table 7.6.

Values of $F_{sedC}(0)$ range from 171 $mg\cdot cm^{-2}\cdot y^{-1}$ to 838 $mg\cdot cm^{-2}\cdot y^{-1}$, with the gradient in F_{sedC} with distance, generated by the relatively short r_{max} (= 50 cm), being fairly sharp. Characteristically, by multiplying $F_{sedC}(r_i)$ ($mg\cdot cm^{-2}\cdot y^{-1}$) with the area of each ring, $A(r_i)$ (cm^2), and comparing the distribution of the material released into each areal ring over a fixed time interval ($mg\cdot y^{-1}$), one finds that 98 % and 99 % of the material falls within the first two areal rings (0 cm to 20 cm) for $F_{matC} = 0.004$ $kg\cdot d^{-1}$ and $F_{matC} = 0.017$ $kg\cdot d^{-1}$, respectively. In this respect, the release and settling of feces, produced by sedentary metazoa and discharged from a point source which is at most 20 cm above the sea floor (the height of the wood parcels in the case study), is reliably reflected.

The model implicitly assumes that all the released material reaches the sediment. This may not be necessarily true for material released from the center of the horizontal surface of the parcel. Material defecated from a distance of more than 20 cm from the edge of the parcel may be transported by the weak but noticeable currents that do characterize the deep sea setting (e.g., Gardner et al. 1984), but may be trapped in unoccupied burrows, depressions, and crevices created by biotic activity. If one assumes that material at least 5 cm from the edge of the horizontal surface of the wood parcels does not reach the sediments, one can calculate the surface area of the parcel which cannot provide material to the sediments. Using parcel dimensions of 240 cm × 45 cm × 20 cm, and considering the area of the five faces of the parcel available for processing

Table 7.6 Calculated values of the area normalization factor, N (cm^{-2}), the dimensionless density function, ρ_f, the dispersal kernel, DK (cm^{-2}), and the TOC sedimentation rate, F_{sedC} ($mg \cdot cm^{-2} \cdot y^{-1}$), at select areal rings, r_l, away from a 120 kg wood parcel. The model was run for the low and high F_{matC} scenaria.

F_{WR} ($kg \cdot d^{-1}$) α (cm^{-1})	r_l to $r_l + r_w$ (cm)	$N(r_l)$ (cm^{-2})	$\rho_f(r_l)$ (-)	DK(r_l) (cm^{-2})	$F_{sedC}(r_l)$ ($mg \cdot cm^{-2} \cdot y^{-1}$)
0.004 1.88×10^{-1}	0-10	1.64×10^{-4}	8.48×10^{-1}	1.39×10^{-4}	171
	10-20	1.45×10^{-4}	1.29×10^{-1}	1.87×10^{-5}	23.0
	20-30	1.30×10^{-4}	1.96×10^{-2}	2.55×10^{-6}	3.13
	30-40	1.18×10^{-4}	2.99×10^{-3}	3.52×10^{-7}	0.43
	40-50	1.08×10^{-4}	4.55×10^{-4}	4.89×10^{-8}	0.06
0.017 2.28×10^{-1}	0-10	1.64×10^{-4}	8.98×10^{-1}	1.47×10^{-4}	838
	10-20	1.45×10^{-4}	9.19×10^{-2}	1.33×10^{-5}	75.8
	20-30	1.30×10^{-4}	9.40×10^{-3}	1.22×10^{-6}	6.95
	30-40	1.18×10^{-4}	9.62×10^{-4}	1.13×10^{-7}	0.64
	40-50	1.08×10^{-4}	9.84×10^{-5}	1.06×10^{-8}	0.06

(30000 cm^2), the area at least 5 cm from the edge of the fall (8050 cm^2) constitutes almost 37 % of the total area available for colonization. Therefore, the effect of material trapping within the eroded horizontal surface of the parcel could be potentially quite significant and may decrease the estimated fluxes to the surrounding sediments by approximately a third. Natural wood falls of similar sizes such as the wood parcels in the case study are, most probably, rounded trunks and are unlikely to have such flat faces lying horizontally. Therefore, the comment above may apply to the case study in this chapter, but not necessarily to natural wood falls.

7.4.3 Whale LOF vs. Wood LOF

A comparison of the model output for the whale fall and the wood parcels used in the case studies (Table 7.7) indicates that the values of F_{matC} generated for the wood falls are up to 2 orders of magnitude lower that those generated for the Santa Cruz Basin whale fall. The difference in F_{matC} values is approximately proportional to the relative sizes of the two falls suggesting comparable removal rates with respect to the fraction of available tissue removed per unit time. Specifically, in the case of wood falls, approximately 9.8×10^{-3} % to 4.1×10^{-2} % of the available C, WtC_{wood}, is released per day to the surroundings, while in the case of whale falls, 1.7×10^{-3} % to 4.8×10^{-2} % of the available C, WtC_{cet}, is released per day. In other words, the F_{matC} values, normalized to the available C of the falls, are very similar for these two fall types of very different quality.

Table 7.7 Comparison of select input and output of the model for the whale fall and wood parcels used as case studies in this chapter. Inputs: Wt – Available wet tissue weight (kg) (Table 7.1), WtC – Carbon content (kg, %) (Table 7.1), r_{max} – the maximum distance at which fall carbon sedimentation is non-negligible (cm) (sections *7.3.3.2* and *7.3.4.2*), Absorption efficiency of ingested material (%), and removal rate of available tissue, F_{SC} for the whale fall and F_{WR} for the wood falls ($kg \cdot d^{-1}$). Output: t_f – estimate of time needed for removal of all available tissue (y) (sections *7.4.1.1* and *7.4.1.2*), F_{matC} – production rate of C available for dispersal ($kg \cdot d^{-1}$) (section *7.4.1.1* and Table 7.3), $F_{sedC}(r_0)$ – estimates of fall C sedimentation at a distance of $r = 0$ cm from the fall ($mg \cdot cm^{-2} \cdot y^{-1}$) (Table 7.5 and Table 7.6).

Parameter	Whale fall	Wood parcel
Wt (kg)	20680	120
WtC (kg, %)	5394, 26	41, 34
r_{max} (cm)	600	50
Absorption efficiency (%)	90	10
Removal rate ($kg \cdot d^{-1}$)	52.0	0.01-0.05
t_f (y)	1.1	6.4-30
F_{matC} ($kg \cdot d^{-1}$)	0.09-2.57	0.004-0.017
$F_{sedC}(r_0)$ ($mg \cdot cm^{-2} \cdot y^{-1}$)	15-6360	171-838

The similarity in normalized F_{matC} values contrasts the difference in tissue removal rates, which are three orders of magnitude greater for the whale fall, and result in a much faster processing time for the whale fall (t_f = 397 d) than for the wood falls (estimated t_f between 6.4 y and 29.9 y). The discrepancy is the outcome of the differences in absorption efficiency by the metazoan that exploit the two types of falls, combined with a significant difference in C content, *WtC*, between the two fall types.

The above comparison is a good illustration of the role of LOF quality in LOF processing rates. Moreover, the comparable normalized F_{matC} values indicate that a fall size may be a good first-order indicator of the C supply rate to the surroundings, regardless of the fall type. I would venture to propose that, based on the results of the comparison of the two fall types of specific size in this study (Table 7.1), the amount of C (kg) released per day to the surroundings (F_{matC}) from a whale fall or a wood fall in the California Borderland Basins is approximately 10^{-3} % of the C (kg) available for consumption at the time point of the fall event, regardless of the fall type.

7.5 Sedimentary processing of dispersed MOM

The major finding from the LOF fragmentation and dispersal modeling calculations described in the previous sections was that estimated fluxes of TOC to sediments adjacent to LOF may exceed background fluxes by as much as three orders of magnitude. Such changes in TOC supply rates can bring about redox shifts, such as those documented using pore water dissolved sulfide (Chapter 6). Sulfide is thought to be primarily responsible for the development of biogenic reducing habitats based on these falls (Deming et al. 1997; Feldman et al. 1998; Smith et al. 2002). However, modeling

pore water sulfide concentrations can be particularly difficult due to its complex geochemistry (Berner 1974). In this section, I discuss a modeling application that might address the problem of linking my LOF-processing model output to early diagenetic processes and, specifically, the shift from oxic-suboxic to anoxic-sulfidic conditions and the development of biogenic reducing habitats.

7.5.1 Early diagenesis and multi-component models

Early diagenesis of organic matter in marine sediments proceeds via a cascade of metabolic reactions (Table 7.8), which are successively less favorable in terms of the energy they yield (e.g., Froelich et al. 1979). A less favorable reaction succeeds a more favorable reaction if the main metabolite involved in the latter is depleted, and sufficient organic matter remains to fuel early diagenesis further. This is typically the case in estuarine, coastal, and upwelling zone sediments, where organic matter supply rates to the sediments are high, and consequently early diagenesis of the supplied material is dominated by sulfate reduction (Berner 1980). In deep sea sediments away from upwelling regions, where the supply rate of organic matter is fairly low and bottom water is oxygenated, the vast majority of the material is degraded at the sediment-water interface (SWI) via aerobic and suboxic pathways (e.g., Rowe and Deming 1985).

Modeling of various aspects of early diagenesis has focused on organic matter decay and its controlling factors, such as concentration, age, temperature, etc. (see overview by Van Cappellen and Gaillard 1996). Efforts over the last fifteen years have expanded to generate multi-component models, which incorporate the re-oxidation of reduced by-products of organic matter oxidation, acid-base speciation, and precipitation

reactions, (e.g., Van Cappellen and Wang 1995; Boudreau 1996; Van Cappellen and Wang 1996).

When modeling the distribution of pore water sulfide concentrations ($\Sigma H_2S = H_2S + HS^- + S^{2-}$) with time and sediment depth, it is necessary to use models which take into account secondary redox reactions (Table 7.9) that implicate the by-products of the main redox reactions as well as other major metabolites. The challenge of modeling pore water sulfide, which was recognized early on (Berner 1974), is illustrated in Figure 7.8. Detailed discussions of the simplifications and assumptions made in multi-component models regarding metal speciation during the primary and secondary redox reactions listed in this section are beyond the scope of this chapter. Instead, the reader is referred to Van Cappellen and Wang (1995) and Boudreau (1996). It is sufficient to state that multi-component models are obligatory to modeling the distribution of species such as sulfide which are affected by multiple, simultaneously active, and inter-connected processes.

7.5.2 The Knowledge-Based Reactive Transport Model (KB-RTM)

As Boudreau (1996) points out, multi-component models have been used very modestly because of the substantial mathematical background required to solve the many coupled, non-linear, differential equations that govern them, and the lack of adequate publicly available codes to aid in solving them. A potentially significant step in bringing multicomponent early diagenetic models to the forefront of aquatic geochemistry was the recent release of the Knowledge-Based Reactive Transport Model (KB-RTM) (Aguilera et al. 2005), which operates as follows:

Table 7.8 Metabolic reactions involved in degradation of organic matter in marine sediments in order of decreasing energetic efficiency (modified from Van Cappellen and Wang 1995).

Reaction code	Reaction
A1	$(CH_2O)x(NH_3)y(H_3PO_4)z + (x+2y)O_2 + (y+2z)HCO_3^- \xrightarrow{R1} (x+y+2z)CO_2 + yNO_3^- + zHPO_4^{2-} + (x+2y+2z)H_2O$
A2	$(CH_2O)x(NH_3)y(H_3PO_4)z + (\frac{4x+3y}{5})NO_3^- \xrightarrow{R2} (\frac{2x+4y}{5})N_2 + (\frac{x-3y+10z}{5})CO_2 + (\frac{4x+3y-10z}{5})HCO_3^- + zPO_4^{2-} + (\frac{3x+6y+10z}{5})H_2O$
A3	$(CH_2O)x(NH_3)y(H_3PO_4)z + 2xMnO_2 + (3x+y-2z)CO_2 + (x+y-2z)H_2O \xrightarrow{R3} 2xMn^{2+} + (4x+y-2z)HCO_3^- + yNH_4^+ + zHPO_4^{2-}$
A4	$(CH_2O)x(NH_3)y(H_3PO_4)z + 4xFe(OH)_3 + (7x+y-2z)CO_2 \xrightarrow{R4} 4xFe^{2+} + (8x+y-2z)HCO_3^- + yNH_4^+ + zHPO_4^{2-} + (3x-y+2z)H_2O$
A5	$(CH_2O)x(NH_3)y(H_3PO_4)z + (x/2)SO_4^{2-} + (y-2z)CO_2 + (y-2z)H_2O \xrightarrow{R5} (x/2)H_2S + (x+y-2z)HCO_3^- + yNH_4^+ + zHPO_4^{2-}$
A6	$(CH_2O)x(NH_3)y(H_3PO_4)z + (y-2z)H_2O \xrightarrow{R6} (x/2)CH_4 + (\frac{x-2y+4z}{2})CO_2 + (y-2z)HCO_3^- + yNH_4^+ + zHPO_4^{2-}$

Table 7.9 Secondary redox reactions involving the production or consumption of H_2S through the reoxidation of products of the degradation of organic matter by the reactions in Table 7.8 (modified from Van Cappellen and Wang 1995).

Source/sink	Reaction code	Reaction
Sinks	A11	$H_2S + 2O_2 + 2HCO_3^- \rightarrow SO_4^{2-} + 2CO_2 + 2H_2O$
	A12	$H_2S + 2CO_2 + MnO_2 \rightarrow Mn^{2+} + S^0 + 2HCO_3^-$
	A13	$H_2S + 4CO_2 + 2Fe(OH)_3 \rightarrow 2Fe^{2+} + S^0 + 4HCO_3^- + 2H_2O$
	A19	$Fe^{2+} + 2HCO_3^- + H_2S \rightarrow FeS + 2CO_2 + 2H_2O$
Sources	A16	$CH_4 + CO_2 + SO_4^{2-} \rightarrow 2HCO_3^- + H_2S$

Figure 7.8 Schematic illustrating the effect of sources and sinks of pore water sulfide on its concentration change with time, as it was elaborated in the model CANDI (Carbon and Nutrient Diagenesis) by Boudreau (1996). Reaction codes refer to reactions in Table 7.8 (A5) and to reactions in Table 7.9 (A11-13, A16, A19).

$$\frac{\partial[\Sigma H_2S]}{\partial t} =$$

Sulfate reduction (A5) + Methane re-oxidation by sulfate (A16)

- Sulfide re-oxidation by oxygen (A11)

- Sulfide re-oxidation by manganese oxide (A12)

- Sulfide re-oxidation by iron hydroxide (A13)

- Iron monosulfide precipitation (A19)

- Molecular diffusion - Burial - Irrigration

a) A world wide web-distributed Knowledge Base facilitates the communication of user and model by the exchange of comprehensive information about the parameters of the model through digital forms filled on-line (http://www.geo.uu.nl/~rtm/index.php).

b) An Automatic Code Generator (Regnier et al. 2002) translates the information in the forms into a complex reaction network algorithm

c) The algorithm can be downloaded onto a personal computer and executed. The KB-RTM output is released in text files which can be exported to most data-management and processing programs for viewing, graphing and further processing.

The KB-RTM is based on the early diagenetic models described in Van Cappellen and Wang (1995; 1996). Further information on the modeled reactions and an example for the continental shelf sea floor is given in Aguilera et al. (2005). I compiled KB-RTM input that could potentially be used to model early diagenesis of Santa Cruz Basin sediments under background conditions, as well as under the influence of LOF-derived MOM. The input is listed in detail in Table 7.10 (physical domain and forcings, and output parameters), and Table 7.11 and Table 7.12 (reaction network parameters). Where possible, values for the different parameters were obtained from the study site (Emery 1960; Shaw et al. 1990; Eganhouse and Venkatesan 1993; Smith et al. 1998; Fornes 1999; Miller et al. 2000). Otherwise, values were obtained from literature reviews used in the past to parameterize deep-sea models (Van Cappellen and Wang 1995; 1996; Boudreau 1997).

The following strategy could be adopted to evaluate the use of the KB-RTM:

a) The data for background conditions should reproduce the background redox state and organic matter content of sediments in Santa Cruz Basin, under steady state conditions.

b) Next, MOM perturbations could be introduced for a period of time, t_f (Table 7.10), which was estimated from the fragmentation module of the model (Table 7.7). Regarding the use of the KB-RTM, perturbations mainly translate into a change of the elemental ratio (C:N:P ratio from Table 7.1 to Table 7.10) and degradation coefficient (kG or kfox in Table 7.11) of the sedimenting organic material, and sedimentation rates calculated from F_{sedC} (Table 7.10).

c) After t_f, the output could be reintroduced into the model and exposed to background conditions for a period of time of 5-10 y.

d) The model output should then be examined with particular attention paid to the contribution of individual processes to organic matter degradation, as well as ΣH_2S pore water concentrations.

Challenges presented by trying to solve the problem of biogenic reducing habitat generation by LOF processing with the KB-RTM include the reproduction of the background sedimentary biogeochemistry of Santa Cruz Basin sediments. These sediments are characterized by particularly high organic matter content (5.4 % ± 0.2 %, Treude et al., in preparation) which remains constant down to at least 10 cm depth, bottom water oxygen concentrations ranging from hypoxic (36 $\mu mol \cdot L^{-1}$) (Emery 1960, p. 108) to near-saturation (250 $\mu mol \cdot L^{-1}$) (Treude et al., in preparation), and sulfide concentrations close to or below detection (Chapter 6). Another challenge is the overlap

Table 7.10 Input for Web Submission Form I of the KB-RTM model. This input defines the physical domain, transport coefficients, forcings, and output parameters, for background conditions at the study site, Santa Cruz Basin.

Parameter category	Parameter (units)	Background	Whale fall scenario	Wood fall scenario
Physical domain	Total time (y)	10-100	t_f [h]	t_f [h]
	Time step (y)	2.5×10^{-3}	2.5×10^{-3}	2.5×10^{-3}
	Total depth (cm)	40	40	40
	Number of nodes (-)	401	401	401
Transport coefficients	Porosity (-)	0.85 [a]	0.85 [a]	0.85 [a]
	Cross section (cm^2)	1.0	1.0	1.0
	Flow velocity ($cm \cdot y^{-1}$)	0 [b]	0 [b]	0 [b]
	Burial velocity ($cm \cdot y^{-1}$)	0.012 [c]	$F_{sed} \div \rho$ [i]	$F_{sed} \div \rho$ [i]
	Bioturbation coeff. ($cm^2 \cdot y^{-1}$)	2 [d]	0 [j]	2 [l]
	Bioturbation mixing depth (cm)	7 [d]	0 [j]	7 [l]
	Longitudinal dispersivity (y)	0 [e]	0 [e]	0 [e]
Forcings	C:N:P ratio	148:16:1 [f]	550:50:1 [k]	4860:20:1 [k]
	Temperature (°C)	4	4	4
	Salinity (PSU)	35	35	35
	Solid phase density ($g \cdot cm^{-3}$)	2.6 [g]	1.030 [k]	0.670 [k]
Output	First output time (y)	2.5×10^{-2}	2.5×10^{-2}	2.5×10^{-2}
	Output interval period (y)	2.5×10^{-2}	2.5×10^{-2}	2.5×10^{-2}

[a] T. Treude et al. (in preparation).

[b] Flow velocity is used in ground-water applications of the model.

[c] The sedimentation rate (burial velocity) was calculated from a total absolute rate of deposition of 32 $mg \cdot cm^{-2} \cdot y^{-1}$ for Santa Cruz Basin (Emery 1960, p. 254) and a density of settling material of 2.6 $g \cdot cm^{-3}$. This agrees with sedimentation rates in California Borderland Basins reported elsewhere (Fornes 1999).

[d] Since no bioturbation values are available for Santa Cruz Basin, values for Santa Catalina Basin are used. The two basins have been grouped together as well populated due to adequate bottom water oxygen content and average macrofaunal abundances, parameters likely to affect bioturbation (Emery 1960, p. 168-175). Bioturbation coefficients in Santa Catalina Basin range between 0.8 $cm^2 \cdot y^{-1}$ and 66 $cm^2 \cdot y^{-1}$ using $^{234}Th_{xs}$ (<100 d time scales), and between 0.1 $cm^2 \cdot y^{-1}$ and 2 $cm^2 \cdot y^{-1}$ using $^{210}Pb_{xs}$ (<100 y time scales) (Smith et al. 1998; Fornes 1999). Based on the time scales modeled (10 y – 100 y) a bioturbation coefficient of 2 $cm^2 \cdot y^{-1}$ was chosen. Mixing depth was set to extend down to 7 cm (Fornes 1999).

[e] The longitudinal dispersivity is defined by the physical regime of the study site. Based on descriptions of other basins (e.g., in Santa Catalina Basin, Miller et al. 2000), the study site could be described as relatively low-energy.

[f] The C:N ratio of material reaching the Santa Cruz Basin sediment was estimated by dividing the sedimentary flux of TOC (1.2 $mg \cdot cm^{-2} \cdot y^{-1}$) by the sedimentary flux of N (0.13 $mg \cdot cm^{-2} \cdot y^{-1}$), with values for the two fluxes from the literature (Emery 1960, p. 254; Eganhouse and Venkatesan 1993). The resulting C:N ratio of 9.2 was complemented by the assumption that N and P degrade equally with respect to C during sinking (Christian et al. 1997), and thus maintain their original ratio, which in this case was assumed to be the Redfield ratio of N:P = 16. Therefore this yields a C:N:P = 148:16:1.

[g] Average value for marine sediments (Berner 1980).

[h] The duration of the runs of the model for the two scenaria depended on the time period, t_f, over which MOM was dispersed to the surrounding sediments, the values of which were determined using the fragmentation module.

[i] The sedimentation rates (burial velocities) of material during the whale and wood fall scenaria were generated after running the fragmentation and dispersal modules. Rates were converted from the material supply rates, F_{sed} ($g \cdot cm^{-2} \cdot y^{-1}$), estimated from the dispersal module, to $cm \cdot y^{-1}$ by dividing by densities, ρ, of settling material of 1.03 $g \cdot cm^{-3}$ and 0.67 $g \cdot cm^{-3}$ for whale and wood falls respectively (Table 7.1).

[j] Assumed to be 0 $cm^2 \cdot y^{-1}$ due to sulfidic conditions observed in sediments adjacent to whale LOF (Chapter 6).

[k] From Table 7.1.

[l] Assumed to be background due to non-sulfidic conditions observed in sediments adjacent to wood LOF (Chapter 6).

---

of multiple (two) sources of organic material, the background source and the LOF source, with different compositions, reactivity coefficients, and fluxes (i.e., the implementation of a multi-G model), within the Knowledge Base. Regardless of the challenges, the KB-RTM is on the cutting edge of ease-of-use multi-component modeling tools, and is the most suitable application for the problem at hand.

Table 7.11 Input for reaction network parameters of Web Submission Form II of the KB-RTM model. This input defines activity constants for primary redox processes, secondary redox processes, acid-base reactions, and precipitation-dissolution reactions at the study site (Aguilera et al. 2005). Constants are listed in the order they appear on the form. Values were taken from van Cappellen and Wang (1995; 1996), and Boudreau (1997, p. 157).

Constant	Symbol in model	Value	Units
KFeCO3	KsFeCO3	4e-9	(mol Fe^{2+})·(mol CO_3^{2-})
KFeS	KsFeS	6.3e-2	(mol Fe^{2+})·(mol HS^-)·(mol H^+)
KMnCO3	KsMnCO3	3.2e-9	(mol Mn^{2+})·(mol CO_3^{2-})
	calrate	18	y^{-1}
	keqcal	4e-7	(mol Ca)·(mol CO_3^{2-})·L^{-2}
kFeCO3	kfeco3precip	1e-6	mol·L^{-1}·y^{-1}
kFeMn	kfemno2	1e4	L·mol^{-1}·y^{-1}
kFeOx	kfeo2	1e9	L·mol^{-1}·y^{-1}
kFeS	kfesprecip	5e-6	mol·L^{-1}·y^{-1}
kFeSOx	kfesreox	2e7	L·mol^{-1}·y^{-1}
kG	kfox	Variable	y^{-1}
kCH4OxO2	kmethox1	1e10	L·mol^{-1}·y^{-1}
kCH4OxSO4	kmethox1	1e10	L·mol^{-1}·y^{-1}
kFe3	kmfeoh3	5e-6	mol·g^{-1}
kMnCo3	kmnco3precip	1e-6	mol·L^{-1}·y^{-1}
	kmno2	2e-6	mol·g^{-1}
	kmno3	1e-5	mol·L^{-1}
kMnOx	kmnox	1e9	L·mol^{-1}·y^{-1}
KO2	kmo2	8e-6	mol·L^{-1}
KSO4	kmso4	1e-3	mol·L^{-1}
KNO3	knit	1.5e7	L·mol^{-1}·y^{-1}
kSOxO2	ksulfox1	6e8	L·mol^{-1}·y^{-1}
kSOxMnO2	ksulfox2	1e4	L·mol^{-1}·y^{-1}
kSOxFe3	ksulfox3	1e4	L·mol^{-1}·y^{-1}

Table 7.12 Input for species-dependent parameters of Web Submission Form II of the KB-RTM model. This input defines the upper and lower boundary conditions and initial conditions for solutes and solid-phase components at the study site. Data were taken from Shaw et al. (1990), van Cappellen and Wang (1995; 1996), from Millero (1996), and Boudreau (1997, p. 157).

		Upper boundary cond.		Lower boundary cond.		Initial
Parameter	Units	Type	Value	Type	Value	condition
boh3	$mol \cdot L^{-1}$	conc.	4e-4	gradient	0	4e-4
boh4	$mol \cdot L^{-1}$	conc.	6e-5	gradient	0	6e-5
ca	$mol \cdot L^{-1}$	conc.	1e-2	gradient	0	1e-2
caco3	$mol \cdot g^{-1}$	flux	3.1e-5	gradient	0	8e-6
ch2o	$mol \cdot g^{-1}$	flux	Variable	conc.	4.2e-3	4.2e-3
ch4	$mol \cdot L^{-1}$	conc.	0	conc.	0	0
co2	$mol \cdot L^{-1}$	conc.	2e-5	conc.	0	2e-5
co3	$mol \cdot L^{-1}$	conc.	1e-4	gradient	0	1e-4
fe2	$mol \cdot L^{-1}$	conc.	0	conc.	7e-5	0
feco3	$mol \cdot g^{-1}$	flux	0	gradient	0	0
feoh3	$mol \cdot g^{-1}$	conc.	2e-4	conc.	5e-5	2e-4
fes	$mol \cdot g^{-1}$	flux	0	gradient	0	0
h2s	$mol \cdot L^{-1}$	conc.	0	gradient	0	0
hco3	$mol \cdot L^{-1}$	conc.	2e-3	gradient	0	2e-3
hplus	$mol \cdot L^{-1}$	conc.	7.8e-9	gradient	0	7.8e-9
hpo4	$mol \cdot L^{-1}$	conc.	1e-6	gradient	0	1e-6
hs	$mol \cdot L^{-1}$	conc.	0	gradient	0	0
mn2	$mol \cdot L^{-1}$	conc.	0	conc.	2e-5	0
mnco3	$mol \cdot g^{-1}$	flux	0	gradient	0	0
mno2	$mol \cdot g^{-1}$	conc.	1e-4	conc.	0	1e-4
nh4	$mol \cdot L^{-1}$	conc.	0	gradient	0	0
no3	$mol \cdot L^{-1}$	conc.	4.5e-5	conc.	0	4.5e-5
o2	$mol \cdot L^{-1}$	conc.	35e-6	conc.	0	35e-6
so4	$mol \cdot L^{-1}$	conc.	2.8e-2	gradient	0	2.8e-2

7.6 Conclusions

A model of fall processing by deep sea floor communities is presented. The proposed model incorporates metazoan processing and dispersal of fragmented material, and its concept was tested using two specific falls from the California Borderland Basins region as case studies. The availability of data from the case studies regarding the characteristics of the falls, processing rates, and impact of fall processing on monitored parameters permitted the assessment of the model output.

Model results indicated that removal rates of available tissue, TOC release rates to the surroundings, and the TOC sedimentation rates to the seafloor are much higher in the case of whale falls than in the case of wood falls. The differences roughly reflect available LOF tissue weight. Specifically, the TOC release rates normalized to tissue weights for the whale fall and wood fall are comparable to each other despite differences in fall characteristics and processing. The explanation lies in the combined effects of absorption efficiency (much higher for the whale fall than for the wood fall) and carbon content of the ingested material (approximately 50 % greater in wood than in whale tissue).

The model highlighted unknown factors that may affect deep sea LOF processing, such as the extent of sloppy feeding, scavenger behavior in the presence of multi-ton-sized LOF, the role of predator-scavenger food webs on wood LOF processing, and bioenergetics of deep-sea wood borers.

Finally, the connection of the model output to an on-line multi-component reaction transport model was discussed, aiming at the study of the development of

biogenic reducing habitats as a result of LOF processing by metazoa during early diagenesis.

7.7 References

Aguilera, D. R., P. Jourabchi, C. Spiteri and P. Regnier (2005) A knowledge-based reactive transport approach for the simulation of biogeochemical dynamics in Earth systems. Geochemistry Geophysics Geosystems, 6: Q07012, doi: 10.1029/2004GC000899.

Allen, C. M. (1982) Numerical simulation of contaminant dispersion in estuary flows. Proceedings of the Royal Society of London A, 381: 179-194.

Baco-Taylor, A. R. (2002) Food-web structure, succession and phylogenetics on deep-sea whale skeletons. Ph.D. Dissertation, University of Hawai'i, pp. 275.

Baco, A. R. and C. R. Smith (2003) High species richness in deep-sea chemoautotrophic whale skeleton communities. Marine Ecology Progress Series, 260: 109-114.

Berelson, W. M., R. F. Anderson, J. A. Dymond, D. DeMaster, D. E. Hammond, R. Collier, S. Honjo, M. Leinen, J. McManus, R. Pope, C. Smith and S. M. (1997) Biogenic budgets of particle rain, benthic remineralization and sediment accumulation in the equatorial Pacific. Deep-Sea Research II, 44: 2251-2282.

Berner, R. A. (1974) Kinetic models for the early diagenesis of nitrogen, sulfur, phosphorus, and silicon in anoxic marine sediments, p. 427-450. *In* Goldberg, E. D. [ed.], The Sea, Vol. 5, Marine Chemistry. Wiley Interscience, New York, New York, U.S.A.

Berner, R. A. (1980) Early diagenesis. Princeton University Press, Princeton, New Jersey, U.S.A., pp. 241.

Boudreau, B. P. (1996) A method-of-lines code for cabon and nutrient diagenesis in aquatic sediments. Computers and Geosciences, 22: 479-496.

Boudreau, B. P. (1997) Diagenetic models and their implementation. Springer, Berlin, Germany, pp. 414.

Brock, V. and V. S. Kennedy (1992) Quantitative analysis of crystalline style carbohydrases in five suspension- and deposit-feeding bivalves. Journal of Experimental Marine Biology and Ecology, 159: 51-58.

Browning, B. L. (1963a) The composition and chemical reactions of wood, p. 57-101. *In* Browning, B. L. [ed.], The chemistry of wood. Wiley Interscience, New York, New York, U.S.A.

Browning, B. L. (1963b) The wood-water relationship, p. 405-439. *In* Browning, B. L. [ed.], The chemistry of wood. Wiley Interscience, New York, New York, U.S.A.

Christian, J. R., M. L. Lewis and D. M. Karl (1997) Vertical fluxes of carbon, nitrogen, and phosphorus in the North Pacific Subtropical Gyre near Hawaii. Journal of Geophysical Research - Oceans, 102: 15667-15677.

Clark, J. S., M. Silman, R. Kern, E. Macklin and J. HilleRisLambers (1999) Seed dispersal near and far: patterns across temperate and tropical forests. Ecology, 80: 1475-1494.

Cromey, C. J., K. D. Black, A. Edwards and I. A. Jack (1998) Modelling the deposition and biological effects of organic carbon from marine sewage discharges. Estuarine, Coastal and Shelf Science, 47: 295-308.

Cromey, C. J., T. D. Nickell and K. D. Black (2002) DEPOMOD - modelling the deposition and biological effects of waste solids from marine cage farms. Aquaculture, 214: 211-239.

Dayton, P. K. and R. R. Hessler (1972) Role of biological disturbance in maintaining diversity in the deep sea. Deep-Sea Research, 19: 199-208.

Deming, J. W., A. L. Reysenbach, S. A. Macko and C. R. Smith (1997) Evidence for the microbial basis of a chemoautotrophic community at a whale fall on the deep seafloor: bone-colonizing bacteria and invertebrate endosymbionts. Microscopy Research and Technique, 37: 162-170.

Distel, D. L. and S. J. Roberts (1997) Bacterial endosymbionts in the gills of the deep-sea wood-boring bivalves *Xylophaga atlantica* and *Xylophaga washingtona*. Biological Bulletin, 192: 253-261.

Drazen, J. C., K. R. Reisenbichler and B. H. Robison (2007) A comparison of absorption and assimilation efficiencies between four species of shallow- and deep-living fishes. Marine Biology, 151: 1551-1558.

Eganhouse, R. P. and M. I. Venkatesan (1993) Chemical oceanography and geochemistry, p. 71-189. *In* Dailey, M. D., D. J. Reish and A. J. W. [eds.], Ecology of the Southern California Bight. University of California Press, Berkeley, California, U.S.A.

Elser, J. J., D. R. Dobberfuhl, N. A. MacKay and J. H. Schampel (1996) Organism size, life history, and N:P stoichiometry. Bioscience, 46: 674-684.

Emery, K. O. (1960) The sea off southern California. John Wiley and sons, New York, New York, U.S.A., pp. 366.

Feldman, R. A., T. M. Shank, M. B. Black, A. R. Baco, C. R. Smith and R. C. Vrijenhoek (1998) Vestimentiferan on a Whale Fall. Biological Bulletin, 194: 116-119.

Fornes, W. L. (1999) Mechanisms and rates of bioturbation and sedimentation in California Borderland sediments. Ph.D. Dissertation, North Carolina State University, pp. 207.

Froelich, P. N., G. P. Klinkhammer, M. L. Bender, N. A. Luedtke, G. R. Heath, D. Cullen, P. Dauphin, D. Hammond, B. Hartman and V. Maynard (1979) Early oxidation of organic matter in pelagic sediments of the eastern equatorial Atlantic: suboxic diagenesis. Geochimica et Cosmochimica Acta, 43: 1075-1090.

Gallager, S. M., R. D. Turner and C. J. Berg (1981) Physiological aspects of wood consumption, growth, and reproduction in the shipworm *Lyrodus pedicellatus* Quatrefages. Journal of Experimental Marine Biology and Ecology, 52: 63-77.

Gardner, W. D., L. G. Sullivan and E. M. Thorndike (1984) Long-term photographic, current, and nephelometer observations of manganese nodule environments in the Pacific. Earth and Planetary Science Letters, 70: 95-109.

Grant, J. and C. Bacher (1998) Comparative models of mussel bioenergetics and their validation at field culture sites. Journal of Experimental Marine Biology and Ecology, 219: 21-44.

Honjo, S., J. Dymond, R. Collier and S. J. Manganini (1995) Export production of particles to the interior of the equatorial Pacific Ocean during the 1992 EqPac experiment. Deep-Sea Research II, 42: 831-870.

Ingalls, A. E., R. C. Aller, C. Lee and S. G. Wakeham (2004) Organic matter diagenesis in shallow water carbonate sediments. Geochimica et Cosmochimica Acta, 68: 4363-4379.

Jones, T. H. [ed.] (1989) The encyclopedia of wood, revised. Sterling Publishing Co., New York, New York, U.S.A., pp. 464.

King, P., H. Kennedy, P. P. Newton, T. D. Jickells, T. Brand, S. Calvert, G. Cauwet, H. Etcheber, B. Head, A. Khripounoff, B. Manighetti and J. C. Miquel (1998) Analysis of total and organic carbon and total nitrogen in settling oceanic particles and a marine sediment: an interlaboratory comparison. Marine Chemistry, 60: 203-216.

Knudsen, J. (1961) The bathyal and abyssal *Xylophaga* (Pholadidae, Bivalvia). Galathea Report, 5: 163-209.

Langdon, C. J. and R. I. E. Newell (1990) Utilization of detritus and bacteria as food sources by two bivalve suspension-feeders, the oyster *Crassostrea virginica* and the mussel *Geukensia demissa*. Marine Ecology Progress Series, 58: 299-310.

McCave, I. N. (1975) Vertical flux of particles in the ocean. Deep-Sea Research, 22: 491-502.

Miller, P. J. O., M. P. Johnson, P. L. Tyack and E. A. Terray (2004) Swimming gaits, passive drag and buoyancy of diving sperm whales *Physeter macrocephalus*. Journal of Experimental Biology, 207: 1953-1967.

Miller, R. J., C. R. Smith, D. J. DeMaster and W. L. Fornes (2000) Feeding selectivity and rapid particle processing by deep-sea megafaunal deposit feeders: a ^{234}Th tracer approach. Journal of Marine Research, 58: 653-673.

Millero, F. J. (1996) Chemical Oceanography. CRC Press, Boca Raton, Florida, U.S.A., pp. 469.

Møller, E. F. (2007) Production of dissolved organic carbon by sloppy feeding in the copepods *Acartia tonsa*, *Centropages typicus*, and *Temora longicornis*. Limnology and Oceanography, 52: 79-84.

Ovington, J. D. and H. A. I. Madgwick (1958) The sodium, potassium and phosphorus contents of tree species grown in close stands. New Phytologist, 57: 273-284.

Parker, W. J. and S. L. LeVan (1989) Kinetic properties of the components of Douglas-fir and the heat of combustion of their volatile pyrolysis products. Wood and Fiber Science, 21: 289-305.

Popham, J. D. and M. R. Dickson (1973) Bacterial associations in the teredo *Bankia australis* (Lamellibranchia, Mollusca). Marine Biology, 19: 338-340.

Priede, I. G., K. L. J. Smith and J. D. Armstrong (1990) Foraging behavior of abyssal grenadier fish: inferences from acoustic tagging and tracking in the North Pacific Ocean. Deep-Sea Research, 37: 81-101.

Priede, I. G., P. M. Bagley, J. D. Armstrong, K. L. J. Smith and N. R. Merrett (1991) Direct measurement of active dispersal of food-falls by deep-sea demersal fishes. Nature, 351: 647-649.

Regnier, P., J. P. O'Kane, C. I. Steefel and J. P. Vanderborght (2002) Modeling complex multi-component reactive-transport systems: towards a simulation environment based on the concept of a Knowledge Base. Applied Mathematical Modelling, 26: 913-927.

Rowe, G. T. and J. W. Deming (1985) The role of bacteria in the turnover of organic carbon in deep-sea sediments. Journal of Marine Research, 43: 925-950.

Shaw, T. J., J. M. Gieskes and R. A. Jahnke (1990) Early diagenesis in differing depositional environments: the response of transition metals in pore water. Geochimica et Cosmochimica Acta, 54: 1233-1246.

Smith, A. H. and N. Pace (1971) Differential component and organ size relationship among whales. Environmental Physiology, 1: 122-136.

Smith, C. R. (1985) Food for the deep sea: utilization, dispersal, and flux of nekton falls at the Santa Catalina basin floor. Deep-Sea Research, 32: 417-442.

Smith, C. R., H. L. Maybaum, A. R. Baco, R. H. Pope, S. H. Carpenter, P. L. Yager, S. A. Macko and J. W. Deming (1998) Sediment community structure around a whale skeleton in the deep Northeast Pacific: Macrofaunal, microbial and bioturbation effects. Deep-Sea Research II, 45: 335-364.

Smith, C. R., A. R. Baco and A. G. Glover (2002) Faunal succession on replicate deep-sea whale falls: time scales and vent-seep affinities. Cahiers de Biologie Marine, 43: 293-297.

Smith, C. R. and A. R. Baco (2003) Ecology of whale falls at the deep-sea floor. Oceanography and Marine Biology: an Annual Review, 41: 311-354.

Stockton, W. L. and T. E. DeLaca (1982) Food falls in the deep sea: occurence, quality and significance. Deep- Sea Research, 29: 157-169.

Turner, R. D. (1973) Wood-boring bivalves, opportunistic species in the deep sea. Science, 180: 1377-1379.

Turner, R. D. (1978) Wood, mollusks, and deep-sea food chains. Bulletin of the American Malacological Union, 1977: 13-19.

Van Cappellen, P. and Y. Wang (1995) Metal cycling in surface sediments: modeling the interplay of transport and reaction, p. 21-64. *In* Allen, H. M. [ed.], Metal contaminated aquatic sediments. Ann Arbor Press, Chelsea, Michigan, U.S.A.

Van Cappellen, P. and Y. Wang (1996) Cycling of iron and manganese in surface sediments: a general theory for the coupled transport and reaction of carbon, oxygen, nitrogen, sulfur, iron, and manganese. American Journal of Science, 296: 197-243.

Van Cappellen, P. and J.-F. Gaillard (1996) Biogeochemical dynamics in aquatic sediments. Reviews in Mineralogy, 34: 335-376.

Watanabe, Y., E. A. Baranov, K. Sato, Y. Naito and N. Miyazaki (2006) Body density affects stroke patterns in Baikal seals. Journal of Experimental Biology, 209: 3269-3280.

Waterbury, J. B., C. B. Calloway and R. D. Turner (1983) A cellulolytic-nitrogen fixing bacterium cultured from the Gland of Deshayes in shipworms (Bivalvia: Teredinidae). Science, 221: 1401-1403.

Woodward, R. L., J. P. Winn and F. E. Fish (2006) Morphological specializations of baleen whales associated with hydrodynamic performance and ecological niche. Journal of Morphology, 267: 1284-1294.

Appendix A

Table A.1 Derived quantities, their units in basic quantities, description, and chapters in which they are used.

Symbol	SI Units	Description	Chapter
A	Le^2	Area, cross-sectional area of sediment column	2, 3, 6
A_{colA}	Le^2	Cross-sectional area of sediment column A	4
A_{plugs}	Le^2	Area of sediment plugs	4
AW_{14N}	M	Atomic weight of ^{14}N	4
AW_{15N}	M	Atomic weight of ^{15}N	4
b	$N \cdot Le^{-3} \cdot T^{-1}$	Slope	4
b_{norm}	$N \cdot Le^{-3} \cdot T^{-1}$	Normalized slope	4
C	$N \cdot Le^{-3}$	Concentration of tracer	3
C_0	$N \cdot Le^{-3}$	Initial concentration of tracer	3
d	Le	Grain diameter	2, 3
d_{50}	Le	Median grain diameter	3
d_{mean}	Le	Mean grain diameter	2, 3
d_o	Le	Grain diameter of 1 mm	2, 3
d_x	Le	Grain diameter > than x % weight of all grains	3
D	$Le^2 \cdot T^{-1}$	Molecular diffusion coefficient	2
D_0	$Le^2 \cdot T^{-1}$	Free solution diffusion coefficient	3
DFC		defecation component (dimensionless)	7

DK	$L e^{-2}$	Dispersal kernel around fall	7
D_s	$L e^{2} \cdot T^{-1}$	Sedimentary diffusion coefficient	3
D_χ	$L e^{2} \cdot T^{-2}$	Displacement coefficient for tracer impulse	3
f	T^{-1}	Frequency	3
f^*		Fraction of $[NO_3^-]_0$ remaining at time t	4
Fa	$N \cdot L e^{-2} \cdot T^{-1}$	Flux of nutrients (by area)	4
F_{abs}	$M \cdot T^{-1}$	Scavenger absorption flux	7
Fa_{NO3-}	$N \cdot L e^{-2} \cdot T^{-1}$	Flux of nitrate (by area)	4
Fa_{PO43-}	$N \cdot L e^{-2} \cdot T^{-1}$	Flux of phosphate (by area)	4
F_{def}	$M \cdot T^{-1}$	Scavenger defecation flux	7
F_{denit}	$N \cdot L e^{-2} \cdot T^{-1}$	Rate of denitrification	4
F_{mat}	$M \cdot T^{-1}$	Organic matter release rate from fall	7
F_{matC}	$M \cdot T^{-1}$	Carbon release rate from fall	7
F_{matN}	$M \cdot T^{-1}$	Nitrogen release rate from fall	7
F_{matP}	$M \cdot T^{-1}$	Phosphorus release rate from fall	7
F_{rel}	$M \cdot T^{-1}$	Dispersal flux	7
F_{SC}	$M \cdot T^{-1}$	Scavenging rate	7
F_{sedC}	$M \cdot L e^{-2} \cdot T^{-1}$	Rate of carbon supply to sediment	7
F_{sf}	$M \cdot T^{-1}$	Sloppy feeding flux	7
Fw	$N \cdot M^{-1} \cdot T^{-1}$	Flux of nutrients (by weight)	4
Fw_{NO3-}	$N \cdot M^{-1} \cdot T^{-1}$	Flux of nitrate (by weight)	4
Fw_{PO43-}	$N \cdot M^{-1} \cdot T^{-1}$	Flux of phosphate (by weight)	4
F_{WR}	$M \cdot T^{-1}$	Removal rate of wood	7

g	$Le \cdot T^{-2}$	Gravitational acceleration	2, 3
h	Le	Height, height of water, head height	3, 6
h_0	Le	Water (wave) height at $t = 0$	3
h_A	Le	Height of water in column A	3
h_{adj}	Le	Water height adjustment in columns A and B	3
h_{Amodel}	Le	Modeled height of water in column A	3
h_B	Le	Height of water in column B	3
h_{Bmodel}	Le	Modeled height of water in column B	3
H	Le	Head difference between reservoirs	2, 3
H_0	Le	Head difference between reservoirs at $t = 0$	3
k	Le^2	Permeability	2, 3
k^*	Le^{-1}	Wave number	3
k_A	Le^2	Permeability of sediment column A	3
k_B	Le^2	Permeability of sediment column B	3
k_T	Le^2	Permeability of sediment columns A and B	3
K	$Le \cdot T^{-1}$	Hydraulic conductivity	2, 3
K_T	$Le \cdot T^{-1}$	Hydraulic conductivity of columns A and B	3
l	Le	Length ofsediment column, large organic fall	2, 3, 7
l_A	Le	Length of sediment column A	3
l_B	Le	Length of sediment column B	3
l_{cet1}	Le	Major axis of whale fall	7
l_{cet2}	Le	Major axis of whale fall	7
l_T	Le	Length of sediment columns A and B	3

l_{wood1}	Le	Length of wood fall	7
l_{wood2}	Le	Width of wood fall	7
L	Le	Length	6
M	M	Mass	6, 7
M_{cet}	M	Weight of whale fall	7
M_d		Median of cumulative grain size distribution	4
M_z		Graphic mean size of sediment grains	4
N	Le^{-2}	Area normalization factor	7
$^{15}N_{missing}$	M	^{15}N missing from system in experiment	4
q	$Le^3 \cdot T^{-1}$	Volume flow rate	2, 3
r	Le	radius	6, 7
r_{AW}		Atomic weight ratio of ^{15}N to ^{14}N	4
$r_{FsedC=bkg}$	Le	r where sedimentation = background	7
r_{max}	Le	Maximum r impacted by fall	7
R		Ratio of $^{15}NO_3^-$ to $^{14}NO_3^-$ at time t	4
R_0		Ratio of $^{15}NO_3^-$ to $^{14}NO_3^-$ at time $t = 0$	4
R_{NO3}		Ratio of ^{15}N to ^{14}N in nitrate	4
R_{sed}		Ratio of ^{15}N to ^{14}N in sediment	4
s_1	Le	Long radius for whale fall area	6
s_2	Le	Short radius for whale fall area	6
SA	Le^2	Surface area	6
SFC		Sloppy feeding component (dimensionless)	7
Sk_1		Skewness of grain size distribution	4

t	T	Time in experiment	3
t_0	T	Experiment start time, initial time	4, 7
t_D	T	Tracer breakthrough time	3
t_f	T	Experiment end time, process end time	4, 7
t_M	T	Tracer peak arrival time	3
T	T	Time period	3
$TN_{sample\text{-}pred}$	N	Total predicted nitrogen value in sample	6
TN_{sed}	N	Total nitrogen value in sediment	6
TN_w	N	Total nitrogen value in wood	6
TOC_{sample}	N	Total organic carbon value in sample	6
TOC_{sed}	N	Total organic carbon value in sediment	6
TOC_w	N	Total organic carbon value in wood	6
u	$Le \cdot T^{-1}$	Sinking velocity	2
v	$Le \cdot T^{-1}$	Fluid velocity	2, 3
v_m	$Le \cdot T^{-1}$	Tracer migration rate	3
V	Le^3	Volume	3, 6
V_{cet}	Le^3	Volume of whale fall	7
V_l	Le^3	Envelope volume per wood block	7
$V_{l\text{-}missing}$	Le^3	Missing volume per wood block	7
V_{OW}	Le^3	Volume of overlying water	4
V_{slice}	Le^3	Volume of sediment slice	4
$V_{T\text{-}missing}$	Le^3	Total volume of missing wood	7
V_{wood}	Le^3	Total volume of wood fall	7

w	Le	Depth in sediment, weight fraction of wood	3, 6
wt_{sed}	M	Weight of plug sediment	4
$\overline{wt}_{plug}$	M	Average weight of sediment plugs	4
W_{DIW}	M	Weight of de-ionized water	4
W_{dry}	M	Weight of dry sediment	4
W_{dry}	M	Weight of dry sediment	4
Wt	M	Tissue weight of fall	7
Wt_{14Nsed}	M	Weight of ^{14}N in sediment	4
Wt_{15NO3}	M	Weight of ^{15}N in nitrate	4
Wt_{15Nsed}	M	Weight of ^{15}N in sediment	4
Wt_{15Ntot}	M	Total weight of N in sediment + nitrate	4
Wt_{abs}	M	Scavenged mass absorbed by the scavenger	7
WtC	M	Carbon weight of fall	7
WtC_{cet}	M	Carbon weight of whale fall	7
Wt_{cet}	M	Tissue weight for whale fall	7
WtC_{wood}	M	Carbon weight of wood fall	7
Wt_{fec}	M	Scavenged mass defecated by the scavenger	7
$WtH20$	M	Water weight of fall	7
WtN	M	Nitrogen weight of fall	7
$Wt_{N\text{-}NO3}$	M	Total weight of N in nitrate	4
Wt_{Nsed}	M	Total weight of N in sediment	4
WtP	M	Phosphorus weight of fall	7
Wt_{rel}	M	Total mass released for dispersal to sediments	7

Wt_{retC}	M	Total carbon released for dispersal	7
Wt_{SC}	M	Scavenged mass	7
Wt_{sf}	M	Scavenged mass released by sloppy feeding	7
Wt_{wood}	M	Tissue weight for wood fall	7
Wt_{WR}	M	Weight of wood removed	7
W_{wet}	M	Weight of wet sediment	4
z	Le	Depth, Displacement of tracer impulse	3
z_{layer}	Le	Depth of separation of sediment layers	3
z_N	Le	Depth for DIN supply and uptake balance	4
z_P	Le	Depth for PO_4^{3-} supply and uptake balance	4
α	Le^{-1}	Distance coefficient	7
ε	-	Diffusion enhancement factor	2, 3
$\in$	-	Isotope fractionation effect	4
ε_{lower}	-	Diffusion enhancement factor for lower layer	3
ε_{upper}	-	Diffusion enhancement factor for upper layer	3
$\delta^{15}N$	-	Nitrogen isotopic composition	4
$\delta^{15}N_{NO3-}$	-	Nitrogen isotopic composition of nitrate	4
$\delta^{15}N_{sed}$	-	Nitrogen isotopic composition of sediment	4
$\Delta^{15}N_{NO3}$	M	Change in ^{15}N in nitrate through experiment	4
$\Delta^{15}N_{sed}$	M	Change in ^{15}N in sediment through experiment	4
ϕ	-	Grain size	2, 3
ϕ_{50}	-	Median of cumulative grain size distribution	2
ϕ_x	-	x % of cumulative grain size distribution	2, 3, 4

φ	-	Porosity	3
λ	Le	Wavelength	3
μ	$M \cdot Le^{-1} \cdot T^{-1}$	Dynamic viscosity	2, 3
θ	-	Sediment tortuosity	3
ρ	$M \cdot Le^{-3}$	Fluid density, Bulk density	2, 3, 7
ρ_{cet}	$M \cdot Le^{-3}$	Density of whale fall	7
ρ_{DIW}	$M \cdot Le^{-3}$	Density of de-ionized water	4
ρ_f	-	Density function	7
ρ_{sw}	$M \cdot Le^{-3}$	Density of seawater	6, 7
ρ_{wet}	$M \cdot Le^{-3}$	Density of wet sediment	4
ρ_{wood}	$M \cdot Le^{-3}$	Density of wood	7
σ_1	-	Sorting of sediment grain size	3
σ_ϕ	-	Sorting of sediment grain size	2

Appendix B

MATLAB Routine 1 (Chapter 3) uses the data from a single relaxation test performed on the microcosm to adjust the collected water level data (if necessary), generating an estimate of the total hydraulic conductivity, and a flow velocity-water height difference relationship. The functions "risinghead" and "droppinghead" are appended. The example given below is for relaxation run 1 of Exp. 11.

```
% Microcosm model: Experiment 11, Run # 1, L = 99.5 cm, 9/25/2006
% When a height difference is set between Columns A and B and the block
% between the two columns is released, the speed of fall is related to
% the hydraulic conductivity. This model takes the data, optimizes the
% Column B height data, and calculates the hydraulic conductivity. It
% also generates a height difference versus velocity graph that helps
% visualize the exchange of water during an oscillation cycle.
% Angelos K. Hannides, 2007

clear;

% DATA ENTRY
XXXXXXXXXXXXXXXXXXXXXXXXXXXXXXXXXXXXXXXXXXXXXXXXXXXXXXXXXXXXXXXXXXXX

% Enter times after release of block between Columns A and B in s
tdata=[0
120
240
420
660
1020
1320
1680
2100
2640
3240
5280];

% Enter Column A water heights above 150 cm mark in cm
hA=[5.3
4.8
4.4
3.8
3.2
2.4
2
```

```
1.5
1.2
0.9
0.7
0.6];

% Enter Column B water heights above 150 cm mark (best guess) in cm
hB=[-6
-5.6
-5.1
-4.5
-3.9
-3.1
-2.6
-2.3
-1.9
-1.2
-1
-0.9];

% The cross-sectional area of the microcosm. In our prototype d = 3
inches
Area = pi*((2.56*3/2)^2);

% The average height of water at equilibrium, usually set at 150 cm
averageh = 150;
hA = hA + averageh;
hB = hB + averageh;

% MODELING
XXXXXXXXXXXXXXXXXXXXXXXXXXXXXXXXXXXXXXXXXXXXXXXXXXXXXXXXXXXXXXXXXXXXXXX

% Column B height adjustment - No adjustment necessary in this
experiment

tmodel = [0:1:max(tdata)]';

% The fit of the two columns' heights with the appropriate equations.
% Please adjust accordingly: match the height data with the right
function.

beta0 = [hB(1,1) max(tdata)/2 0.1];
[beta,r,J] = nlinfit(tdata, hB, 'risinghead', beta0);
predColB = risinghead(beta, tmodel);
predicted_hB = beta(1)+beta(2)*(1-exp(-(beta(3))*tmodel));
ColBfitting_coeffs = beta;
ColumnBasymptote = beta(1) + beta(2);

beta0 = [hA(1,1) max(tdata)/2 0.1];
[beta,r,J] = nlinfit(tdata, hA, 'droppinghead', beta0);
predColA = droppinghead(beta, tmodel);
predicted_hA = beta(1)+beta(2)*exp(-(beta(3))*tmodel);
ColAfitting_coeffs = beta;
ColumnAasymptote = beta(1);
```

```
% Plotting the data and the models
figure('Color','w');
subplot(2,2,1);
plot(tdata,hA,'or');
hold on;
plot(tdata,hB,'db');
plot(tmodel,predicted_hA,'--r');
plot(tmodel,predicted_hB,':b');
text(max(tdata)*0.99,ColumnAasymptote*1.09,['h_{A} =
',num2str(ColAfitting_coeffs(1)),...
        ' + ',num2str(ColAfitting_coeffs(2)),'e^{-
',num2str(ColAfitting_coeffs(3)),'t}'],...
    'HorizontalAlignment','right','Color','r')
text(max(tdata)*0.99,ColumnAasymptote*1.07,['h_{B} =
',num2str(ColBfitting_coeffs(1)),...
        ' + ',num2str(ColBfitting_coeffs(2)),'(1-e^{-
',num2str(ColBfitting_coeffs(3)),'t})'],...
    'HorizontalAlignment','right','Color','b')

% Calculating hadj and adjusting the water height data
hadj = (ColumnAasymptote - ColumnBasymptote)/2;
hA = hA-hadj;
hB = hB+hadj;

% Plotting the adjusted Column B data
xlabel('Time (s)','FontWeight','bold');
ylabel('Water level (cm)','FontWeight','bold');
legend('Col. A data','Col. B data','Eq. 3.2a fit','Eq. 3.2b fit',0);
text(10,max(hA),['h_{adj} = ',num2str(hadj),'
cm'],'HorizontalAlignment',...
   'left');
title('Experiment 11, Run # 1, 9/25/2006, L =99.5 cm'); % Enter the
data date, experiment, measurement #,
% or any other meaningful description of the data source
hold off;

% Estimate of water transfer velocity, v (cm/s)

ColA(1,1) = hA(1,1);
ColB(1,1) = hB(1,1);
length = 99.5; % The length of the sediment column in cm
K = 0.04179; % no independent permeability measurement in Experiment 1

% In this experiment, the starting value of K was guessed
% Afterwards, vary this by inspection of Figure 2 so that you get a
minimum
% in the value of the summed square of residuals (SSR) with K.
K_range = [0.02:0.0001:0.06]';

% The following routine varies K as you defined above, calculates the
% SSR at each K, and stores it in an array
Kcounter = 1;
maxKcounter = size(K_range)+1;
while Kcounter < maxKcounter(1,1);
```

```
    v(1,1) = K_range(Kcounter)*((ColA(1,1)-ColB(1,1))/length);
    counter = 2;
    maxcounter = size(tmodel)+1;
    while counter < maxcounter(1,1);
        ColA(counter,1) = ColA(counter-1,1) - v(counter-1,1);
        ColB(counter,1) = ColB(counter-1,1) + v(counter-1,1);
        v(counter,1) = K_range(Kcounter)*((ColA(counter,1)-
ColB(counter,1))/length);
        counter = counter+1;
    end

    % SSR determination
    % - indexing the time points
    counter = 1;
    maxcounter = size(tdata)+1;
    while counter < maxcounter(1,1);
        index(counter,1) = find(tdata(counter,1) == tmodel);
        counter = counter + 1;
    end
    % - calculating the square of residuals for the Column A data
    ydifferenceA = hA - ColA(index);
    ydifferencesquaredA = ydifferenceA.^2;
    % - calculating the square of residuals for the Column B data
    ydifferenceB = hB - ColB(index);
    ydifferencesquaredB = ydifferenceB.^2;
    % - calculating the summed square of residuals
    S(Kcounter,1) =
(sum(ydifferencesquaredA)+sum(ydifferencesquaredA))/2;

    Kcounter = Kcounter + 1;
end

% Plotting the SSR versus K
subplot(2,2,2);
plot(K_range,S,'-b');
hold on;
xlabel('K (cm s^{-1})','FontWeight','bold');
ylabel('SSR (Eq. 3.4)','FontWeight','bold');
text(K,max(S)*0.1,'\downarrow','FontSize',18);
text(max(K_range),max(S)*0.9,['K_{Measured} = ',num2str(K),' cm s^{-
1}'],...
   'HorizontalAlignment','right','FontSize',12,'Color','k');

% Finding the minimum SSR and matching it to the optimal K
[minSSR,i] = min(S);
K = K_range(i);
text(K,max(S)*0.1,'\downarrow','HorizontalAlignment','center',...
    'FontSize',18,'Color','b');
text(max(K_range),max(S)*0.8,['K_{Optimal} = ',num2str(K),' cm s^{-
1}'],...
   'HorizontalAlignment','right','FontSize',12,'Color','b');

% Modeling the head difference and velocity with the optimal K
v(1,1) = K.*((ColA(1,1)-ColB(1,1))/length);
counter = 2;
```

```
maxcounter = size(tmodel)+1;
while counter < maxcounter(1,1);
    ColA(counter,1) = ColA(counter-1,1) - v(counter-1,1);
    ColB(counter,1) = ColB(counter-1,1) + v(counter-1,1);
    v(counter,1) = K.*((ColA(counter,1)-ColB(counter,1))/length);
    counter = counter+1;
end

% Plotting the actual data against the model

subplot(2,2,3);
plot(tdata,hA,'or');
hold on;
plot(tdata,hB,'db');
plot(tmodel,ColA,'--r');
[AX,H1,H2] = plotyy(tmodel,ColB,tmodel,v,'plot');
xlabel('Time (s)','FontWeight','bold');
set(get(AX(1),'Ylabel'),'String','Water level
(cm)','FontWeight','bold','Color','black')
set(get(AX(2),'Ylabel'),'String','v (cm s^{-1})','FontWeight','bold')
set(H1,'LineStyle',':')
set(H2,'LineStyle','-')
legend('Col. A data','Col. B data','Col. A model (Eq. 3.3)','Col. B
model (Eq. 3.3)',1);
legend(H2,'v model (Eq. 3.3)',0);

% H vs v
XXXXXXXXXXXXXXXXXXXXXXXXXXXXXXXXXXXXXXXXXXXXXXXXXXXXXXXXXXXXXXXXXXXXXXX

% Generating H
H = ColA-ColB;

% Calculating the relationship
Hvsvfit=polyfit(H,v,1);

subplot(2,2,4);
plot(H,v,'-k');
xlabel('Column water height difference, H(t)
(cm)','FontWeight','bold');
ylabel('Model velocity (Eq. 3.3), v(t) (cm s^{-
1})','FontWeight','bold');
text(max(H)*0.08,max(v)*0.9,['v = ',num2str(Hvsvfit(1,1)),'H + ',...
        num2str(Hvsvfit(1,2))]);

% CLEAN-UP
XXXXXXXXXXXXXXXXXXXXXXXXXXXXXXXXXXXXXXXXXXXXXXXXXXXXXXXXXXXXXXXXXXXXXXX

clear Area Column*asymptote J K_range S Kcounter averageh beta* counter
i index;
clear leftyaxis length max* predCol* r rightyaxis* tdata ydifference*;
```

Function "risinghead"

```
function pred_risinghead=risinghead(beta,tmodel)

y0=beta(1);
a=beta(2);
b=beta(3);
pred_risinghead = y0+a*(1-exp(-(b)*tmodel));
```

Function "droppinghead"

```
function pred_droppinghead=droppinghead(beta,tmodel)

y0=beta(1);
a=beta(2);
b=beta(3);
pred_droppinghead = y0+a*exp(-(b)*tmodel);
```

Appendix C

MATLAB Routine 2 (Chapter 3) uses all the hydraulic conductivity estimates (generated by Routine 1, Appendix B) from a single microcosm experiment to calculate the individual hydraulic conductivities and permeabilities of the two columns. The function composite_permeability is appended. The example presented below is for microcosm Exp. 1.

```
clear;

kT=[5.07942E-06
6.13618E-06
5.72743E-06
6.18004E-06
4.87505E-06
4.79828E-06
4.16124E-06
4.20111E-06
4.0765E-06
3.80832E-06];

LT=[110
110
110
120
120
150
150
175
175];

LTmodel = [100:1:200]';

beta0 = [0.0000062 0.0000025];
[beta,r,J] = nlinfit(LT, kT, 'composite_permeability', beta0);
predks = composite_permeability(beta, LTmodel);
kA=beta(1);
kB=beta(2);
stcomp = 100/kA;
ndcomp = (LTmodel-100)/kB;
denom = stcomp + ndcomp;
kTmodel = LTmodel./denom;
```

```
figure('Color','w');
plot(LT,kT,'or');
hold on;
plot(LTmodel,kTmodel,'-r');
xlabel('Total length (cm)');
ylabel('Total column permeability, k_{T} (cm^{2})');
legend('Data','Model (Eq. 3.6)',0);
kAm2 = kA/(10^4);
kBm2 = kB/(10^4);
text(max(LTmodel)*0.95,max(kTmodel),['k_{A} = ',num2str(kAm2),'
m^{2}'],...
    'HorizontalAlignment','right','FontWeight','bold');
text(max(LTmodel)*0.95,max(kTmodel)*0.95,['k_{B} = ',num2str(kBm2),'
m^{2}'],...
    'HorizontalAlignment','right','FontWeight','bold');
```

Function "composite_permeability"

```
function pred_kT=composite_permeability(beta,LTmodel)

kA=beta(1);
kB=beta(2);
stcomp = 100/kA;
ndcomp = (LTmodel-100)/kB;
denom = stcomp + ndcomp;
pred_kT = LTmodel./denom;
```

Appendix D

The Rao and Jahnke (2004) model, developed to calculate enhanced transport in benthic chamber studies, was transformed from Fortran to MATLAB, and used to calculate the loss into the sediment of a pulse of bromide released in the overlying water of a chamber. The Example given is for Tracer Exp. 11-1.

```
% Rao and Jahnke (2004) Limnol. Oceanogr. Methods, 2: 75-90
% Model EDIF.f converted to MATLAB by A. K. Hannides, 2007
% Comments in model are both from EDIF.F and from A. K. Hannides

% Diffusion only code, implemented changes 10/13/2001.
% Assume: dphi/dx is negligible for the purposes of calculating dC/dt.
% Result: total mass decreasing with time (imperfect mass balance).
% Values are in microL (mm3), mm, mol

% clear;
%
% timedata = [0.0006
% 0.267
% 0.550
% 0.750
% 1.283
% 4.617];
%
% OWdata=[9 26    26
% 905 26    26
% 722 26    26
% 752 26    26
% 729 26    26
% 707 26    26];
%
% PWtsdata_50mm=[0.0006 2     26    26
% 0.767     -7    26    26
% 1.3 -4    26    26
% 2.033     91    26    26
% 2.567     105   26    26
% 3.117     94    26    26
% 3.85      168   26    26
% 4.633     157   26    26
% 5.3 186   26    26];

% Establish initial distribution tracer distribution
c = ones(999,1); % tracer concentration mol/microL
c = c-1;
```

```
% Calculate initial mass
vol = 3.48*10^6; % microL
area = 4632; % mm2
mass = 0.00254; % mol
cw = mass/vol; % mol/microL

% Establish depth domain
delz = 1; % mm
z(1) = delz/2;
counter = 2;
while counter < 1001;
    z(counter) = z(counter-1) + delz;
    counter = counter + 1;
end

% Establish porosity array
counter = 1;
while counter < 1001;
    % pore(counter) = 0.712 + 0.156*exp(-0.512*0.1*(z(counter)-
(delz/2))); % use according to Martin and Sayles (1996)
    pore (counter) = 0.47; % use if porosity is known and unchanging
with depth
    counter = counter + 1;
end

% Establish array of diffusion coefficients
% edif1 = 112; % epsilon, the diffusion enhancement factor
(dimensionless), top layer
% edif2 = 112; % epsilon, the diffusion enhancement factor
(dimensionless), bottom layer
% toplayer = 0; % mm, top layer's cut-off
adif = 6.9340; % Do, the free solution diffusion coefficient mm2/h

% Calculating transport functions

if toplayer > 0;
    vdif(1) = pore(1)*pore(1)*pore(1)*adif*edif1/(delz/2); % mm/h
else
    vdif(1) = pore(1)*pore(1)*pore(1)*adif*edif2/(delz/2); % mm/h
end
counter = 2;
while counter < toplayer;
    vdif(counter) =
edif1*adif*pore(counter)*pore(counter)*pore(counter)/delz;
    counter = counter + 1;
end
while counter < 1000;
    vdif(counter) =
edif2*adif*pore(counter)*pore(counter)*pore(counter)/delz;
    counter = counter + 1;
end

% % Calculate modulus value
% delt = 0.001;
```

```
% counter = 1;
% while counter < 1000;
%     modulus(counter) = ((dif*pore(counter)))*delt/(delz*delz);
%     counter = counter + 1;
% end
%
totsample = 0; % mol
tottim = 0; % h
delt = 0.001; % h
corr = 1e-4;
fintim = max(PWtsdata_50mm(:,1)); % h
prtfreq = 0.1;

recorder = 1;

while ((tottim-fintim) < 0);
    prtt = 0;

    if ((prtt + corr - prtfreq) < 0);

% Transport functions to bypass instabilities due to high modulus
values
%         if cw - c(1) > 0;
%             vdif(1) = pore(1)*pore(1)*pore(1)*adif*edif1/(delz/2); %
mm/h
%         else
%             vdif(1) = 0;
%         end
%         counter = 2;
%         while counter < toplayer;
%             if c(counter-1) - c(counter) > 0;
%                 vdif(counter) =
edif1*adif*pore(counter)*pore(counter)*pore(counter)/delz;
%             else
%                 vdif(counter) = 0;
%             end
%             counter = counter + 1;
%         end
%         while counter < 1000;
%             if c(counter-1) - c(counter) > 0;
%                 vdif(counter) =
edif2*adif*pore(counter)*pore(counter)*pore(counter)/delz;
%             else
%                 vdif(counter) = 0;
%             end
%             counter = counter + 1;
%         end

        % Calculate array of dC/dt
        dc(1) = (vdif(1)*(cw-c(1))) + (vdif(2)*(c(2)-c(1))); %
mol/mm2.h
        counter = 2;
        while counter < 999;
            dc(counter) = (vdif(counter)*(c(counter-1)-c(counter))) +
(vdif(counter+1)*(c(counter+1)-c(counter)));
```

```
            counter = counter + 1;
        end
        dc(999) = (vdif(999)*(c(998)-c(998)));


%         % Remove sample volume
%         sample = cw*(0); % mol
%         t = tottim - delt; %h
%
%         timedatasize = size(timedata); % Determine size of time
points matrix
%         timedatasize = timedatasize(2);
%         counter = 1;
%         while counter < timedatasize + 1;
%             if ((t <= timedata(counter)) & (tottim >=
timedata(counter)));
%                 cw1 = cw; % mol/microL
%                 cw = ((cw*vol) - sample)/vol; % mol/microL
%                 totsample = totsample + sample; % mol
%                 counter = counter + 1;
%             else counter = counter + 1;
%             end
%         end

        % Calculate benthic flux
        bf = (vdif(1)*(cw-c(1))); % mol/mm2.h

        % Calculate new concentrations, and correct chamber water
concentration for non-local exchange
        counter = 1;
        while counter < 1000;
            c(counter) = (c(counter)*pore(counter)*delz +
delt*dc(counter))/(delz*pore(counter)); % mol/microL
            counter = counter + 1;
        end

        % Calculate new chamber concentration - correct for benthic
diffusive flux
        ch = vol/area; % mm
        cw = ((cw*ch) - bf*delt)/ch; % mol/microL

        % Calculate total mass
        mass = (vol*cw) + totsample; % mol
        counter = 1;
        while counter < 1000;
            mass = mass + (c(counter)*pore(counter)*delz*area); % mol
            counter = counter + 1;
        end

        % Increment time counters
        tottim = tottim + delt; % h
        prtt = prtt + delt; % h

        % Iterate
```

```
    else
    end

%     OWmodel(recorder,1)=tottim;
%     OWmodel(recorder,2)=cw*(10^6)*(10^6); % converts mol/microL to
micromol/L
%     OWmodel(recorder,3)=bf;
%     OWmodel(recorder,4)=mass;

    PWtsmodel(recorder,1)=tottim;
    PWtsmodel(recorder,2)=((c(50)+c(51))/2)*(10^6)*(10^6);

%     if (tottim >= fintim);
%         counter = 1;
%         while counter < 1000;
%             PWmodel(counter,1)=z(counter);
%             PWmodel(counter,2)=pore(counter);
%             PWmodel(counter,3)=c(counter)*(10^6)*(10^6);
%             counter = counter + 1;
%         end
%     else
%     end

    recorder = recorder + 1;

end

% figure;
% plot(OWmodel(:,1),OWmodel(:,2),'-b');
% hold on;
% plot(PWtsmodel(:,1),PWtsmodel(:,2),'-k');
% errorbar(timedata,OWdata(:,1),OWdata(:,2),OWdata(:,3),'ob');
%
errorbar(PWtsdata_50mm(:,1),PWtsdata_50mm(:,2),PWtsdata_50mm(:,3),PWtsd
ata_50mm(:,4),'sk');

loopsize = size(PWtsdata_50mm);
loopsize = loopsize(1,1);
chisquare = 0;

counter = 1;
while counter < loopsize + 1;
    time(counter) = PWtsdata_50mm(counter,1);
    observed(counter) = PWtsdata_50mm(counter,2);
    timeexpected(counter) = find((PWtsmodel(:,1) < time(counter)) &
(PWtsmodel(:,1) > time(counter)-delt));
    expected(counter) = PWtsmodel(timeexpected(counter),2);
    if expected(counter) < 26 & expected(counter) > -26;
        expected(counter) = 0;
    else
        chisquare = chisquare + (((observed(counter)-
expected(counter))^2)/expected(counter));
    end
    counter = counter + 1;
end
```

```
% text(max(PWtsmodel(:,1)),min(PWtsmodel(:,2)),['\epsilon =
',num2str(edif1),...
%         ', \chi^{2} = ',num2str(chisquare)],...
%     'HorizontalAlignment','right','FontSize',12,'Color','k');
% text(max(PWmodel(:,1)),max(PWmodel(:,3))*0.9,['Top layer: z = 0-',
num2str(toplayer/10),...
%         ' cm, \epsilon =
',num2str(edif1),],'HorizontalAlignment','right','FontSize',12,'Color',
'k');
% text(max(PWmodel(:,1)),max(PWmodel(:,3))*0.8,['Lower layer: z < ',
num2str(toplayer/10),...
%         ' cm, \epsilon =
',num2str(edif2),],'HorizontalAlignment','right','FontSize',12,'Color',
'k');
% text(max(PWmodel(:,1)),max(PWmodel(:,3))*0.7,['\chi^{2} =
',num2str(chisquare)],...
%         'HorizontalAlignment','right','FontSize',12,'Color','k');
```

Appendix E

The whale fall fragmentation and dispersal modules as implemented in MATLAB.

```
% FRAGMENTATION MODULE

% Model inputs
InitMcet = 24300; % initial carcass mass, kg
MunSC = InitMcet * 0.15; % unscavengeable carcass mass (skeleton
weight), kg
WtCcet = 0.26; % Carbon content of carcass soft tissue (26 %)
SFC = 0.01 % proportion of scavenged material which is released by
sloppy feeding
DFC = 0.1; % proportion of ingested material which is defecated
DefDelay = 10; % defecation delay, d, after ingestion
dt = 0.25; % time step, d

% Model run set-up

counter = 1;
t(counter,1) = 0; % time, d

% Reservoirs

Mcet(counter,1) = InitMcet; % carcass mass, kg
WtSC(counter,1) = 0; % scavenged mass, kg
Wtabs(counter,1) = 0; % scavenged mass absorbed by the scavenger, kg
Wtfec(counter,1) = 0; % scavenged mass defecated by the scavenger, kg
Wtsf(counter,1) = 0; % scavenged mass released by sloppy feeding, kg
Wtrel(counter,1) = Wtfec(counter,1) + Wtsf(counter,1); % total mass
released for dispersal to sediments, kg

% Fluxes

FSC = 0; % scavenging flux, kg d-1
Fabs(counter,1) = 0; % scavenger absorption flux, kg d-1
Fdef(counter:counter+(DefDelay/dt),1) = 0; % scavenger defecation flux,
kg d-1
Fsf(counter,1) = 0; % sloppy feeding flux, kg d-1
Frel(counter,1) = 0; % total release flux, kg d-1

% Model run

counter = counter + 1;
t(counter,1) = t(counter-1,1) + dt; % time, d

while Mcet(counter-1,1) > MunSC; % if there is still scavengeable
carcass mass
```

```
    FSC = 4.993 * log(InitMcet) + 1.5996; % scavenging flux, kg d-1, kg

    Mcet(counter,1) = Mcet(counter-1,1) - FSC*dt; % new carcass mass,
kg
    WtSC(counter,1) = WtSC(counter-1,1) + FSC*dt; % new scavenged mass
at beginning of iteration, kg

    Fabs(counter,1) = WtSC(counter,1) * (1 - SFC) * (1 - DFC); % new
scavenger absorption flux, kg d-1
    Fdef(counter+(DefDelay/dt),1) = WtSC(counter,1) * (1 - SFC) * DFC;
% new scavenger defecation flux, kg d-1
    Fsf(counter,1) = WtSC(counter,1) * SFC; % new sloppy feeding flux,
kg d-1
    Frel(counter,1) = Fdef(counter,1) + Fsf(counter,1); % new total
release flux, kg d-1

    WtSC(counter,1) = WtSC(counter,1) - (Fabs(counter,1) +
Fdef(counter,1) + Fsf(counter,1)) * dt; % new scavenged mass at end of
iteration, kg
    Wtabs(counter,1) = Wtabs(counter-1,1) + (Fabs(counter,1) * dt); %
new scavenged mass absorbed by the scavenger, kg
    Wtfec(counter,1) = Wtfec(counter-1,1) + (Fdef(counter,1) * dt); %
new scavenged mass defecated by the scavenger, kg
    Wtsf(counter,1) = Wtsf(counter-1,1) + (Fsf(counter,1) * dt); %
scavenged mass released by sloppy feeding, kg
    Wtrel(counter,1) = Wtfec(counter,1) + Wtsf(counter,1); % new total
mass released for dispersal to sediments, kg

    counter = counter + 1;
    t(counter,1) = t(counter-1,1) + dt; % time, d

end

t = t(1:size(t)-1,1); % eliminates the last time point, which is not
accompanied by model data
Fdef = Fdef(1:size(Fsf),1); % eliminates the time-displaced defecation
flux data
Fmat = Frel(round(max(counter) / 2),1); % Activate to include
defecation in release flux during carcass processing, kg d-1
% Fmat = Fsf(round(max(counter) / 2),1); % Activate to exclude
defecation from release flux during carcass processing, kg d-1
FmatC = Fmat*WtCcet; % combined Carbon release flux during carcass
processing, kg d-1, using C content of 26 %
FmatN = FmatC*50/555; % combined Nitrogen release flux during carcass
processing, kg d-1, using a N:C of 50/555
FmatP = FmatC*1/555; % combined Phosphate release flux during carcass
processing, kg d-1, using a P:C of 1/555
```

```
% DISPERSAL MODULE

% Calculating the dispersal kernel, DK (m-2)

% Model input

dr = 10; % areal band width, cm
rmax = 600; % maximum distance, cm, beyond which MOM supply is
negligible, defined as >= 0.001 of that at r=0 %
alphaadj = -0.002179; % adjustment of alpha to bring FsedC(rmax) at
background organic carbon accumulation values; set to 0 at first run
alpha = alphaadj + (-log(0.00001)/rmax) % exponential coefficient
needed to drive ratio of FsedC(rmax)/FsedC(r=0) to 0.001 %
s1 = 650; % major radius, cm, of the whale fall
s2 = 115; % minor radius, cm, of the whale fall

% Component 1: the density function, roefofr with distance, r, from the
perimeter of the fall

% Calculating the boundaries, cm, of the areal rings of width dr away
from the fall:
rint = [0:dr:rmax-dr  % minimum
    0+dr:dr:rmax % maximum
    (0+dr)/2:dr:rmax-(dr/2)]; % mid-point

roefofr_int_0tormax = (-1 / alpha) * exp(-rmax * alpha) - (-1 / alpha);
% the definite integral of the density function from r=0 cm to r=rmax
cm

% create density function distribution through the areal rings
counter = 1;
while counter <= rmax/dr % distance, cm, of the remaining areal bands
of width dr away from the fall
    roefofr_int_rtorplusdr(counter) = (-1 / alpha) * exp(-
rint(2,counter) * alpha) - (-1 / alpha) * exp(- rint(1,counter) *
alpha); % the definite integral of the dispersal kernel from r=0 cm to
r=rmax cm
    roefofr(counter) = roefofr_int_rtorplusdr(counter) /
roefofr_int_0tormax; % roefofr calculation
    counter = counter + 1;
end

% Component 2: the areal normalization factor, N (cm-2), with distance,
r (cm), from the perimeter of the fall

ring_area = pi * dr * (s1 + s2 + (2*rint(1,:)) + dr);
counter = 1;
while counter <= rmax/dr;
    Normfac(1,counter) = 1 / ring_area(1,counter); % cm-2
    counter = counter + 1;
end

% Calculation of the dispersal kernel, DK (cm-2), with distance, r
(cm), from the perimeter of the fall
```

```
counter = 1;
while counter <= rmax/dr;
    DKofr(1,counter) = Normfac(1,counter) * roefofr(1,counter); % cm-2
    counter = counter + 1;
end

% Conversion of FmatC from kg m-2 d-1 to mg cm-2 y-1

FmatCnew = FmatC * 3.65 * 10^8;

% Calculation of the settling rate, mg cm-2 y-1, of released material
with distance, r, from the perimeter of the fall
FsedC = FmatCnew * DKofr;
```

Appendix F

The wood fall fragmentation and dispersal modules, as implemented in MATLAB.

```
% FRAGMENTATION MODULE

% Model inputs
InitMwood = 120; % initial wood parcel mass, kg
WtCwood = 0.34; % Carbon content of wood (34 %)
DFC = 0.9; % proportion of ingested material which is defecated
dt = 1; % time step, d

% Model run set-up

counter = 1;
t(counter,1) = 0; % time, d

% Reservoirs

Mwood(counter,1) = InitMwood; % wood parcel mass, kg
WtWR(counter,1) = 0; % consumed mass, kg
Wtabs(counter,1) = 0; % consumed mass absorbed by the borer, kg
Wtfec(counter,1) = 0; % consumed mass defecated by the borer, kg
Wtrel(counter,1) = Wtfec(counter,1); % total mass released for
dispersal to sediments, kg

% Fluxes

FWR = 0.051; % released wood flux, kg d-1
Fabs(counter,1) = 0; % borer absorption flux, kg d-1
Fdef(counter,1) = 0; % borer defecation flux, kg d-1
Frel(counter,1) = 0; % total release flux, kg d-1

% Model run

counter = counter + 1;
t(counter,1) = t(counter-1,1) + dt; % time, d

while Mwood(counter-1,1) > 0; % if there is still consumeable carcass
mass

    Mwood(counter,1) = Mwood(counter-1,1) - FWR*dt; % new wood parcel
mass, kg
    WtWR(counter,1) = WtWR(counter-1,1) + FWR*dt; % new consumeded mass
at beginning of iteration, kg

    Fabs(counter,1) = WtWR(counter,1) * (1 - DFC); % new borer
absorption flux, kg d-1
```

```
    Fdef(counter,1) = WtWR(counter,1) * DFC; % new borer defecation
flux, kg d-1
    Frel(counter,1) = Fdef(counter,1); % new total release flux, kg d-1

    WtWR(counter,1) = WtWR(counter,1) - (Fabs(counter,1) +
Fdef(counter,1) ) * dt; % new consumed mass at end of iteration, kg
    Wtabs(counter,1) = Wtabs(counter-1,1) + (Fabs(counter,1) * dt); %
new consumed mass absorbed by the borer, kg
    Wtfec(counter,1) = Wtfec(counter-1,1) + (Fdef(counter,1) * dt); %
new consumed mass defecated by the borer, kg
    Wtrel(counter,1) = Wtfec(counter,1); % new total mass released for
dispersal to sediments, kg

    counter = counter + 1;
    t(counter,1) = t(counter-1,1) + dt; % time, d

end

t = t(1:size(t)-1,1); % eliminates the last time point, which is not
accompanied by model data
Fmat = Frel(round(max(counter) / 2),1); % Activate to include
defecation in release flux during wood parcel processing, kg d-1
FmatC = Fmat*WtCwood; % combined Carbon release flux during wood parcel
processing, kg d-1, using C content of 34 %
FmatN = FmatC*20/4860; % combined Nitrogen release flux during wood
parcel processing, kg d-1, using a N:C of 20/4860
FmatP = FmatC*1/4860; % combined Phosphate release flux during wood
parcel processing, kg d-1, using a P:C of 1/20

% DISPERSAL MODULE

% Calculating the dispersal kernel, DK (m-2)

% Model input

dr = 10; % areal band width, cm
rmax = 50; % maximum distance, cm, beyond which MOM supply is
negligible, defined as >= 0.001 of that at r=0 %
alphaadj = -0.0023; % adjustment of alpha to bring FsedC(rmax) at
background organic carbon accumulation values; set to 0 at first run
alpha = alphaadj + (-log(0.00001)/rmax) % exponential coefficient
needed to drive ratio of FsedC(rmax)/FsedC(r=0) to 0.001 %
lwood1 = 240; % length, cm, of the wood parcel
lwood2 = 45; % width, cm, of the wood parcel

% Component 1: the density function, roefofr with distance, r, from the
perimeter of the fall

% Calculating the boundaries, cm, of the areal rings of width dr away
from the fall:
rint = [0:dr:rmax-dr  % minimum
    0+dr:dr:rmax % maximum
    (0+dr)/2:dr:rmax-(dr/2)]; % mid-point
```

```
roefofr_int_0tormax = (-1 / alpha) * exp(-rmax * alpha) - (-1 / alpha);
% the definite integral of the density function from r=0 cm to r=rmax
cm

% create density function distribution through the areal rings
counter = 1;
while counter <= rmax/dr % distance, cm, of the remaining areal bands
of width dr away from the fall
    roefofr_int_rtorplusdr(counter) = (-1 / alpha) * exp(-
rint(2,counter) * alpha) - (-1 / alpha) * exp(- rint(1,counter) *
alpha); % the definite integral of the dispersal kernel from r=0 cm to
r=rmax cm
    roefofr(counter) = roefofr_int_rtorplusdr(counter) /
roefofr_int_0tormax; % roefofr calculation
    counter = counter + 1;
end

% Component 2: the areal normalization factor, N (cm-2), with distance,
r (cm), from the perimeter of the fall

ring_area = 2 * dr * ( lwood1 + lwood2 + (4*rint(1,:)) + (2*dr) );
counter = 1;
while counter <= rmax/dr;
    Normfac(1,counter) = 1 / ring_area(1,counter); % cm-2
    counter = counter + 1;
end

% Calculation of the dispersal kernel, DK (cm-2), with distance, r
(cm), from the perimeter of the fall

counter = 1;
while counter <= rmax/dr;
    DKofr(1,counter) = Normfac(1,counter) * roefofr(1,counter); % cm-2
    counter = counter + 1;
end

% Conversion of FmatC from kg m-2 d-1 to mg cm-2 y-1

FmatCnew = FmatC * 3.65 * 10^8;

% Calculation of the settling rate, mg cm-2 y-1, of released material
with distance, r, from the perimeter of the fall
Fsed = FmatCnew * DKofr;

Fsed(1,5)
```